TÉCNICO LISBOA

UNIVERSIDADE DE LISBOA

INSTITUTO SUPERIOR TÉCNICO

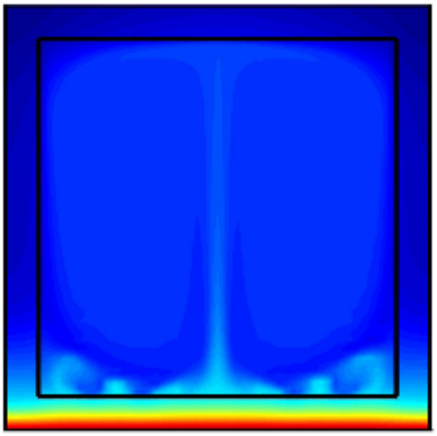

Numerical modelling of the thermomechanical behaviour of GFRP pultruded profiles subjected to fire

Cristina López Sánchez

Supervisor: Doctor Carlos Manuel Tiago Tavares Fernandes
Co-supervisor: Doctor João Pedro Ramôa Ribeiro Correia

Thesis approved in public session to obtain the PhD Degree in Civil Engineering

Jury final classification: Pass with Merit

Jury:

Chairperson: Chairman of the IST Scientific Board
Members of the committee: Doctor Paulo Jorge de Melo Matias Faria de Vila Real
Doctor Joaquim António Oliveira de Barros
Doctor Nuno Miguel Rosa Pereira Silvestre
Doctor João Pedro Ramôa Ribeiro Correia
Doctor Luís Rego da Cunha de Eça
Doctor Carlos Manuel Tiago Tavares Fernandes

2017

TÉCNICO LISBOA

UNIVERSIDADE DE LISBOA

INSTITUTO SUPERIOR TÉCNICO

Numerical modelling of the thermomechanical behaviour of GFRP pultruded profiles subjected to fire

Cristina López Sánchez

Supervisor: Doctor Carlos Manuel Tiago Tavares Fernandes
Co-supervisor: Doctor João Pedro Ramôa Ribeiro Correia

Thesis approved in public session to obtain the PhD Degree in Civil Engineering

Jury final classification: Pass with Merit

Jury:

Chairperson: Chairman of the IST Scientific Board

Members of the committee:

Doctor Paulo Jorge de Melo Matias Faria de Vila Real, *Professor Catedrático da Universidade de Aveiro*

Doctor Joaquim António Oliveira de Barros, *Professor Catedrático da Escola de Engenharia da Universidade de Minho*

Doctor Nuno Miguel Rosa Pereira Silvestre, *Professor Associado do Instituto Superior Técnico da Universidade de Lisboa*

Doctor João Pedro Ramôa Ribeiro Correia, *Professor Associado (com agregação) do Instituto Superior Técnico da Universidade de Lisboa*

Doctor Luís Rego da Cunha de Eça, *Professor Auxiliar (com agregação) do Instituto Superior Técnico da Universidade de Lisboa*

Doctor Carlos Manuel Tiago Tavares Fernandes, *Professor Auxiliar do Instituto Superior Técnico da Universidade de Lisboa*

Funding institutions:
FCT — Fundação para a Ciência e a Tecnologia
FIRE-FRP project: Fire Protection Systems for GFRP Pultruded Profiles
(PTCD/ECM/100779/2008)

2017

Abstract

The present thesis addresses the numerical modelling of the fire behaviour of pultruded glass fibre reinforced polymer (GFRP) profiles. An uncoupled finite element (FE) formulation is developed to evaluate the thermal (heat flux and temperature fields) and mechanical (generalized stresses, strains and displacements) behaviour of GFRP profiles (beams and columns) with generic cross section, for both protected and unprotected situations, subjected to fire.

An in-house software is developed in MATLAB comprising four nonlinear FE moduli: (i) heat transfer, (ii) non-isothermal fluid dynamics, (iii) mechanical, and (iv) thermomechanical. All codes are thoroughly verified using benchmark solutions available in the literature.

A coupled nonlinear two-dimensional FE model is developed to solve the system of equations derived from the conjugate heat transfer and fluid dynamics problems. The code considers the possible radiative heat exchanges between the faces of a cavity, as well as the natural convection, allowing to evaluate the temperature field in a GFRP cross section while the flow is laminar. A nonlinear one-dimensional FE code is developed to compute the mechanical response of the GFRP profiles. A geometrically exact beam theory is implemented by considering the Reissner–Simo kinematic assumptions, in order to avoid any restrictions on the magnitude of the displacements and rotations. The generalized displacement field is computed using a total Lagrangian scheme.

The ability of the code to evaluate the thermomechanical performance of GFRP profiles is assessed by simulating experimental tests on GFRP beams and columns with different cross sections, fire scenarios, fire protection systems and loading conditions. The thermal simulations showed that the model proposed is able to reproduce with reasonable accuracy the thermal response of the cross sections tested, highlighting the importance of considering simultaneously the radiative heat exchange between the faces of a cavity and the natural convection. However, the simulation of the natural convective flow showed that, at high temperatures, very reduced time steps are required to obtain a converged a solution. This fact increases strongly the CPU time, making the calculation of the complete thermal response not feasible in some of the cases studied.

Numerical simulations for profiles subjected to different fire scenarios were performed. In these applications, the thermal response of the profiles was simulated: in almost all cases, the model provided results for 60 minutes.

The mechanical behaviour of the GFRP beams was simulated with good accuracy by the thermomechanical model proposed. However, in most of the cases studied, the simulation of the mechanical behaviour of the GFRP columns was less accurate, probably due to the uncertainties in some GFRP material properties (namely, the compressive modulus and the thermal expansion coefficient) and the non consideration of creep effects.

Keywords: GFRP profiles, fire behaviour, fire protection systems, finite element formulation, heat radiation in a cavity, heat transfer FE code, fluid dynamics FE code, conjugate heat transfer FE code, geometrically exact beam theory, thermomechanical behaviour.

Resumo

Esta tese aborda a modelação numérica do comportamento ao fogo de perfis pultrudidos de polímero reforçado com fibras de vidro (GFRP). Foi utilizada uma formulação desacoplada de elementos finitos (EF) para avaliar a resposta térmica (distribuição de fluxos e temperaturas) e mecânica (tensões, deformações e deslocamentos generalizados) de elementos estruturais formados por perfis de GFRP (vigas e colunas) de secção genérica, com e sem protecção térmica e sujeitos à acção do fogo.

Com recurso ao programa MATLAB, foi desenvolvido um código que incorpora quatro módulos não lineares de EF: (i) transferência de calor, (ii) dinâmica de fluidos não isotérmicos, (iii) mecânico e (iv) termomecânico. Todos os módulos foram verificados com base em soluções de referência disponíveis na bibliografia.

Para resolver o sistema de equações não lineares resultante da combinação dos problemas de transferência de calor e de dinâmica de fluidos, foi desenvolvido um modelo bidimensional de EF. O código simula as trocas de calor por radiação entre as faces da cavidade dos perfis de GFRP e a convecção natural do ar, permitindo calcular a distribuição de temperaturas na secção transversal enquanto o comportamento do fluido se encontra em regime laminar. Relativamente à simulação da resposta mecânica dos perfis de GFRP, foi desenvolvido um modelo unidimensional não linear de EF, em que foi implementada a teoria de vigas geometricamente exacta, admitindo as hipóteses cinemáticas de Reissner–Simo (sem restrições à magnitude dos deslocamentos e rotações). O campo de deslocamentos foi calculado com recurso à formulação Lagrangiana total.

A capacidade do código desenvolvido em prever a resposta termomecânica de perfis de GFRP foi avaliada através da simulação de ensaios experimentais realizados em vigas e colunas com diferentes secções transversais e protecções ao fogo, e sujeitos a vários níveis de carga e condições de exposição térmica. Os resultados numéricos, além de reproduzirem com uma precisão razoável as distribuições de temperatura obtidas experimentalmente, evidenciaram a importância da consideração simultânea das trocas de calor por convecção e por radiação entre as faces das cavidades dos perfis. Contudo, estes resultados mostraram que quando são atingidas temperaturas elevadas na cavidade, são necessários incrementos de tempo muito reduzidos para obter convergência da solução. Este facto causa um forte incremento do tempo de cálculo, não sendo possível, em termos práticos, calcular a resposta térmica completa em alguns dos casos analisados.

Foram efectuadas simulações numéricas de perfis submetidos a diferentes exposições ao fogo. Nestas aplicações a resposta térmica dos perfis é obtida, em praticamente todos os casos, até aos 60 minutos.

O modelo termomecânico permitiu simular a resposta mecânica de vigas de GFRP com uma boa precisão. A simulação dos resultados mecânicos das colunas foi menos precisa, provavelmente devido à incerteza nos valores das propriedades mecânicas do material GFRP a temperaturas elevadas (nomeadamente, o módulo de elasticidade em compressão e o coeficiente de expansão térmica) e ao facto de os efeitos de fluência não terem sido considerados.

Palavras-chave: Perfis de GFRP, comportamento ao fogo, sistemas de protecção, programa de EF, radiação em cavidades, código de EF transferência de calor, código de EF de dinâmica de fluidos, código de EF transferência de calor sólido-fluido, teoria de vigas geometricamente exacta, comportamento termomecânico.

Acknowledgements

In developing and writing this thesis I had the assistance and help of many people that I would like to acknowledge.

First of all, I would like to thank Professor Carlos Tiago for his dedication to the work and guidance. His rigour and tireless search for improvement allowed the progression of the present project.

I would like to express my most sincere gratitude to Professor João Ramôa Correia, for his valuable advice, guidance and encouragement. He has substantially contributed to my professional and, mainly, personal development. I am greatly indebted to him for his constructive suggestions and his endless enthusiasm for the work. He made sense to the cite,

> *Não voltes atrás, pois é fraqueza desistir-se da cousa começada.*
> Os Lusíadas. Luís de Camões.

thus becoming a remarkable example to follow.

I would also like to thank João Pedro Firmo and Tiago Morgado for their valuable comments and assistance during the research.

In addition, I express my thanks to the Professors of the Department of Civil Engineering, Architecture and Georesources for their cordiality and hospitality.

Many thanks also go to my colleagues, office mates and friends — Mário Arruda, João Pedro Firmo, Francisco Nunes, João Sousa, Tiago Morgado, Luís Valarinho, Mário Garrido, José Sampaio, Pham Tien Cuong, José Gonilha, Mário Sá and Giovanni Chiumento — for creating a comfortable and propitious working environment and for being positive, amazing and friendly all the time.

I would like also to acknowledge the IST and the Civil Engineering, Architecture and Georesources Department for giving me the chance to pursue my PhD and FCT for funding the present research through the project PTDC/ECM/100779/2008.

In the same way, I would also like to express my gratitude to all the persons who made my staying in Lisbon so fantastic and have contributed during these years for my life experiences, which I will never forget. Among them, I would like to mention Pablo Garrido, Ana Melo, Marco Neves, Sophia Kalakou, Inês Macedo and David Rondán.

I would like to specially mention Diego Lisi, for his motivation and for understanding and respecting all my decisions during these years.

Most important, I would like to appreciate and thank my mother for her infinite support and unconditional love. I am particularly grateful for her advices, which were and will always be useful.

Finally, I would like to mention Pim Braspenning for his continuous support and pragmatic advices.

Contents

List of Figures

List of Tables

Notation, list of symbols and abbreviations

Notation

The direct notation is used to express the algebraic operations and the nature of the variables, as carried out by Tiago (2007). In specific cases, the matrix notation is also utilised.

Italic Latin or Greek lowercase letters (a, b,...α, β,...) denote scalar quantities, bold italic Latin or Greek lowercase letters ($\boldsymbol{a}$, $\boldsymbol{b}$,...$\boldsymbol{\alpha}$, $\boldsymbol{\beta}$,...) indicate vectors and bold italic Latin or Greek capital letters ($\boldsymbol{A}$, $\boldsymbol{B}$,...$\boldsymbol{\Omega}$, $\boldsymbol{\Theta}$,...) represent second order tensors. Furthermore, they also represent the skew-symmetric second order tensors, while the associated axial vector are denote by ($\boldsymbol{a}$, $\boldsymbol{b}$,...$\boldsymbol{\omega}$, $\boldsymbol{\theta}$,...).

For implementation purposes, the unknown vectors resulting after replacing the spatial discretization are represented by bold Latin or Greek lowercase letters ($\mathbf{a}$, $\mathbf{b}$,...$\boldsymbol{\alpha}$, $\boldsymbol{\beta}$,...) and the resulting matrices are denoted by bold Latin or Greek capital letters ($\mathbf{A}$, $\mathbf{B}$,...$\boldsymbol{\Omega}$, $\boldsymbol{\Theta}$,...).

The indicial notation, where summation convention over repeated indices is implied, is adopted. The italic Greek indices range from 1 to 2 and italic Latin subscripts from 1 to 3.

Punctual notation conflicts exist along the text. Most of them are duly pointed out and the remaining should be easily understood from the context.

The applications and examples presented are in a coherent system of units, even if this system is not always specified.

Regarding the derivatives, the comma notation is occasionally used where, for example, $(\cdot)_{,i} = \partial(\cdot)/\partial x_i$. The derivatives of a variable with respect to time are represented by $\dot{(\cdot)}$ and, finally, the notation $(\cdot)' = \partial(\cdot)/\partial\zeta$ is employed to define derivatives with respect to ζ.

Furthermore, the following sets, operators and operations are defined:

Sets	
$\mathbb{R}$	Real number
$\cup$	Set union
$\cap$	Set intersection
$\emptyset$	Empty set
$\in$	Belongs to
$\subset$	Is a subset of
$\forall$	For all

Operators

$\delta(\cdot)$	Variation of, virtual quantity, iterative quantity
$\Delta(\cdot)$	Incremental perturbation
$\dot{(\cdot)}$	Time variation
$\boldsymbol{\nabla}(\cdot)$	Gradient of, differential operator
$\|(\cdot)\|$	Norm of
axial$(\cdot)$	Axial vector of skew-symmetric second order tensor
div $(\cdot)$	Divergence of
tr$(\cdot)$	Trace operator of
$\Delta^2(\cdot)$	Laplace operator

Operations

$\cdot$	Internal product of vectors
$\times$	Vectorial product of vectors
:	Scalar product between second order tensors

Finite element formulation

$\mathbf{A}$	Assembly operator
(e)	Generic element e

List of symbols

Roman letters

Symbol	Description
A	Pre-exponential factor, cross section area
A^*	Reduced cross section area
c_p	Specific heat capacity
c_{pc}	Specific heat capacity of the char material
c_{pf}	Specific heat capacity of the fibres
c_{pg}	Specific heat capacity of the gas
c_{pm}	Specific heat capacity of the matrix
c_{pv}	Specific heat capacity of the virgin material
d	Distance between the points of two surfaces that exchange radiative heat flux in a three-dimensional space
E	Activation energy, Young's modulus
E_f	Young's modulus of the fibres
E_m	Young's Modulus of the matrix
F	Fraction of virgin material computed using densities ($\frac{\rho-\rho_c}{\rho_v-\rho_c}$), shape factor
$\overline{F}_i$	Prescribed loads in the i-direction
f_c	Mass fraction of char material (m_c/m)
f_v	Mass fraction of virgin material (m_v/m)
G	Heat flux generation, shear modulus
Gr	Grashof number
h	Enthalpy of the composite, convective heat transfer coefficient, cross section height
h_g	Enthalpy of the gas

I	Second order area moment of the cross section
k	Thermal conductivity
k^*	Constant describing the breadth of the distribution
k_c	Thermal conductivity of the char material
k_f	Thermal conductivity of the fibres
k_m	Thermal conductivity of the matrix
k_v	Thermal conductivity of the virgin material
L	Length
L_0	Initial length
M	Internal moment
$\overline{M}$	Prescribed moment
m	Mass of the composite, number of nodes where the pressure is approximated
m_c	Mass of the char material
m_v	Mass of the virgin material
$\overline{m}$	Prescribed distributed moment
$\dot{m}_g$	Mass flux of the pyrolysis gas
n	Number of nodes where the velocity/temperature are approximated, outward normal to the cross-section of the beam
n_G	Gauss points number
N	Internal axial force
Nu	Nusselt number
P	Generic mechanical property, applied concentrated load
P_R	Residual generic mechanical property value at high temperature
P_U	Generic mechanical property value at ambient temperature
Pr	Prandtl number
p	Pressure divided by the density, polynomial degree
$\overline{p}_i$	Prescribed distributed loads in the i-direction
$\tilde{p}$	Absolute pressure
$\tilde{p}_r$	Relative pressure
$\tilde{p}_s$	Hydrostatic pressure
Q_p	Heat of decomposition
q_i	Heat flux in the i direction
$\overline{q}$	Normal prescribed heat flux
q_h	Convective heat flux
q_r	Radiative heat flux
q_R	Radiative heat flux in a generic surface
R	Universal gas constant, radiosity variable
R^n	Power law factor related to the residual resin content
Ra	Rayleigh number
Re	Reynolds number
r	Distance between the points of two faces that exchange radiative heat flux in a two-dimensional space
S	First order area moment of the cross section
S_R^e	Gray-diffusive surface e
t	Time and traction on a boundary
U	Energy, characteristic flow velocity
$\widehat{U}$	Exact energy of the solution
u_i	Displacements in the i-direction

$\overline{u}_i$	Prescribed displacements in the i-direction
V	Volume of the composite, internal shear force
V_f	Relative volume of the fibres
V_m	Relative volume of the matrix
W_{ext}	External virtual work
W_{int}	Internal virtual work
x_i	Spatial coordinate

Greek symbols

Symbol	Description
α	Thermal expansion coefficient of solids, thermal diffusivity
α_c	Thermal expansion of the char material
α_v	Pyrolysis expansion factor
α^e	Angle between the surface normal and the joining line of two points
β	Thermal expansion of fluids
β^e	Angle between the face normal and the joining line of two points
Γ	Boundary
$\Gamma_{\overline{q}}$	Prescribed heat flux boundary
Γ_h	Convective heat transfer boundary
Γ_R	Radiosity heat transfer boundary
Γ_r	Radiative heat transfer boundary
Γ_t	Prescribed traction boundary
Γ_v	Prescribed velocity boundary
Γ_θ	Prescribed temperature boundary
Γ_t	Static boundary
Γ_d	Kinematic boundary
γ	Angular distortion of the points laid in the axis bar
$\tilde{\gamma}$	Angular distortion at any point of the cross section
$\gamma^{\Delta\theta}$	Angular distortion due to the temperature gradient
ΔL	Length variation
$\Delta\eta$	Length variation
$\Delta\theta$	Temperature gradient
$\Delta\theta_L$	Linear temperature gradient
$\Delta\theta_U$	Uniform temperature gradient
ϵ	Emissivity, axial deformation at any point of the cross section
$\epsilon^{\Delta\theta}$	Axial deformation due to the temperature gradient
ε	Axial deformation of the points laid in the axis bar
ζ	Arc-length parameter
θ	Temperature, rotation
$\overline{\theta}$	Prescribed temperature, prescribed rotation
θ_a	Ambient temperature
θ_{cr}	Critical temperature
θ_g	Glass transition temperature
$\theta_{g,mech}$	Mechanically observed glass transition temperature
θ_U	Room temperature
κ	Curvature of the points laid in the axis bar, shear correction factor

λ	Load parameter
μ	Fluid viscosity
ν	Poisson modulus, kinematic viscosity
ν_f	Poisson modulus of the fibres
ν_m	Poisson modulus of the matrix
ξ	Natural coordinate, perpendicular distance between the point and the bar axis
ρ	Density
ρ_c	Density of the char material
ρ_v	Density of the virgin material
σ	Stefan–Boltzmann's constant, normal stress
τ	Tangential stress
τ_{SUPG}	Constant SUPG method
φ	Stream function
χ	Curvature in the planar problem
Ω	Domain
$\overline{\Omega}$	Closure domain

Tensors

Symbol	Description
$\boldsymbol{a}$	Position of the points of the cross section
$\boldsymbol{a}^r$	Relative position with respect to the axis of a point located in an arbitrary cross section
$\boldsymbol{b}$	Body force
$\boldsymbol{D}$	Conductivity tensor, constitutive matrix
$\boldsymbol{d}$	Distance tensor, generalized displacement field of a point laid in the axis bar
$\boldsymbol{e}_i$	Orthonormal base vectors coordinate system in the deformed configuration
$\boldsymbol{e}_i^r$	Orthonormal base vectors coordinate system in the reference configuration
$\boldsymbol{F}$	Deformation gradient
$\boldsymbol{F}^r$	Deformation gradient in the reference position
$\boldsymbol{f}$	Load tensor
$\boldsymbol{f}_B$	Buoyancy force
$\boldsymbol{g}$	Gravity force
$\boldsymbol{m}$	Moment resultant
$\boldsymbol{m}^r$	Moment resultant in the reference position
$\boldsymbol{n}$	Normal vector, stress resultant
$\boldsymbol{n}^r$	Stress resultant in the reference configuration
$\boldsymbol{P}$	First Piola–Kirchhoff stress tensor
$\boldsymbol{P}^r$	Back-rotated first Piola–Kirchhoff stress tensor
$\boldsymbol{Q}$	Rotation tensor
$\boldsymbol{q}$	Heat flux vector
$\boldsymbol{r}$	Distance, two-dimensional vector
$\boldsymbol{t}$	Traction tensor
$\boldsymbol{u}$	Position of any point of the cross section after the deformation
$\boldsymbol{v}$	Velocity tensor
$\boldsymbol{x}$	Displacement vector of the points lying on the beam axis
$\boldsymbol{z}$	Position of any point laid on the rod axis
$\boldsymbol{\gamma}$	Total deformation tensor

$\boldsymbol{\gamma}^r$	Total deformation tensor in the reference position
$\boldsymbol{\delta}$	Displacement field at a generic point
$\boldsymbol{\varepsilon}$	Deformation tensor
ε^r	Cross sectional generalized strains in the reference configuration
$\boldsymbol{\zeta}$	Position of the points situated in the axis bar
$\boldsymbol{\eta}$	Deformation tensor in the mechanical problem
$\boldsymbol{\eta}^r$	Deformation tensor in the mechanical problem (in the reference position)
$\boldsymbol{\kappa}$	Curvature
$\boldsymbol{\kappa}^r$	Curvature in the reference position
$\boldsymbol{\xi}$	Position of any point of the cross section
$\boldsymbol{\sigma}$	Cauchy stress tensor
$\boldsymbol{\sigma}^r$	Back-rotated cross sectional generalized stress resultants
$\boldsymbol{\tau}$	Viscous stress tensor
$\boldsymbol{\tau}_i$	Stress tensor

Vectors and matrices

Symbol	Description
$\mathbf{B}$	Matrix that gathers the differentiate shape functions
$\mathbf{B}_\theta$	Matrix that gathers the differentiate temperature shape functions
$\mathbf{C}$	Convection matrix
$\mathbf{d}$	Nodal generalized displacement vector
$\mathbf{f}$	Nodal equivalent heat flux vector
$\mathbf{f}_R$	Nodal radiative heat flux between the faces of the element
$\mathbf{f}_v$	Force vector
$\mathbf{g}$	Heat generation nodal vector
$\mathbf{G}$	Discrete gradient operator of the pressure
$\mathbf{G}^T$	Discrete divergence operator
$\mathbf{K}$	Conductivity matrix, tangential stiffness matrix
$\mathbf{K}_R$	Radiosity matrix
$\mathbf{K}_g$	Geometric term of the tangential stiffness matrix
$\mathbf{K}_m$	Material term of the tangential stiffness matrix
$\mathbf{K}_v$	Viscosity matrix
$\mathbf{M}$	Capacitance matrix
$\mathbf{M}_v$	Standard finite element mass matrix
$\overline{\mathbf{q}}$	Prescribed heat flux nodal vector
$\mathbf{R}$	Radiosity nodal vector
$\mathbf{r}$	Residual vector
$\mathbf{r}_{ext}$	External residual vector
$\mathbf{r}_{int}$	Internal residual vector
$\overline{\boldsymbol{v}}$	Prescribed velocity vector
$\boldsymbol{\theta}$	Nodal temperature vector
$\boldsymbol{\Phi}$	Shape functions of the mechanical problem
$\boldsymbol{\psi}$	Generic matrix of approximation functions
$\boldsymbol{\psi}_p$	Approximation functions of pressure
$\boldsymbol{\psi}_R$	Approximation functions of radiosity
$\boldsymbol{\psi}_v$	Approximation functions of velocity
$\boldsymbol{\psi}_\theta$	Approximation functions of temperature

Abbreviations

ACI	American Concrete Institute
ADINA	Automatic Dynamic Incremental Nonlinear Analysis (commercial software)
ATD	Apparent Thermal Diffusivity model
ASCE	American Society of Civil Engineers
CFD	Computational Fluid Dynamics
CFRP	Carbon Fibre-Reinforced Polymer
CS	Calcium Silicate
DMA	Dynamic Mechanical Analysis
DSC	Differential Scanning Calorimetry tests
FCT	Fundação para a Ciência e a Tecnologia
FDM	Finite Difference Method
FEM	Finite Element Method
FRP	Fibre Reinforced Polymer
FVM	Finite Volume Method
GEBT	Geometrically Exact Beam Theory
GFRP	Glass Fibre Reinforced Polymer
GLS	Galerkin/Least-Squares
HRR	Heat Release Rate
IABSE	International Association for Bridge and Structural Engineering
ICIST	Instituto de Engenharia de Estruturas, Território e Construção
IIFC	International Institute for FRP in Construction
INEGI	Instituto de Engenharia Mecânica e Gestão Industrial
ISO	International Standards Organization
IST	Instituto Superior Técnico
LBB	Ladyzhenskaya-Babŭska-Brezzi condition
LS	Least-Squares
MATLAB	MATrix LABoratory (commercial software)
PHRR	Peak Heat Release Rate
SGS	Subgrid Scale Method
SUPG	Streamline Upwind/Petrov-Galerkin method
TBT	Timoshenko Beam Theory
TGA	Thermogravimetric Analysis

Chapter 1

Introduction

1.1 Context

The increasing high performance requirements of most recent civil engineering structures motivates the use of new materials, whose behaviour during the structural lifespan conditions has to be studied in depth. Among these materials, glass fibre reinforced polymer (GFRP) profiles are starting to be used relatively often in civil construction as they offer several advantages when compared to traditional materials, namely in what concerns strength, self-weight, insulation properties, maintenance and durability. Although they also offer competitive life-cycle costs, their use is still restricted due to well-founded concerns about their fire behaviour. This issue is yet to be addressed in a comprehensive manner and has hampered the widespread use of GFRP profiles in buildings, where construction elements must have adequate fire reaction behaviour and sufficient fire resistance.

The mechanical performance of GFRP composites decreases when they are exposed to high temperatures, mainly due to the decomposition of the organic matrix. When heated to temperatures ranging between 100-200 °C, these composites start to soften, creep and distort, suffering considerable strength and stiffness reductions due to the glass transition of the resin. Subsequently, at around 300-500 °C, the organic matrix decomposes, releasing heat, smoke, soot and toxic volatiles. These fire reaction properties of GFRP (a flammable material) may prevent their use for certain applications and conditions. However, fibre reinforced polymer (FRP) materials also present some advantages under fire conditions, *e.g.*, low thermal conductivity (composites are very good heat insulators) and reasonable burn-through resistance, providing an effective barrier against flame, heat, smoke and toxic gases (Dodds *et al.*, 2000).

Fire reaction experiments (Brown and Mathys, 1997, Scudamore, 1994, Burchill *et al.*, 2005, Mouritz *et al.*, 2006) enable a reasonable level of understanding of the fire reaction properties of most common FRPs and show that both commercial flame retardants and phenolic resins allow most flammability requirements to be fulfilled (Troitzsch, 1983, Lu and Hamerton, 2002). However, even if changing the matrix formulation allows overcoming fire reaction restrictions, in terms of fire resistance this approach does not allow achieving the performance typically required for primary structural building elements in terms of fire endurance (60-90 min). In fact, most flame retardants cause considerable reductions in the mechanical properties of FRPs; similarly, the FRPs produced with phenolic resins usually have lower resistance than those made of standard polyester or vinylester resins. It was also shown that the thermal insulation and post-fire mechanical properties of phenolic and polyester composites exposed to fire are similar (Dodds *et al.*, 2000, Mouritz and Mathys,

2001, Mouritz, 2002, 2003). In order to enable the use of composites in civil engineering applications, the development of fire protection systems seems to be necessary to improve their fire resistance. These fire protection systems can be classified as (i) passive (*e.g.* calcium silicate boards or vermiculite/perlite cement based mortar) and (ii) active (*e.g.* internal water cooling or sprinklers).

In what concerns passive protection, it has been proved that the use of intumescent coatings/mats and ceramic mats improve the fire reaction properties of FRPs (Davies and Dewhurst, 1999, Keller *et al.*, 2005), namely regarding the post-fire mechanical performance (Mouritz and Mathys, 2001, Mouritz, 2002, 2003). Sorathia *et al.* (1993) measured significant improvements of the flexural strength retention and temperature profiles of FRP laminates protected with a wide range of fire barrier treatments (ceramic fabric, ceramic coating, different intumescent coatings, a hybrid of ceramic and intumescent coating, silicone foam and a phenolic sacrificial layer). An active protection system consisting of internal water cooling has been successfully tested with FRP tubes (Davies and Dewhurst, 1999). In the particular case of GFRP profiles, experimental campaigns were performed by Tracy (2005) and Correia *et al.* (2010a,b, 2013b), indicating that passive and active fire protection systems enable the considerable improvement of the fire reaction and fire resistance behaviour of GFRP profiles. In these previous experiments, the water cooling system was the most effective fire protection solution. However, since it is only applicable to tubular shapes, the development of alternative protection systems for other structural cross sections is necessary.

The structural response of an element/component subjected to fire has been traditionally assessed through specific fire tests, which, in general, are costly and unable to predict the behaviour of the component when subjected to other fire scenarios (*e.g.* Kim *et al.*, 2008). In this context, the availability of mathematical models able to simulate the performance of generic GFRP members under different fire situations is of paramount importance.

The burning process of materials in general and of FRP composites in particular is complex and involves chemical and physical changes. Heat transfer and fluid dynamic theories are of fundamental importance as they allow evaluating the fire effect in the structures and the calculation of temperatures and heat flux distributions in the constructive elements. In order to numerically solve the differential equations deriving from the aforementioned problems, the finite element method (FEM) constitutes an adequate tool due to the following reasons:

- It is a powerful method for determining approximate (and accurate) solutions to a large class of engineering problems, as for example, heat transfer, structural or flow dynamics problems;
- it is applicable to problems with irregular or arbitrary geometries;
- once the boundary conditions and the finite element (FE) mesh are correctly defined, it is relatively easy to implement; and
- it is simple to couple the thermal and mechanical behaviour of the profiles, calculating the transversal thermal response (using a two-dimensional model representing the cross-section) and a longitudinal mechanical behaviour (adopting a one-dimensional model).

In recent studies, mathematical models started to be developed in order to reproduce the experimental results of fire resistance tests of structures with FRP components, *e.g.*, Keller *et al.* (2006c) and Nigro *et al.* (2011). In the same way, this thesis addresses the study of the fire behaviour of GFRP profiles under fire exposure by developing an in-house FE code that allows computing the thermomechanical behaviour of unprotected and protected GFRP elements subjected to different fire exposures. Furthermore, the numerical results obtained allow a deeper understanding of the heat transfer process in GFRP cross sections.

1.2 Motivation and aims

As mentioned in the previous section, the widespread use of GFRP profiles in buildings is still restricted due to their fire performance. Flame retardants and phenolic resins were seen to induce significant improvements on the GFRP fire reaction properties, despite reducing their fire resistance. The few studies addressing this subject suggest that adequate fire protection systems need to be developed to allow the structural use of GFRP profiles in buildings (Correia *et al.*, 2015).

The effectiveness of both passive and active fire protection systems, nowadays well established for steel structures, needs also to be evaluated to assess the structural use of GFRP profiles in buildings. Based on this purpose, mathematical models able to predict the thermal and mechanical behaviour of FRP structures need to be developed. Nowadays, the FEM is one of the most used numerical tools to compute the mechanical behaviour of structures and it was already used to evaluate the thermomechanical behaviour of composites. In fact, several commercial software packages are available and are suitable to develop FE models. However, for the problem studied in this thesis, which involves different subjects (heat transfer, fluid dynamics and mechanical theories), only three-dimensional FE models can be developed using commercial software. These models are complex and their use presents the following disadvantages:

- The generation of compatible meshes can be laborious and difficult in the presence of complex geometries;
- models that couple fluid dynamics, heat transfer and solid mechanics entail the definition of boundary conditions of different origins;
- complex simulations involve the development of models with wide disparity in length and time scales; and
- three-dimensional mechanical models do not directly return engineering quantities required to structural design, *i.e.*, axial forces, shear forces and moments.

The main target of this thesis is to develop a special-purpose FE code to carefully assess the thermomechanical behaviour of GFRP profiles (with arbitrary cross sections) subjected to fire, avoiding the difficulties previously mentioned.

In this context, the following objectives are defined for this thesis: (i) the development of a FE code that allows simulating the thermal and structural behaviour of generic GFRP beams and columns subjected to mechanical loads and fire exposure, considering the non-linear and temperature-dependent thermophysical and mechanical properties of the GFRP and fire protection materials, (ii) to numerically simulate the experiments developed within

the *Fundação para a Ciência e a Tecnologia* (FCT) funded research project *FIRE-FRP — Fire Protection Systems for GFRP Pultruded Profiles* (PTDC/ECM/100779/2008), using the experimental data available regarding the thermophysical and mechanical properties of the GFRP composite, and (iii) to assess the applicability of the FE code developed in simulating the complete thermal response of tubular and I-profiles subjected to fire exposures different than those tested.

1.3 Methodology

1.3.1 Preliminary comments

As mentioned, this thesis was developed in the frame of the FCT-funded research project *FIRE-FRP*, which comprises experimental and numerical investigations regarding the fire performance of pultruded GFRP profiles. This section first presents a brief description of the experimental programme and then describes in more detail the methodology used for the mathematical modelling, the object of this thesis. Further information regarding the experimental programme can be consulted in the following project reports: Gomes *et al.* (2011, 2012c,b,a), Correia *et al.* (2013a) and Morgado *et al.* (2013d,c,b,a).

1.3.2 Experimental programme

The experimental programme centres on the study of the fire behaviour of protected and unprotected GFRP profiles and includes the following tests: (i) dynamic mechanical analysis, thermogravimetric and differential scanning calorimetry tests, to evaluate the thermophysical and thermomechanical properties of GFRP and fire protection materials, (ii) mechanical tests (tension, compression and shear loading) on GFRP laminates at varying temperatures, in order to estimate the temperature-dependent material stiffness and strength, (iii) fire reaction tests on GFRP profiles, and (iv) full-scale fire resistance tests on loaded GFRP beams and columns.

The first objective of the experimental campaign was to evaluate the thermophysical and thermomechanical properties of both GFRP and different fire protection materials, namely: the glass transition temperature (θ_g), the GFRP temperature-dependent stiffness, the polymeric matrix temperature of decomposition, the density, the thermal conductivity and the specific heat capacity (the last three properties as a function of temperature).

In order to obtain the aforementioned properties, the following tests were performed:

1. Dynamic mechanical analysis (DMA): the results of these tests allow obtaining the θ_g of the resin and the temperature-dependent stiffness relationship, following the process of degradation of both the polymeric matrix and the fibre-matrix adhesion.

2. Thermogravimetric analysis (TGA) and differential scanning calorimetry tests (DSC): the objective of these tests is to evaluate the mass and enthalpy changes in the materials as a function of temperature and the kinetic parameters describing the reactions taking place in both the GFRP and the fire protection materials.

The second objective of the experimental programme was to provide the temperature-dependent mechanical properties of the GFRP material in tension, compression and shear at elevated temperatures. Small-scale tests have been carried out on GFRP laminates according to the following procedure: (i) the specimens were heated uniformly until they

reached a constant target temperature (ambient temperature, 60, 90, 120, 150, 200 and 220/250 °C) and, subsequently, (ii) a mechanical load was applied until failure. The load-deformation curves and maximum loads were measured for the different temperatures and types of loading (tension, compression and shear), providing the temperature and loading dependent stiffness and strength curves.

Fire reaction tests were also performed at *Instituto de Engenharia Mecânica e Gestão Industrial* (INEGI) to evaluate the fire reaction properties of GFRP profiles made of polyester resin, either unprotected or protected with different fire protection materials. This task is not detailed as the results obtained are not relevant for the modelling of the fire resistance behaviour of GFRP beams and columns.

Finally, full-scale fire resistance tests were carried out at *Instituto Superior Técnico* (IST) in the framework of the PhD thesis of Tiago Morgado (in course) to evaluate the fire resistance properties of GFRP beams and columns, both unprotected and protected with different passive and active systems. Two different cross-sections with similar principal inertia moments were tested: square tubular section and I-section. In these tests the efficacy of the different fire protection systems was studied in terms of temperature distributions and mechanical responses of the GFRP members.

The tests were carried out using an intermediate-scale furnace with 6 gas burners controlled by a computer and 3 internal thermocouples to record the air temperatures.

The temperature profiles and the evolution of midspan deflections, as well as the fire resistances of loaded GFRP beams and columns submitted to fire were assessed. In the columns tests, the axial elongation was also measured. These results were used to evaluate the accuracy of the mathematical model in the simulation of the experimental data. Tables 1.1 and 1.2 summarize the fire resistance tests carried out in GFRP beams and columns, respectively.

The passive fire protection materials used in the beams were applied either in the bottom surface (one-surface fire exposure) or in the bottom and lateral faces (three-surfaces fire exposure) of the GFRP profiles. The materials used in the protection systems were: agglomerated cork, rockwool, calcium silicate (CS) boards and intumescent (INT) mats and coatings. The active fire protection system consisted of filling the cavity of the tubular GFRP pultruded profile with circulating water.

In the case of the GFRP columns, one-surface and three-surfaces fire exposure conditions have also been tested. The passive protection system comprised only CS boards, while the active protection system consisted of filling the cavity of the tubular GFRP pultruded profile with water, either stagnant or flowing (strictly, only the latter system is active), which are identified in table 1.2 as (s) and (f), respectively.

For both GFRP beams and columns, two different load levels were considered causing midspan deflections in the beams of $L/400$ and $L/250$ (L being the beam span) or axial deflections in the columns of $L/1500$ and $L/750$ (L being the column length).

1.3.3 Thermomechanical modelling

The first objective of the thesis is the elaboration of a thermomechanical model to compute the thermal and mechanical behaviour of GFRP beams and columns subjected to fire. This task comprised, mainly, the following four stages of development:

1. Thermal two-dimensional FE model to compute the temperature and flux fields in the cross section of a beam or column (conjugate heat transfer problem).

Cross section	Experimental series	Fire exposure	Fire protection	Load level
Square tubular section	S1	1-face	Unprotected	—
			Unprotected	11.7 kN ($L/400$)
			Cork	
			Rockwool	
			CS	
			INT	
			INT	
			Water cooling	
	S2	3-faces	Unprotected	—
			Unprotected	11.7 kN ($L/400$)
			CS	
			Water cooling	
	S3	1-face	Unprotected	18.7 kN ($L/250$)
			CS	
I-section	I1	1-face	Unprotected	7.4 kN ($L/400$)
			CS	
	I2	3-faces	Unprotected	7.4 kN ($L/400$)
			CS	
	I3	1-face	Unprotected	11.7 kN ($L/250$)
			CS	

Table 1.1: Experimental campaign for GFRP beams.

2. Mechanical one-dimensional FE model to simulate the generalized displacement field of a beam or column and the associated generalized stresses.

3. An uncoupled thermomechanical FE code.

4. A final unique code that allows performing the above mentioned different analyses.

All the codes are implemented in MATLAB (2012) using double-precision floating point in the calculations.

In the first stage, a two-dimensional thermal model was implemented by developing the following three numerical codes: (i) FE heat transfer code, (ii) fluid dynamics FE code for non-isothermal fluids, and (iii) coupled heat transfer/fluid dynamics FE code (conjugate heat transfer problem).

The heat transfer FE code allows computing the temperature and heat flux fields. The thermophysical properties of the material (thermal conductivity, density, specific heat capacity and emissivity) and the convective heat coefficient can either be considered as temperature-dependent or not. The following boundary conditions can be imposed: prescribed temperature, prescribed heat flux and convective and radiative heat flux; the last three items can coexist in the same boundary. The code allows performing both steady state and transient analyses.

Cross section	Experimental series	Fire exposure	Fire protection	Load level
Square tubular section	S1	1-face	Unprotected CS Water cooling (s) Water cooling (f)	55 kN (L/1500)
	S2	3-faces	Unprotected CS Water cooling (s) Water cooling (f)	55 kN (L/1500)
	S3	1-face	Unprotected CS	110 kN (L/750)
I-section	I1	1-face	Unprotected CS	25 kN (L/1500)
	I2	3-faces	Unprotected CS	25 kN (L/1500)
	I3	1-face	Unprotected CS	50 kN (L/750)

Table 1.2: Experimental campaign for GFRP columns.

The GFRP cross section to be analysed is either tubular or I-shaped. In both cases the computation of the radiative heat flux exchange between the walls of the cavity is required. This type of heat transfer is only not relevant in unprotected I-shaped profiles subjected to fire in three-surfaces.

The cross section cavity highlights the influence of the enclosed air on the temperature field of the GFRP material. Therefore, a fluid dynamics FE code was developed, considering that the fluid is viscous, incompressible and non-isothermal. The physical properties of the fluid (viscosity and density) were assumed as constant and, in order to artificially introduce the changes in the fluid density due to the temperature, the Boussinesq approximation was included. The thermal properties of the fluid were also set as constant. Furthermore, the Streamline Upwind/Petrov–Galerkin (SUPG) method was implemented to avoid possible instabilities in the temperature and velocity fields due to the convection.

The final thermal model is constituted by a combination of the two FE codes previously defined, where the resulting system of equations is obtained adopting a coupled scheme and is solved using the Newton–Raphson method.

In a second stage, a one-dimensional FE code to compute the mechanical behaviour of the beams and columns subjected to mechanical loads and fire exposure was implemented, according to the following steps: (i) the implementation of a FE code considering the geometrically exact beam theory and the Reissner–Simo kinematic assumptions, and (ii) the inclusion of the effect of the temperature in the previous code. The mechanical properties of the GFRP material are considered nonlinear and temperature-dependent. The code developed allows computing the displacement, stress and strain generalized fields.

In a third stage, once the temperature field and the beam/column behaviour were defined, the thermomechanical model was implemented using an uncoupled scheme where, for each time step, the temperature and the displacement field are computed. In a first

step, the temperature profile in the cross section is obtained using the thermal model and in a second step, the mechanical code computes the displacement field at the current time step using the temperatures previously computed. Furthermore, because several analyses may be performed using the same cross section (namely, for varying beam/column lengths), a second option was implemented. In this second case, the temperature field is first computed for all time steps and stored in a worksheet data-file and, subsequently, the displacement field is computed for all the time steps, using as input the temperature fields from the mentioned data-file generated.

In a fourth and final stage, a unique FE code was assembled allowing to perform the following analyses:

- Two-dimensional steady state and transient heat transfer analyses in plane elements, taking into account the thermophysical properties of the materials (GFRP and fire protection), considered to be either constant or temperature-dependent;
- two-dimensional fluid dynamic analyses in steady state and transient regime, whether accounting or not for the advection-diffusion in a fluid;
- two-dimensional heat transfer/fluid dynamic analyses;
- one-dimensional mechanical analyses, considering mechanical loads and temperature gradients; and
- uncoupled thermomechanical analyses.

The second objective of the thesis is the application of the model proposed to reproduce the thermal and mechanical response of the GFRP beams and columns tested in the laboratory by Morgado *et al.* (2013b,a) and described in section 1.3.2. In order to carry out this task, the following steps were defined:

1. Definition of the thermophysical properties of the GFRP and CS materials. The variation of the density of the GFRP with temperature is estimated using the data obtained from the experimental programme (TGA tests), while the thermal properties of the GFRP were computed using different mathematical models available in the literature. The thermophysical properties of the CS were provided by the manufacturer.
2. Evaluation of the mechanical properties of the GFRP as a function of temperature, using the experimental tests defined in the project.
3. Definition of the boundary conditions and characteristics of the model. In what concerns the boundary conditions, to simulate the fire exposure of a given surface and the heat exchange between the surface and the surrounding environment, three possibilities were considered: (i) prescribed temperature, (ii) convective and radiative heat flux and (iii) adiabatic. Regarding the simulation of the heat transfer in the cavity, four scenarios were simulated: (i) the cavity is insulated, (ii) there is radiative heat exchange between the cavity walls, (iii) there is convective natural convection due to the presence of air in the cavity, and (iv) natural convective heat transfer and exchange of radiative heat flux coexist in the cavity.
4. Validation of the final model by comparing the numerical results obtained with the experimental ones.

5. Numerical simulations of the beams and columns tested and comparison between the numerical and experimental temperature and displacement fields.

The third objective of the thesis consists of assessing the applicability of the model to reproduce the complete thermal response of GFRP profiles subjected to fire exposures different from those used in the experimental programme of the FIRE-FRP project. These applications were set by considering possible fire scenarios during the service life of a GFRP profile. Fire durations of 30 min or 60 min were set as goals, as these correspond to particular fire resistance ratings defined in building codes.

1.4 Thesis outline

The present document is organized in eight chapters, whose content is briefly summarized as follows.

Chapter 1 corresponds to the introduction of the thesis, describing its context, motivation, aims and methodology.

Chapter 2 provides an overview about composite materials, addressing their evolution and applications in engineering, with special attention being given to GFRP composites. The combustion process and the development of a fire are also briefly introduced. Subsequently, a brief state of the art review about the fire performance of composites is presented, divided in two parts: (i) the fire behaviour of GFRP laminates, and (ii) the fire behaviour of GFRP structural elements (beams, columns and slabs), including the numerical modelling of such behaviour.

Chapter 3 describes a transient nonlinear finite element formulation to evaluate heat transfer problems. It includes the computation of prescribed, convective and radiative heat fluxes. A coupled formulation using the radiosity equation is also introduced to compute the radiative heat flux exchange in enclosures.

Chapter 4 presents a transient nonlinear finite element formulation to solve the Navier–Stokes equations coupled with the advection-diffusion equation, allowing to obtain the velocity, pressure and temperature fields of the fluid. As the fluid is considered incompressible, the Boussinesq approximation is introduced to consider the variability of the density due to temperature changes.

Chapter 5 presents a compact finite element procedure to solve conjugate problems where conduction, convection, radiation and natural convection are involved. The radiosity is also included in the system of equations. In fact, this formulation can be considered as a compact treatment of the formulations presented in the preceding chapters 3 and 4.

Chapter 6 describes a one-dimensional finite element formulation to solve structural mechanics problems using a geometrically exact beam theory. The advantages of this theory with respect to the classical theories is illustrated with different numerical examples.

In chapters 3 to 6 benchmark examples are presented in order to verify the numerical codes implemented. The numerical results are compared with the analytical solution of the problem or, in case there is no analytical solution, with numerical results available in the literature or calculated using a commercial FE software.

Chapter 7 presents the main results of this thesis, namely the temperature and displacement fields obtained from the numerical simulations of the thermomechanical behaviour of GFRP profiles (beams and columns) subjected to fire. This chapter is divided into five parts:

- Calibration of the thermal model, in which the thermal properties of the GFRP are assessed, as well as different aspects related to the numerical simulations: spatial and temporal discretization, boundary conditions considered and influence of the singularities in the radiosity field in the results.
- Comparison between the numerical and experimental temperature results obtained for GFRP profiles subjected to fire, both protected and unprotected.
- Calibration of the mechanical model, in which the mechanical properties of the GFRP are assessed, as well as the spatial discretization and the temperature distribution along the bars and the boundary conditions defined.
- Comparison between the numerical and experimental mechanical results obtained for GFRP beams and columns subjected to fire, both protected and unprotected.
- Further applications of the thermal code for different fire scenarios from those used in the experimental tests, in which the applicability of the model to retrieve the thermal response of the profiles for durations of at least 30 min and 60 min was assessed.

Finally, chapter 8 summarizes the main conclusions of the work developed and presents suggestions for possible future developments and improvements of the finite element model proposed.

Complementary numerical information and additional benchmark solutions are presented in the appendixes.

Chapter 2

State of the art

2.1 Overview of composite materials

Composite materials result from the combination of two or more materials which together produce desirable properties that cannot be achieved with any of the constituents alone (Reddy, 2004c). In this context, fibre reinforce polymer (FRP) materials are non-homogeneous and anisotropic (orthotropic) composites that contain fibres in a polymeric matrix (bulk). Chawla (1998) and Chung (2011) present a discussion about the different types of fibres and matrices, respectively, used nowadays.

The concept of FRP materials was first developed in the 1930s. However, it was only in the early 1940s that FRP composites, as we know them today, appeared with the production of fibreglass reinforced plastics (Pilato and Michno, 1994). Initially, the use of FRP composites was limited to automotive, aeronautic and naval applications (Correia, 2008); however, in the last years, their application in several engineering areas has increased. In fact, the advantages and potential shown by these new materials (light weight, corrosion resistance and high strength) in those early applications created a growing interest in researchers and the composites industry, namely in understanding their behaviour. In addition, it also promoted the improvement of the effectiveness of the manufacturing processes, with new production techniques being developed, for example, the pultrusion process.

Figure 2.1 shows different applications of FRP composites in naval and automotive industries and in offshore structures.

(a) KRI Klewang boat (PT. Lundin Industry Invest, 2014).

(b) Offshore structures (Team One Composites, 2014).

(c) Suzuki Swift S1600 (Suzuki, 2014).

Figure 2.1: Applications of composite materials.

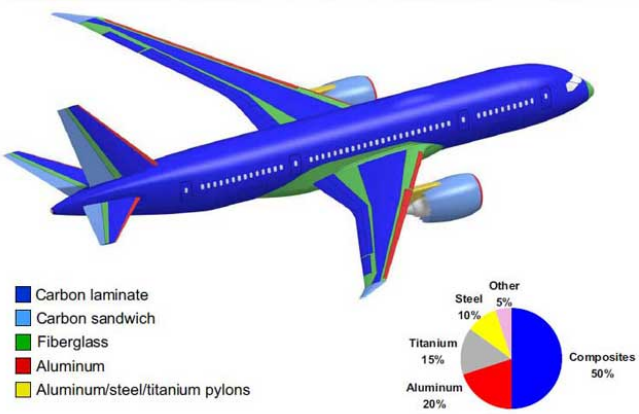

Figure 2.2: Distribution of materials in the commercial Boeing 787 Dreamliner (Campbell, 2006).

An increasing use of composites in aircraft construction has been observed in recent years with the aim of reducing weight and obtaining fuel savings. Figure 2.2 illustrates the distribution of the materials used in the Boing 787 Dreamliner, which comprises 50% in weight of composite materials (website of the Federal Aviation Administration, 2014).

Regarding civil engineering, the first known applications of FRP composites date back to the late 1960s/early 1970s, being remarkable: (i) the dome structure in Benghazi in 1968 and (ii) the roof structure at Dubai airport in 1972 (Zoghi, 2014).

Nowadays, the (lack of) durability of traditional materials and the need for higher construction speed are stimulating the development of innovative structural materials. In this respect, FRP materials and GFRP profiles have great potential, due to their high mechanical performance, lightness, good insulation and low maintenance requirements (Keller, 2003, Bank, 2006). Consequently, their use has been increasing consistently since the 1960s (Adams *et al.*, 2003). Figure 2.3a shows the Eyecatcher Building, built in Basel (Switzerland) in 1998, which is the tallest (15 m) residential/office building with load-bearing GFRP members in the world. Figure 2.3b shows a view of the GFRP bridge built in Kolding (Denmark) in 1997. The book edited by Nicolais *et al.* (2011) illustrates some possible future applications of these composite materials.

The GFRP profiles dealt in this thesis are produced by pultrusion, which is a process where a continuous fibrous reinforcement (in the present case, E-glass fibres) is impregnated with a polymeric matrix (in this case, isophthalic polyester) and continuously consolidated into a solid composite (Campbell, 2006). This process is cost-effective in the production of long constant cross section elements, but it can be costly when used in a high volume process due to the time required for production. Figure 2.4 shows some of the most typical cross sections of GFRP pultruded profiles used in civil engineering.

Despite of the above mentioned advantages, the fire performance of composites could be inadequate in civil engineering applications. In fact, Mouritz *et al.* (2009) identify fire performance as *one of the most significant factors affecting the wider use of composites in engineering structures*. Among the disadvantages of FRPs, it is possible to identify an inadequate fire reaction: standard FRP materials are flammable, not preventing fire ignition, flame spread and excessive generation of smoke. Furthermore, there are well-founded concerns regarding their fire resistance behaviour, which has been object of a

(a) GFRP Eyecatcher Building Basel, Switzerland (Composite Construction Laboratory, 2014).

(b) Bridge at Kolding, Denmark (Fiberline Composites, 2014).

Figure 2.3: Applications of composite materials in civil engineering.

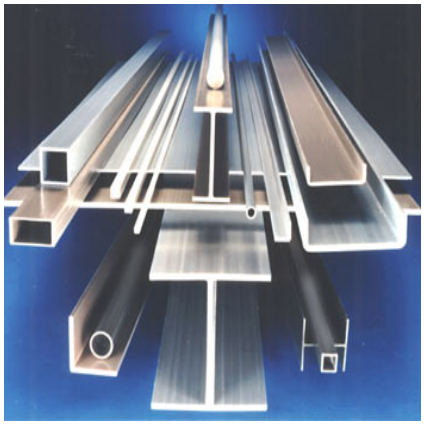

Figure 2.4: Typical GFRP pultruded profiles (Campbell, 2006).

relatively limited number of studies. Therefore, there has been a growing research interest about the behaviour of FRP materials when subjected to thermal loads (Dodds *et al.*, 2000, Kharbari *et al.*, 2003, Mouritz and Gibson, 2006). In several international scientific committees (*e.g.* IABSE WG2, IIFC, ASCE, ACI440-FRP), the fire behaviour of FRPs has been recognized as one of the most critical research issues.

The current chapter first presents an introduction about the different stages of development of a fire, describing also different analytical time-temperature curves typically used to simulate the evolution of the temperatures in a room during a fire scenario. Subsequently, the chapter provides an overview of the literature available regarding the fire performance (fire reaction and fire resistance) of FRP composites, with special attention being given to the mathematical models developed to simulate and characterize such behaviour.

2.2 Combustion process and development of a fire

Combustion is a mass and energy conversion process where chemical bond energy is transformed into thermal energy (Peters, 2011). The combustion initiation involves the coexistence of an oxidizing agent and a fuel source in a sufficient concentration to ignite as a reaction of an energy source that heats the fuel until it reaches its ignition temperature. The combustion can be flaming (with turbulent flames developing) or smouldering (without flames).

The development of a fire is a complex phenomenon that depends on several factors and is difficult to parametrize. However, it is possible to define different stages of development. The objective of the present section is to illustrate the basic concepts of fire and flame. Further information is provided in Babrauskas and Grayson (2006), Quintiere (2006) and Drysdale (2011).

Figure 2.5 illustrates (black curve) five stages of development that can be identified in terms of enclosure temperatures (Karlsson and Quintiere, 2000, Mouritz and Gibson, 2006, Correia, 2008):

1. Ignition: is an exothermic process that increases the ambient temperature greatly. This process can be initiated by pilot ignition (*e.g.* by flaming a match) or by spontaneous ignition (accumulation of heat in the fuel).

2. Growth: in the case of flaming combustion, which is the case dealt in this thesis, this process occurs very rapidly, releasing elevated rates of energy and generating toxic gases. *A priori*, the growth period does not depend on the combustion material, only on the fuel and oxygen available.

3. Flashover: is a rapid transition from the growth period to the fully developed fire, where the combustible material reaches its ignition temperature and bursts into flames. This stage is not always present in fire and the compartment temperature is typically considered around 500-600 °C.

4. Fully developed fire: in this stage the heat released to the room and the temperature attain their maxima. The energy generated is often limited by the oxygen available. The gas temperature in the room is often in the range of 700-1200 °C.

5. Decay: occurs when the fuel and the combustible materials become consumed. In this moment, the energy released is reduced and, as a consequence, the room temperature declines.

The fire development can also be divided as a function of the mass flows in and out through the room openings during the fire (Karlsson and Quintiere, 2000). It is also pertinent to notice that the fire event becomes especially complex when polymer composite materials are involved, because they confer a source of fuel and can influence significantly the evolution of the temperature, size and spread of the flame (Mouritz and Gibson, 2006).

In structural design, time-temperature curves are adopted to represent the post-flashover development of fires. Figure 2.5 depicts two different curves available in standards: (i) Eurocode 1 (1995) parametric curves (red and blue, different curves depending on the degree of ventilation of the room) and (ii) ISO 834 (1975) curve (green). The fire design curves are independent of various parameters that can affect the fire intensity, as for example ventilation areas or building thermal properties. The importance of these curves stems

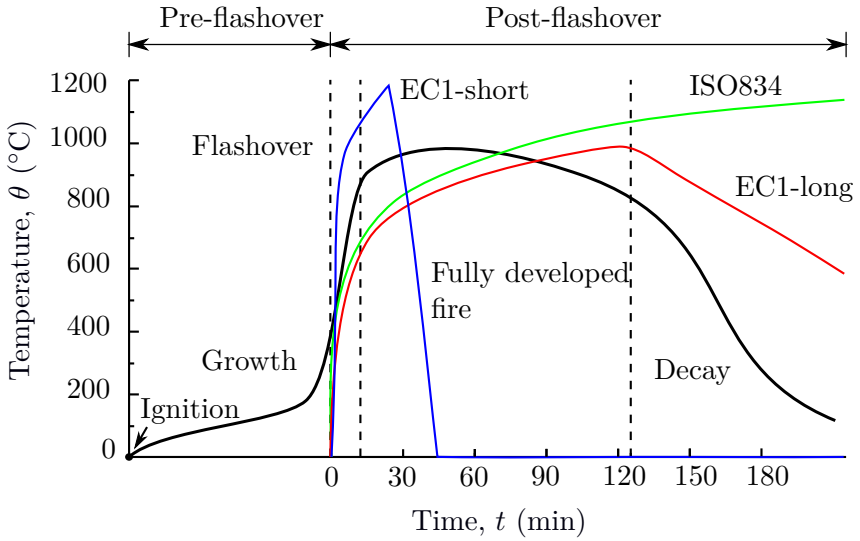

Figure 2.5: Idealized description of the fire development (black) and different fire design curves (red, green and blue). Figure adapted from Karlsson and Quintiere (2000).

from the fact that they are used in fire resistance tests and numerical simulations, even if they do not represent exactly the development of a fire and some of them do not consider a reduction of temperatures corresponding to the decay stage.

2.3 Fire behaviour of GFRP composites

2.3.1 Thermal decomposition of composites in fire

The combustion of composite materials is a complex process where thermal, chemical and physical transformations are involved. The current section presents a general description of the decomposition process underwent by polymeric composites at high temperatures (additional information is available in Mouritz and Gibson, 2006). Schematically, the combustion process of composites can be divided in four stages (Hilado, 1990):

- Heating: in this phase, the polymeric matrix absorbs the energy required to reach its decomposition temperature.
- Decomposition: the composite continues absorbing energy to break the covalent bonds of the organic compounds. Several decomposition products are generated, namely solid residue (char and ash), partially decomposed polymer (various liquids), entrained particles (smoke) and incombustible and combustible gases.
- Ignition: it is the instant when the combustion begins.
- Combustion: it corresponds to the final phase where the exothermic reactions between the combustible gases and the oxidizing agent (usually oxygen) provide the energy required for the total decomposition of the composite. This process constitutes a self-propagating cycle, as the combustion generates heat, then more decomposition occurs and more fuel is created (combustible gases), thus allowing the continuity of the fire.

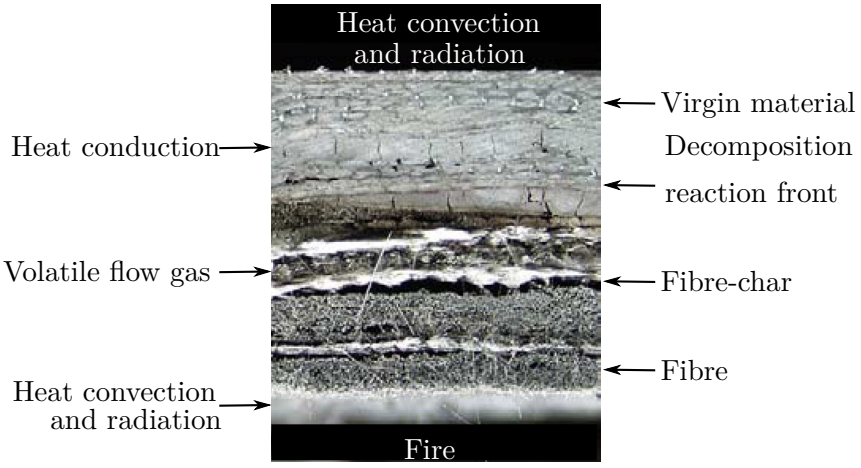

Figure 2.6: Schematic description of the burning process throughout the thickness of a composite laminate (adapted from Tracy, 2005, Mouritz *et al.*, 2009).

The combustion of a polymeric composite involves different processes, that Mouritz *et al.* (2009) summarize as follows:

- Thermal processes: involve heat transfer from the fire to the composite, heat generation/absorption of the polymer matrix and the organic fibres, convective heat flux due to the flow of the gases generated from the composite into the fire, heat generation in the char and fibres zone and, finally, heat generation due to the ignition of the flammable volatiles.

- Chemical processes: involve phase transformations, viscous softening, melting, decomposition and volatilisation of the polymer matrix and organic fibres, as well as the formation, growth and oxidation of char and char-fibre reactions.

- Physical processes: include thermal expansion/contraction, thermally-induced strains, internal pressure build-up due to the formation of volatile gases, formation of gas-filled pores, matrix cracking, fibre-matrix interfacial debonding, delamination damage, surface ablation and, finally, softening, melting and fusion of fibres.

- Failure processes: are complex phenomena depending on temperature, heat flux and duration of the fire and magnitude and type of load.

During the combustion process, the composite material suffers different types of damage, being possible to distinguish different zones as a function of the decomposition degree. Figure 2.6 illustrates the evolution of the fire damage in a composite laminate (right hand side of the figure) and the various heat transfer processes that occur through the thickness of the laminate (left hand side).

During a fire, the temperature of the composite increases progressively. When the polymer matrix attains the glass transition temperature (usually around 100-200 °C), a change from the initial hard and brittle condition to a viscous state occurs. During this stage of the heating process no relevant chemical reactions take place. At 200-300°C, a chemical reaction known as pyrolysis initiates and the material starts decomposing,

releasing volatile gases (flammable and non-flammable) and smoke. The decomposition of the polymeric matrix commonly occurs between 300-600°C.

Regarding the E-glass fibre[1] reinforcement, the fibres used in the GFRP composite studied in this thesis, the softening and viscous flow starts at 830°C, while melting only occurs at 1070°C. Hence, they do not interfere significantly in the decomposition process as this is mainly controlled by the decomposition of the matrix. However, a significant reduction of the mechanical properties of the fibres can be observed for temperatures around the softening temperature (Correia, 2008), and this is relevant for the tensile behaviour of the composite.

2.3.2 Fire reaction performance of composites

According to Mouritz and Gibson (2006), fire reaction *is used to describe the flammability and combustion properties of a material that affect the early stages of fire, generally from ignition to flashover.* The most relevant fire reaction properties encompass the time to ignition, the smoke toxicity, the heat release rate, the flame spread rate and the oxygen index.

The time to ignition is the period of time required for a material to ignite and to sustain flaming combustion when subjected to a certain radiant heat flux. GFRP laminates can ignite in a few minutes when exposed to radiant heat fluxes of 25 to 50 kW/m^2 (Correia *et al.*, 2010a).

The smoke toxicity and density are two parameters of important relevance in buildings design due to their influence in the possibility of human survival during a fire.

The heat release rate (HRR) is considered the most important fire reaction property as it represents the best indicator of the fire hazard of a material. The HRR is a quantitative measure of the amount of thermal energy released — during the thermochemical decomposition processes — by a material per unit area when exposed to a fire, simulated by radiating a constant heat flux or temperature (Mouritz and Gibson, 2006). The HRR is usually defined by means of two parameters: the peak HRR (PHRR, maximum instantaneous value of heat released) and the average HRR (AHRR, average value of heat released, typically during a period of time between 3 and 5 minutes after the PHRR is attained). Composites with low values of peak and average HRR are recommended for engineering applications. Figure 2.7 illustrates a typical time-HRR curve for a composite material reinforced with non-combustible fibres. The presented curve (Mouritz *et al.*, 2006), corresponds to a glass/vinylester composite subjected to a constant heat flux of 50 kW/m^2. The PHRR is situated at around 400 °C due to the decomposition of the matrix, that starts at 350 °C.

The flame spread rate refers to the velocity of the flame front propagating in the surface of a combustible material.

Finally, the oxygen index is the minimum oxygen content in the air required to maintain the flaming combustion of a material and it is usually used to quantify the flammability of organic polymers and composite materials.

[1] E-glass fibres are the most commonly used in the reinforcement of FRP materials. The letter *E* refers to their electrical insulation.

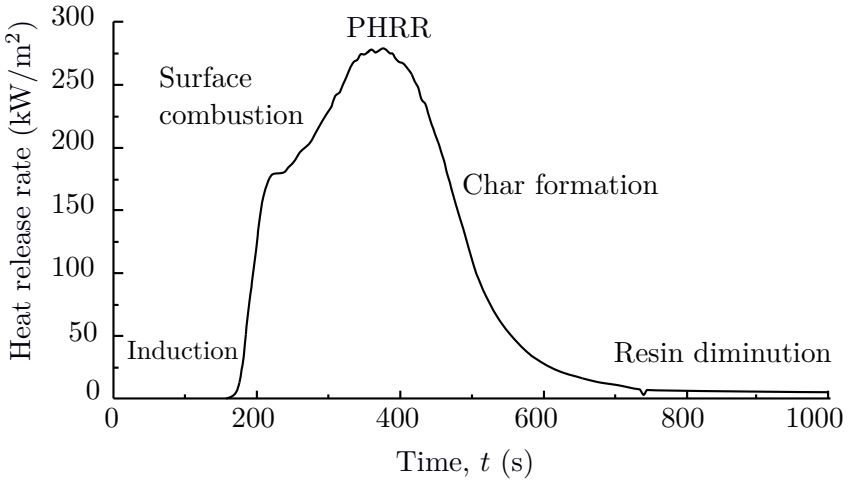

Figure 2.7: Typical heat release rate curve for a composite reinforced with non-combustible fibres (adapted from Mouritz *et al.*, 2006, Mouritz and Gibson, 2006).

2.3.3 Thermophysical properties of GFRP composites

The characterization of the thermophysical properties of FRP composites has been thoroughly pursued in the last years. In the literature, there is reference to many experimental studies which usually are complemented with numerical expressions to predict the evolution of the thermal properties as a function of temperature. This knowledge is essential to obtain accurate predictions of the thermal response of composite laminates. However, as discussed later, there is still limited information about some properties that are relevant for the thermomechanical response of FRP composites. The anisotropic behaviour of FRP composites and its combustibility make very challenging to determine the thermophysical properties as a function of temperature.

The thermophysical properties of composites relevant to their thermal behaviour comprise the density (ρ), the thermal conductivity (k) and the specific heat capacity (c_p) of both the virgin and the char (fully decomposed) material and the emissivity (ϵ). They are variable with temperature due to the physical-chemical reactions that occur when the material is subjected to high temperatures.

Dimitrienko (1995) presented a model to estimate the thermomechanical behaviour of composites under high temperatures by considering the variation of the thermophysical material properties with temperature. The model incorporates the physicochemical processes of pyrolysis and charring of the composite. Figure 2.8 illustrates the typical variation of the conductivity, the heat deformation, the density and the gas permeability as a function of the temperature for a glass/epoxy composite.

According to this model, the density reduction occurs, mainly, due to the decomposition and volatilisation of the polymeric matrix and, hence, when the matrix is totally decomposed, the density remains constant and equal to the density of the inorganic components of the composite. Furthermore, a minor loss of mass takes place at 100 °C due to the water evaporation. The evolution of the composite mass with the temperature can be obtained experimentally through DSC/TGA analysis (as done in the project that frames the present thesis). Several mathematical models are available in the literature, most of them being based in the Arrhenius decomposition kinetics, *e.g.*, Bai *et al.* (2008a)

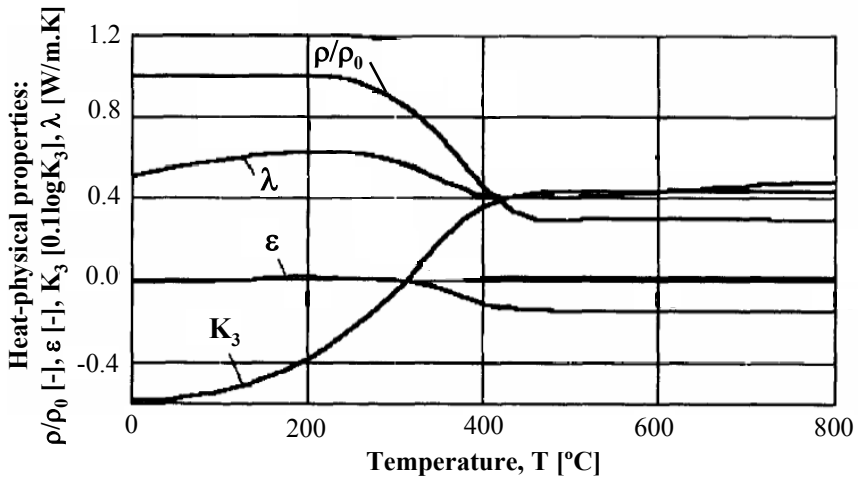

Figure 2.8: Temperature-dependent properties of the glass/epoxy composite, being K_3 the gas permeability, ϵ the heat deformation, λ the thermal conductivity and ρ/ρ_0 the relative density (adapted from Dimitrienko, 1995).

and Lattimer *et al.* (2011). The variation of the density with time is given by equations in the following form,

$$\frac{\partial \rho}{\partial t} = -\left(\rho_v - \rho_c\right)\left(\frac{\rho - \rho_c}{\rho_v - \rho_c}\right)^n A\, e^{-E/R\theta} \tag{2.1}$$

where n is the order of reaction, A is the pre-exponential factor, E is the activation energy, R is the universal gas constant and θ is the temperature, with v and c corresponding to the virgin and char material, respectively.

The composite thermal conductivity progression follows three phases: (i) a slight rise due to the intrinsic behaviour of the matrix, (ii) a decrease due to the formation of pores originated by the decomposition of the matrix, and (iii) a stabilization when the pyrolysis process is finished and the material is composed basically of fibres.

Regarding the evolution of the specific heat capacity with temperature, two important increases are observed at (i) 100 °C, due to the water evaporation, and (ii) between 250 and 400 °C, due to the endothermic decomposition of the matrix, while for the remaining temperature ranges the specific heat capacity remains approximately constant.

The literature offers several mathematical models to predict the evolution of the thermophysical properties of composites. Samanta *et al.* (2004) presented a model to compute the thermal conductivity based in the rule of mixtures where the volume of fibres and matrix is related without considering the thermal expansion and the concentration of gases. The equation proposed is,

$$\frac{1}{k} = \frac{V_f}{k_f} + \frac{(1 - V_f)}{k_m} \tag{2.2}$$

where V_f represents the volume of fibres and the subscripts f and m correspond to the fibres and the matrix, respectively. For the specific heat capacity, the following equation is proposed:

$$\frac{1}{c_p} = \frac{V_f}{c_{pf}} + \frac{(1 - V_f)}{c_{pm}} \tag{2.3}$$

In both expressions, the influence of the humidity evaporation is considered.

Regarding the emissivity of the GFRP, Samanta *et al.* (2004) proposed a linear variation between 0.75 and 0.95 for temperatures ranging from 20 °C to 1000 °C.

Samanta *et al.* (2004) reported empirical curve-fit polynomial equations to compute the thermal conductivity and the specific heat capacity as a function of temperature. Subsequently, Tracy (2005) improved the previous model by adding the effect of the total loss of matrix at around 830 °C. During the combustion, the burnt material can confer a protection to the virgin material, but when the decomposition is in an advanced stage of development, the char material dissociates and only the fibres remain, these having a five times higher thermal conductivity compared to the matrix. In this model, the evaporation of the water and the concentration of gases in the pores are not considered. In the modelling of the specific heat capacity, the dehydration of the material and the endothermic decomposition of the matrix are considered. However, only numerical values of thermal conductivity and specific heat capacity are reported based on experimental measurements and no analytical expressions are proposed.

Lua *et al.* (2006) presented a temperature and mass dependent heat diffusion model to characterize the temperature and mass dependent heat conduction in a composite laminate. In this work, analytical expressions are proposed to evaluate the variation of thermophysical properties with temperature. These expressions are validated using experimental results.

Several analytical and mathematical models consider composite laminates exposed to heat or fire divided into two layers as a function of the degradation underwent by the material: virgin (v) and char (c). They usually estimate the thermal conductivity and the specific heat capacity during the decomposition process as a combination of the properties corresponding to virgin (ρ_v, k_v, c_{pv}) and char (ρ_v, k_c, c_{pc}) material.

Based on this concept, Bai *et al.* (2007) developed a decomposition model for GFRP composites subjected to fire. Temperature-dependent mass variation is obtained using a decomposition model of the resin, whose kinetic parameters have to be determined experimentally (for example, from TGA tests). The thermal conductivity of the composite is evaluated as,

$$\frac{1}{k} = \frac{V_v}{k_v} + \frac{V_c}{k_c} \tag{2.4}$$

and, similarly, the specific heat capacity is given by,

$$c_p = c_{pv}\, f_v + c_{pc}\, f_c \tag{2.5}$$

where f_c and f_v are, respectively, the mass fraction of char and virgin material expressed as $f_c = m_c/m$ and $f_v = m_v/m$, where m is the composite instantaneous mass. In the same way, V_c and V_v are, respectively, the relative volume of char and virgin material with respect to the composite instantaneous volume.

Lattimer *et al.* (2011) presented a decomposition model where the mass fraction of virgin material is calculated considering constant volume and is given by,

$$F = \frac{\rho - \rho_c}{\rho_v - \rho_c} \tag{2.6}$$

and the thermal conductivity and the specific heat capacity are calculated as:

$$k = F\, k_v + (1 - F)\, k_c \tag{2.7a}$$

$$c_p = F\, c_{pv} + (1 - F)\, c_{pc} \tag{2.7b}$$

Advanced models developed recently start to include the effect of fire-induced damage, as for example the formation of delamination or cracking, in the variation of the thermo-physical properties of the composite material.

Regarding the mechanical behaviour, the thermal expansion coefficient represents the expansion or contraction of a composite due to the conduction of heat and this physical property is also dependent on temperature. Furthermore, as composites are anisotropic materials, this coefficient presents different values in the longitudinal, transversal and through-thickness directions.

Mouritz and Gibson (2006) presented an overview of the numerical and experimental studies carried out to evaluate the thermal expansion of a glass-filled polymer composite (glass fibres embedded in a phenolic resin). Figure 2.9 illustrates the typical variation of the thermal expansion coefficient as a function of temperature, for two different heating rates. Four stages can be identified:

- Stage I: the composite initially expands due to the thermal expansion of the fibres and polymeric matrix and due to the vaporization of the traces of moisture. In this phase, the temperatures are lower than the glass transition temperature of the matrix and, hence, the amount of expansion can be determined by the linear coefficient of thermal expansion of the virgin material.

- Stage II: a sharp expansion of the composite can be observed when the pyrolysis of the matrix commences. This process continues while the temperature increases and the generation of gases persists. The expansion peak is reached when the corresponding rate of diffusion of the gases out of the material surpasses the rate of production. It can be observed that the peak depends on the heating flux and it is greater for the higher heating rate, as it also presents an elevated gas generation rate.

- Stage III: an abrupt contraction is observed immediately after the expansion peak due to the pyrolysis gases released and the consequent reduction of pressure in the composite. Subsequently, a slow contraction can be observed due to char formation and to the elastic recovery of the solid residue.

- Stage IV: an additional contraction or expansion may occur after 1000 °C due to structural changes in the composite resulting from char reactions.

Figure 2.9 confirms that the thermal expansion coefficient depends strongly on the temperature and, hence, in a generic composite element where a thermal gradient exists, the material expansion will be non-uniform in the through-thickness direction, *i.e.*, the expansion will be greatest at the hot surfaces (until the beginning of stage III). However, for very high temperatures following the resin matrix decomposition, further (positive) temperature variation may cause contraction in the composite material.

Tant *et al.* (1985) reported graphical results about the variation of the thermal expansion coefficients of glass/phenolic composites at different temperatures. These values were obtained experimentally by testing cylindrical (6 mm outer diameter and 50 mm long) composite samples heated at different heating rates[2]. Figure 2.10 shows the fractional length change for two glass/phenolic composites that differ only in the curing scheme of

[2]During the tests, it was guaranteed that all the material was at the same temperature, thus avoiding the possible influence of thermal gradients on the results.

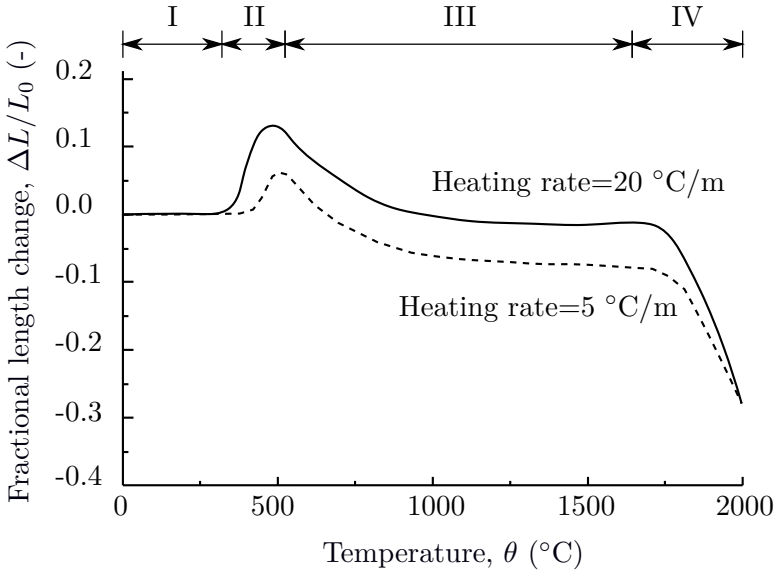

Figure 2.9: Fractional length change of a glass/phenolic composite as a function of temperature for two different heating rates (adapted from Mouritz and Gibson, 2006).

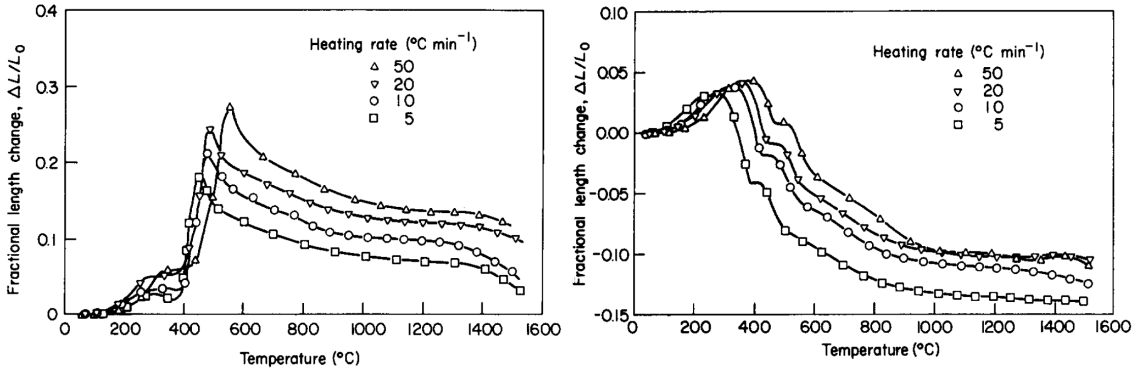

(a) Composite 1.

(b) Composite 2.

Figure 2.10: Fractional length change of two glass/phenolic composites *vs.* temperature for various heating rates (Tant *et al.*, 1985).

the matrix. The plots demonstrate that variations in the method of preparation of the samples have a dramatic effect upon the expansion behaviour. Furthermore, the magnitude of the maximum fractional length changes can be very high. However, it is very likely that the experimental results measured are dependent on a scale factor, as the samples tested had very reduced dimensions (compared with the structural members tested in the present research project). Consequently, Tant *et al.* (1985) could have obtained higher thermal expansion coefficients, these values not being directly applicable to full-scale composite elements as beams, columns or slabs.

The mathematical model proposed in Tant *et al.* (1985) was originally developed by Buch (1982). The thermal expansion of a composite is evaluated as a combination of

the thermal expansion coefficient of the char material, α_c, and of the virgin material, α_v,

$$\frac{1}{L_0}\frac{\partial L}{\partial t} = \alpha_v\, f_v \frac{\partial \theta}{\partial t} + \alpha_c\, f_c \frac{\partial \theta}{\partial t} + \Delta\eta \frac{\partial f_v}{\partial t} \tag{2.8}$$

where L is the length at each instant, L_0 is the initial length, t is the time and $\Delta\eta$ is the dimensionless pyrolysis expansion factor, which accounts for the rapid expansion/contraction during the pyrolysis reactions.

Tracy (2005) also proposed an analytical model to compute the thermal expansion coefficient based on the rule of mixtures. As the material is anisotropic, three expressions were reported to calculate the thermal expansion in the longitudinal (axis x_1), transversal (axis x_2) and through-thickness (axis x_3) directions,

$$\alpha_1 = \frac{E_f\,\alpha_f\,V_f + E_m\,\alpha_m\,V_m}{E} \tag{2.9a}$$

$$\alpha_2 = (1+\nu_m)\,\alpha_m\,V_m + (1+\nu_f)\,\alpha_f\,V_f - \alpha_1\,(\nu_f\,V_f + \nu_m\,V_m) \tag{2.9b}$$

$$\alpha_3 = \alpha_m\,V_m + \alpha_f\,V_f \tag{2.9c}$$

where f and m refer to the fibres and the matrix, respectively, E is the Young's modulus and ν is the Poisson ratio. The values reported by this author for a glass/polymer composite are $\alpha_1 = 12.6\cdot10^{-6}$ K^{-1}, $\alpha_2 = 21.8\cdot10^{-6}$ K^{-1} and $\alpha_3 = 37.0\cdot10^{-6}$ K^{-1}. However, this formulation only allows computing the thermal expansion coefficient at ambient temperature.

2.3.4 Thermal analysis of GFRP composites

The main objective of the thermal analysis of GFRP composites (both numerical and experimental) is to study their thermal response, namely determining the temperature profiles in the material when subjected to elevated temperatures.

The challenge of numerical thermal models is to reproduce the temperature evolution of FRPs under fire and the complex material processes (thermal, chemical, physical and failure) that occur during fire exposure.

There are several thermal models reported in the literature differing, mainly, in the processes modelled. One of the most frequently cited thermal model is the one proposed by Henderson *et al.* (1985). The formulation is based on the thermochemical models previously developed to wood, as for example Kung (1972) and Kanury (1972). The proposed thermal model analyses the temperature distribution within a composite laminate considering: (i) the heat transfer in both the virgin and the char material, (ii) the decomposition of the matrix and the fibres (when organic), and (iii) the diffusion of the decomposition gases from the reaction zone through the char zone. The one-dimensional nonlinear equation reported is,

$$\rho\,c_p\frac{\partial \theta}{\partial t} = \frac{\partial}{\partial x_1}\left(k_1\frac{\partial \theta}{\partial x_1}\right) - \dot{m}_g\,c_{pg}\frac{\partial \theta}{\partial x_1} - \frac{\partial \rho}{\partial t}\,(Q_p + h - h_g) \tag{2.10}$$

where ρ, c_p and k_1 are, respectively, the density, the specific heat capacity and the conductivity coefficient of the composite in the considered direction, $\dot{m}_g$ is the mass flux of the pyrolysis gas flowing through the char structure, c_{pg} is the specific heat of the gas, Q_p is the heat of decomposition at a reference temperature and, finally, h and h_g are the enthalpy of the composite and the gas, respectively. The first term of the left hand side describes the temporal variation of the temperature, the first term of the right part of the

equation is the heat conduction term, the second one represents the endothermic effect of the resin decomposition and the last one describes the small cooling effect that happens when the volatile decomposition products pass through the thickness of the laminate. In this kind of models, the resin decomposition process is usually modelled by an Arrhenius relationship (Mouritz and Gibson, 2006), which can cause numerical instabilities.

Florio Jr. *et al.* (1991) presented a more sophisticated one-dimensional transient thermal model which considers heat transfer conduction in a solid, decomposition gas due to the temperature, solid mass loss, pressure rise due to the formation of volatile gases, permeability and porosity of the material, gas mass flux and storage and, finally, the expansion of the material.

Sullivan and Salamon (1992a) presented a finite element model to simulate the thermochemical decomposition of polymeric materials considering, as the previous model, heat transfer conduction, pyrolysis in the matrix and fibres, flow of the decomposition gases, thermal expansion/contraction of the material and the pressure rise. The referred study uses the thermochemical model to generate the input data for mechanical analysis and, as a result, the validation of the model is carried out by means of the experimentally measured strain variations depending on the temperature (Sullivan and Salamon, 1992b).

More recently, Dimitrienko (1995) developed a mechanical-mathematical model for ablating composites [3] where the composite is considered a porous multiphase media with phase transformations and chemical reactions when heated. The innovation of the model is the simulation of the influence of the physical-chemical transformations in the stress-strain state of the material.

Recently, a wealth of literature was published about thermal models, in which the numerical results are validated with experimental data, as for example, Dodds *et al.* (2000), who analysed the thermal response of laminated GFRP panels under fire exposure.

Looyeh and Bettess (1998) presented a transient nonlinear FE model and analysed the thermal performance of a composite panel by considering temperature-dependent thermal properties, testing different mixed boundary conditions at the unexposed surface. This study is based on a previous work, Looyeh *et al.* (1997). The results reported are the temperature profiles in a polyester-based GFRP panel and the density distribution in the panel.

Miller and Weaver (2003) presented a numerical tool to estimate the temperature distribution through a multi-layered specimen subject to convection and, for the first time, radiation boundary conditions.

Lua *et al.* (2006) reported a temperature and mass dependent heat diffusion model based on Henderson *et al.* (1985) to characterize the temperature and mass dependent heat conduction, considering the decomposition of the material and the vapour migration.

Milano and Gibson (2009) reported a new model to predict the thermal field in FRP composites exposed to high heat flux in one side of the laminate, known as *apparent thermal diffusivity* (ATD) model. It represents a simplified approach to model the temperature evolution in a composite avoiding the use of the Arrhenius decomposition relations. The decomposition of the resin and the changes in the specific heat capacity and thermal conductivity of the composite are considered.

Riccio *et al.* (2013) presented a three dimensional thermochemical model to study the thermal behaviour of a composite plate. The code was implemented in a commercial software and allows computing the mass loss rate, the heat release rate and the total heat

[3] Composites that can experience removal of mass from the surface by thermochemical and mechanical processes.

released during the heating source application. The composite plate comprises GFRP layers with different fibre orientations. The orthotropic thermal conductivities and the specific heat capacity in each layer are estimated with the rule of mixtures and the degree of decomposition function. The mathematical model was validated by comparing the numerical results with experimental data taken from the literature.

2.3.5 Fire resistance of GFRP composite laminates

Fire resistance refers to the ability of a composite material to retain its mechanical integrity (Mouritz and Gibson, 2006), *i.e.*, preserving its mechanical properties, such as the stiffness, the creep resistance and the strength during the fire exposure and after the fire has been extinguished (post-fire mechanical behaviour).

The mechanical properties of composite laminates under fire conditions can be obtained experimentally through tension, compression and shear tests. The main objective of these tests is to determine in a particular specimen each elastic parameter (Young's modulus and shear modulus) or strength value (tensile, compressive and shear strength) as a function of temperature. However, this data is not available for all composite systems. Alternatively, it can be considered that the mechanical properties fit relationships similar to that shown in figure 2.11 (Mouritz and Gibson, 2006). In the depicted curve, P_U represents the mechanical property value at ambient temperature, which experiments a rapid reduction after a certain critical temperature (θ_{cr}) is reached. At the mechanically observed glass transition temperature ($\theta_{g,mech}$), the mechanical property of the composite is reduced to 50%. This temperature is typically about 15-20 °C below the glass transition temperature (θ_g) measured by thermal techniques (*e.g.* DSC). Finally, after the glass transition temperature, a residual value of the mechanical property (P_R) remains. Hence, according to this curve, the reduction of the mechanical properties happens before the glass transition temperature, which is lower than the decomposition temperature of thermosetting resins. It has been demonstrated that this kind of curves describes with reasonable accuracy the variation with temperature of matrix-dominated properties of composite materials (Mouritz *et al.*, 2006).

This raises the problem of fitting a suitable relationship between a given mechanical property and temperature, mainly between the critical and glass transition temperatures. In the literature it is usual to find polynomial series (Liu *et al.*, 2006), Weibull distributions (Mouritz and Gibson, 2006) and tanh functions (Gibson *et al.*, 2006). In this way, the actual approach to model the mechanical response of composites subjected to fire uses empirical curve-fit equations to calculate the reduction of the mechanical properties at different points throughout the composite section based on its thermal profile (Mouritz *et al.*, 2009). The different thermomechanical models differ in the mechanical theories considered to calculate the mechanical response and to predict failure of the composite.

Most of the literature consulted includes the development of a thermomechanical model to predict the evolution of the mechanical properties as a function of temperature. These models are calibrated using experimental data and usually they are complemented with a thermochemical model, as the former is required to estimate the temperature distribution in the composite (Tracy, 2005).

One of the first thermomechanical studies carried out on composites was presented by Springer (1984). The paper describes a thermochemical model in conjunction with a thermomechanical model. The mechanical model allows calculating changes in the tensile,

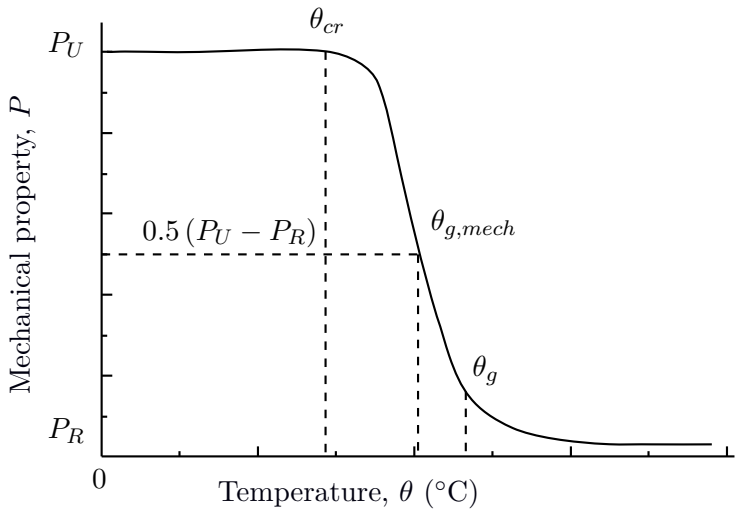

Figure 2.11: Typical reduction of the mechanical properties of composite materials (adapted from Mouritz *et al.*, 2006, Mouritz and Gibson, 2006).

compressive and shear strengths as a function of the fire exposure time, but no experimental data was used to validate the numerical results.

Griffis *et al.* (1986) described a mathematical model for predicting the integrity loss of composite structures subjected to simultaneous intense heating and applied mechanical loads. A nonlinear two dimensional FE model was developed to represent the degradation of mechanical properties with stepped functions at discretized temperature points. The FE model uses the Mindlin theory of plates and considers the effects of surface ablation, re-irradiation losses and temperature-dependent thermophysical properties. The Tsai-Wu failure criterion was also included. In this case, the numerical results were validated with experimental data.

McManus and Springer (1992a,b) presented the first model combining thermal, chemical and mechanical fire phenomena. The interaction between mechanically-induced stresses and the pressures created due to the generation of decomposition gases was considered. The numerically computed stress state of the composite was compared with experimental results.

Gibson *et al.* (2004) developed a thermomechanical model that couples with the two-layer post-fire mechanical model of Mouritz and Mathys (2001), in which the laminate is divided into two regions as a function of the decomposition degree (virgin and char zones). This model allows calculating the thickness of the virgin material, which was also verified using experimentally measured values. The results obtained with the model are the stiffness and strength in tension or compression, the flexural stiffness, the Euler buckling load and the apparent stress at which buckling occurs, and the failure load and corresponding apparent stress.

Subsequently, Gibson *et al.* (2006) presented an upgraded version of the model described in Gibson *et al.* (2004), where the degradation of mechanical properties between the critical and glass transition temperature is fitted by a semi-empirical function that considers the effects of both viscous softening and decomposition of the polymer matrix.

Liu *et al.* (2006) performed an experimental and numerical study about the response of

GFRP columns under axial compression and thermal loads obtained by keeping one side of the specimen exposed to heat flux. As a result, a non-uniform temperature distribution through the thickness was observed. A model based on polynomial equations was developed to represent the degradation of the elastic moduli (elasticity and shear modulus) with the temperature. One interesting effect of the non-uniform temperature applied is that the neutral axis moves away from the centroid of the cross section, resulting in an additional moment due to the eccentric loading, which would tend to bend the structure away from the heat source. Hence, it was concluded that the thermal moment tends to bend the structure away or towards the heat source when respectively low or large temperatures are developed. On the contrary, the moment induced due to the eccentric loading always tends to bend the structure away from the heat source.

Bausano *et al.* (2006) developed an experimental investigation regarding the lifetime of E-glass vinylester composite laminates subjected to centric compression and one-sided simulated fire exposure. A finite element analysis was performed to simulate the behaviour of the laminates and different values of the elastic modulus as a function of temperature.

Feih *et al.* (2007a) reported an experimental and numerical study about the thermal decomposition, softening and failure of polymer matrix laminates under combined compressive loading and one-sided heating. A thermochemical and thermomechanical coupled model was presented for predicting the temperature field and the time to failure of laminates.

The evaluation of the structural response of composites subjected to fire under tension is more complicated than under compression, because both matrix and fibres softening and failure have to be analysed. Feih *et al.* (2007b) presented an investigation about the thermomechanical response of fibreglass laminates under tension and one-sided heating. An average strength model was developed considering the matrix and the fibres contributions. The model presented does not consider the effects of the thermal strains, pore formation, delamination and fibre-matrix debonding.

Bai *et al.* (2008a) developed thermochemical and thermomechanical models in which the composite is considered as a mixture of materials that are in a glassy, leathery to rubbery or decomposed state[4]. The mechanical properties of the mixture are determined by the content and the property of each state. The equations presented are based on the Arrhenius equation and they allow predicting the temperature-dependent E-modulus, G-modulus, viscosity and effective coefficient of thermal expansion. The model is structurally validated in Bai *et al.* (2008b,c).

Correia *et al.* (2013b) reported an experimental investigation that addresses the mechanical characterization of GFRP laminates under tension, compression and shear loads at temperatures varying from 20 to 250 °C. The load-deflection curves, stiffness, failure modes and the ultimate strength are evaluated. Different empirical models available in the literature are used to estimate the tensile, shear and compressive strengths of GFRP pultruded material as a function of temperature.

As mentioned, the fire resistance of a composite also comprises its post-fire behaviour. Accordingly, the mechanical properties of composite materials shall be quantified after the event of a fire or exposure to elevated temperature. The experimental studies carried out in the last years reveal that the post-fire properties of a composite depend on the fire temperature, heating time, load condition and matrix decomposition properties. In

[4]According to Bai *et al.* (2008a) four different states (glassy, leathery, rubbery and decomposed) and three transitions or processes (glass transition, leathery-to-rubbery transition and decomposition) can be defined.

this context, Mouritz and Mathys (2001) and Mouritz (2002) proposed a two-layer model to compute the mechanical properties of fire-damaged composite materials. Analytical expressions that consider the properties of the fibre-char and virgin materials are also reported. The validation of the model was carried out with experimental data measured in a set of tests performed on laminates subjected to a range of heat flux and heating time conditions.

2.4 Fire behaviour of GFRP structures

In the present section, a literature review about the thermal and mechanical analyses of full-scale GFRP structures is reported.

Miller and Weaver (2003) reported an analytical tool to compute the thermal behaviour of composites and multi-layered systems. Convection and radiation boundary conditions are modelled, being the inclusion of radiation a novel feature in the analysis of composite structures. The results reported were verified with a commercial FE software.

Keller *et al.* (2005, 2006a) presented an experimental study about the thermal response of FRP laminates and unloaded cellular FRP components in which an internal liquid cooling system was used. Results showed that cellular FRP components subjected to the ISO 834 (1975) fire conditions and liquid cooling can satisfy the fire resistance rating of 90 minutes required by the Swiss building code (Swiss Society of Engineers and Architects, 1997) for structural members of multi-storey buildings. Keller *et al.* (2006b) presented the calculation of the thermo-physical properties of the GFRP material based on experimental data obtained from full-scale fire tests on loaded and unloaded slabs. Moreover, a numerical study of the post-fire behaviour using the two-layer and the three-layer models was reported. Keller *et al.* (2006c) presented a numerical simulation of the thermomechanical behaviour of the GFRP slabs using the FEM, where the thermal and the mechanical properties of the material were considered temperature-dependent. A two dimensional FE thermochemical model was developed to predict the temperature progression in the liquid-cooled and non-cooled slab components. The thermomechanical model presented consists of a three dimensional FEM that predicts the measured midspan deflections and axial strains under serviceability loads (only in the liquid-cooled case) during the fire exposure. It uses as input the temperatures computed with the thermochemical model following a coupled scheme. Both models were validated with the experimental results. The thermomechanical model was able to predict the hot face temperatures, which, as the authors mention, are *very difficult to experimentally measure*. An important aspect for the present thesis is that the modelling of the heat exchange in the cavity was carried out considering simply free convection: the air temperature was set as 20 °C and the convective heat transfer coefficient was considered. In this paper the authors mentioned that in the empty cells:

> *a large amount of heat was transferred from the lower to the upper face sheet through convection and radiation. In order to properly simulate this effect, however, a complex modelling of the air including computational fluid dynamics (CFD) would have been necessary.*

The solution adopted is justified because the main objective of the paper was to present a model to reproduce the thermal and mechanical behaviour of liquid-cooled slabs, where only forced convection occurs in the cells. In this context, no literature addressing the

simulation of natural convection and radiation in enclosed spaces of composite sections was found.

Bai and Keller (2009) developed a study about the liquid-cooling fire protection system applied to columns. The GFRP tubular columns were subjected simultaneously to thermal and mechanical loads. The objective of the study was to maintain the material temperature below the critical glass transition temperature using the liquid-cooling system. Different flows of water were tested. The experimental thermal and mechanical results were reproduced using thermal and strength degradation models. The models used were previously described in Bai *et al.* (2008a). Regarding the thermal simulation, a transient one-dimensional heat transfer in the through-thickness direction was assumed and the resulting system of equations was solved using the finite difference method. The boundary condition considered between the GFRP interior wall of the tube and the water was forced convection. Regarding the mechanical simulation, a compressive strength degradation model was employed in which it was assumed that, at a certain temperature, the FRP material can be modelled as a mixture of materials that are in different states (glassy, leathery and decomposed).

Correia (2008) presented a fire resistance experimental study about the thermal and mechanical behaviour of tubular GFRP beams when subjected to fire and mechanical loading (four point bending). Several protection systems, both passive and active, were also tested in order to evaluate their effectiveness. Specifically, calcium silicate boards, vermiculite/perlite based mortar, intumescent coating and water cooling were tested. The experimental results obtained were later published in Correia *et al.* (2010b).

Bai *et al.* (2010) presented thermochemical and thermomechanical models of the beams tested by Correia (2008), using the models described in Bai *et al.* (2007, 2008a,b). The main objective of this study was to reproduce numerically the beneficial effects of passive fire protection systems and, thus, to propose a model that can be used for the selection and design of passive fire protection systems. The thermal behaviour of the tubular cross section was reproduced by performing a transient one-dimensional heat transfer analysis, where the thermophysical properties of the materials are temperature-dependent. In this model, only heat transfer in the bottom flange of the cross section was modelled by discretizing it into 23 layers. The resulting system of one-dimensional equations was obtained using the finite difference method. The heating of the lower face (GFRP or passive fire protection material) was modelled by means of a variable prescribed temperature according to ISO 834 (1975), while in the upper face convective and radiative heat transfer was considered with a constant ambient temperature equal to 20 °C and a convective heat transfer coefficient equal to 2 W/m^2 K (determined by minimizing the differences between the experimental and modelling temperatures). In the case of GFRP profiles protected to fire with a water cooling system, the boundary condition in the upper face was set as a convective heat flux with a convective heat transfer coefficient equal to 18 W/m^2 K. Figure 2.12 shows the complete geometry of the cross section and the simulated flange with the boundary conditions described above (θ_a represents the ambient temperature and $\overline{\theta}$ is the prescribed temperature). The mechanical response was computed using the Timoshenko beam theory, where the E-modulus was evaluated as a combination of the E-modulus in the top flange, bottom flange and web. These moduli take different values as they are temperature-dependent (the reduction of the G-modulus with temperature was also considered). The mathematical model was validated using the experimental results reported in Correia (2008) and, according to the authors, the modelling approach is applicable to structural GFRP profiles incorporating either passive or active fire protection systems.

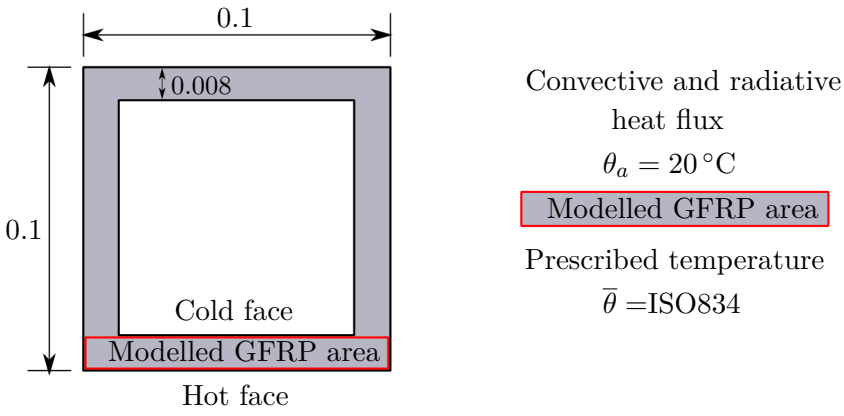

(a) Complete geometry. (b) Geometry modelled.

Figure 2.12: GFRP cross section modelled in Bai *et al.* (2010).

The previous one-dimensional heat transfer model was later extended to a two dimensional heat transfer model with the work of Fernandes (2009). A finite element formulation using a commercial software was presented to reproduce the thermal behaviour of the GFRP profiles tested by Correia (2008). The complete square tubular section was modelled considering the following boundary conditions: (i) convective and radiative heat fluxes in the bottom and top face of the cross section, and (ii) radiative heat flux on the walls of the cavity. Hence, in this work no convective heat flux was considered in the cavity. The dissertation also presents an analysis of the thermophysical properties of the GFRP estimated through three analytical models: Samanta *et al.* (2004), Tracy (2005) and Bai *et al.* (2007). No mechanical analyses were carried out.

Kodur and Ahmed (2010) presented an investigation where the strategy adopted to simulate the thermal (2D) and mechanical (1D) behaviour of beams is similar to the one used in the present thesis. The paper presents a coupled mechanical and thermal FE model to evaluate the performance of concrete beams strengthened with carbon fibre-reinforced polymer (CFRP) laminates subjected to flexural loads and fire conditions. The thermal model consists of a two-dimensional FE code, where the thermophysical properties of the constituent materials are temperature-dependent. The heat transfer between the fire and the beam is modelled by considering convective and radiative heat flux. The mechanical model consists of a one-dimensional FE code that uses as input the temperature field computed previously with the thermal model. The strains on each material (concrete, steel and CFRP) are evaluated considering different phenomena, *e.g.*, mechanical loading, temperature gradient in the cross sections, creep and transient effects. Subsequently, the stresses and the resultant forces in each element are computed and used to check the force equilibrium. An iterative procedure is repeated until equilibrium, compatibility and convergence criteria are satisfied. The model does not include the relative slip between concrete and CFRP or between concrete and steel rebars. The numerical results were compared with experimental data and a very good agreement was reported.

2.5 Concluding remarks

The literature review shows that the experimental and numerical study of the fire performance of composites is a complex task. Comprehensive mathematical models that attempt to address all the thermal, mechanical and chemical phenomena are still to be developed. Nevertheless, several models that consider some of those phenomena are available and can be classified as thermochemical, thermomechanical and post-fire mechanical models.

The literature also shows that a recent progress took place concerning the development of thermochemical and thermomechanical models to evaluate the fire behaviour of FRP composites. However, most of them assume that weakening is caused solely by matrix softening, not taking into account other damaging processes, *e.g.*, pore formation and delamination. Furthermore, most of the studies referred focus on the compressive behaviour without addressing in similar depth the tensile and shear responses. Hence, further analysis integrating all softening processes and thermally-induced strains involved in tensile, compressive and shear loading are to be developed.

Regarding the fire response of full-scale GFRP structural elements (as for example, beams, columns or slabs), very few studies presented results of fire resistance tests and the corresponding numerical simulations. Consequently, only a few thermomechanical models simulating the thermal and mechanical responses of GFRP structural elements were developed; they usually constitute simple thermal and mechanical models that, in general, are not able to reproduce the gross geometrical and thermal changes that occur under long fire exposures.

In the particular case of the thermomechanical simulation of tubular GFRP profiles, no thermal models that consider simultaneously the radiative and convective heat transfer in the cavity of the cross section were found. Most of the thermal models do not include important effects, such as the delamination and loss of reinforcement layers, that are relevant when beams or columns are exposed to fire during long periods. The mechanical models available are based on classical beam theories that do not include the geometrical nonlinearities of the deformation process and are not able to evaluate large displacements and rotations.

In the last years, an important increase in the use of GFRP profiles for civil engineering and buildings applications was observed. However, the (few) experimental data available indicates that unprotected GFRP structural components may present fire endurances below 30 minutes, this period of time being insufficient for most building applications. Hence, most of the literature reviewed point out the need of developing efficient fire protection systems in order to increase the use of these composites in building construction (Buchanan, 2002). In this sense, reliable mathematical models that enable the design of fire-protected FRP components still need to be developed, this being the main motivation and objective of the present thesis.

Chapter 3

Conduction heat transfer and radiative heat exchange between surfaces

3.1 Introduction

Heat transfer is a branch of the thermal sciences that studies the energy transport between material bodies due to a temperature gradient. The following concepts can be defined:

- Temperature: is a physical property of matter that quantitatively expresses the degree or intensity of heat present in a substance or object (adapted from Maxwell, 1972).
- Heat: form of energy that can be transferred from one system to another as a result of temperature difference (Çengel, 2003).

The mathematical modelling of the heat transfer process has been thoroughly explored in the past. The works of Kern (1950), Arpaci (1966), Patankar and Spalding (1972) or Holman (1986) describe the heat transfer processes (conduction, convection and radiation) and report the mathematical equations to quantify it.

The phenomenon of the radiative heat flux between walls was investigated by several authors and it proved to be a relevant way to exchange heat between solids. Detailed information about the radiative heat flux between walls can be found in the following references: Sparrow (1962), Holman (1986), Li (2006), Bergheau and Fortunier (2008), Reddy and Gartling (2010) and Lienhard IV and Lienhard V (2011).

The advancement of computers enabled the development of numerical methods in structural applications. The most commonly used were the finite difference method (FDM) and the finite element method (FEM) and both were quickly extended to non-structural applications, as the heat transfer analyses. However, due to the difficulties in using the FDM in irregular geometries and in unusual boundary conditions, many scientists continued to prefer the FEM. The works of, for example, Bathe (1996), Zienkiewicz *et al.* (2005a), Lewis *et al.* (2004), Hughes (2000) and Reddy (2004b) contributed to the expansion of the FEM.

In the present chapter, the heat transfer modes and the corresponding quantification laws are presented. The finite element formulation developed in the present thesis to

solve heat transfer problems in a solid is reported. Furthermore, the particular radiative exchange between the walls of an enclosed cavity is analysed.

Numerical applications are presented to illustrate the notions introduced to simulate steady state and transient heat transfer. The finite element code is verified by comparing the solutions computed with the analytical solutions of the problem or with numerical results available in the literature or calculated using a commercial FE software.

3.2 Modes of heat transfer and physical laws

3.2.1 Conduction

Conduction is the heat transfer mode that occurs when a temperature gradient exists in a body. Conduction can be defined as the transfer of energy from the more energetic particles to the less energetic particles of a substance due to interactions between them: higher temperatures are associated with higher molecular energies, and when neighbouring molecules collide an energy transfer occurs.

The heat transfer rate by conduction is proportional to the thermal gradient and it can be calculated with *Fourier's law*, which is expressed for the i-direction as follows,

$$q_i = -k_{ij} \frac{\partial \theta}{\partial x_j} \tag{3.1}$$

where q_i is the heat flux in the i-direction, k_{ij} are the conductivity tensor components and $\partial\theta/\partial x_j$ is the temperature gradient in the j-direction. The minus sign in equation (3.1) is a consequence of the fact that heat is transferred in the direction of decreasing temperatures (*i.e.*, from higher to lower temperatures).

The thermal conductivity is a positive material property that represents the material's ability to conduct heat (*i.e.*, materials with high thermal conductivity will transfer large amounts of heat over time and they are called *good thermal conductors* and materials with low thermal conductivity will transfer small amounts of heat over time, being known as *poor thermal conductors* or *insulators*). This property depends on the type of material and it can change as a function of temperature.

3.2.2 Convection

The definition of convection is given by Lewis *et al.* (2004) as follows:

> *The transfer of heat from one region to another, due to such macroscopic motion in a liquid or gas, added to the energy transfer by conduction within the fluid, is called heat transfer by convection.*

The convection heat transfer mode comprises two mechanisms: diffusion (due to random molecular motion) and advection (due to macroscopic motion of the fluid). The following types of convection can occur:

- Free or natural: when fluid motion occurs because of a density variation caused, for example, due to pressure or temperature;
- Forced: when fluid motion is caused by an external force;
- Mixed: when natural and forced convection are present.

For convective heat transfer, the rate equation is given by the *Newton's law of cooling*,

$$q_h = h\ (\theta_a - \theta) \tag{3.2}$$

where q_h is the convective heat flux, h is the convection heat transfer coefficient, θ_a is the ambient temperature and θ is the body temperature.

The convection heat transfer coefficient is a physical property of the fluid — it depends on the viscosity and thermal properties of the fluid, as referred in Holman (1986) — and it is positive. This property is influenced by the surface geometry, the nature of the fluid motion and it may depend on the temperature, as indicated in Incropera *et al.* (2006) and Lienhard IV and Lienhard V (2011).

In equation (3.2), q_h is defined positive when the heat transfer is produced from the ambient to the body (*i.e.*, $\theta_a > \theta$).

3.2.3 Radiation

Thermal radiation refers to the energy emitted by matter that is at nonzero temperature. This energy is transported by electromagnetic waves in all directions.

The maximum flux that can be emitted by radiation from an ideal black-body is given by the *Stefan–Boltzmann's law*,

$$q_r(max) = \sigma\, \theta^4 \tag{3.3}$$

where $q_r(max)$ is the maximum radiative heat flux, σ is the Stefan–Boltzmann's constant[1] and θ is the body temperature.

The heat flux emitted by a real surface, q_r, is less than that emitted by a black surface and is given by,

$$q_r = \epsilon\, \sigma\, \theta^4 \tag{3.4}$$

where ϵ is a material property called emissivity, which provides a measure of how efficiently a surface emits energy compared to a black-body. It can be temperature-dependent and takes values in the range $0 \leq \epsilon \leq 1$.

The radiative net heat flux exchange between the solid and the ambient can be expressed as:

$$q_r = \epsilon\, \sigma\, \left(\theta_a^4 - \theta^4\right) \tag{3.5}$$

3.2.4 Heat radiation between surfaces

The heat flux due to the radiative heat interchange between two or more surfaces of a cavity is accounted using a new parameter called *radiosity*. Following Bahrami (2005), the radiosity, R, represents the *total emitted and reflected radiation leaving a surface*.

The radiative heat flux in a generic surface, e, can be expressed as,

$$q_R = -\frac{\epsilon^e}{1-\epsilon^e}\, \left(\sigma\ (\theta^e)^4 - R^e\right) \tag{3.6}$$

where θ^e, R^e and ϵ^e are, respectively, the temperature, the radiosity and the emissivity in the surface e.

[1] In the SI unit system, the value of the Stefan–Boltzmann's constant is usually expressed in watt, metre and Kelvin, taking a value of $\sigma = 5.669 \cdot 10^{-8}$ W/(m^2 K^4). In this case, the temperature of the body in equation (3.3) will be given in Kelvin.

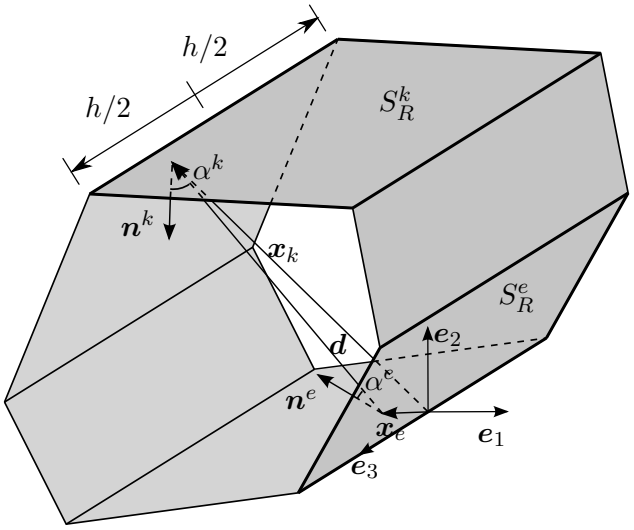

Figure 3.1: Schematic radiative exchanges among the surfaces of a cavity.

The radiosity in a gray[2] and diffuse[3] face is given by,

$$R^e = \sigma\,\epsilon^e\,(\theta^e)^4 + (1-\epsilon^e)\sum_{\substack{k=1\\k\neq e}}^{n}\int_{S_R^k} R^k\,\frac{\cos\alpha^e\cos\alpha^k}{\pi\,d^2}\,\mathrm{d}S_R^k \tag{3.7}$$

where the angles α^e and α^k are defined for two generic faces, e and k — schematically represented in figure 3.1 —, d is the distance from a point on S_R^e to a point on S_R^k and n is the number of surfaces that intervene in the interchange of radiative heat flux. It is useful to remark that the previous expression is valid for three-dimensional problems[4], being $\boldsymbol{d}$ the three-dimensional distance vector $\boldsymbol{d} = \boldsymbol{x}^k - \boldsymbol{x}^e$ and d its norm.

Equation (3.7) depends on the dimension of the space. Hence, in the following, two notations will be used to denominate the dimension of the element where the radiative heat exchange is applied: (i) S_R to surfaces and (ii) Γ_R to lines.

3.3 Heat transfer equation

The main objective of the conduction analysis is to determine the temperature distribution in a medium. Once this temperature distribution is known, the heat flux at any point may be computed from Fourier's law (3.1).

The heat transfer equation is obtained by applying the principle of conservation of the energy to a three-dimensional differential control volume considering the following hypotheses:

1. Homogeneous solid;

[2]A surface is gray when its properties are independent from the wavelength.

[3]A surface is diffuse when its properties are independent of the direction.

[4]In the present thesis a two-dimensional heat transfer formulation is discussed. Hence, in the next sections, the radiosity expression will be particularized for the two-dimensional space.

2. constant density and specific heat transfer in the volume;
3. continuous medium.

The heat transfer equation is given by,

$$-\operatorname{div} \boldsymbol{q} + G = \rho\, c_p \frac{\partial \theta}{\partial t} \tag{3.8}$$

where $\boldsymbol{q}$ is the heat flux vector, G is the heat generation per unit volume and time, ρ is the density of the material and c_p is the specific heat, which, similarly to density, depends on the material and can vary with the temperature and space. The heat generation constant will be positive when the body generates heat and negative when the body consumes it.

The heat flux $\boldsymbol{q}$ given by the Fourier's law (3.1) can be rewritten as,

$$\boldsymbol{q} = -\boldsymbol{D}\, \boldsymbol{\nabla} \theta \tag{3.9}$$

where $\boldsymbol{D}$ is the conductivity matrix that gathers the conductivity coefficients and $\boldsymbol{\nabla}$ is the gradient differential operator.

The divergence of a generic vector, $\operatorname{div} \boldsymbol{f}$, is defined using the Einstein's summation notation as:

$$\operatorname{div} \boldsymbol{f} = f_{i,i} \tag{3.10}$$

The notation $f_{i,i} = (f_i)_{,i}$ is introduced to represent the partial derivative of the i^{th} component of a generic vector with respect to the i^{th} coordinate of the cartesian reference system, $\frac{\partial f_i}{\partial x_i}$, defined with the base of vectors $\boldsymbol{e}_i$.

Considering the Fourier's law (3.1) and taking the notation $\dot{\theta} = \frac{\partial \theta}{\partial t}$, the *heat transfer equation* becomes:

$$\frac{\partial}{\partial x_i}\left(k_{ij} \frac{\partial \theta}{\partial x_j}\right) + G = \rho\, c_p\, \dot{\theta} \tag{3.11}$$

The solution of the equation (3.11) provides the temperature distribution in the body and it can be particularized for the following cases when an isotropic material with constant thermal conductivity ($k = k_{ij}$) is considered:

- The transient heat transfer equation is known as the *Fourier-Biot equation*,

$$\nabla^2 \theta + \frac{G}{k} = \frac{1}{\alpha}\, \dot{\theta} \tag{3.12}$$

  where $\alpha{=}k/(\rho\, c_p)$ is the *thermal diffusivity* of the material (it represents the velocity of the heat propagation through a material) and ∇^2 is the Laplace operator defined, for a generic scalar field u, as:

$$\nabla^2 u = u_{,ii} \tag{3.13}$$

  If there is no heat generation ($G = 0$), the previous equation is called the *diffusion equation* and renders:

$$\nabla^2 \theta = \frac{1}{\alpha}\, \dot{\theta} \tag{3.14}$$

- The steady state heat transfer is known as *Poisson equation* and is given by,

$$\nabla^2 \theta + \frac{G}{k} = 0 \tag{3.15}$$

  and when there is no heat generation ($G = 0$), the equation is referred to the *Laplace equation*:

$$\nabla^2 \theta = 0 \tag{3.16}$$

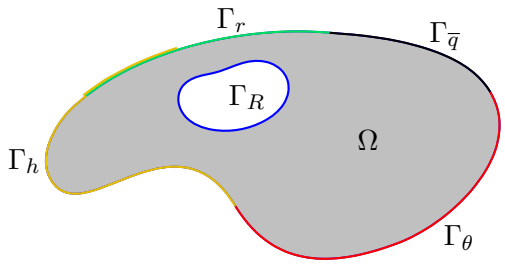

Figure 3.2: Boundary conditions of the heat transfer problem.

3.4 Strong form of the heat transfer problem

The heat transfer equation is a differential equation that requires boundary conditions and an initial condition to be solved.

If Ω is the domain of the solution and Γ is the boundary contour (figure 3.2), the following three types of boundary conditions can be defined:

- Dirichlet or essential condition: prescribed temperature on Γ_θ,

$$\theta = \overline{\theta} \qquad \text{on} \quad \Gamma_\theta \tag{3.17}$$

- Neumann or natural condition: prescribed heat flux on $\Gamma_{\overline{q}}$,

$$q_n = -\overline{q} \qquad \text{on} \quad \Gamma_{\overline{q}} \tag{3.18}$$

  where q_n is the heat flux in the n direction given by $q_n = q_i\, n_i$ and $\overline{q}$ is a heat flux in the normal direction. This constant can assume a positive or negative value, where the former means supplied heat and the latter subtracted heat.

- Robin condition: convective heat flux on Γ_h and/or radiative heat flux on Γ_r and radiative heat exchange between walls on Γ_R,

$$q_n = -h\,(\theta_a - \theta) \qquad \text{on} \quad \Gamma_h \tag{3.19}$$

$$q_n = -\epsilon\,\sigma\,(\theta_a^4 - \theta^4) \qquad \text{on} \quad \Gamma_r \tag{3.20}$$

$$q_n = \frac{\epsilon^e}{1-\epsilon^e}\left(\sigma\,(\theta^e)^4 - R^e\right) \qquad \text{on} \quad \Gamma_R \tag{3.21}$$

Hence, in the current problem, the boundary is expressed as $\Gamma = \Gamma_\theta \cup \Gamma_{q_n}$ such that $\Gamma_\theta \cap \Gamma_{q_n} = \emptyset$ and $\Gamma_{q_n} = \Gamma_{\overline{q}} \cup \Gamma_h \cup \Gamma_r \cup \Gamma_R$. The convective and radiative heat fluxes can simultaneously be present in the same contour, being possible that $\Gamma_h \cap \Gamma_r \neq \emptyset$.

The initial condition can be expressed as,

$$\theta_0 = \overline{\theta}_0 \qquad \text{in} \quad \Omega \quad \text{at} \quad t = t_0 \tag{3.22}$$

where t_0 is the reference time and $\overline{\theta}_0$ is the known initial temperature.

The strong form of the heat transfer problem is constituted by the nonlinear partial differential governing equation, the mentioned boundary conditions for the physical system and the initial condition.

The classical formulation of the strong form for the transient heat transfer problem[5] can be stated as,

,

Obtain $\theta \in \overline{\Omega}$ and $R \in \Gamma_R$ for each point $\boldsymbol{x} = x_i\,\boldsymbol{e}_i \in \overline{\Omega}$ and $t \in [t_0, t_f]$ such that:

$$-\operatorname{div}\boldsymbol{q} + G = \rho\, c_p\, \dot{\theta} \qquad \text{in } \Omega \tag{3.23a}$$
$$\theta = \overline{\theta} \qquad \text{on } \Gamma_\theta \tag{3.23b}$$
$$q_n + \overline{q} = 0 \qquad \text{on } \Gamma_{\overline{q}} \tag{3.23c}$$
$$q_n + h\,(\theta_a - \theta) = 0 \qquad \text{on } \Gamma_h \tag{3.23d}$$
$$q_n + \epsilon\,\sigma\,\left(\theta_a^4 - \theta^4\right) = 0 \qquad \text{on } \Gamma_r \tag{3.23e}$$
$$q_n - \frac{\epsilon}{1-\epsilon}\,\left(\sigma\,\theta^4 - R\right) = 0 \qquad \text{on } \Gamma_R \tag{3.23f}$$
$$\theta_0 = \overline{\theta}_0 \qquad \text{at } t = t_0 \quad \text{in } \overline{\Omega} \tag{3.23g}$$

where $\overline{\Omega} = \Omega \cup \Gamma$ is the closure of the domain, t_f is the final time.

3.5 Weak form

The weak form is the integral form of the strong formulation problem obtained by multiplying equations (3.23) by an arbitrary virtual function, $\delta\theta$, and integrating the result over the domains on which they hold:

$$\begin{aligned}\int_\Omega \delta\theta\left(-\operatorname{div}\boldsymbol{q} + G - \rho\, c_p\,\dot{\theta}\right)\,\mathrm{d}\Omega + \int_{\Gamma_{\overline{q}}} \delta\theta\,\left(q_n + \overline{q}\right)\,\mathrm{d}\Gamma_{\overline{q}} + \\ + \int_{\Gamma_h} \delta\theta\,\left(q_n + h\,\left(\theta_a - \theta\right)\right)\,\mathrm{d}\Gamma_h + \int_{\Gamma_r} \delta\theta\,\left(q_n + \epsilon\,\sigma\,\left(\theta_a^4 - \theta^4\right)\right)\,\mathrm{d}\Gamma_r + \\ + \int_{\Gamma_R} \delta\theta\,\left(q_n - \frac{\epsilon}{1-\epsilon}\,\left(\sigma\,\theta^4 - R\right)\right)\,\mathrm{d}\Gamma_R = 0\end{aligned} \tag{3.24}$$

Considering that θ and $\delta\theta$ are differentiable with respect to the space and applying the divergence theorem and the integration by parts rule in equation (3.24), the final expression of the weak form is obtained:

$$\begin{aligned}\int_\Omega \left(\boldsymbol{\nabla}\delta\theta\cdot\,\boldsymbol{q} - \delta\theta\,\rho\, c_p\,\dot{\theta}\right)\,\mathrm{d}\Omega + \int_\Omega \delta\theta\, G\,\mathrm{d}\Omega + \int_{\Gamma_{\overline{q}}} \delta\theta\,\overline{q}\,\mathrm{d}\Gamma_{\overline{q}} + \int_{\Gamma_h} \delta\theta\, h\,\left(\theta_a - \theta\right)\,\mathrm{d}\Gamma_h + \\ + \int_{\Gamma_r} \delta\theta\,\epsilon\,\sigma\,\left(\theta_a^4 - \theta^4\right)\,\mathrm{d}\Gamma_r + \int_{\Gamma_R} \delta\theta\,\frac{\epsilon}{1-\epsilon}\,\left(\sigma\,\theta^4 - R\right)\,\mathrm{d}\Gamma_R = 0\end{aligned} \tag{3.25}$$

Further information about the operations carried out can be consulted in appendix A.1. In the previous expression, the thermophysical properties of the material (k_{ij}, ρ, c_p and ϵ) and the convective coefficient, h, may be temperature-dependent.

[5] The reader should notice that equation (3.7) is not included in the strong form of the problem even if it has to be solved together in assemblage with the governing equation.

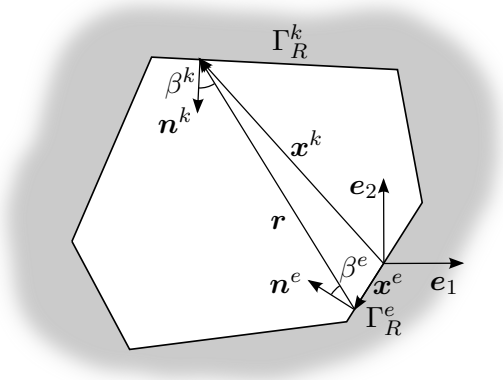

Figure 3.3: Schematic radiative exchanges between the edges of a cavity.

The weak form of the radiosity equation will be obtained considering that the current calculus surface is identified by e, while the remaining interacting surfaces (all the heat radiative interchange faces) are generically designated by k.

Multiplying equation (3.7) by an arbitrary virtual function, δR^e, dividing by $(1-\epsilon^e)$ and integrating the result over the surface S_R^e, the respective weak form is obtained:

$$\int_{S_R^e} \delta R^e \frac{R^e}{(1-\epsilon^e)}\,\mathrm{d}S_R^e = \int_{S_R^e} \delta R^e\,\sigma\,\frac{\epsilon^e}{(1-\epsilon^e)}\,(\theta^e)^4\,\mathrm{d}S_R^e + \\ + \sum_{\substack{k=1\\k\neq e}}^{n} \int_{S_R^e}\int_{S_R^k} \delta R^e\,R^k\,\frac{\cos\alpha^e\cos\alpha^k}{\pi\,d^2}\,\mathrm{d}S_R^k\,\mathrm{d}S_R^e \quad (3.26)$$

The particularization of equation (3.26) for a two-dimensional case can be consulted in appendix A.2 and renders,

$$\int_{\Gamma_R^e} \delta R^e \frac{R^e}{(1-\epsilon^e)}\,\mathrm{d}\Gamma_R^e = \int_{\Gamma_R^e} \delta R^e\,\sigma\,\frac{\epsilon^e}{(1-\epsilon^e)}\,(\theta^e)^4\,\mathrm{d}\Gamma_R^e + \\ + \sum_{\substack{k=1\\k\neq e}}^{n} \int_{\Gamma_R^e}\int_{\Gamma_R^k} \delta R^e\,R^k\,\frac{\cos\beta^e\cos\beta^k}{2\,r}\,\mathrm{d}\Gamma_R^k\,\mathrm{d}\Gamma_R^e \quad (3.27)$$

where r is the norm of the two-dimensional distance vector given by $\boldsymbol{r} = \boldsymbol{x}^k - \boldsymbol{x}^e$. Equation (3.27) is the weak form of the radiosity equation. Figure 3.3 shows schematically the radiative heat interchange among the edges of an arbitrary two-dimensional closed cavity.

The reader should observe that equation (3.27) is not a mechanical law and its origin is not a variational principle. As a consequence, the mentioned equation is not integrated by parts and no boundary conditions are associated to it. In the case the radiosity is constant over the surfaces, the expression (3.27) can be rewritten as,

$$\delta R^e \frac{R^e}{(1-\epsilon^e)} = \delta R^e\,\sigma\,\frac{\epsilon^e}{(1-\epsilon^e)}\,(\theta^e)^4 + \sum_{\substack{k=1\\k\neq e}}^{n} \delta R^e\,F^{ek}\,R^k \quad (3.28)$$

where F^{ek} is the *view factor*[6], which represents the proportion of radiation that leaves one surface and strikes another, and can be computes as,

$$F^{ek} = \frac{1}{\Gamma_R^e} \int_{\Gamma_R^e} \int_{\Gamma_R^k} \frac{\cos\beta^e \cos\beta^k}{2\,r} \, \mathrm{d}\Gamma_R^k \, \mathrm{d}\Gamma_R^e \tag{3.29}$$

or, in the case of closed two-dimensional cavities, using the geometrical expressions obtained by the *Hottel's crossed string method* (Bergheau and Fortunier, 2008). The advantage of equation (3.28) *vs.* equation (3.27) is that it is not necessary to compute the complicated integrals involving cosines, as the view factor can be obtained using geometrical expressions or a catalogue where its value is reported for different common configurations (Howell, 1982).

3.6 Spatial discretization and residual vector

In the finite element method, the domain $\overline{\Omega}$ is divided into a set of subdomains $\overline{\Omega}^{(\mathrm{e})} = \Omega^{(\mathrm{e})} \cup \Gamma^{(\mathrm{e})}$ called *finite elements*. Any geometric shape for which the approximation functions can be derived uniquely qualifies as an element.

The present formulation considers a two-dimensional domain and one-dimensional boundaries dicretized with standard 2D and 1D isoparametric finite elements, respectively.

The independent unknowns, *temperature* and *radiosity*, are approximated over a typical element, (e), by the following expressions,

$$\theta^{(e)} = \sum_{i=1}^{n} \psi_i \, \theta_i = \boldsymbol{\psi}_\theta^{(e)} \, \boldsymbol{\Theta}^{(e)} \qquad \text{in} \quad \Omega^{(e)} \tag{3.30a}$$

$$R^{(e)} = \sum_{i=1}^{m} \psi_i \, R_i = \boldsymbol{\psi}_R^{(e)} \, \mathbf{R}^{(e)} \qquad \text{on} \quad \Gamma_R^{(e)} \tag{3.30b}$$

and, consequently,

$$\delta\theta^{(e)} = \boldsymbol{\psi}_\theta^{(e)} \, \delta\boldsymbol{\Theta}^{(e)} \qquad \text{in} \quad \Omega^{(e)} \tag{3.31a}$$

$$\delta R^{(e)} = \boldsymbol{\psi}_R^{(e)} \, \delta\mathbf{R}^{(e)} \qquad \text{on} \quad \Gamma_R^{(e)} \tag{3.31b}$$

where $\boldsymbol{\Theta}^{(e)}$ and $\mathbf{R}^{(e)}$ are, respectively, the elemental nodal vector of temperatures and radiosities[7] , $\boldsymbol{\psi}_\theta^{(e)}(\xi_1, \xi_2) = \begin{bmatrix} \psi_1 & \psi_2 & \dots & \psi_n \end{bmatrix}$ is the matrix that gathers the two-dimensional nodal shape functions, defining n as the number of nodes of the element where the temperature is approximated and, finally, $\boldsymbol{\psi}_R^{(e)}(\xi_1) = \begin{bmatrix} \psi_1 & \psi_2 & \dots & \psi_m \end{bmatrix}$ is the matrix that gathers the one-dimensional nodal shape functions, being m the number of nodes of the side element where the radiosity is approximated. In the in-house code developed in this thesis, equal order shape functions are used to approximate both temperature and radiosity. Further information about the finite element method and the shape functions and their derivatives can be consulted in the appendixes B.1 and B.2 .

[6] It is also referred in the bibliography as *radiation form factor*, *shape factor*, *angle factor* and *configuration factor*.

[7] A notation conflict exists as, in this case, a capital letter is being used to define a vector and not a matrix.

In the following, it is assumed that the heat generation in the domain, the heat flux vector on the static boundary and the ambient temperature on the convective and radiative boundaries can be expressed over an element as,

$$G^{(e)} = \boldsymbol{\psi}_\theta^{(e)}\, \mathbf{g}^{(e)} \qquad \text{in} \quad \Omega^{(e)} \tag{3.32a}$$

$$\overline{q}^{(e)} = \boldsymbol{\psi}_\theta^{(e)}\, \overline{\mathbf{q}}^{(e)} \qquad \text{on} \quad \Gamma_{\overline{q}}^{(e)} \tag{3.32b}$$

$$\theta_a^{(e)} = \boldsymbol{\psi}_\theta^{(e)}\, \boldsymbol{\theta}_a{}^{(e)} \qquad \text{on} \quad \Gamma_h^{(e)} \cup \Gamma_r^{(e)} \tag{3.32c}$$

where $\mathbf{g}^{(e)}$, $\overline{\mathbf{q}}^{(e)}$ and $\boldsymbol{\theta}_a{}^{(e)}$ are the nodal values of $G^{(e)}$, $\overline{q}^{(e)}$ and $\theta_a^{(e)}$, respectively. Replacing the mentioned spatial discretizations into the weak form (3.25) of the heat transfer problem one obtains, term by term,

$$\int_{\Omega^{(e)}} \boldsymbol{\nabla}\delta\theta^{(e)} \cdot \boldsymbol{q}^{(e)}\, \mathrm{d}\Omega^{(e)} = -\delta\boldsymbol{\theta}^{(e)T} \int_{\Omega^{(e)}} \mathbf{B}_\theta^{(e)T} \mathbf{D}\, \mathbf{B}_\theta^{(e)}\, \mathrm{d}\Omega^{(e)}\, \boldsymbol{\theta}^{(e)} \tag{3.33a}$$

$$-\int_{\Omega^{(e)}} \delta\theta^{(e)}\, \rho\, c_p\, \dot{\theta}^{(e)}\, \mathrm{d}\Omega^{(e)} = -\delta\boldsymbol{\theta}^{(e)T} \int_{\Omega^{(e)}} \boldsymbol{\psi}_\theta^{(e)T} \rho\, c_p\, \boldsymbol{\psi}_\theta^{(e)}\, \mathrm{d}\Omega^{(e)}\, \dot{\boldsymbol{\theta}}^{(e)} \tag{3.33b}$$

$$\int_{\Omega^{(e)}} \delta\theta^{(e)}\, G^{(e)}\, \mathrm{d}\Omega^{(e)} = \delta\boldsymbol{\theta}^{(e)T} \int_{\Omega^{(e)}} \boldsymbol{\psi}_\theta^{(e)T} \boldsymbol{\psi}_\theta^{(e)}\, \mathrm{d}\Omega^{(e)}\, \mathbf{g}^{(e)} \tag{3.33c}$$

$$\int_{\Gamma_{\overline{q}}^{(e)}} \delta\theta^{(e)}\, \overline{q}^{(e)}\, \mathrm{d}\Gamma_{\overline{q}}^{(e)} = \delta\boldsymbol{\theta}^{(e)T} \int_{\Gamma_{\overline{q}}^{(e)}} \boldsymbol{\psi}_\theta^{(e)T} \boldsymbol{\psi}_\theta^{(e)}\, \mathrm{d}\Gamma_{\overline{q}}^{(e)}\, \overline{\mathbf{q}}^{(e)} \tag{3.33d}$$

$$\int_{\Gamma_h^{(e)}} \delta\theta^{(e)}\, h\, \left(\theta_a^{(e)} - \theta^{(e)}\right) \mathrm{d}\Gamma_h^{(e)} = \delta\boldsymbol{\theta}^{(e)T} \int_{\Gamma_h^{(e)}} \boldsymbol{\psi}_\theta^{(e)T}\, h\, \boldsymbol{\psi}_\theta^{(e)} \left(\boldsymbol{\theta}_a^{(e)} - \boldsymbol{\theta}^{(e)}\right) \mathrm{d}\Gamma_h^{(e)} \tag{3.33e}$$

$$\begin{aligned} &\int_{\Gamma_r^{(e)}} \delta\theta^{(e)}\, \epsilon\, \sigma\, \left(\theta_a^{(e)4} - \theta^{(e)4}\right) \mathrm{d}\Gamma_r^{(e)} = \\ &\qquad = \delta\boldsymbol{\theta}^{(e)T} \int_{\Gamma_r^{(e)}} \epsilon\, \sigma\, \boldsymbol{\psi}_\theta^{(e)T} \left(\left(\boldsymbol{\psi}_\theta \boldsymbol{\theta}_a^{(e)}\right)^4 - \left(\boldsymbol{\psi}_\theta^{(e)} \boldsymbol{\theta}^{(e)}\right)^4\right) \mathrm{d}\Gamma_r^{(e)} \end{aligned} \tag{3.33f}$$

$$\begin{aligned} &\int_{\Gamma_R^{(e)}} \delta\theta^{(e)}\, \frac{\epsilon}{1-\epsilon} \left(\sigma\, \theta^{(e)4} - R^{(e)}\right) \mathrm{d}\Gamma_R^{(e)} = \\ &\qquad = \delta\boldsymbol{\theta}^{(e)T} \int_{\Gamma_R^{(e)}} \frac{\epsilon}{1-\epsilon}\, \boldsymbol{\psi}_\theta^{(e)T} \left(\sigma\, \left(\boldsymbol{\psi}_\theta^{(e)}\, \boldsymbol{\theta}^{(e)}\right)^4 - \boldsymbol{\psi}_R^{(e)}\, \mathbf{R}^{(e)}\right) \mathrm{d}\Gamma_R^{(e)} \end{aligned} \tag{3.33g}$$

where $\mathbf{D}$ is the conductivity matrix in a two-dimensional space and $\mathbf{B}_\theta^{(e)}$ gathers the derivative of the shape functions with respect to the space coordinates. They are defined as:

$$\mathbf{D} = \begin{bmatrix} k_{11} & 0 \\ 0 & k_{22} \end{bmatrix} \tag{3.34a}$$

$$\boldsymbol{\nabla}^T = \begin{Bmatrix} \partial/\partial x_1 & \partial/\partial x_2 \end{Bmatrix} \tag{3.34b}$$

$$\mathbf{B}_\theta^{(e)} = \boldsymbol{\nabla}\, \boldsymbol{\psi}_\theta^{(e)} = \begin{bmatrix} \psi_{1,1} & \psi_{2,1} & \cdots & \psi_{n,1} \\ \psi_{1,2} & \psi_{2,2} & \cdots & \psi_{n,2} \end{bmatrix} \tag{3.34c}$$

Similarly, the spatial discretization of the temperature and radiosity will be replaced into the weak form (3.27) of the radiosity weak form equation and, term by term, one

obtains:

$$\int_{\Gamma_R^{(e)}} \delta R^{(e)} \frac{1}{1-\epsilon} R^{(e)} \, \mathrm{d}\Gamma_R^{(e)} = \delta \mathbf{R}^{(e)T} \int_{\Gamma_R^{(e)}} \frac{1}{1-\epsilon} \boldsymbol{\psi}_R^{(e)T} \boldsymbol{\psi}_R^{(e)} \, \mathrm{d}\Gamma_R^{(e)} \, \mathbf{R}^{(e)} \tag{3.35a}$$

$$\begin{aligned} -\int_{\Gamma_R^{(e)}} \int_{\Gamma_R^{(k)}} \delta R^{(e)} \, R^{(k)} \, \frac{\cos\beta^{(e)} \cos\beta^{(k)}}{2\,r} \, \mathrm{d}\Gamma_R^{(k)} \, \mathrm{d}\Gamma_R^{(e)} = \\ = -\delta \mathbf{R}^{(e)T} \int_{\Gamma_R^{(e)}} \boldsymbol{\psi}_R^{(e)T} \int_{\Gamma_R^{(k)}} \boldsymbol{\psi}_R^{(k)} \, \frac{\cos\beta^{(e)} \cos\beta^{(k)}}{2\,r} \, \mathrm{d}\Gamma_R^{(k)} \, \mathrm{d}\Gamma_R^{(e)} \, \mathbf{R}^{(k)} \end{aligned} \tag{3.35b}$$

$$-\int_{\Gamma_R^{(e)}} \delta R^{(e)} \, \sigma \, \frac{\epsilon}{(1-\epsilon)} \, \theta^{(e)4} \, \mathrm{d}\Gamma_R^{(e)} = -\delta \mathbf{R}^{(e)T} \int_{\Gamma_R^{(e)}} \sigma \, \frac{\epsilon}{1-\epsilon} \, \boldsymbol{\psi}_R^{(e)T} \left(\boldsymbol{\psi}_\theta^{(e)} \, \boldsymbol{\theta}^{(e)} \right)^4 \mathrm{d}\Gamma_R^{(e)} \tag{3.35c}$$

Hence, the elemental weak form of both problems can be expressed as:

$$\begin{aligned} -\delta \boldsymbol{\theta}^{(e)T} \Bigg(& \int_{\Omega^{(e)}} \mathbf{B}_\theta^{(e)T} \mathbf{D} \, \mathbf{B}_\theta^{(e)} \, \mathrm{d}\Omega^{(e)} \, \boldsymbol{\theta}^{(e)} + \int_{\Omega^{(e)}} \boldsymbol{\psi}_\theta^{(e)T} \rho \, c_p \, \boldsymbol{\psi}_\theta^{(e)} \, \mathrm{d}\Omega^{(e)} \, \dot{\boldsymbol{\theta}}^{(e)} - \\ & - \int_{\Omega^{(e)}} \boldsymbol{\psi}_\theta^{(e)T} \boldsymbol{\psi}_\theta^{(e)} \, \mathrm{d}\Omega^{(e)} \, \mathbf{g}^{(e)} - \int_{\Gamma_{\overline{q}}^{(e)}} \boldsymbol{\psi}_\theta^{(e)T} \boldsymbol{\psi}_\theta^{(e)} \, \mathrm{d}\Gamma_{\overline{q}}^{(e)} \, \overline{\mathbf{q}}^{(e)} - \\ & - \int_{\Gamma_h^{(e)}} \boldsymbol{\psi}_\theta^{(e)T} \, h \, \boldsymbol{\psi}_\theta^{(e)} \left(\boldsymbol{\theta}_a^{(e)} - \boldsymbol{\theta}^{(e)} \right) \mathrm{d}\Gamma_h^{(e)} - \\ & - \int_{\Gamma_r^{(e)}} \epsilon \, \sigma \, \boldsymbol{\psi}_\theta^{(e)T} \left(\left(\boldsymbol{\psi}_\theta \boldsymbol{\theta}_a^{(e)} \right)^4 - \left(\boldsymbol{\psi}_\theta^{(e)} \boldsymbol{\theta}^{(e)} \right)^4 \right) \mathrm{d}\Gamma_r^{(e)} - \\ & - \int_{\Gamma_R^{(e)}} \frac{\epsilon}{1-\epsilon} \, \boldsymbol{\psi}_\theta^{(e)T} \left(\sigma \left(\boldsymbol{\psi}_\theta^{(e)} \, \boldsymbol{\theta}^{(e)} \right)^4 - \boldsymbol{\psi}_R^{(e)} \, \mathbf{R}^{(e)} \right) \mathrm{d}\Gamma_R^{(e)} \Bigg) = 0 \end{aligned} \tag{3.36a}$$

$$\begin{aligned} \delta \mathbf{R}^{(e)T} \Bigg(& \int_{\Gamma_R^{(e)}} \frac{1}{1-\epsilon} \, \boldsymbol{\psi}_R^{(e)T} \boldsymbol{\psi}_R^{(e)} \, \mathrm{d}\Gamma_R^{(e)} \, \mathbf{R}^{(e)} - \\ & - \sum_{\substack{k=1 \\ k \neq e}}^{n} \int_{\Gamma_R^{(e)}} \boldsymbol{\psi}_R^{(e)T} \int_{\Gamma_R^{(k)}} \boldsymbol{\psi}_R^{(k)} \, \frac{\cos\beta^{(e)} \cos\beta^{(k)}}{2\,r} \, \mathrm{d}\Gamma_R^{(k)} \, \mathrm{d}\Gamma_R^{(e)} \, \mathbf{R}^{(k)} - \\ & - \int_{\Gamma_R^{(e)}} \sigma \, \frac{\epsilon}{1-\epsilon} \, \boldsymbol{\psi}_R^{(e)T} \left(\boldsymbol{\psi}_\theta^{(e)} \, \boldsymbol{\theta}^{(e)} \right)^4 \mathrm{d}\Gamma_R^{(e)} \Bigg) = 0 \end{aligned} \tag{3.36b}$$

The equations (3.36) constitute a set of nonlinear equations that will be solved following a coupled scheme. Since $\delta\boldsymbol{\theta}^{(e)}$ and $\delta\mathbf{R}^{(e)}$ are arbitrary nodal vectors, the only possible solution is,

$$\mathbf{r}^{(e)} = \mathbf{0} \tag{3.37}$$

where $\mathbf{r}^{(e)}$ is the elemental residual vector given by,

$$\mathbf{r}^{(e)} = \begin{Bmatrix} \mathbf{r}_\theta^{(e)} \\ \mathbf{r}_R^{(e)} \end{Bmatrix} \tag{3.38}$$

and its components are:

$$\begin{aligned}\mathbf{r}_\theta^{(e)} = &\int_{\Omega^{(e)}} \mathbf{B}_\theta^{(e)T}\mathbf{D}\,\mathbf{B}_\theta^{(e)}\,\mathrm{d}\Omega^{(e)}\,\boldsymbol{\theta}^{(e)} + \int_{\Omega^{(e)}} \boldsymbol{\psi}_\theta^{(e)T}\rho\,c_p\,\boldsymbol{\psi}_\theta^{(e)}\,\mathrm{d}\Omega^{(e)}\,\dot{\boldsymbol{\theta}}^{(e)} - \\ &- \int_{\Omega^{(e)}} \boldsymbol{\psi}_\theta^{(e)T}\boldsymbol{\psi}_\theta^{(e)}\,\mathrm{d}\Omega^{(e)}\,\mathbf{g}^{(e)} - \int_{\Gamma_{\overline{q}}^{(e)}} \boldsymbol{\psi}_\theta^{(e)T}\boldsymbol{\psi}_\theta^{(e)}\,\mathrm{d}\Gamma_{\overline{q}}^{(e)}\,\overline{\mathbf{q}}^{(e)} - \\ &- \int_{\Gamma_h^{(e)}} \boldsymbol{\psi}_\theta^{(e)T}\,h\,\boldsymbol{\psi}_\theta^{(e)}\,\mathrm{d}\Gamma_h^{(e)}\,\left(\boldsymbol{\theta}_a^{(e)} - \boldsymbol{\theta}^{(e)}\right) - \\ &- \int_{\Gamma_r^{(e)}} \epsilon\,\sigma\,\boldsymbol{\psi}_\theta^{(e)T}\left(\left(\boldsymbol{\psi}_\theta\boldsymbol{\theta}_a^{(e)}\right)^4 - \left(\boldsymbol{\psi}_\theta^{(e)}\boldsymbol{\theta}^{(e)}\right)^4\right)\mathrm{d}\Gamma_r^{(e)} - \\ &- \int_{\Gamma_R^{(e)}} \frac{\epsilon}{1-\epsilon}\,\boldsymbol{\psi}_\theta^{(e)T}\left(\sigma\,\left(\boldsymbol{\psi}_\theta^{(e)}\,\boldsymbol{\theta}^{(e)}\right)^4 - \boldsymbol{\psi}_R^{(e)}\,\mathbf{R}^{(e)}\right)\mathrm{d}\Gamma_R^{(e)}\end{aligned} \tag{3.39a}$$

$$\begin{aligned}\mathbf{r}_R^{(e)} = &\int_{\Gamma_R^{(e)}} \frac{1}{1-\epsilon}\,\boldsymbol{\psi}_R^{(e)T}\boldsymbol{\psi}_R^{(e)}\,\mathrm{d}\Gamma_R^{(e)}\,\mathbf{R}^{(e)} - \\ &- \sum_{\substack{k=1\\k\neq e}}^{n} \int_{\Gamma_R^{(e)}} \boldsymbol{\psi}_R^{(e)T}\int_{\Gamma_R^{(k)}} \boldsymbol{\psi}_R^{(k)}\,\frac{\cos\beta^{(e)}\cos\beta^{(k)}}{2\,r}\,\mathrm{d}\Gamma_R^{(k)}\,\mathrm{d}\Gamma_R^{(e)}\,\mathbf{R}^{(k)} - \\ &- \int_{\Gamma_R^{(e)}} \sigma\,\frac{\epsilon}{1-\epsilon}\,\boldsymbol{\psi}_R^{(e)T}\left(\boldsymbol{\psi}_\theta^{(e)}\,\boldsymbol{\theta}^{(e)}\right)^4\,\mathrm{d}\Gamma_R^{(e)}\end{aligned} \tag{3.39b}$$

Hence, the elemental set of nonlinear differential equations (3.37) can be written in the following matrix form,

$$\begin{bmatrix}\mathbf{M}^{(e)} & \mathbf{O} & \cdots & \mathbf{O}\\ \mathbf{O} & \mathbf{O} & \cdots & \mathbf{O}\end{bmatrix}\begin{Bmatrix}\dot{\boldsymbol{\theta}}^{(e)}\\ \dot{\mathbf{R}}^{(1)}\\ \vdots\\ \dot{\mathbf{R}}^{(n)}\end{Bmatrix} + \\ + \begin{bmatrix}\mathbf{K}^{(e)} & \mathbf{O} & \cdots & \mathbf{O}\\ \mathbf{O} & \mathbf{K}_R^{(1)} & \cdots & \mathbf{K}_R^{(n)}\end{bmatrix}\begin{Bmatrix}\boldsymbol{\theta}^{(e)}\\ \mathbf{R}^{(1)}\\ \vdots\\ \mathbf{R}^{(n)}\end{Bmatrix} - \begin{Bmatrix}\mathbf{f}^{(e)}\\ \mathbf{f}_R^{(1)}\\ \vdots\\ \mathbf{f}_R^{(n)}\end{Bmatrix} = \begin{Bmatrix}\mathbf{0}\\ \mathbf{0}\\ \vdots\\ \mathbf{0}\end{Bmatrix} \tag{3.40}$$

where $\mathbf{K}^{(e)}$ is the conductivity matrix, $\mathbf{M}^{(e)}$ is the capacitance matrix, $\mathbf{K}_R^{(e)}$ is the radiosity matrix, $\mathbf{f}^{(e)}$ is the nodal equivalent heat flux vector and $\mathbf{f}_R^{(e)}$ is the nodal radiative heat flux between the faces of the element. They can be expressed as:

$$\mathbf{K}^{(e)} = \int_{\Omega^{(e)}} \mathbf{B}_\theta^{(e)T}\,\mathbf{D}\,\mathbf{B}_\theta^{(e)}\,\mathrm{d}\Omega^{(e)} \tag{3.41a}$$

$$\mathbf{M}^{(e)} = \int_{\Omega^{(e)}} \boldsymbol{\psi}_\theta^{(e)T}\,\rho\,c_p\,\boldsymbol{\psi}_\theta^{(e)}\,\mathrm{d}\Omega^{(e)} \tag{3.41b}$$

$$\mathbf{K}_R^{(k)} = \begin{cases}\displaystyle\int_{\Gamma_R^{(e)}} \frac{1}{1-\epsilon}\,\boldsymbol{\psi}_R^{(e)T}\,\boldsymbol{\psi}_R^{(e)}\,\mathrm{d}\Gamma_R^{(e)} & \text{if } k = e\\ \displaystyle -\int_{\Gamma_R^{(e)}} \boldsymbol{\psi}_R^{(e)T}\int_{\Gamma_R^{(k)}} \boldsymbol{\psi}_R^{(k)}\,\frac{\cos\beta^{(e)}\cos\beta^{(k)}}{2\,r}\,\mathrm{d}\Gamma_R^{(k)}\,\mathrm{d}\Gamma_R^{(e)} & \text{if } k \neq e\end{cases} \tag{3.41c}$$

$$\begin{aligned}\mathbf{f}^{(e)} = &\int_{\Omega^{(e)}} \boldsymbol{\psi}_\theta^{(e)T}\boldsymbol{\psi}_\theta^{(e)}\,\mathrm{d}\Omega^{(e)}\,\mathbf{g}^{(e)} + \int_{\Gamma_{\overline{q}}^{(e)}} \boldsymbol{\psi}_\theta^{(e)T}\boldsymbol{\psi}_\theta^{(e)}\,\mathrm{d}\Gamma_{\overline{q}}^{(e)}\,\overline{\mathbf{q}}^{(e)} + \\ &+ \int_{\Gamma_h^{(e)}} \boldsymbol{\psi}_\theta^{(e)T}\,h\,\boldsymbol{\psi}_\theta^{(e)}\,\mathrm{d}\Gamma_h^{(e)}\,\left(\boldsymbol{\theta}_a^{(e)} - \boldsymbol{\theta}^{(e)}\right) + \\ &+ \int_{\Gamma_r^{(e)}} \epsilon\,\sigma\,\boldsymbol{\psi}_\theta^{(e)T}\left(\left(\boldsymbol{\psi}_\theta\boldsymbol{\theta}_a^{(e)}\right)^4 - \left(\boldsymbol{\psi}_\theta^{(e)}\boldsymbol{\theta}^{(e)}\right)^4\right)\mathrm{d}\Gamma_r^{(e)} + \\ &+ \int_{\Gamma_R^{(e)}} \frac{\epsilon}{1-\epsilon}\,\boldsymbol{\psi}_\theta^{(e)T}\left(\sigma\,\left(\boldsymbol{\psi}_\theta^{(e)}\,\boldsymbol{\theta}^{(e)}\right)^4 - \boldsymbol{\psi}_R^{(e)}\,\mathbf{R}^{(e)}\right)\mathrm{d}\Gamma_R^{(e)}\end{aligned} \tag{3.41d}$$

$$\mathbf{f}_R^{(k)} = \begin{cases} \int_{\Gamma_R^{(e)}} \sigma\,\frac{\epsilon}{1-\epsilon}\,\boldsymbol{\psi}_R^{(e)T}\,\left(\boldsymbol{\psi}_\theta^{(e)}\,\boldsymbol{\theta}^{(e)}\right)^4\,\mathrm{d}\Gamma_R^{(e)} & \text{if } k = e \\ \mathbf{0} & \text{if } k \neq e \end{cases} \tag{3.41e}$$

By replacing the temporal discretization of $\dot{\boldsymbol{\theta}}^{(e)}$ (see expression (B.13) in appendix B.3) into equation (3.38), the residual vector for the instant $(t+\Delta t)$ is given by,

$$\mathbf{r}^{(e)t+\Delta t} = \begin{Bmatrix} \mathbf{r}_\theta^{(e)t+\Delta t} \\ \mathbf{r}_R^{(e)t+\Delta t} \end{Bmatrix} \tag{3.42}$$

where:

$$\begin{aligned}\mathbf{r}_\theta^{(e)t+\Delta t} = &\int_{\Omega^{(e)}} \Big(\mathbf{B}_\theta^{(e)T}\mathbf{D}^{t+\Delta t}\mathbf{B}_\theta^{(e)}\,\boldsymbol{\theta}^{(e)t+\Delta t} + \\ &+ \rho^{t+\Delta t}\,c_p^{t+\Delta t}\,\boldsymbol{\psi}_\theta^{(e)T}\,\boldsymbol{\psi}_\theta^{(e)}\,\frac{1}{\gamma\,\Delta t}\left(\boldsymbol{\theta}^{(e)t+\Delta t} - \boldsymbol{\theta}^{(e)t} - (1-\gamma)\,\Delta t\,\dot{\boldsymbol{\theta}}^{(e)t}\right)\Big)\,\mathrm{d}\Omega^{(e)} - \\ &- \Bigg[\int_{\Omega^{(e)}} \boldsymbol{\psi}_\theta^{(e)T}\boldsymbol{\psi}_\theta^{(e)}\,\mathrm{d}\Omega^{(e)}\,\mathbf{g}^{(e)t+\Delta t} + \int_{\Gamma_{\overline{q}}^{(e)}} \boldsymbol{\psi}_\theta^{(e)T}\boldsymbol{\psi}_\theta^{(e)}\,\mathrm{d}\Gamma_{\overline{q}}^{(e)}\,\overline{\mathbf{q}}^{(e)t+\Delta t} + \\ &+ \int_{\Gamma_h^{(e)}} \boldsymbol{\psi}_\theta^{(e)T}\,h^{t+\Delta t}\,\boldsymbol{\psi}_\theta^{(e)}\,\mathrm{d}\Gamma_h^{(e)}\,\left(\boldsymbol{\theta}_a^{(e)t+\Delta t} - \boldsymbol{\theta}^{(e)t+\Delta t}\right) + \\ &+ \int_{\Gamma_r^{(e)}} \epsilon^{t+\Delta t}\,\sigma\,\boldsymbol{\psi}_\theta^{(e)T}\left(\left(\boldsymbol{\psi}_\theta\boldsymbol{\theta}_a^{(e)t+\Delta t}\right)^4 - \left(\boldsymbol{\psi}_\theta^{(e)}\boldsymbol{\theta}^{(e)t+\Delta t}\right)^4\right)\mathrm{d}\Gamma_r^{(e)}\Bigg] - \\ &- \int_{\Gamma_R^{(e)}} \frac{\epsilon^{t+\Delta t}}{1-\epsilon^{t+\Delta t}}\,\boldsymbol{\psi}_\theta^{(e)T}\left(\sigma\,\left(\boldsymbol{\psi}_\theta^{(e)}\,\boldsymbol{\theta}^{(e)t+\Delta t}\right)^4 - \boldsymbol{\psi}_R^{(e)}\,\mathbf{R}^{(e)t+\Delta t}\right)\mathrm{d}\Gamma_R^{(e)}\end{aligned} \tag{3.43a}$$

$$\begin{aligned}\mathbf{r}_R^{(e)t+\Delta t} = &\int_{\Gamma_R^{(e)}} \frac{1}{1-\epsilon^{t+\Delta t}}\,\boldsymbol{\psi}_R^{(e)T}\,\boldsymbol{\psi}_R^{(e)}\,\mathrm{d}\Gamma_R^{(e)}\,\mathbf{R}^{(e)t+\Delta t} - \\ &- \int_{\Gamma_R^{(e)}} \boldsymbol{\psi}_R^{(e)T} \int_{\Gamma_R^{(k)}} \boldsymbol{\psi}_R^{(k)}\,\frac{\cos\beta^{(e)}\cos\beta^{(k)}}{2\,r}\,\mathrm{d}\Gamma_R^{(k)}\,\mathrm{d}\Gamma_R^{(e)}\,\mathbf{R}^{(k)t+\Delta t} - \\ &- \int_{\Gamma_R^{(e)}} \sigma\,\frac{\epsilon^{t+\Delta t}}{1-\epsilon^{t+\Delta t}}\,\boldsymbol{\psi}_R^{(e)T}\,\left(\boldsymbol{\psi}_\theta^{(e)}\,\boldsymbol{\theta}^{(e)t+\Delta t}\right)^4\,\mathrm{d}\Gamma_R^{(e)}\end{aligned} \tag{3.43b}$$

The elemental transient system of nonlinear equations to solve can be written as,

$$\mathbf{r}^{(e)t+\Delta t} = \mathbf{0} \tag{3.44}$$

or in its matrix form:

$$\begin{bmatrix} -\frac{1-\gamma}{\gamma}\mathbf{M}^{(e)} & \mathbf{O} & \cdots & \mathbf{O} \\ \mathbf{O} & \mathbf{O} & \cdots & \mathbf{O} \end{bmatrix}^{t+\Delta t} \begin{Bmatrix} \dot{\boldsymbol{\theta}}^{(e)} \\ \dot{\mathbf{R}}^{(1)} \\ \vdots \\ \dot{\mathbf{R}}^{(n)} \end{Bmatrix}^{t} + \\ + \begin{bmatrix} -\frac{1}{\gamma\,\Delta t}\mathbf{M}^{(e)} & \mathbf{O} & \cdots & \mathbf{O} \\ \mathbf{O} & \mathbf{O} & \cdots & \mathbf{O} \end{bmatrix}^{t+\Delta t} \begin{Bmatrix} \boldsymbol{\theta}^{(e)} \\ \mathbf{R}^{(1)} \\ \vdots \\ \mathbf{R}^{(n)} \end{Bmatrix}^{t} + \\ + \begin{bmatrix} \mathbf{K}^{(e)} + \frac{1}{\gamma\,\Delta t}\mathbf{M}^{(e)} & \mathbf{O} & \cdots & \mathbf{O} \\ \mathbf{O} & \mathbf{K}_R^{(1)} & \cdots & \mathbf{K}_R^{(n)} \end{bmatrix}^{t+\Delta t} \begin{Bmatrix} \boldsymbol{\theta}^{(e)} \\ \mathbf{R}^{(1)} \\ \vdots \\ \mathbf{R}^{(n)} \end{Bmatrix}^{t+\Delta t} - \begin{Bmatrix} \mathbf{f}^{(e)} \\ \mathbf{f}_R^{(1)} \\ \vdots \\ \mathbf{f}_R^{(n)} \end{Bmatrix}^{t+\Delta t} = \begin{Bmatrix} \mathbf{0} \\ \mathbf{0} \\ \vdots \\ \mathbf{0} \end{Bmatrix} \tag{3.45}$$

The time derivative of the temperature and radiation at the initial time can be calculated particularizing the equation (3.40) for $t = 0$ and solving the resultant system of equations in terms of $\dot{\boldsymbol{\theta}}^{(e)}$ and $\dot{\mathbf{R}}^{(k)}$.

The global residual vector will be obtained by assembling (see appendix B.5) all the elemental ones and it will constitute the global system of nonlinear differential equations to be solved.

3.7 Solution of the nonlinear system of equations and tangent matrix

The global system of equations obtained in the previous section will be solved for the free degrees of freedom by using the Newton–Raphson method (see appendix B.6). In order to carry out this process, the tangent matrix of the problem has to be computed by differentiating the residual elemental vector with respect to the variables or by perturbing the weak form of the problem. In the present thesis, the latter case is presented considering that the perturbation of the variables and its time derivatives are given by,

$$\Delta\theta^{(e)} = \boldsymbol{\psi}_\theta^{(e)}\,\Delta\boldsymbol{\theta}^{(e)} \tag{3.46a}$$

$$\Delta R^{(e)} = \boldsymbol{\psi}_R^{(e)}\,\Delta\mathbf{R}^{(e)} \tag{3.46b}$$

$$\Delta\dot{\theta}^{(e)} = \boldsymbol{\psi}_\theta^{(e)}\,\Delta\dot{\boldsymbol{\theta}}^{(e)} \tag{3.46c}$$

$$\Delta\dot{R}^{(e)} = \boldsymbol{\psi}_R^{(e)}\,\Delta\dot{\mathbf{R}}^{(e)} \tag{3.46d}$$

and the perturbation of its variation by:

$$\Delta\delta\theta^{(e)} = 0 \tag{3.47a}$$

$$\Delta\delta R^{(e)} = 0 \tag{3.47b}$$

Hence, by perturbing the weak form (3.24), one obtains, term by term,

$$\Delta \int_{\Omega^{(e)}} \boldsymbol{\nabla}\delta\theta^{(e)} \cdot \boldsymbol{q}^{(e)} \, \mathrm{d}\Omega^{(e)} = -\delta\boldsymbol{\theta}^{(e)T} \int_{\Omega^{(e)}} \Big(\mathbf{B}_\theta^{(e)T} \, \mathbf{D} \, \mathbf{B}_\theta^{(e)} + \\ + \mathbf{B}_\theta^{(e)T} \, \frac{\partial \mathbf{D}}{\partial \theta} \, \mathbf{B}_\theta^{(e)} \, \boldsymbol{\theta}^{(e)} \, \boldsymbol{\psi}_\theta^{(e)} \Big) \, \mathrm{d}\Omega^{(e)} \, \Delta\boldsymbol{\theta}^{(e)} \tag{3.48a}$$

$$-\Delta \int_{\Omega^{(e)}} \delta\theta^{(e)} \, \rho \, c_p \, \dot{\theta}^{(e)} \, \mathrm{d}\Omega^{(e)} = -\delta\boldsymbol{\theta}^{(e)T} \int_{\Omega^{(e)}} \boldsymbol{\psi}_\theta^{(e)T} \rho \, c_p \, \boldsymbol{\psi}_\theta^{(e)} \, \mathrm{d}\Omega^{(e)} \, \Delta\dot{\boldsymbol{\theta}}^{(e)} - \\ - \delta\boldsymbol{\theta}^{(e)T} \int_{\Omega^{(e)}} \boldsymbol{\psi}_\theta^{(e)T} \left(\frac{\partial \rho}{\partial \theta} \, c_p \boldsymbol{\psi}_\theta^{(e)} \, \dot{\boldsymbol{\theta}}^{(e)} + \rho \, \frac{\partial c_p}{\partial \theta} \boldsymbol{\psi}_\theta^{(e)} \, \dot{\boldsymbol{\theta}}^{(e)} \right) \boldsymbol{\psi}_\theta^{(e)} \, \mathrm{d}\Omega^{(e)} \, \Delta\dot{\boldsymbol{\theta}}^{(e)} \tag{3.48b}$$

$$\Delta \int_{\Omega^{(e)}} \delta\theta^{(e)} \, G^{(e)} \, \mathrm{d}\Omega^{(e)} = 0 \tag{3.48c}$$

$$\Delta \int_{\Gamma_{\overline{q}}^{(e)}} \delta\theta^{(e)} \, \overline{q}^{(e)} \, \mathrm{d}\Gamma_{\overline{q}}^{(e)} = 0 \tag{3.48d}$$

$$\Delta \int_{\Gamma_h^{(e)}} \delta\theta^{(e)} \, h \, \left(\theta_a^{(e)} - \theta^{(e)} \right) \mathrm{d}\Gamma_h^{(e)} = \delta\boldsymbol{\theta}^{(e)T} \int_{\Gamma_h^{(e)}} \boldsymbol{\psi}_\theta^{(e)T} \, (-h + \\ + \frac{\partial h}{\partial \theta} \, \left(\boldsymbol{\psi}_\theta^{(e)} \boldsymbol{\theta}_a^{(e)} - \boldsymbol{\psi}_\theta^{(e)} \boldsymbol{\theta}^{(e)} \right) \Big) \, \boldsymbol{\psi}_\theta^{(e)} \, \mathrm{d}\Gamma_h^{(e)} \, \Delta\boldsymbol{\theta}^{(e)} \tag{3.48e}$$

$$\Delta \int_{\Gamma_r^{(e)}} \delta\theta^{(e)} \, \epsilon \, \sigma \, \left(\theta_a^{(e)4} - \theta^{(e)4} \right) \mathrm{d}\Gamma_r^{(e)} = \\ = \delta\boldsymbol{\theta}^{(e)T} \int_{\Gamma_r^{(e)}} \sigma \, \boldsymbol{\psi}_\theta^{(e)T} \, \left(\frac{\partial \epsilon}{\partial \theta} \, \left(\left(\boldsymbol{\psi}_\theta \boldsymbol{\theta}_a^{(e)} \right)^4 - \left(\boldsymbol{\psi}_\theta^{(e)} \boldsymbol{\theta}^{(e)} \right)^4 \right) - \\ - 4 \, \epsilon \, \left(\boldsymbol{\psi}_\theta \boldsymbol{\theta}_a^{(e)} \right)^3 \right) \boldsymbol{\psi}_\theta^{(e)} \, \mathrm{d}\Gamma_r^{(e)} \, \Delta\boldsymbol{\theta}^{(e)} \tag{3.48f}$$

$$\Delta \int_{\Gamma_R^{(e)}} \delta\theta^{(e)} \, \frac{\epsilon}{1-\epsilon} \, \left(\sigma \, \theta^{(e)4} - R^{(e)} \right) \mathrm{d}\Gamma_R^{(e)} = \\ = \delta\boldsymbol{\theta}^{(e)T} \int_{\Gamma_R^{(e)}} \boldsymbol{\psi}_\theta^{(e)T} \, \left(\frac{1}{(1-\epsilon)^2} \, \frac{\partial \epsilon}{\partial \theta} \, \left(\sigma \, \left(\boldsymbol{\psi}_\theta^{(e)} \, \boldsymbol{\theta}^{(e)} \right)^4 - \boldsymbol{\psi}_R^{(e)} \, \mathbf{R}^{(e)} \right) + \\ + \frac{\epsilon}{1-\epsilon} \, 4 \, \sigma \, \left(\boldsymbol{\psi}_\theta^{(e)} \, \boldsymbol{\theta}^{(e)} \right)^3 \Big) \, \boldsymbol{\psi}_\theta^{(e)} \, \mathrm{d}\Gamma_R^{(e)} \, \Delta\boldsymbol{\theta}^{(e)} - \\ - \delta\boldsymbol{\theta}^{(e)T} \int_{\Gamma_R^{(e)}} \boldsymbol{\psi}_\theta^{(e)T} \, \frac{\epsilon}{1-\epsilon} \, \boldsymbol{\psi}_R^{(e)} \, \mathrm{d}\Gamma_R^{(e)} \, \Delta\mathbf{R}^{(e)} \tag{3.48g}$$

and, in the same way, by perturbing the weak form (3.27) of the radiosity problem one obtains, term by term:

$$\Delta \int_{\Gamma_R^{(e)}} \delta R^{(e)} \frac{1}{1-\epsilon} \, R^{(e)} \, \mathrm{d}\Gamma_R^{(e)} = \delta\mathbf{R}^{(e)T} \int_{\Gamma_R^{(e)}} \frac{1}{1-\epsilon} \, \boldsymbol{\psi}_R^{(e)T} \, \boldsymbol{\psi}_R^{(e)} \, \mathrm{d}\Gamma_R^{(e)} \, \Delta\mathbf{R}^{(e)} + \\ + \delta\mathbf{R}^{(e)T} \int_{\Gamma_R^{(e)}} \boldsymbol{\psi}_R^{(e)T} \, \frac{1}{(1-\epsilon)^2} \, \frac{\partial \epsilon}{\partial \theta} \, \boldsymbol{\psi}_R^{(e)} \mathbf{R}^{(e)} \, \boldsymbol{\psi}_\theta^{(e)} \, \mathrm{d}\Gamma_R^{(e)} \, \Delta\boldsymbol{\theta}^{(e)} \tag{3.49a}$$

$$-\Delta \int_{\Gamma_R^{(e)}} \int_{\Gamma_R^{(k)}} \delta R^{(e)} \, R^{(k)} \, \frac{\cos\beta^{(e)} \cos\beta^{(k)}}{2\,r} \, \mathrm{d}\Gamma_R^{(k)} \, \mathrm{d}\Gamma_R^{(e)} = \\ = -\delta\mathbf{R}^{(e)T} \int_{\Gamma_R^{(e)}} \boldsymbol{\psi}_R^{(e)T} \int_{\Gamma_R^{(k)}} \boldsymbol{\psi}_R^{(k)} \, \frac{\cos\beta^{(e)} \cos\beta^{(k)}}{2\,r} \, \mathrm{d}\Gamma_R^{(k)} \, \mathrm{d}\Gamma_R^{(e)} \, \Delta\mathbf{R}^{(k)} \tag{3.49b}$$

$$-\Delta \int_{\Gamma_R^{(e)}} \delta R^{(e)}\, \sigma\, \frac{\epsilon}{1-\epsilon}\, \theta^{(e)4}\, \mathrm{d}\Gamma_R^{(e)} = -\delta \mathbf{R}^{(e)T} \int_{\Gamma_R^{(e)}} \sigma\, \boldsymbol{\psi}_R^{(e)T} \left(\frac{1}{(1-\epsilon)^2}\, \frac{\partial \epsilon}{\partial \theta} \left(\boldsymbol{\psi}_\theta^{(e)}\, \boldsymbol{\theta}^{(e)} \right)^4 + \right.$$
$$\left. +4\, \frac{\epsilon}{1-\epsilon} \left(\boldsymbol{\psi}_\theta^{(e)}\, \boldsymbol{\theta}^{(e)} \right)^3 \right) \boldsymbol{\psi}_\theta^{(e)}\, \mathrm{d}\Gamma_R^{(e)} \Delta \boldsymbol{\theta}^{(e)} \tag{3.49c}$$

The thermal properties of the materials and the convective coefficient are considered temperature-dependent and, consequently, they contribute to the computation of the tangent matrix while the prescribed heat flux, $\overline{q}^{(e)}$, and the volumetric heat source term, $G^{(e)}$, are not temperature-dependent.

The tangent matrix can be obtained using the expressions (3.48) and (3.49), which can be written in the matrix form, as follows,

$$\begin{Bmatrix} \delta \boldsymbol{\theta}^{(e)} \\ \delta \mathbf{R}^{(e)} \end{Bmatrix}^T \left(\begin{bmatrix} \frac{\partial \mathbf{r}_\theta^{(e)}}{\partial \dot{\boldsymbol{\theta}}^{(e)}} & \mathbf{O} & \cdots & \mathbf{O} \\ \mathbf{O} & \mathbf{O} & \cdots & \mathbf{O} \end{bmatrix} \begin{Bmatrix} \Delta \dot{\boldsymbol{\theta}}^{(e)} \\ \Delta \dot{\mathbf{R}}^{(1)} \\ \vdots \\ \Delta \dot{\mathbf{R}}^{(n)} \end{Bmatrix} + \right.$$
$$\left. + \begin{bmatrix} \frac{\partial \mathbf{r}_\theta^{(e)}}{\partial \boldsymbol{\theta}^{(e)}} & \frac{\partial \mathbf{r}_\theta^{(e)}}{\partial \mathbf{R}^{(1)}} & \cdots & \frac{\partial \mathbf{r}_\theta^{(e)}}{\partial \mathbf{R}^{(n)}} \\ \frac{\partial \mathbf{r}_R^{(e)}}{\partial \boldsymbol{\theta}^{(e)}} & \frac{\partial \mathbf{r}_R^{(e)}}{\partial \mathbf{R}^{(1)}} & \cdots & \frac{\partial \mathbf{r}_R^{(e)}}{\partial \mathbf{R}^{(n)}} \end{bmatrix} \begin{Bmatrix} \Delta \boldsymbol{\theta}^{(e)} \\ \Delta \mathbf{R}^{(1)} \\ \vdots \\ \Delta \mathbf{R}^{(n)} \end{Bmatrix} \right) \tag{3.50}$$

where:

$$\frac{\partial \mathbf{r}_\theta^{(e)}}{\partial \dot{\boldsymbol{\theta}}^{(e)}} = \int_{\Omega^{(e)}} \boldsymbol{\psi}_\theta^{(e)T}\, \rho\, c_p\, \boldsymbol{\psi}_\theta^{(e)}\, \mathrm{d}\Omega^{(e)} + \int_{\Omega^{(e)}} \boldsymbol{\psi}_\theta^{(e)T} \left(\frac{\partial \rho}{\partial \theta}\, c_p + \frac{\partial c_p}{\partial \theta}\, \rho \right) \boldsymbol{\psi}_\theta^{(e)} \dot{\boldsymbol{\theta}}^{(e)} \boldsymbol{\psi}_\theta^{(e)}\, \mathrm{d}\Omega^{(e)} \tag{3.51a}$$

$$\begin{aligned} \frac{\partial \mathbf{r}_\theta^{(e)}}{\partial \boldsymbol{\theta}^{(e)}} = {} & \int_{\Omega^{(e)}} \mathbf{B}_\theta^{(e)T}\, \frac{\partial \mathbf{D}}{\partial \theta}\, \mathbf{B}_\theta^{(e)}\, \boldsymbol{\theta}^{(e)}\, \boldsymbol{\psi}_\theta^{(e)}\, \mathrm{d}\Omega^{(e)} + \int_{\Omega^{(e)}} \mathbf{B}_\theta^{(e)T}\, \mathbf{D}\, \mathbf{B}_\theta^{(e)}\, \mathrm{d}\Omega^{(e)} - \\ & - \left[\int_{\Gamma_h^{(e)}} \boldsymbol{\psi}_\theta^{(e)T}\, \frac{\partial h}{\partial \theta}\, \boldsymbol{\psi}_\theta^{(e)} \left(\boldsymbol{\psi}_\theta^{(e)} \boldsymbol{\theta}_a^{(e)} - \boldsymbol{\psi}_\theta^{(e)}\, \boldsymbol{\theta}^{(e)} \right) \mathrm{d}\Gamma_h^{(e)} - \int_{\Gamma_h^{(e)}} \boldsymbol{\psi}_\theta^{(e)T}\, h\, \boldsymbol{\psi}_\theta^{(e)}\, \mathrm{d}\Gamma_h^{(e)} + \right. \\ & + \int_{\Gamma_r^{(e)}} \sigma\, \boldsymbol{\psi}_\theta^{(e)T}\, \frac{\partial \epsilon}{\partial \theta}\, \boldsymbol{\psi}_\theta^{(e)} \left(\left(\boldsymbol{\psi}_\theta^{(e)}\, \boldsymbol{\theta}_a^{(e)} \right)^4 - \left(\boldsymbol{\psi}_\theta^{(e)}\, \boldsymbol{\theta}^{(e)} \right)^4 \right) \mathrm{d}\Gamma_r^{(e)} - \\ & \left. - \int_{\Gamma_r^{(e)}} 4\, \epsilon\, \sigma\, \boldsymbol{\psi}_\theta^{(e)T}\, \boldsymbol{\psi}_\theta^{(e)} \left(\boldsymbol{\psi}_\theta^{(e)}\, \boldsymbol{\theta}^{(e)} \right)^3 \mathrm{d}\Gamma_r^{(e)} \right] - \\ & - \int_{\Gamma_R^{(e)}} \boldsymbol{\psi}_\theta^{(e)T}\, \frac{1}{(1-\epsilon)^2}\, \frac{\partial \epsilon}{\partial \theta}\, \boldsymbol{\psi}_\theta^{(e)} \left(\sigma \left(\boldsymbol{\psi}_\theta^{(e)}\, \boldsymbol{\theta}^{(e)} \right)^4 - \boldsymbol{\psi}_R^{(e)}\, \mathbf{R}^{(e)} \right) \mathrm{d}\Gamma_R^{(e)} - \\ & - \int_{\Gamma_R^{(e)}} 4\, \sigma\, \frac{\epsilon}{1-\epsilon}\, \boldsymbol{\psi}_\theta^{(e)T}\, \boldsymbol{\psi}_\theta^{(e)} \left(\boldsymbol{\psi}_\theta^{(e)}\, \boldsymbol{\theta}^{(e)} \right)^3 \mathrm{d}\Gamma_R^{(e)} \end{aligned} \tag{3.51b}$$

$$\frac{\partial \mathbf{r}_\theta^{(e)}}{\partial \mathbf{R}^{(k)}} = \begin{cases} \int_{\Gamma_R^{(e)}} \frac{\epsilon}{1-\epsilon}\, \boldsymbol{\psi}_\theta^{(e)T}\, \boldsymbol{\psi}_R^{(e)}\, \mathrm{d}\Gamma_R^{(e)} & \text{if } k = e \\ \mathbf{O} & \text{if } k \neq e \end{cases} \tag{3.51c}$$

$$\frac{\partial \mathbf{r}_R^{(e)}}{\partial \boldsymbol{\Theta}^{(e)}} = \int_{\Gamma_R^{(e)}} \frac{1}{(1-\epsilon)^2} \frac{\partial \epsilon}{\partial \theta}\, \boldsymbol{\psi}_R^{(e)T}\, \boldsymbol{\psi}_R^{(e)}\, \mathbf{R}^{(e)} \boldsymbol{\psi}_\theta^{(e)}\, \mathrm{d}\Gamma_R^{(e)} - \\ - \int_{\Gamma_R^{(e)}} \sigma \frac{1}{(1-\epsilon)^2} \frac{\partial \epsilon}{\partial \theta}\, \boldsymbol{\psi}_R^{(e)T}\, \left(\boldsymbol{\psi}_\theta^{(e)}\, \boldsymbol{\Theta}^{(e)}\right)^4\, \boldsymbol{\psi}_\theta^{(e)}\, \mathrm{d}\Gamma_R^{(e)} - \\ - \int_{\Gamma_R^{(e)}} 4\,\sigma\, \frac{\epsilon}{1-\epsilon}\, \boldsymbol{\psi}_R^{(e)T}\, \left(\boldsymbol{\psi}_\theta^{(e)}\, \boldsymbol{\Theta}^{(e)}\right)^3\, \boldsymbol{\psi}_\theta^{(e)}\, \mathrm{d}\Gamma_R^{(e)} \tag{3.51d}$$

$$\frac{\partial \mathbf{r}_R^{(e)}}{\partial \mathbf{R}^{(k)}} = \begin{cases} \int_{\Gamma_R^{(e)}} \frac{1}{1-\epsilon}\, \boldsymbol{\psi}_R^{(e)T}\, \boldsymbol{\psi}_R^{(e)}\, \mathrm{d}\Gamma_R^{(e)} & \text{if } k = e \\ -\int_{\Gamma_R^{(e)}} \boldsymbol{\psi}_R^{(e)T} \int_{\Gamma_R^{(k)}} \boldsymbol{\psi}_R^{(k)}\, \frac{\cos\beta^{(e)} \cos\beta^{(k)}}{2\,r}\, \mathrm{d}\Gamma_R^{(k)}\, \mathrm{d}\Gamma_R^{(e)} & \text{if } k \neq e \end{cases} \tag{3.51e}$$

By replacing the temporal discretization of the temperature into (3.50), the final form of the elemental tangent matrix is obtained,

$$\overline{\mathbf{K}}^{(e)t+\Delta t} = \begin{bmatrix} \frac{\partial \mathbf{r}_\theta^{(e)t+\Delta t}}{\partial \boldsymbol{\Theta}^{(e)}} & \frac{\partial \mathbf{r}_\theta^{(e)t+\Delta t}}{\partial \mathbf{R}^{(1)}} & \cdots & \frac{\partial \mathbf{r}_\theta^{(e)t+\Delta t}}{\partial \mathbf{R}^{(n)}} \\ \frac{\partial \mathbf{r}_R^{(e)t+\Delta t}}{\partial \boldsymbol{\Theta}^{(e)}} & \frac{\partial \mathbf{r}_R^{(e)t+\Delta t}}{\partial \mathbf{R}^{(1)}} & \cdots & \frac{\partial \mathbf{r}_R^{(e)t+\Delta t}}{\partial \mathbf{R}^{(n)}} \end{bmatrix} \tag{3.52}$$

where:

$$\frac{\partial \mathbf{r}_\theta^{(e)t+\Delta t}}{\partial \boldsymbol{\Theta}^{(e)}} = \int_{\Omega^{(e)}} \mathbf{B}_\theta^{(e)T}\, \frac{\partial \mathbf{D}^{t+\Delta t}}{\partial \theta}\, \mathbf{B}_\theta^{(e)}\, \boldsymbol{\Theta}^{(e)t+\Delta t}\, \boldsymbol{\psi}_\theta^{(e)}\, \mathrm{d}\Omega^{(e)} + \\ + \int_{\Omega^{(e)}} \mathbf{B}_\theta^{(e)T}\, \mathbf{D}^{t+\Delta t}\, \mathbf{B}_\theta^{(e)}\, \mathrm{d}\Omega^{(e)} + \int_{\Omega^{(e)}} \boldsymbol{\psi}_\theta^{(e)T}\, \rho^{t+\Delta t}\, c_p^{t+\Delta t}\, \boldsymbol{\psi}_\theta^{(e)}\, \frac{1}{\gamma\, \Delta t}\, \mathrm{d}\Omega^{(e)} + \\ + \int_{\Omega^{(e)}} \boldsymbol{\psi}_\theta^{(e)T} \left(\frac{\partial \rho^{t+\Delta t}}{\partial \theta}\, c_p^{t+\Delta t} + \frac{\partial c_p^{t+\Delta t}}{\partial \theta}\, \rho^{t+\Delta t}\right) \boldsymbol{\psi}_\theta^{(e)}\ (...) \\ (...)\, \frac{1}{\gamma\, \Delta t} \left(\boldsymbol{\psi}_\theta^{(e)}\, \boldsymbol{\Theta}^{(e)t+\Delta t} - \boldsymbol{\psi}_\theta\, \boldsymbol{\Theta}^{(e)t} - (1-\gamma)\, \Delta t\, \boldsymbol{\psi}_\theta^{(e)}\, \dot{\boldsymbol{\theta}}^{(e)t}\right) \mathrm{d}\Omega^{(e)} - \\ - \left[\int_{\Gamma_h^{(e)}} \boldsymbol{\psi}_\theta^{(e)T}\, \frac{\partial h^{t+\Delta t}}{\partial \theta}\, \boldsymbol{\psi}_\theta^{(e)} \left(\boldsymbol{\psi}_\theta^{(e)} \boldsymbol{\Theta}_a^{(e)t+\Delta t} - \boldsymbol{\psi}_\theta^{(e)}\, \boldsymbol{\Theta}^{(e)t+\Delta t}\right)\, \mathrm{d}\Gamma_h^{(e)} - \right. \\ \left. - \int_{\Gamma_h^{(e)}} \boldsymbol{\psi}_\theta^{(e)T}\, h^{t+\Delta t}\, \boldsymbol{\psi}_\theta^{(e)}\, \mathrm{d}\Gamma_h^{(e)} + \right. \\ + \int_{\Gamma_r^{(e)}} \sigma\, \boldsymbol{\psi}_\theta^{(e)T}\, \frac{\partial \epsilon^{t+\Delta t}}{\partial \theta}\, \boldsymbol{\psi}_\theta^{(e)} \left(\left(\boldsymbol{\psi}_\theta^{(e)}\, \boldsymbol{\Theta}_a^{(e)t+\Delta t}\right)^4 - \left(\boldsymbol{\psi}_\theta^{(e)}\, \boldsymbol{\Theta}^{(e)t+\Delta t}\right)^4\right)\, \mathrm{d}\Gamma_r^{(e)} - \\ \left. - \int_{\Gamma_r^{(e)}} 4\, \epsilon^{t+\Delta t}\, \sigma\, \boldsymbol{\psi}_\theta^{(e)T}\, \boldsymbol{\psi}_\theta^{(e)} \left(\boldsymbol{\psi}_\theta^{(e)}\, \boldsymbol{\Theta}^{(e)t+\Delta t}\right)^3\, \mathrm{d}\Gamma_r^{(e)}\right] - \\ - \int_{\Gamma_R^{(e)}} \boldsymbol{\psi}_\theta^{(e)T}\, \frac{1}{\left(1-\epsilon^{t+\Delta t}\right)^2}\, \frac{\partial \epsilon^{t+\Delta t}}{\partial \theta}\, \boldsymbol{\psi}_\theta^{(e)} \left(\sigma \left(\boldsymbol{\psi}_\theta^{(e)}\, \boldsymbol{\Theta}^{(e)t+\Delta t}\right)^4 - \right. \\ \left. - \boldsymbol{\psi}_R^{(e)}\, \mathbf{R}^{(e)t+\Delta t}\right)\, \mathrm{d}\Gamma_R^{(e)} - \int_{\Gamma_R^{(e)}} 4\,\sigma\, \frac{\epsilon^{t+\Delta t}}{1-\epsilon^{t+\Delta t}}\, \boldsymbol{\psi}_\theta^{(e)T}\, \boldsymbol{\psi}_\theta^{(e)} \left(\boldsymbol{\psi}_\theta^{(e)}\, \boldsymbol{\Theta}^{(e)t+\Delta t}\right)^3\, \mathrm{d}\Gamma_R^{(e)} \tag{3.53a}$$

$$\frac{\partial \mathbf{r}_\theta^{(e)t+\Delta t}}{\partial \mathbf{R}^{(k)}} = \begin{cases} + \int_{\Gamma_R^{(e)}} \frac{\epsilon^{t+\Delta t}}{1-\epsilon^{t+\Delta t}}\, \boldsymbol{\psi}_\theta^{(e)T}\, \boldsymbol{\psi}_R^{(e)}\, \mathrm{d}\Gamma_R^{(e)} & \text{if } k = e \\ \mathbf{O} & \text{if } k \neq e \end{cases} \tag{3.53b}$$

$$\frac{\partial \mathbf{r}_R^{(e)t+\Delta t}}{\partial \boldsymbol{\Theta}^{(e)}} = \int_{\Gamma_R^{(e)}} \frac{1}{\left(1-\epsilon^{t+\Delta t}\right)^2} \frac{\partial \epsilon^{t+\Delta t}}{\partial \theta} \boldsymbol{\psi}_R^{(e)T} \boldsymbol{\psi}_R^{(e)} \mathbf{R}^{(e)t+\Delta t} \boldsymbol{\psi}_\theta^{(e)} \, \mathrm{d}\Gamma_R^{(e)} -$$
$$- \int_{\Gamma_R^{(e)}} \sigma \frac{1}{\left(1-\epsilon^{t+\Delta t}\right)^2} \frac{\partial \epsilon^{t+\Delta t}}{\partial \theta} \boldsymbol{\psi}_R^{(e)T} \left(\boldsymbol{\psi}_\theta^{(e)} \, \boldsymbol{\theta}^{(e)t+\Delta t}\right)^4 \boldsymbol{\psi}_\theta^{(e)} \, \mathrm{d}\Gamma_R^{(e)} -$$
$$- \int_{\Gamma_R^{(e)}} 4\,\sigma \, \frac{\epsilon^{t+\Delta t}}{1-\epsilon^{t+\Delta t}} \boldsymbol{\psi}_R^{(e)T} \left(\boldsymbol{\psi}_\theta^{(e)} \, \boldsymbol{\theta}^{(e)t+\Delta t}\right)^3 \boldsymbol{\psi}_\theta^{(e)} \, \mathrm{d}\Gamma_R^{(e)} \tag{3.53c}$$

$$\frac{\partial \mathbf{r}_R^{(e)t+\Delta t}}{\partial \mathbf{R}^{(k)}} = \begin{cases} \int_{\Gamma_R^{(e)}} \frac{1}{1-\epsilon^{t+\Delta t}} \boldsymbol{\psi}_R^{(e)T} \boldsymbol{\psi}_R^{(e)} \, \mathrm{d}\Gamma_R^{(e)} & \text{if } k = e \\ - \int_{\Gamma_R^{(e)}} \boldsymbol{\psi}_R^{(e)T} \int_{\Gamma_R^{(k)}} \boldsymbol{\psi}_R^{(k)} \, \frac{\cos\beta^{(e)} \cos\beta^{(k)}}{2\,r} \, \mathrm{d}\Gamma_R^{(k)} \, \mathrm{d}\Gamma_R^{(e)} & \text{if } k \neq e \end{cases} \tag{3.53d}$$

The computation of the tangent matrix term $\frac{\partial \mathbf{r}_R^{(e)t+\Delta t}}{\partial \mathbf{R}^{(k)}}$ in the finite element (e) involves the calculation of the radiative heat exchange of the element (e) face with all the visible sides of the remaining elements (k). The elemental tangent matrix is not symmetric, as expression (3.50) shows. The elemental tangent matrices will be assembled to obtain the global tangent matrix required to solve the nonlinear system of equations using the Newton–Raphson method.

3.8 Computational aspects

The implemented code allows simulating two-dimensional heat transfer problems, where the domain can be discretized with isoparametric triangular or quadrilateral elements and the radiosity boundary with isoparametric one-dimensional elements.

The following two-dimensional elements are programmed: (i) triangular with 3, 6 or 10 nodes, and (ii) quadrilateral with 4, 8, 9, 12 or 16 nodes. In the boundary where radiative heat flux between walls is applied, one-dimensional elements of 2, 3 or 4 nodes can be employed. Figure 3.4 illustrates the different element types.

In general, the weak form derived in the previous sections may not be integrated in closed form. In the developed code, Gauss integration rule is programmed which is based on choosing the weights and the integration points so that the highest possible polynomial is integrated exactly using a minimum number of points. Further information can be consulted in appendix B.4.

A discussion about the number of Gauss points to use in the integration in order to compute exactly the integrals of the nonlinear system of equations is carried out. The mentioned study considers the isoparametric transformation Jacobian and the nonlinear terms constant.

For one-dimensional elements it is possible to prove that a number of integration points n_G needed to integrate exactly a polynomial of order p is given by:

$$n_G \geq \frac{p+1}{2} \tag{3.54}$$

For quadrilateral elements, the tensor product of the previous rule is used.

The integral term in the domain with the maximum polynomial degree is,

$$\int_{\Omega^{(e)}} \boldsymbol{\psi}_\theta^{(e)T} \left(\frac{\partial \rho}{\partial \theta} \, c_p \boldsymbol{\psi}_\theta^{(e)} \, \dot{\boldsymbol{\theta}}^{(e)} + \rho \, \frac{\partial c_p}{\partial \theta} \boldsymbol{\psi}_\theta^{(e)} \, \dot{\boldsymbol{\theta}}^{(e)} \right) \boldsymbol{\psi}_\theta^{(e)} \, \mathrm{d}\Omega^{(e)} \tag{3.55}$$

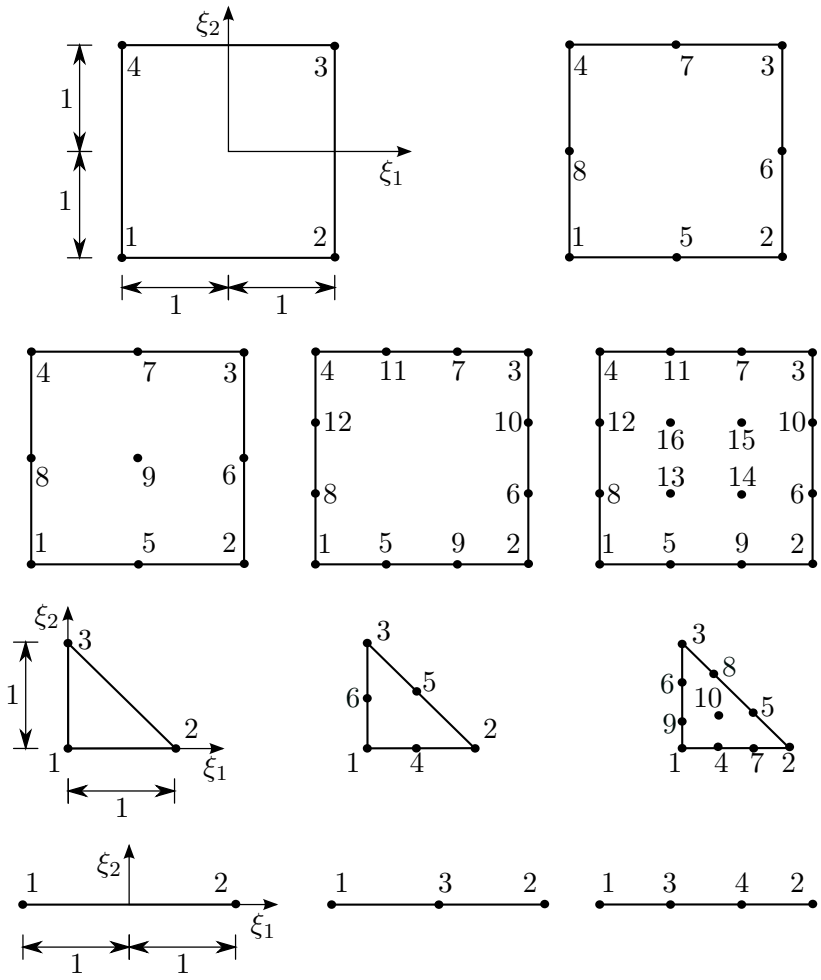

Figure 3.4: One- and two-dimensional elements.

whose polynomial degree is 3 (linear functions), 6 (quadratic functions) and 9 (cubic functions), being employed 4, 12 and 19 Gauss points for triangular elements and 2×2, 4×4 and 5×5 for quadrilateral elements.

The integral term on the boundary with the maximum polynomial degree is,

$$\int_{\Gamma_R^{(e)}} \sigma \frac{1}{\left(1-\epsilon^{t+\Delta t}\right)^2} \frac{\partial \epsilon^{t+\Delta t}}{\partial \theta} \boldsymbol{\psi}_R^{(e)T} \left(\boldsymbol{\psi}_\theta^{(e)}\, \boldsymbol{\theta}^{(e)t+\Delta t}\right)^4 \boldsymbol{\psi}_\theta^{(e)}\, \mathrm{d}\Gamma_R^{(e)} \tag{3.56}$$

being required 4, 7 and 10 Gauss points to evaluate the integral in a linear, quadratic and cubic element, respectively. Table 3.1 summarizes this information.

Regarding the integral which involves rational and trigonometric functions,

$$\int_{\Gamma_R^{(e)}} \boldsymbol{\psi}_R^{(e)T} \int_{\Gamma_R^{(k)}} \boldsymbol{\psi}_R^{(k)} \frac{\cos\beta^{(e)} \cos\beta^{(k)}}{2\,r}\, \mathrm{d}\Gamma_R^{(k)}\, \mathrm{d}\Gamma_R^{(e)} \tag{3.57}$$

in most of the problems presented, 10 Gauss points were used in each element to determine with accuracy the value of the integrals without increasing excessively the computation time. This number of points is enough when there are no discontinuities in the radiosity field that can influence the temperature evolution.

Element type	Expression (3.55)	
	p	n_G
T3	3	4
T6	6	12
T10	9	19
Q4	3	2×2
Q8	6	4×4
Q9	6	4×4
Q12	9	5×5
Q16	9	5×5

(a) Tn and Qn denote Triangular and Quadrilateral elements with n nodes, respectively.

Element type	Expression (3.56)	
	p	n_G
L2	3	2
L3	12	7
L4	21	11

(b) Ln denotes Line elements with n nodes.

Table 3.1: Polynomial degree (p) of the integrand function and number of Gauss points (n_G) required for the numerical integration.

3.9 Verification of the model

3.9.1 Introduction

In the current section, seven numerical applications are presented in order to illustrate the concepts introduced in the preceding sections. The problems reported are solved using the developed code and the numerical results obtained are verified by comparing them with analytical or numerical solutions available in the literature or with numerical solutions computed with a commercial FE software (code-to-code comparison). The objective of this comparison is to guarantee that the code is implemented correctly.

The verification examples presented are the following:

- Linear steady state heat transfer analysis (section 3.9.2). This problem is designed to demonstrate the accuracy of the solution and the convergence of the code using different elements and meshes.
- Linear steady state heat convective analysis (section 3.9.3). This one-dimensional example illustrates the computation of the heat transfer problems in steady state regime when linear thermal material properties are considered.
- Nonlinear steady state temperature of a slab (section 3.9.4). This one-dimensional example, similar to the previous one, demonstrates the computation of the heat transfer problems when nonlinear thermal material properties are employed.
- Linear transient heat transfer analysis of a slab with prescribed heat flux (section 3.9.5). This one-dimensional example is used to verify the code developed in a transient analysis.
- Nonlinear transient heat transfer analysis of a slab with convective and radiative heat fluxes applied (section 3.9.6). This example demonstrates the use of the code in transient analysis with nonlinear boundary conditions (radiative heat transfer) involved.

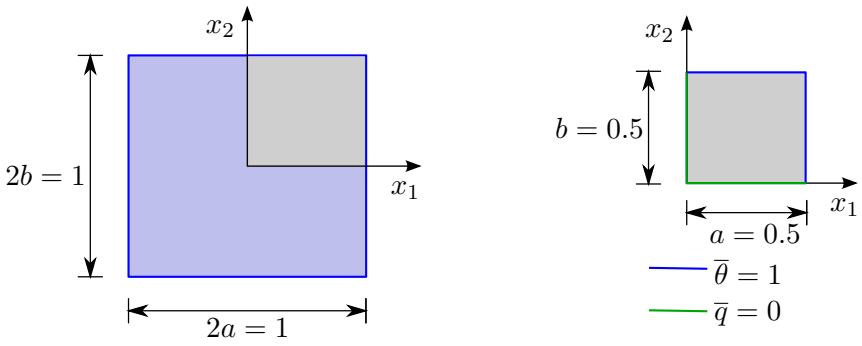

(a) Geometry and boundary conditions of the plate.

(b) Modelled plate and boundary conditions.

Figure 3.5: Geometry of the problem.

- Radiative heat flux between two parallel walls (section 3.9.7). This application instances the radiative heat exchange between parallel walls of a closed cavity, in which the effect of the fluid is not included.
- Radiative heat flux between two adjacent walls (section 3.9.8). This example is employed to discuss the computational time for the calculation and the effect of the singularities in the radiosity field.

The resulting system of equations is solved using the iterative Newton–Raphson method until the solution is reached (see details on appendix B.6).

3.9.2 Linear steady state heat transfer analysis

The problem to solve consists of a 1 m long square plate with a prescribed temperature equal to unity in all sides ($\overline{\theta} = 1\,^{\circ}\mathrm{C}$), as illustrated in figure 3.5a. The source (or internal heat generation) term is equal to $G = 1\ \mathrm{W/m^2}$ in the domain ($1 \times 1\,\mathrm{m^2}$) and the material is isotropic with a thermal conductivity set as $k = 1\ \mathrm{W/(m\,^{\circ}C)}$.

The exact solution is given by Arpaci (1966),

$$\theta\left(x_1,\, x_2\right) = \overline{\theta} + \frac{G\,a^2}{k}\left(\frac{1}{2}\left(1 - \left(\frac{x_1}{a}\right)^2\right) - \right.$$
$$\left. -2\sum_{n=1}^{\infty}\frac{(-1)^n\,\cosh\left((2n+1)\,\frac{\pi}{2}\,\frac{x_2}{a}\right)\,\cos\left((2n+1)\,\frac{\pi}{2}\,\frac{x_1}{a}\right)}{\left((2n+1)\,\frac{\pi}{2}\right)^3\,\cosh\left((2n+1)\,\frac{\pi}{2}\,\frac{b}{a}\right)}\right) \tag{3.58}$$

where $2a$ and $2b$ are the plate dimension sides.

Only a quarter of the slab is modelled using the symmetry conditions, as depicted in figure 3.5b.

In order to analyse the accuracy of the finite element code and of the elements implemented, four different meshes with 1, 4, 16 and 64 elements are tested, see figure 3.6. The element types employed are quadrilateral elements of 4, 8 and 9 nodes. Hence, a total of 12 finite element models were generated.

Figure 3.7 depicts the temperature field obtained using the M14 mesh (M1 mesh with 4-node elements) and M39 mesh (M3 mesh with 9-node elements). It can be seen that the

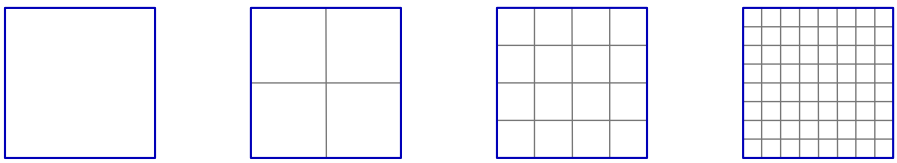

(a) M1 (b) M2 (c) M3 (d) M4

Figure 3.6: Meshes with 1, 4, 16 and 64 elements.

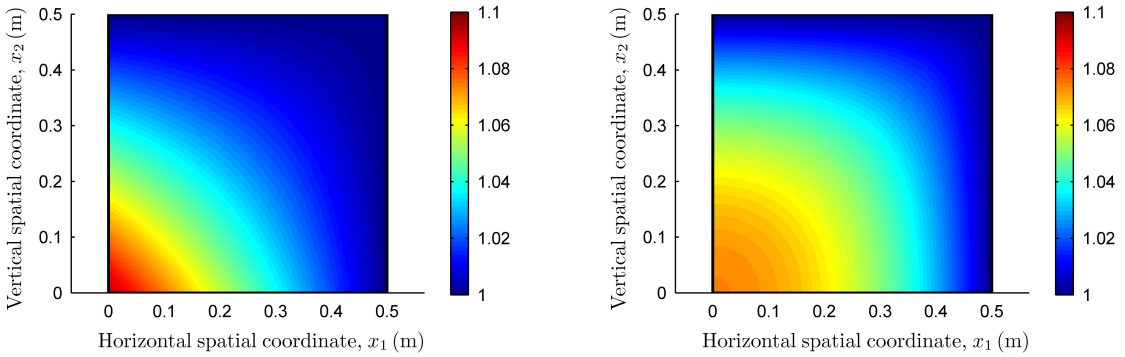

(a) Mesh M1, Q4 elements. (b) Mesh M3, Q9 elements.

Figure 3.7: Temperature field.

temperature distribution depicted in figure 3.7a is bilinear and that the mesh is excessively coarse to represent correctly the solution, while the results obtained with a refined mesh (figure 3.7b) are closer to the exact solution. This fact will be discussed once more in the following.

The error of each FE solution evaluated at any mesh is quantified as follows,

$$error = U - \widehat{U} \tag{3.59}$$

where $\widehat{U}$ is the energy calculated using the known exact solution and U is the energy obtained with the finite element code.

The exact energy is computed from the exact heat flux,

$$\widehat{U} = \frac{1}{2k} \int_{-a}^{a} \int_{-b}^{b} \boldsymbol{q} \cdot \boldsymbol{q} \, \mathrm{d}x_1 \, \mathrm{d}x_2 \tag{3.60}$$

where $\boldsymbol{q} = \boldsymbol{q}(x_1, x_2)$ can be obtained by deriving equation (3.58), rendering for each heat flux component:

$$q_1 = G\, a^2 \left(\frac{x_1}{a^2} - \right.$$
$$\left. -2 \sum_{n=1}^{\infty} \frac{4\,(-1)^n \cosh\left((2n+1)\,\frac{\pi}{2}\,\frac{x_2}{a}\right) \operatorname{sech}\left((2n+1)\,\frac{\pi}{2}\,\frac{b}{a}\right) \sin\left((2n+1)\,\frac{\pi}{2}\,\frac{x_1}{a}\right)}{a\,(1+2\,n)^2\,\pi^2} \right) \tag{3.61a}$$

$$q_2 = G\, a^2\, 2 \sum_{n=1}^{\infty} \frac{4\,(-1)^n \cos\left((2n+1)\,\frac{\pi}{2}\,\frac{x_1}{a}\right) \operatorname{sech}\left((2n+1)\,\frac{\pi}{2}\,\frac{b}{a}\right) \sinh\left((2n+1)\,\frac{\pi}{2}\,\frac{x_2}{a}\right)}{a\,(1+2\,n)^2\,\pi^2} \tag{3.61b}$$

Meshes	h	Q4	Q8	Q9
M1	0.5	0.00292969	0.00430126	0.00436254
M2	0.25	0.00399693	0.00438569	0.00438979
M3	0.125	0.00429170	0.00439250	0.00439275
M4	0.0625	0.00436752	0.00439300	0.00439304
	SLOPE	1:1.949	1:3.933	1:3.716
Exact	0.0043930250	—	—	—

Table 3.2: Energy values obtained.

The numerical energy computed in the complete domain of the problem is given by:

$$U = \frac{1}{2}\int_{\Omega} \boldsymbol{\theta}^T \mathbf{B}_\theta^T \mathbf{D}\, \mathbf{B}_\theta\, \boldsymbol{\theta}\, \mathrm{d}\Omega = \frac{1}{2}\, \boldsymbol{\theta}^T \mathbf{K}\, \boldsymbol{\theta} \tag{3.62}$$

Table 3.2 summarizes the energy obtained for each numerical test. The line *SLOPE* in the table represents the double of the rate of convergence of the elements. The theoretical rates of convergence for the different elements employed are verified: linear for the element Q4 and quadratic for Q8 and Q9. Figure 3.8 shows the error convergence results as a function of the characteristic element length, h. Each point on the plot represents the error in a finite element approximation obtained with the tested meshes.

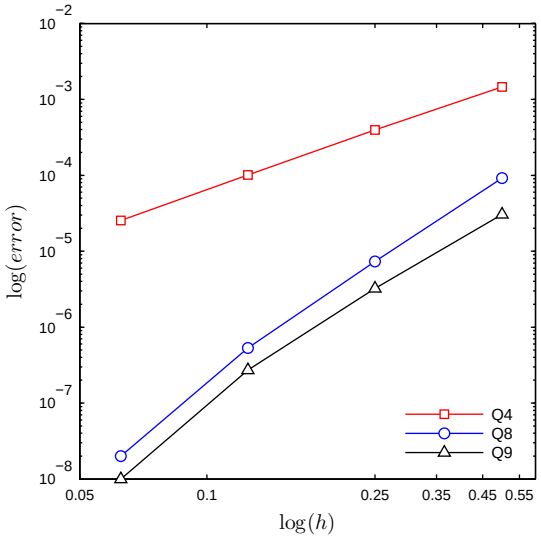

Figure 3.8: Convergence of the error.

An additional analysis employing the commercial software ADINA-T (2010) is performed using the M3 mesh with 9-node elements. Table 3.3 reports the temperature values in the node 1 (point with coordinates $x_1 = x_2 = 0$ m). It can be observed that both ADINA-T (2010) and the code developed are able to reproduce the exact solution with the 9-node element M3 mesh.

Excellent agreement between the numerical and the analytical solution is observed.

Meshes	h	Q4	Q8	Q9
M1	0.5	1.093750	1.067416	1.073718
M2	0.25	1.077679	1.073524	1.073652
M3	0.125	1.074598	1.073662	1.073670
M4	0.0625	1.073899	1.073671	1.073670
Exact	1.073670	—	—	—
ADINA M39	1.073670	—	—	—

Table 3.3: Temperature values at node 1 (middle of the plate).

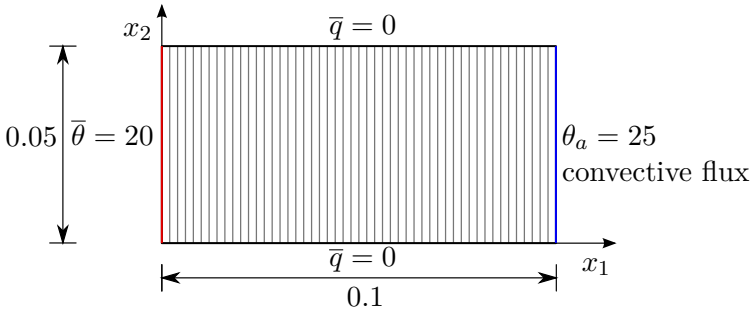

Figure 3.9: Induction heated plate.

3.9.3 Linear steady state heat convective analysis

Consider now a plate heated by induction which has an uniform width of 0.05 m and a length of $L = 0.1$ m.

On the left side of the plate ($x_1 = 0$ m), the temperature is prescribed and equal to $\overline{\theta} = 20\,^{\circ}\text{C}$, while on the right side of the plate ($x_1 = 0.1$ m) a convective heat flux is applied. The top and bottom sides of the plate are considered insulated. The thermal conductivity is $k = k_{11} = k_{22} = 30$ W/(m °C), the ambient temperature is $\theta_a = 20\,^{\circ}\text{C}$ and the convection heat transfer coefficient is $h = 2000$ W/(m^2 °C).

Induction heating is represented by the heat superficial density,

$$G(x_1) = G_0\, e^{\frac{x_1 - L}{P}} \tag{3.63}$$

where G_0 corresponds to the heating superficial power and has a value of $5 \cdot 10^7$ W/m^2 and P is a characteristic heating depth depending on the inductor frequency set as $P = 0.02$ m. Figure 3.9 shows the geometry plate, the boundary conditions and the mesh used. The heat generation was introduced in the code developed as nodal values.

The current problem was solved using a mesh with 50 two-dimensional 4-node elements. The results were compared with the exact solution reported in Bergheau and Fortunier (2008):

$$\theta(x_1) = \overline{\theta} + \frac{G_0\, P}{k + L\, h}\left(1 + \frac{P\, h}{k}\left(1 - e^{-\frac{L}{P}}\right)\right) x_1 + \frac{G_0\, P^2}{k}\, e^{-\frac{L}{P}}\, \left(1 - e^{\frac{x_1}{P}}\right) \tag{3.64}$$

Figure 3.10 illustrates the temperature distribution along the x_1-direction and table 3.4 summarizes the numerical values of the temperature, where "Exact" stands for the results obtained with the expression (3.64), and "Num." corresponds to the results computed with

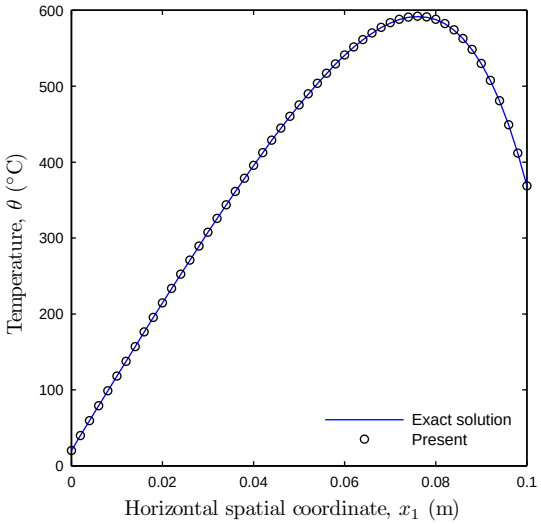

Figure 3.10: Temperature distribution within the plate length in steady state heat transfer.

x_1 (m)	Exact (°C)	Num. (°C)
0.00	20.0000000	20.0000000
0.01	118.1446367	118.2264406
0.02	214.3988782	214.5609100
0.03	307.5363849	307.7760459
0.04	395.5352647	395.8482706
0.05	475.0619809	475.4412681
0.06	540.6204609	541.0543833
0.07	583.1492127	583.6185693
0.08	587.7083618	588.1814954
0.09	529.6662192	530.0909360
0.10	368.4119954	368.7022424

Table 3.4: Summary of the nodal temperature results (exact and numerical).

the code implemented in MATLAB (2012). The error computed as the relative difference between the exact and the numerical solution is approximately 0.08% (average error). The results reported show good agreement between numerical and analytical solutions.

3.9.4 Nonlinear steady state temperature of a slab

An infinitely long slab with $2L$ width is considered in this example. The internal heat generation is set as $G = 2$ W/m^2.

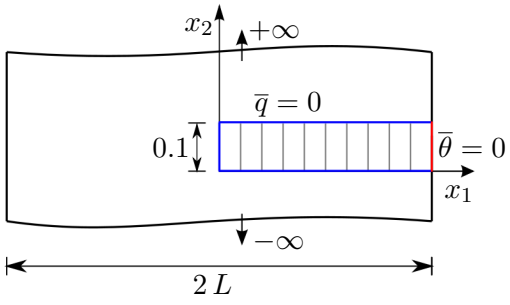

(a) Geometry of the slab and boundary conditions.

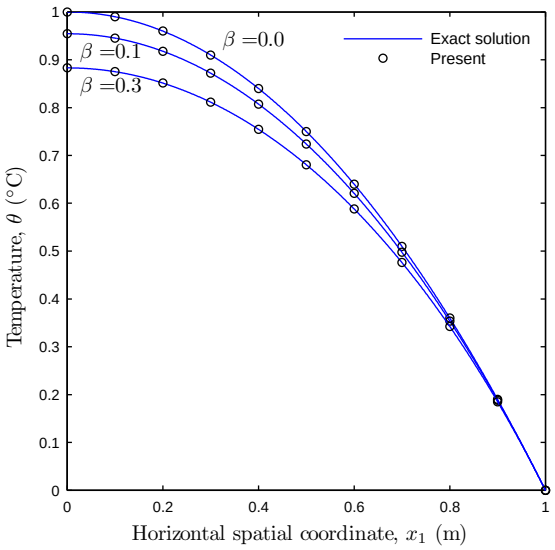

(b) Steady state temperature of slab for different values of β.

Figure 3.11: Nonlinear steady state temperature of a slab.

As the slab presents symmetric conditions with respect to the x_2 axis, only half of the slab is modelled. The finite element model consists of a 0.1×0.05 m^2 rectangle, that is discretized spatially by ten equally spaced two-dimensional 4-node quadrilateral elements. The top, bottom and right sides of the slab modelled are considered insulated, while a temperature of 0 °C is prescribed in the right side. Figure 3.11a illustrates the finite element model and the boundary conditions.

Regarding the thermophysical properties of the material, a linear variation of the thermal conductivity with the temperature following $k = k_{11} = k_{22} = k_0\,(1 + \beta\,\theta)$ is assumed (k_0 is set equal to 1 W/(m °C)). The parameter β is a dimensionless constant set equal to 0, 0.1 and 0.3, for the three simulations carried out. The density and specific heat capacity of the material are constant and equal to unity.

The analytical solution is given by Arpaci (1966):

$$\frac{\theta(x_1) - \overline{\theta}}{G\,L^2/(2\,k_0)} = \frac{1}{\beta\,G\,L^2/(2\,k_0)} \left(-1 + \sqrt{1 + 2\,\frac{\beta\,G\,L^2}{2\,k_0} \left(1 - \left(\frac{x_1}{L} \right)^2 \right)} \right) \tag{3.65}$$

Expression (3.65) also reports the solution for a temperature-independent material (constant thermal conductivity) when $\beta \to 0$.

Figure 3.11b depicts the steady state temperature along the x_1 axis. Excellent agreement between the numerical and the analytical temperatures can be observed.

3.9.5 One-dimensional linear transient heat transfer analysis of a slab with prescribed heat flux

The slab analysed in the present example has dimensions $0 \leq x_1 \leq L_1$ and $0 \leq x_2 \leq L_2$, where $L_1 = \pi$ m and $L_2 = 1$ m. The initial temperature is set as 0 °C. A constant prescribed heat flux, $\overline{q} = 10$ W/m^2, is applied on the side $x_1 = L_1$. The slab sides $x_1 = 0$, $x_2 = 0$ and $x_2 = L_2$ are insulated. Figure 3.12 illustrates the geometry and the boundary conditions of the slab modelled.

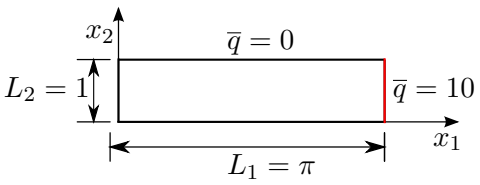

Figure 3.12: Geometry and boundary conditions of the slab with prescribed flux.

The analytical solution is given by (Carslaw and Jaeger, 1959):

$$\theta(x_1, t) = \frac{\overline{q}\,t}{\rho\,c_p\,L_1} + \frac{\overline{q}\,L_1}{k} \left(\frac{3\,x_1^2 - L_1^2}{6\,L_1^2} - \frac{2}{\pi^2} \sum_{i=1}^{\infty} \frac{(-1)^i}{i^2}\, e^{-\rho\,c_p\,i^2\,\pi^2\,t/L_1^2} \cos \frac{i\,\pi\,x_1}{L_1} \right) \tag{3.66}$$

A transient two-dimensional finite element simulation is carried out using a mesh of 50 quadrilateral 4-node elements. The numerical data of the problem is: $\rho = 1$ kg/m^2, $c_p = 1$ J/(kg °C), $k = k_{11} = k_{22} = 1$ W/(m °C), $t = 20$ s, $\Delta t = 0.5$ s and $\gamma = 0.5$ (Crank–Nicolson scheme).

Figure 3.13 depicts the evolution of the temperature field along the x_1 axis for different computational times. The code implemented is capable of accurately reproducing the analytical solution of the problem, when an adequate time step and mesh size is employed.

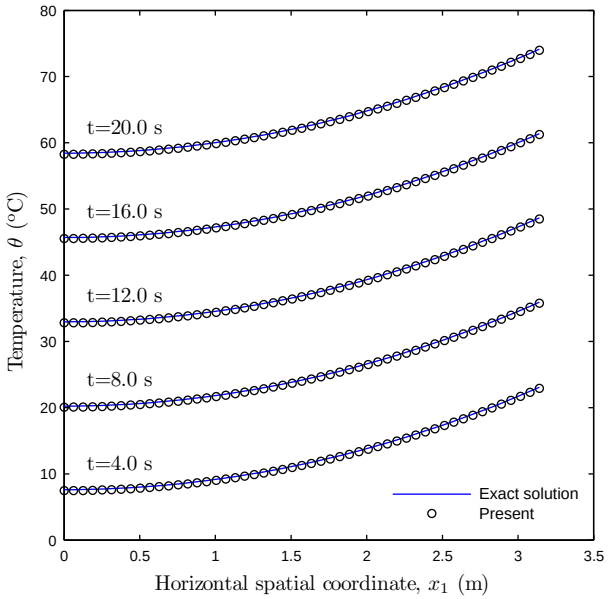

Figure 3.13: Temperature evolution for different computational times.

3.9.6 Nonlinear transient heat transfer analysis of a slab with convective and radiative heat fluxes applied

In the present section, a transient analysis of a slab subjected simultaneously to convective and radiative heat flux is presented. This problem is reported by Bathe and Khoshgoftaar (1979), where the imperial system of units is employed.

The initial temperature of the slab is equal to 1498.1505 °F. At $t = 0$ h, a convective and radiative heat flux is applied on the right side of the slab, where the ambient temperature is $\theta_a = 0\,°\text{F}$. The bottom, top and left faces are insulated. Figure 3.14 shows the geometry of the slab and schematically represents the boundary conditions.

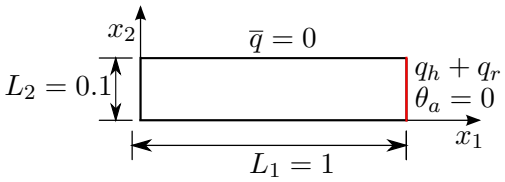

Figure 3.14: Geometry and boundary conditions of the slab with convective and radiative heat flux.

The convective coefficient is $h = 0.04$ Btu/(in^2 h °F) and the emissivity is set as $\epsilon = 1$. The conductivity and the specific heat are considered constant and equal to 0.01 Btu/(in h °F) and 0.01 Btu/(lb °F), respectively. The density is $\rho = 1$ lb/in^2 and the Stefan–Boltzmann's constant is $\sigma = 1.18958 \cdot 10^{-11}$ Btu/(in^2 h °F^4).

A nonlinear transient heat transfer analysis using the Euler backward method is carried out considering a mesh of 20 equally spaced two-dimensional quadrilateral 4-node conduction elements. The final time considered is $t = 3.66$ h with a time step of $\Delta t = 0.001$ h.

Figure 3.15 illustrates the evolution of the temperature in two points situated on the edges $x_1 = 0$ in and $x_1 = 1$ in. The numerical results obtained are compared with those

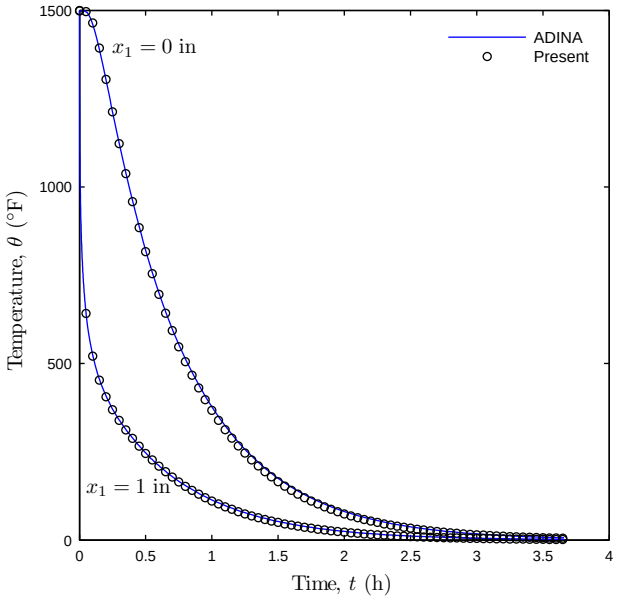

Figure 3.15: Transient temperature results for a slab with radiative and convective boundary conditions.

calculated employing the commercial finite element package ADINA-T (2010). Once again, very good agreement can be observed.

3.9.7 Radiative heat flux between two parallel walls

A radiative heat flux problem between two parallel walls of an enclosure is presented in this section. The exterior edge of the left wall has a prescribed temperature of 0 °C, while the temperature in the exterior of the right wall is 1000 °C. The thermal conductivity of the walls is taken as 1.5 W/(m °C) and the emissivities are 0.1 and 0.3 in the left and right walls, respectively. The Stefan–Boltzmann's constant is set as $\sigma = 5.669 \cdot 10^{-8}$ W/(m^2 K^4). The geometry of the problem is illustrated in figure 3.16, where the dimensions are given in meters. The discontinuous lines emphasise that the problem consists of an closed cavity with finite length walls. This problem was originally proposed by Bergheau and Fortunier (2008) and was adapted in this thesis for finite walls[8].

A steady state nonlinear analysis is carried out using a regular mesh of 450 4-node quadrilateral elements (10×30 on the left wall and 5×30 on the right one). The exchange of radiative heat transfer takes place between the interior faces of the walls, where the radiosities are approximated by 30 2-node linear elements on each face. Figure 3.17 depicts the temperature field obtained. It can be observed that a reduced variation of temperatures is obtained between the faces of the left wall (variation of temperatures between 0 °C and 11.6 °C). However, in the right wall, an elevated gradient of temperatures can be observed. This result leads to a higher heat flux in the right wall (especially in the horizontal direction, even if the heat flux is two-dimensional).

[8]The results presented in this thesis are not coincident with those reported in the reference book, as in that original problem there is a radiative heat flux between two infinite parallel walls, hence leading to a solution where the radiative heat flux is equal in both walls and the heat transfer is one-dimensional.

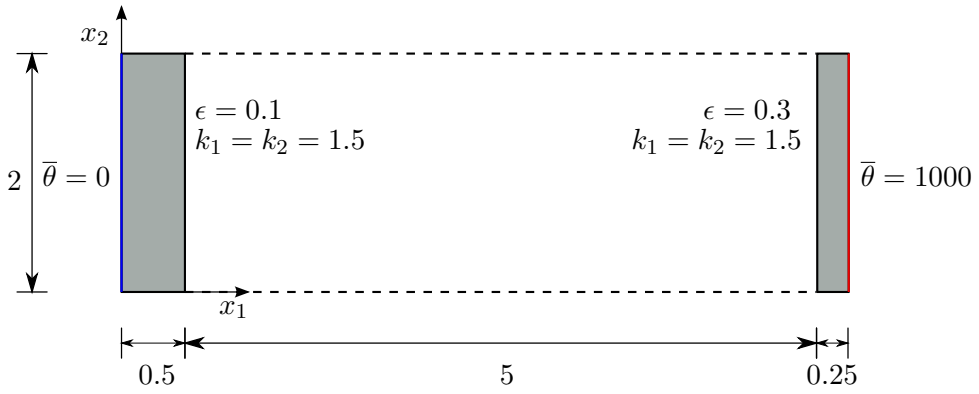

Figure 3.16: Geometry of the radiative exchange among two parallel walls of a close cavity.

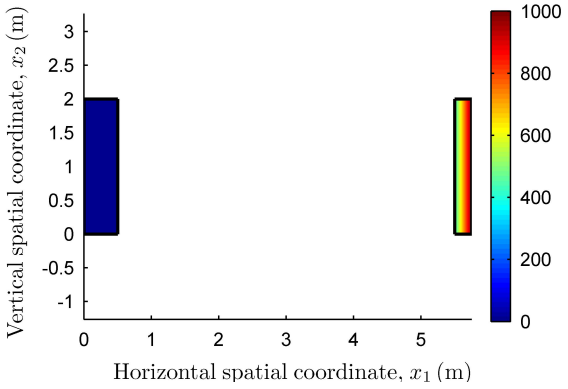

Figure 3.17: Temperature distribution on the walls.

The numerical solution is compared with that obtained using the commercial software ADINA-T (2010). Figure 3.18 illustrates the evolution of the temperature (it can be observed clearly that the problem is two-dimensional) and of the radiosity along the line $x_1 = 0.5$ m. An excellent agreement is observed for both temperature and radiosity distributions.

3.9.8 Radiative heat flux between two adjacent walls

The present example consists of two 1 m long walls with 0.1 m of width and a relative angle between them of 60°. The external edges of the walls have a prescribed temperature equal to 100 °C and the internal faces of the walls exchange radiative heat flux. The lateral faces of the walls are adiabatic. The thermal conductivity is taken as 1.5 W/(m °C) and the emissivity as 0.1. A steady state finite element analysis is carried out considering a mesh of 80 conduction 4-node elements and 20 linear one-dimensional elements to discretize the radiative boundary. Figure 3.19 shows the geometry of the problem and the mesh employed.

The temperature and heat flux distributions obtained are represented in figure 3.20. It can be observed that, due to the two-dimensional heat flux, the temperature distribution along the internal faces of the walls is not uniform, with the zone close to the contact

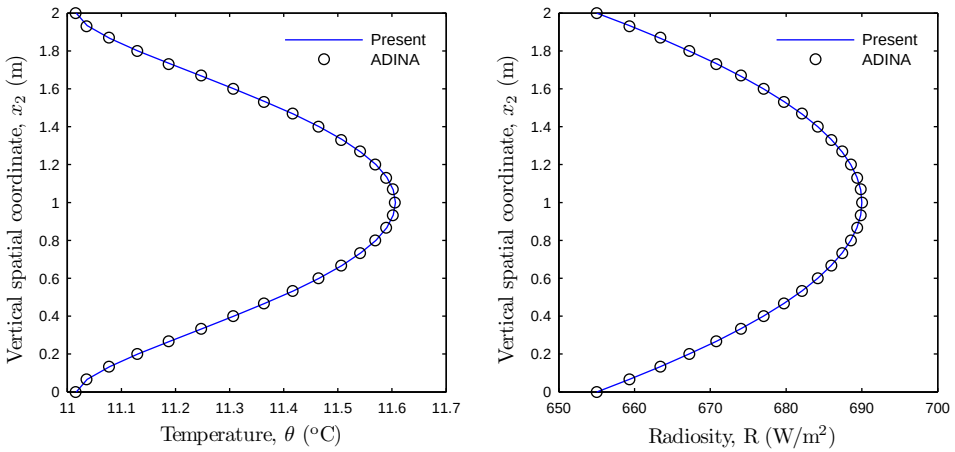

(a) Temperature distribution. (b) Radiosity distribution.

Figure 3.18: Temperature and radiosity distributions along $x_1 = 0.5$ m (interior face of the left wall).

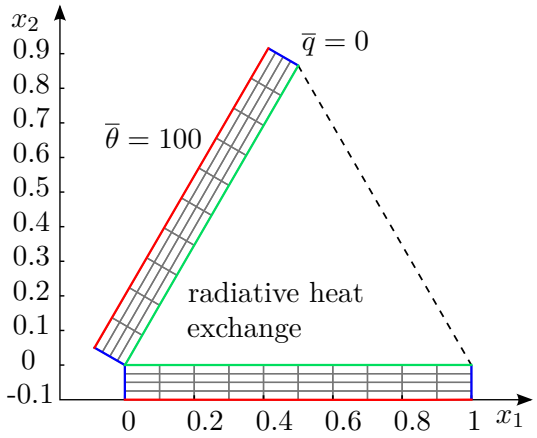

Figure 3.19: Mesh and geometry of two adjacent walls problem.

point being warmer. Furthermore, it can be seen that the heat flux in the horizontal wall is mainly vertical, while in the leaning wall, both components of the heat flux are relevant.

Figure 3.21 depicts non-zero elements of the tangent matrix when radiative heat flux is considered or not considered. It can be observed that the consideration of the radiative heat flux increments the size of the tangent matrix and that the radiosity matrix is full (see the lower right corner of figure 3.21b).

Based on the previously defined mesh, the commercial software ADINA-T (2010) was used to verify the results obtained by means of a code-to-code comparison. Figure 3.22 plots the comparative graphs of the temperature and radiosity distributions. Once more, an excellent agreement between both numerical results is observed. In both cases, the solution is obtained considering 10 Gauss points at each element to integrate the expression (3.57).

Figure 3.22 also depicts the temperature and radiosity distributions obtained consid-

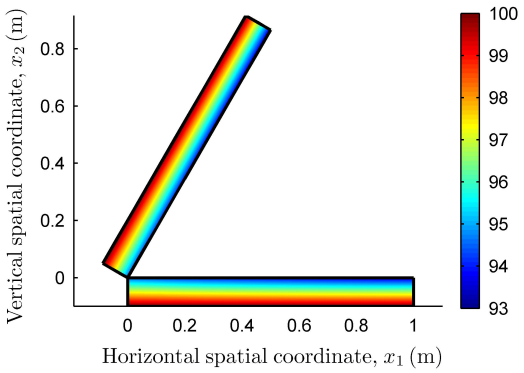

(a) Temperature field.

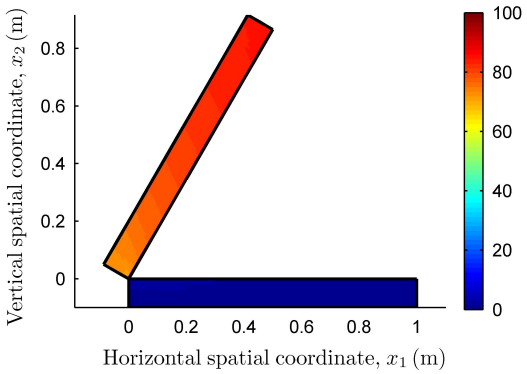

(b) Horizontal heat flux component.

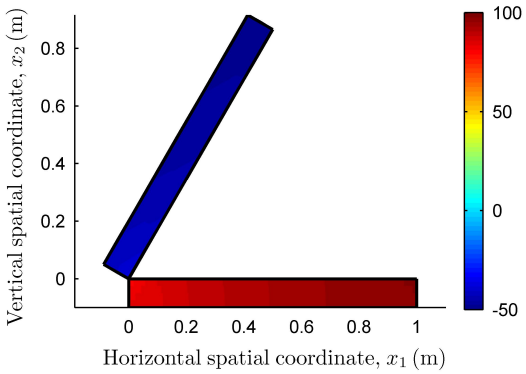

(c) Vertical heat flux component.

Figure 3.20: Temperature and heat flux distribution in the adjacent walls.

ering 20 and 50 Gauss points in the integration of the radiosity matrix. A difference can be observed in the temperature and radiosity values computed in the vicinity of the point located in the coordinates $x_1 = 0, x_2 = 0$. In fact, it can be verified that in that points a singularity in the radiosity field exists and the mesh is not able to reproduce correctly the temperature and radiosity fields. This is consistent with Modest (2003), who referred that the evaluation of the term (3.57) using numerical quadrature can be problematic due to the singularities in the integrand. In this case, the numerical results depend strongly on the number of Gauss points considered and the convergence is slow.

A refined mesh, depicted in figure 3.23, is designed to represent more accurately the temperature and radiosity fields. Figure 3.24 depicts the temperature and radiosity fields evolution obtained taking 10, 20 and 50 Gauss points. In this case, it can be observed that the solutions obtained using different number of Gauss points are similar, although the differences in the radiosity field are kept in the singularity.

These results demonstrate that the singularity in the radiosity field influences strongly the temperature results. Hence, a refined mesh in this zone has to be generated in order to obtain an acceptable solution without increasing excessively the number of Gauss points in the integration of the term (3.57).

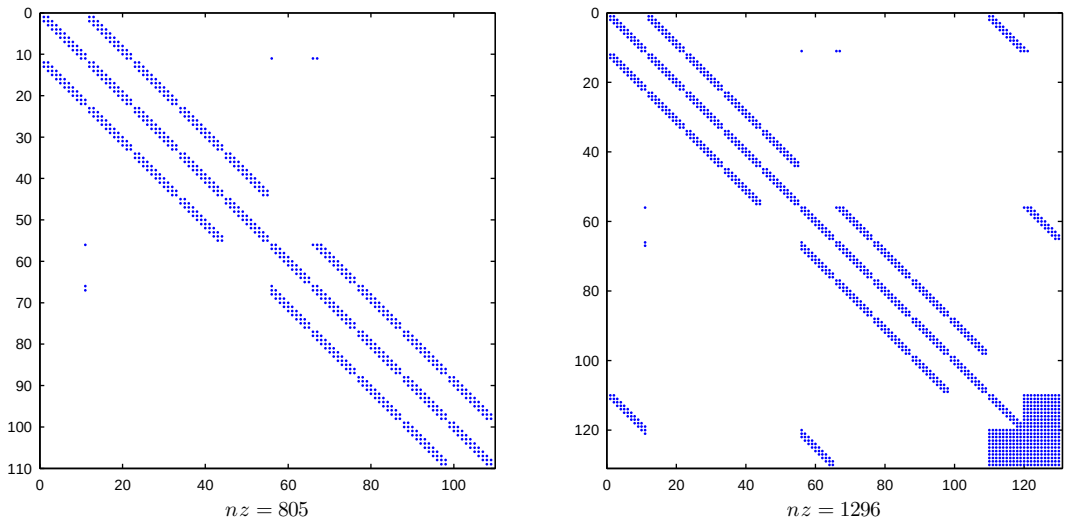

(a) Without including radiosity equations. (b) Including radiosity equations.

Figure 3.21: Sparsity pattern of the tangent matrix (the axes of both figures refer to the dimension of the matrix and nz is the number of non-zero elements).

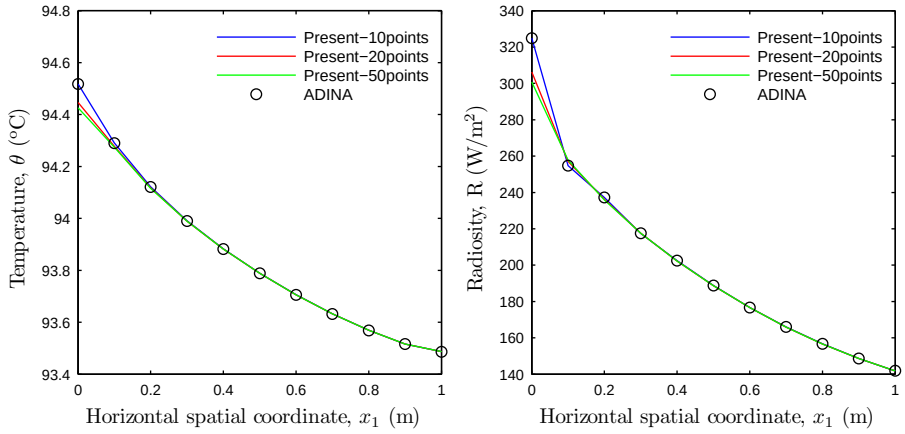

(a) Temperature distribution. (b) Radiosity distribution.

Figure 3.22: Temperature and radiosity values along the line $x_2 = 0$ m.

3.10 Concluding remarks

In the present chapter, the FE formulation of the coupled problem between conduction heat transfer and radiative heat exchange in a cavity was presented. The code developed computes the temperature field as a primary variable and, subsequently, it allows the evaluation of the heat flux fields. The programme implemented allows performing steady state and transient analyses considering that the thermal properties of the material are constant or temperature-dependent. In the same way, the convection coefficient can be considered temperature-dependent.

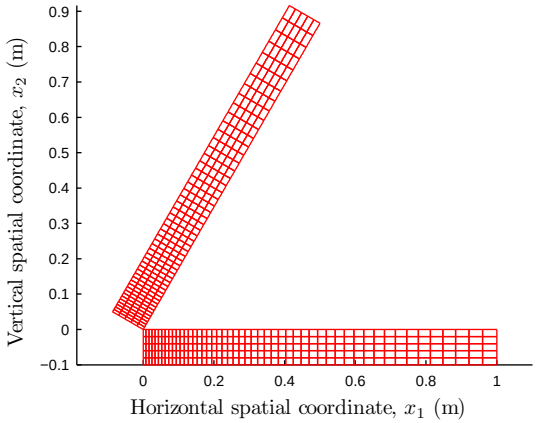

Figure 3.23: Refined mesh.

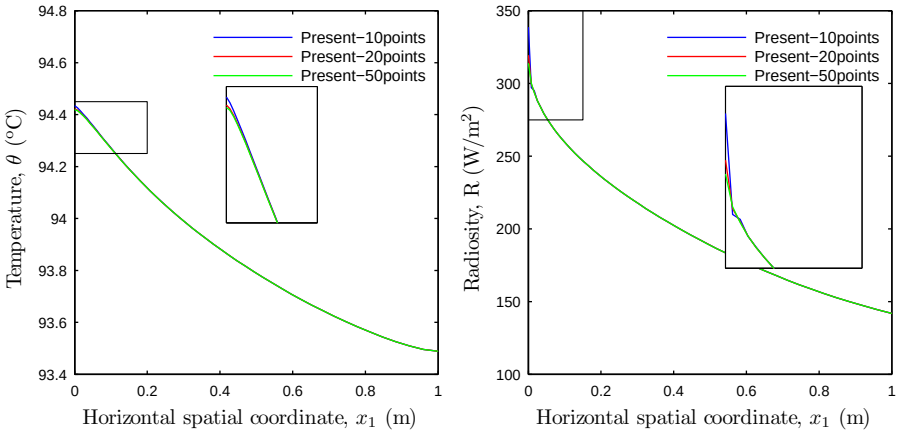

(a) Temperature distribution. (b) Radiosity distribution.

Figure 3.24: Temperature and radiosity values along the line $x_2 = 0$ m (refined mesh).

A significant increment of the computational time was observed when radiative exchanges between faces are considered in the problem, as (i) the matrix of the radiosity equation is full and the evaluation of the terms $\mathbf{r}_R^{(e)t+\Delta t}$, $\frac{\partial \mathbf{r}_R^{(e)t+\Delta t}}{\partial \boldsymbol{\theta}^{(e)}}$ and $\frac{\partial \mathbf{r}_R^{(e)t+\Delta t}}{\partial \mathbf{R}^{(k)}}$ requires more computational time, (ii) the number of equations in the system of equations to be solved increases (besides the temperature degrees of freedom, the radiosity degrees of freedom are included), and (iii) some of the integrals involve rational and trigonometric functions. Consequently, in most problems, generate the radiosity equations is more expensive in terms of computational speed and memory usage than solving the heat transfer equations system. One possible action to reduce the computational time could be the approximation of the radiosity (3.30b) and its variation (3.31b) by constant functions. In this case, $\mathbf{r}_R^{(e)t+\Delta t}$, $\frac{\partial \mathbf{r}_R^{(e)t+\Delta t}}{\partial \boldsymbol{\theta}^{(e)}}$ and $\frac{\partial \mathbf{r}_R^{(e)t+\Delta t}}{\partial \mathbf{R}^{(k)}}$ could be evaluated only once.

Furthermore, a singularity in the radiosity field was detected when there are sharp corners in the geometry. This fact influences considerably the results obtained and makes it necessary to use refined meshes or a higher number of Gauss points to integrate the radiosity equations. This conclusion is of special importance as the thermal modelling

presented in chapter 7 for GFRP profiles includes the computation of the radiative heat exchange in cavities with sharp corners.

The code implemented in MATLAB (2012) was verified using several benchmark solutions and, in all cases, excellent results were observed, as well as quadratic convergence of the iterative method in the asymptotic limit of the solution.

Chapter 4

Finite element method for the non-isothermal fluid dynamic problems

4.1 Introduction

The governing equations of a viscous and incompressible fluid flow are known as the Navier–Stokes equations. They are nonlinear differential equations whose analytical solution can only be obtained for very particular — and usually simple — problems. Hence, numerical techniques were applied in the last years to obtain approximate solutions for these equations (Fernández-Carvajal, 2001). The most popular methods are the finite volume method (FVM), the finite element method (FEM) and the finite difference method (FDM).

The FDM is based on the spatial and temporal finite difference approximation of the derivatives included in the governing equations. This method was used by many authors, as for example Roache (1973), Katopodes (1984) or Smith (1985). The FEM began to be used in fluid dynamics with the works of Jamet and Raviart (1974), Shen and Habashi (1976) and Kim (1988). This method presents specific numerical difficulties when applied to fluid problems: conservation of the mass of the fluid, approximation of velocities and pressures, asymmetric tangent matrix due to the convective terms and the treatment of viscous forces between the particles of the fluid. In particular, the numerical instabilities of the method due to the convective terms and the need to satisfy the Ladyzhenskaya–Babŭska–Brezzi (LBB) condition are the main reasons why other authors prefer to use the FVM, which was born as a special case of the FDM based upon the splitting of the domain into a finite number of control volumes (Patankar and Spalding, 1972). However, the FEM is still considered a powerful tool for solving flow problems and different authors postulated solutions for the numerical instabilities. Taylor and Hood (1973) detected numerical oscillations when inappropriate element types were used to solve non-isothermal fluid dynamic problems. These elements, in particular those that approximate the velocity and the pressure with the same degree polynomials, did not satisfy the LBB condition. In the same publication, the elements known as *Taylor–Hood* were proposed. They strictly satisfy strictly the LBB condition and were used in fluid problems providing excellent results.

The second source of instability stems directly from the Galerkin formulation as it deals

with the convective term in a symmetric way. It causes the occurrence of wiggles[1] in the velocity and temperature fields, which will be more important as more significant is the convection in the problem, *i.e.*, in problems with high number of Reynolds. These oscillations can be mitigated using adapted meshes, very refined in the areas where the flux changes drastically the flow conditions. This procedure can increment very significantly the computational cost making it impracticable to solve the problem in due time. Hence, in Heinrich *et al.* (1977) a Petrov–Galerkin stabilization method for the advection-diffusion equation was presented, thus contributing to the expansion of the FEM (Fernández-Carvajal, 2001). This method was extended for the Navier–Stokes equations and Brooks and Hughes (1982) reported the streamline upwind/Petrov–Galerkin method (SUPG), which consists of the inclusion of an artificial diffusive term in the Navier–Stokes equations. Different versions of the SUPG method are available in the literature: Franca and Frey (1992), Kondo (1994), Hannani *et al.* (1995) and Tezduyar and Osawa (2000). Furthermore, other stabilization techniques as GLS (Galerkin/least-squares), SGS (subgrid scale method) or LS (least-squares) were also developed.

In the present chapter, a mixed finite element formulation for the non-isothermal fluid dynamic problems is presented. The finite element method is based on the transformation of the differential governing equations into $3\,n + m$ (n and m are the number of nodes where the velocity/temperature and pressure are approximated, respectively) nonlinear algebraic equations for the three-dimensional problems. These equations, in general, can demand big storing memory requirements. During the implementation process it was set as a priority to obtain, at each time step, quadratic convergence in the asymptotic limit of the solution. This allows reducing the number of iterations and, consequently, lessen the computational time. Hence, the resulting nonlinear system of equations will be solved using the Newton–Raphson method. At the end of the chapter several examples are presented in order to verify the code.

4.2 Basic concepts

Fluids are substances whose molecular structure offers no resistance to external shear forces. The intermolecular forces are weaker in liquids and extremely small in gases. The stress in a fluid is proportional to the time rate of strain, while in solids it is proportional to the strain. In the case of fluids, the proportionality parameter is known as viscosity and, in general, it is a function of the thermodynamic variables, *i.e.*, temperature and pressure of the fluid (Ferziger and Perić, 2000).

As stated in Reddy and Gartling (2010), fluid mechanics is a broad area and is typically divided into smaller areas based on the characteristics of the fluid or on the basic nature of the flow. An inviscid fluid is one where the viscosity is assumed to be zero. An incompressible fluid is one with constant density and an incompressible flow is one in which the density variations are negligible. A perfect or ideal fluid is an inviscid fluid. Otherwise, a real fluid has a finite viscosity and it may or may not be incompressible. A Newtonian fluid is a fluid whose viscosity depends only on the thermodynamic properties and in which the stress is linearly related to the strain rate. A non-Newtonian fluid is one that does not obey the linear stress-strain rate relation (Reddy, 2004a, Hauke, 2008).

The speed of the fluid affects its properties and, then, the flow. At low speeds, the inertia of the fluid may be ignored and the flow is called creep flow. This regime is

[1] Spurious node-to-node numerical oscillations.

important in flows containing small particles in suspension or in flows through porous media. As the speed is increased, inertia effects become relevant, but if each fluid particle follows a smooth trajectory, the flow is laminar. Further increases in speed may lead to instability that produces a more random type of flow that is called turbulent flow (Reddy, 2004a, Hauke, 2008). Some dimensionless parameters can be used to characterize a flow. In viscous fluids, the Reynolds number is defined as the ratio of inertial forces to viscous forces,

$$Re = \frac{\rho U L}{\mu} \tag{4.1}$$

where ρ is the density of the fluid, μ is the fluid viscosity, U is the characteristic flow velocity and L is a characteristic dimension of the flow region. A small Reynolds number (high viscosity and/or small velocities) produces a laminar flow. In opposition, a high Reynolds number flow develops transitional or turbulent flows.

The motion of a fluid is governed by the global laws of conservation of mass and momentum and the energy equation. The equations of motion resulting from the application of the conservation of linear momentum principle are known as the Navier–Stokes equations, which can be expressed in terms of the Reynolds number (dimensionless equations). When the temperature effects are not important, the energy equation is uncoupled from the Navier–Stokes equations and, therefore, for isothermal flows only the Navier–Stokes equations and the continuity equation are solved. For non-isothermal flows the energy equation is coupled with the others and it considers the possibility of density differences (due to temperature variation), which give rise to buoyancy (Reddy and Gartling, 2010).

In the case of non-isothermal fluids, the study of the motion of the fluid involves joining two different areas: fluid dynamics and heat transfer. In these fluids, convective fluxes appear, being classified as natural/free, forced or mixed convective fluxes. In the present thesis only the natural convection is considered, as the final objective of the work is to reproduce the thermal behaviour of the GFRP profiles tested in the laboratory conditions and, during the tests, the profiles were protected from the wind using a system featuring four flame retardant blankets and two agglomerated cork structures Morgado *et al.* (2013a,b). As a result of this setup, it can be considered that no forced convection developed in the top face of the GFRP profiles.

In the present chapter, a coupled fluid-solid thermal problem is presented. The current formulation involves a coupled solution scheme of the Navier–Stokes equations, the advection-diffusion equation and the heat transfer equation. As the fluid is considered incompressible, the forces due to the changes of the density as a result of the variation of the temperature in the fluid are computed using the Boussinesq approximation (Reddy and Gartling, 2010). This approach was considered in the computation of nonisothermal incompressible fluids, as its inclusion in the formulation only requires a minimal variation in the body force term. However, this hypothesis is limited to reduced temperature gradients in the fluid.

Furthermore, the FE formulation presented contains the stabilization terms of the convection in the Navier–Stokes equation and in the advection-diffusion equation. These terms can be important in problems where the Reynolds and Rayleigh numbers are significant. This stabilization allows solving complex fluid dynamics problems using a not particularly refined mesh and with a reasonable time step and, as referred in Tezduyar and Osawa (2000), it can also improve the convergence to the solution. However, the stabilization is unnecessary in the benchmark problems presented as: (i) the respective Reynolds numbers are relatively low, and (ii) their geometry is particularly simple.

4.3 Governing equations

4.3.1 Preliminary comments

The mathematical model to describe the motion of a fluid is governed by the conservation of mass equation and the Navier–Stokes equations (momentum equations), which are a set of nonlinear coupled partial differential equations in terms of velocity and pressure.

In order to define a flow, two alternative descriptions can be used:

- *Eulerian*: the motion of all matter passing through a fixed spatial location is considered. In this formulation, the control volume remains fixed in the space and the displacements of the particles are ignored.
- *Lagrangian*: the displacements of a set of particles is a primary dependent variable. In this formulation, the control volume is variable.

Eulerian description is commonly used to study fluid-flow and coupled fluid-flow with heat transfer problems, hence this is the system used in this work.

Regarding the condition of incompressibility, a fluid can be considered incompressible when the density does not change due to the pressure. In these cases, the density can be treated as a parameter instead of as a variable. In formulations that consider compressible fluids, an extra equation, relating density, temperature and pressure, has to be introduced. This equation is known as the state equation and, in the case of perfect gases, it is given by (Versteeg and Malalasekera, 1995),

$$p = \rho\, R\, \theta \tag{4.2}$$

where ρ is the density, p is the pressure, θ is the temperature and R is the ideal gas constant.

4.3.2 Conservation of mass

The principle of conservation of mass can be stated as the time rate of change of mass in a fixed volume being equal to the rate of inflow of mass through the surface. The application of this principle to the control volume leads to the continuity equation:

$$\frac{\partial \rho}{\partial t} + \operatorname{div}\,(\rho \boldsymbol{v}) = 0 \tag{4.3}$$

Equation (4.3) can be developed to obtain,

$$\frac{\partial \rho}{\partial t} + \frac{\partial \rho v_i}{\partial x_i} = 0$$

where v_i are the components of the velocity vector, $\boldsymbol{v}$, in a three-dimensional space.

For steady state conditions, the equation (4.3) becomes,

$$\frac{\partial \rho v_i}{\partial x_i} = 0 \tag{4.4}$$

and if the density changes following a fluid particle are negligible, the continuity equation is referred to as the *incompressibility condition*, which expresses that the volume change for an incompressible fluid during its deformation is zero:

$$\frac{\partial v_i}{\partial x_i} = 0 \Leftrightarrow \operatorname{div} \boldsymbol{v} = 0 \tag{4.5}$$

4.3.3 Conservation of momentum

The principle of conservation of linear momentum states that the time rate of change of linear momentum of a given set of particles is equal to the vector sum of all external forces acting on this set. The equation can be written as,

$$\rho \frac{\mathrm{D}\boldsymbol{v}}{\mathrm{D}t} = \operatorname{div} \boldsymbol{\sigma} + \rho \boldsymbol{b} \tag{4.6}$$

where $\mathrm{D}/\mathrm{D}t$ is the material derivative, $\operatorname{div} \boldsymbol{\sigma}$ is the divergence of the Cauchy stress tensor and $\boldsymbol{b}$ is the body force vector measured per unit mass. Equation (4.6) is known as Navier–Stokes equation. The material derivative of a vector and the operator *divergence* of a tensor are defined as:

$$\frac{\mathrm{D}\boldsymbol{v}}{\mathrm{D}t} = \frac{\partial \boldsymbol{v}}{\partial t} + (\boldsymbol{\nabla v})\ \boldsymbol{v} \tag{4.7a}$$

$$\operatorname{div} \boldsymbol{\sigma} = \sigma_{ij,j}\, \boldsymbol{e}_i \tag{4.7b}$$

Considering an Eulerian reference system, the acceleration of the fluid can be decomposed in two terms: (i) local acceleration and (ii) convective acceleration. Hence, equation (4.6) can be written as,

$$\rho\ (\dot{\boldsymbol{v}} + (\boldsymbol{\nabla v})\ \boldsymbol{v}) = \operatorname{div} \boldsymbol{\sigma} + \rho \boldsymbol{b} \tag{4.8}$$

where $\dot{\boldsymbol{v}}$ represents the partial derivative of the velocity vector with respect to time and $\boldsymbol{\nabla v}$ is the gradient of the velocity defined as:

$$\boldsymbol{\nabla v} = \boldsymbol{v}_{,i} \otimes \boldsymbol{e}_i \tag{4.9}$$

For viscous incompressible and Newtonian fluids, the Cauchy stress tensor can be calculated as,

$$\boldsymbol{\sigma} = \boldsymbol{\tau} + (-\tilde{p})\, \boldsymbol{I} \tag{4.10}$$

where $\tilde{p}$ is the absolute pressure (hydrostatic and relative pressure), $\boldsymbol{I}$ the unit tensor and $\boldsymbol{\tau}$ is the viscous stress tensor, which can be computed using the shear stress constitutive relation expressed, in the linear case, as,

$$\boldsymbol{\tau} = 2\, \mu\, \boldsymbol{\varepsilon} \tag{4.11}$$

where μ is the shear viscosity that depends on the fluid and $\boldsymbol{\varepsilon}$ is the deformation tensor of the velocity depending on the velocity vector:

$$\boldsymbol{\varepsilon} = \frac{1}{2} \left(\boldsymbol{\nabla v} + (\boldsymbol{\nabla v})^T \right) \tag{4.12}$$

Replacing equation (4.12) into (4.11) and the resulting expression into (4.10), the stress tensor can be expressed as,

$$\boldsymbol{\sigma} = \mu \left(\boldsymbol{\nabla v} + (\boldsymbol{\nabla v})^T \right) + (-\tilde{p})\, \boldsymbol{I} \tag{4.13}$$

and, then, the divergence of $\boldsymbol{\sigma}$ is given by,

$$\operatorname{div} \boldsymbol{\sigma} = \mu\, \boldsymbol{\nabla}^2 \boldsymbol{v} + \mu \boldsymbol{\nabla} (\operatorname{div} \boldsymbol{v}) - \boldsymbol{\nabla} \tilde{p} \tag{4.14}$$

where $\boldsymbol{\nabla}^2\boldsymbol{v} = v_{i,jj}\,\boldsymbol{e}_i$ is the Laplacian of $\boldsymbol{v}$.

Considering that $\operatorname{div}\boldsymbol{v} = 0$, as equation (4.5) shows, replacing (4.14) into (4.8) and dividing the resultant equation by the density of the fluid, the motion equation for an incompressible Newtonian fluid is expressed as,

$$\dot{\boldsymbol{v}} + (\boldsymbol{\nabla}\boldsymbol{v})\,\boldsymbol{v} - \nu\,\boldsymbol{\nabla}^2\boldsymbol{v} + \boldsymbol{\nabla}p = \boldsymbol{b} \tag{4.15}$$

where ν is the kinematic viscosity, $\nu = \mu/\rho$, and p is the absolute pressure divided by the density, $p = \tilde{p}/\rho$.

4.3.4 Conservation of the energy equation

The first law of thermodynamics for viscous incompressible fluids stands,

$$\rho_0\,c_p\,\frac{\mathrm{D}\theta}{\mathrm{D}t} + \operatorname{div}\boldsymbol{q} - G = 0 \tag{4.16}$$

where θ represents the temperature, c_p is the specific heat of the fluid, G is the heat generation per unit volume and q_i is the heat transfer flux in the i-direction.

Replacing the definition of material derivative into (4.16), the advection-diffusion equation in viscous incompressible fluids, is then expressed as:

$$\rho_0\,c_p\,\left(\dot{\theta} + \boldsymbol{v}\cdot\boldsymbol{\nabla}\theta\right) + \operatorname{div}\boldsymbol{q} - G = 0 \tag{4.17}$$

The conservation of momentum equation represents the motion of a viscous and incompressible fluid when the density variations are not important. However, when the fluid is subjected to high temperatures, the variation of the density with the temperature may be significant and buoyancy forces are developed. In order to consider their effects, an extended form of the Boussinesq approximation is used in the conservation of momentum equations. The artificial linear variation of the density with the temperature is expressed as,

$$\rho = \rho_0\,\left(1 - \beta\,(\theta - \theta_0)\right) \tag{4.18}$$

where β is the thermal expansion coefficient and θ_0 is the reference temperature. This equation is valid for the description of the body forces. Thus, the density in all other situations is assumed to be that of the reference state, ρ_0.

The gravitational force due to the artificial variation of the density with the temperature is included in the conservation of momentum equation by means of,

$$\boldsymbol{f}_g = \rho_0\,\boldsymbol{g}\,(1 - \beta\,(\theta - \theta_0)) \tag{4.19}$$

where $\boldsymbol{g}$ is the gravity acceleration vector.

At this point, it is deemed relevant to make a remark about the pressure (manual of the ADINA-F, 2010). In equation (4.15), p is the rate between the absolute pressure, $\tilde{p}$, and the density of the fluid, ρ. The absolute pressure is the sum of the relative pressure, $\tilde{p}_r$, and the hydrostatic pressure, $\tilde{p}_s$, but, in many fluid flow problems, the value of the hydrostatic pressure is much larger than the relative pressure. This fact can create numerical instabilities and, in these cases, the relative pressure is usually taken as a variable of the problem instead of the absolute pressure.

In order to avoid possible numerical instabilities, in the present implementation it was decided to use a formulation where p in the conservation of momentum equation (4.15)

is the relative pressure divided by the density[2] and, then, only the buoyancy force also divided by the density, $\boldsymbol{f}_B$, will be included in the referred equation,

$$\dot{\boldsymbol{v}} + (\boldsymbol{\nabla v})\,\boldsymbol{v} - \nu\,\boldsymbol{\nabla}^2\boldsymbol{v} + \boldsymbol{\nabla} p = \boldsymbol{b} + \boldsymbol{f}_B \tag{4.20}$$

and:

$$\boldsymbol{f}_B = -\beta\,\boldsymbol{g}\,(\theta - \theta_0) \tag{4.21}$$

The non-isothermal flows are characterized by the following dimensionless numbers (Çengel, 2003):

- Grashof number, Gr: it is the ratio between buoyancy forces and viscous forces,

$$Gr = \frac{g\beta L_{ref}^3 \Delta\theta}{\nu^2} \tag{4.22}$$

  where g is the Euclidean norm of gravity acceleration vector, $\Delta\theta$ is the gradient of temperatures and α is the thermal diffusivity:

$$\alpha = \frac{k}{\rho_0\, c_p} \tag{4.23}$$

- Prandtl number, Pr: it is computed as the ratio between the momentum diffusivity and thermal diffusivity:

$$Pr = \frac{\nu}{\alpha} \tag{4.24}$$

- Rayleigh number, Ra: it is the most often used natural convection parameter:

$$Ra = Gr\,Pr = \frac{g\beta L_{ref}^3 \Delta\theta}{\nu\alpha} \tag{4.25}$$

Additionally, the relation between the Grashof and the square Reynolds number (Gr/Re^2) is also referred in the literature to classify the convection. The ratio Gr/Re^2 represents the importance of natural convection relative to forced convection. In the literature it is usually accepted that natural convection is negligible when $Gr/Re^2 < 0.1$, forced convection is negligible when $Gr/Re^2 > 10$ and both natural and forced convection are not negligible when $0.1 > Gr/Re^2 > 10$.

4.4 Strong form of the problem

Consider the thermodynamic problem schematically represented in figure 4.1, where Ω is the domain of the problem and $\Gamma = \Gamma_t \cup \Gamma_v = \Gamma_\theta \cup \Gamma_{\overline{q}}$ represents the boundary.

The set of governing differential equations presented in section 4.3 constitute a nonlinear system of partial differential equations in the domain of the problem, Ω, which require appropriate boundary conditions on the contour, Γ, and initial conditions in the domain to be solved.

The boundary conditions can be subdivided in two groups: (i) those regarding the heat transfer problem ($\Gamma_\theta \cup \Gamma_{\overline{q}}$ such that $\Gamma_\theta \cap \Gamma_{\overline{q}} = \emptyset$) and (ii) those regarding the fluid-flow problem ($\Gamma_t \cup \Gamma_v$ such that $\Gamma_t \cap \Gamma_v = \emptyset$). Both conditions are applied simultaneously.

[2] From now on, p denotes the relative pressure divided by the density.

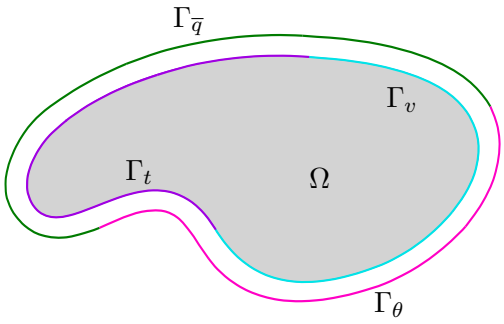

Figure 4.1: Boundary conditions of the fluid dynamics problem.

The boundary and initial conditions that can be defined in the in-house code developed within the thesis are the following,

$$\boldsymbol{v} = \overline{\boldsymbol{v}} \quad \text{on} \quad \Gamma_v \tag{4.26a}$$
$$\boldsymbol{t} = \overline{\boldsymbol{t}} \quad \text{on} \quad \Gamma_t \tag{4.26b}$$
$$\theta = \overline{\theta} \quad \text{on} \quad \Gamma_\theta \tag{4.26c}$$
$$q_n + \overline{q} = 0 \quad \text{on} \quad \Gamma_{\overline{q}} \tag{4.26d}$$
$$\boldsymbol{v}_0 = \overline{\boldsymbol{v}}_0 \quad \text{at} \quad t = t_0 \text{ in } \overline{\Omega} \tag{4.26e}$$
$$\theta_0 = \overline{\theta}_0 \quad \text{at} \quad t = t_0 \text{ in } \overline{\Omega} \tag{4.26f}$$

where $\overline{\Omega} = \Omega \cup \Gamma$ is the closure of the fluid domain, $\boldsymbol{t} = (\nu\, \boldsymbol{\nabla}\boldsymbol{v} - p\, \boldsymbol{I})\, \boldsymbol{n}$ is the ratio between the traction[3] and the density on the boundary Γ_t and $\overline{\boldsymbol{v}}$, $\overline{\boldsymbol{t}}$ and $\overline{\theta}$ are the prescribed values of the velocity, traction and temperature on the boundaries, respectively.

The classical formulation of the strong form of the transient non-isothermal fluid-flow problem reads as follows:

Obtain $\boldsymbol{v}$, p and θ for each point $\boldsymbol{x} = x_i\, \boldsymbol{e}_i \in \overline{\Omega}$ for all $t \in [t_0, t_1]$, such that:

$$\operatorname{div} \boldsymbol{v} = 0 \quad \text{in} \quad \Omega \tag{4.27a}$$
$$\dot{\boldsymbol{v}} + (\boldsymbol{\nabla}\boldsymbol{v})\, \boldsymbol{v} - \nu\, \boldsymbol{\nabla}^2 \boldsymbol{v} + \boldsymbol{\nabla} p = \boldsymbol{b} + \boldsymbol{f}_B \quad \text{in} \quad \Omega \tag{4.27b}$$
$$-\operatorname{div} \boldsymbol{q} + G = \rho_0\, c_p \left(\dot{\theta} + \boldsymbol{v} \cdot \boldsymbol{\nabla}\theta\right) \quad \text{in} \quad \Omega \tag{4.27c}$$
$$\boldsymbol{v} = \overline{\boldsymbol{v}} \quad \text{on} \quad \Gamma_v \tag{4.27d}$$
$$\boldsymbol{t} = \overline{\boldsymbol{t}} \quad \text{on} \quad \Gamma_t \tag{4.27e}$$
$$\theta = \overline{\theta} \quad \text{on} \quad \Gamma_\theta \tag{4.27f}$$
$$q_n + \overline{q} = 0 \quad \text{on} \quad \Gamma_{\overline{q}} \tag{4.27g}$$
$$\boldsymbol{v}_0 = \overline{\boldsymbol{v}}_0 \quad \text{at} \quad t = t_0 \text{ in } \overline{\Omega} \tag{4.27h}$$
$$\theta_0 = \overline{\theta}_0 \quad \text{at} \quad t = t_0 \text{ in } \overline{\Omega} \tag{4.27i}$$

[3] In the literature it is common to refer $\boldsymbol{t}$ as a *pseudotraction* as it is not the real traction, $\hat{\boldsymbol{t}}$, computed as: $\hat{\boldsymbol{t}} = \boldsymbol{\sigma}\boldsymbol{n}$. In this text, the formulation using the pseudotraction is presented even if it is referred to as a traction.

4.5 Weak form of the problem

The weak form associated to the system of governing equations and the respective boundary and initial conditions renders a set of equations amenable to a (i) finite element space discretization, and (ii) a finite difference time discretization.

Consider $\delta\boldsymbol{v}$, δp and $\delta\theta$ arbitrary virtual functions such that $\delta\boldsymbol{v} = \boldsymbol{o}$ on Γ_v and $\delta\theta = 0$ on Γ_θ. Using these functions to weigh the governing equations on the domain and the static boundary equilibrium equations, respectively, integrating the result and using the definition of the pseudotraction, one obtains:

$$\int_\Omega \delta\boldsymbol{v}\cdot\left(\dot{\boldsymbol{v}} + (\boldsymbol{\nabla}\boldsymbol{v})\,\boldsymbol{v} - \nu\,\boldsymbol{\nabla}^2\boldsymbol{v} + \boldsymbol{\nabla}p - \boldsymbol{b} - \boldsymbol{f}_B\right)\,\mathrm{d}\Omega + \\ + \int_{\Gamma_t}\delta\boldsymbol{v}\cdot\left((\nu\,\boldsymbol{\nabla}\boldsymbol{v} - p\,\boldsymbol{I})\,\boldsymbol{n} - \overline{\boldsymbol{t}}\right)\,\mathrm{d}\Gamma_t = 0 \tag{4.28a}$$

$$-\int_\Omega \delta p\,\mathrm{div}\,\boldsymbol{v}\,\mathrm{d}\Omega = 0 \tag{4.28b}$$

$$\int_\Omega \delta\theta\,\left(-\mathrm{div}\,\boldsymbol{q} + G - \rho_0\,c_p\,\left(\dot{\theta} + \boldsymbol{v}\cdot\boldsymbol{\nabla}\theta\right)\right)\,\mathrm{d}\Omega + \int_{\Gamma_{\overline{q}}}\delta\theta\,(q_n + \overline{q})\,\mathrm{d}\Gamma_{\overline{q}} = 0 \tag{4.28c}$$

Applying the divergence theorem and parts integration to the latter (see details on appendix C.1) renders the weak form of the problem:

$$\int_\Omega \delta\boldsymbol{v}\cdot\dot{\boldsymbol{v}}\,\mathrm{d}\Omega + \int_\Omega \delta\boldsymbol{v}\cdot(\boldsymbol{\nabla}\boldsymbol{v})\,\boldsymbol{v}\,\mathrm{d}\Omega + \int_\Omega \boldsymbol{\nabla}\delta\boldsymbol{v} : \nu\boldsymbol{\nabla}\boldsymbol{v}\,\mathrm{d}\Omega - \\ - \int_\Omega \mathrm{div}\,\delta\boldsymbol{v}\,p\,\mathrm{d}\Omega - \int_{\Gamma_t}\delta\boldsymbol{v}\cdot\overline{\boldsymbol{t}}\,\mathrm{d}\Gamma_t - \int_\Omega \delta\boldsymbol{v}\cdot\boldsymbol{b}\,\mathrm{d}\Omega - \int_\Omega \delta\boldsymbol{v}\cdot\boldsymbol{f}_B\,\mathrm{d}\Omega = 0 \tag{4.29a}$$

$$-\int_\Omega \delta p\,\mathrm{div}\,\boldsymbol{v}\,\mathrm{d}\Omega = 0 \tag{4.29b}$$

$$\int_\Omega \left(\boldsymbol{\nabla}\delta\theta\cdot\boldsymbol{q} - \delta\theta\,\rho_0\,c_p\,\dot{\theta}\right)\,\mathrm{d}\Omega - \int_\Omega \delta\theta\,\rho_0\,c_p\,\boldsymbol{v}\cdot\boldsymbol{\nabla}\theta\,\mathrm{d}\Omega + \\ + \int_\Omega \delta\theta\,G\,\mathrm{d}\Omega + \int_{\Gamma_{\overline{q}}}\delta\theta\,\overline{q}\,\mathrm{d}\Gamma_{\overline{q}} = 0 \tag{4.29c}$$

The operator : in equation (4.29a) represents the scalar product between general second-order tensors, $\boldsymbol{A}$ and $\boldsymbol{B}$, and it is defined as:

$$\boldsymbol{A} : \boldsymbol{B} = \mathrm{tr}\left(\boldsymbol{A}^T\,\boldsymbol{B}\right) = A_{ij}\,B_{ij} \tag{4.30}$$

where $\mathrm{tr}(\cdot)$ is the trace operator.

4.6 Spatial discretization and residual vector

Considering that the closure of the domain, $\overline{\Omega}$, is subdivided into finite elements, a spatial discretization of the weak form can be done.

The independent variables $\boldsymbol{v}^{(e)}$ and $p^{(e)}$ in each element can be approximated by the expressions,

$$\boldsymbol{v}^{(e)} = \boldsymbol{\psi}_v^{(e)}\,\mathbf{v}^{(e)} \tag{4.31a}$$

$$p^{(e)} = \boldsymbol{\psi}_p^{(e)}\,\mathbf{p}^{(e)} \tag{4.31b}$$

where $\mathbf{v}^{(e)}$ and $\mathbf{p}^{(e)}$ are the nodal vectors of velocity and pressure, respectively, and $\boldsymbol{\psi}_v^{(e)}$ and $\boldsymbol{\psi}_p^{(e)}$ are the shape functions in an element defined as,

$$\boldsymbol{\psi}_v^{(e)} = \begin{bmatrix} \psi_1 \mathbf{I} & \psi_2 \mathbf{I} & \dots & \psi_n \mathbf{I} \end{bmatrix} \tag{4.32a}$$

$$\boldsymbol{\psi}_p^{(e)} = \begin{Bmatrix} \psi_1 & \psi_2 & \dots & \psi_m \end{Bmatrix} \tag{4.32b}$$

where n and m are, respectively, the number of nodes of the element where the velocity and pressure fields are approximated and $\mathbf{I}$ is the identity matrix. The variation of the expressions (4.31) can be written as:

$$\delta \boldsymbol{v}^{(e)} = \boldsymbol{\psi}_v^{(e)} \, \delta \mathbf{v}^{(e)} \tag{4.33a}$$

$$\delta p^{(e)} = \boldsymbol{\psi}_p^{(e)} \, \delta \mathbf{p}^{(e)} \tag{4.33b}$$

The spatial discretization of the temperature is given by the expression (3.30a) and, consequently, the variation of that expression is given by (3.31a).

In the following it is considered that the body force vector in the domain and the traction vector on the static boundary can be expressed as,

$$\boldsymbol{b}^{(e)} = \boldsymbol{\psi}_v^{(e)} \, \mathbf{b}^{(e)} \tag{4.34a}$$

$$\bar{\boldsymbol{t}}^{(e)} = \boldsymbol{\psi}_v^{(e)} \, \bar{\mathbf{t}}^{(e)} \tag{4.34b}$$

where $\mathbf{b}^{(e)}$ and $\bar{\mathbf{t}}^{(e)}$ are the nodal values of $\boldsymbol{b}^{(e)}$ and $\bar{\boldsymbol{t}}^{(e)}$, respectively. The internal heat generation, G, is approximated over the elemental domain as (3.32a). In the program developed, the prescribed heat flux can only be null, *i.e.*, $\overline{q} = 0$. Consequently, the term regarding the prescribed heat is not included in the following equations.

Considering the weak form (4.29) over a typical finite element and replacing the expressions (4.31), (4.33), (3.30a), (3.31a), (4.34) and (3.32a) into the mentioned equation, one obtains term by term,

$$\int_{\Omega^{(e)}} \delta \boldsymbol{v}^{(e)} \cdot \dot{\boldsymbol{v}}^{(e)} \, \mathrm{d}\Omega^{(e)} = \delta \mathbf{v}^{(e)T} \int_{\Omega^{(e)}} \boldsymbol{\psi}_v^{(e)T} \boldsymbol{\psi}_v^{(e)} \, \mathrm{d}\Omega^{(e)} \, \dot{\mathbf{v}}^{(e)} \tag{4.35a}$$

$$\begin{aligned} &\int_{\Omega^{(e)}} \delta \boldsymbol{v}^{(e)} \cdot \left(\boldsymbol{\nabla} \boldsymbol{v}^{(e)} \right) \boldsymbol{v}^{(e)} \, \mathrm{d}\Omega^{(e)} = \int_{\Omega^{(e)}} \delta \boldsymbol{v}^{(e)} \cdot \left(\boldsymbol{v}_{,i}^{(e)} \otimes \boldsymbol{e}_i \right) \boldsymbol{v}^{(e)} \, \mathrm{d}\Omega^{(e)} = \\ &= \int_{\Omega^{(e)}} \delta \boldsymbol{v}^{(e)} \cdot \left(\boldsymbol{e}_i \cdot \boldsymbol{v}^{(e)} \right) \boldsymbol{v}_{,i}^{(e)} \, \mathrm{d}\Omega^{(e)} = \delta \mathbf{v}^{(e)T} \int_{\Omega^{(e)}} \boldsymbol{\psi}_v^{(e)T} \left(\mathbf{e}_i^T \, \boldsymbol{\psi}_v^{(e)} \mathbf{v}^{(e)} \right) \left(\boldsymbol{\psi}_v^{(e)} \right)_{,i} \mathrm{d}\Omega^{(e)} \, \mathbf{v}^{(e)} \end{aligned} \tag{4.35b}$$

$$\begin{aligned} &\int_{\Omega^{(e)}} \boldsymbol{\nabla} \delta \boldsymbol{v}^{(e)} : \nu \boldsymbol{\nabla} \boldsymbol{v}^{(e)} \, \mathrm{d}\Omega^{(e)} = \int_{\Omega^{(e)}} \left(\delta \boldsymbol{v}_{,i}^{(e)} \otimes \boldsymbol{e}_i \right) : \left(\nu \boldsymbol{v}_{,j}^{(e)} \otimes \boldsymbol{e}_j \right) \mathrm{d}\Omega^{(e)} = \\ &\quad = \int_{\Omega^{(e)}} \delta \, v_{i,j}^{(e)} \, \nu \, v_{i,j}^{(e)} \, \mathrm{d}\Omega^{(e)} = \int_{\Omega^{(e)}} \left(\delta \boldsymbol{v}_{,j}^{(e)} \cdot \boldsymbol{e}_i \right) \nu \left(\boldsymbol{v}_{,j}^{(e)} \cdot \boldsymbol{e}_j \right) \mathrm{d}\Omega^{(e)} = \\ &\quad = \delta \mathbf{v}^{(e)T} \int_{\Omega^{(e)}} \left(\left(\boldsymbol{\psi}_v^{(e)T} \right)_{,j} \mathbf{e}_i \right) \nu \left(\mathbf{e}_i^T \left(\boldsymbol{\psi}_v^{(e)} \right)_{,j} \right) \mathrm{d}\Omega^{(e)} \, \mathbf{v}^{(e)} \end{aligned} \tag{4.35c}$$

$$\begin{aligned} &- \int_{\Omega^{(e)}} \operatorname{div} \delta \boldsymbol{v}^{(e)} \, p^{(e)} \, \mathrm{d}\Omega^{(e)} = - \int_{\Omega^{(e)}} \delta v_{i,i}^{(e)} \, p^{(e)} \, \mathrm{d}\Omega^{(e)} = \\ &\quad = - \int_{\Omega^{(e)}} \left(\delta \boldsymbol{v}_{,i}^{(e)} \cdot \boldsymbol{e}_i \right) p^{(e)} \, \mathrm{d}\Omega^{(e)} = -\delta \mathbf{v}^{(e)T} \int_{\Omega^{(e)}} \left(\boldsymbol{\psi}_v^{(e)T} \right)_{,i} \mathbf{e}_i \, \boldsymbol{\psi}_p^{(e)} \, \mathrm{d}\Omega^{(e)} \, \mathbf{p}^{(e)} \end{aligned} \tag{4.35d}$$

$$\begin{aligned} &- \int_{\Omega^{(e)}} \delta p^{(e)} \operatorname{div} \boldsymbol{v}^{(e)} \, \mathrm{d}\Omega^{(e)} = - \int_{\Omega^{(e)}} \delta p^{(e)} \left(\boldsymbol{e}_i \cdot \boldsymbol{v}_{,i}^{(e)} \right) \mathrm{d}\Omega^{(e)} = \\ &\quad = -\delta \mathbf{p}^{(e)T} \int_{\Omega^{(e)}} \boldsymbol{\psi}_p^{(e)T} \, \mathbf{e}_i^T \left(\boldsymbol{\psi}_v^{(e)} \right)_{,i} \mathrm{d}\Omega^{(e)} \, \mathbf{v}^{(e)} \end{aligned} \tag{4.35e}$$

$$-\int_{\Omega^{(e)}} \delta\boldsymbol{v}^{(e)} \cdot \boldsymbol{b}^{(e)}\,\mathrm{d}\Omega^{(e)} = -\delta\mathbf{v}^{(e)T}\int_{\Omega^{(e)}} \boldsymbol{\psi}_v^{(e)T}\,\boldsymbol{\psi}_v^{(e)}\,\mathrm{d}\Omega^{(e)}\,\mathbf{b}^{(e)} \tag{4.35f}$$

$$-\int_{\Gamma_t^{(e)}} \delta\boldsymbol{v}^{(e)} \cdot \bar{\boldsymbol{t}}^{(e)}\,\mathrm{d}\Gamma_t^{(e)} = -\delta\mathbf{v}^{(e)T}\int_{\Gamma_t^{(e)}} \boldsymbol{\psi}_v^{(e)T}\,\boldsymbol{\psi}_v^{(e)}\,\mathrm{d}\Gamma_t^{(e)}\,\bar{\mathbf{t}}^{(e)} \tag{4.35g}$$

$$-\int_{\Omega^{(e)}} \delta\boldsymbol{v}^{(e)} \cdot \boldsymbol{f}_B^{(e)}\,\mathrm{d}\Omega^{(e)} = \delta\mathbf{v}^{(e)T}\int_{\Omega^{(e)}} \boldsymbol{\psi}_v^{(e)T}\,\beta\,\boldsymbol{g}\,\boldsymbol{\psi}_\theta^{(e)}\left(\boldsymbol{\theta}^{(e)} - \boldsymbol{\theta}_0^{(e)}\right)\,\mathrm{d}\Omega^{(e)} \tag{4.35h}$$

$$\int_{\Omega^{(e)}} \boldsymbol{\nabla}\delta\theta^{(e)} \cdot \boldsymbol{q}^{(e)}\,\mathrm{d}\Omega^{(e)} = -\delta\boldsymbol{\theta}^{(e)T}\int_{\Omega^{(e)}} \mathbf{B}_\theta^{(e)T}\mathbf{D}\,\mathbf{B}_\theta^{(e)}\,\mathrm{d}\Omega^{(e)}\,\boldsymbol{\theta}^{(e)} \tag{3.33a}$$

$$-\int_{\Omega^{(e)}} \delta\theta^{(e)}\,\rho\,c_p\,\dot{\theta}^{(e)}\,\mathrm{d}\Omega^{(e)} = -\delta\boldsymbol{\theta}^{(e)T}\int_{\Omega^{(e)}} \boldsymbol{\psi}_\theta^{(e)T}\rho\,c_p\,\boldsymbol{\psi}_\theta^{(e)}\,\mathrm{d}\Omega^{(e)}\,\dot{\boldsymbol{\theta}}^{(e)} \tag{3.33b}$$

$$\int_{\Omega^{(e)}} \delta\theta^{(e)}\,G^{(e)}\,\mathrm{d}\Omega^{(e)} = \delta\boldsymbol{\theta}^{(e)T}\int_{\Omega^{(e)}} \boldsymbol{\psi}_\theta^{(e)T}\boldsymbol{\psi}_\theta^{(e)}\,\mathrm{d}\Omega^{(e)}\,\mathbf{g}^{(e)} \tag{3.33c}$$

$$-\int_{\Omega} \delta\theta\,\rho_0\,c_p\,\boldsymbol{v}\cdot\boldsymbol{\nabla}\theta\,\mathrm{d}\Omega = -\delta\boldsymbol{\theta}^{(e)T}\int_{\Omega^{(e)}} \boldsymbol{\psi}_\theta^{(e)T}\,\rho_0\,c_p\left(\boldsymbol{\psi}_v^{(e)}\mathbf{v}^{(e)}\right)^T\,\mathbf{B}_\theta^{(e)}\,\mathrm{d}\Omega^{(e)}\,\boldsymbol{\theta}^{(e)} \tag{4.35i}$$

where the last terms of each of the expressions are written using the matrix notation, being this the form implemented in the numerical code.

Hence, the weak form of the problem can be obtained replacing the expressions (4.35) into (4.28):

$$\begin{aligned}
&\delta\mathbf{v}^{(e)T}\left(\int_{\Omega^{(e)}} \boldsymbol{\psi}_v^{(e)T}\boldsymbol{\psi}_v^{(e)}\dot{\mathbf{v}}^{(e)}\,\mathrm{d}\Omega^{(e)} + \int_{\Omega^{(e)}} \boldsymbol{\psi}_v^{(e)T}\,\mathbf{e}_i^T\,\boldsymbol{\psi}_v^{(e)}\mathbf{v}^{(e)}\,\left(\boldsymbol{\psi}_v^{(e)}\right)_{,i}\mathbf{v}^{(e)}\,\mathrm{d}\Omega^{(e)} + \right.\\
&+\int_{\Omega^{(e)}} \left(\boldsymbol{\psi}_v^{(e)T}\right)_{,j}\,\mathbf{e}_i\,\nu\,\mathbf{e}_i^T\,\left(\boldsymbol{\psi}_v^{(e)}\right)_{,j}\,\mathbf{v}^{(e)}\,\mathrm{d}\Omega^{(e)} - \int_{\Omega^{(e)}} \left(\boldsymbol{\psi}_v^{(e)T}\right)_{,i}\,\mathbf{e}_i\,\boldsymbol{\psi}_p^{(e)}\mathbf{p}^{(e)}\,\mathrm{d}\Omega^{(e)} - \\
&\qquad - \int_{\Gamma_t^{(e)}} \boldsymbol{\psi}_v^{(e)T}\,\boldsymbol{\psi}_v^{(e)}\,\mathrm{d}\Gamma_t^{(e)}\,\bar{\mathbf{t}}^{(e)} - \int_{\Omega^{(e)}} \boldsymbol{\psi}_v^{(e)T}\,\boldsymbol{\psi}_v^{(e)}\,\mathrm{d}\Omega^{(e)}\,\mathbf{b}^{(e)} + \\
&\qquad\qquad \left. + \int_{\Omega^{(e)}} \boldsymbol{\psi}_v^{(e)T}\,\beta\,\boldsymbol{g}\,\boldsymbol{\psi}_\theta^{(e)}\left(\boldsymbol{\theta}^{(e)} - \boldsymbol{\theta}_0^{(e)}\right)\,\mathrm{d}\Omega^{(e)}\right) = 0
\end{aligned} \tag{4.36a}$$

$$-\delta\mathbf{p}^{(e)T}\left(\int_{\Omega^{(e)}} \boldsymbol{\psi}_p^{(e)T}\,\mathbf{e}_i^T\,\left(\boldsymbol{\psi}_v^{(e)}\right)_{,i}\,\mathbf{v}^{(e)}\,\mathrm{d}\Omega^{(e)}\right) = 0 \tag{4.36b}$$

$$\begin{aligned}
&-\delta\boldsymbol{\theta}^{(e)T}\left(\int_{\Omega^{(e)}} \mathbf{B}_\theta^{(e)T}\mathbf{D}\,\mathbf{B}_\theta^{(e)}\,\mathrm{d}\Omega^{(e)}\,\boldsymbol{\theta}^{(e)} + \int_{\Omega^{(e)}} \boldsymbol{\psi}_\theta^{(e)T}\rho\,c_p\,\boldsymbol{\psi}_\theta^{(e)}\,\mathrm{d}\Omega^{(e)}\,\dot{\boldsymbol{\theta}} + \right.\\
&\left. + \int_{\Omega^{(e)}} \boldsymbol{\psi}_\theta^{(e)T}\,\rho_0\,c_p\left(\boldsymbol{\psi}_v^{(e)}\mathbf{v}^{(e)}\right)^T\,\mathbf{B}_\theta^{(e)}\,\mathrm{d}\Omega^{(e)}\,\boldsymbol{\theta}^{(e)} - \int_{\Omega^{(e)}} \boldsymbol{\psi}_\theta^{(e)T}\boldsymbol{\psi}_\theta^{(e)}\,\mathrm{d}\Omega^{(e)}\,\mathbf{g}^{(e)}\right) = 0
\end{aligned} \tag{4.36c}$$

Since $\delta\mathbf{v}^{(e)}$, $\delta\mathbf{p}^{(e)}$ and $\delta\boldsymbol{\theta}^{(e)}$ are arbitrary nodal vectors, the only possible solution of the equation (4.36) is,

$$\mathbf{r}^{(e)} \equiv \begin{Bmatrix} \mathbf{r}_v^{(e)} \\ \mathbf{r}_p^{(e)} \\ \mathbf{r}_\theta^{(e)} \end{Bmatrix} = \mathbf{0} \tag{4.37}$$

where $\mathbf{r}_v^{(e)}$, $\mathbf{r}_p^{(e)}$ and $\mathbf{r}_\theta^{(e)}$ are the components of the elemental residual vector defined as:

$$\begin{aligned}\mathbf{r}_v^{(e)} = &\int_{\Omega^{(e)}} \boldsymbol{\psi}_v^{(e)T}\boldsymbol{\psi}_v^{(e)}\,\mathrm{d}\Omega^{(e)}\,\dot{\mathbf{v}}^{(e)} + \int_{\Omega^{(e)}} \boldsymbol{\psi}_v^{(e)T}\,\mathbf{e}_i^T\,\boldsymbol{\psi}_v^{(e)}\mathbf{v}^{(e)}\,\left(\boldsymbol{\psi}_v^{(e)}\right)_{,i}\,\mathrm{d}\Omega^{(e)}\,\mathbf{v}^{(e)} + \\ &+ \int_{\Omega^{(e)}} \left(\boldsymbol{\psi}_v^{(e)T}\right)_{,j}\,\mathbf{e}_i\,\nu\,\mathbf{e}_i^T\,\left(\boldsymbol{\psi}_v^{(e)}\right)_{,j}\,\mathrm{d}\Omega^{(e)}\,\mathbf{v}^{(e)} - \\ &- \int_{\Omega^{(e)}} \left(\boldsymbol{\psi}_v^{(e)T}\right)_{,i}\,\mathbf{e}_i\,\boldsymbol{\psi}_p^{(e)}\,\mathrm{d}\Omega^{(e)}\,\mathbf{p}^{(e)} - \int_{\Gamma_t^{(e)}} \boldsymbol{\psi}_v^{(e)T}\,\boldsymbol{\psi}_v^{(e)}\,\mathrm{d}\Gamma_t^{(e)}\,\overline{\mathbf{t}}^{(e)} - \\ &- \int_{\Omega^{(e)}} \boldsymbol{\psi}_v^{(e)T}\,\boldsymbol{\psi}_v^{(e)}\,\mathrm{d}\Omega^{(e)}\,\mathbf{b}^{(e)} + \int_{\Omega^{(e)}} \boldsymbol{\psi}_v^{(e)T}\,\beta\,\boldsymbol{g}\,\boldsymbol{\psi}_\theta^{(e)}\left(\boldsymbol{\theta}^{(e)} - \boldsymbol{\theta}_0^{(e)}\right)\,\mathrm{d}\Omega^{(e)}\end{aligned} \tag{4.38a}$$

$$\mathbf{r}_p^{(e)} = -\int_{\Omega^{(e)}} \boldsymbol{\psi}_p^{(e)T}\,\mathbf{e}_i^T\,\left(\boldsymbol{\psi}_v^{(e)}\right)_{,i}\,\mathrm{d}\Omega^{(e)}\,\mathbf{v}^{(e)} \tag{4.38b}$$

$$\begin{aligned}\mathbf{r}_\theta^{(e)} = &\int_{\Omega^{(e)}} \mathbf{B}_\theta^{(e)T}\mathbf{D}\,\mathbf{B}_\theta^{(e)}\,\mathrm{d}\Omega^{(e)}\,\boldsymbol{\theta}^{(e)} + \int_{\Omega^{(e)}} \boldsymbol{\psi}_\theta^{(e)T}\rho\,c_p\,\boldsymbol{\psi}_\theta^{(e)}\,\mathrm{d}\Omega^{(e)}\,\dot{\boldsymbol{\theta}} + \\ &+ \int_{\Omega^{(e)}} \boldsymbol{\psi}_\theta^{(e)T}\,\rho_0\,c_p\left(\boldsymbol{\psi}_v^{(e)}\mathbf{v}^{(e)}\right)^T\,\mathbf{B}_\theta^{(e)}\,\mathrm{d}\Omega^{(e)}\,\boldsymbol{\theta}^{(e)} - \int_{\Omega^{(e)}} \boldsymbol{\psi}_\theta^{(e)T}\boldsymbol{\psi}_\theta^{(e)}\,\mathrm{d}\Omega^{(e)}\,\mathbf{g}^{(e)}\end{aligned} \tag{4.38c}$$

The matrix form of the set of nonlinear system of differential equations (4.37) is,

$$\begin{aligned}\mathbf{r}^{(e)} = &\begin{bmatrix}\mathbf{M}_v^{(e)} & \mathbf{O} & \mathbf{O}\\ \mathbf{O} & \mathbf{O} & \mathbf{O}\\ \mathbf{O} & \mathbf{O} & \mathbf{M}^{(e)}\end{bmatrix}\begin{Bmatrix}\dot{\mathbf{v}}^{(e)}\\ \dot{\mathbf{p}}^{(e)}\\ \dot{\boldsymbol{\theta}}^{(e)}\end{Bmatrix} + \\ &+ \begin{bmatrix}\mathbf{K}_v^{(e)} + \mathbf{C}^{(e)} & \mathbf{G}^{(e)} & \mathbf{B}^{(e)}\\ \mathbf{G}^{(e)T} & \mathbf{O} & \mathbf{O}\\ \mathbf{O} & \mathbf{O} & \mathbf{K}^{(e)} + \mathbf{L}^{(e)}\end{bmatrix}\begin{Bmatrix}\mathbf{v}^{(e)}\\ \mathbf{p}^{(e)}\\ \boldsymbol{\theta}^{(e)}\end{Bmatrix} - \begin{Bmatrix}\mathbf{f}_v^{(e)}\\ \mathbf{0}\\ \mathbf{f}_\theta^{(e)}\end{Bmatrix}\end{aligned} \tag{4.39}$$

where $\mathbf{K}_v^{(e)}$ is the viscosity matrix, $\mathbf{C}^{(e)}$ is the convection matrix, $\mathbf{G}^{(e)}$ is the discrete gradient operator of the pressure, $\mathbf{G}^{(e)T}$ is the discrete divergence operator, $\mathbf{M}_v^{(e)}$ is the standard finite element mass matrix and $\mathbf{f}_v^{(e)}$ is the force vector, which includes the contributions of the body forces and the prescribed pseudotraction on the static boundary. They can be computed as,

$$\mathbf{K}_v^{(e)} = \int_{\Omega^{(e)}} \mathbf{B}_v^{(e)T}\,\nu\,\mathbf{B}_v^{(e)}\,\mathrm{d}\Omega^{(e)} \tag{4.40a}$$

$$\mathbf{C}^{(e)} = \int_{\Omega^{(e)}} \boldsymbol{\psi}_v^{(e)T}\,\left(\left(\boldsymbol{\psi}_v^{(e)}\,\mathbf{v}^{(e)}\right)^T\,\mathbf{e}_i\right)\,\left(\boldsymbol{\psi}_v^{(e)}\right)_{,i}\,\mathrm{d}\Omega^{(e)} \tag{4.40b}$$

$$\mathbf{G}^{(e)} = -\int_{\Omega^{(e)}} \left(\boldsymbol{\nabla}\boldsymbol{\psi}_v^{(e)}\right)^T\,\boldsymbol{\psi}_p^{(e)}\,\mathrm{d}\Omega^{(e)} \tag{4.40c}$$

$$\mathbf{M}_v^{(e)} = \int_{\Omega^{(e)}} \boldsymbol{\psi}_v^{(e)T}\,\boldsymbol{\psi}_v^{(e)}\,\mathrm{d}\Omega^{(e)} \tag{4.40d}$$

$$\mathbf{B}^{(e)} = \int_{\Omega^{(e)}} \beta\,\boldsymbol{\psi}_v^{(e)T}\,\boldsymbol{g}\,\boldsymbol{\psi}_\theta^{(e)}\,\mathrm{d}\Omega^{(e)} \tag{4.40e}$$

$$\mathbf{L}^{(e)} = \int_{\Omega^{(e)}} \rho_0\,c_p\,\boldsymbol{\psi}_\theta^{(e)T}\,\left(\boldsymbol{\psi}_v^{(e)}\,\mathbf{v}^{(e)}\right)^T\,\mathbf{B}_\theta^{(e)}\,\mathrm{d}\Omega^{(e)} \tag{4.40f}$$

$$\begin{aligned}\mathbf{f}_v^{(e)} = &\int_{\Omega^{(e)}} \boldsymbol{\psi}_v^{(e)T}\,\boldsymbol{\psi}_v^{(e)}\mathbf{b}^{(e)}\,\mathrm{d}\Omega^{(e)} + \int_{\Gamma_t^{(e)}} \boldsymbol{\psi}_v^{(e)T}\,\boldsymbol{\psi}_v^{(e)}\overline{\mathbf{t}}^{(e)}\,\mathrm{d}\Gamma_t^{(e)} + \\ &+ \int_{\Omega^{(e)}} \beta\,\boldsymbol{\psi}_v^{(e)T}\,\boldsymbol{g}\,\boldsymbol{\psi}_\theta^{(e)}\,\boldsymbol{\theta}_0^{(e)}\,\mathrm{d}\Omega^{(e)}\end{aligned} \tag{4.40g}$$

$$\mathbf{f}_\theta^{(e)} = \int_{\Omega^{(e)}} \boldsymbol{\psi}_\theta^{(e)T}\boldsymbol{\psi}_\theta^{(e)}\,\mathrm{d}\Omega^{(e)}\,\mathbf{g}^{(e)} \tag{4.40h}$$

where $\mathbf{g}^{(e)}$ is the elemental internal heat generation vector, $\boldsymbol{\theta}_0^{(e)}$ is the elemental nodal vector of initial temperatures and $\mathbf{B}_v^{(e)}$ is the matrix that gathers the derivatives of the shape functions defined as:

$$\mathbf{B}_v^{(e)} = \begin{bmatrix} \psi_{1,1}\mathbf{I} & \psi_{2,1}\mathbf{I} & ... & \psi_{n,1}\mathbf{I} \\ \psi_{1,2}\mathbf{I} & \psi_{2,2}\mathbf{I} & ... & \psi_{n,2}\mathbf{I} \end{bmatrix} \tag{4.41}$$

where $\mathbf{I}$ is the identity matrix. Matrices $\mathbf{M}^{(e)}$ and $\mathbf{K}^{(e)}$ are defined in equations (3.41b) and (3.41a), respectively.

Replacing the temporal discretization of the velocities and temperature, given by equation (B.13) in appendix B.3, into (4.39), the elemental residual vector is given by:

$$\begin{aligned} \mathbf{r}^{(e)t+\Delta t} = & \begin{bmatrix} \mathbf{K}_v^{(e)} + \mathbf{C}^{(e)} + \frac{1}{\gamma\Delta t}\mathbf{M}_v^{(e)} & \mathbf{G}^{(e)} & \mathbf{B}^{(e)} \\ \mathbf{G}^{(e)T} & \mathbf{O} & \mathbf{O} \\ \mathbf{O} & \mathbf{O} & \mathbf{K}^{(e)} + \mathbf{L}^{(e)} + \frac{1}{\gamma\Delta t}\mathbf{M}^{(e)} \end{bmatrix}^{t+\Delta t} \begin{Bmatrix} \mathbf{v}^{(e)} \\ \mathbf{p}^{(e)} \\ \boldsymbol{\theta}^{(e)} \end{Bmatrix}^{t+\Delta t} - \\ & - \begin{Bmatrix} \mathbf{f}_v^{(e)} \\ \mathbf{0} \\ \mathbf{f}_\theta^{(e)} \end{Bmatrix}^{t+\Delta t} - \begin{bmatrix} \frac{1}{\gamma\Delta t}\mathbf{M}_v^{(e)} & \mathbf{O} & \mathbf{O} \\ \mathbf{O} & \mathbf{O} & \mathbf{O} \\ \mathbf{O} & \mathbf{O} & \frac{1}{\gamma\Delta t}\mathbf{M}^{(e)} \end{bmatrix}^{t+\Delta t} \begin{Bmatrix} \mathbf{v}^{(e)} \\ \mathbf{p}^{(e)} \\ \boldsymbol{\theta}^{(e)} \end{Bmatrix}^{t} - \\ & - \begin{bmatrix} \frac{1-\gamma}{\gamma}\mathbf{M}_v^{(e)} & \mathbf{O} & \mathbf{O} \\ \mathbf{O} & \mathbf{O} & \mathbf{O} \\ \mathbf{O} & \mathbf{O} & \frac{1-\gamma}{\gamma}\mathbf{M}^{(e)} \end{bmatrix}^{t} \begin{Bmatrix} \dot{\mathbf{v}}^{(e)} \\ \dot{\mathbf{p}}^{(e)} \\ \dot{\boldsymbol{\theta}}^{(e)} \end{Bmatrix}^{t} \end{aligned} \tag{4.42}$$

The global residual vector can be obtained by assembling the elemental vectors (4.42) into their global counterparts. The nonlinear system of equations is,

$$\mathbf{r}^{t+\Delta t} = \mathbf{0} \tag{4.43}$$

and it will be solved to the free degrees of freedom using the Newton–Raphson method.

4.7 Tangent matrix

The tangent matrix of the presented problem can be computed through the perturbation of the set of expressions (4.35). Hence, by imposing

$$\Delta\boldsymbol{v}^{(e)} = \boldsymbol{\psi}_v^{(e)}\,\Delta\mathbf{v}^{(e)} \tag{4.44a}$$

$$\Delta p^{(e)} = \boldsymbol{\psi}_v^{(e)}\,\Delta\mathbf{p}^{(e)} \tag{4.44b}$$

$$\Delta\theta^{(e)} = \boldsymbol{\psi}_\theta^{(e)}\,\Delta\boldsymbol{\theta}^{(e)} \tag{3.46a}$$

$$\Delta\dot{\boldsymbol{v}}^{(e)} = \boldsymbol{\psi}_v^{(e)}\,\Delta\dot{\mathbf{v}}^{(e)} \tag{4.44c}$$

$$\Delta\dot{p}^{(e)} = \boldsymbol{\psi}_v^{(e)}\,\Delta\dot{\mathbf{p}}^{(e)} \tag{4.44d}$$

$$\Delta\dot{\theta}^{(e)} = \boldsymbol{\psi}_\theta^{(e)}\,\Delta\dot{\boldsymbol{\theta}}^{(e)} \tag{3.46c}$$

and

$$\Delta\delta\boldsymbol{v}^{(e)} = \boldsymbol{o} \tag{4.45a}$$

$$\Delta\delta p^{(e)} = 0 \tag{4.45b}$$

$$\Delta\delta\theta^{(e)} = 0 \tag{3.47a}$$

one obtains:

$$\Delta \int_{\Omega^{(e)}} \delta \boldsymbol{v}^{(e)} \cdot \dot{\boldsymbol{v}}^{(e)} \, \mathrm{d}\Omega^{(e)} = \delta \mathbf{v}^{(e)T} \int_{\Omega^{(e)}} \boldsymbol{\psi}_v^{(e)T} \boldsymbol{\psi}_v^{(e)} \, \mathrm{d}\Omega^{(e)} \, \Delta \dot{\mathbf{v}}^{(e)} = \delta \mathbf{v}^{(e)T} \mathbf{M}_v^{(e)} \Delta \dot{\mathbf{v}}^{(e)} \tag{4.46a}$$

$$\begin{aligned} \Delta \int_{\Omega^{(e)}} \delta \boldsymbol{v}^{(e)} \cdot \left(\boldsymbol{\nabla} \boldsymbol{v}^{(e)} \right) \boldsymbol{v}^{(e)} \, \mathrm{d}\Omega^{(e)} &= \Delta \int_{\Omega^{(e)}} \delta \boldsymbol{v}^{(e)} \cdot \left(\boldsymbol{e}_i \cdot \boldsymbol{v}^{(e)} \right) \boldsymbol{v}_{,i}^{(e)} \, \mathrm{d}\Omega^{(e)} = \\ &= \int_{\Omega^{(e)}} \delta \boldsymbol{v}^{(e)} \cdot \left(\left(\boldsymbol{e}_i \cdot \boldsymbol{v}^{(e)} \right) \Delta \boldsymbol{v}_{,i}^{(e)} + \left(\boldsymbol{e}_i \cdot \Delta \boldsymbol{v}^{(e)} \right) \boldsymbol{v}_{,i}^{(e)} \right) \mathrm{d}\Omega^{(e)} = \\ &= \delta \mathbf{v}^{(e)T} \left(\int_{\Omega^{(e)}} \boldsymbol{\psi}_v^{(e)T} \left(\mathbf{e}_i^T \, \boldsymbol{\psi}_v^{(e)} \mathbf{v}^{(e)} \right) \left(\boldsymbol{\psi}_v^{(e)} \right)_{,i} \mathrm{d}\Omega^{(e)} + \right. \\ &\left. + \int_{\Omega^{(e)}} \boldsymbol{\psi}_v^{(e)T} \left(\left(\boldsymbol{\psi}_v^{(e)} \right)_{,i} \mathbf{v}^{(e)} \mathbf{e}_i^T \right) \boldsymbol{\psi}_v^{(e)} \, \mathrm{d}\Omega^{(e)} \right) \Delta \mathbf{v}^{(e)} = \delta \mathbf{v}^{(e)T} \mathbf{C}_T^{(e)} \Delta \mathbf{v}^{(e)} \end{aligned} \tag{4.46b}$$

$$\begin{aligned} \Delta \int_{\Omega^{(e)}} \boldsymbol{\nabla} \delta \boldsymbol{v}^{(e)} : \nu \boldsymbol{\nabla} \boldsymbol{v}^{(e)} \, \mathrm{d}\Omega^{(e)} &= \\ &= \delta \mathbf{v}^{(e)T} \int_{\Omega^{(e)}} \left(\left(\boldsymbol{\psi}_v^{(e)T} \right)_{,j} \mathbf{e}_i \right) \nu \left(\mathbf{e}_i^T \left(\boldsymbol{\psi}_v^{(e)} \right)_{,j} \right) \mathrm{d}\Omega^{(e)} \, \Delta \mathbf{v}^{(e)} = \\ &= \delta \mathbf{v}^{(e)T} \mathbf{K}_v^{(e)} \Delta \mathbf{v}^{(e)} \end{aligned} \tag{4.46c}$$

$$\begin{aligned} -\Delta \int_{\Omega^{(e)}} \operatorname{div} \delta \boldsymbol{v}^{(e)} \, p^{(e)} \, \mathrm{d}\Omega^{(e)} &= -\int_{\Omega^{(e)}} \delta v_{i,i}^{(e)} \, \Delta p^{(e)} \, \mathrm{d}\Omega^{(e)} = \\ &= -\delta \mathbf{v}^{(e)T} \int_{\Omega^{(e)}} \left(\boldsymbol{\psi}_v^{(e)T} \right)_{,i} \mathbf{e}_i \, \boldsymbol{\psi}_p^{(e)} \, \mathrm{d}\Omega^{(e)} \, \Delta \mathbf{p}^{(e)} = \delta \mathbf{v}^{(e)T} \mathbf{G}^{(e)} \Delta \mathbf{p}^{(e)} \end{aligned} \tag{4.46d}$$

$$\begin{aligned} -\Delta \int_{\Omega^{(e)}} \delta p^{(e)} \operatorname{div} \boldsymbol{v}^{(e)} \, \mathrm{d}\Omega^{(e)} &= -\int_{\Omega^{(e)}} \delta p^{(e)} \left(\boldsymbol{e}_i \cdot \Delta \boldsymbol{v}_{,i}^{(e)} \right) \mathrm{d}\Omega^{(e)} = \\ &= -\delta \mathbf{p}^{(e)T} \int_{\Omega^{(e)}} \boldsymbol{\psi}_p^{(e)T} \, \mathbf{e}_i^T \left(\boldsymbol{\psi}_v^{(e)} \right)_{,i} \mathrm{d}\Omega^{(e)} \, \Delta \mathbf{v}^{(e)} = \delta \mathbf{p}^{(e)T} \mathbf{G}^{(e)T} \Delta \mathbf{v}^{(e)} \end{aligned} \tag{4.46e}$$

$$-\Delta \int_{\Omega^{(e)}} \delta \boldsymbol{v}^{(e)} \cdot \boldsymbol{b}^{(e)} \, \mathrm{d}\Omega = 0 \tag{4.46f}$$

$$-\Delta \int_{\Gamma_t^{(e)}} \delta \boldsymbol{v}^{(e)} \cdot \bar{\boldsymbol{t}}^{(e)} \, \mathrm{d}\Gamma_t^{(e)} = 0 \tag{4.46g}$$

$$-\Delta \int_{\Omega^{(e)}} \delta \boldsymbol{v}^{(e)} \cdot \boldsymbol{f}_B^{(e)} \, \mathrm{d}\Omega^{(e)} = \delta \mathbf{v}^{(e)T} \int_{\Omega^{(e)}} \boldsymbol{\psi}_v^{(e)T} \, \beta \, \boldsymbol{g} \, \boldsymbol{\psi}_\theta^{(e)} \, \mathrm{d}\Omega^{(e)} \Delta \boldsymbol{\theta}^{(e)} \tag{4.46h}$$

$$\Delta \int_{\Omega^{(e)}} \boldsymbol{\nabla} \delta \theta^{(e)} \cdot \boldsymbol{q}^{(e)} \, \mathrm{d}\Omega^{(e)} = -\delta \boldsymbol{\theta}^{(e)T} \int_{\Omega^{(e)}} \mathbf{B}_\theta^{(e)T} \, \mathbf{D} \, \mathbf{B}_\theta^{(e)} \, \mathrm{d}\Omega^{(e)} \, \Delta \boldsymbol{\theta}^{(e)} \tag{4.46i}$$

$$-\Delta \int_{\Omega^{(e)}} \delta \theta^{(e)} \, \rho \, c_p \, \dot{\theta}^{(e)} \, \mathrm{d}\Omega^{(e)} = -\delta \boldsymbol{\theta}^{(e)T} \int_{\Omega^{(e)}} \boldsymbol{\psi}_\theta^{(e)T} \rho \, c_p \, \boldsymbol{\psi}_\theta^{(e)} \, \mathrm{d}\Omega^{(e)} \, \Delta \dot{\boldsymbol{\theta}}^{(e)} \tag{4.46j}$$

$$\Delta \int_{\Omega^{(e)}} \delta \theta^{(e)} \, G^{(e)} \, \mathrm{d}\Omega^{(e)} = 0 \tag{3.48c}$$

$$-\Delta \int_{\Omega} \delta \theta \, \rho_0 \, c_p \, \boldsymbol{v} \cdot \boldsymbol{\nabla} \theta \, \mathrm{d}\Omega = -\delta \boldsymbol{\theta}^{(e)T} \int_{\Omega^{(e)}} \boldsymbol{\psi}_\theta^{(e)T} \, \rho_0 \, c_p \left(\boldsymbol{\psi}_v^{(e)} \mathbf{v}^{(e)} \right)^T \mathbf{B}_\theta^{(e)} \, \mathrm{d}\Omega^{(e)} \, \Delta \boldsymbol{\theta}^{(e)} \tag{4.46k}$$

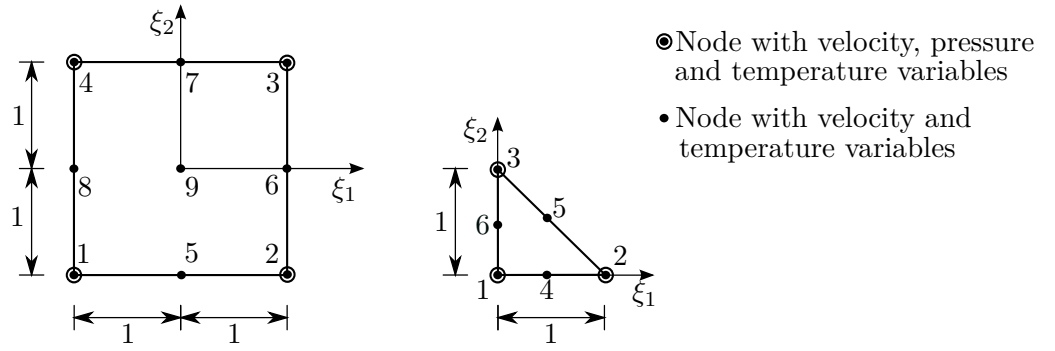

Figure 4.2: Quadrilateral $Q2Q1$ and triangular $P2P1$ elements for the coupled fluid-flow and heat transfer problem.

After replacing the temporal discretization into the (4.46) expressions, the elemental tangent matrix is given by,

$$\overline{\mathbf{K}}^{(e)t+\Delta t} = \begin{bmatrix} \mathbf{K}_v^{(e)} + \mathbf{C}_T^{(e)} + \frac{1}{\gamma\Delta t}\mathbf{M}_v^{(e)} & \mathbf{G}^{(e)} & \mathbf{B}^{(e)} \\ \mathbf{G}^{(e)T} & \mathbf{O} & \mathbf{O} \\ \mathbf{E}^{(e)} & \mathbf{O} & \mathbf{F}^{(e)} \end{bmatrix}^{t+\Delta t} \tag{4.47}$$

where:

$$\mathbf{E}^{(e)t+\Delta t} = \int_{\Omega^{(e)}} \rho_0\, c_p\, \boldsymbol{\psi}_\theta^{(e)T} \left(\boldsymbol{\psi}_\theta^{(e)}\right)_{,i} \boldsymbol{\theta}^{(e)t+\Delta t}\, \mathbf{e}_i^T\, \boldsymbol{\psi}_v^{(e)}\, \mathrm{d}\Omega^{(e)} \tag{4.48a}$$

$$\mathbf{F}^{(e)t+\Delta t} = \mathbf{K}^{(e)t+\Delta t} + \mathbf{L}^{(e)} + \frac{1}{\gamma\Delta t}\,\mathbf{M}^{(e)} \tag{4.48b}$$

In the code developed, the thermal and fluid properties were considered constant and, hence, they do not depend on the temperature, velocity and pressure. The formulation presented constitutes a strict Boussinesq model where the thermophysical properties are treated as constant and the work done by pressure and viscous dissipation is neglected (Reddy and Gartling, 2010).

The global tangent matrix is obtained by assembling of all elemental tangent matrices.

4.8 Computational considerations and element types

The considered element types are the isoparametric quadratic $Q2Q1$ and $P2P1$ introduced by Taylor and Hood (1973) and referred in the literature as *Taylor–Hood elements*. Figure 4.2 shows the elements shape and the independent variables defined per node.

In both elements the number of degrees of freedom per node is variable and, consequently, the polynomial degree of the shape functions is also changeable: (i) in the case of the elements $P2P1$, linear shape functions are used to interpolate the pressure field, while those used to interpolate the velocities are quadratic; (ii) in the case of the elements $Q2Q1$, the shape functions to interpolate the pressure are bilinear and those used to interpolate the velocities are biquadratic.

These elements were chosen as they satisfy the Ladyzhenskaya-Babŭska-Brezzi (*LBB*) stability condition — see Brezzi and Fortin (1991, page 57) — and present quadratic

Element type	$\mathbf{M}^{(e)}$		$\mathbf{K}^{(e)}$		$\mathbf{C}^{(e)}, \mathbf{C}_T^{(e)}$		$\mathbf{G}^{(e)}$		$\mathbf{f}_b^{(e)}$		$\mathbf{f}_t^{(e)}$	
	p	n_G	p	n_G	p	n_G	p	n_G	p	n_G	p	n_G
$P2P1$	4	6	2	3	5	7	2	3	4	6	4	6
$Q2Q1$	4	3×3	4	3×3	6	4×4	3	2×2	4	3×3	4	3

Table 4.1: Polynomial degree (p) of the integrand function and number of Gauss points (n_G) required for the numerical integration.

convergence rates. Further information about the LBB condition can be consulted in appendix C.2.

The representation of the geometry is the same as the one used for the velocity variable, *i.e.*, $\boldsymbol{x} = \boldsymbol{\psi}_v \, \mathbf{x}$.

The numerical integration is computed using the Gauss quadrature. The number of Gauss points required to integrate exactly the residual vector terms and the tangent matrix were determined considering a constant determinant of the Jacobian. In the case of quadrilateral elements, the Gauss–Legendre quadrature was employed, while in the case of triangular elements specific rules were programmed (Cowper, 1973).

The integrand with a maximum polynomial degree is the term regarding the convective matrix. In the case of $Q2Q1$ elements, 4×4 Gauss points were used in the integration, while in the case of $P2P1$ elements, 7 points were employed. Table 4.1 shows the polynomial degree of the integrands and the number of Gauss points required to integrate the matrices $\mathbf{M}^{(e)}$, $\mathbf{K}^{(e)}$, $\mathbf{C}^{(e)}$, $\mathbf{C}_T^{(e)}$ and $\mathbf{G}^{(e)}$ and the vectors $\mathbf{f}_b^{(e)}$ and $\mathbf{f}_t^{(e)}$, given by:

$$\mathbf{f}_b^{(e)} = \int_{\Omega^{(e)}} \boldsymbol{\psi}_v^{(e)T} \, \boldsymbol{\psi}_v^{(e)} \, \mathrm{d}\Omega^{(e)} \, \mathbf{b}^{(e)} \tag{4.49a}$$

$$\mathbf{f}_t^{(e)} = \int_{\Gamma_t^{(e)}} \boldsymbol{\psi}_v^{(e)T} \, \boldsymbol{\psi}_v^{(e)} \, \mathrm{d}\Gamma_t^{(e)} \, \bar{\mathbf{t}}^{(e)} \tag{4.49b}$$

4.9 Stabilization of the convective term: SUPG method

In problems with dominant convection, the hyperbolic Navier–Stokes equations and the heat transfer equation (or advection-diffusion equation) can present numerical instabilities when solved using the FEM. Brooks and Hughes (1982) originally proposed a formulation to stabilize the convective term using the concept of *SUPG* (streamline upwind/Petrov–Galerkin). In the present text, a stabilized formulation of the equation based in the works of Tezduyar and Osawa (2000) and Campelo (2013) is presented.

The weak form of the coupled heat transfer and fluid-flow equations including the convective stabilization term can be written as follows,

$$\begin{aligned} \int_\Omega \delta\boldsymbol{v} \cdot \dot{\boldsymbol{v}} \, \mathrm{d}\Omega + \int_\Omega \delta\boldsymbol{v} \cdot (\boldsymbol{\nabla}\boldsymbol{v}) \, \boldsymbol{v} \, \mathrm{d}\Omega + \int_\Omega \boldsymbol{\nabla}\delta\boldsymbol{v} : \nu\boldsymbol{\nabla}\boldsymbol{v} \, \mathrm{d}\Omega - \\ - \int_\Omega \operatorname{div} \delta\boldsymbol{v} \, p \, \mathrm{d}\Omega - \int_{\Gamma_t} \delta\boldsymbol{v} \cdot \bar{\boldsymbol{t}} \, \mathrm{d}\Gamma_t - \int_\Omega \delta\boldsymbol{v} \cdot \boldsymbol{b} \, \mathrm{d}\Omega - \int_\Omega \delta\boldsymbol{v} \cdot \boldsymbol{f}_B \, \mathrm{d}\Omega + \\ + \int_\Omega \tau_{SUPG} \, (\boldsymbol{\nabla}\delta\boldsymbol{v}) \, \boldsymbol{v} \cdot \boldsymbol{r}_{SUPG} \, \mathrm{d}\Omega = 0 \end{aligned} \tag{4.50a}$$

$$-\int_\Omega \delta p \,\mathrm{div}\,\boldsymbol{v}\,\mathrm{d}\Omega = 0 \tag{4.29b}$$

$$\begin{aligned}\int_\Omega (\boldsymbol{\nabla}\delta\theta\cdot\boldsymbol{q} - \delta\theta\,\rho\,c_p\,\cdot\theta)\,\mathrm{d}\Omega - \int_\Omega \delta\theta\,\rho\,c_p\,\boldsymbol{v}\cdot\boldsymbol{\nabla}\theta\,\mathrm{d}\Omega + \\ + \int_\Omega \delta\theta\,G\,\mathrm{d}\Omega + \int_\Omega \tau_{SUPG\theta}\;\boldsymbol{v}\cdot\boldsymbol{\nabla}\delta\theta\,r_{SUPG\theta}\,\mathrm{d}\Omega = 0\end{aligned} \tag{4.50b}$$

where τ_{SUPG} and $\tau_{SUPG\theta}$ are the stabilization parameters.

The stabilization terms are computed over a finite element and, introducing the spatial discretization at $(t+\Delta t)$, they are:

$$\begin{aligned}\int_{\Omega^{(e)}} \tau^{(e)}_{SUPG}\,\left(\boldsymbol{\nabla}\delta\boldsymbol{v}^{(e)}\right)\boldsymbol{v}^{(e)}\cdot\boldsymbol{r}^{(e)}_{SUPG}\,\mathrm{d}\Omega^{(e)} = \\ = \delta\mathbf{v}^{(e)T}\left(\tau^{(e)t}_{SUPG}\int_{\Omega^{(e)}}\left(\boldsymbol{\psi}^{(e)T}_v\right)_{,i}\left(\mathbf{e}_i^T\,\boldsymbol{\psi}^{(e)}_v\mathbf{v}^{(e)}\right)\boldsymbol{r}^{(e)}_{SUPG}\,\mathrm{d}\Omega^{(e)}\right)\end{aligned} \tag{4.51a}$$

$$\begin{aligned}\int_{\Omega^{(e)}} \tau^{(e)}_{SUPG\theta}\,\boldsymbol{v}^{(e)}\cdot\boldsymbol{\nabla}\delta\theta^{(e)}\,r^{(e)}_{SUPG\theta}\,\mathrm{d}\Omega^{(e)} = \\ = \delta\boldsymbol{\theta}^{(e)T}\left(\tau^{(e)t}_{SUPG\theta}\int_{\Omega^{(e)}}\mathbf{B}^{(e)T}_\theta\,\boldsymbol{\psi}^{(e)}_v\mathbf{v}^{(e)}\,r^{(e)}_{SUPG\theta}\,\mathrm{d}\Omega^{(e)}\right)\end{aligned} \tag{4.51b}$$

The elemental residual vectors of the conservation of momentum equation, $\boldsymbol{r}^{(e)}_{SUPG}$, and the residual of the advection-diffusion equation, $r^{(e)}_{SUPG\theta}$, are calculated as:

$$\boldsymbol{r}^{(e)}_{SUPG} = \dot{\boldsymbol{v}}^{(e)} + \left(\boldsymbol{\nabla}\boldsymbol{v}^{(e)}\right)\boldsymbol{v}^{(e)} - \nu\,\boldsymbol{\nabla}^2\boldsymbol{v}^{(e)} + \boldsymbol{\nabla}p^{(e)} - \boldsymbol{b}^{(e)} - \boldsymbol{f}^{(e)}_B \tag{4.52a}$$

$$r^{(e)}_{SUPG\theta} = \rho_0\,c_p\,\left(\dot\theta^{(e)} + \boldsymbol{v}^{(e)}\cdot\boldsymbol{\nabla}\theta^{(e)}\right) + \mathrm{div}\,\boldsymbol{q}^{(e)} - G^{(e)} \tag{4.52b}$$

The $\tau^{(e)t}_{SUPG}$ and $\tau^{(e)t}_{SUPG\theta}$ are considered constant over each element[4] and they are computed with the data of the previous time step t[5]. There are several definitions of these constants; the interested reader can consult the works of Shakib *et al.* (1991), Tezduyar *et al.* (1992), Franca and Frey (1992) or Codina (2000). Following Tezduyar and Osawa (2000), in the present formulation, the stabilization constant of the Navier–Stokes equations is computed as the inverse of the r-norm (set equal to 2) of a vector $\boldsymbol{\tau}^{(e)t}_{SUPG}$ with components $1/\tau^{(e)t}_{S1}$, $1/\tau^{(e)t}_{S2}$ and $1/\tau^{(e)t}_{S3}$. The same assumption is considered for the stabilization term of the advection-diffusion equation, hence,

$$\tau^{(e)t}_{SUPG} = \left(\frac{1}{\left(\tau^{(e)t}_{S1}\right)^r} + \frac{1}{\left(\tau^{(e)t}_{S2}\right)^r} + \frac{1}{\left(\tau^{(e)t}_{S3}\right)^r}\right)^{-1/r} \tag{4.53a}$$

$$\tau^{(e)t}_{SUPG\theta} = \left(\frac{1}{\left(\tau^{(e)t}_{S1\theta}\right)^r} + \frac{1}{\left(\tau^{(e)t}_{S2\theta}\right)^r} + \frac{1}{\left(\tau^{(e)t}_{S3\theta}\right)^r}\right)^{-1/r} \tag{4.53b}$$

[4]The paper of Tezduyar and Osawa (2000) refers literally: "it is *conceivable* that we calculate a separate τ for each element node, or degree of freedom, or element equation".

[5]It can be also computed at $t+\Delta t$ but, in this case, the scalars τ_{SUPG} will introduce additional terms in the tangent matrix.

where τ_{S1}, τ_{S2} and τ_{S3} introduce the stabilization for the advection-, transient- and diffusion-dominated problems, respectively. Each component of the vector can be computed as,

$$\tau_{S1}^{(e)t} = \frac{\|\mathbf{C}^{(e)t}\|}{\|\mathbf{C}_{\tau}^{(e)t}\|} \qquad \tau_{S1\theta}^{(e)t} = \frac{\|\mathbf{C}_{\theta}^{(e)t}\|}{\|\mathbf{C}_{\theta\tau}^{(e)t}\|}$$

$$\tau_{S2}^{(e)t} = \frac{\Delta t}{2}\frac{\|\mathbf{C}^{(e)t}\|}{\|\mathbf{M}_{\tau}^{(e)t}\|} \qquad \tau_{S2\theta}^{(e)t} = \frac{\Delta t}{2}\frac{\|\mathbf{C}_{\theta}^{(e)t}\|}{\|\mathbf{M}_{\theta\tau}^{(e)t}\|}$$

$$\tau_{S3}^{(e)t} = \tau_{S1}^{(e)t}\, Re^{(e)t} \qquad \tau_{S3\theta}^{(e)t} = \tau_{S1\theta}^{(e)t}\, Re_{\theta}^{(e)t}$$

where $Re^{(e)t}$ is the finite element Reynolds number and $\mathbf{C}_{\tau}^{(e)t}$ and $\mathbf{M}_{\tau}^{(e)t}$ are the elemental stabilization matrices defined by the following expressions:

$$Re^{(e)t} = \frac{\|\boldsymbol{v}^{(e)t}\|^2}{\nu}\frac{\|\mathbf{C}^{(e)t}\|}{\|\mathbf{C}_{\tau}^{(e)t}\|} \tag{4.55a}$$

$$\mathbf{C}_{\tau}^{(e)t} = \int_{\Omega^{(e)}} \left(\boldsymbol{\psi}_v^{(e)}\right)_{,i}^{T} \left(\left(\boldsymbol{\psi}_v^{(e)}\,\mathbf{v}^{(e)t}\right)^{T}\mathbf{e}_i\right)\left(\left(\boldsymbol{\psi}_v^{(e)}\,\mathbf{v}^{(e)t}\right)^{T}\mathbf{e}_j\right)\left(\boldsymbol{\psi}_v^{(e)}\right)_{,j}\mathrm{d}\Omega^{(e)} \tag{4.55b}$$

$$\mathbf{M}_{\tau}^{(e)t} = \int_{\Omega^{(e)}} \left(\boldsymbol{\psi}_v^{(e)}\right)_{,i}^{T} \left(\left(\boldsymbol{\psi}_v^{(e)}\,\mathbf{v}^{(e)t}\right)^{T}\mathbf{e}_i^{(e)}\right)\boldsymbol{\psi}_v^{(e)}\,\mathrm{d}\Omega^{(e)} \tag{4.55c}$$

The equivalent stabilization terms of the advection-diffusive equations are:

$$Re_{\theta}^{(e)t} = \frac{\rho_0\, c_p\, \|\boldsymbol{v}^{(e)t}\|^2}{k}\frac{\|\mathbf{C}_{\theta}^{(e)t}\|}{\|\mathbf{C}_{\theta\tau}^{(e)t}\|} \tag{4.56a}$$

$$\mathbf{C}_{\theta}^{(e)t} = \int_{\Omega^{(e)}} \boldsymbol{\psi}_{\theta}^{(e)T}\left(\boldsymbol{\psi}_v^{(e)}\,\mathbf{v}^{(e)t}\right)^{T}\mathbf{B}_{\theta}^{(e)}\,\mathrm{d}\Omega^{(e)} \tag{4.56b}$$

$$\mathbf{C}_{\theta\tau}^{(e)t} = \int_{\Omega^{(e)}} \mathbf{B}_{\theta}^{(e)T}\left(\boldsymbol{\psi}_v^{(e)}\,\mathbf{v}^{(e)t}\right)\left(\boldsymbol{\psi}_v^{(e)}\,\mathbf{v}^{(e)t}\right)^{T}\mathbf{B}_{\theta}^{(e)}\,\mathrm{d}\Omega^{(e)} \tag{4.56c}$$

$$\mathbf{M}_{\theta\tau}^{(e)t} = \int_{\Omega^{(e)}} \mathbf{B}_{\theta}^{(e)T}\,\boldsymbol{\psi}_v^{(e)}\,\mathbf{v}^{(e)t}\boldsymbol{\psi}_{\theta}^{(e)}\,\mathrm{d}\Omega^{(e)} \tag{4.56d}$$

The L^2 norms used are defined in Layton (2008) and for a generic vector, $\boldsymbol{v}$, and matrix, $\mathbf{A}$, such that $A_{ij} = \int_{\Omega} a_{ij}\,(\boldsymbol{x})\,\mathrm{d}\Omega$, they can be written as,

$$\|\boldsymbol{v}\|^2 = \int_{\Omega}\sum_{i=1}^{n} v_i\, v_i\,\mathrm{d}\Omega = \int_{\Omega}\boldsymbol{v}^T\,\boldsymbol{v}\,\mathrm{d}\Omega \tag{4.57a}$$

$$\|\mathbf{A}\|^2 = \int_{\Omega}\sum_{i,j=1}^{m} a_{ij}\, a_{ij}\,\mathrm{d}\Omega = \sum_{i,j=1}^{m} A_{ij}\, A_{ij} = \mathrm{tr}\left(\mathbf{A}^T\,\mathbf{A}\right) \tag{4.57b}$$

where n is the number of components of the vector and m is the dimension of the matrix. The reader should notice that $\mathbf{M}_{\tau}^{(e)t} = \left(\mathbf{C}^{(e)t}\right)^T$ and $\mathbf{M}_{\theta\tau}^{(e)t} = \left(\mathbf{C}_{\theta}^{(e)t}\right)^T$, as it is reported in Tezduyar and Osawa (2000, Remark 12, page 417).

The elemental residual vector can be obtained from (4.51),

$$\mathbf{r}^{(e)t+\Delta t} = \begin{Bmatrix} \mathbf{r}_v^{(e)} + \mathbf{r}_{SUPGv}^{(e)} \\ \\ \mathbf{r}_p^{(e)} \\ \\ \mathbf{r}_{\theta}^{(e)} + \mathbf{r}_{SUPG\theta}^{(e)} \end{Bmatrix}^{t+\Delta t} \tag{4.58}$$

where the elemental terms due to the stabilization are:

$$\mathbf{r}_{SUPGv}^{(e)t+\Delta t} = \tau_{SUPG}^{(e)t} \int_{\Omega^{(e)}} \left(\boldsymbol{\psi}_v^{(e)}\right)_{,i}^T \left(\mathbf{e}_i^T \boldsymbol{\psi}_v^{(e)} \mathbf{v}^{(e)}\right) \boldsymbol{r}_{SUPG}^{(e)} \, \mathrm{d}\Omega^{(e)} \tag{4.59a}$$

$$\mathbf{r}_{SUPG\theta}^{(e)t+\Delta t} = \tau_{SUPG\theta}^{(e)t} \int_{\Omega^{(e)}} \mathbf{B}_\theta^{(e)T} \boldsymbol{\psi}_v^{(e)} \mathbf{v}^{(e)} \, r_{SUPG\theta}^{(e)} \, \mathrm{d}\Omega^{(e)} \tag{4.59b}$$

The global residual vector can be obtained by assembling the elemental ones.

The inclusion of the stabilization terms into the elemental tangent matrix leads to,

$$\overline{\mathbf{K}}^{(e)t+\Delta t} = \begin{bmatrix} \mathbf{K}_v^{(e)} + \mathbf{C}_T^{(e)} + \frac{1}{\gamma\Delta t}\mathbf{M}_v^{(e)} + \mathbf{C}_{SUPG}^{(e)} & \mathbf{G}^{(e)} + \mathbf{G}_{SUPG}^{(e)} & \mathbf{B}^{(e)} + \mathbf{B}_{SUPG}^{(e)} \\ \mathbf{G}^{(e)T} & \mathbf{O} & \mathbf{O} \\ \mathbf{E}^{(e)} + \mathbf{E}_{SUPG\theta}^{(e)} & \mathbf{O} & \mathbf{F}^{(e)} + \mathbf{F}_{SUPG\theta}^{(e)} \end{bmatrix}^{t+\Delta t} \tag{4.60}$$

where the additional matrices $\mathbf{C}_{SUPG}^{(e)}$, $\mathbf{G}_{SUPG}^{(e)}$, $\mathbf{B}_{SUPG}^{(e)}$, $\mathbf{E}_{SUPG}^{(e)}$ and $\mathbf{F}_{SUPG}^{(e)}$ can be computed as:

$$\begin{aligned} \mathbf{C}_{SUPG}^{(e)t+\Delta t} = \tau_{SUPG}^{(e)t} \int_{\Omega^{(e)}} \Bigg[& \left(\boldsymbol{\psi}_v^{(e)}\right)_{,i}^T \boldsymbol{r}_{SUPG}^{(e)} \, \mathbf{e}_i^T \boldsymbol{\psi}_v^{(e)} + \\ & + \left(\boldsymbol{\psi}_v^{(e)}\right)_{,i}^T \left(\left(\boldsymbol{\psi}_v^{(e)} \, \mathbf{v}^{(e)t+\Delta t}\right)^T \mathbf{e}_i\right) \left(\frac{1}{\gamma\Delta t} \boldsymbol{\psi}_v^{(e)} + \left(\mathbf{e}_j^T \boldsymbol{\psi}_v^{(e)} \, \mathbf{v}^{(e)t+\Delta t}\right) \left(\boldsymbol{\psi}_v^{(e)}\right)_{,j} + \right. \\ & \left. + \left(\left(\boldsymbol{\psi}_v^{(e)}\right)_{,i} \mathbf{v}^{(e)t+\Delta t} \, \mathbf{e}_j^T\right) \boldsymbol{\psi}_v^{(e)} - \nu \left(\boldsymbol{\psi}_v^{(e)}\right)_{,jj}\right) \Bigg] \, \mathrm{d}\Omega^{(e)} \end{aligned} \tag{4.61a}$$

$$\mathbf{G}_{SUPG}^{(e)t+\Delta t} = \tau_{SUPG}^{(e)t} \int_{\Omega^{(e)}} \left(\boldsymbol{\psi}_v^{(e)}\right)_{,i}^T \left(\left(\boldsymbol{\psi}_v^{(e)} \, \mathbf{v}^{(e)t+\Delta t}\right)^T \mathbf{e}_i\right) \left(\mathbf{e}_j \left(\boldsymbol{\psi}_p^{(e)}\right)_{,j}\right) \, \mathrm{d}\Omega^{(e)} \tag{4.61b}$$

$$\mathbf{B}_{SUPG}^{(e)t+\Delta t} = \tau_{SUPG}^{(e)t} \int_{\Omega^{(e)}} \left(\boldsymbol{\psi}_v^{(e)}\right)_{,i}^T \left(\left(\boldsymbol{\psi}_v^{(e)} \, \mathbf{v}^{(e)t+\Delta t}\right)^T \mathbf{e}_i\right) \beta \, \boldsymbol{g} \, \boldsymbol{\psi}_\theta^{(e)} \, \mathrm{d}\Omega^{(e)} \tag{4.61c}$$

$$\begin{aligned} \mathbf{E}_{SUPG\theta}^{(e)t+\Delta t} = \tau_{SUPG\theta}^{(e)t} \int_{\Omega^{(e)}} \mathbf{B}_\theta^{(e)T} \boldsymbol{\psi}_v^{(e)} \, \Big[& r_{SUPG\theta}^{(e)} + \\ & + \mathbf{v}^{(e)} \left(\mathbf{B}_\theta^{(e)} \, \boldsymbol{\theta}^{(e)t+\Delta t}\right)^T \boldsymbol{\psi}_v^{(e)} \Big] \, \mathrm{d}\Omega^{(e)} \end{aligned} \tag{4.61d}$$

$$\begin{aligned} \mathbf{F}_{SUPG}^{(e)t+\Delta t} = \tau_{SUPG\theta}^{(e)t} \int_{\Omega^{(e)}} \mathbf{B}_\theta^{(e)T} \boldsymbol{\psi}_v^{(e)} \mathbf{v}^{(e)t+\Delta t} \, \Big(& \frac{\rho_0 \, c_p}{\gamma\Delta t} \boldsymbol{\psi}_\theta^{(e)} + \\ & + \rho_0 \, c_p \left(\boldsymbol{\psi}_v^{(e)} \, \mathbf{v}^{(e)t+\Delta t}\right)^T \mathbf{B}_\theta^{(e)} - k_{ij} \left(\boldsymbol{\psi}_\theta^{(e)}\right)_{,ij} \Big) \, \mathrm{d}\Omega^{(e)} \end{aligned} \tag{4.61e}$$

The evaluation of the first and second derivatives of the shape functions required for the computation of the previous expressions can be consulted in appendix B.2.

The global tangent matrix necessary to solve the nonlinear system of equations will be obtained by assembling the elemental ones.

An additional term proposed by Tezduyar and Osawa (2000), LSIC (least-squares on incompressibility constant), can be included to improve the stability of flows at large Reynolds number.

4.10 Stream function computation

The stream function is often used as an output in problems of fluid dynamics. The stream function is, by definition, a function φ such that,

$$v_1 = \frac{\partial \varphi}{\partial x_2} \quad \text{and} \quad v_2 = -\frac{\partial \varphi}{\partial x_1} \tag{4.62}$$

and it represents the remaining nonzero component of the vector potential, as it was defined in Reddy and Gartling (2010), or the locus of points that are everywhere tangent to the instantaneous velocity vector, as it is defined in Diersch (2014).

The stream function has to be obtained for each node and the results are presented in form of *streamlines*[6], *i.e.*, lines with constant stream function value.

The most common methods to compute the stream function in the finite element theory are: (i) boundary integral method and (ii) vorticity equation integrator. The first method consists of considering the value of the stream function in each node by integrating all sides of the finite element using the following expression reported in Reddy and Gartling (2010):

$$\delta\varphi = \int_A^B (v_1 n_1 + v_2 n_2)\, \mathrm{d}s \tag{4.63}$$

Proceeding as in Diersch (2014), *i.e.*, using the shape functions for the velocity and the transformation of coordinates to integrate numerically, the following expression is obtained,

$$\delta\varphi = \int_{-1}^{1} \left(\frac{\partial \boldsymbol{\psi}_\theta}{\partial \xi} \mathbf{x}_2\, \boldsymbol{\psi}_\theta \mathbf{v}_1 + \frac{\partial \boldsymbol{\psi}_\theta}{\partial \xi} \mathbf{x}_1\, \boldsymbol{\psi}_\theta \mathbf{v}_2 \right) \mathrm{d}\xi \tag{4.64}$$

where $\boldsymbol{\psi}_\theta$ is the shape function for a one-dimensional element, $\mathbf{x}_1$ and $\mathbf{x}_2$ are respectively vectors which group the horizontal and vertical coordinates of the side nodes and $\mathbf{v}_1$ and $\mathbf{v}_2$ are vectors whose components are the horizontal and vertical velocity at each side node.

The second method consists of solving the Poisson equation,

$$-\boldsymbol{\nabla}^2 \varphi = \omega \tag{4.65}$$

where ω is the vorticity function.

The previous equation can be cast into a finite element formulation, generating the following elemental matrix problem,

$$\int_{\Omega^{(e)}} \left(\boldsymbol{\nabla} \boldsymbol{\psi}_\theta^{(e)} \right)^T \left(\boldsymbol{\nabla} \boldsymbol{\psi}_\theta^{(e)} \right) \mathrm{d}\Omega^{(e)}\, \boldsymbol{\varphi}^{(e)} = \int_{\Omega^{(e)}} \left(\boldsymbol{\psi}_{\theta,1}^{(e)T} \boldsymbol{\psi}_\theta^{(e)}\, \mathbf{v}_2^{(e)} - \boldsymbol{\psi}_{\theta,2}^{(e)T} \boldsymbol{\psi}_\theta^{(e)}\, \mathbf{v}_1^{(e)} \right) \mathrm{d}\Omega^{(e)} \tag{4.66}$$

where:

$$\boldsymbol{\psi}_{\theta,1}^{(e)} = \frac{\partial \boldsymbol{\psi}_\theta^{(e)}}{\partial x_1} \tag{4.67a}$$

$$\boldsymbol{\psi}_{\theta,2}^{(e)} = \frac{\partial \boldsymbol{\psi}_\theta^{(e)}}{\partial x_2} \tag{4.67b}$$

By assembling the previous elemental system of equations, the global matrix problem is obtained and can be solved by prescribing the value of the stream function at one point.

The developed routine uses the above mentioned method (ii) for the computation of the stream functions.

[6] Several definitions of streamlines are possible as function of the considered fluid dynamics problem.

4.11 Verification examples

4.11.1 Preliminary comments

In the present section, six examples are presented. The objective is to verify the code by comparing the results obtained with solutions given by other authors or with the analytical solution described in the literature. The verification examples presented and discussed are the following:

- Stokes flow with applied body forces in the domain (section 4.11.2). It is a simple problem where the analytical solution is known. The rate of convergence of the quadrilateral and triangular elements is also evaluated.
- Laminar Couette steady state flow (section 4.11.3). This problem is designed to verify the code when a steady state regime is considered and to illustrate the prescription of traction in the boundaries.
- Lid-driven cavity flow (section 4.11.4). It is a typical problem of fluids that is solved for different Reynolds numbers.
- Laminar Couette transient flow (section 4.11.5). This application is designed to verify the code developed in a transient analysis.
- Differentially heated square cavity (section 4.11.6). This example demonstrates the use of the code when non-isothermal fluids are involved.
- Uniform heating at bottom wall (section 4.11.7). This case aims at explaining the development of convective cells in cavities (or Bénard cells), similar to those expected to be developed in the cavity of the tubular GFRP profiles subjected to fire.

The Newton–Raphson is used to solve the resulting system of equations (see appendix B.6 for further information).

4.11.2 Stokes flow with body forces in the domain

In this first verification example, the domain of the flow problem is a square of 1 m side length with both components of the velocity vector equal to 0 m/s on the boundaries. The volume forces are applied in all the domain and the components in each direction are,

$$\begin{aligned} b_1 = {} & (12 - 24x_2)\, x_1^4 + (-24 + 48x_2)\, x_1^3 + \left(-48x_2 + 72x_2^2 - 48x_2^3 + 12\right) x_1^2 + \\ & + \left(-2 + 24x_2 - 72x_2^2 + 48x_2^3\right) x_1 + 1 - 4x_2 + 12x_2^2 - 8x_2^3 \end{aligned} \tag{4.68a}$$

$$\begin{aligned} b_2 = {} & \left(8 - 48x_2 + 48x_2^2\right) x_1^3 + \left(-12 + 72x_2 - 72x_2^2\right) x_1^2 + \\ & + \left(4 - 24x_2 + 48x_2^2 - 48x_2^3 + 24x_2^4\right) x_1 - 12x_2^2 + 24x_2^3 - 12x_2^4 \end{aligned} \tag{4.68b}$$

where x_1 and x_2 are the components of the position vector.

The body forces applied are quadratic, according to the expression (4.34a). Hence, in order to exactly consider the body forces defined by equations (4.68), these expressions were directly introduced in the code and computed in all Gauss points — making the transformation of the natural coordinates, (ξ, η), into the global ones, (x_1, x_2).

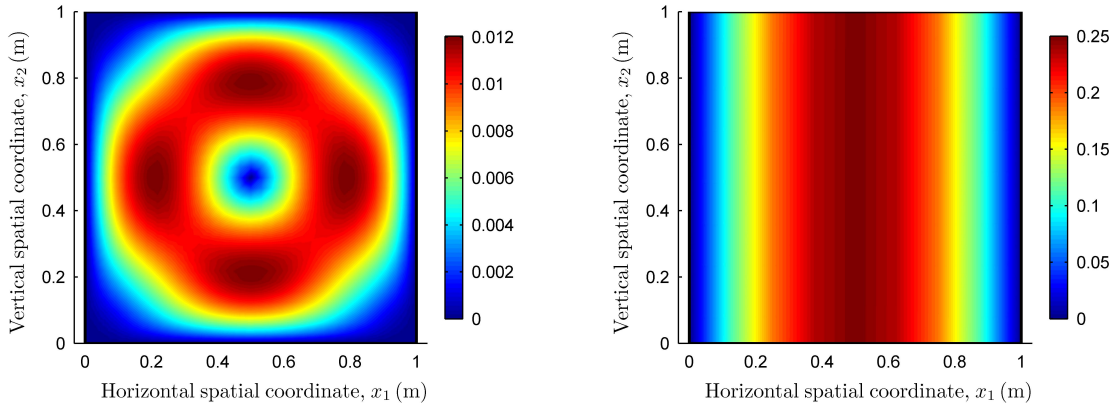

(a) Velocity resultant field. (b) Pressure field.

Figure 4.3: Numerical results of the Stokes flow problems.

The exact solution of the problem is provided by Donea and Huerta (2003):

$$v_1 = x_1^2 (1 - x_1)^2 \left(2x_2 - 6x_2^2 + 4x_2^3\right) \tag{4.69a}$$

$$v_2 = -x_2^2 (1 - x_2)^2 \left(2x_1 - 6x_1^2 + 4x_1^3\right) \tag{4.69b}$$

$$p = x_1 (1 - x_1) \tag{4.69c}$$

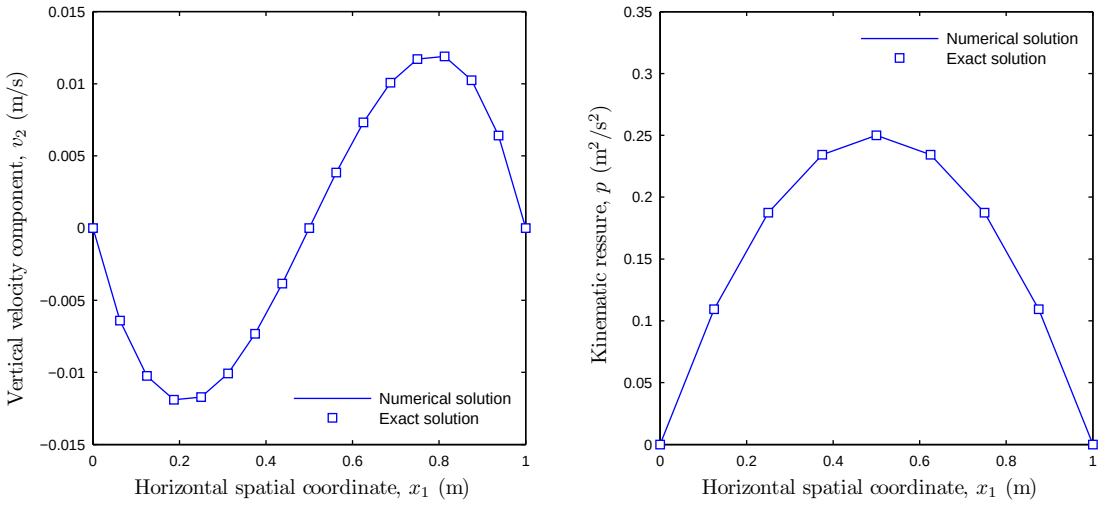

(a) Vertical velocity component distribution. (b) Kinematic pressure distribution.

Figure 4.4: Comparison between exact and numerical solutions along the line $x_2 = 0.5$.

The viscosity and density of the fluid are taken equal to the unity. A prescribed pressure equal to zero is imposed in the node located at $x_1 = 0$ and $x_2 = 0$. Figure 4.3 shows the resultant velocity and pressure fields obtained using a regular mesh of 8×8 quadrilateral elements. Figure 4.4 displays the vertical component of the velocity and

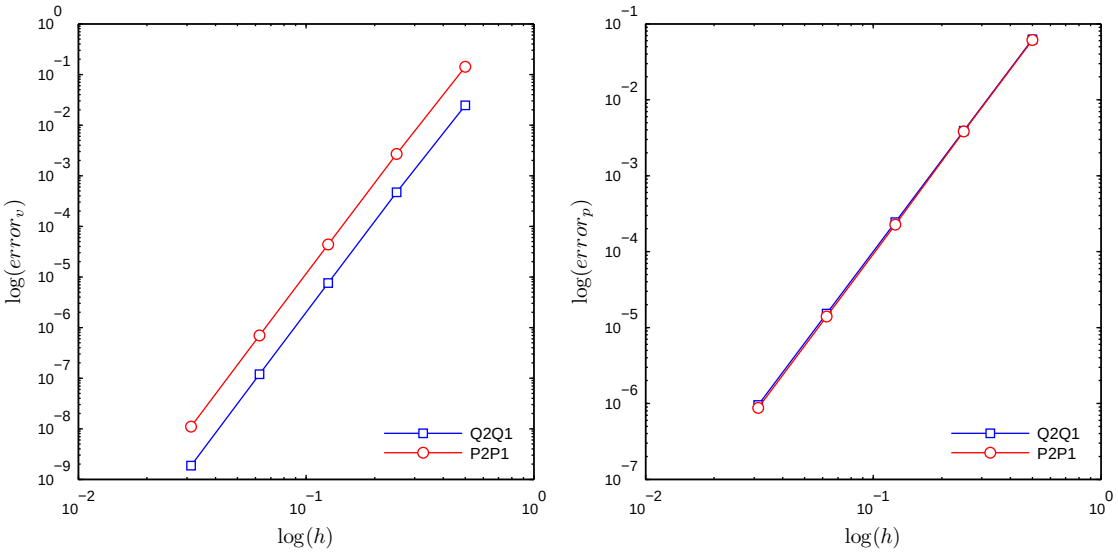

(a) Convergence of velocity.

(b) Convergence of pressure.

Figure 4.5: Convergence of the error norms with h refinement.

pressure along the line $x_2 = 0.5$. An excellent agreement between the numerical and the exact results is observed.

A convergence study considering different meshes was carried out. The velocity and pressure error norms,

$$error_v = \frac{\int_\Omega (\mathbf{v}_{ex} - \mathbf{v}_{num}) \cdot (\mathbf{v}_{ex} - \mathbf{v}_{num}) \, \mathrm{d}\Omega}{\int_\Omega \mathbf{v}_{ex} \cdot \mathbf{v}_{ex} \, \mathrm{d}\Omega} \tag{4.70a}$$

$$error_p = \frac{\int_\Omega (p_{ex} - p_{num})^2 \, \mathrm{d}\Omega}{\int_\Omega p_{ex}^2 \, \mathrm{d}\Omega} \tag{4.70b}$$

were employed to assess the convergence of the results with the mesh refinement, for both elements. The superscript *num* means *numerical* (result computed using the finite element method) and *ex* means *exact* (results obtained using the analytical solution). The error convergence results are plotted in figure 4.5 and reported in table 4.2. The geometry of the meshes employed is plotted in figure 4.6.

The convergence rate obtained for the velocity is 6, as quadratic shape functions are used to approximate the velocity field, and that obtained for the pressure is 4, as linear shape functions are used to approximate the pressure. These values can be compared with those reported by Thatcher (1990, Table 1, page 351), where the convergence rates of the velocity and the pressure are 3 and 2, respectively. At this point the reader should notice that the rates obtained in the reference paper are half of those presented in the current work, as the error measure is different. The definition of the error used in the mentioned paper is,

$$\|e\| = c\, h^\alpha \Rightarrow \log\|e\| = \log c + \alpha \log h \tag{4.71}$$

where $\|e\|$ is the error and α is the convergence rate. In the present work, the results for the error squared are presented, being easy to demonstrate that the convergence rate obtained in the present work is twice the one presented in the reference. For both elements the optimal convergence rate is observed.

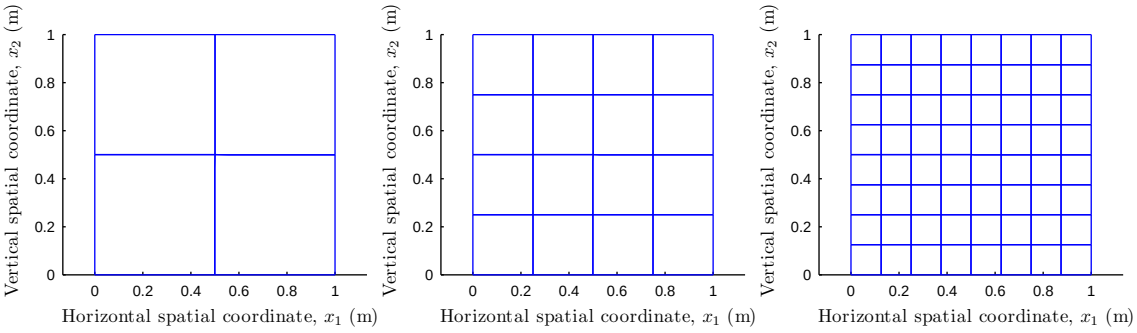

(a) $2 \times 2\, Q2Q1$. (b) $4 \times 4\, Q2Q1$. (c) $8 \times 8\, Q2Q1$.

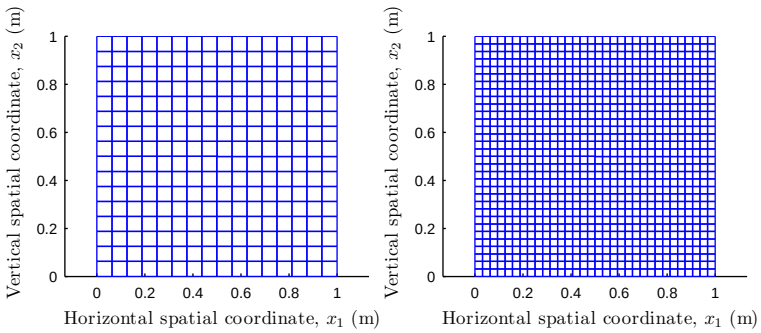

(d) $16 \times 16\, Q2Q1$. (e) $32 \times 32\, Q2Q1$.

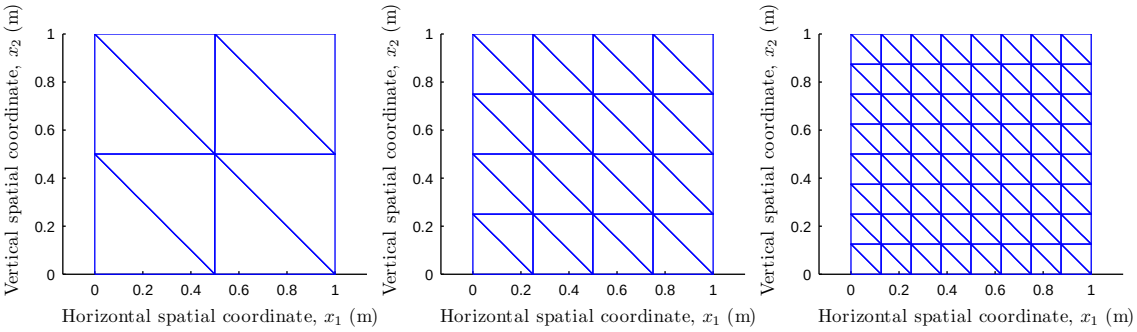

(f) $2 \times 2\, P2P1$. (g) $4 \times 4\, P2P1$. (h) $8 \times 8\, P2P1$.

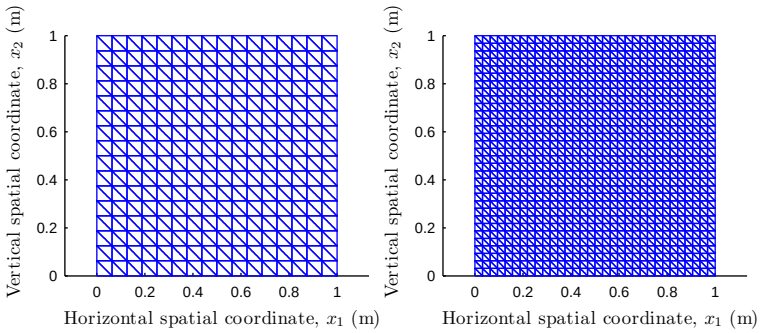

(i) $16 \times 16\, P2P1$. (j) $32 \times 32\, P2P1$.

Figure 4.6: Meshes used for the convergence study.

Meshes	h	$Q2Q1$	$P2P1$
2×2	0.5	0.024593364444810	0.142185231568019
4×4	0.25	$4.706966526871706 \cdot 10^{-4}$	0.002681018324911
8×8	0.125	$7.576532572879776 \cdot 10^{-6}$	$4.372319249098789 \cdot 10^{-5}$
16×16	0.0625	$1.190251088290493 \cdot 10^{-7}$	$6.973661797906820 \cdot 10^{-7}$
32×32	0.03125	$1.861956159615986 \cdot 10^{-9}$	$1.101939070327104 \cdot 10^{-8}$
	SLOPE	1:5.9259	1:5.9151

(a) Velocity error norm value for each mesh.

Meshes	h	$Q2Q1$	$P2P1$
2×2	0.5	0.062499999998323	0.061054973821512
4×4	0.25	0.003908197073506	0.003827536665808
8×8	0.125	$2.441520720932675 \cdot 10^{-4}$	$2.263938183118387 \cdot 10^{-4}$
16×16	0.0625	$1.525885251115168 \cdot 10^{-5}$	$1.400812572463752 \cdot 10^{-5}$
32×32	0.03125	$9.536746956778950 \cdot 10^{-7}$	$8.743568722643320 \cdot 10^{-7}$
	SLOPE	1:4.0001	1:4.0277

(b) Pressure error norm value for each mesh.

Table 4.2: Error norms computed for the velocity and the pressure using meshes with 2, 4, 8, 16 and 32 divisions.

4.11.3 Laminar Couette steady state flow

A Couette flow consists of a laminar flow between two infinite parallel plates, one of which is moving with a horizontal velocity V_1 (the vertical velocity is equal to 0). Figure 4.7a discloses the geometry of the problem.

The exact solution of this problem is given by,

$$v_1 = \frac{V_1}{h}\left(x_2 + \frac{h}{2}\right) - \frac{1}{2\,\mu}\frac{\partial p}{\partial x_1}\left(\frac{h^2}{4} - x_2^2\right) \tag{4.72a}$$

$$v_2 = 0 \tag{4.72b}$$

which shows that the horizontal component of the velocity depends on the pressure gradient in the horizontal direction.

In order to reproduce the results obtained by Taylor and Hood (1973), the gradients of pressure considered were 0.25, 0 and (-0.25), the velocity of the top plate was set as 3 and the density and viscosity of the fluid were taken as unity. The value of h was taken equal to 6. A mesh with 3 quadrilateral elements with side length equal to 2 was created, as depicted in figure 4.7b. The value of the traction vector on the right and left sides of the domain are presented in table 4.3. Figure 4.8 portrays the computed horizontal velocity component *vs.* the exact solution.

The exact solution for the velocity field (4.72) is biquadratic. The exact pressure field is constant. As the adopted approximation for the discretization of the problem is biquadratic and bilinear for the velocity and pressure fields, respectively, the exact solution was reproduced. Notice that this was only possible due to the simplicity of the geometry of the problem: the Jacobian of the transformation is constant, hence leading to the exact

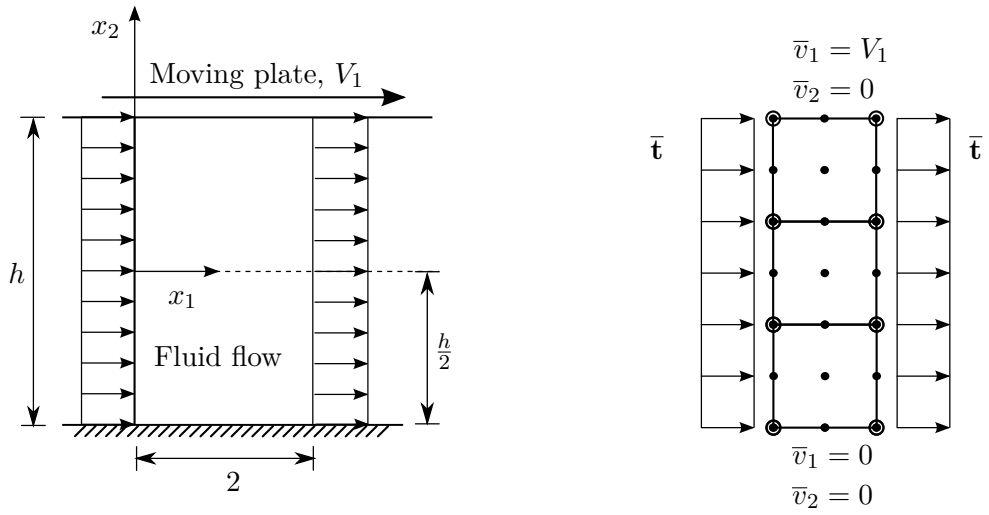

(a) Couette flow problem.

(b) Mesh and boundary conditions.

Figure 4.7: Geometry of the Couette flow problem and the respective finite element model.

$\frac{\partial p}{\partial x_1}$	left side		right side	
	$\overline{t}_1$	$\overline{t}_2$	$\overline{t}_1$	$\overline{t}_2$
-0.25	0.5	0	0	0
0.00	0	0	0	0
0.25	0	0	-0.5	0

Table 4.3: Traction value at the boundaries for the studied cases.

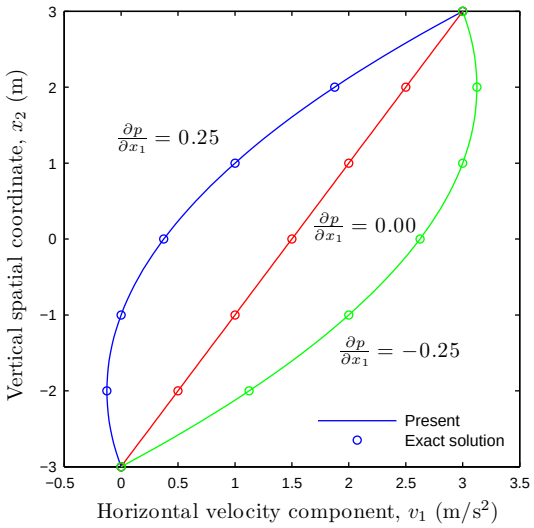

Figure 4.8: Horizontal component of the velocity in a Couette flow between parallel plates.

evaluation of all the integrals. Moreover, one element would be sufficient to exactly solve the problem.

4.11.4 Lid-driven cavity flow

The lid-driven cavity flow problem is a typical benchmark problem, whose solution, for different Reynolds number, can be consulted in several publications as, *e.g.*, Donea and Huerta (2003), Campelo (2013), Ramaswamy (1988), Reddy and Gartling (2010) and Holdeman (2010), among others.

The square cavity with unit length side has three fixed walls and one — top side —

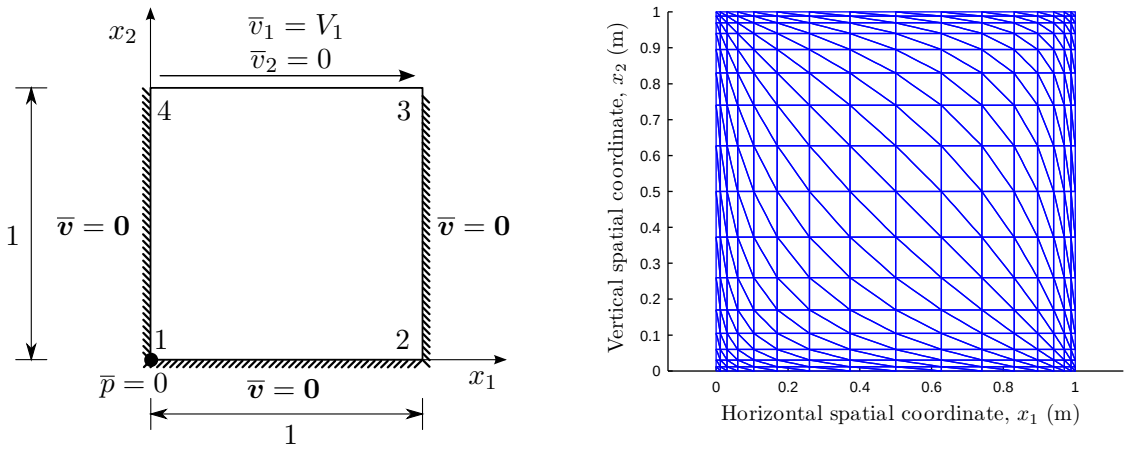

(a) Geometry problem and boundary conditions.

(b) Nonuniform mesh of $16 \times 16\, P2P1$ elements.

Figure 4.9: Lid-driven cavity.

moving with an horizontal velocity equal to V_1 (the vertical velocity is equal to 0). Figure 4.9a shows the geometry of the problem and the boundary conditions. In the lower left corner, the pressure value is prescribed as zero in order to archive a nonsingular system of equations. The horizontal velocity of the upper corners can be assumed equal to 0 (non-leaky cavity) or equal to V_1. In the present work, the second possibility is considered and, consequently, in these points a singularity in the pressure field is introduced, being the respective value equal to infinity.

The cavity is discretized with a nonuniform mesh of $16 \times 16\, P2P1$ elements, see figure 4.9b. The Navier–Stokes solution is characterized by the Reynolds number, which can be calculated for the present problem as,

$$Re = \frac{V_1\, L_{ref}}{\nu} \tag{4.73}$$

where the reference length, L_{ref}, is the side of the cavity. In the presented solutions, the velocity of the upper side, V_1, is variable as a function of the Reynolds number and the kinematic viscosity of the fluid, ν, is taken as 1 m^2/s. The problem is solved for Reynolds numbers equal to 1, 100, 400 and 1000.

The nonlinear system of equations is solved using the iterative Newton–Raphson method in which an initial solution is required. Hence, for the problems with Reynolds numbers of 1, 100 and 400, the initial solution is set to null velocity and pressure in all nodes. In the problem with $Re = 1000$ the initial solution is the solution of the problem with $Re = 400$, as no convergence is attained considering null initial velocity and pressure. All the numerical analyses were carried out in steady state regime and using a pure Galerkin formulation without including any stabilization method.

Figure 4.10 depicts a comparison between the horizontal velocity along $x_1 = 0.5$ computed using the implemented code and that presented by Donea and Huerta (2003). The continuous line is the solution obtained using the developed code and the marks are the results presented in the reference. The code implemented is capable of accurately reproducing the numerical solution of the problem, when an adequate mesh size is employed.

Figure 4.11 shows the resultant velocity and the streamlines obtained for different Reynolds numbers. These results were also compared with Campelo (2013) and good

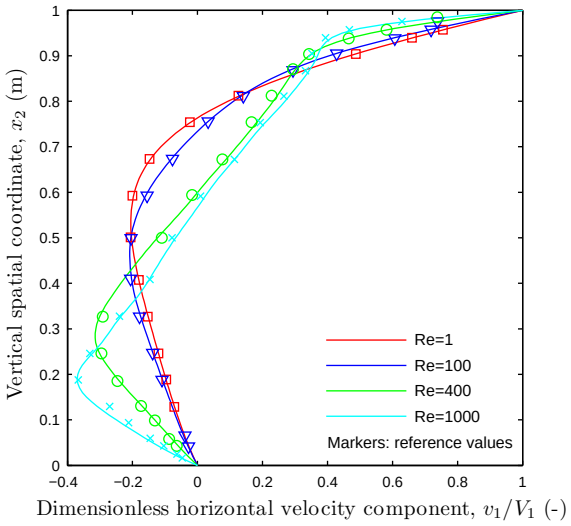

Figure 4.10: Dimensionless horizontal velocity profile at the vertical centerline for the lid-flow cavity with different Reynolds numbers.

agreement between both solutions is observed.

A study of the mesh convergence to the solution of the problem when $Re = 1000$ was carried out considering different meshes with uniform and nonuniform configurations. Figure 4.12 shows the geometry of the meshes and figure 4.13 displays the norm of the residual vector obtained for each iterative step using the different meshes.

Figure 4.13 shows that no convergence is attained with the $8 \times 8\, Q2Q1$ uniform mesh, see figure 4.12a, as this mesh is not able to reproduce the velocity gradient in the vicinity of the walls. For all the other meshes a quadratic convergence of the iterative error in the asymptotic limit of the solution is observed.

In appendix D the reader can consult further verifications of the code for higher Reynolds numbers.

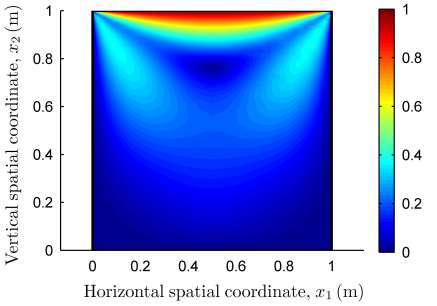

(a) Velocity resultant field, $Re = 1$.

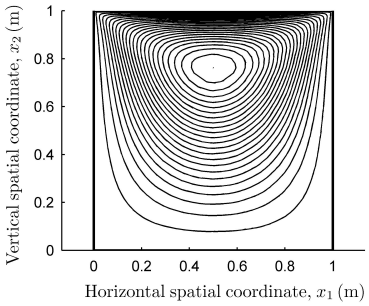

(b) Streamlines, $Re = 1$.

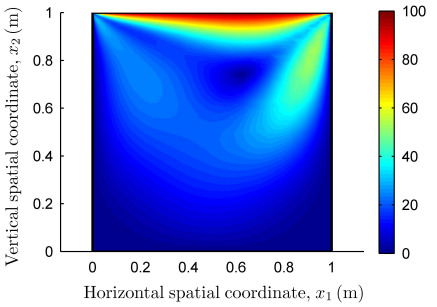

(c) Velocity resultant field, $Re = 100$.

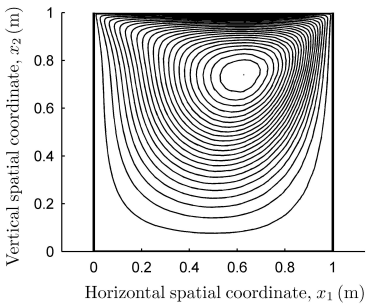

(d) Streamlines, $Re = 100$.

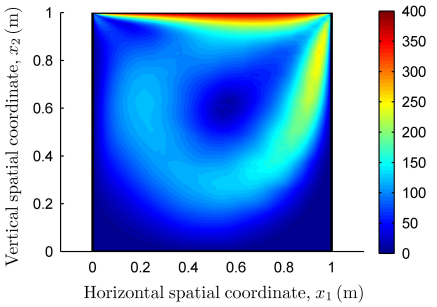

(e) Velocity resultant field, $Re = 400$.

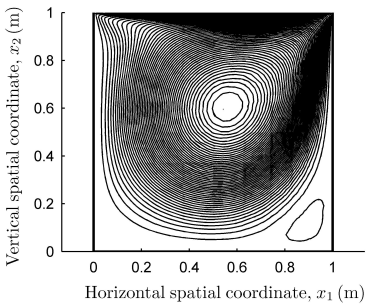

(f) Streamlines, $Re = 400$.

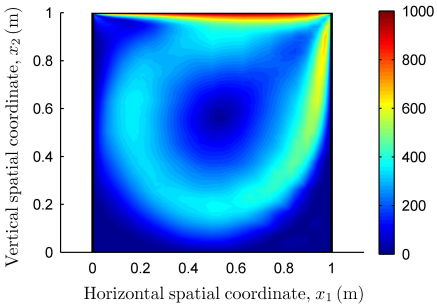

(g) Velocity resultant field, $Re = 1000$.

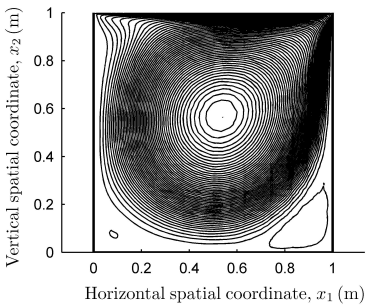

(h) Streamlines, $Re = 1000$.

Figure 4.11: Resultant velocity and streamlines obtained for different Reynolds numbers.

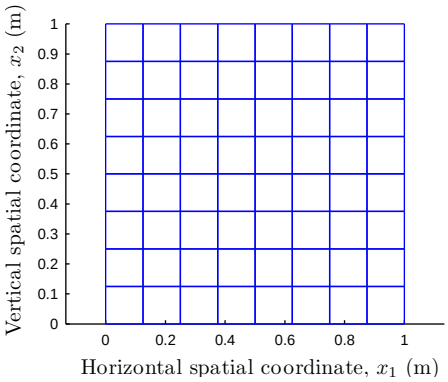

(a) Uniform $8 \times 8\, Q2Q1$.

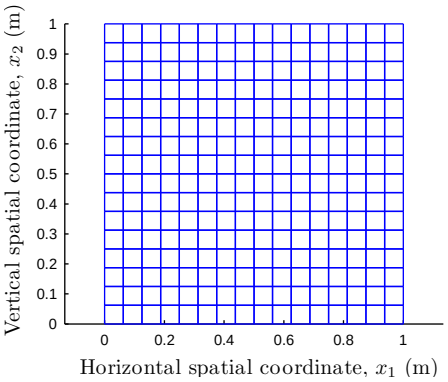

(b) Uniform $16 \times 16\, Q2Q1$.

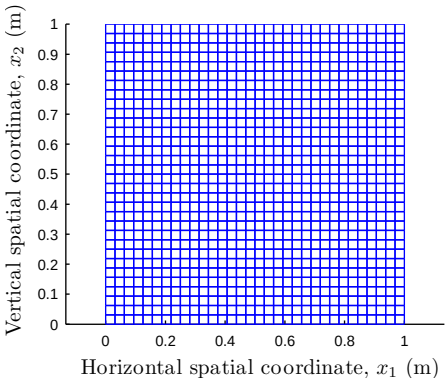

(c) Uniform $32 \times 32\, Q2Q1$.

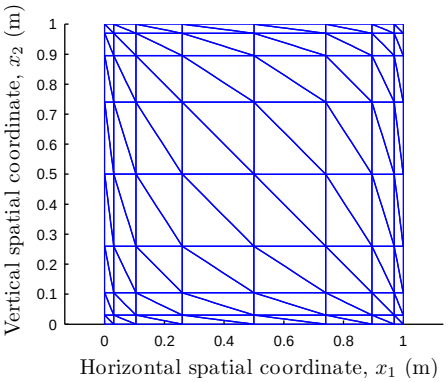

(d) Nonuniform $8 \times 8\, P2P1$.

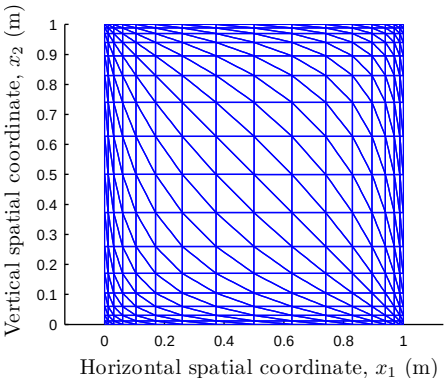

(e) Nonuniform $16 \times 16\, P2P1$.

Figure 4.12: Meshes defined for the mesh convergence study.

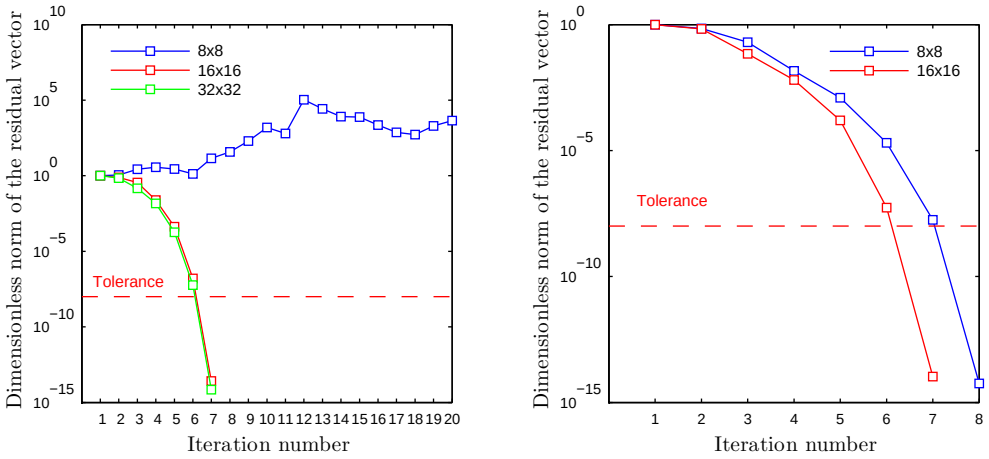

(a) Uniform meshes ($Q2Q1$ elements). (b) Nonuniform meshes ($P2P1$ elements).

Figure 4.13: Results of the convergence mesh study.

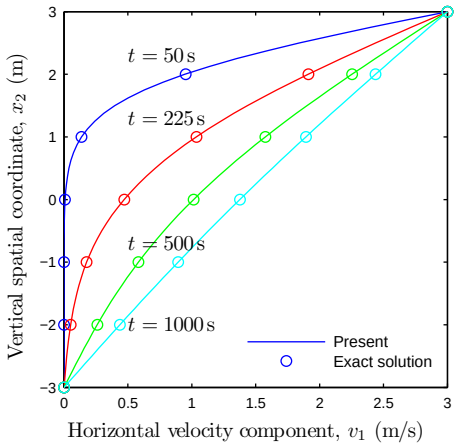

Figure 4.14: Transient Couette problem.

4.11.5 Laminar Couette transient flow

This section outlines the transient development of a Couette flow, which was defined in section 4.11.3, when $\frac{\partial p}{\partial x_1} = 0$. The analytical solution of the problem is reported in Schlichting (1960, page 92) and is given by,

$$\frac{v_1}{V_1} = \sum_{n=0}^{\infty} \operatorname{erfe}\left(2\,n\,\eta_1 + \eta\right) - \sum_{n=0}^{\infty} \operatorname{erfe}\left(2\,(n+1)\,\eta_1 - \eta\right) \tag{4.74}$$

where $\operatorname{erfe}(x)$ is the error function and:

$$\eta_1 = \frac{h}{2\sqrt{\nu t}} \tag{4.75a}$$

$$\eta = \frac{x_2}{2\sqrt{\nu t}} \tag{4.75b}$$

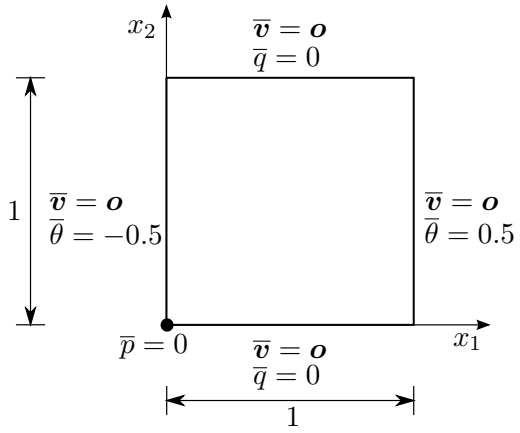

Figure 4.15: Geometry and boundary conditions of the differentially heated square cavity.

Ra	ν and κ	β
10^3	1.0	100
10^5	1.0	10 000
10^6	1.0	100 000

Table 4.4: Parameters of the differentially heated square cavity.

In this example, 100 terms of the series were considered to compute the approximation of the exact solution, which are sufficient for the required precision.

The finite element model consists of a mesh of 6 quadrilateral elements with dimensions 2×1. The kinematic viscosity was set as 0.01 m^2/s and, initially, the fluid is at rest, being the pressure equal to zero at all points. The transient analysis was carried out considering a total time of 1000 seconds and a time step of 1 second. The Euler backward scheme was used. Figure 4.14 shows the results obtained for different time steps.

It can be deemed that the numerical results represent with good accuracy the exact solution.

4.11.6 Differentially heated square cavity

This verification example is a classical benchmark test that consists of a square cavity with a temperature gradient between two opposite walls. Numerical results of this problem are provided by several authors, *e.g.*, Donea and Huerta (2003) and De Vahl Davis (1983). The geometry of the problem and the boundary conditions are depicted in figure 4.15.

The numerical solution is obtained using a regular mesh of 8×8 quadrilateral elements. The value of the constants considered are reported in table 4.4. The Rayleigh number defined in equation (4.25) is evaluated considering $\boldsymbol{g} = g\,\boldsymbol{e}_2$, where g is set to (-10), L_{ref} is the side length of the cavity and $\Delta\theta$ is the temperature difference between the horizontal walls. All thermal constants and properties of the fluid which are not explicitly mentioned in the text are taken as unity. The problems with a Rayleigh number $Ra = 10^3$ and $Ra = 10^5$ were solved using a steady state analysis, while that with $Ra = 10^6$ was performed using a transient analysis with a total time of 1.0, a time step of 0.01 and the Crank–Nicolson scheme. For problems with high Rayleigh number no convergence is attained when a steady state analysis is performed. Figure 4.16 shows the comparison between the temperature fields obtained in the developed code and those reported in De Vahl Davis (1983). A good agreement can be observed for the different problems tested.

However, regarding the numerical results obtained for $Ra = 10^5$ and $Ra = 10^6$, the mesh is visible in the vicinity of the walls and, consequently, more refined meshes have to

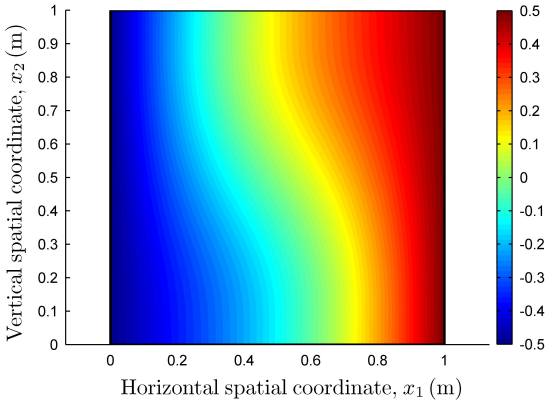

(a) Temperature field $Ra = 10^3$.

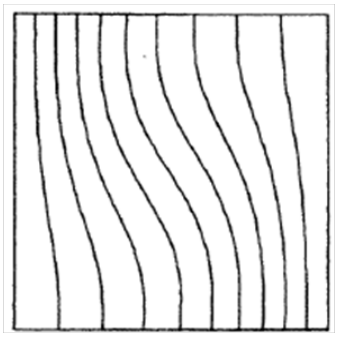

(b) Reference (De Vahl Davis, 1983).

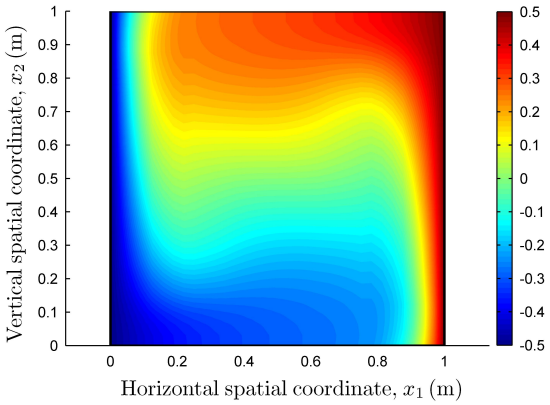

(c) Temperature field $Ra = 10^5$.

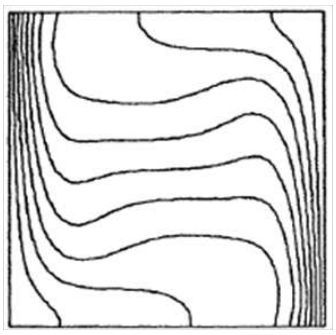

(d) Reference (De Vahl Davis, 1983).

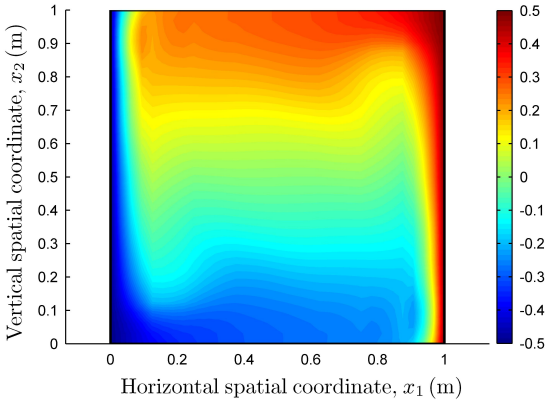

(e) Temperature field $Ra = 10^6$.

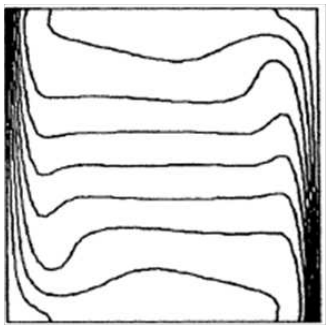

(f) Reference (De Vahl Davis, 1983).

Figure 4.16: Graphical results of the *differentially heated square cavity* problem.

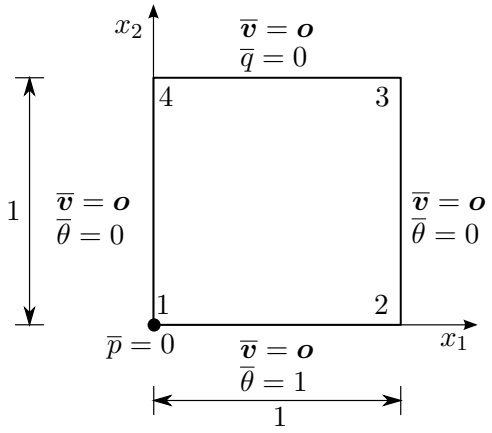

Figure 4.17: Geometry and boundary conditions of the bottom heated square cavity.

Ra	Pr	ν	β
10^3	0.7	0.7	70
10^6	10	10	100 000

Table 4.5: Bottom heated square cavity.

be employed to obtain accurate results. A study about this fact is discussed in appendix E, where further verifications of the numerical results of this problem can be consulted for different meshes.

4.11.7 Uniform heating at bottom wall

The objective of this example is to illustrate that the code is able to simulate the generation of convective cells due to natural convection, similar to those that should appear in the air enclosed in the cavities of GFRP tubular cross sections. This example is reported in Basak *et al.* (2006). The geometry of the problem and boundary conditions are summarized in figure 4.17.

The cavity has a unit length and the different values of the constants used in the cases analysed are reported in table 4.5. The gravity acceleration is taken as (-10) in the vertical direction and the kinematic viscosity of the fluid and $\Delta\theta$ are set equal to unity.

All analyses are carried out using a regular quadrilateral mesh of 32×32 elements. The problem with $Ra = 10^3$ is solved as a steady state problem, while for $Ra = 10^5$ a transient analysis is performed with a total time of 0.3 and setting Δt equal to 0.01 and $\gamma = 0.5$. Figures 4.18 and 4.19 show the numerical results obtained, in terms of temperature field and streamlines. Once again, a very good agreement is obtained between the present results and those reported in Basak *et al.* (2006).

4.12 Concluding remarks

In the present chapter a finite element formulation of the non-isothermal fluid dynamics problem is presented. In this formulation, the fluid is considered viscous, incompressible and Newtonian. In addition, a laminar flow is assumed. The Boussinesq approximation is introduced to represent artificially the variation of the density due to the temperature gradient. The Taylor–Hood elements ($Q2Q1$ and $P2P1$) are implemented to ensure that the LBB condition is satisfied. The code developed allows performing steady state and transient analyses following different time schemes. Several benchmark problems are solved

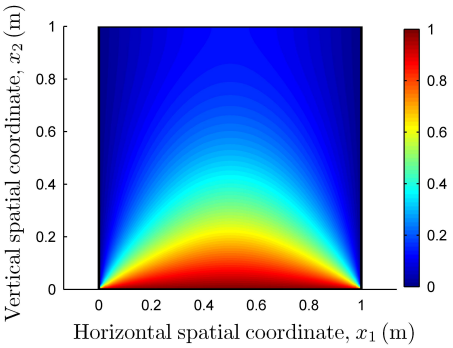

(a) Temperature field.

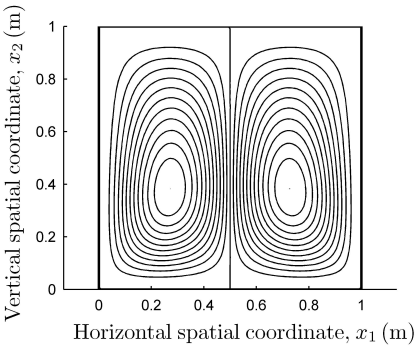

(b) Streamlines.

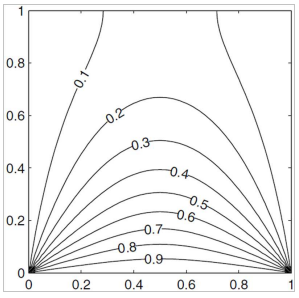

(c) Temperature field (Basak *et al.*, 2006).

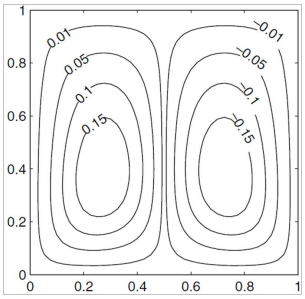

(d) Streamlines (Basak *et al.*, 2006).

Figure 4.18: Graphical results of the *uniform heated bottom wall* problem, $Ra = 10^3$.

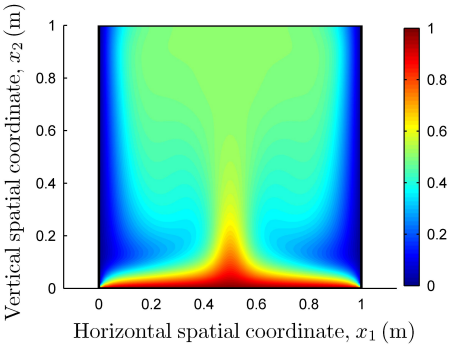

(a) Temperature field.

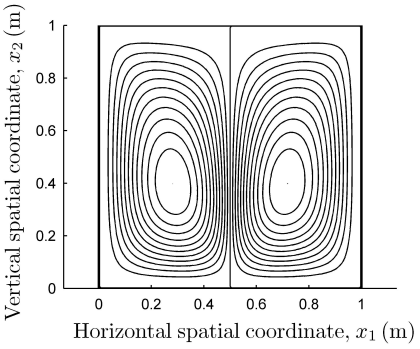

(b) Streamlines.

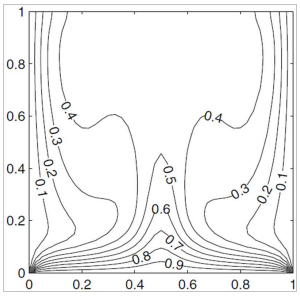

(c) Temperature field (Basak *et al.*, 2006).

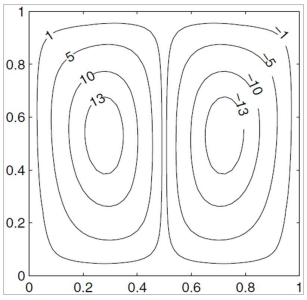

(d) Streamlines (Basak *et al.*, 2006).

Figure 4.19: Graphical results of the *uniform heated bottom wall* problem, $Ra = 10^5$.

using the in-house code in order to verify the numerical results obtained and to illustrate some important concepts regarding the fluid dynamics theory.

The example presented in section 4.11.7 illustrates that the natural convection in the fluid has an important influence on the temperature distribution, especially on the top wall of the cavity. In fact, when a fluid is heated from below, the warmer fluid rises (in the centre), while the colder descends (around the edges) due to the differences in density at different temperatures. These movements originate the Bénard cells, which are expected to develop in the cavity of the GFRP square tubular cross-section. Furthermore, due to the ascending movement of the warm air, the upper flange of the cross section is also heated due to the natural convection of the fluid. This phenomenon is assessed and discussed in detail in chapter 7.

Chapter 5

Conjugate heat transfer problem

5.1 Introduction

The term *conjugate heat transfer* is used to describe processes that involve temperature variations within solids and fluids due to their thermal interaction.

Traditionally, the conjugate heat transfer problems were solved using the classical convective heat transfer modelling through the heat transfer coefficient (Dorfman and Renner, 2009), and it was only since the 1960s, that the conjugate and coupled formulation began to be used.

Luikov *et al.* (1971) were one of the first researchers to point out the need to take into account wall conduction in problems where convective heat transfer occurs on the surfaces of a conducting solid wall of finite thickness. Since then, numerous studies about the coupling of solid wall conduction with fluid convection have been reported in the literature. In recent years, the conjugate heat transfer, especially in cavities, has gained the attention of many scientists due to its application, as for example, in thermal design of buildings, furnace design or solar collectors. Furthermore, the present needs and demands of engineering applications dictate extremely strict requirements for thermally loaded surfaces and, hence, a deep knowledge of the conjugate heat transfer process. In order to accomplish this goal, researchers have performed experimental studies about the effect of the conduction on natural convection, as well as numerical investigations to develop effective numerical tools for solving conjugate convective-conductive heat transfer problems (Zudin, 2011).

Regarding the thermal simulation of cavities, namely the consideration of both the natural convection in a fluid and the conductivity on the walls, the literature available is relatively extensive. One of the most referred studies is the one carried out by Kaminski and Prakash (1986). It analyzes the natural convection in a square enclosure with three zero thickness walls and one finite thickness right vertical wall, for different Grashof numbers. A temperature gradient is created by prescribing different temperatures in both vertical faces and the resulting conjugate heat transfer problem is solved taking into account the conduction in the right vertical wall. Multiple variations of this paper can be found in the literature, as for example, Belazizia *et al.* (2012), where different Rayleigh numbers and thermal conductivities of the wall are considered, or Du and Bilgen (1972), where different parameters — Rayleigh numbers, wall thickness, conductivity of the wall and dimensions of the enclosure — are tested in order to determine the influence of the conduction in the solid wall and convection in the fluid during the heat transfer process. Mobedi (2008) presented a numerical study about the heat transfer in cavities where the

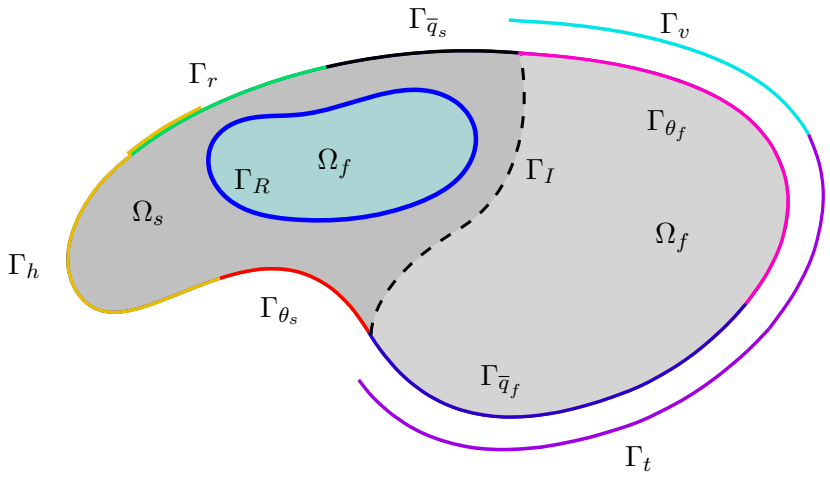

Figure 5.1: Boundary conditions of the coupled problem.

two lateral walls have null thickness and the horizontal walls have finite thickness. A gradient of temperature is applied between the two vertical walls and the steady state results are obtained for a wide range of Rayleigh numbers and thermal conductivity ratios (ratios between the wall and fluid conductivities).

While the natural convection heat transfer in cavities and its interaction with the conductivity on the walls has been widely explored, in only a few studies the thermal radiation is considered together with heat convection. However, as Yücel *et al.* (1989) refers, radiation can strongly influence the natural convective flow. One of the first numerical studies about conjugate heat transfer with radiative heat flux was presented by Kim and Viskanta (1984), where a two-dimensional rectangular cavity with four finite thickness walls is analysed. A gradient of temperatures is imposed between the exterior faces of the vertical walls, while the exterior faces of the internal walls are insulated. The fluid inside the cavity is considered to be nonparticipating, and only radiation heat exchange between the walls, that are assumed to be gray diffuse emitters, is considered. Recently, Nouanegue *et al.* (2009) presented a numerical study where the influence of the radiative heat exchange in the problem solved by Kaminski and Prakash (1986) is studied.

The current chapter presents a compact coupled procedure for modelling transient conjugate heat transfer problems using the FEM. The resulting system of equations is obtained by coupling the fluid dynamics equations (presented in chapter 4) with the heat transfer equations (described in chapter 3). Furthermore, boundary conditions in the fluid-solid interface have to be defined. The code developed is verified by solving the following two problems:

- Conjugate heat transfer in a square cavity with a finite thickness wall.

- Conjugate heat transfer problem of a differentially heated cavity where the finite thickness walls are gray-diffusive.

5.2 Governing equations and strong form of the problem

Consider the coupled conjugate heat transfer problem schematically represented in figure 5.1, where Ω_s and Ω_f are the solid and fluid domains, respectively. The interface between the solid and fluid domains is represented by Γ_I, when no radiative heat exchange is present, and Γ_R, when there is radiative heat exchange between the walls of the cavity. Along the present chapter, the subindex s, f and I are used to refer the *solid*, *fluid* and *interface* variables.

The classical formulation of the strong form of the conjugate heat transfer problem reads as follows:

Obtain $\theta \in \overline{\Omega}_s$, $R \in \Gamma_R$ and $\{\boldsymbol{v}, p, \theta\} \in \overline{\Omega}_f$ for $\boldsymbol{x} = x_i\,\boldsymbol{e}_i \in \left(\overline{\Omega}_s \cup \overline{\Omega}_f\right)$ and at all $t \in [t_0, t_1]$, such that:

$$\rho\, c_p\, \dot{\theta} + \operatorname{div} \boldsymbol{q} - G = 0 \qquad \text{in} \quad \Omega_s \tag{5.1a}$$

$$\operatorname{div} \boldsymbol{v} = 0 \qquad \text{in} \quad \Omega_f \tag{5.1b}$$

$$\dot{\boldsymbol{v}} + (\boldsymbol{\nabla} \boldsymbol{v})\, \boldsymbol{v} - \nu\, \boldsymbol{\nabla}^2 \boldsymbol{v} + \boldsymbol{\nabla} p = \boldsymbol{b} + \boldsymbol{f}_B \qquad \text{in} \quad \Omega_f \tag{5.1c}$$

$$\rho_0\, c_p \left(\dot{\theta} + \boldsymbol{v} \cdot \boldsymbol{\nabla} \theta\right) + \operatorname{div} \boldsymbol{q} - G = 0 \qquad \text{in} \quad \Omega_f \tag{5.1d}$$

$$\theta - \overline{\theta} = 0 \qquad \text{on} \quad \Gamma_{\theta_s} \tag{5.1e}$$

$$q_n + \overline{q} = 0 \qquad \text{on} \quad \Gamma_{\overline{q}_s} \tag{5.1f}$$

$$q_n + h\, (\theta_a - \theta) = 0 \qquad \text{on} \quad \Gamma_h \tag{5.1g}$$

$$q_n + \epsilon\, \sigma \left(\theta_a^4 - \theta^4\right) = 0 \qquad \text{on} \quad \Gamma_r \tag{5.1h}$$

$$\boldsymbol{v} - \overline{\boldsymbol{v}} = 0 \qquad \text{on} \quad \Gamma_v \tag{5.1i}$$

$$\boldsymbol{t} - \overline{\boldsymbol{t}} = 0 \qquad \text{on} \quad \Gamma_t \tag{5.1j}$$

$$\theta - \overline{\theta} = 0 \qquad \text{on} \quad \Gamma_{\theta_f} \tag{5.1k}$$

$$q_n + \overline{q} = 0 \qquad \text{on} \quad \Gamma_{\overline{q}_f} \tag{5.1l}$$

$$\boldsymbol{v} = \boldsymbol{o} \qquad \text{on} \quad \Gamma_I \text{ and } \Gamma_R \tag{5.1m}$$

$$\theta|_f = \theta|_s \qquad \text{on} \quad \Gamma_I \text{ and } \Gamma_R \tag{5.1n}$$

$$q_n|_s + q_n|_f = 0 \qquad \text{on} \quad \Gamma_I \tag{5.1o}$$

$$q_n|_s + q_n|_f - \frac{\epsilon}{1-\epsilon} \left(\sigma\, \theta^4 - R\right) = 0 \qquad \text{on} \quad \Gamma_R \tag{5.1p}$$

$$\theta_0 = \overline{\theta}_0 \qquad \text{at} \quad t = t_0 \text{ in } \overline{\Omega}_s \tag{5.1q}$$

$$\boldsymbol{v}_0 = \overline{\boldsymbol{v}}_0 \qquad \text{at} \quad t = t_0 \text{ in } \Omega_f \tag{5.1r}$$

$$\theta_0 = \overline{\theta}_0 \qquad \text{at} \quad t = t_0 \text{ in } \overline{\Omega}_f \tag{5.1s}$$

No-slip boundary conditions (the velocity in the interface is null) and ideal thermal contact (continuous temperature field) are considered in the interface (equations (5.1m) and (5.1n), respectively). Equation (5.1p) imposes equilibrium of fluxes when the radiative heat flux between the faces of a solid is calculates assuming nonparticipating medium, *i.e.*, neglecting the contribution of the fluid in the radiative heat exchange.

5.3 Finite element formulation

5.3.1 Weak form

The compact weak form of the conjugate problem is formed by the set of the weak forms presented in chapters 3 and 4 and can be written as:

$$\begin{aligned}\int_{\Omega_s}\left(\boldsymbol{\nabla}\delta\theta\cdot\boldsymbol{q}-\delta\theta\,\rho\,c_p\,\dot{\theta}\right)\mathrm{d}\Omega_s+\int_{\Omega_s}\delta\theta\,G\,\mathrm{d}\Omega_s+\int_{\Gamma_{\overline{q}_s}}\delta\theta\,\overline{q}\,\mathrm{d}\Gamma_{\overline{q}_s}+\int_{\Gamma_h}\delta\theta\,h\,(\theta_a-\theta)\,\mathrm{d}\Gamma_h+\\+\int_{\Gamma_r}\delta\theta\,\epsilon\,\sigma\,\left(\theta_a^4-\theta^4\right)\mathrm{d}\Gamma_r+\int_{\Gamma_R}\delta\theta\,\frac{\epsilon}{1-\epsilon}\,\left(\sigma\,\theta^4-R\right)\mathrm{d}\Gamma_R+\\+\int_{\Omega_f}\left(\boldsymbol{\nabla}\delta\theta\cdot\boldsymbol{q}-\delta\theta\,\rho_0\,c_p\,\dot{\theta}\right)\mathrm{d}\Omega_f-\int_{\Omega_f}\delta\theta\,\rho_0\,c_p\,\boldsymbol{v}\cdot\boldsymbol{\nabla}\theta\,\mathrm{d}\Omega_f+\\+\int_{\Omega_f}\delta\theta\,G\,\mathrm{d}\Omega_f+\int_{\Gamma_{\overline{q}_f}}\delta\theta\,\overline{q}\,\mathrm{d}\Gamma_{\overline{q}_f}=0\end{aligned}\tag{5.2}$$

$$\begin{aligned}\int_{\Gamma_R^e}\delta R^e\frac{R^e}{(1-\epsilon^e)}\,\mathrm{d}\Gamma_R^e=\int_{\Gamma_R^e}\delta R^e\,\sigma\,\frac{\epsilon^e}{(1-\epsilon^e)}\,(\theta_I^e)^4\,\mathrm{d}\Gamma_R^e+\\+\sum_{\substack{k=1\\k\neq e}}^{n}\int_{\Gamma_R^e}\int_{\Gamma_R^k}\delta R^e\,R^k\,\frac{\cos\beta^e\cos\beta^k}{2\,r}\,\mathrm{d}\Gamma_R^k\,\mathrm{d}\Gamma_R^e\end{aligned}\tag{5.3}$$

$$\begin{aligned}&\int_\Omega\delta\boldsymbol{v}\cdot\dot{\boldsymbol{v}}\,\mathrm{d}\Omega+\int_\Omega\delta\boldsymbol{v}\cdot(\boldsymbol{\nabla}\boldsymbol{v})\,\boldsymbol{v}\,\mathrm{d}\Omega+\int_\Omega\boldsymbol{\nabla}\delta\boldsymbol{v}:\nu\boldsymbol{\nabla}\boldsymbol{v}\,\mathrm{d}\Omega-\\&\quad-\int_\Omega\operatorname{div}\delta\boldsymbol{v}\,p\,\mathrm{d}\Omega-\int_{\Gamma_t}\delta\boldsymbol{v}\cdot\bar{\boldsymbol{t}}\,\mathrm{d}\Gamma_t-\int_\Omega\delta\boldsymbol{v}\cdot\boldsymbol{b}\,\mathrm{d}\Omega-\int_\Omega\delta\boldsymbol{v}\cdot\boldsymbol{f}_B\,\mathrm{d}\Omega=0\end{aligned}\tag{4.29a}$$

$$-\int_\Omega\delta p\operatorname{div}\boldsymbol{v}\,\mathrm{d}\Omega=0\tag{4.29b}$$

5.3.2 Spatial discretization, residual vector and tangent matrix

Consider that the independent variables $\boldsymbol{v}^{(e)}$, $p^{(e)}$, $\theta^{(e)}$ and $R^{(e)}$ in each element can, in general, be approximated by the expressions,

$$\boldsymbol{v}^{(e)}=\boldsymbol{\psi}_v^{(e)}\,\mathbf{v}^{(e)}\qquad\text{in}\quad\Omega_f^{(e)}\tag{5.5a}$$

$$p^{(e)}=\boldsymbol{\psi}_p^{(e)}\,\mathbf{p}^{(e)}\qquad\text{in}\quad\Omega_f^{(e)}\tag{5.5b}$$

$$\theta^{(e)}=\boldsymbol{\psi}_{\theta_s}^{(e)}\,{\boldsymbol{\Theta}_s}^{(e)}+\boldsymbol{\psi}_{\theta_I}^{(e)}\,{\boldsymbol{\Theta}_I}^{(e)}\qquad\text{in}\quad\Omega_s^{(e)}\tag{5.5c}$$

$$\theta^{(e)}=\boldsymbol{\psi}_{\theta_f}^{(e)}\,{\boldsymbol{\Theta}_f}^{(e)}+\boldsymbol{\psi}_{\theta_I}^{(e)}\,{\boldsymbol{\Theta}_I}^{(e)}\qquad\text{in}\quad\Omega_f^{(e)}\tag{5.5d}$$

$$R^{(e)}=\boldsymbol{\psi}_R^{(e)}\,\mathbf{R}^{(e)}\qquad\text{on}\quad\Gamma_R^{(e)}\tag{5.5e}$$

where $\boldsymbol{\Theta}_s^{(e)}$, ${\boldsymbol{\Theta}_I}^{(e)}$ and ${\boldsymbol{\Theta}_f}^{(e)}$ are the nodal temperatures at the solid, the interface (Γ_I or Γ_R) and the fluid.

In particular, if the element does not have nodes along the interface, then the expressions (5.5c) and (5.5d) render:

$$\theta^{(e)}=\boldsymbol{\psi}_{\theta_s}^{(e)}\,{\boldsymbol{\Theta}_s}^{(e)}\qquad\text{in}\quad\Omega_s^{(e)}\tag{5.6a}$$

$$\theta^{(e)}=\boldsymbol{\psi}_{\theta_f}^{(e)}\,{\boldsymbol{\Theta}_f}^{(e)}\qquad\text{in}\quad\Omega_f^{(e)}\tag{5.6b}$$

As the trace of the shape functions $\boldsymbol{\psi}_{\theta_s}^{(e)}$ and $\boldsymbol{\psi}_{\theta_f}^{(e)}$ along the interface is zero, then the approximation along the interface is given by:

$$\theta^{(e)} = \boldsymbol{\psi}_{\theta_I}^{(e)}\, \boldsymbol{\theta}_I{}^{(e)} \quad \text{on} \quad \Gamma_I^{(e)} \tag{5.7}$$

The elemental residual vector is calculated by replacing the expressions (5.5), their variations, (3.32) and (4.34) into the weak form presented in section 5.3.1.

The elemental residual vector at a generic computation time, $(t+\Delta t)$, can be expressed as:

$$\mathbf{r}^{(e)t+\Delta t} = \begin{Bmatrix} \mathbf{r}_v^{(e)} \\ \mathbf{r}_p^{(e)} \\ \mathbf{r}_{\theta_f}^{(e)} \\ \mathbf{r}_{\theta_I}^{(e)} \\ \mathbf{r}_{\theta s}^{(e)} \\ \mathbf{r}_R^{(e)} \end{Bmatrix}^{t+\Delta t} \tag{5.8}$$

Using the matrix notation, the elemental residual vector is given by (5.12). This vector is valid for all the elements. The first three lines refer to elements in the fluid domain, the forth line refers to the nodes in the interface, the fifth line refers to elements in the solid domain and the remaining lines refer to the radiosity elements. The matrices regarding the solid domain can be consulted in section 3.6, while the matrices regarding the fluid domain are defined in section 4.6. Due to the coupling of the solid and fluid domain, new matrices/vectors referring to the interface have to be defined,

$$\mathbf{K}_{ff}^{(e)} = \mathbf{K}^{(e)} + \mathbf{L}^{(e)} + \frac{1}{\gamma \Delta t}\, \mathbf{M}^{(e)} \tag{5.9a}$$

$$\mathbf{K}_{fI}^{(e)} = \int_{\Omega_f^{(e)}} \mathbf{B}_{\theta_f}^{(e)T} \mathbf{D}\, \mathbf{B}_{\theta_I}^{(e)}\, \mathrm{d}\Omega_f^{(e)} \tag{5.9b}$$

$$\mathbf{K}_{II}^{(e)} = \int_{\Omega_f^{(e)}} \mathbf{B}_{\theta_I}^{(e)T} \mathbf{D}\, \mathbf{B}_{\theta_I}^{(e)}\, \mathrm{d}\Omega_f^{(e)} + \int_{\Omega_s^{(e)}} \mathbf{B}_{\theta_I}^{(e)T} \mathbf{D}\, \mathbf{B}_{\theta_I}^{(e)}\, \mathrm{d}\Omega_s^{(e)} \tag{5.9c}$$

$$\mathbf{K}_{Is}^{(e)} = \int_{\Omega_s^{(e)}} \mathbf{B}_{\theta_I}^{(e)T} \mathbf{D}\, \mathbf{B}_{\theta_s}^{(e)}\, \mathrm{d}\Omega_s^{(e)} \tag{5.9d}$$

$$\mathbf{K}_{ss}^{(e)} = \mathbf{K}_s^{(e)} + \frac{1}{\gamma \Delta t}\, \mathbf{M}_s^{(e)} \tag{5.9e}$$

$$\begin{aligned} \mathbf{f}_{\theta_I}^{(e)} = & \int_{\Omega_f^{(e)}} \boldsymbol{\psi}_{\theta_I}^{(e)T} \boldsymbol{\psi}_{\theta_f}^{(e)} \mathbf{g}^{(e)}\, \mathrm{d}\Omega_f^{(e)} + \int_{\Omega_s^{(e)}} \boldsymbol{\psi}_{\theta_I}^{(e)T} \boldsymbol{\psi}_{\theta_s}^{(e)} \mathbf{g}^{(e)}\, \mathrm{d}\Omega_s^{(e)} - \\ & - \int_{\Gamma_R^{(e)}} \boldsymbol{\psi}_{\theta_I}^{(e)T} \frac{\epsilon}{1-\epsilon} \left(\sigma \left(\boldsymbol{\psi}_{\theta_I}^{(e)}\, \boldsymbol{\theta}_I^{(e)} \right)^4 - \boldsymbol{\psi}_R^{(e)}\, \mathbf{R}^{(e)} \right) \mathrm{d}\Gamma_R^{(e)} \end{aligned} \tag{5.9f}$$

where, $\mathbf{B}_{\theta_s}^{(e)}$, $\mathbf{B}_{\theta_I}^{(e)}$ and $\mathbf{B}_{\theta_f}^{(e)}$ are the matrix that gather the derivatives of the shapes functions in the solid, interface and fluid:

$$\mathbf{B}_{\theta_s}^{(e)} = \boldsymbol{\nabla}\, \boldsymbol{\psi}_{\theta_s}^{(e)} \tag{5.10a}$$

$$\mathbf{B}_{\theta_I}^{(e)} = \boldsymbol{\nabla}\, \boldsymbol{\psi}_{\theta_I}^{(e)} \tag{5.10b}$$

$$\mathbf{B}_{\theta_f}^{(e)} = \boldsymbol{\nabla}\, \boldsymbol{\psi}_{\theta_f}^{(e)} \tag{5.10c}$$

The resultant nonlinear system of equations is obtained by assembling the elemental ones and solved using the iterative/incremental Newton–Raphson method.

The elemental tangent matrix at the instant $(t + \Delta t)$ is given by (5.13), where the sub-matrices are defined in expressions (3.53), (4.61), (4.40) and (4.48). The matrices due to the coupling of the solid and fluid domain are also included.

5.3.3 Adaptive time stepping

Adaptive time stepping schemes can be used to solve several types of transient nonlinear problems. The formulation presented in the current and previous chapters is given for a constant time step, but it is possible to extend it to variable time step size.

In the code developed, a simple automatic time stepping scheme is implemented to obtain a converged solution when equilibrium iterations fail because the time step used is too large. In this scheme, when convergence is reached with a certain time increment, Δt, the next time increment, Δt^*, is given by (adapted from Tiago, 2007),

$$\Delta t^* = \Delta t \sqrt{\frac{n}{n_i}} \tag{5.11}$$

where n is the desired number of iterations and n_i was the required number of iterations to archive a converged solution on the last step. In the code developed, n was set equal to 6.

When convergence is not reached after a prescribed maximum number of iterations with Δt, the program automatically calculates the new time increment as $\Delta t^* = \Delta t/2$. In the code developed, the maximum number of allowed iterations is 20. The solution of the problem is computed at the updated time step. If the convergence is not attained, a new subdivision of the time increment is done. This process continues until the maximum number of subdivisions (10, in the code developed) is attained without reaching a converged solution. More efficient and complex algorithms can be found in Turek (1998).

5.4 Verification examples

5.4.1 Introduction

In the present section two typical benchmark problems are tested to verify the code developed.

Section 5.4.2 presents a two-dimensional conjugate problem consisting of a natural convection flow taking into account the conduction of the solid elements. The numerical solution obtained is compared with those available in the literature.

Section 5.4.3 reports a conjugate problem where a square cavity is differentially heated. Two finite thickness horizontal walls close the square cavity. The effect of the exchange of radiative heat flux between the mentioned walls in the natural convection is analysed. In this case, the numerical results are compared with those obtained using the commercial software ADINA-F (2010).

5.4.2 Wall conductivity conjugate problem

A benchmark test consisting of a cavity with a finite thickness wall of 0.2 m in the right side is considered. The configuration of the problem is depicted in figure 5.2a. The

$$
\mathbf{r}^{(e)t+\Delta t} = \begin{bmatrix}
\mathbf{K}_v^{(e)} + \mathbf{C}^{(e)} + \frac{1}{\gamma\Delta t}\mathbf{M}_v^{(e)} & \mathbf{G}^{(e)} & \mathbf{B}^{(e)} & \mathbf{O} & \mathbf{O} & \mathbf{O} & \mathbf{O} \\
\mathbf{G}^{(e)T} & \mathbf{O} & \mathbf{O} & \mathbf{O} & \mathbf{O} & \mathbf{O} & \mathbf{O} \\
\mathbf{O} & \mathbf{O} & \mathbf{K}_{ff}^{(e)} & \mathbf{K}_{fI}^{(e)} & \mathbf{O} & \mathbf{O} & \mathbf{O} \\
\mathbf{O} & \mathbf{O} & \mathbf{K}_{fI}^{(e)T} & \mathbf{K}_{II}^{(e)} & \mathbf{K}_{Is}^{(e)} & \mathbf{O} & \mathbf{O} \\
\mathbf{O} & \mathbf{O} & \mathbf{O} & \mathbf{K}_{Is}^{(e)T} & \mathbf{K}_{ss}^{(e)} & \mathbf{O} & \mathbf{O} \\
\mathbf{O} & \mathbf{O} & \mathbf{O} & \mathbf{O} & \mathbf{O} & \mathbf{K}_R^{(1)} & \\
 & & & & & & \mathbf{K}_R^{(n)}
\end{bmatrix}^{t+\Delta t}
\begin{Bmatrix}
\mathbf{v}^{(e)} \\ \mathbf{p}^{(e)} \\ \boldsymbol{\theta}_f^{(e)} \\ \boldsymbol{\theta}_I^{(e)} \\ \boldsymbol{\theta}_s^{(e)} \\ \mathbf{R}^{(1)} \\ \cdots \\ \mathbf{R}^{(n)}
\end{Bmatrix}^{t+\Delta t}
-
$$

$$
\begin{Bmatrix}
\mathbf{f}_v^{(e)} \\ \mathbf{0} \\ \mathbf{f}_{\theta_f}^{(e)} \\ \mathbf{f}_{\theta_I}^{(e)} \\ \mathbf{f}_{\theta_s}^{(e)} \\ \mathbf{f}_R^{(1)} \\ \cdots \\ \mathbf{f}_R^{(n)}
\end{Bmatrix}^{t+\Delta t}
-
\begin{bmatrix}
\frac{1}{\gamma\Delta t}\mathbf{M}_v^{(e)} & \mathbf{O} & \mathbf{O} & \mathbf{O} & \mathbf{O} & \mathbf{O} & \mathbf{O} \\
\mathbf{O} & \mathbf{O} & \mathbf{O} & \mathbf{O} & \mathbf{O} & \mathbf{O} & \mathbf{O} \\
\mathbf{O} & \mathbf{O} & \frac{1}{\gamma\Delta t}\mathbf{M}^{(e)} & \mathbf{O} & \mathbf{O} & \mathbf{O} & \mathbf{O} \\
\mathbf{O} & \mathbf{O} & \mathbf{O} & \mathbf{O} & \mathbf{O} & \mathbf{O} & \mathbf{O} \\
\mathbf{O} & \mathbf{O} & \mathbf{O} & \mathbf{O} & \frac{1}{\gamma\Delta t}\mathbf{M}_s^{(e)} & \mathbf{O} & \mathbf{O} \\
\mathbf{O} & \mathbf{O} & \mathbf{O} & \mathbf{O} & \mathbf{O} & \mathbf{O} & \mathbf{O}
\end{bmatrix}^{t+\Delta t}
\begin{Bmatrix}
\mathbf{v}^{(e)} \\ \mathbf{p}^{(e)} \\ \boldsymbol{\theta}_f^{(e)} \\ \boldsymbol{\theta}_I^{(e)} \\ \boldsymbol{\theta}_s^{(e)} \\ \mathbf{R}^{(1)} \\ \cdots \\ \mathbf{R}^{(n)}
\end{Bmatrix}^{t}
-
$$

$$
\begin{bmatrix}
\frac{1-\gamma}{\gamma}\mathbf{M}_v^{(e)} & \mathbf{O} & \mathbf{O} & \mathbf{O} & \mathbf{O} & \mathbf{O} & \mathbf{O} \\
\mathbf{O} & \mathbf{O} & \mathbf{O} & \mathbf{O} & \mathbf{O} & \mathbf{O} & \mathbf{O} \\
\mathbf{O} & \mathbf{O} & \frac{1-\gamma}{\gamma}\mathbf{M}^{(e)} & \mathbf{O} & \cdots & \mathbf{O} & \mathbf{O} \\
\mathbf{O} & \mathbf{O} & \mathbf{O} & \mathbf{O} & \mathbf{O} & \mathbf{O} & \mathbf{O} \\
\mathbf{O} & \mathbf{O} & \mathbf{O} & \mathbf{O} & \frac{1-\gamma}{\gamma}\mathbf{M}_s^{(e)} & \mathbf{O} & \mathbf{O} \\
\mathbf{O} & \mathbf{O} & \mathbf{O} & \mathbf{O} & \mathbf{O} & \mathbf{O} & \mathbf{O}
\end{bmatrix}^{t+\Delta t}
\begin{Bmatrix}
\dot{\mathbf{v}}^{(e)} \\ \dot{\mathbf{p}}^{(e)} \\ \dot{\boldsymbol{\theta}}_f^{(e)} \\ \dot{\boldsymbol{\theta}}_I^{(e)} \\ \dot{\boldsymbol{\theta}}_s^{(e)} \\ \dot{\mathbf{R}}^{(1)} \\ \cdots \\ \dot{\mathbf{R}}^{(n)}
\end{Bmatrix}^{t}
+
\begin{Bmatrix}
\mathbf{r}_{SUPGv}^{(e)} \\ \mathbf{0} \\ \mathbf{r}_{SUPG\theta}^{(e)} \\ \mathbf{0} \\ \mathbf{0} \\ \mathbf{0} \\ \cdots \\ \mathbf{0}
\end{Bmatrix}^{t+\Delta t}
\tag{5.12}
$$

$$\overline{\mathbf{K}}^{(e)t+\Delta t} = \begin{bmatrix} \mathbf{K}_v^{(e)} + \mathbf{C}_T^{(e)} + \frac{1}{\gamma\Delta t}\mathbf{M}_v^{(e)} + \mathbf{C}_{SUPG}^{(e)} & \mathbf{G}^{(e)} + \mathbf{G}_{SUPG}^{(e)} & \mathbf{B}^{(e)} + \mathbf{B}_{SUPG}^{(e)} & \mathbf{O} & \mathbf{O} & \mathbf{O} & \mathbf{O} \\ \mathbf{G}^{(e)T} & \mathbf{O} & \mathbf{O} & \mathbf{O} & \mathbf{O} & \mathbf{O} & \mathbf{O} \\ \mathbf{E}^{(e)} + \mathbf{E}_{SUPG\theta}^{(e)} & \mathbf{O} & \mathbf{F}^{(e)} + \mathbf{F}_{SUPG\theta}^{(e)} & \mathbf{F}_{fI}^{(e)} & \mathbf{O} & \mathbf{O} & \cdots \quad \mathbf{O} \\ \mathbf{O} & \mathbf{O} & \mathbf{F}_{fI}^{(e)T} & \mathbf{F}_{II}^{(e)} & \mathbf{F}_{Is}^{(e)} & \mathbf{O} & \mathbf{O} \\ \mathbf{O} & \mathbf{O} & \mathbf{O} & \mathbf{F}_{Is}^{(eT)} & \frac{\partial \mathbf{r}_{\theta_s}^{(e)t+\Delta t}}{\partial \boldsymbol{\theta}_s^{(e)}} & \frac{\partial \mathbf{r}_{\theta_s}^{(e)t+\Delta t}}{\partial \mathbf{R}^{(1)}} & \frac{\partial \mathbf{r}_{\theta_s}^{(e)t+\Delta t}}{\partial \mathbf{R}^{(n)}} \\ \mathbf{O} & \mathbf{O} & \mathbf{O} & \mathbf{O} & \frac{\partial \mathbf{r}_R^{(e)t+\Delta t}}{\partial \boldsymbol{\theta}_s^{(e)}} & \frac{\partial \mathbf{r}_R^{(e)t+\Delta t}}{\partial \mathbf{R}^{(1)}} & \frac{\partial \mathbf{r}_R^{(e)t+\Delta t}}{\partial \mathbf{R}^{(n)}} \end{bmatrix}^{t+\Delta t} \tag{5.13}$$

$$\mathbf{F}_{fI}^{(e)} = \mathbf{K}_{fI}^{(e)} \tag{5.14}$$

$$\mathbf{F}_{II}^{(e)} = \mathbf{K}_{II}^{(e)} + \int_{\Omega_s^{(e)}} \mathbf{B}_{\theta_I}^{(e)T} \frac{\partial \mathbf{D}^{t+\Delta t}}{\partial \theta} \mathbf{B}_{\theta_I}^{(e)} \, \boldsymbol{\theta}_I^{(e)t+\Delta t} \boldsymbol{\psi}_{\theta_I}^{(e)} \, \mathrm{d}\Omega_s^{(e)} - \int_{\Gamma_R^{(e)}} \boldsymbol{\psi}_{\theta_I}^{(e)T} \frac{1}{\left(1-\epsilon^{t+\Delta t}\right)^2} \frac{\partial \epsilon^{t+\Delta t}}{\partial \theta} \boldsymbol{\psi}_{\theta_I}^{(e)} \left(\sigma \left(\boldsymbol{\psi}_{\theta_I}^{(e)} \, \boldsymbol{\theta}_I^{(e)t+\Delta t} \right)^4 - \right.$$
$$\left. - \boldsymbol{\psi}_R^{(e)} \, \mathbf{R}^{(e)t+\Delta t} \right) \mathrm{d}\Gamma_R^{(e)} - \int_{\Gamma_R^{(e)}} 4\,\sigma \frac{\epsilon^{t+\Delta t}}{1-\epsilon^{t+\Delta t}} \boldsymbol{\psi}_{\theta_I}^{(e)T} \boldsymbol{\psi}_{\theta_I}^{(e)} \left(\boldsymbol{\psi}_{\theta_I}^{(e)} \, \boldsymbol{\theta}_I^{(e)t+\Delta t} \right)^3 \mathrm{d}\Gamma_R^{(e)} \tag{5.15}$$

$$\mathbf{F}_{Is}^{(e)} = \mathbf{K}_{Is}^{(e)} + \int_{\Omega_s^{(e)}} \mathbf{B}_{\theta_I}^{(e)T} \frac{\partial \mathbf{D}^{t+\Delta t}}{\partial \theta} \mathbf{B}_{\theta_s}^{(e)} \, \boldsymbol{\theta}_s^{(e)t+\Delta t} \boldsymbol{\psi}_{\theta_s}^{(e)} \, \mathrm{d}\Omega_s^{(e)} \tag{5.16}$$

$$\mathbf{F}_{sI}^{(e)} = \mathbf{K}_{Is}^{(e)T} + \int_{\Omega_s^{(e)}} \mathbf{B}_{\theta_s}^{(e)T} \frac{\partial \mathbf{D}^{t+\Delta t}}{\partial \theta} \mathbf{B}_{\theta_I}^{(e)} \, \boldsymbol{\theta}_I^{(e)t+\Delta t} \boldsymbol{\psi}_{\theta_I}^{(e)} \, \mathrm{d}\Omega_s^{(e)} \tag{5.17}$$

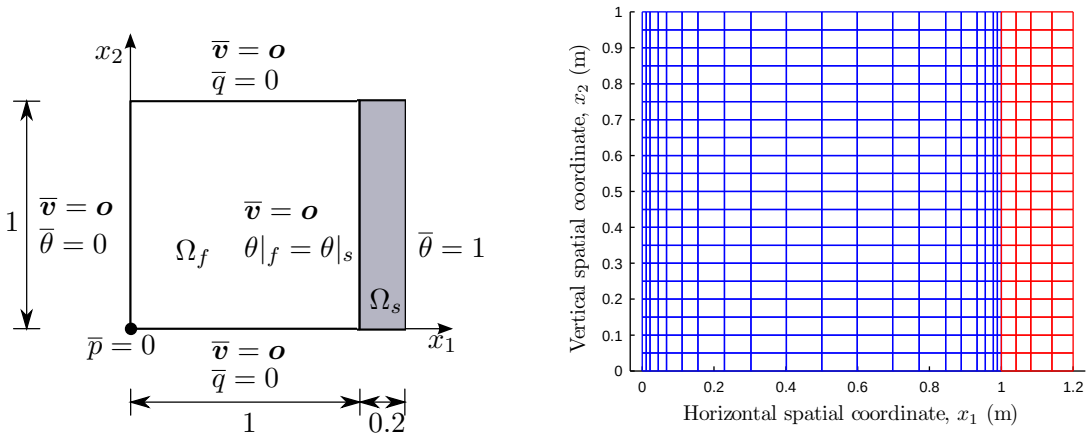

(a) Geometrical configuration.

(b) Mesh.

Figure 5.2: Cavity-wall problem.

top and bottom walls of the cavity are insulated, while the left wall and the exterior face of the right wall are isothermal.

The problem is solved using a nonuniform mesh of 20×20 and 20×5 $Q2Q1$ elements in the cavity and on the wall, respectively (figure 5.2b). The Prandtl number is set as $Pr = 0.7$ (the kinematic viscosity is equal to 0.7 m^2/s and the thermal conductivity, the density and the specific heat capacity in the fluid are set as unity). The vertical component of the gravity acceleration is considered equal to (-10) $\mathrm{m/s}^2$.

Three nonlinear finite element semi-implicit transient analyses are carried out until attaining the steady state solution. The total time is set as 200 seconds and the time step is 10 seconds. The initial temperature and velocity are set as zero, as well as their derivatives with respect to time.

The analyses performed are function of the Rayleigh number, Ra, and of the ratio between the thermal conductivities of the wall and of the fluid ($k_r = k_w/k_f$):

- In order to compare the numerical results with those reported in Kaminski and Prakash (1986) and Belazizia *et al.* (2012), a first simulation was carried out with $Ra = 7 \cdot 10^4$ (the thermal expansion coefficient is equal to 4900) and $k_r = \infty$, *i.e.*, with the conductivity of the wall being much higher than that of the fluid. The thermal conductivity of the wall is set as 10^8, while the specific heat capacity and the density of the solid are equal to 1.

- To evaluate if the code developed is capable of simulating the effect of the wall conductivity in the natural convection, a value of $Ra = 10^5$ (the thermal expansion coefficient is equal to 7000) was set and two analyses were carried out with $k_r = 0.1$ (the thermal conductivity of the wall is set as 0.1) and $k_r = 1$ (the thermal conductivity of the solid is equal to 1). The specific heat capacity and the density of the solid are, once more, equal to 1. The results were compared with those presented by Belazizia *et al.* (2012).

Figure 5.3 shows the temperature field and the streamlines obtained when $Ra = 7 \cdot 10^4$ and $k_r = \infty$. Once more, a good agreement is observed when results are compared with those of Kaminski and Prakash (1986).

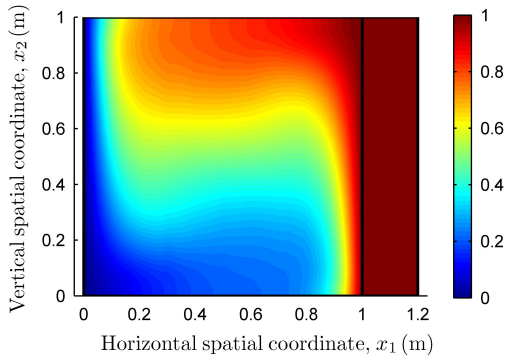

(a) Temperature field.

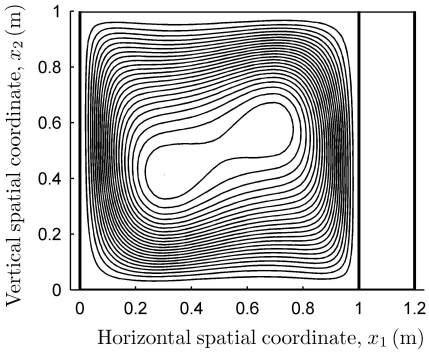

(b) Streamlines.

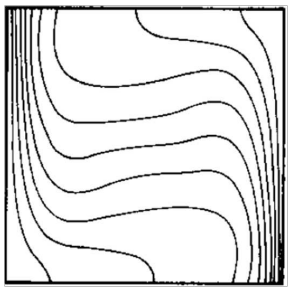

(c) Temperature field (Kaminski and Prakash, 1986).

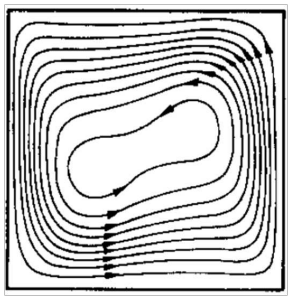

(d) Streamlines (Kaminski and Prakash, 1986).

Figure 5.3: Graphical results of the problem when $Ra = 7 \cdot 10^4$ and $k_r = \infty$.

It can be observed that $k_r = \infty$ implies that k_w is much higher than k_f and, thus, this case provides the same results of the cavity without wall and a right side with prescribed temperature (this example was also analysed in section 4.11.6 setting different prescribed temperatures in the vertical walls).

Figures 5.4 and 5.5 depict the numerical results obtained in terms of temperature and streamlines when $Ra = 10^5$ and the relative conductivity equal to $k_r = 0.1$ and $k_r = 1$. Good agreement between the presented results and the corresponding numerical results reported in the literature can be observed.

The results depicted in figures 5.4 and 5.5 illustrate the effect of the wall conductivity in the natural convection. It can be observed that for the same Rayleigh number ($Ra = 10^5$), the temperatures in the fluid are lower for reduced values of k_r. In fact, a reduced k_r implies reduced thermal conductivity of the solid and, in this case, the wall acts as an insulation. Consequently, the temperature difference between the interior face of the wall and the cold boundary (left side of the cavity) is lower.

5.4.3 Effect of the radiation on a conjugate problem

A square cavity with two finite thickness walls in the horizontal faces is considered. The length of the cavity is 1 m and the thickness of the walls is set as 0.1 m. The vertical walls of the cavity are maintained at constant temperature equal to $-0.5\,^{\circ}\mathrm{C}$ on the right

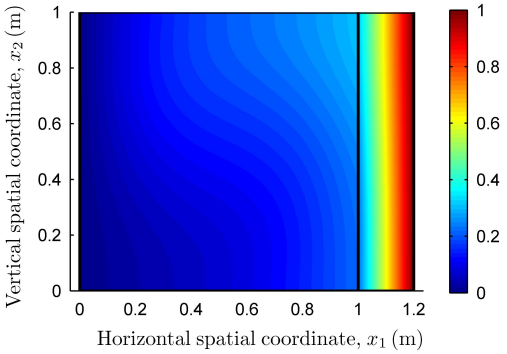

(a) Temperature field.

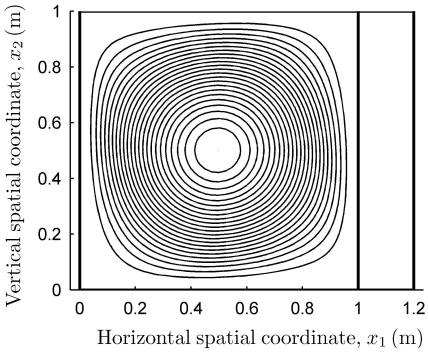

(b) Streamlines.

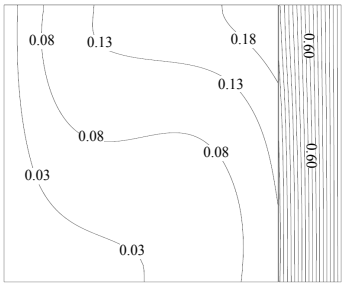

(c) Temperature field (Belazizia *et al.*, 2012).

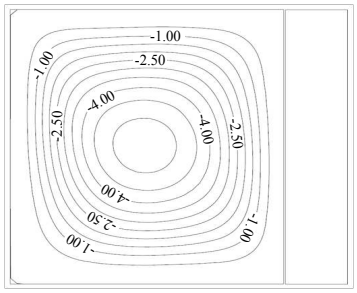

(d) Streamlines (Belazizia *et al.*, 2012).

Figure 5.4: Graphical results of the problem when $Ra = 10^5$ and $k_r = 0.1$.

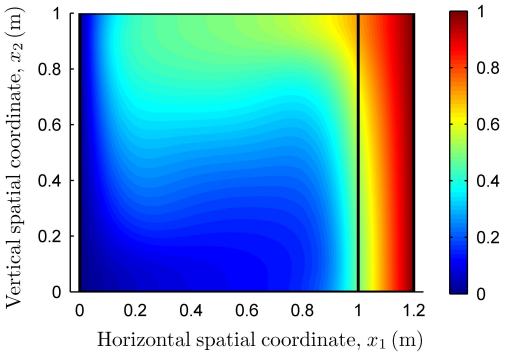

(a) Temperature field.

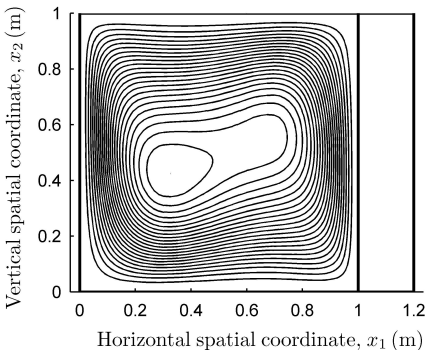

(b) Streamlines.

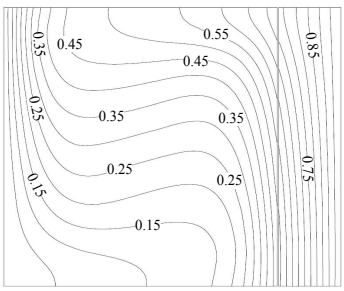

(c) Temperature field (Belazizia *et al.*, 2012).

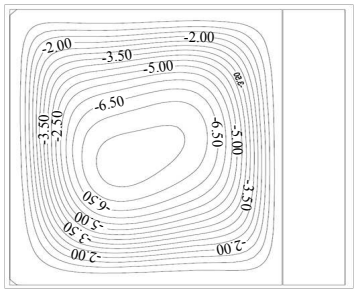

(d) Streamlines (Belazizia *et al.*, 2012).

Figure 5.5: Graphical results of the problem when $Ra = 10^5$ and $k_r = 1.0$.

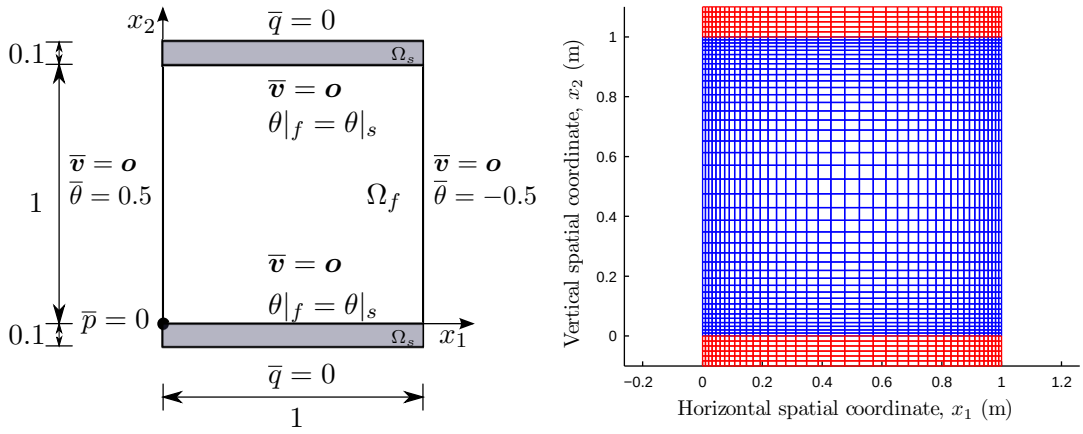

(a) Schematic view of the square cavity.

(b) Mesh.

Figure 5.6: Square cavity with finite thickness horizontal walls.

face and 0.5 °C on the left face. Figure 5.6a illustrates the geometry of the problem and the boundary conditions. The enclosure is fullfilled by air ($Pr = 0.71$) and the laminar heat transfer is computed for $Ra = 10^6$ and $Ra = 10^7$. The vertical component of the gravity is set as (-10) m/s^2. In all the cases studied, the density, the heat specific capacity and the thermal conductivity of the fluid are set as unity, the kinematic viscosity is equal to 0.71 m^2/s and the density and the specific heat capacity of the solid are both set as unity.

Regarding the walls, different boundary conditions are considered, namely the following:

- In order to compare the effect of the wall conduction in the natural convection, different relative thermal conductivities, k_r, are adopted. The dimensionless k_r value is computed as the ratio between the thermal conductivity of the wall and that of the fluid ($k_r = k_w/k_f$) and, in the present example, two values are considered: (i) $k_r = 0.0$ (thermal conductivity of the solid equal to 10^{-6}) and (ii) $k_r = 1.0$ (thermal conductivity of the solid equal to 1). In both cases, the external faces of the horizontal walls are insulated. The Rayleigh number is fixed to $Ra = 10^6$ (thermal expansion coefficient equal to 71000).

- To evaluate the effect of the Rayleigh number in the natural convection, a problem with $Ra = 10^7$ (thermal expansion coefficient equal to 710000) and $k_r = 0.0$ (thermal conductivity of the solid equal to 10^{-6}) is also computed. The external faces of the horizontal walls are insulated.

- To assess the influence of the radiative heat flux in the natural convection, a problem where the walls are considered gray and diffusive and, consequently, emit heat radiation is considered. The external faces of the wall are modelled as adiabatic and the thermal conductivity of the wall is set large enough to obtain one dimensional heat transfer on the walls ($k_r = \infty$, the thermal conductivity of the walls is set as 10^6). The same example is computed without considering the radiative heat exchange and, in both cases, the Rayleigh number of the problems is set as $Ra = 10^6$ (thermal ex-

Ra	k_r	No radiation	Radiation
10^6	0.0	0.1	—
	1.0	0.01	—
	∞	0.001	0.001
10^7	0.0	0.001	—

Table 5.1: Time steps used in each analysis.

pansion coefficient equal to 71000) and, when radiative heat flux exists, the emissivity is equal to 0.5 and the Stefan–Boltzmann's constant is $\sigma = 5.669 \cdot 10^{-8}$ W/(m^2 K^4).

Furthermore, in all the examples, the no-slip condition is prescribed (null velocity) in all the cavity walls.

A non-uniform mesh with 40×40 $Q2Q1$ elements is used to discretizate the fluid area, while a mesh of 5×40 mesh with $Q2Q1$ elements is used at each wall. This mesh refinement is based on the meshes used in the reference papers and is considered sufficient to model accurately the heat transfer and to obtain numerical results where the spatial discretization error can be neglected. Figure 5.6b illustrates the mesh employed.

Nonlinear transient analyses are carried out using the Euler backward scheme until the steady state regime is reached. The initial temperature and velocity are set as zero, as well as their derivatives with respect to time. The time steps used depend on the problem and are reported in table 5.1. It is possible to conclude that shorter time steps are required when more complex problems are analysed.

Figure 5.7 illustrates the isotherms for $k_r = 0.0$ and $k_r = 1.0$ when $Ra = 10^6$. It can be observed that when $k_r = 1.0$ the temperature distribution on the walls is two-dimensional, and since there is heat transfer between the wall and the fluid, the temperatures in the fluid are lower compared to the case in which $k_r = 0.0$.

In order to solve the problem with $Ra = 10^6$ and $k_r = 1.0$ using a constant time step of 0.01 s until a final time of 5 s, a total of 500 computational steps are required. This calculation is extremely time consuming and also requires huge memory capacities as the results have to be stored for all the computational times and all the degrees of freedom. In order to reduce the CPU time, this problem was also solved using the adaptive time stepping algorithm presented in section 5.3.3. Figure 5.8 shows the evolution of the adimensional norm of the residual vector for the first ten time steps. It can be observed that no convergence is attained for the two first time steps, while for the remaining convergence is obtained. Table 5.2 summarizes the time steps employed in the first ten calculations. The desired number of iterations is set as 5 and the solution of the problem at 5 s is calculated in 32 steps, instead of the previous 500.

Figure 5.9 shows the steady state solution of the natural convection problem when $Ra = 10^7$. Comparing figures 5.7a and 5.9a, it can be observed that high Rayleigh numbers lead to more uniform temperatures in the cavity by maintaining the temperature of the upper and lower walls almost constant.

The comparison of the previous results with the reference solutions attests the good accuracy of the code developed in this thesis.

Figure 5.10 depicts the temperature contour in the fluid cavity when there is no radiative heat flux (figure 5.10a) and when radiation is involved (figure 5.10b). In both figures the isotherms on the walls are linear and, consequently, the heat transfer can be considered

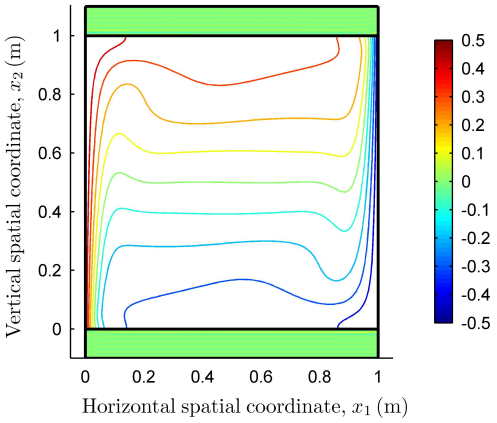

(a) $k_r = 0.0$

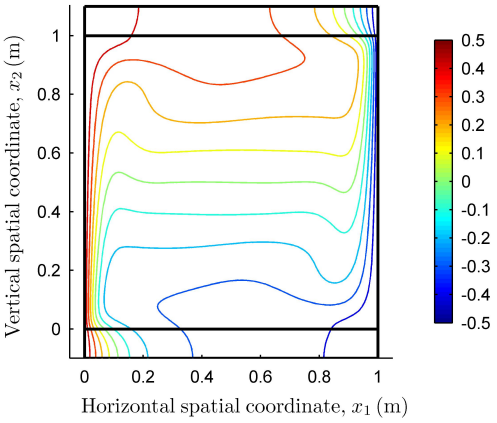

(b) $k_r = 1.0$

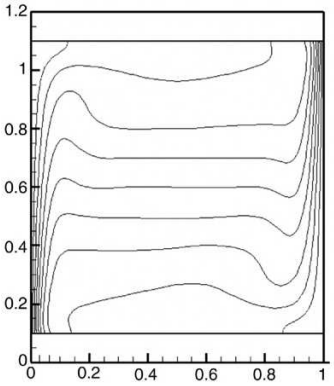

(c) $k_r = 0.0$ (Mobedi, 2008).

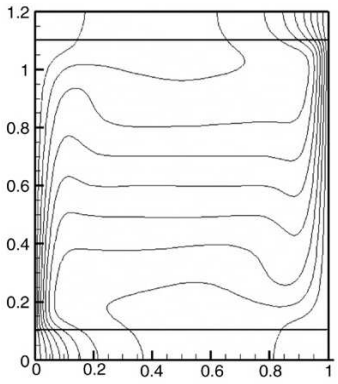

(d) $k_r = 1.0$ (Mobedi, 2008).

Figure 5.7: Temperature fields computed when $Ra = 10^6$.

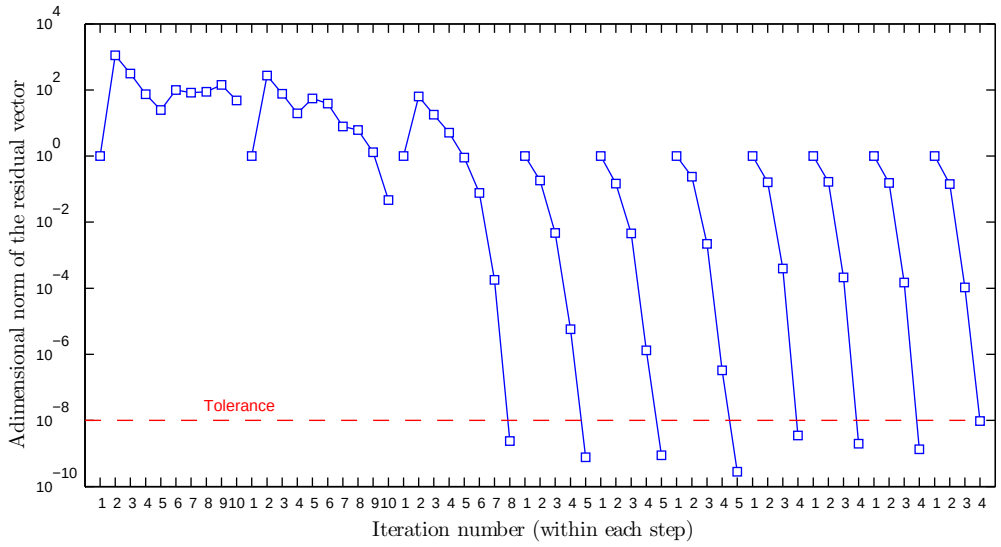

Figure 5.8: Convergence at the first ten time steps when $Ra = 10^6$ and $k_r = 1.0$.

Time step	Δt	
1	0.02500	no convergence is attained
2	0.01250	no convergence is attained
3	0.00625	
4	0.00494	
5	0.00494	
6	0.00494	
7	0.00494	
8	0.00552	
9	0.00618	
10	0.00691	

Table 5.2: Time steps used in the first ten time steps when $Ra = 10^6$ and $k_r = 1.0$.

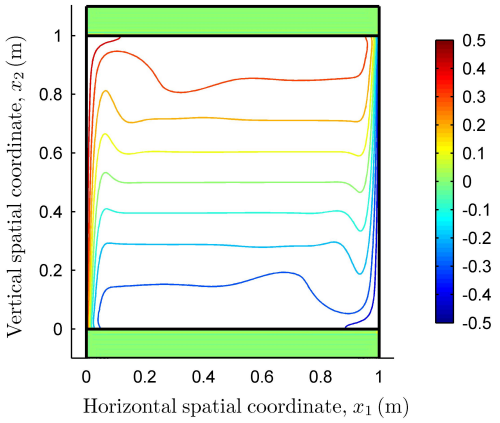

(a) $k_r = 0.0$

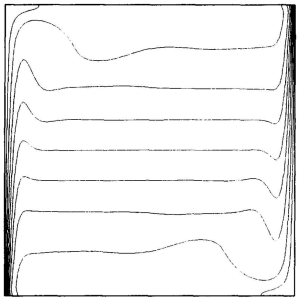

(b) $k_r = 0.0$ (Le Quéré, 1991).

Figure 5.9: Isotherms when $Ra = 10^7$.

as one-dimensional. This result is contrary to that observed in figure 5.7b where the heat conduction on the walls is two-dimensional. Similar conclusions are reported in Mobedi (2008). Moreover, it can be observed that the radiative heat flux between the walls causes a reduction of the temperature distribution along the vicinity of the upper and lower walls.

Figure 5.11 illustrates the vertical and horizontal components of the velocity vector and the temperature along the vertical line $x_1 = 0.5$ m. The numerical results are compared with those obtained using the commercial software ADINA-F (2010) and again a good agreement can be noticed. In figure 5.11c it can be observed once more that the radiation causes a reduction of the temperatures in the fluid.

5.5 Concluding remarks

A compact FE formulation developed in order to solve conjugate problems with presence of heat transfer exchange between faces is presented. An adaptive time stepping scheme is also introduced.

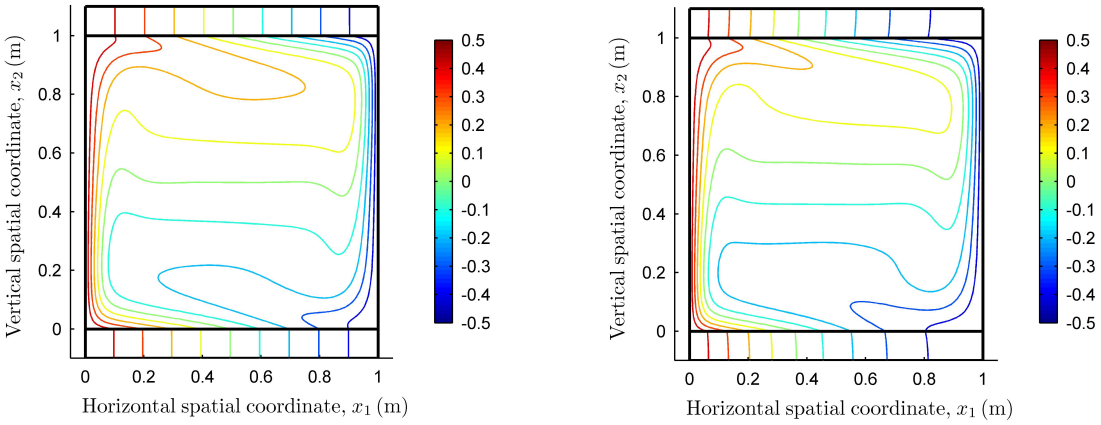

(a) $\epsilon = 0.0$ (b) $\epsilon = 0.5$

Figure 5.10: Temperature fields computed when $k_r = \infty$ and $Ra = 10^6$.

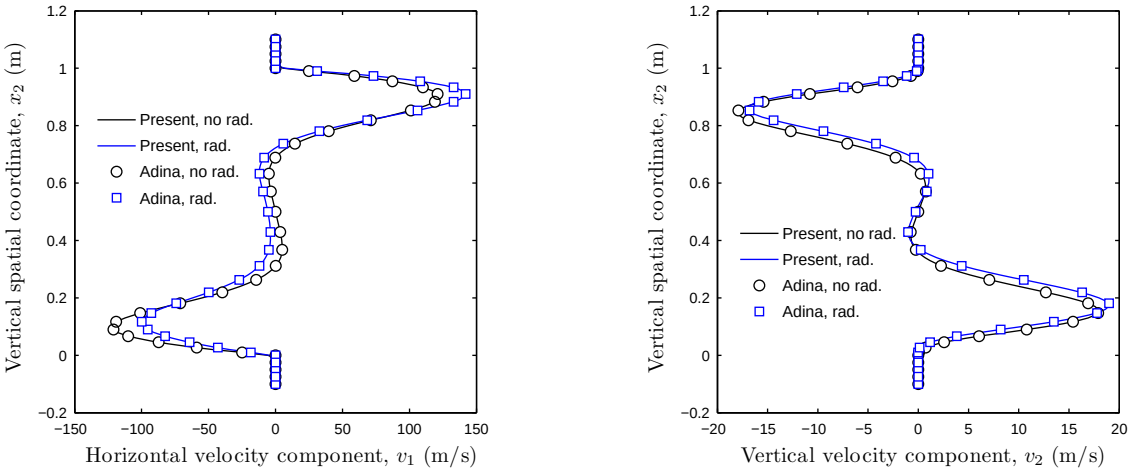

(a) Horizontal velocity distribution.

(b) Vertical velocity distribution.

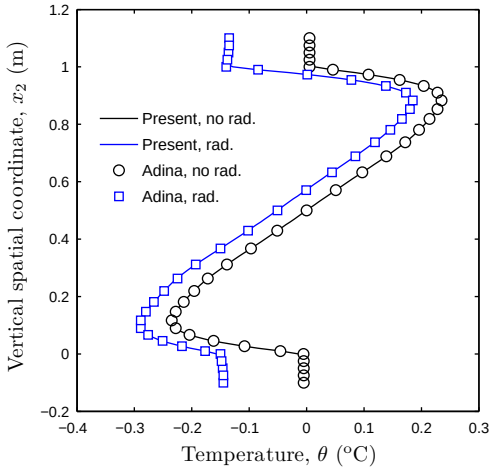

(c) Temperature distribution.

Figure 5.11: Velocity and temperature distribution along the line $x_1 = 0.5$ m.

The code developed is used to solve, firstly, a benchmark problem consisting of the heat transfer in an air-filled square cavity with thick and conductive vertical walls and, secondly, a problem where there is radiative heat exchange between the cavity walls. A study about the influence of the radiative heat flux in the natural convection is presented, allowing to conclude that the radiative heat exchange between the faces of a solid influences the temperature distribution in the solid and the fluid. In both examples, non-uniform meshes more refined in the vicinity of the walls (interface between the solid and the fluid) are employed in order to reproduce accurately the velocity field (high velocity gradient in the vicinity of the wall).

In both cases, the developed code is capable of reproducing accurate solutions, attested by the good agreement with the results reported in the literature or obtained by using the commercial FE software ADINA-F (2010).

Chapter 6

Thermomechanical finite element model

6.1 Introduction

A *beam* is a one-dimensional continuum used to represent three-dimensional bodies with one dimension significantly larger than the other two. The classical beam theories (Euler–Bernoulli theory or Timoshenko theory) have application in several engineering areas, as for example, civil, mechanical and aero-space engineering. Currently, the complexity of some of the mechanical phenomena to simulate makes it necessary to develop exact and nonlinear beam theories that allow to compute the displacements, strains and stresses with more precision. The interested reader can consult the evolution of the beam theories in Timoshenko (1953).

The derivation of a beam theory was traditionally based on some simplifying static and kinematic hypotheses. While the former introduces constraints on the stress distribution, the latter imposes artificial constraints on the continuum motion of the model and, thus, into the deformation process.

Originally, Reissner (1972) proposed a geometrically exact beam theory in the two-dimensional space. The scientific community recovered the interest in this work due to its posterior generalization made, again, by Reissner (1981), where a three-dimensional model capable of dealing with arbitrary large displacements and deformations and moderate rotations was presented. However, this model was only approximate, based on a simplification of the rotation matrix (which is nontrivial in the three-dimensional space due to the non commutative character of the rotations).

The work of Simo (1985) presented the first compact 3D geometrically exact beam theory based on the rotation tensor. Subsequently, Simo and Vu-Quoc (1986) presented the weak form of the governing equations of the problem in the context of the finite element formulation.

In the current chapter, a geometrically exact beam theory using the Reissner–Simo kinematic assumptions is presented. The advantage of the geometrically exact beam theories, with respect to other nonlinear theories, is that all the geometrical effects are taken into account and, therefore, no restrictions on the magnitude of the displacements and rotations are imposed *a priori*. However, a kinematical hypothesis is introduced: the plane sections remain plane after the deformation, which is inherited from the Timoshenko beam theory.

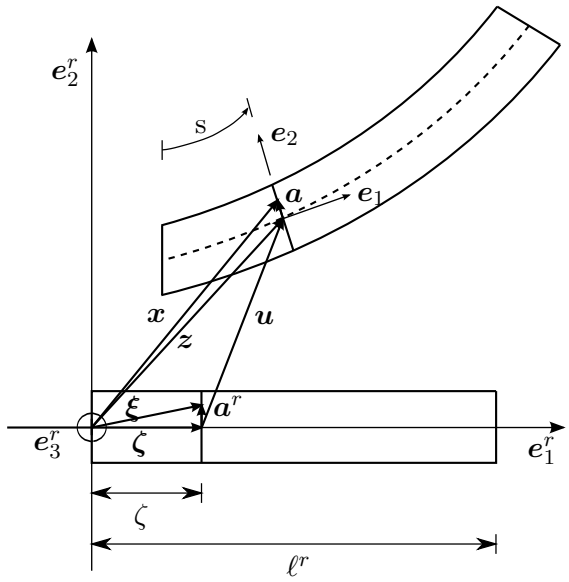

Figure 6.1: Reference and deformed configuration of a straight rod.

In the present chapter a plane formulation of this theory is exposed following the works of Zienkiewicz and Taylor (2005, chapter 17, page 517), Wriggers (2008, chapter 9, page 325) and Tiago (2007, chapter 6, from page 169 to 210). Section 6.2 reports the geometrically exact beam theory, including the weak form of the problem and its perturbation. Section 6.3 presents the finite element formulation where the elemental and global residual vector and tangent matrix are obtained. Finally, section 6.4 illustrates a set of applications of the code developed.

6.2 Geometrically exact beam theory formulation

6.2.1 The rod model

Consider a rod where the reference or undeformed configuration is defined in the orthonormal base vectors coordinate system, denoted by the superscript r, *i.e.*, $\boldsymbol{e}_i^r$.

Attending to figure 6.1, the position of any point of the cross section can be defined as,

$$\boldsymbol{\xi} = \boldsymbol{\zeta} + \boldsymbol{a}^r \tag{6.1}$$

and

$$\boldsymbol{\zeta} = \zeta\, \boldsymbol{e}_1^r \tag{6.2a}$$
$$\boldsymbol{a}^r = \xi\, \boldsymbol{e}_2^r \tag{6.2b}$$

where $\boldsymbol{\zeta}$ describes the position of the points situated in the axis bar, ζ is the arc-length parameter, $\boldsymbol{a}^r$ represents the relative position with respect to the axis of a point located in an arbitrary cross section and ξ is the perpendicular distance between the point and the bar axis.

6.2.2 Kinematics

Displacement field

The deformed position is defined in the coordinate system denoted as $\boldsymbol{e}_i$, where the vector $\boldsymbol{e}_1$, in general, is not tangent to the beam axis on the deformed configuration and $\boldsymbol{e}_2$ fits with the cross section position. The position of any point laid on the rod axis is given by,

$$\boldsymbol{z} = \boldsymbol{\zeta} + \boldsymbol{u} \tag{6.3}$$

where $\boldsymbol{u} = \boldsymbol{u}(\zeta)$ is the displacement vector of the points lying on the beam axis. The position of any point of the cross section after the deformation, $\boldsymbol{x} = \boldsymbol{x}(\xi)$, can be expressed as,

$$\boldsymbol{x} = \boldsymbol{z} + \boldsymbol{a} \tag{6.4}$$

where $\boldsymbol{a}$ describes the position of the points of the cross section given by:

$$\boldsymbol{a} = \xi\, \boldsymbol{e}_2 \tag{6.5}$$

Hence, replacing (6.3) in (6.4), one obtains:

$$\boldsymbol{x} = \boldsymbol{\zeta} + \boldsymbol{u} + \boldsymbol{a} \tag{6.6}$$

The assumed kinematical hypothesis is that the sections remain plane after the deformation, *i.e.*, after the application of the loading and imposed displacements. Thus, the vector $\boldsymbol{a}$ can be expressed by,

$$\boldsymbol{a} = \boldsymbol{Q}\, \boldsymbol{a}^r \tag{6.7}$$

where $\boldsymbol{Q} = \boldsymbol{Q}(\theta)$ is the rotation tensor, which can be calculated as follows:

$$[\boldsymbol{Q}] = \begin{bmatrix} \cos\theta & -\sin\theta & 0 \\ \sin\theta & \cos\theta & 0 \\ 0 & 0 & 1 \end{bmatrix} \tag{6.8}$$

Replacing (6.2b) into (6.7) and using the resulting expression in (6.6), it is obtained,

$$\boldsymbol{x} = \boldsymbol{\zeta} + \boldsymbol{u} + \xi\, \boldsymbol{Q}\, \boldsymbol{e}_2^r \tag{6.9}$$

whose matrix form is:

$$\begin{Bmatrix} x_1 \\ x_2 \\ x_3 \end{Bmatrix} = \begin{Bmatrix} \zeta \\ 0 \\ 0 \end{Bmatrix} + \begin{Bmatrix} u_1 \\ u_2 \\ 0 \end{Bmatrix} + \xi \begin{Bmatrix} -\sin\theta \\ \cos\theta \\ 0 \end{Bmatrix} \tag{6.10}$$

The generalized displacement field of a point laid in the axis bar is defined by,

$$\boldsymbol{d} = \begin{Bmatrix} u_1 \\ u_2 \\ \theta \end{Bmatrix} \tag{6.11}$$

where u_1 and u_2 are the displacements in the direction of the vectors $\boldsymbol{e}_1^r$ and $\boldsymbol{e}_2^r$, respectively, and θ is the rotation of the cross section.

The displacement field at a generic point can be calculated as the difference between the deformed position and the initial or undeformed position:

$$\boldsymbol{\delta} = \boldsymbol{x} - \boldsymbol{\xi} \tag{6.12}$$

Deformation gradient

The deformation gradient is given by:

$$\boldsymbol{F} = \frac{\partial \boldsymbol{x}}{\partial \boldsymbol{\xi}} = \frac{\partial x_i}{\partial \xi_j}\, \boldsymbol{e}_i^r \otimes \boldsymbol{e}_j^r = \frac{\partial \boldsymbol{x}}{\partial \xi_i} \otimes \boldsymbol{e}_i^r = \frac{\partial \boldsymbol{x}}{\partial \zeta} \otimes \boldsymbol{e}_1^r + \frac{\partial \boldsymbol{x}}{\partial \xi} \otimes \boldsymbol{e}_2^r \tag{6.13}$$

The term concerning the variation of the cross section can be written as,

$$\frac{\partial \boldsymbol{x}}{\partial \xi} = \frac{\partial}{\partial \xi}\left(\boldsymbol{\zeta} + \boldsymbol{u} + \boldsymbol{a}\right) = \frac{\partial \boldsymbol{a}}{\partial \xi} = \frac{\partial}{\partial \xi}\left(\xi\, \boldsymbol{e}_2\right) = \boldsymbol{e}_2 \tag{6.14}$$

and the term associated to the variation along the axis can be expressed as,

$$\frac{\partial \boldsymbol{x}}{\partial \zeta} = \frac{\partial}{\partial \zeta}\left(\boldsymbol{\zeta} + \boldsymbol{u} + \boldsymbol{a}\right) = \boldsymbol{e}_1^r + \boldsymbol{u}' + \frac{\partial}{\partial \zeta}\left(\boldsymbol{Q}\, \boldsymbol{a}^r\right) = \underbrace{\boldsymbol{e}_1^r + \boldsymbol{u}'}_{\boldsymbol{z}'} + \underbrace{\boldsymbol{Q}'\, \boldsymbol{Q}^T}_{\boldsymbol{K}}\, \boldsymbol{a} \tag{6.15}$$

where the notation for derivatives $(\cdot)' = \partial(\cdot)/\partial\zeta$ was employed and the tensor $\boldsymbol{K}$ was introduced:

$$\boldsymbol{K} = \boldsymbol{Q}'\boldsymbol{Q}^T = \begin{bmatrix} 0 & -1 & 0 \\ 1 & 0 & 0 \\ 0 & 0 & 0 \end{bmatrix} \theta' \tag{6.16}$$

The curvature can be computed as,

$$\boldsymbol{\kappa} = \text{axial}\left(\boldsymbol{K}\right) = \theta'\, \boldsymbol{e}_3^r \tag{6.17}$$

where $\boldsymbol{\kappa}$ is the vector associated with the skew-symmetric[1] tensor $\boldsymbol{K}$.

Hence, the gradient of the transformation can be written as,

$$\begin{aligned} \boldsymbol{F} = \left(\boldsymbol{e}_1^r + \boldsymbol{u}' + \boldsymbol{\kappa} \times \boldsymbol{a}\right) \otimes \boldsymbol{e}_1^r + \boldsymbol{e}_2 \otimes \boldsymbol{e}_2^r = \\ = \boldsymbol{Q}\, \boldsymbol{e}_2^r \otimes \boldsymbol{e}_2^r + \left(\boldsymbol{z}' - \boldsymbol{e}_1 + \boldsymbol{e}_1 + \boldsymbol{\kappa} \times \boldsymbol{a}\right) \otimes \boldsymbol{e}_1^r = \\ = \boldsymbol{Q}\, \left(\boldsymbol{e}_1^r \otimes \boldsymbol{e}_1^r + \boldsymbol{e}_2^r \otimes \boldsymbol{e}_2^r\right) + \left(\underbrace{\boldsymbol{z}' - \boldsymbol{e}_1}_{\boldsymbol{\eta}} + \boldsymbol{\kappa} \times \boldsymbol{a}\right) \otimes \boldsymbol{e}_1^r = \\ = \boldsymbol{Q}\, \left(\boldsymbol{e}_\alpha^r \otimes \boldsymbol{e}_\alpha^r\right) + \left(\underbrace{\boldsymbol{\eta} + \boldsymbol{\kappa} \times \boldsymbol{a}}_{\boldsymbol{\gamma}}\right) \otimes \boldsymbol{e}_1^r \end{aligned} \tag{6.19}$$

where $\boldsymbol{\eta}$ is the deformation vector in the $\boldsymbol{e}_1$ and $\boldsymbol{e}_2$ directions (axial deformation of the beam axis and the average angular distortion of the cross section), and $\boldsymbol{\gamma}$ is the total deformation vector (axial strain and angular distortion).

The deformation gradient in the reference position can be computed as follows,

$$\boldsymbol{F}^r = \boldsymbol{Q}^T\, \boldsymbol{F} = \boldsymbol{Q}^T \boldsymbol{Q}\, \left(\boldsymbol{e}_\alpha^r \otimes \boldsymbol{e}_\alpha^r\right) + \underbrace{\left(\underbrace{\boldsymbol{Q}^T \boldsymbol{\eta}}_{\boldsymbol{\eta}^r} + \underbrace{\left(\boldsymbol{Q}^T \boldsymbol{\kappa}\right)}_{\boldsymbol{\kappa}^r} \times \underbrace{\left(\boldsymbol{Q}^T \boldsymbol{a}\right)}_{\boldsymbol{a}^r}\right)}_{\boldsymbol{\gamma}^r} \otimes \boldsymbol{e}_1^r \tag{6.20}$$

[1] Consider a general vector $\boldsymbol{t}$. Hence, $\boldsymbol{t} = \text{axial}\left(\boldsymbol{T}\right)$, where:

$$[\boldsymbol{T}] = \begin{bmatrix} 0 & -t_3 & t_2 \\ t_3 & 0 & -t_1 \\ -t_2 & t_1 & 0 \end{bmatrix} \tag{6.18}$$

or, in its matrix form:

$$[\boldsymbol{F}^r] = \begin{bmatrix} 1 & 0 & 0 \\ 0 & 1 & 0 \\ 0 & 0 & 0 \end{bmatrix} + \begin{bmatrix} \cos\theta + \cos\theta\, u_1' + \sin\theta\, u_2' - 1 & 0 & 0 \\ -\sin\theta - \sin\theta\, u_1' + \cos\theta\, u_2' & 0 & 0 \\ 0 & 0 & 0 \end{bmatrix} + \xi\,\theta' \begin{bmatrix} -1 & 0 & 0 \\ 0 & 0 & 0 \\ 0 & 0 & 0 \end{bmatrix} \tag{6.21}$$

Then, using the previous expression, the generalized deformations can be computed as,

$$\boldsymbol{\varepsilon}^r = \begin{Bmatrix} \varepsilon \\ \gamma \\ \kappa \end{Bmatrix}^r = \begin{Bmatrix} u_2' \sin\theta + (1 + u_1')\cos\theta - 1 \\ u_2' \cos\theta - (1 + u_1')\sin\theta \\ \theta' \end{Bmatrix} \tag{6.22}$$

where ε, γ and κ are, respectively, the axial deformation, the angular distortion and the curvature of the points laid in the bar axis.

The axial deformation, ϵ, and the angular distortion, $\tilde{\gamma}$, at any point of the cross section can be computed as:

$$\epsilon = \varepsilon - \xi\kappa \tag{6.23a}$$

$$\tilde{\gamma} = \gamma \tag{6.23b}$$

As the angular distortion is constant in all points of the cross section and equal to γ, in the following formulation no distinction between $\tilde{\gamma}$ and γ will be done, in order to simplify the notation.

6.2.3 Statics

Generalized stresses and constitutive relation

The first Piola-Kirchhoff stress tensor, $\boldsymbol{P}$, is written as,

$$\boldsymbol{P} = \boldsymbol{\tau}_i \otimes \boldsymbol{e}_i^r \tag{6.24}$$

where $\boldsymbol{\tau}_i$ is the stress tensor acting in the plane whose perpendicular direction is defined by $\boldsymbol{e}_i^r$ on the reference configuration. The tensor $\boldsymbol{P}$ can be decomposed as a sum of the term regarding the beam axis and those concerning the cross section:

$$\boldsymbol{P} = \boldsymbol{\tau}_1 \otimes \boldsymbol{e}_1^r + \underbrace{\boldsymbol{\tau}_2 \otimes \boldsymbol{e}_2^r + \boldsymbol{\tau}_3 \otimes \boldsymbol{e}_3^r}_{=\boldsymbol{o}} \tag{6.25}$$

The stress resultants in the cross section can be computed as follows:

$$\boldsymbol{n} = \int_{A^r} \boldsymbol{\tau}_1 \,\mathrm{d}A^r \tag{6.26a}$$

$$\boldsymbol{m} = \int_{A^r} \boldsymbol{a} \times \boldsymbol{\tau}_1 \,\mathrm{d}A^r \tag{6.26b}$$

The back-rotated first Piola-Kirchhoff stress tensor is obtained as:

$$\boldsymbol{P}^r = \boldsymbol{Q}^T \boldsymbol{P} \tag{6.27}$$

Hence, the generalized cross section resultants are:

$$\boldsymbol{n}^r = \int_{A^r} \boldsymbol{\tau}_1^r \,\mathrm{d}A^r = \int_{A^r} \sigma \,\mathrm{d}A^r \boldsymbol{e}_1^r + \int_{A^r} \tau \,\mathrm{d}A^r \boldsymbol{e}_2^r \tag{6.28a}$$

$$\boldsymbol{m}^r = \int_{A^r} \boldsymbol{a}^r \times \boldsymbol{\tau}_1^r \,\mathrm{d}A^r = -\int_{A^r} \xi\sigma \,\mathrm{d}A^r \boldsymbol{e}_3^r \tag{6.28b}$$

The back-rotated cross sectional generalized stress resultants, $\boldsymbol{\sigma}^r$, are energetically conjugated with the cross sectional generalized strains, $\boldsymbol{\varepsilon}^r$, and can be written as,

$$\boldsymbol{\sigma}^r = \begin{Bmatrix} N \\ V \\ M \end{Bmatrix}^r = \begin{Bmatrix} \int_{A^r} \sigma \, \mathrm{d}A^r \\ \int_{A^r} \tau \, \mathrm{d}A^r \\ -\int_{A^r} \xi\sigma \, \mathrm{d}A^r \end{Bmatrix} \tag{6.29}$$

where N, V and M are the internal axial force, shear force and moment, respectively, acting in the reference configuration.

The general constitutive relations for the material, which could be nonlinear, can be written as:

$$\sigma = \sigma\left(\epsilon - \epsilon^{\Delta\theta}\right) \tag{6.30a}$$

$$\tau = \tau\left(\gamma\right) \tag{6.30b}$$

where $\epsilon^{\Delta\theta}$ is the axial deformation due to the temperature gradient[2], $\Delta\theta$.

6.2.4 Variational formulation of the problem

Using the results reported in Tiago (2007), the internal virtual work may be written as:

$$\delta W_{int} = \int_\Omega \boldsymbol{P} : \delta\boldsymbol{F} \, \mathrm{d}\Omega = \int_0^{\ell^r} \int_{A^r} \boldsymbol{P} : \delta\boldsymbol{F} \, \mathrm{d}A^r \, \mathrm{d}\xi = \int_0^{\ell^r} \boldsymbol{\sigma}^r \cdot \delta\boldsymbol{\varepsilon}^r \, \mathrm{d}\zeta \tag{6.31}$$

The variation of the cross sectional generalized strains renders,

$$\delta\boldsymbol{\varepsilon}^r = \begin{Bmatrix} \delta\varepsilon \\ \delta\gamma \\ \delta\chi \end{Bmatrix} = \begin{Bmatrix} -\sin\theta\,\delta\theta + \cos\theta\,\delta u_1' - u_1'\,\sin\theta\,\delta\theta + u_2'\,\cos\theta\,\delta\theta + \sin\theta\,\delta u_2' \\ -\cos\theta\,\delta\theta - \sin\theta\,\delta u_1' - u_1'\cos\theta\,\delta\theta - u_2'\,\sin\theta\,\delta\theta + \cos\theta\,\delta u_2' \\ \delta\theta' \end{Bmatrix} \tag{6.32}$$

or, using matricial notation,

$$\delta\boldsymbol{\varepsilon}^r = \boldsymbol{\Psi}\,\boldsymbol{\Delta}\,\delta\boldsymbol{d} \tag{6.33}$$

where

$$\boldsymbol{\Psi} = \begin{bmatrix} \cos\theta & \sin\theta & 0 & -(1+u_1')\sin\theta + u_2'\cos\theta \\ -\sin\theta & \cos\theta & 0 & -(1+u_1')\cos\theta - u_2'\sin\theta \\ 0 & 0 & 1 & 0 \end{bmatrix} \tag{6.34a}$$

$$\boldsymbol{\Delta} = \begin{bmatrix} \frac{\partial}{\partial\zeta} & 0 & 0 \\ 0 & \frac{\partial}{\partial\zeta} & 0 \\ 0 & 0 & \frac{\partial}{\partial\zeta} \\ 0 & 0 & 1 \end{bmatrix} \tag{6.34b}$$

$$\delta\boldsymbol{d} = \begin{Bmatrix} \delta u_1 \\ \delta u_2 \\ \delta\theta \end{Bmatrix} \tag{6.34c}$$

Hence, replacing (6.33) into (6.31), one obtains,

$$\delta W_{int} = \int_0^{\ell^r} \boldsymbol{\sigma}^r \cdot \delta\boldsymbol{\varepsilon}^r \, \mathrm{d}\zeta = \int_0^{\ell^r} \left(\boldsymbol{\Delta}\,\delta\boldsymbol{d}\right)^T \boldsymbol{\Psi}^T\boldsymbol{\sigma}^r \, \mathrm{d}\zeta \tag{6.35}$$

[2]There is a notation conflict, as $\Delta\theta$ is used to represent the temperature variation and, also, the incremental rotation. The correct meaning of this variable should be interpreted from the context.

where $\boldsymbol{\sigma}^r = \boldsymbol{\sigma}^r(\boldsymbol{\varepsilon}^r)$.

The external virtual work is,

$$\delta W_{ext} = \int_0^{\ell^r} \delta \boldsymbol{d}^T (\lambda \boldsymbol{f}) \, \mathrm{d}\zeta \tag{6.36}$$

where λ is a load parameter and $\boldsymbol{f}$ is the load vector whose components are the prescribed distributed loads along the $\boldsymbol{e}_1^r$ direction, the $\boldsymbol{e}_2^r$ direction and the distributed moment:

$$\boldsymbol{f} = \begin{Bmatrix} \overline{p}_1 \\ \overline{p}_2 \\ \overline{m} \end{Bmatrix} \tag{6.37}$$

The weak form of the equilibrium of the rod is calculated using the virtual work principle,

$$\delta W \equiv \delta W_{int} - \delta W_{ext} = 0 \quad \forall \delta \boldsymbol{d} \tag{6.38}$$

where $\delta \boldsymbol{d}$ is the variation of the generalized displacements field.

Equilibrium equations in the domain

The governing equation can be derived from the weak form (6.38), which can be expressed as:

$$\int_0^{\ell^r} (\boldsymbol{n}^r \cdot \delta \boldsymbol{\eta}^r + \boldsymbol{m}^r \cdot \delta \boldsymbol{\kappa}^r) \, \mathrm{d}\zeta - \int_0^{\ell^r} (\lambda \boldsymbol{f}) \cdot \delta \boldsymbol{d} \, \mathrm{d}\zeta = 0 \tag{6.39}$$

Rewriting the expression (6.32) as,

$$\delta \boldsymbol{\eta}^r = \boldsymbol{Q}^T \delta \boldsymbol{u}' + \begin{Bmatrix} -(1+u_1')\sin\theta + u_2'\cos\theta \\ -(1+u_1')\cos\theta - u_2'\sin\theta \\ 0 \end{Bmatrix} \delta\theta \tag{6.40a}$$

$$\delta \boldsymbol{\kappa}^r = \delta\theta' \boldsymbol{e}_3^r \tag{6.40b}$$

replacing the result into (6.39) and integrating by parts on $\delta \boldsymbol{u}'$ and $\delta\theta'$, the equilibrium equations in the domain are given by,

$$\boldsymbol{n}' + \lambda \overline{\boldsymbol{n}} = \boldsymbol{o} \quad \forall \delta \boldsymbol{u} \tag{6.41a}$$

$$\boldsymbol{m}' + \boldsymbol{z}' \times \boldsymbol{n} + \lambda \overline{\boldsymbol{m}} = \boldsymbol{o} \quad \forall \delta \boldsymbol{\theta} \tag{6.41b}$$

where, for the plane case:

$$\boldsymbol{n} = N \boldsymbol{e}_1 + V \boldsymbol{e}_2 = N \boldsymbol{Q} \boldsymbol{e}_1^r + V \boldsymbol{Q} \boldsymbol{e}_2^r \tag{6.42a}$$

$$\boldsymbol{n}' = \partial(\boldsymbol{n})/\partial\zeta \tag{6.42b}$$

$$\overline{\boldsymbol{n}} = \lambda \overline{p}_1 \boldsymbol{e}_1^r + \lambda \overline{p}_2 \boldsymbol{e}_2^r \tag{6.42c}$$

$$\boldsymbol{m} = M \boldsymbol{e}_3 = M \boldsymbol{Q} \boldsymbol{e}_3^r \tag{6.42d}$$

$$\boldsymbol{m}' = \partial(\boldsymbol{m})/\partial\zeta \tag{6.42e}$$

$$\boldsymbol{z}' = \boldsymbol{e}_1^r + \boldsymbol{u}' \tag{6.42f}$$

$$\overline{\boldsymbol{m}} = \lambda \overline{m} \boldsymbol{e}_3^r \tag{6.42g}$$

Replacing the expressions (6.42) into (6.41), the equilibrium equations of the plane case are obtained and render:

$$(N\,\cos\theta - V\,\sin\theta)' + \lambda\,\overline{p}_1 = 0 \tag{6.43a}$$
$$(N\,\sin\theta + V\,\cos\theta)' + \lambda\,\overline{p}_2 = 0 \tag{6.43b}$$
$$M' + (1+u_1')\,(N\,\sin\theta + V\,\cos\theta) - u_2'\,(N\,\cos\theta - V\,\sin\theta) + \lambda\,\overline{m} = 0 \tag{6.43c}$$

The previous equilibrium equations can be obtained considering the equilibrium in the deformed configuration, as carried out in Reissner (1972).

Boundary conditions

Boundary conditions are required to solve the governing equations in the domain. If Ω is the domain of the solution (length of the beam) and Γ is the boundary contour (extreme points of the beam), the following types of boundary conditions can be defined:

- Static condition: prescribed forces ($\overline{F}_1$ and $\overline{F}_2$) and moment ($\overline{M}$) on the boundary Γ_t,

$$n\,(N\cos\theta - V\sin\theta) - \lambda\,\overline{F}_1 = 0 \tag{6.44}$$
$$n\,(N\sin\theta + V\cos\theta) - \lambda\,\overline{F}_2 = 0 \tag{6.45}$$
$$n\,M - \lambda\,\overline{M} = 0 \tag{6.46}$$

  where n is the outward normal to the cross-section of the beam, that takes the values $(+1)$ or (-1).

- Kinematic condition: prescribed displacements ($\overline{u}_1$ and $\overline{u}_2$) and rotation ($\overline{\theta}$) on the boundary Γ_d,

$$u_1 = \lambda\,\overline{u}_1 \tag{6.47}$$
$$u_2 = \lambda\,\overline{u}_2 \tag{6.48}$$
$$\theta = \lambda\,\overline{\theta} \tag{6.49}$$

In the current problem, the boundary is expressed as $\Gamma = \Gamma_t \cup \Gamma_d$ such that $\Gamma_t \cap \Gamma_d = \emptyset$.

6.2.5 Linearization of the weak form

Internal virtual work

The incremental perturbation of the internal virtual work is given by:

$$\Delta\delta W_{int} = \int_0^{\ell^r} \Delta\boldsymbol{\sigma}^r \cdot \delta\boldsymbol{\varepsilon}^r \,\mathrm{d}\zeta + \int_0^{\ell^r} \boldsymbol{\sigma}^r \cdot \Delta\delta\boldsymbol{\varepsilon}^r \,\mathrm{d}\zeta \tag{6.50}$$

The first term contains the generalized material stiffness and the second term includes a generalized geometric stiffness.

Developing the integrands, one obtains,

$$\Delta\boldsymbol{\sigma}^r \cdot \delta\boldsymbol{\varepsilon}^r = (\boldsymbol{D}\,\Delta\boldsymbol{\varepsilon}^r) \cdot \delta\boldsymbol{\varepsilon}^r \tag{6.51a}$$
$$\boldsymbol{\sigma}^r \cdot \Delta\delta\boldsymbol{\varepsilon}^r = N\,\Delta\delta\varepsilon + V\,\Delta\delta\gamma + M\,\Delta\delta\chi \tag{6.51b}$$

where the perturbations of the generalized strains are explicitly given by,

$$\Delta\delta\varepsilon = \delta u_1' \left(-\sin\theta\right)\Delta\theta + \left(1+u_1'\right)\left(-\cos\theta\right)\delta\theta\Delta\theta + \Delta u_1' \left(-\sin\theta\right)\delta\theta + \\ + \delta u_2' \cos\theta\,\Delta\theta + \Delta u_2' \cos\theta\,\delta\theta + u_2' \left(-\sin\theta\right)\delta\theta\Delta\theta \tag{6.52a}$$

$$\Delta\delta\gamma = \delta u_2' \left(-\sin\theta\right)\Delta\theta + \Delta u_2' \left(-\sin\theta\right)\delta\theta + u_2' \left(-\cos\theta\right)\delta\theta\Delta\theta - \\ - \delta u_1' \cos\theta\,\Delta\theta - \Delta u_1' \cos\theta\,\delta\theta - \left(1+u_1'\right)\left(-\sin\theta\right)\delta\theta\Delta\theta \tag{6.52b}$$

$$\Delta\delta\kappa = \Delta\left(\delta\theta'\right) = 0 \tag{6.52c}$$

and the constitutive matrix, $\boldsymbol{D}$, can be computed as:

$$\boldsymbol{D} = \frac{\partial \boldsymbol{\sigma}^r}{\partial \boldsymbol{\varepsilon}^r} \Leftrightarrow \boldsymbol{D} = \begin{bmatrix} \frac{\partial N}{\partial \varepsilon} & \frac{\partial N}{\partial \gamma} & \frac{\partial N}{\partial \kappa} \\ \frac{\partial V}{\partial \varepsilon} & \frac{\partial V}{\partial \gamma} & \frac{\partial V}{\partial \kappa} \\ \frac{\partial M}{\partial \varepsilon} & \frac{\partial M}{\partial \gamma} & \frac{\partial M}{\partial \kappa} \end{bmatrix} \tag{6.53}$$

Each coefficient of the matrix $\boldsymbol{D}$ defined in the expression (6.53) can be developed as:

$$\frac{\partial N}{\partial \varepsilon} = \int_{A^r} \frac{\partial \sigma\left(\epsilon-\epsilon^{\Delta\theta}\right)}{\partial \varepsilon}\,\mathrm{d}A^r = \int_{A^r} \frac{\partial \sigma\left(\epsilon-\epsilon^{\Delta\theta}\right)}{\partial\left(\epsilon-\epsilon^{\Delta\theta}\right)} \frac{\partial\left(\epsilon-\epsilon^{\Delta\theta}\right)}{\partial \varepsilon}\,\mathrm{d}A^r = \\ = \int_{A^r} \frac{\partial \sigma\left(\epsilon\right)}{\partial \epsilon} \underbrace{\frac{\partial\left(\epsilon-\epsilon^{\Delta\theta}\right)}{\partial \epsilon}}_{=1} \underbrace{\frac{\partial \epsilon}{\partial \varepsilon}}_{=1}\,\mathrm{d}A^r = \int_{A^r} \frac{\partial \sigma\left(\epsilon\right)}{\partial \epsilon}\,\mathrm{d}A^r \tag{6.54a}$$

$$\frac{\partial N}{\partial \gamma} = 0 \tag{6.54b}$$

$$\frac{\partial N}{\partial \kappa} = \int_{A^r} \frac{\partial \sigma\left(\epsilon-\epsilon^{\Delta\theta}\right)}{\partial \kappa}\,\mathrm{d}A^r = \int_{A^r} \frac{\partial \sigma\left(\epsilon-\epsilon^{\Delta\theta}\right)}{\partial\left(\epsilon-\epsilon^{\Delta\theta}\right)} \frac{\partial\left(\epsilon-\epsilon^{\Delta\theta}\right)}{\partial \kappa}\,\mathrm{d}A^r = \\ = \int_{A^r} \frac{\partial \sigma\left(\epsilon\right)}{\partial \epsilon} \underbrace{\frac{\partial\left(\epsilon-\epsilon^{\Delta\theta}\right)}{\partial \epsilon}}_{=1} \underbrace{\frac{\partial \epsilon}{\partial \kappa}}_{=-\xi}\,\mathrm{d}A^r = -\int_{A^r} \xi\,\frac{\partial \sigma\left(\epsilon\right)}{\partial \epsilon}\,\mathrm{d}A^r \tag{6.54c}$$

$$\frac{\partial V}{\partial \varepsilon} = 0 \tag{6.54d}$$

$$\frac{\partial V}{\partial \gamma} = \int_{A^r} \frac{\partial \tau\left(\gamma\right)}{\partial \gamma}\,\mathrm{d}A^r \tag{6.54e}$$

$$\frac{\partial V}{\partial \kappa} = 0 \tag{6.54f}$$

$$\frac{\partial M}{\partial \varepsilon} = \int_{A^r} \frac{\partial\left(-\xi\sigma\left(\epsilon-\epsilon^{\Delta\theta}\right)\right)}{\partial \varepsilon}\,\mathrm{d}A^r = -\int_{A^r} \xi \frac{\partial \sigma\left(\epsilon\right)}{\partial \epsilon}\,\mathrm{d}A^r \tag{6.54g}$$

$$\frac{\partial M}{\partial \gamma} = 0 \tag{6.54h}$$

$$\frac{\partial M}{\partial \kappa} = \int_{A^r} \frac{\partial\left(-\xi\sigma\left(\epsilon-\epsilon^{\Delta\theta}\right)\right)}{\partial \kappa}\,\mathrm{d}A^r = -\int_{A^r} \xi \frac{\partial\left(\sigma\left(\epsilon-\epsilon^{\Delta\theta}\right)\right)}{\partial \kappa}\,\mathrm{d}A^r = \\ = -\int_{A^r} \xi \frac{\partial\left(\sigma\left(\epsilon-\epsilon^{\Delta\theta}\right)\right)}{\partial\left(\epsilon-\epsilon^{\Delta\theta}\right)} \underbrace{\frac{\partial\left(\epsilon-\epsilon^{\Delta\theta}\right)}{\partial \kappa}}_{=-1}\,\mathrm{d}A^r = \int_{A^r} \xi^2 \frac{\partial \sigma\left(\epsilon\right)}{\partial \epsilon}\,\mathrm{d}A^r \tag{6.54i}$$

hence,

$$\boldsymbol{D} = \int_{A^r} \begin{bmatrix} \frac{\partial \sigma(\epsilon)}{\partial \epsilon} & 0 & -\xi \frac{\partial \sigma(\epsilon)}{\partial \epsilon} \\ 0 & \frac{\partial V}{\partial \gamma} & 0 \\ -\xi \frac{\partial \sigma(\epsilon)}{\partial \epsilon} & 0 & \xi^2 \frac{\partial \sigma(\epsilon)}{\partial \epsilon} \end{bmatrix} \mathrm{d}A^r \tag{6.55}$$

Similarly to (6.33), $\Delta\boldsymbol{\varepsilon}^r = \boldsymbol{\Psi}\,(\boldsymbol{\Delta}\Delta\boldsymbol{d})$. Replacing this result and (6.33) into (6.51a) renders,

$$\Delta\boldsymbol{\sigma}^r \cdot \delta\boldsymbol{\varepsilon}^r = (\boldsymbol{\Delta}\delta\boldsymbol{d})^T\ \boldsymbol{\Psi}^T\,\boldsymbol{D}\,\boldsymbol{\Psi}\,(\boldsymbol{\Delta}\Delta\boldsymbol{d}) \tag{6.56}$$

and the matrix form of (6.51b) is,

$$\begin{aligned} \boldsymbol{\sigma}^r \cdot \Delta\delta\boldsymbol{\varepsilon}^r = \boldsymbol{\sigma}^r \cdot \Delta\,(\,\boldsymbol{\Psi}\boldsymbol{\Delta}\delta\boldsymbol{d}) = \Delta\,(\boldsymbol{\sigma}^r \cdot \boldsymbol{\Psi}\boldsymbol{\Delta}\delta\boldsymbol{d}) = \Delta\left(\boldsymbol{\Psi}^T\boldsymbol{\sigma}^r \cdot \boldsymbol{\Delta}\delta\boldsymbol{d}\right) = \\ = \frac{\partial\left(\boldsymbol{\Psi}^T\boldsymbol{\sigma}^r\right)}{\partial\,(\boldsymbol{\Delta}\boldsymbol{d})}\Delta\,(\boldsymbol{\Delta}\boldsymbol{d}) \cdot \boldsymbol{\Delta}\delta\boldsymbol{d} = (\boldsymbol{\Delta}\delta\boldsymbol{d})^T\,\boldsymbol{G}\,(\boldsymbol{\Delta}\Delta\boldsymbol{d}) \end{aligned} \tag{6.57}$$

where, considering the expressions (6.52),

$$\boldsymbol{\Delta}\delta\boldsymbol{d} = \begin{Bmatrix} \delta u_1' \\ \delta u_2' \\ \delta\theta' \\ \delta\theta \end{Bmatrix} \tag{6.58a}$$

$$\boldsymbol{G} = \begin{bmatrix} 0 & 0 & & \\ 0 & 0 & & \\ 0 & 0 & \cdots & \\ -N\sin\theta - V\cos\theta & N\cos\theta - V\sin\theta & & \end{bmatrix} \begin{bmatrix} 0 & -N\sin\theta - V\cos\theta \\ 0 & N\cos\theta - V\sin\theta \\ \cdots\ 0 & 0 \\ 0 & (1+u_1')(V\sin\theta - N\cos\theta) - u_2'(N\sin\theta + V\cos\theta) \end{bmatrix} \tag{6.58b}$$

$$\boldsymbol{\Delta}\Delta\boldsymbol{d} = \begin{Bmatrix} \Delta u_1 \\ \Delta u_2 \\ \Delta\theta' \\ \Delta\theta \end{Bmatrix} \tag{6.58c}$$

External virtual work

The incremental perturbation of the external virtual work is given by:

$$\Delta\delta W_{ext} = \Delta\int_0^{\ell^r} \delta\boldsymbol{d}^T\,(\lambda\,\boldsymbol{f})\,\mathrm{d}\zeta \tag{6.59}$$

which, for non configuration dependent loadings, is null.

6.3 Spatial discretization by finite elements

6.3.1 Implementation of the elemental system

A displacement-based formulation in which the displacements at the nodes are the fundamental unknowns is used. It is considered a discretization of the form,

$$\boldsymbol{d}^{(e)} = \boldsymbol{\Phi}^{(e)}\,\mathbf{d}^{(e)} \tag{6.60}$$

where $\boldsymbol{d}^{(e)}$ is the generalized displacement vector, $\boldsymbol{\Phi}^{(e)}$ are shape functions and $\mathbf{d}^{(e)}$ is the nodal generalized displacement vector at each finite element. The approximation for the iterative and incremental generalized displacement vectors is:

$$\delta\boldsymbol{d}^{(e)} = \boldsymbol{\Phi}^{(e)}\,\delta\mathbf{d}^{(e)} \tag{6.61a}$$

$$\Delta\boldsymbol{d}^{(e)} = \boldsymbol{\Phi}^{(e)}\,\Delta\mathbf{d}^{(e)} \tag{6.61b}$$

By substituting the approximation (6.61a) into the internal virtual work expression (6.35), it is obtained:

$$\delta W_{int} = \int_0^{\ell^{(e)r}} \left(\boldsymbol{\Delta}\,\delta\boldsymbol{d}^{(e)}\right)^T \boldsymbol{\Psi}^{(e)T}\boldsymbol{\sigma}^{(e)r}\,\mathrm{d}\zeta^{(e)} = \\ = \delta\mathbf{d}^{(e)T}\int_0^{\ell^{(e)r}} \left(\boldsymbol{\Delta}\,\boldsymbol{\Phi}^{(e)}\right)^T \boldsymbol{\Psi}^{(e)T}\boldsymbol{\sigma}^{(e)r}\,\mathrm{d}\zeta^{(e)} \tag{6.62}$$

Proceeding in the same way, the external virtual work can be written as,

$$\delta W_{ext} = \delta\mathbf{d}^{(e)T}\,\lambda\int_0^{\ell^{(e)r}} \boldsymbol{\Phi}^{(e)T}\boldsymbol{f}^{(e)}\,\mathrm{d}\zeta^{(e)} \tag{6.63}$$

and the weak form of the equilibrium (6.38) is:

$$\delta W \equiv \delta\mathbf{d}^{(e)T}\left(\int_0^{\ell^{(e)r}} \left(\boldsymbol{\Delta}\,\boldsymbol{\Phi}^{(e)}\right)^T \boldsymbol{\psi}^{(e)T}\boldsymbol{\sigma}^{(e)r}\,\mathrm{d}\zeta^{(e)} - \lambda\int_0^{\ell^{(e)r}} \boldsymbol{\Phi}^{(e)T}\boldsymbol{f}^{(e)}\,\mathrm{d}\zeta^{(e)}\right) = 0 \tag{6.64}$$

Besides the trivial solution, $\delta\mathbf{d}^{(e)} = \mathbf{0}$, the previous equation renders $\mathbf{r}^{(e)} = \mathbf{0}$, where $\mathbf{r}^{(e)}$ is the elemental residual vector,

$$\mathbf{r}^{(e)} = \int_0^{\ell^{(e)r}} \left(\boldsymbol{\Delta}\,\boldsymbol{\Phi}^{(e)}\right)^T \boldsymbol{\Psi}^{(e)T}\boldsymbol{\sigma}^{(e)r}\,\mathrm{d}\zeta^{(e)} - \lambda\int_0^{\ell^{(e)r}} \boldsymbol{\Phi}^{(e)T}\boldsymbol{f}^{(e)}\,\mathrm{d}\zeta^{(e)} \tag{6.65}$$

which can be subdivided in the internal and external elemental residual vectors:

$$\mathbf{r}_{int}^{(e)} = \int_0^{\ell^{(e)r}} \left(\boldsymbol{\Delta}\,\boldsymbol{\Phi}^{(e)}\right)^T \boldsymbol{\Psi}^{(e)T}\boldsymbol{\sigma}^{(e)r}\,\mathrm{d}\zeta^{(e)} \tag{6.66a}$$

$$\mathbf{r}_{ext}^{(e)} = -\lambda\int_0^{\ell^{(e)r}} \boldsymbol{\Phi}^{(e)T}\boldsymbol{f}^{(e)}\,\mathrm{d}\zeta^{(e)} \tag{6.66b}$$

For a generic element (e), the results presented in section 6.2.5 can be written as:

$$\Delta\delta W_{int} = \int_0^{\ell^{(e)r}} \left(\boldsymbol{\Delta}\delta\boldsymbol{d}^{(e)}\right)^T \boldsymbol{\Psi}^{(e)T}\boldsymbol{D}\,\boldsymbol{\Psi}^{(e)}\left(\boldsymbol{\Delta}\Delta\boldsymbol{d}^{(e)}\right)\mathrm{d}\zeta^{(e)} + \\ + \int_0^{\ell^{(e)r}} \left(\boldsymbol{\Delta}\delta\boldsymbol{d}^{(e)}\right)^T \boldsymbol{G}\left(\boldsymbol{\Delta}\Delta\boldsymbol{d}^{(e)}\right)\mathrm{d}\zeta^{(e)} \tag{6.67}$$

Replacing (6.61) into (6.67), one obtains:

$$\Delta\delta W_{int} = \delta\mathbf{d}^{(e)T}\left(\int_0^{\ell^{(e)r}} \left(\boldsymbol{\Delta}\boldsymbol{\Phi}^{(e)}\right)^T \boldsymbol{\Psi}^{(e)T}\boldsymbol{D}\,\boldsymbol{\Psi}^{(e)}\left(\boldsymbol{\Delta}\boldsymbol{\Phi}^{(e)}\right)\mathrm{d}\zeta^{(e)} + \right. \\ \left. + \int_0^{\ell^{(e)r}} \left(\boldsymbol{\Delta}\boldsymbol{\Phi}^{(e)}\right)^T \boldsymbol{G}\left(\boldsymbol{\Delta}\boldsymbol{\Phi}^{(e)}\right)\mathrm{d}\zeta^{(e)}\right)\Delta\mathbf{d}^{(e)} \tag{6.68}$$

Element type	$\mathbf{r}_{int}^{(e)}$		$\mathbf{r}_{ext}^{(e)}$		$\mathbf{K}_g^{(e)}, \mathbf{K}_m^{(e)}$	
	p	n_G	p	n_G	p	n_G
L2	0	1	1	1	2	2
L3	1	1	2	2	4	3
L4	2	2	3	2	6	4

Table 6.1: Polynomial degree (p) of the integrand function and number of Gauss points (n_G) required for the exact numerical integration, where Ln denotes Lagrange element with n nodes.

Hence, the tangent stiffness matrix can be calculated as,

$$\boldsymbol{K}^{(e)} = \boldsymbol{K}_g^{(e)} + \boldsymbol{K}_m^{(e)} \tag{6.69}$$

where $\boldsymbol{K}_g^{(e)}$ and $\boldsymbol{K}_m^{(e)}$ are the geometric and material terms in the element (e), respectively:

$$\boldsymbol{K}_g^{(e)} = \int_0^{\ell^{(e)r}} \left(\boldsymbol{\Delta\Phi}^{(e)}\right)^T \boldsymbol{G} \left(\boldsymbol{\Delta\Phi}^{(e)}\right) \mathrm{d}\zeta^{(e)} \tag{6.70a}$$

$$\boldsymbol{K}_m^{(e)} = \int_0^{\ell^{(e)r}} \left(\boldsymbol{\Delta\Phi}^{(e)}\right)^T \boldsymbol{\Psi}^{(e)T} \boldsymbol{D}\, \boldsymbol{\Psi}^{(e)} \left(\boldsymbol{\Delta\Phi}^{(e)}\right) \mathrm{d}\zeta^{(e)} \tag{6.70b}$$

The global tangent matrix and residual vector will be obtained by assembly of the elemental vectors and matrices described in the present section. The nonlinear system of equations will be solved for the free degrees of freedom.

6.3.2 Computational considerations

The developed code requires two different meshes: (i) a one-dimensional mesh to discretize the length of the bar, and (ii) a two-dimensional mesh to discretize the cross section.

One-dimensional elements of n nodes can be used and an isoparametric formulation is used to compute the Lagrangian shape functions of the elements, which are polynomial functions. The two-dimensional finite elements can be quadrilateral of 4, 8, 9, 12 and 16 nodes, or triangular with 3, 6 and 10 nodes, which were already defined in figure 3.4. The two-dimensional mesh employed is the one used for the computation of the temperature field using the formulation described in chapter 5.

The Gauss–Legendre quadrature was programmed to compute the integrals involved in the residual vector and tangent matrix. The number of Gauss points required to integrate exactly the polynomial expressions that appear in the integrands was calculated, assuming that the nonlinear operators are constant (see table 6.1).

In order to alleviate the shear locking phenomenon, a simple selective/reduced integration scheme is employed.

The numerical integration of the internal residual vector is explicitly showed due the complexity regarding the calculation of the stresses, as these depend on the strains and temperature.

The generalized stresses in a cross section can be computed using the equation (6.29). Applying the numerical integration, each component of the generalized stress vector can

be computed knowing the generalized strain vector, $\boldsymbol{\varepsilon}^r$, as,

$$N = \int_{A^r} \sigma \, \mathrm{d}A^r = \sum_{e=1}^{n} \sum_{pG=1}^{nG} \sigma \left(\varepsilon_{pG}\right) \, |\mathbf{J}|_{pG} \, w_{pG} \tag{6.71a}$$

$$V = \int_{A^r} \tau \, \mathrm{d}A^r = \sum_{e=1}^{n} \sum_{pG=1}^{nG} \tau \left(\gamma_{pG}\right) \, |\mathbf{J}|_{pG} \, w_{pG} \tag{6.71b}$$

$$M = -\int_{A^r} \xi_2 \, \sigma \, \mathrm{d}A^r = -\sum_{e=1}^{n} \sum_{pG=1}^{nG} \left(\xi_2\right)_{pG} \, \sigma \left(\varepsilon_{pG}\right) \, |\mathbf{J}|_{pG} \, w_{pG} \tag{6.71c}$$

where $\left(\xi_1, \xi_2\right)_{pG}$ are the natural coordinates of the Gauss point, $|\mathbf{J}|_{pG}$ is the determinant of the Jacobian matrix evaluated at the Gauss point, w_{pG} is the weight value and ϵ_{pG} and γ_{pG} are the longitudinal deformation and angular distortion, respectively, computed at a Gauss point as:

$$\epsilon_{pG} = \varepsilon - \left(\xi_2\right)_{pG} \, \kappa - \epsilon_{pG}^{\Delta\theta} \tag{6.72a}$$

$$\gamma_{pG} = \gamma \tag{6.72b}$$

The equations (6.71) depend on the constitutive equation and n is the number of elements of the mesh used for the spatial discretization of the cross section.

Hence, the global internal residual vector can be computed as,

$$\mathbf{r}_{int} = \mathop{\mathsf{A}}_{e=1}^{m} \sum_{pG=1}^{nG} \left(\boldsymbol{\Delta} \, \boldsymbol{\Phi}^{(e)}\right)_{pG}^{T} \, \boldsymbol{\Psi}_{pG}^{(e)T} \, \boldsymbol{\sigma}_{pG}^{(e)r} \, J_{pG} \, w_{pG} \tag{6.73}$$

where J_{pG} is the Jacobian of the one-dimensional transformation. Notice that the value of the weight, the Jacobian and the number of Gauss points in expression (6.73) are different from those shown in equation (6.71). The integral of the cross section in equation (6.71) is computed using the number of Gauss points defined in chapter 3.

The same process can be applied to compute the geometric and material tangent matrices. In this case, instead of the value of the stresses in the Gauss points in expressions (6.71), the derivative of the generalized stresses with respect to the strain has to be computed.

The resulting nonlinear system of equations is solved using the incremental/iterative Newton–Raphson method, which is described in the appendix B.6.

6.4 Numerical examples

6.4.1 Introduction

In the present section mechanical and thermomechanical applications of the developed code are shown. The selected problems allow verifying the accuracy of the numerical results obtained with the employed theory, as they can be compared with the exact solutions of the problems or with results proposed by different authors.

In all the examples presented, the constitutive relation is linear and expressed by,

$$\sigma = E \left(\epsilon - \epsilon^{\Delta\theta}\right) \tag{6.74a}$$

$$\tau = G \left(\gamma - \gamma^{\Delta\theta}\right) \tag{6.74b}$$

where E is the Young's modulus, G is the shear modulus and ϵ and $\epsilon^{\Delta\theta}$ are the axial deformation due to the mechanical loads and to the temperature gradient, respectively.

The following benchmark problems were analysed:

- Cantilever beam loaded with a transversal point load (section 6.4.2).
- Square diamond frame (section 6.4.3).
- Square frame (section 6.4.4).
- Pure bending of a cantilever beam (section 6.4.5).

The first three examples present simple applications of the geometrically exact beam theory. These examples are used for the verification of the FE code developed.

The last example, presented in 6.4.5, illustrates the computation of the generalized strains, stresses and displacements of a beam subjected to a uniform, $\Delta\theta_U$, and linear, $\Delta\theta_L$, temperature gradient. In this particular problem, the axial deformation and the angular distortion at any point of the cross section can be computed as,

$$\epsilon^{\Delta\theta} = \alpha\,\Delta\theta\,(\xi_2) = \alpha\,\left(\Delta\theta_U - \xi_2\,\frac{\Delta\theta_L}{h}\right) \tag{6.75a}$$

$$\gamma^{\Delta\theta} = 0 \tag{6.75b}$$

where α is the thermal expansion coefficient and h is the height of the cross section.

The generalized stress vector is given by,

$$\boldsymbol{\sigma}^r = \boldsymbol{D}\left(\boldsymbol{\varepsilon}^r - (\boldsymbol{\varepsilon}^r)^{\Delta\theta}\right) \tag{6.76}$$

whose matricial form is,

$$\begin{Bmatrix} N \\ V \\ M \end{Bmatrix} = \begin{bmatrix} EA & 0 & -ES \\ 0 & GA^* & 0 \\ -ES & 0 & EI \end{bmatrix} \left(\begin{Bmatrix} \varepsilon \\ \gamma \\ \kappa \end{Bmatrix} - \begin{Bmatrix} \alpha\,\Delta\theta_U \\ 0 \\ \alpha\frac{\Delta\theta_L}{h} \end{Bmatrix} \right) \tag{6.77}$$

where A, S and I are the zero, first and second order area moments of the cross section in the undeformed position, *i.e.*, the area, the static and the inertia moment. The variable A^* is the reduced area, which can be computed as $A^* = \kappa\,A$ where κ is the shear correction factor[3].

In all the following examples, the load parameter, λ, varies between 0 and 1.

6.4.2 Cantilever beam loaded with a transversal point load

A cantilever beam with a vertical point load applied in the free end, as figure 6.2a shows, is analysed using the geometrically exact beam theory. The cross section of the unit length beam has a second order moment (or inertia moment) equal to $8.(3)\cdot10^{-6}$ and an area equal 10. The shear correction factor is set as 1. The Young´s modulus is equal to 10^6. The shear modulus was computed considering that the material is elastic and the Poisson ratio is 0, thus, the shear modulus is equal to $0.5\cdot10^6$. The vertical load is applied in 50 steps until reaching the maximum value, which is equal to 83.(3) in this simulation.

[3]There is a notation conflict as in the current expression, κ refers to the shear correction factor used in the Timoshenko's beam theory and not the curvature of the beam axis.

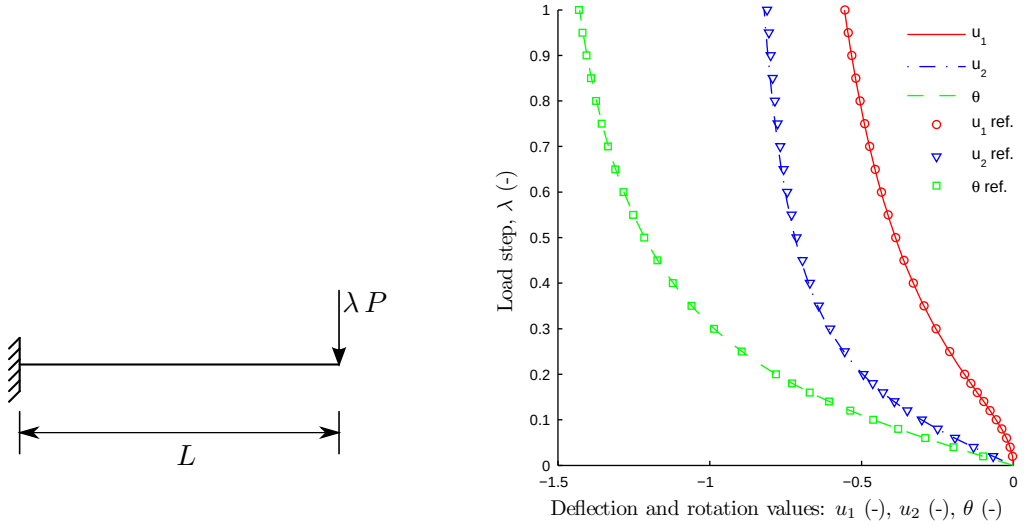

(a) Cantilever geometry.

(b) Load-deflection and load-rotation curves at the free end of the beam.

Figure 6.2: Cantilever beam.

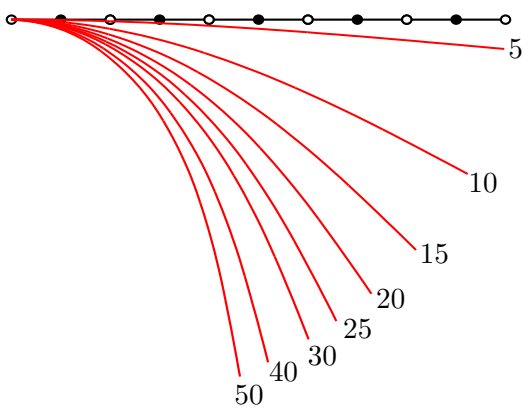

Figure 6.3: Deformed configurations for the cantilever beam, where the numbers are the different load steps.

Figure 6.2b illustrates the load-deflections and load-rotation curves obtained at the free end and figure 6.3 displays the mesh of 5 quadratic elements used and the deformed shapes for different load steps (the white and black dots indicate the start-end and the central nodes of the element, respectively). Table 6.2 summarizes the numerical results obtained and the reference values (Mattiasson, 1981), for different values of the parameter, λ. A good agreement is observed between the reference and the computed results. It can be noticed that the horizontal displacement at the free end is not null and the length of the beam is approximately constant in all load steps.

Figure 6.4 depicts the iterative norm of the residual vector obtained in the computation of the first 5 load steps and it can be observed that quadratic convergence of the computational process in the asymptotic limit of the solution is obtained.

λ	Reference values			Numerical values		
	$-u_1$	$-u_2$	$-\theta$	$-u_1$	$-u_2$	$-\theta$
0.02	0.00265	0.06636	0.09964	0.002646515	0.066364802	0.099636148
0.04	0.01035	0.13098	0.19716	0.010353786	0.130975804	0.197154509
0.06	0.02249	0.19235	0.29074	0.022487355	0.192350937	0.290737391
0.08	0.03817	0.24945	0.37906	0.038165040	0.249452097	0.379062153
0.1	0.05643	0.30172	0.46135	0.056432310	0.301720994	0.461350364
0.12	0.07640	0.34901	0.53730	0.076398944	0.349009716	0.537301499
0.14	0.09732	0.39147	0.60698	0.097314865	0.391464536	0.606971696
0.16	0.11860	0.42941	0.67065	0.118593452	0.429410504	0.670648408
0.18	0.13981	0.46326	0.72876	0.139802026	0.463260351	0.728747644
0.2	0.16064	0.49346	0.78175	0.160637381	0.493452473	0.781740770
0.3	0.25442	0.60325	0.98602	0.254409652	0.603238695	0.985995906
0.4	0.32894	0.66996	1.12124	0.328922266	0.669937066	1.121204377
0.5	0.38763	0.71379	1.21537	0.387599235	0.713750427	1.215318766
0.6	0.43459	0.74457	1.28370	0.434548218	0.744514952	1.283633868
0.7	0.47293	0.76737	1.33496	0.472874238	0.767296944	1.334883084
0.8	0.50483	0.78498	1.37443	0.504761027	0.784893556	1.374342287
0.9	0.53182	0.79906	1.40547	0.531739519	0.798949448	1.405364667
1.0	0.55500	0.81061	1.43029	0.554899476	0.810485171	1.430174454

Table 6.2: Generalized displacement values obtained when a vertical load is applied at the free end of the beam $P = 83.(3)$.

In addition, a further test was carried out in which the load is increased (100 times) until an almost vertical straight position is attained. Figure 6.5 shows the evolution of the deformed shapes and the load-deflection/load-rotation curves in the free end. At the end of the process, the horizontal displacement at the free end of the beam is near to its original length. The rotation at that point is approximately equal to -1.57 rad, which corresponds to 89.95°.

6.4.3 Square diamond frame

Figure 6.6a shows a square diamond frame loaded with two point loads, which is the verification example analysed in the present subsection. To minimize the computational time, symmetry conditions were used and, thus, only half of the geometry of the square diamond was modelled, as depicted in figures 6.6b and 6.6c. All the beams are unit length.

The cross section has a second order moment equal to $8.(3) \cdot 10^{-6}$ and an area equal 0.01. The shear correction factor is set as 1. The Young's modulus is equal to 10^6. The shear modulus was computed considering that the material is elastic and the Poisson ratio is 0, thus, the shear modulus is equal to $0.5 \cdot 10^6$. The absolute value of the vertical load applied, P, is equal to 83.(3). This problem is analysed in tension and in compression, as figure 6.6 shows.

Figure 6.7 shows the numerical results obtained using a mesh of 10 linear elements in each bar and the reference values provided in Mattiasson (1981).

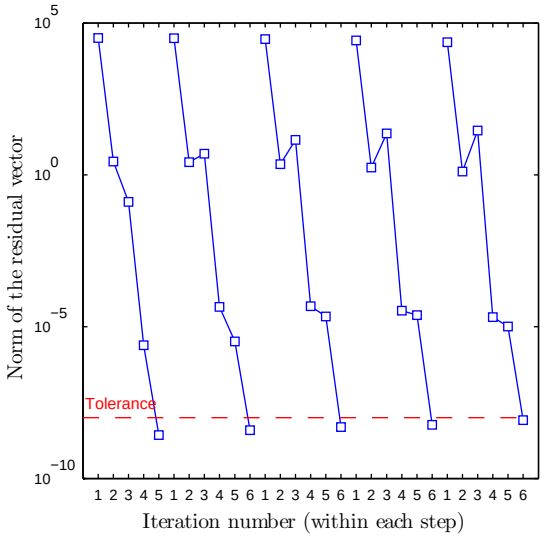

Figure 6.4: Norm of the residual vector obtained at each iteration in the cantilever beam problem (first 5 load steps).

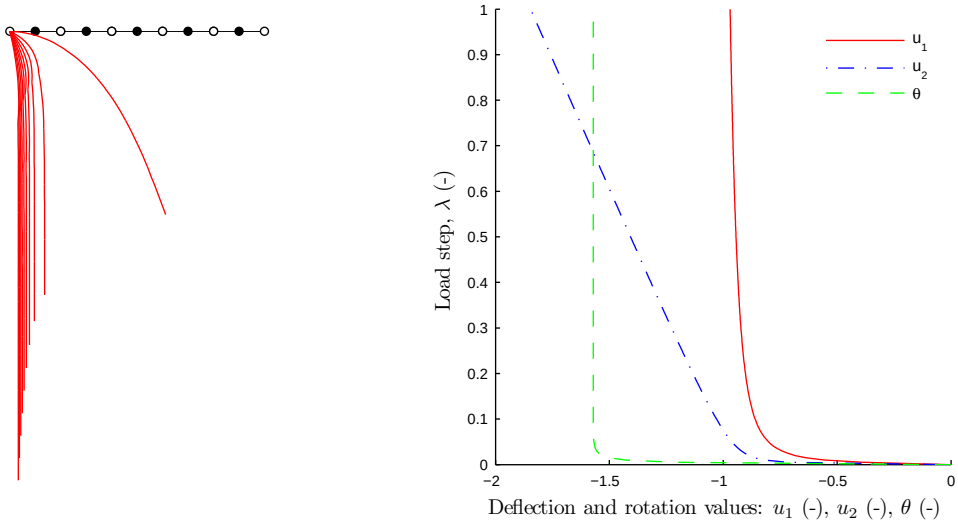

(a) Deformed configurations.

(b) Load-displacement and load-rotation at the free end.

Figure 6.5: Cantilever results for a load equal to $P = 8333$.

The horizontal displacement represented is that computed in the node 11 of the model (the vertical displacement and the rotation are null), while the vertical displacement and the rotation are those computed in node 21 (the horizontal displacement is equal to 0). The nodes are identified in figure 6.6b. Figure 6.8 illustrates the deformed shape for different load steps (5, 10, 15, 20, 25, 30, 35, 40, 45 and 50). The load was applied in 50 steps in order to obtain numerical results comparable with those presented in Mattiasson (1981) and, in both cases, good agreement between the numerical and the reference results is observed.

Figure 6.9 plots the norm of the residual vector at each iteration for the first 5 load

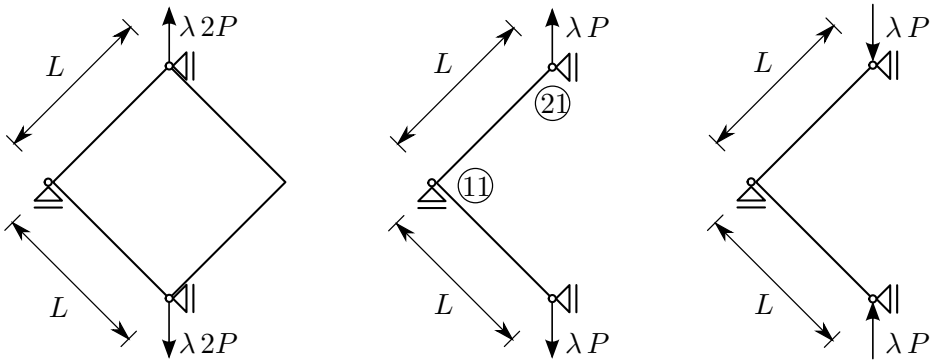

(a) Complete geometry of square diamond loaded in tension.

(b) Half-diamond loaded in tension.

(c) Half-diamond loaded in compression.

Figure 6.6: Pinned-fix square diamond.

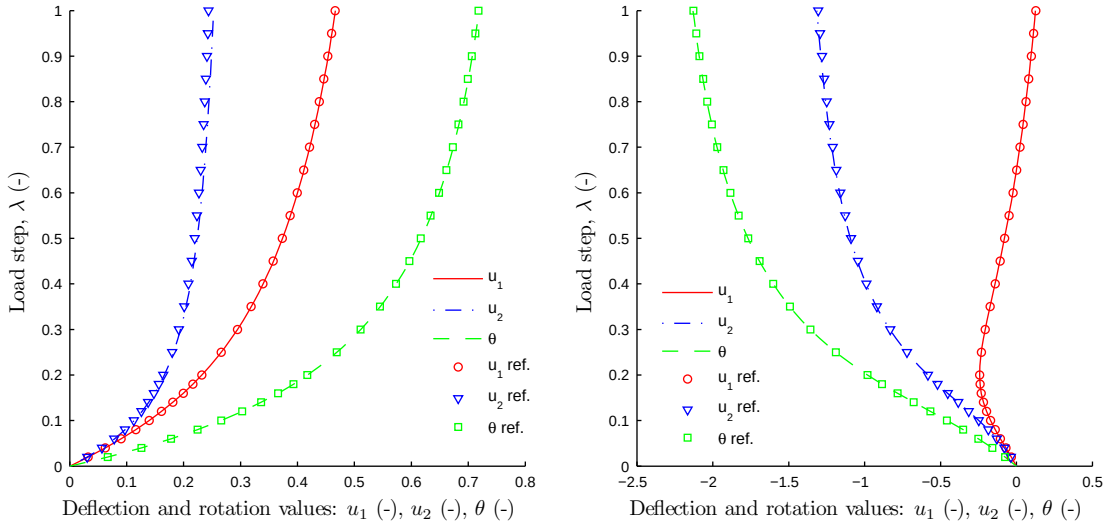

(a) Tension.

(b) Compression.

Figure 6.7: Load-displacement and load-rotation in the square diamond.

steps. In the asymptotic limit of the solution, the convergence of the iterative error is quadratic.

During the computation of the shape function it was considered that there is no contact between the frames. Figure 6.10 shows the deformed shapes of the diamond square loaded in compression obtained at different load steps. It can be observed that the horizontal displacement at node 11 changes of signal, being positive until the load step 12 and being negative after that. This fact is illustrated in figure 6.10 and also in 6.7b.

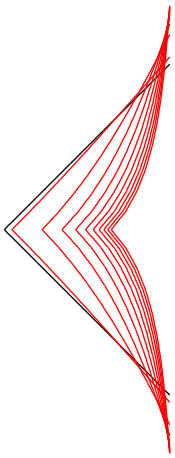

Figure 6.8: Deformed shape plots of the square half-diamond for different load steps (tension).

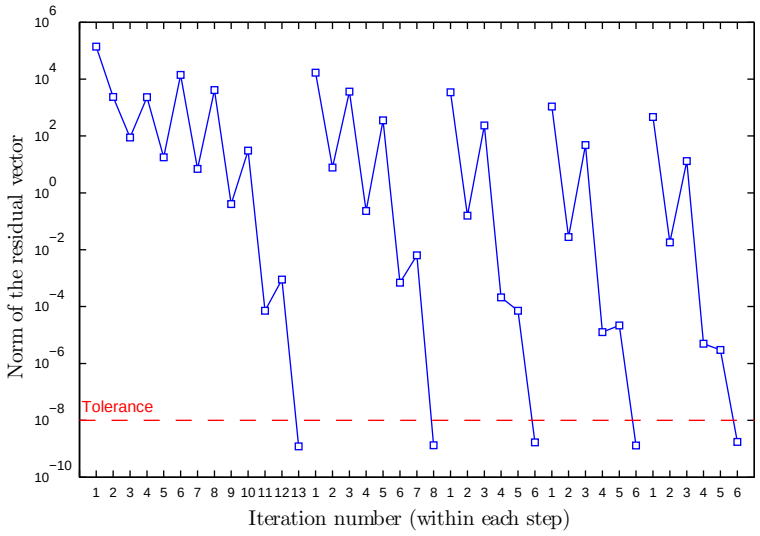

Figure 6.9: Norm of the residual vector obtained for the half-diamond loaded in tension (during the computation of the first 5 load steps).

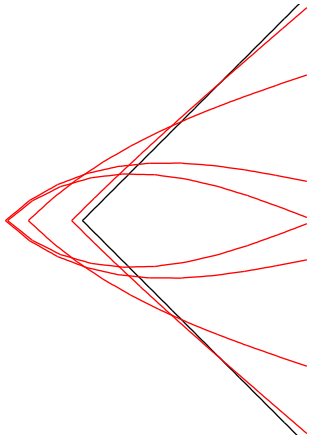

(a) Load steps 1, 5, 10 and 12.

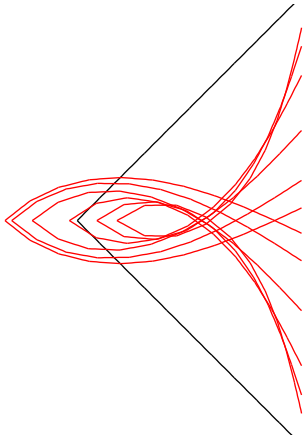

(b) Load steps 13, 15, 20, 30, 40 and 50.

Figure 6.10: Deformed shape plots of the square half-diamond loaded in compression.

6.4.4 Square frame

A square frame with the geometry showed in figure 6.11 is analysed in the present subsection. All the beams are unit length and present the same characteristics than those in section 6.4.3. The absolute value of the vertical applied load, P, is equal to 33.(3). Again, tension and compression loadings are considered.

The numerical results reported in this work were obtained using a mesh with 160 linear elements, *i.e.*, each frame of length L was divided in 20 linear elements. The numerical results obtained are compared with those presented in Mattiasson (1981) and depicted in in figures 6.12 and 6.13. The deformed shapes for different load steps are also illustrated.

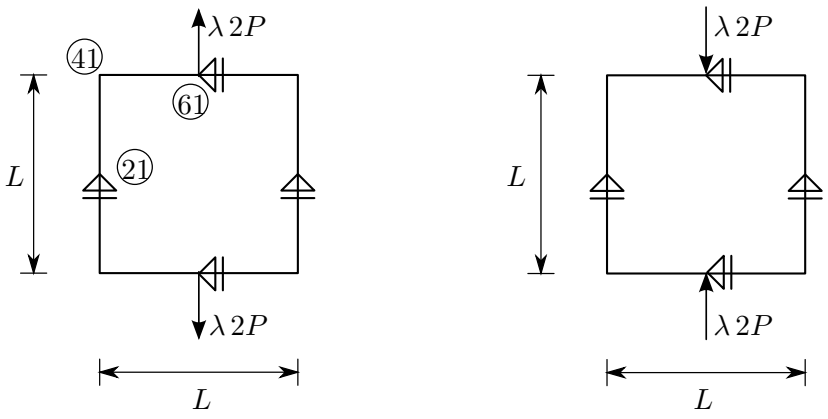

(a) Tension loading. (b) Compression loading.

Figure 6.11: Square frame and boundary conditions.

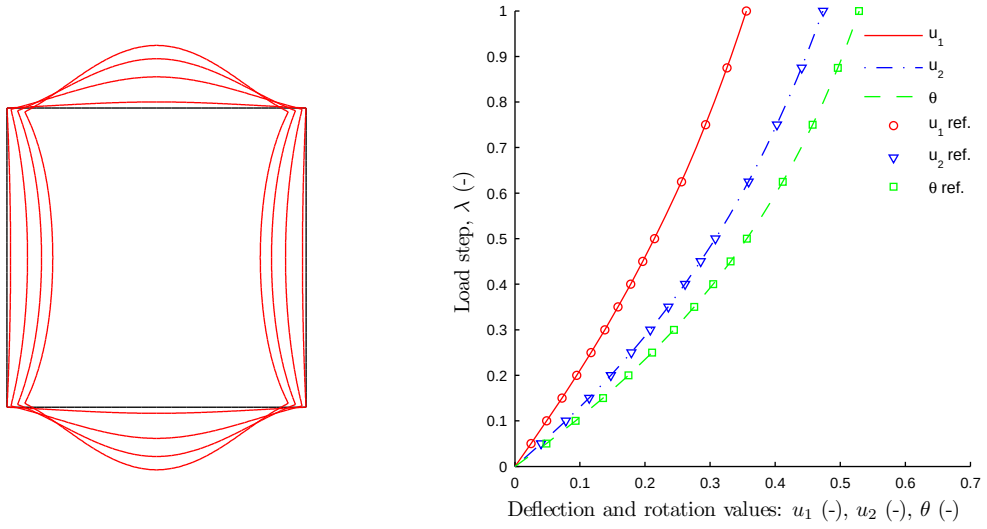

(a) Deformed shape at steps 5, 10, 15 and 20. (b) Displacement and rotation curves.

Figure 6.12: Results of the square frame loaded in tension.

The horizontal displacement, the vertical displacement and the rotation plotted are those computed in nodes 21, 61 and 41, respectively. The position of the nodes can be consulted in figure 6.11a. As in the previous example, a good agreement between the numerical and the reference results is observed.

6.4.5 Pure bending of a cantilever beam

Simo and Vu-Quoc (1986) solved the problem of a straight beam of unit length with a

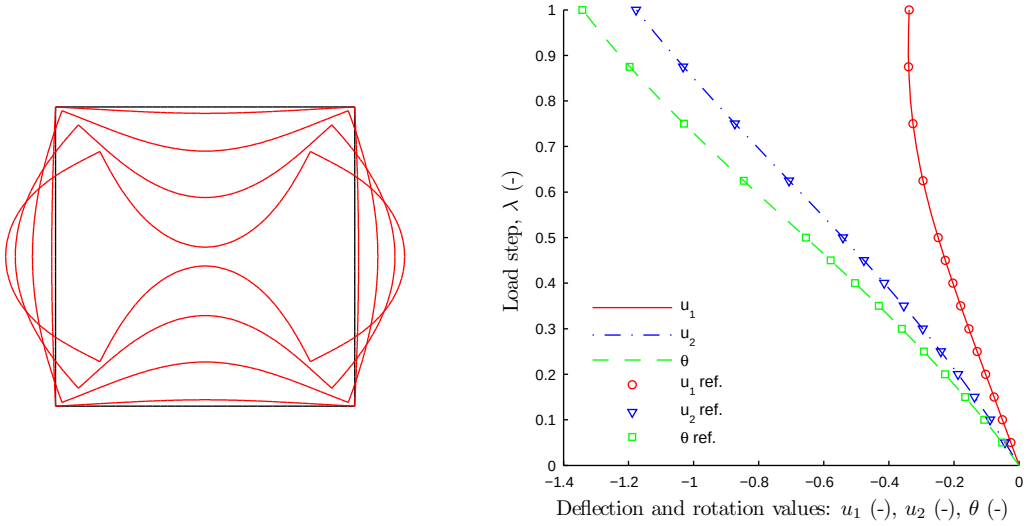

(a) Deformed shape at steps 5, 10, 15 and 20. (b) Vertical displacement and rotation curves.

Figure 6.13: Results of the square frame loaded in compression.

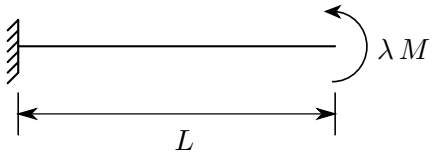

Figure 6.14: Pure bending cantilever beam.

moment applied on the right end using the geometrically exact beam theory, see figure 6.14.

The cross section has a second order moment equal to 2 and an area equal to 1. The shear correction factor is set as 1. The Young´s modulus is equal to 1. The shear modulus was computed considering that the material is elastic and the Poisson ratio is 0, thus, the shear modulus is equal to 0.5.

In this section, the referred problem was solved applying a bending moment such that the rotation is $\theta = 4\,\pi$. Hence, knowing that the bending stiffness is $EI = 2$, the bending moment, M, required to force the rod to deform into two fully closed circles is given by:

$$M = \kappa EI = \frac{\theta}{L}\,EI = 8\pi \tag{6.78}$$

The moment is applied in 6 steps, getting the convergence to the solution in five iterations for each step.

The exact generalized displacements at the free end of the cantilever are:

$$u_1 = -L\left(1 - \frac{\sin\frac{\lambda ML}{EI}}{\frac{\lambda ML}{EI}}\right) \tag{6.79a}$$

$$u_2 = \frac{EI}{\lambda M}\left(1 - \cos\frac{\lambda ML}{EI}\right) \tag{6.79b}$$

$$\theta = \frac{\lambda ML}{EI} \tag{6.79c}$$

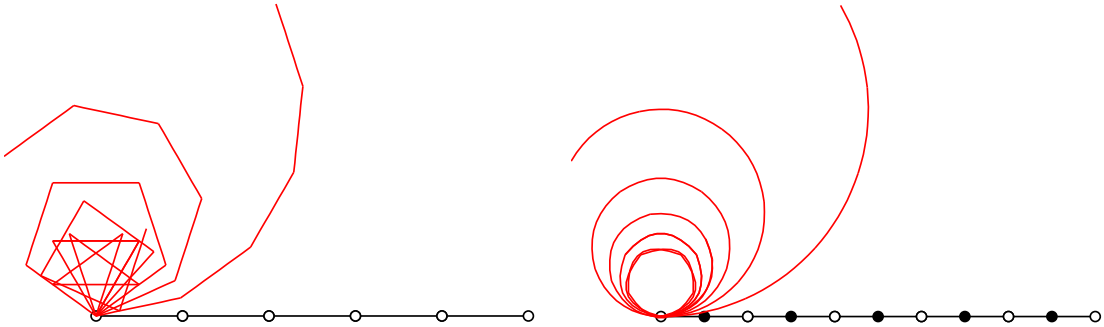

(a) Five one-dimensional linear elements. (b) Five one-dimensional quadratic elements.

Figure 6.15: Rod deformed position at each load step.

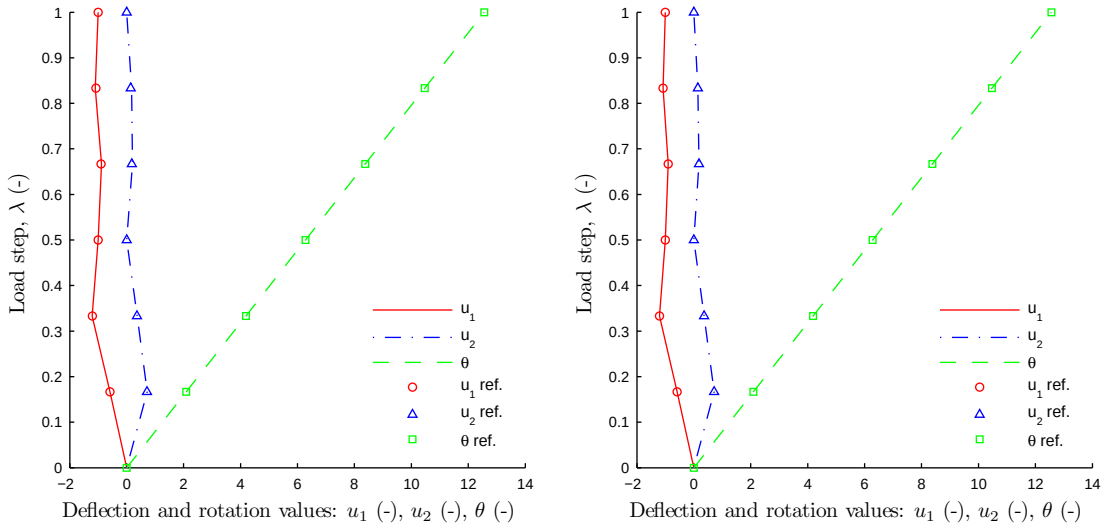

(a) Five one-dimensional linear elements. (b) Five one-dimensional quadratic elements.

Figure 6.16: Evolution of the generalized displacement at the point situated at the end of the rod.

The presented problem was solved employing two different one-dimensional meshes with: (i) five linear and (ii) five quadratic elements. Figures 6.15 and 6.16 illustrate the computed beam's deformed configurations and the corresponding evolution of the generalized displacement vector at the free end of the beam, respectively. The latest figure also presents the exact solution of the problem (markers), being possible to conclude that both the meshes are able to evaluate an accurate displacement field at the tip of the rod. However, figure 6.15 indicates that only the mesh with quadratic elements is able to represent properly the displacement field of all the points in the rod. In order to obtain a similar results with linear elements, a more refined mesh is required.

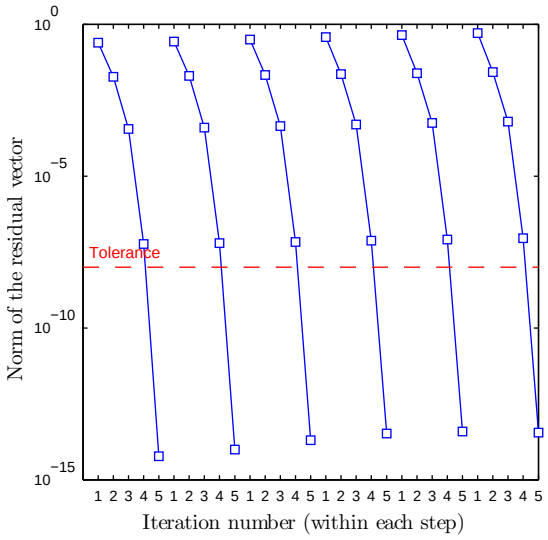

Figure 6.17: Norm of the residual vector for the pure bending cantilever beam problem (6 load steps).

Figure 6.17 displays the relative iterative errors obtained in the computational analysis in 6 load steps, attesting the quadratic convergence in the asymptotic limit when the error of the numerical solution tends to zero.

The same example was solved using the Timoshenko beam theory (TBT), as an exercise to compare the results and observe the potential use of the geometrically exact beam theory ($GEBT$). Table 6.3 summarizes the displacement and rotation values obtained in the free end of the rod. It can be observed that the TBT is not able to represent the displacement field of the rod.

Similar behaviour can be obtained by applying a linear variation of the temperature, $\Delta\theta_L$, in all the cross sections along the span of the beam. In this simulation, the temperature gradient is imposed directly, *i.e.*, without using the routine to integrate the temperatures along the cross section. In fact, one of the possibilities of the developed program to apply temperature gradients is to prescribe temperatures in the bottom and top faces of the beam. To solve the same problem using the integration of the temperatures in the section, a vector with the temperatures at each node of the cross section should be created previously as an input.

Generalized	Quadratic elements		Linear elements	
displacement	$GEBT$	TBT	$GEBT$	TBT
u_1	-1	0	-1	0
u_2	0	6.283185	0	6.283185
θ	12.566371	12.566371	12.566371	12.566371

Table 6.3: Generalized displacement values obtained when $M = 8\pi$.

The nodal equivalent moment due to the temperature distribution is given by,

$$M = \frac{EI\alpha\Delta\theta_L}{h} = \frac{4\pi}{L}EI \Rightarrow \Delta\theta_L = \frac{4\pi h}{\alpha L} \tag{6.80}$$

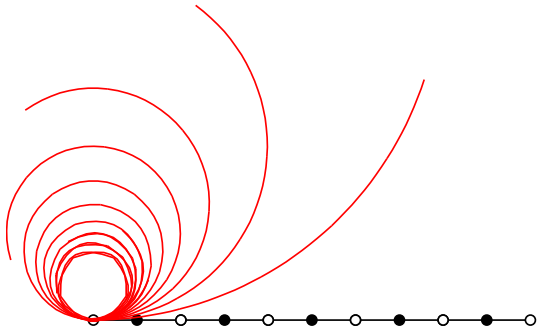

Figure 6.18: Deformed shape for 10 steps of the cantilever beam when a linear gradient of temperature is applied.

Step	u_1	u_2	θ
0	0.000000000000	0.000000000000	0.000000000000
1	−0.24317397180	0.549866295872	1.256637061498
2	−0.76613116303	0.719774269590	2.513274122934
3	−1.15590300291	0.479820105319	3.769911184370
4	−1.18916047181	0.137433127360	5.026548245806
5	−0.99999999997	−0.00000000000	6.283185307242
6	−0.87402479244	0.091526345778	7.539822368677
7	−0.93334337254	0.205148005029	8.796459430113
8	−1.05821511003	0.179167685689	10.05309649155
9	−1.08348658462	0.060656554230	11.30973355298
10	−0.99999999999	0.000000000000	12.56637061442
Exact (step 10)	−1.000000000000	0.000000000000	$4\pi \approx$12.56637061435

Table 6.4: Generalized displacements in the free end of the cantilever beam.

where h is the cross section height. The temperature at the bottom face will be equal to $\Delta\theta_L/2$ and in the top face it will be $(-\Delta\theta_L/2)$, which are applied in 10 steps. All variables are considered equal to 1, as the example presented is theoretical. The results obtained in a cantilever using a mesh of 5 one-dimensional quadratic elements are reported in figure 6.18 and table 6.4. Once again, a good agreement was obtained between the numerical results and the exact solution.

6.5 Concluding remarks

In the present chapter a compact finite element formulation of the thermomechanical problem based on the geometrically exact beam theory is presented.

The in-house code developed constitutes a powerful tool to compute the mechanical behaviour of beams and columns with large displacements, considering the nonlinearities

due to the geometry and the temperature-dependent mechanical properties of the material. The mechanical code was verified through benchmark solutions available in the literature. In all the examples presented, an excellent agreement between the numerical and the reference results was observed. Quadratic convergence of the iterative error was always achieved in the asymptotic limit of the solution.

Chapter 7

Thermomechanical simulations in GFRP beams and columns

7.1 Introduction

In the present chapter, nonlinear thermomechanical transient numerical simulations of GFRP beams and columns using the code described in the previous chapters are presented. The numerical results obtained are compared with the experimental data obtained in the tests carried out by Morgado *et al.* (2013a,b) at IST/ICIST (Portugal) within the project PTDC/ECM/100779/2008.

The chapter is organized in the following nine main sections:

1. Brief summary of the experimental programme (section 7.2).

2. Analysis of the thermal properties of the GFRP and calcium silicate (CS) materials (section 7.3).

3. General characteristics of the thermal modelling (boundary conditions, mesh, time step size and geometry of the cross section) of the tubular cross section exposed to fire in the bottom face and definition of the thermal properties of the GFRP that provide the best agreement with the experimental data (section 7.4).

4. Thermal simulations of the unprotected and protected square-tubular and I-section GFRP profiles exposed to different fire scenarios (section 7.5).

5. General characteristics of the thermomechanical modelling of beams and columns (boundary conditions, mesh and temperature distribution along the length of the bars) and temperature-dependent mechanical properties of the GFRP and CS (section 7.6).

6. Thermomechanical simulations of GFRP beams and columns exposed to different fire scenarios and comparison between the numerical and the experimental temperatures (section 7.7).

7. Additional numerical tests, in which the ability of the thermal code to simulate the thermal response of the GFRP profiles subjected to different fire scenarios (compared to those used in the experiments) for a sufficiently long duration of fire exposure (for practical applications) was investigated (section 7.8).

8. Conclusions (section 7.9).

7.2 General description of the problem and of the thermomechanical modelling

The present chapter centres on the thermomechanical simulation of protected and unprotected GFRP beams and columns. The numerical results obtained are compared with the experimental data resulting from fire resistance tests developed by Morgado *et al.* (2013a,b) at IST. In those tests, the setups presented in figures 7.1a and 7.1b were used for beams and columns, respectively.

GFRP profiles with square-tubular and I-section were experimentally tested as beams and columns. In all the fire resistance tests, thermocouples were installed at different positions to record the temperature evolution. These data were used to define the most adequate mathematical model for reproducing the thermal behaviour of the GFRP profiles. Furthermore, in the experiments, displacement transducers were installed to measure the deflections at the midspan of the beams and at the central section of columns; the axial shortening was also measured in columns.

In the fire resistance tests, the bars (both beams and columns) were mechanically loaded and a temperature variation according with the standard ISO 834 (1975) was imposed: (i) in the bottom face, keeping the lateral faces insulated, or (ii) in the bottom and lateral faces. In all the tests, the top face was exposed to the ambient temperature and, in order to protect the profiles from the wind, a system comprising four flame retardant blankets and two agglomerated cork panels (Morgado *et al.*, 2013b) was installed around the setup. As a result, it can be considered that no forced convection occurred in the top of the profile and, thus, the exchange of heat on the top face can be modelled as natural convection and radiation.

The thermomechanical model proposed consists of an uncoupled two-dimensional thermal and one-dimensional mechanical model. The former allows computing the temperature field in the cross section of the profile, while the latter allows obtaining the displacement field in the bar.

Table 7.1 summarizes the thermomechanical simulations performed for the beams and their main characteristics. All analyses were performed considering a beam span, L, of 1.3 m, as in the experimental tests. Point loads required to cause vertical displacements in the midspan section of $L/400$ or $L/250$ were applied.

Table 7.2 summarizes the thermomechanical simulations performed for the columns. The columns' length, L, was set as 1.5 m, in agreement with the experimental tests. Axial loads required to cause axial shortening in the columns of $L/1500$ (55 kN and 25 kN in the tubular and I sections, respectively) or $L/750$ (110 kN in the tubular section) were applied.

7.3 Thermal properties of the materials

7.3.1 GFRP material

The thermal conductivity and the specific heat capacity are thermophysical material properties that depend on factors such as the temperature, the density, the humidity, the porosity and the permeability. Due to the absence of experimental results, the men-

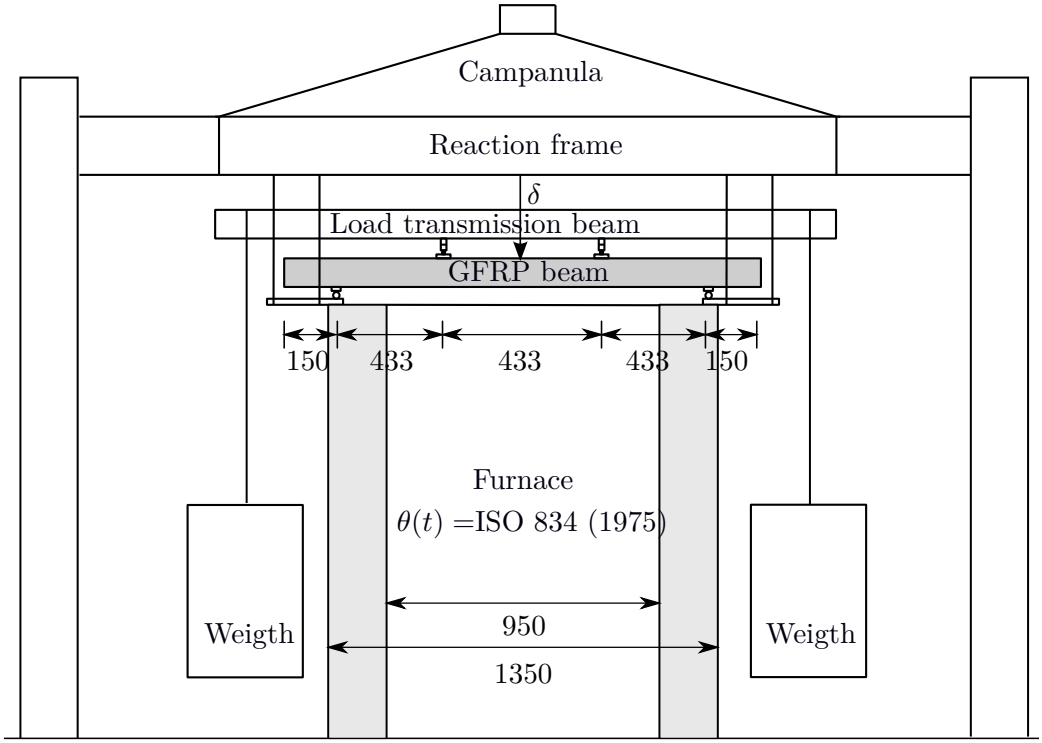

(a) Beam setup.

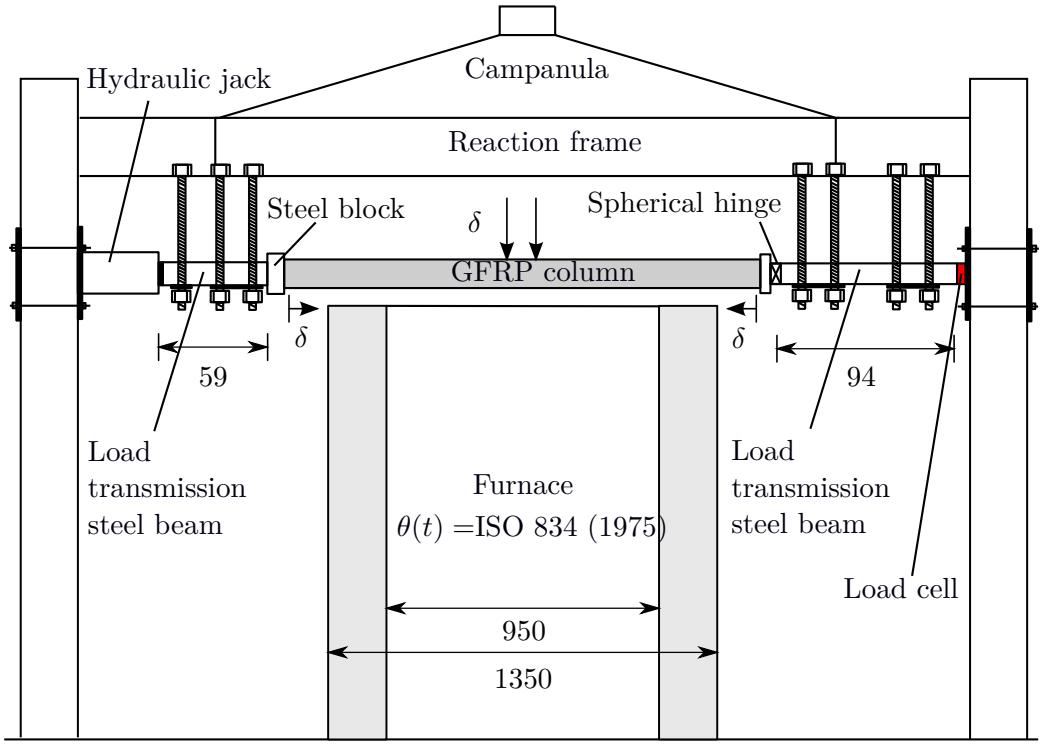

(b) Column setup.

Figure 7.1: Setup of the experimental full-scale fire resistance tests in GFRP (a) beams and (b) columns, where the dimensions are in millimetres (adapted from Morgado *et al.*, 2013a,b).

Cross section	Experimental series	Fire exposure	Fire protection	Load level
Square tubular section	S1	1-face	— / CS	$L/400$ (11.7 kN)
	S2	3-faces	— / CS	$L/400$ (11.7 kN)
	S3	1-face	— / CS	$L/250$ (18.7 kN)
I-section	I2	3-faces	— / CS	$L/400$ (7.4 kN)

Table 7.1: Numerical simulations of the beams.

Cross section	Experimental series	Fire exposure	Fire protection	Load level
Square tubular section	S1	1-face	— / CS	$L/1500$ (55 kN)
	S2	3-faces	— / CS	$L/1500$ (55 kN)
	S3	1-face	— / CS	$L/750$ (110 kN)
I-section	I2	3-faces	— / CS	$L/1500$ (25 kN)

Table 7.2: Numerical simulations of the columns.

tioned properties were computed using the analytical models proposed by Samanta *et al.* (2004), Tracy (2005) and Bai *et al.* (2007). In the present section, a brief description of the models is reported. Further information can be consulted in Fernandes (2009).

Samanta *et al.* (2004) present an analytical model based on the rule of mixtures to estimate the thermal conductivity and the specific heat capacity of GFRP. The material is considered to be formed by the matrix and the fibres. The thermal conductivity of the composite can be computed as a combination of the thermal conductivity of the matrix and the fibres. The specific heat capacity can be computed in the same way. Figure 7.2 represents the evolution of the thermal conductivity and the specific heat capacity as a function of temperature, according to the model of Samanta *et al.* (2004).

Tracy (2005) presents numerical values of thermal conductivity and specific heat capacity based on experimental tests; no analytical expressions are proposed. Figure 7.3a illustrates the evolution of the thermal conductivity as a function of temperature, as suggested by Tracy (2005). It can be observed that the thermal conductivity remains constant until approximately 250 °C (decomposition temperature of the matrix), when it suffers a pronounced reduction due to the protection that the burnt material confers to the virgin material. However, when the state of decomposition is advanced, the char material dissociates and only the fibres remain. Consequently, at around 800 °C, the thermal conductivity increases because the fibres have five times higher thermal conductivity than the matrix.

Figure 7.3b shows the progression of the specific heat capacity as a function of tem-

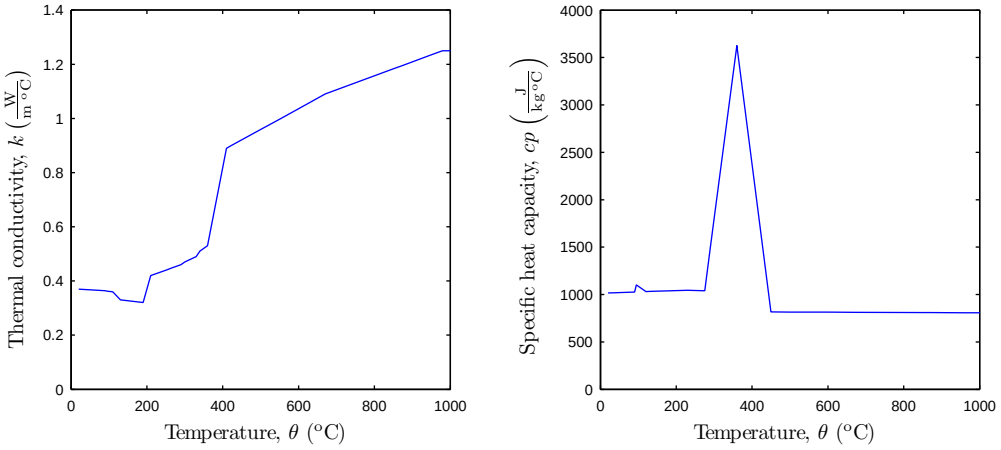

(a) Thermal conductivity. (b) Specific heat capacity.

Figure 7.2: Thermo-physical properties of the GFRP composite as a function of temperature (Samanta *et al.*, 2004).

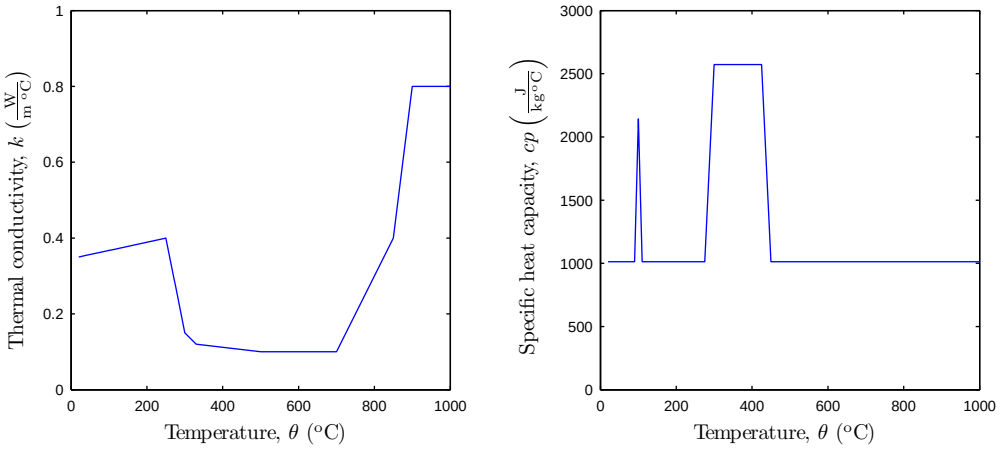

(a) Thermal conductivity. (b) Specific heat capacity.

Figure 7.3: Thermo-physical properties of the GFRP composite as a function of temperature (Tracy, 2005).

perature according to Tracy (2005). In the modelling of the specific heat capacity, the dehydration of the material and the endothermic reaction of the matrix are considered. The specific heat capacity remains constant with the exception of two abrupt increments. The first one occurs at 90-110 °C, due to the evaporation of the water contained in the material. The second one occurs between 275-450 °C, being due to the endothermic reactions that take place during the decomposition of the matrix.

Both Samanta *et al.* (2004) and Tracy (2005) presented models where the thermophysical properties of the composite are obtained as a mixture of the individual properties of the fibres and the matrix. In these models, the delamination of the composite during the burning process is not considered.

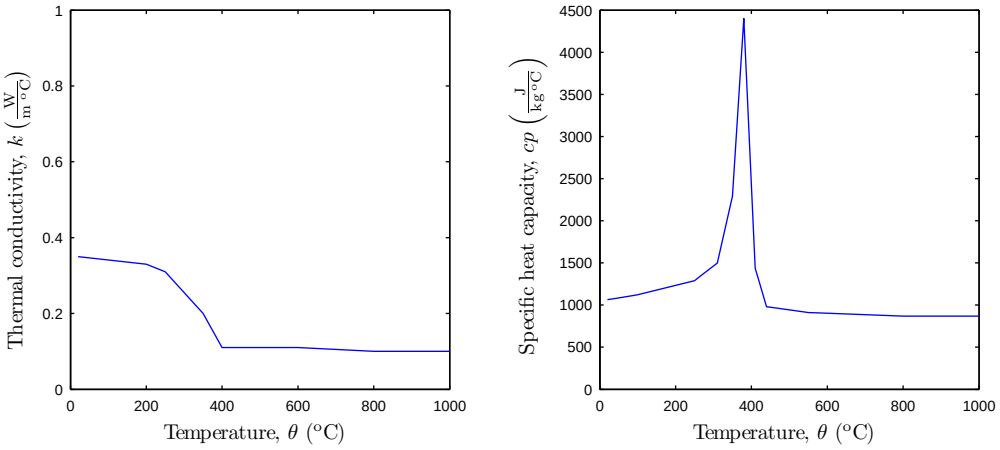

(a) Thermal conductivity. (b) Specific heat capacity.

Figure 7.4: Thermo-physical properties of the GFRP composite as a function of temperature (Bai *et al.*, 2007).

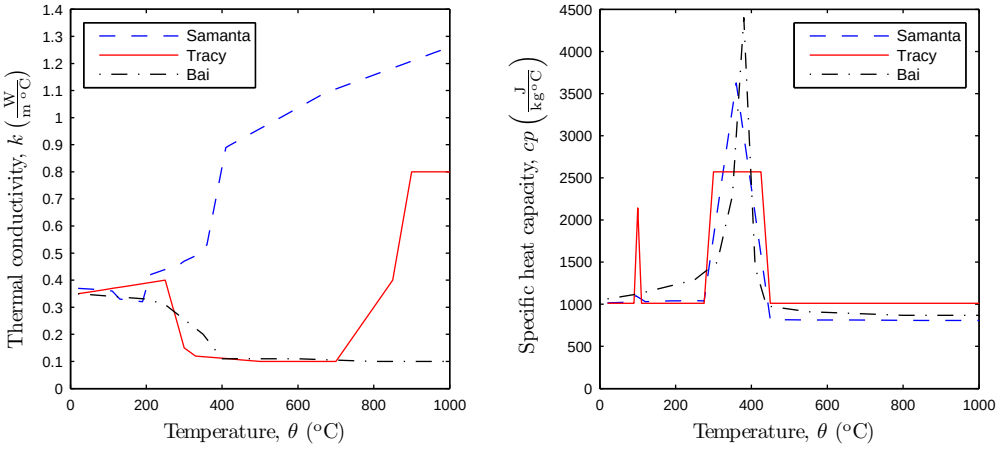

(a) Thermal conductivity. (b) Specific heat capacity.

Figure 7.5: Thermo-physical properties of the GFRP composite as a function of temperature.

Bai *et al.* (2007) presented a model where the composite is assumed to be divided in two layers, whose difference is the degree of degradation of the material. Two states are designated: virgin (v) material, when it is not degraded; and char (c) material, when it is damaged. The thermal conductivity and the specific heat capacity of the composite can be obtained as a combination of those properties for the different degrees of degradation of the composite. Figure 7.4 illustrates the evolution of the thermal conductivity and specific heat capacity proposed by Bai *et al.* (2007).

Figure 7.5 plots the evolution of the thermal conductivity and the specific heat capacity for all the models exposed.

Observing figure 7.5 some important differences in the values of the thermal conduc-

tivity and specific heat capacity provided by the different models available in the literature can be perceived. Regarding the thermal conductivity, the model proposed by Samanta *et al.* (2004) provides significant differences when compared with the others, especially after 200 °C. These are caused mainly by two reasons: (i) the model of Samanta *et al.* (2004) does not consider the gas generated due to the matrix decomposition and allocated in the pores of the matrix (this gas causes a reduction of the thermal conductivity); and (ii) the analytical expressions proposed by Samanta *et al.* (2004) were adapted to the material employed in the related experimental tests, which can be different from that used by Tracy (2005) and Bai *et al.* (2007), which is roughly similar to the one used in the present study. The latter models present similar values of the thermal conductivity, differing mainly after 700 °C, where Tracy (2005) considers an increase of the thermal conductivity due to the delamination and, subsequently, dissociation of the decomposed material.

Regarding the specific heat capacity, in all models the maximum value is in the range of temperatures for which the matrix decomposition occurs, *i.e.*, between 275-450 °C. The maximum value is not coincident in all models, but the area contained under the curve between the mentioned 275-450 °C temperature range is similar. Furthermore, it can be observed that the dehydration of the matrix at 100 °C is only significant in the model of Tracy (2005); in the model of Bai *et al.* (2007) it is not considered.

The internal heat generation, G, of the GFRP was set as null, as the values of the specific heat capacity presented in all models take into account the generation of internal heat due to the water evaporation (except the model of Bai *et al.* (2007)) and matrix decomposition.

The density of the GFRP composite was obtained by means of TGA tests. These tests provide the loss of mass of the composite when heated. The material was tested under air (O) and nitrogen (N) atmospheres at heating rates of 5, 10, 15 and 20 °C/min. Mouritz *et al.* (2006) refer that the results obtained under nitrogen conditions represent with more accuracy the variation of the density in thick composites, as the results obtained in air atmosphere are more representative of the superficial behaviour of the composite and not of the bulk of the material. Hence, in the present thesis the evolution of the density with the temperature considered is the one obtained under nitrogen conditions. Figure 7.6 displays the variation of the density as a function of temperature. A moderate decrease of density takes place until the decomposition temperature (approximately 370 °C) is attained. In this moment, an abrupt reduction of the density occurs due to the decomposition of the matrix and, subsequently, the density remains roughly constant corresponding to the inorganic components of the GFRP composite, *i.e.*, the glass fibres and the fillers.

The emissivity is a temperature-dependent physical property of the material. Samanta *et al.* (2004) suggest a linear variation of the emissivity of the GFRP between 0.75 at 20 °C and 0.95 at 1000 °C. The Eurocode 1 (1995) recommends using an emissivity equal to 0.7 if this material property is unknown. As the only reference found regarding the emissivity of the GFRP is that of Samanta *et al.* (2004), numerical simulations considering both situations were carried out in order to assess their influence in the agreement between numerical and experimental results. The Stefan–Boltzmann's constant is set as $\sigma = 5.669 \cdot 10^{-8}$ W/(m^2 K^4).

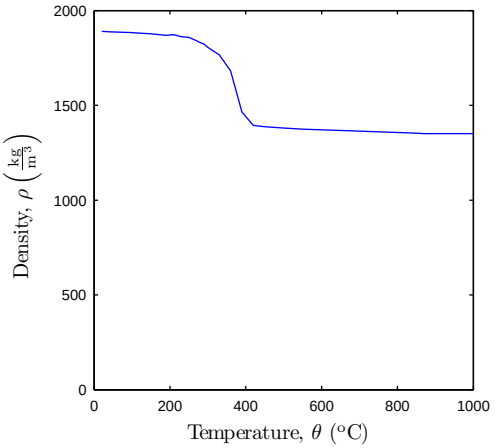

Figure 7.6: GFRP density as a function of temperature.

7.3.2 Air

The thermal properties of the air are assumed as constant and equal to those at 20 °C: $\nu = 1.67 \cdot 10^{-5}$ m^2/s, $k_{11} = k_{22} = 0.0256912$ W/(m °C), $c_p = 1004.592$ J/(kg °C) and $\rho = 1.2$ kg/m^3. The Boussinesq model implemented requires also the thermal expansion coefficient, $\beta = 0.003$ °C^{-1}, and of the gravity force, whose vertical component is set equal to -9.81 m/s^2.

7.3.3 CS boards

The temperature-dependent thermal properties (thermal conductivity and specific heat) of the CS boards were provided by the manufacturer. The temperature-dependent density was obtained experimentally (TGA tests) and reported in Correia (2008). The emissivity is set constant and equal to $\epsilon = 0.7$, following the recommendation of the Eurocode 1 (1995), since no references were found for this material. Figure 7.7 illustrates the variation of the mentioned properties between 20 and 1000 °C.

7.4 Thermal modelling of the tubular profile exposed to fire in 1-face

7.4.1 Preliminary comments

The present section contains different thermal studies regarding the thermal modelling of the GFRP tubular profile exposed to fire in the bottom face. As mentioned, this test was set as reference for the calibration of the mathematical model. The following aspects were studied and discussed:

1. Boundary conditions in the cross section (section 7.4.2).
2. Spatial and temporal discretization (sections 7.4.3 and 7.4.4).
3. Influence in the temperature field of modelling the corners of the cavity as either sharp or round (section 7.4.5).

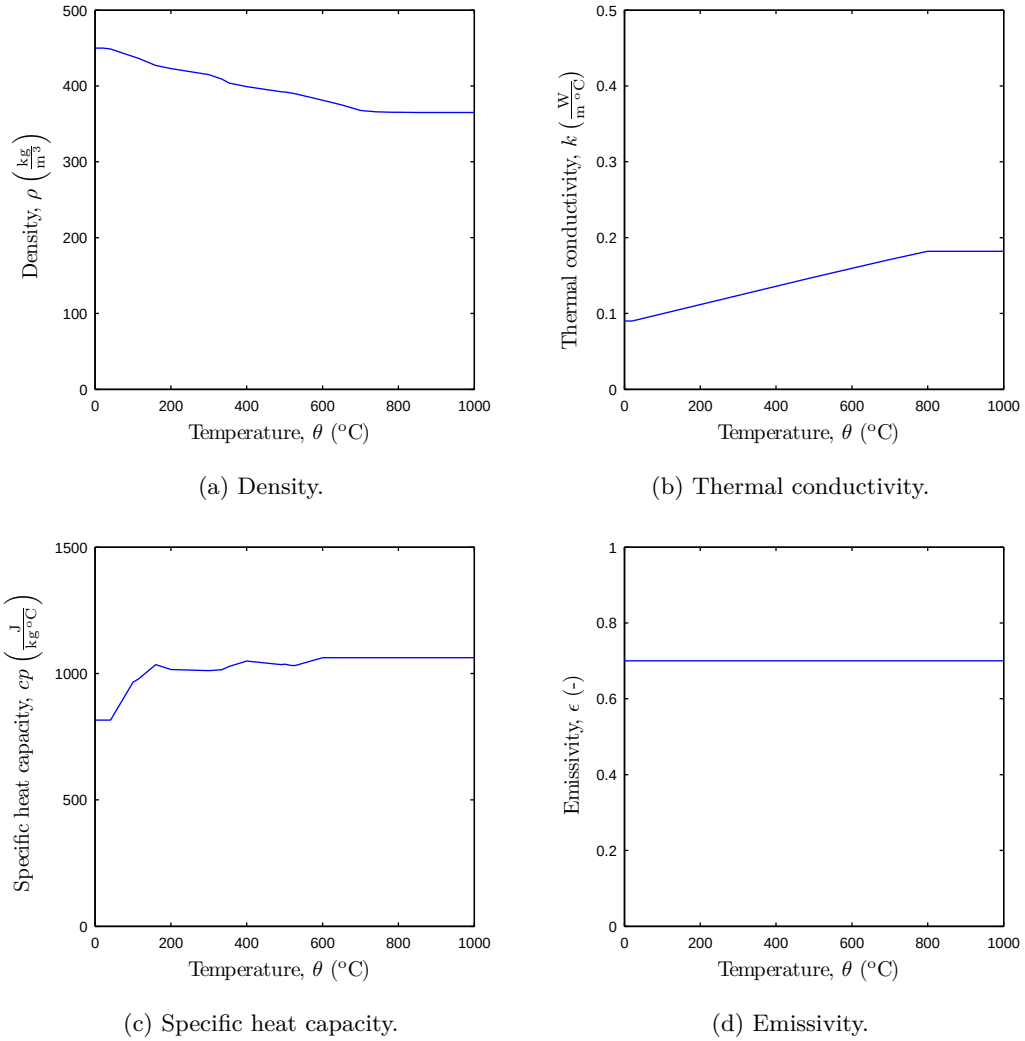

(a) Density.

(b) Thermal conductivity.

(c) Specific heat capacity.

(d) Emissivity.

Figure 7.7: Thermo-physical properties of the calcium silicate as a function of temperature.

4. Influence of the GFRP temperature-dependent thermal properties on the agreement between numerical and experimental temperatures (section 7.4.6).

The conclusions obtained from the studies reported are presented in section 7.4.7 and they will be used on the modelling of the profiles simulated in section 7.5. In all the thermal simulations presented, the stabilization SUPG was employed.

7.4.2 Discussion about the definition of the boundary conditions adopted in the modelling

This section presents the analyses carried out about the boundary conditions used to model the thermal response of the unprotected GFRP tubular profiles. The main goal of this study is to compare the numerical and experimental time-temperature curves in the thermocouples position, thus allowing to evaluate the capacity of the models to reproduce with accuracy the measured results.

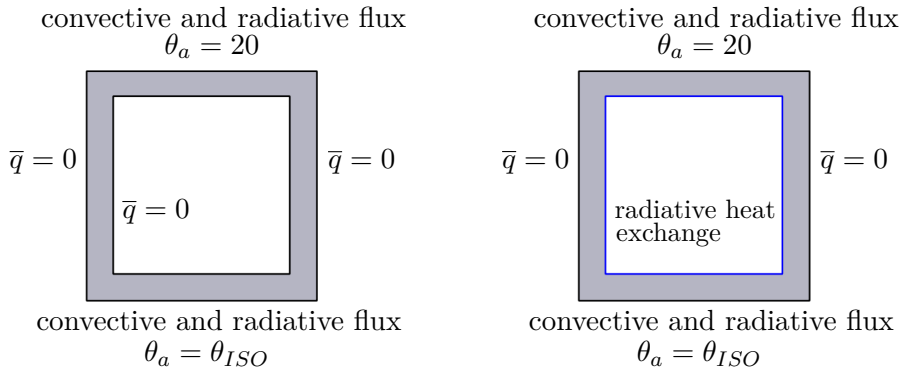

(a) Model (i).

(b) Model (ii).

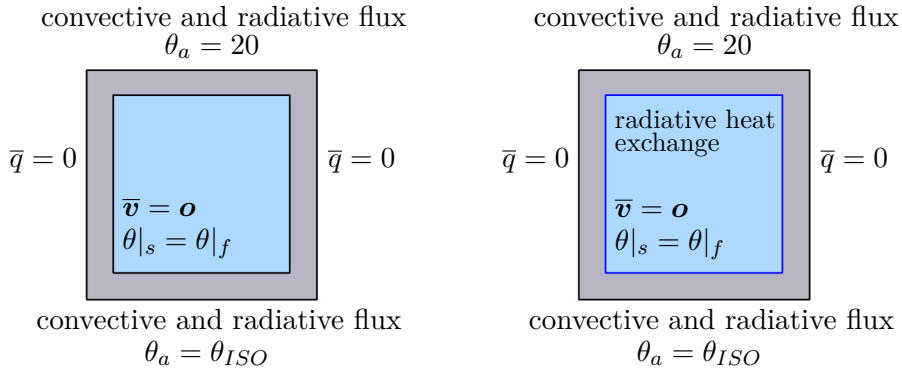

(c) Model (iii).

(d) Model (iv).

Figure 7.8: Thermal boundary conditions prescribed in the different models of the GFRP tubular cross section.

In all the models, convective and radiative heat fluxes are considered in the top and in the bottom faces of the cross section, while the lateral faces are modelled as insulated, *i.e.*, adiabatic. The ambient temperature in the top face is fixed as 20 °C, while in the bottom face the exterior air temperature is time dependent and given by (ISO 834, 1975),

$$\theta_{ISO} = \theta_0 + 345 \log(8t + 1) \tag{7.1}$$

where θ_0 (°C) is the initial temperature and t (minutes) is the time of fire exposure. The following four situations are considered to model the heat exchange in the cavity: (i) adiabatic walls; (ii) radiative heat exchange between the walls of the cavity; (iii) natural convection due to the air located in the cavity; and (iv) both natural convection and radiative heat exchanges in the cavity. In all models the initial temperature is set equal to 20 °C.

The boundary conditions considered in the thermal models are shown in figure 7.8 and can be summarized as follows:

1. Top face: convective and radiative heat flux with constant ambient temperature equal to 20 °C.

2. Bottom face: convective and radiative heat flux considering that the ambient temperature follows the ISO 834 (1975) curve.

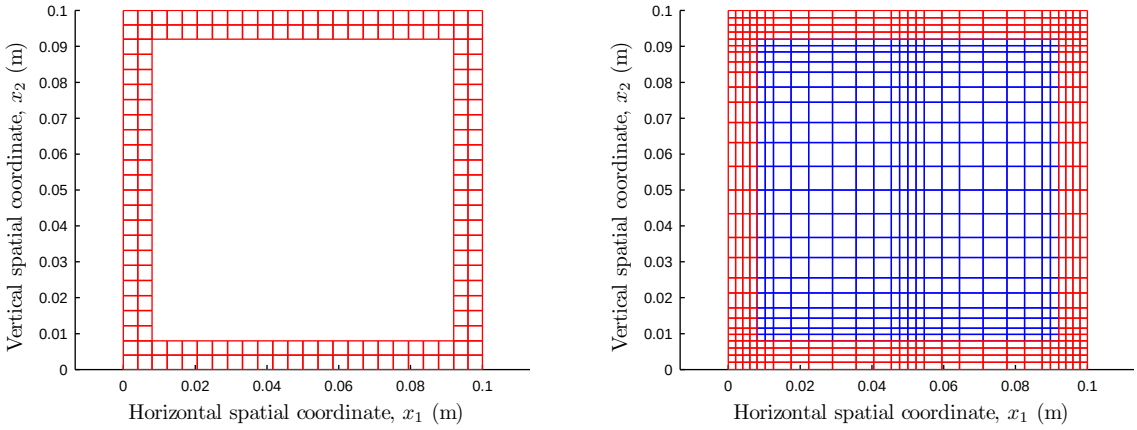

(a) Mesh used in the models (i) and (ii).

(b) Mesh used in the models (iii) and (iv).

Figure 7.9: Meshes designed for the boundary condition study.

3. Lateral faces: insulated.
4. Cavity faces:
   a) Model (i): insulated.
   b) Model (ii): radiative heat exchange between the cavity faces.
   c) Model (iii): natural heat convection, wall condition (null normal velocity) and no-slip condition (null tangential velocity).
   d) Model (iv): both natural heat convection and radiative heat exchange.

The evaluation of the convective heat flux between the cross section and the exterior air required the definition of the convective coefficient, h. This parameter depends on the physical (or geometrical) configuration, the properties of the fluid involved (density, viscosity, thermal conductivity, specific heat and coefficient of thermal expansion), the velocity of the flow and the angle of attack of the flow. The analytical evaluation of h is possible for simple systems. However, in general, it must be determined experimentally. Tracy (2005) presented a test in a GFRP panel subjected to the ISO 834 (1975) standard fire curve and proposed a linear variation of the convective coefficient from 5 to 50 W/(m^2 °C), for temperatures between 20 and 1000 °C. In the present thesis, these values are assumed in the thermal simulations.

In these analyses about the boundary conditions, the thermal properties assumed for the GFRP are those suggested by Tracy (2005) and the emissivity is set as constant.

The different meshes generated are illustrated in figure 7.9. In models (i) and (ii) a mesh with regular 9-nodes quadrilateral elements of 4 mm length was designed, as depicted in figure 7.9a. The mesh contains a total of 880 nodes and 176 quadrilateral elements. The radiative and convective heat flux in the bottom and top faces is imposed in 48 element sides. Additionally, the model (ii) contains 80 one-dimensional radiosity quadratic elements to quantify the internal heat flux exchange between the faces of the cavity. Figure 7.9b shows the mesh used in the models (iii) and (iv). The mesh is formed by 3249 nodes and 784 quadrilateral elements (400 $Q2Q1$ elements in the fluid and 384 9-nodes elements in the solid). Furthermore, 56 element sides are used to impose the

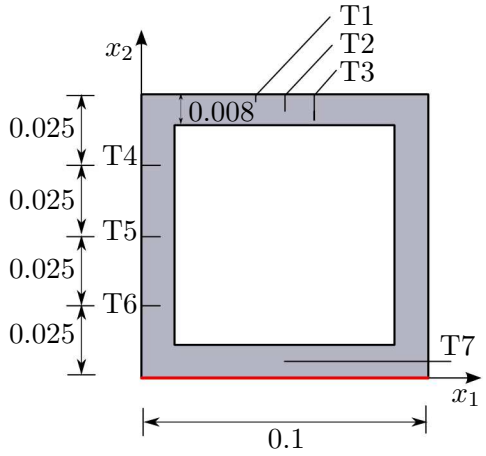

Figure 7.10: Cross section geometry and thermocouples distribution (dimensions in meters).

Thermocouples	x_1 (m)	x_2 (m)
T1	0.040	0.098
T2	0.050	0.096
T3	0.060	0.094
T4	0.004	0.075
T5	0.004	0.050
T6	0.004	0.025
T7	0.050	0.004

Table 7.3: Thermocouples position in the GFRP cross section.

radiative and convective heat exchanges of the GFRP with the ambient and the air of the furnace. Additionally, in the model (iv) 80 one-dimensional radiosity quadratic elements are employed to approximate the radiative heat exchange in the cavity.

The transient nonlinear analyses were carried out using the Euler backward scheme and for a total time of 1800 seconds (30 minutes). The time step is selected as a function of the complexity of the problem. A time step of 20 s is set in the models (i) and (ii), while 1 s is fixed in the models (iii) and (iv). The initial temperature was set at 24 °C, which was the temperature measured at the beginning of the test.

Figure 7.10 shows the geometry of the cross section and the position of the thermocouples and table 7.3 summarizes their coordinates.

Figures 7.11, 7.12, 7.13 and 7.14 present comparative graphs depicting the experimental and numerical temperatures in the position of the thermocouples, the latter having been obtained with the models (i), (ii), (iii) and (iv), respectively. The numerical results are presented until 1800 s (whenever possible), the duration of the experimental test.

Model (i) considers that the walls of the cavity are insulated and, consequently, the heat transfer in the solid occurs exclusively by conduction. This fact explains the relatively high numerical temperatures in the bottom flange and the relatively low temperatures in the top flange, when compared with the experimental results. In fact, for these boundary conditions, numerical temperatures in the top flange present very little variation during the 1800 s. This result points out the importance of considering the heat exchanges between the walls that define the section cavity. Regarding the web, the numerical results provide lower temperatures than those observed experimentally. The elevated temperatures measured in the web can be due to an inefficient insulation of the lateral faces of the profile in the experiments, this being impossible for the model to accurately reproduce them.

Model (ii) considers that the faces of the cavity exchange heat by radiation. It can be observed that the mathematical model is now able to reproduce better the temperature distribution in the top flange, with a good agreement being obtained between the numerical and experimental results. However, in the bottom flange the numerical temperatures are significantly higher than the experimental ones. Furthermore, in the web the model still underestimates the experimental temperature distribution. Overall, when compared with

model (i), the model (ii) provides a better agreement between the numerical temperatures and those measured in all thermocouples, especially in the bottom and top flanges.

Model (iii) takes into account that the air contained in the cavity transmits heat by natural convection. Similarly to model (ii), this model is able to represent the temperature evolution in the top flange, providing slightly higher numerical temperatures between 25 and 30 minutes compared with the experimental results. This fact can be due to the consideration of the Boussinesq hypothesis, when it is only valid for reduced temperature gradients. Consequently, for high temperatures the error induced by this hypothesis can be relevant. In the bottom flange a worse estimation of the temperature distribution compared with model (ii) is observed. In fact, the temperature distribution obtained in the bottom flange is similar to that computed with model (i), the temperatures being slightly lower in this case. In the lateral face, once again, the numerical results underestimate the experimental data.

The previous results point out that the heat transfer in the bottom flange occurs mainly by conduction, while the heating in the top face stems mostly from natural convection and radiative heat exchange between the faces of the cavity walls.

Model (iv) assumes that both natural convection and radiative heat exchange occur simultaneously in the cavity. In this model, the temperature distributions obtained in the top flange are higher than those observed experimentally, but the overall tendency of the numerical results is coherent with the experimental data. The numerical temperature distribution in the bottom flange is closer to the experimental results and the temperatures obtained with this model are lower than those obtained with the other models. In the lateral face, again and due to the reasons already explained, the numerical results underestimate the experimental data. Furthermore, convergence of the solution was only obtained until 1161 s. In order to obtain the complete thermal response, very small time steps are required. This aspect is discussed further in section 7.4.4.

The results also illustrate the high non linearity of the problem solved, where the solution of the model (iv) cannot be calculated as the combination of the solutions in the models (ii) and (iii).

Table 7.4 summarizes the CPU time required to complete the analyses of models (i) and (ii) — using the mesh presented in figure 7.9a — with a time step of 20 s and a total time of 3600 s (1 hour). Moreover, the same analyses, but using constant thermophysical properties, were also performed and the respective required CPU time is included in the table. During the numerical tests carried out, a significant increase of the CPU time required in the computations was observed when the radiative heat exchange between the faces of the cavity is considered (from 19 min to 841 min) and when the GFRP thermal properties are temperature-dependent (from 19 min to 64 min). It can be observed that when nonlinear material is considered simultaneously with radiative heat exchange between the faces of the cavity, a CPU time increment from 19 min to 1647 min occurs.

In all models, the quadratic convergence of the algorithm in the asymptotic limit of the solution was guaranteed due to the use of the Newton–Raphson method. This is an important factor to reduce the computational time required to run the model. Figure 7.15 depicts the value of the dimensionless norm of the residual vector at each iteration in the first six time steps in model (ii).

Overall, the most accurate model regarding the simulation of the temperature field in the cross section was model (ii). However, this model is not realistic (as in the cavity there is fluid and convective and radiative heat exchange between the walls is expected) and could not represent accurately the experimental results obtained in the protected

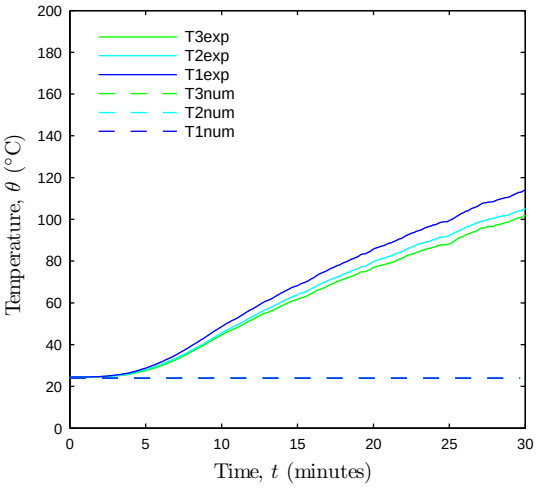

(a) Top flange.

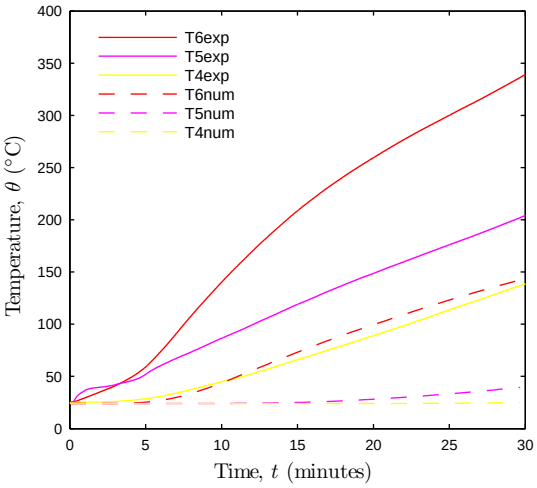

(b) Web.

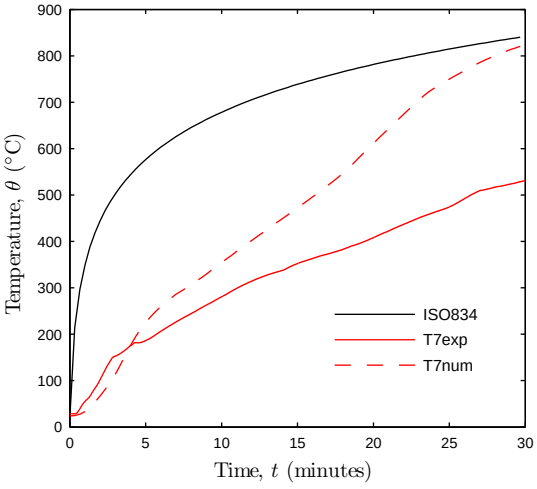

(c) Bottom flange.

Figure 7.11: Temperature in the thermocouples obtained with model (i).

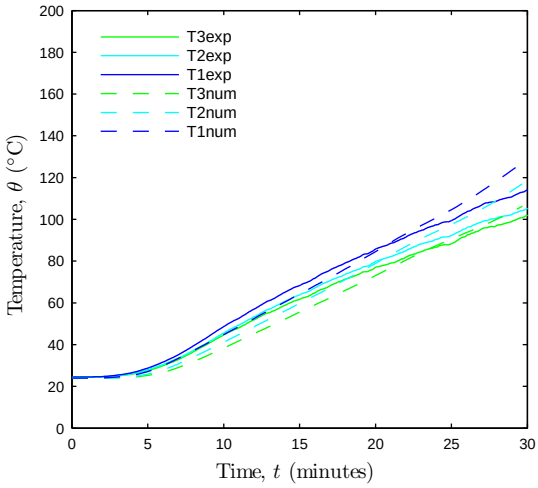

(a) Top flange.

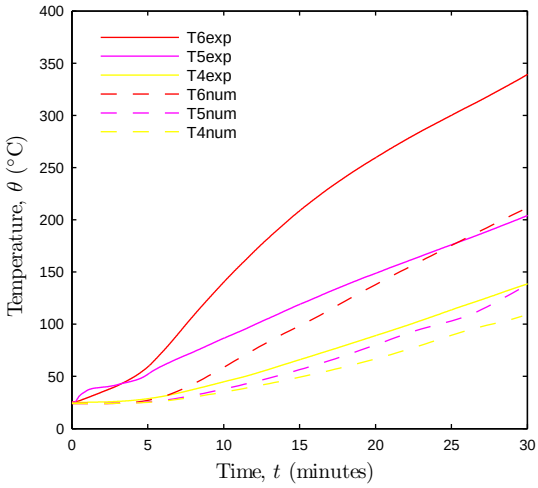

(b) Web.

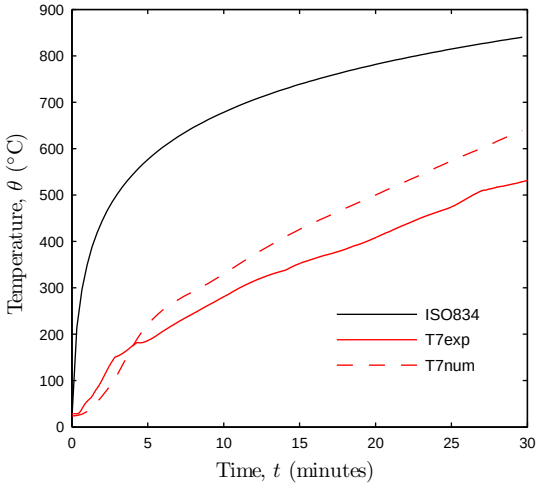

(c) Bottom flange.

Figure 7.12: Temperature in the thermocouples obtained with model (ii).

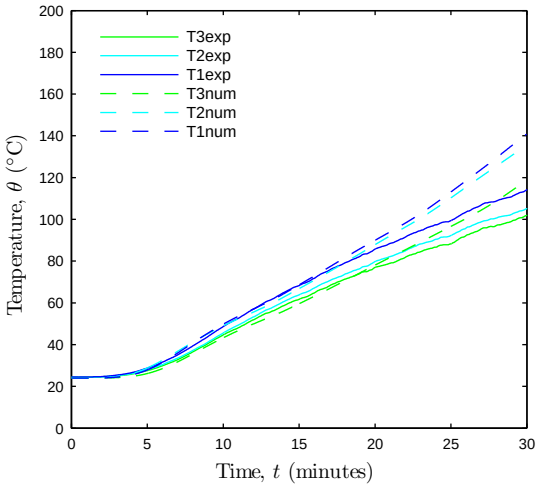

(a) Top flange.

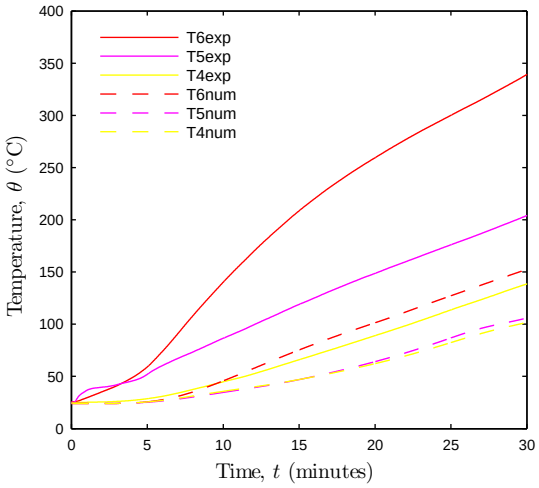

(b) Web.

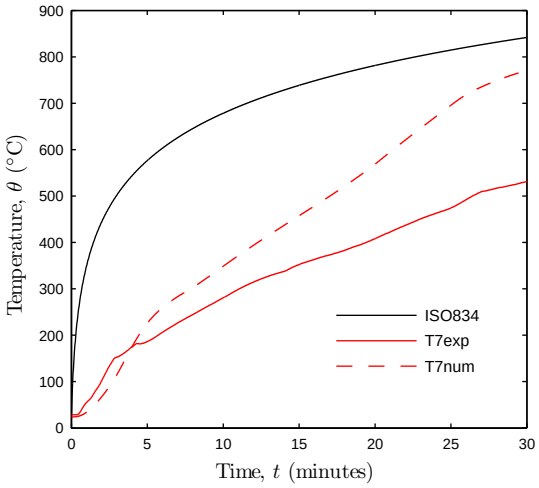

(c) Bottom flange.

Figure 7.13: Temperature in the thermocouples obtained with model (iii).

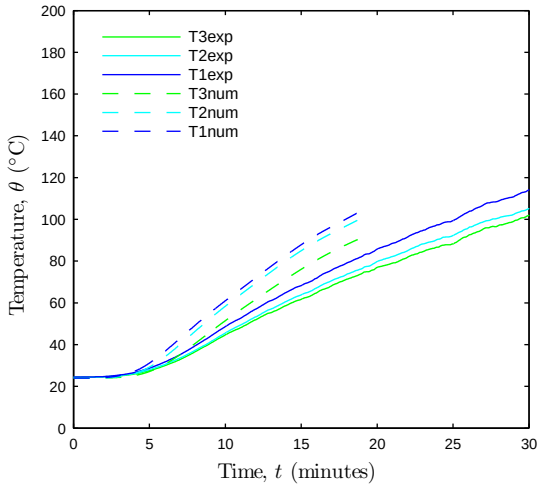

(a) Top flange.

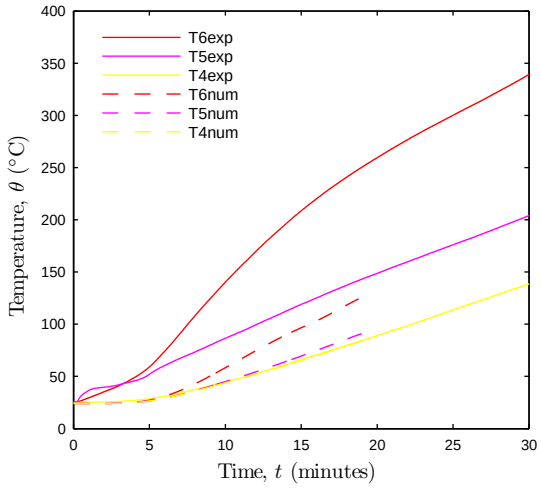

(b) Web.

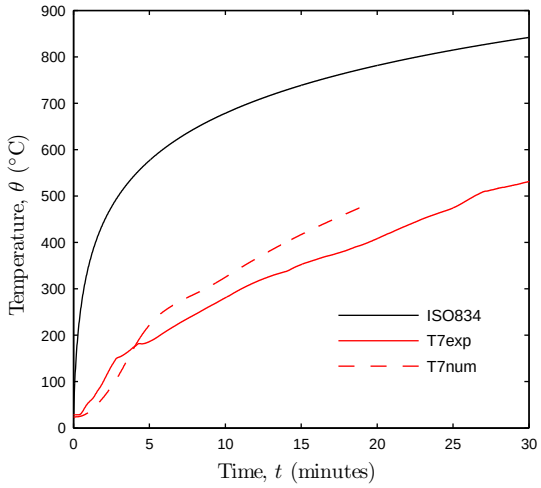

(c) Bottom flange.

Figure 7.14: Temperature in the thermocouples obtained with model (iv).

Thermophysical properties	Boundary conditions in the cavity	CPU time (min)
Constant	Adiabatic	19
	Radiative heat flux	841
Nonlinear	Adiabatic	64
	Radiative heat flux	1647

Table 7.4: Computational CPU time for different models.

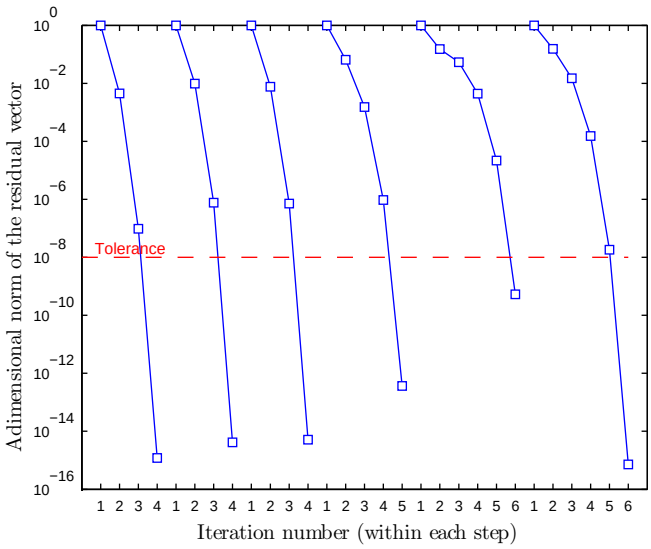

Figure 7.15: Convergence at the first six time steps in model (ii).

tubular profile with the bottom face subjected to fire (see appendix G). Consequently, model (iv) was considered more appropriate for the numerical simulations presented in the following.

7.4.3 Spatial discretization

The present section reports a study about the spatial discretization of the unprotected tubular cross section. This analysis was performed to assess if the results obtained can be considered independent of the mesh employed, *i.e.*, if spatial the discretization error tends to zero with the grid refinement.

In the numerical tests carried out, the boundary conditions defined in model (iv) were considered. The thermal properties of the GFRP are those suggested by Tracy (2005), considering a linear variation of the emissivity with the temperature. The transient nonlinear simulations were carried out using the Euler backward scheme, a total time of 1800 seconds (30 minutes) and a constant time step equal to 1 second.

Four non-regular meshes were tested, which are depicted in figure 7.16. All meshes are formed with 9-nodes quadrilateral elements in the solid, $Q2Q1$ elements in the fluid and one-dimensional quadratic radiosity elements. In terms of total nodes and elements, mesh 1 (the coarsest) has 1449 nodes and 364 elements, mesh 2 has 3409 nodes and 864 elements, mesh 3 contains 7465 nodes and 1784 elements, and mesh 4 (the most refined) has 13089

Meshes properties	Mesh 1	Mesh 2	Mesh 3	Mesh 4
Number of elements in the solid	224	384	864	1536
Number of elements in the fluid	100	400	900	1600
Number of radiosity elements	40	80	120	160
Total number of elements	364	864	1784	3296
Total number of nodes	1449	3409	7465	13089

Table 7.5: Number of nodes and elements in the meshes considered for the spatial discretization study.

Compared meshes	T1	T2	T3	T4	T5	T6	T7
Mesh 2	0.947	2.789	0.468	0.487	0.458	0.223	0.244
Mesh 3	(2.4%)	(6.4%)	(0.9%)	(1.4%)	(1.3%)	(0.5%)	(0.1%)
Mesh 2	1.012	1.191	0.411	0.521	0.471	1.925	0.296
Mesh 4	(2.6%)	(2.6%)	(0.8%)	(1.5%)	(1.4%)	(4.2%)	(0.1%)
Mesh 3	0.065	1.598	0.057	0.034	0.013	2.148	0.052
Mesh 4	(0.2%)	(3.5%)	(0.1%)	(0.1%)	(0.04%)	(4.7%)	(0.02%)

Table 7.6: Difference between the temperatures in the thermocouples at $t = 500$ s.

nodes and 3296 elements. Table 7.5 summarizes the number of nodes and elements in the different meshes.

Figure 7.17 illustrates the evolution of numerical temperatures in the thermocouples locations obtained with the different meshes.

It can be observed that the temperature evolution obtained with the different meshes is similar, the main difference being the last computational time converged (marked with an $\times$ in the graphics). The last converged time of mesh 1 is 155 s, probably because the mesh is too coarse to represent correctly the fluid flow in the cavity. Hence, this mesh was discarded. Regarding meshes 2, 3 and 4, the last converged time is 1058 s, 630 s and 504 s, respectively. In order to evaluate the difference of the temperature in the thermocouples computed using these different meshes, a common computational time of 500 s (8.3 minutes) was selected. Table 7.6 summarizes the absolute difference between the temperatures in the thermocouples computed with those meshes. The maximum difference between meshes 2 and 3 occurs in thermocouple T2, while the maximum difference between meshes 2 and 4 occurs in thermocouple T6. The values in parentheses represent the percentage difference regarding the finest mesh.

The difference in the final converged computational time between the meshes 2, 3 and 4 is associated to the time step size required. Refined meshes require, in general, smaller times steps than coarser meshes for the calculation of a converged solution.

Figure 7.18 illustrates the velocity and temperature fields computed with mesh 2 at different times (250, 500, 1000 and 1058 s). It can be observed that at $t = 1058$ s small convective cells appear in the bottom corners of the cross section.

Figure 7.18g shows the formation of multiple vortex in the vicinity of the bottom face of the cavity that reduce the dimensions of the Bénard cells and separate them from the bottom face. Figure 7.18h depicts the formation of multiples plumes, which can be induced

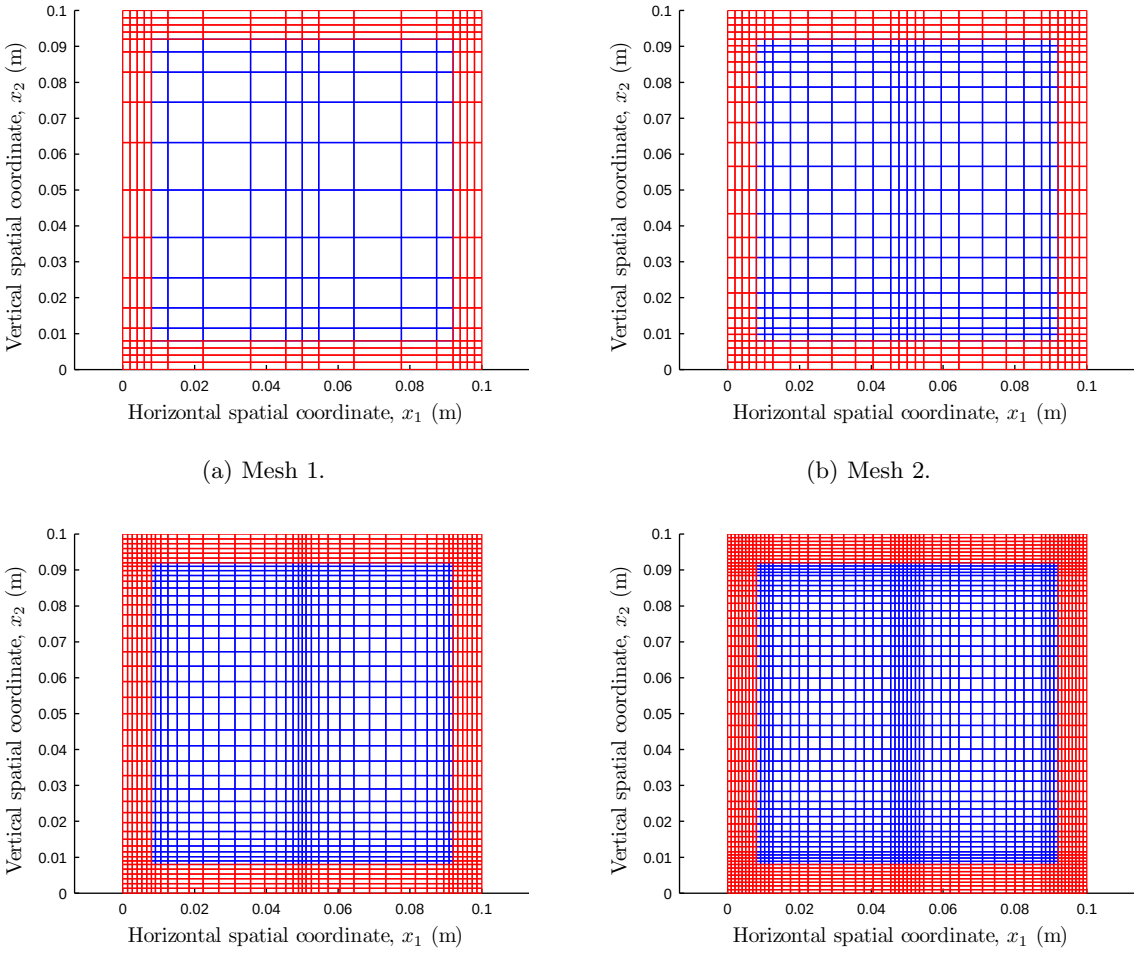

(a) Mesh 1.

(b) Mesh 2.

(c) Mesh 3.

(d) Mesh 4.

Figure 7.16: Meshes designed for spatial discretization study.

due to the effect of the radiative heat exchange between the cavity faces. A similar effect was experimentally observed and referred in the works of, for example, Sparrow *et al.* (1970) and Solomon and Gollub (1990). This effect is also observable in the numerical results computed using the meshes 3 and 4.

Due to the complexity of the problem and the objective of the analysis (to reproduce the temperature distribution in the thermocouples), it was considered that the relative differences obtained in the temperatures for meshes 2 to 4 were acceptable and, consequently, mesh 2 was adopted for the thermal modelling of the tubular GFRP profiles, as the computational time required to compute one time step is lower than the time required for the refined mesh 4.

In order to guarantee that the spatial discretization error tends to zero in all the cases analysed in section 7.5, the spatial discretization study was extended for the unprotected tubular cross section exposed to fire in 3-faces. The geometry of the cross section studied and the thermocouples location are depicted in figure 7.19. Table 7.7 provides the position of the thermocouples.

In the faces exposed to fire (bottom face and 3/4 of the lateral faces), convective

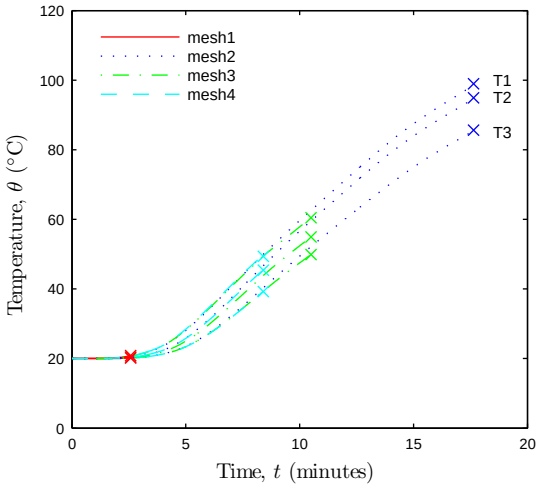

(a) Top flange.

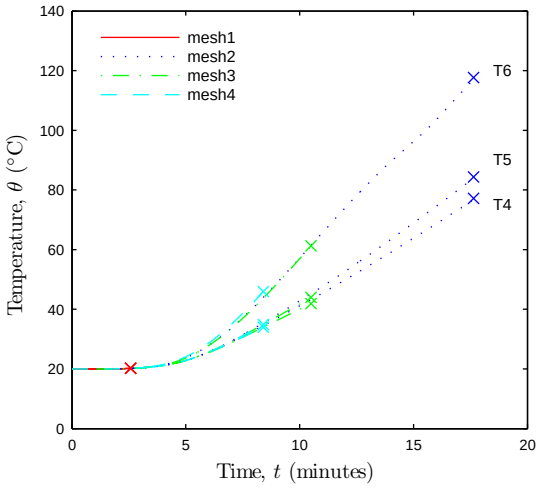

(b) Web.

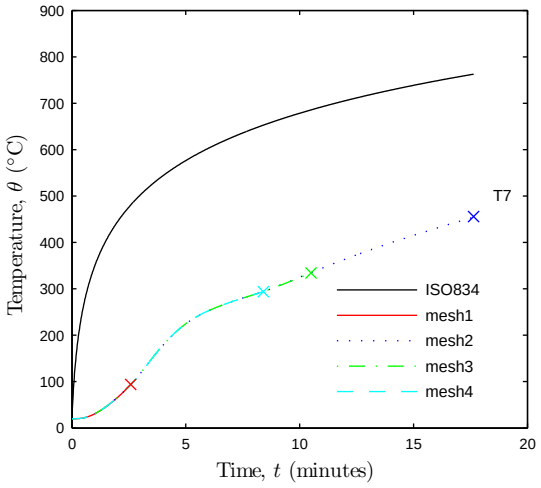

(c) Bottom flange.

Figure 7.17: Comparative graphics of the temperature evolution in the thermocouples position obtained using different meshes.

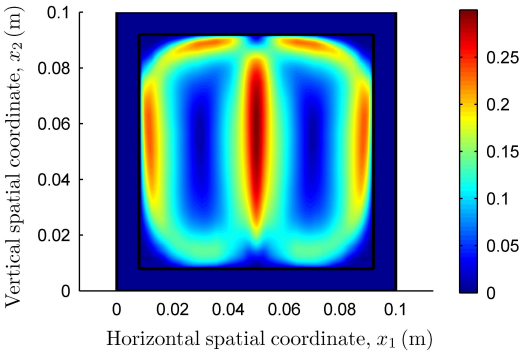

(a) Resultant velocity field, $t = 250$ s.

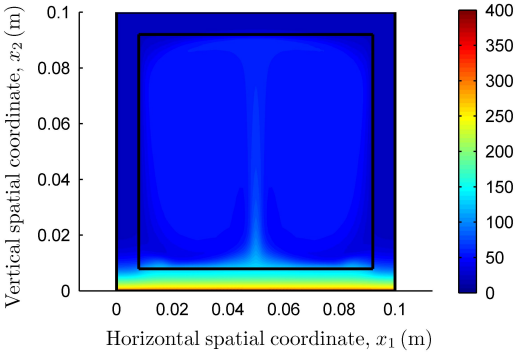

(b) Temperature field, $t = 250$ s.

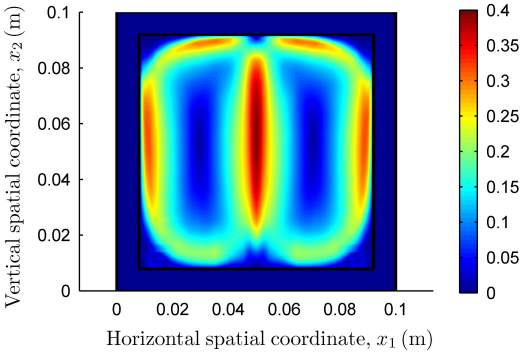

(c) Resultant velocity field, $t = 500$ s.

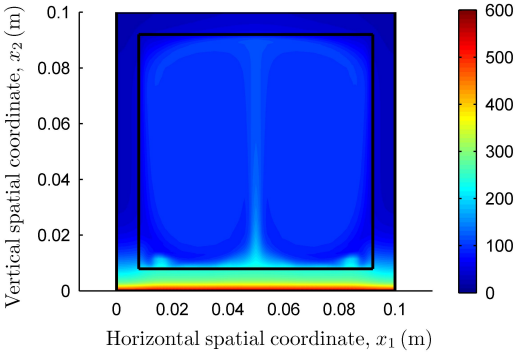

(d) Temperature field, $t = 500$ s.

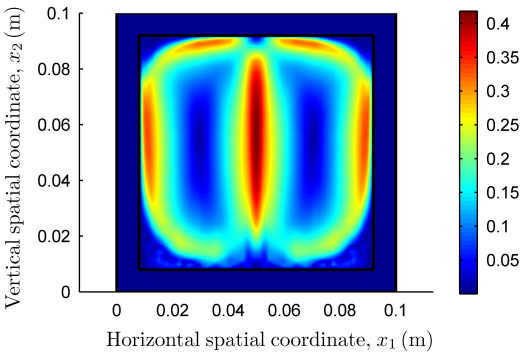

(e) Resultant velocity field, $t = 1000$ s.

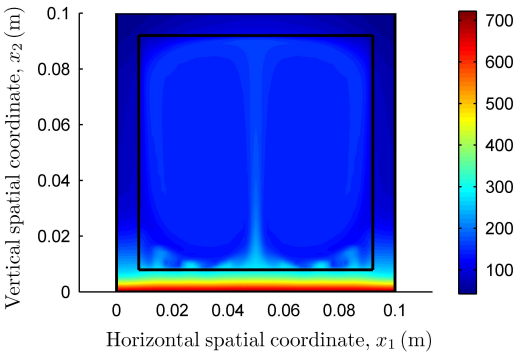

(f) Temperature field, $t = 1000$ s.

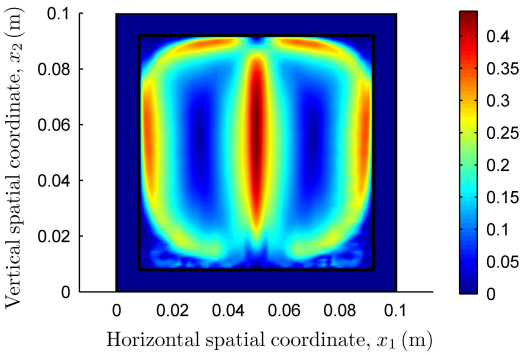

(g) Resultant velocity field, $t = 1058$ s.

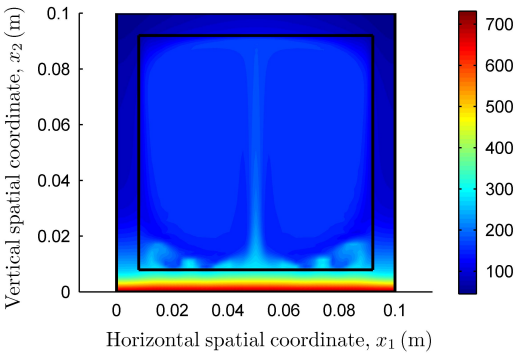

(h) Temperature field, $t = 1058$ s.

Figure 7.18: Velocity resultant and temperature field at different instants.

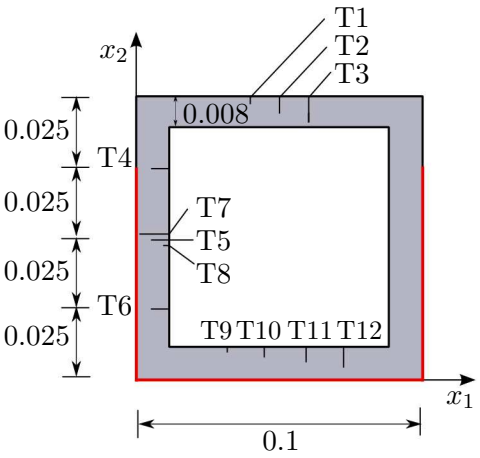

Figure 7.19: Cross section geometry and thermocouples distribution of the GFRP tubular cross section exposed to fire in 3-faces (in meters).

Thermocouples	x_1 (m)	x_2 (m)
T1	0.04	0.098
T2	0.05	0.096
T3	0.06	0.094
T4	0.004	0.075
T5	0.004	0.05
T6	0.004	0.025
T7	0.007	0.05
T8	0.001	0.05
T9	0.05	0.007
T10	0.05	0.005
T11	0.05	0.003
T12	0.05	0.001

Table 7.7: Thermocouples position in the GFRP tubular cross section for 3-faces fire exposure.

and radiative heat flux were prescribed, with the exterior temperature varying with time according to the nominal curve reported in the ISO 834 (1975) standard. The top 2.5 cm of the lateral faces were considered insulated, as in the experiment. In the top face, convective and radiative heat flux were considered, the ambient temperature being equal to 20 °C. In the cavity, natural convection and radiative heat exchange were applied. Figure 7.20 illustrates the boundary conditions defined in the model.

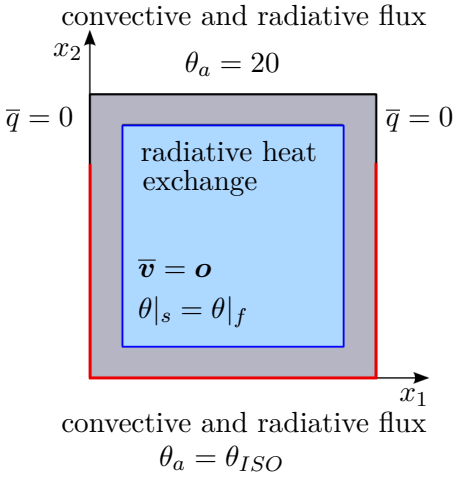

Figure 7.20: Unprotected tubular profile partially exposed to fire in 3-faces.

Numerical simulations were carried out considering the meshes 2, 3 and 4 depicted in figure 7.16. Figure 7.21 represents the temperature evolution in the thermocouples obtained with the three meshes.

It can be seen that the temperature in the thermocouples obtained with all the meshes

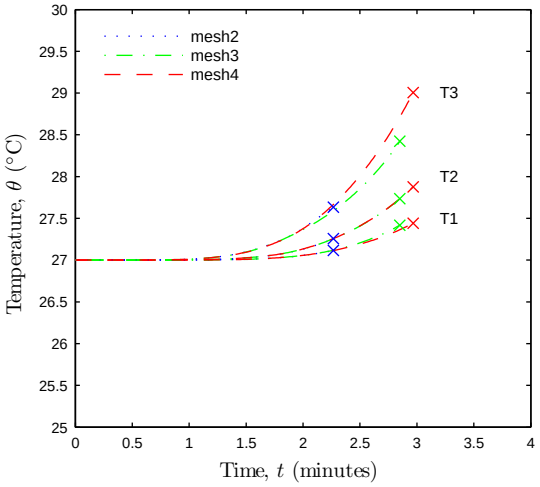

(a) Top flange.

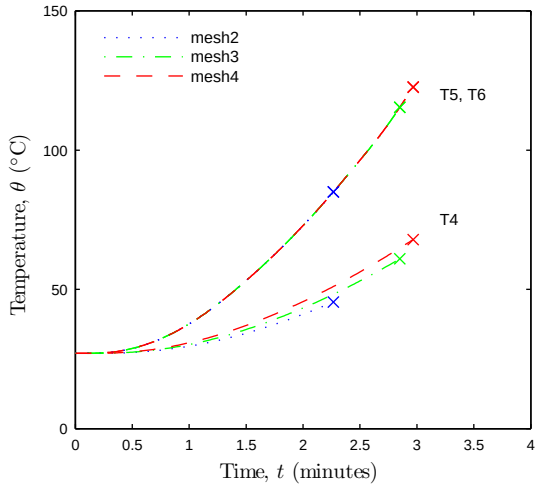

(b) Web.

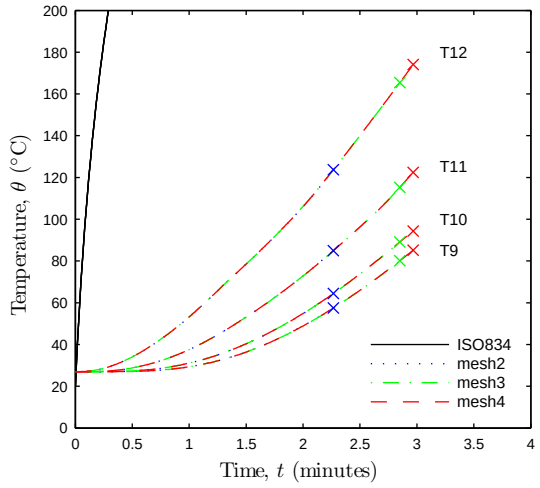

(c) Bottom flange.

Figure 7.21: Temperature evolution in the thermocouples position obtained using different meshes in a tubular cross section partially subjected to fire in 3-faces.

is almost coincident, the maximum differences being obtained in the thermocouples situated in the top flange and in the thermocouple T4. The radiative heat exchange between the faces of the cavity depends on the mesh, as in refined meshes more Gauss points are considered for the evaluation of the geometrical terms given by equation (3.57) and the convergence of the radiosity equation is slower. Consequently, in the thermocouples where the heat transfer is mainly by conduction (all thermocouples in the bottom face and thermocouples T5 and T6 in the lateral face) the temperature values computed with the different meshes are similar, while some differences can be found in the thermocouples that are more dependent on the natural convective heat flux and radiative heat exchange (all thermocouples in the top flange and thermocouple T4 in the lateral face). The difference in the last converged solution is associated to the time step size required to obtain a converged solution. The time step size needed depends on the mesh size. This is further discussed in the following section.

7.4.4 Temporal discretization

This section reports a study about the dependency of the numerical results on the time step size. Nonlinear transient analyses using mesh 2 and the Euler backward scheme, in order to guarantee an unconditionally stable algorithm, are performed by defining different time step values.

In these calculations, the GFRP conductivity and specific heat capacity were considered temperature-dependent according to the model of Bai *et al.* (2007). The density was also temperature-dependent, while the emissivity was set as constant and equal to 0.7. Three constant time steps of 1, 5 and 10 seconds were considered. Figure 7.22 illustrates the temperature evolution in the thermocouples locations, using the different time steps.

For the time steps of 1 and 5 seconds, the last computational time for which a converged solution is attained is similar (1421 and 1400 s, respectively), while for the time step of 10 seconds, it was significantly different and lower (740 s). After those instants, the temperature and velocity variation in the fluid is too elevated and, consequently, a smaller time step size is required in order to obtain a converged solution.

The Courant number is a dimensionless number that relates the temporal and spatial discretization. The elemental Courant number in a two-dimensional domain can be calculated as,

$$Cu^{(e)} = \left(\frac{v_1^{(e)}}{\Delta x_1} + \frac{v_2^{(e)}}{\Delta x_2} \right) \Delta t \tag{7.2}$$

where $Cu^{(e)}$ is the Courant number in a generic element (e), $v_1^{(e)}$ and $v_2^{(e)}$ are the velocities along the axes x_1 and x_2, Δx_1 and Δx_2 are the two main dimensions of the element and Δt is the time step size.

In general, low Courant numbers are required to solve highly nonlinear problems, decreasing the oscillations and improving the accuracy of the solution. When using explicit methods, the Courant number must be lower than 1 for stability reasons, but when using implicit methods, higher Courant number maybe adopted, depending on the complexity of the problem (FLUENT, 2016). This topic is further developed in appendix F.

By comparing the temperature evolution in the thermocouples until 740 s (last common time), no significant differences can be observed. Hence, the time discretization error can be considered negligible for the selected time steps.

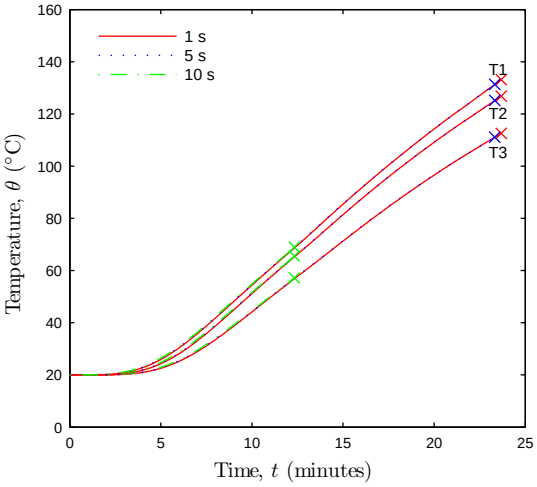

(a) Top flange.

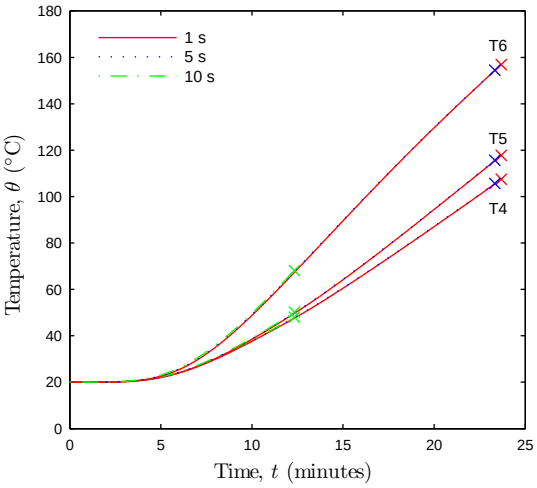

(b) Web.

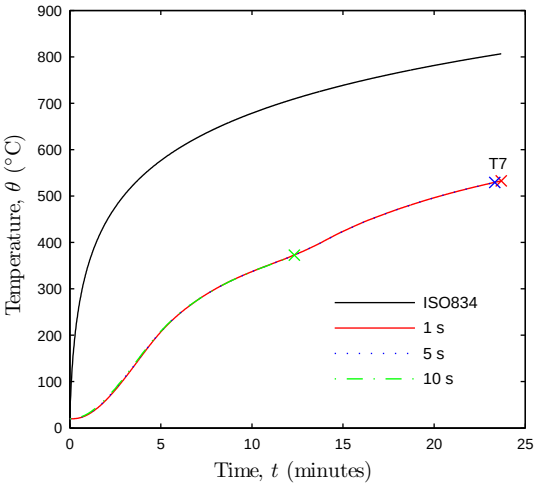

(c) Bottom flange.

Figure 7.22: Temperature evolution in the thermocouples position obtained using different constant time steps.

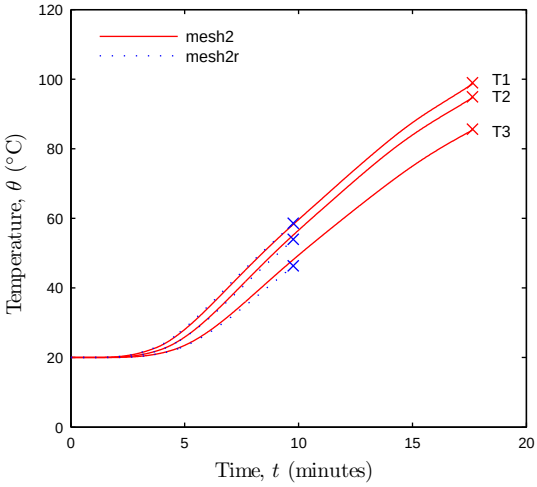

(a) Top flange.

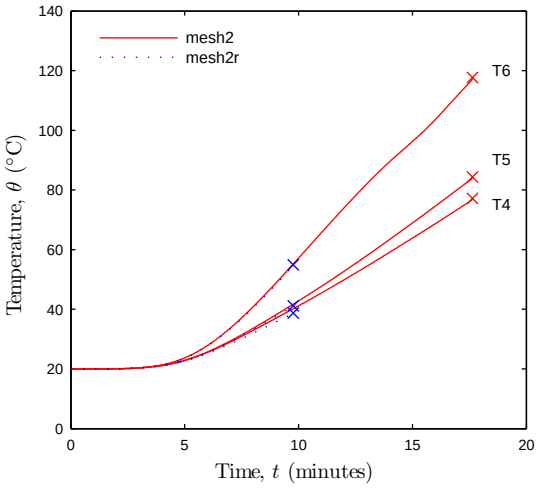

(b) Web.

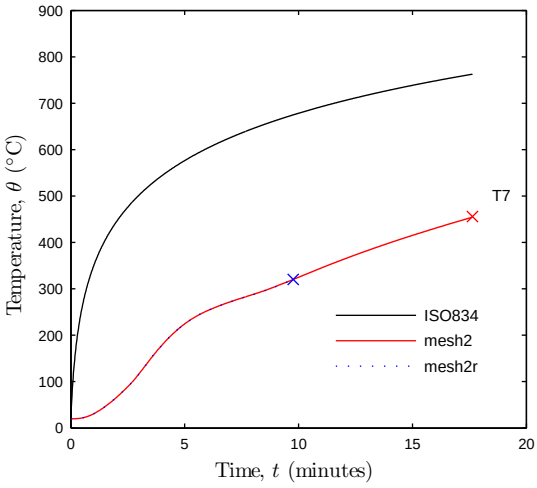

(c) Bottom flange.

Figure 7.23: Temperature evolution in the thermocouples position obtained using mesh 2 and mesh 2r.

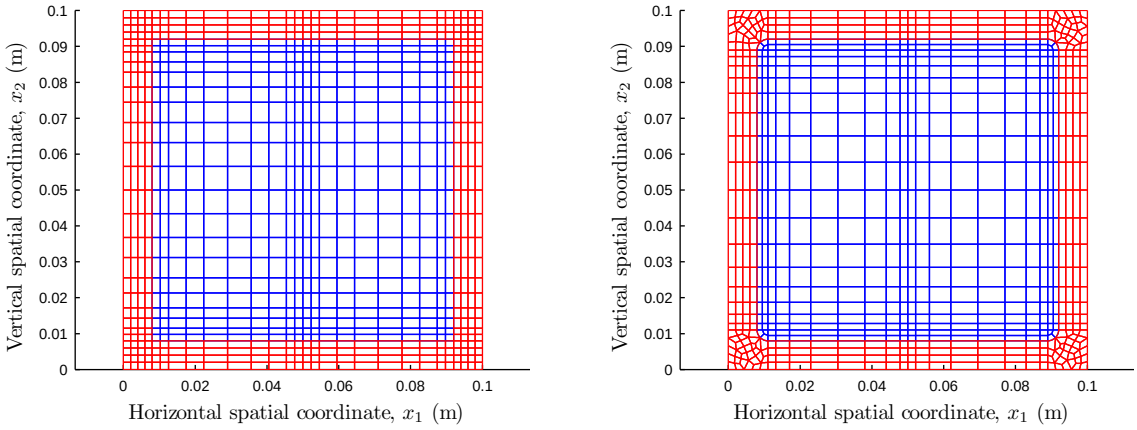

(a) Mesh 2.

(b) Mesh 2r.

Figure 7.24: Meshes designed for spatial discretization study.

In order to avoid convergence problems due to the time step size, the adaptive time step scheme presented in section 5.3.3 must be employed. However, very reduced time step sizes are needed to obtain the complete thermal response of the cross section. This fact implies an elevated CPU time and, consequently, an optimized algorithm should be implemented[1] to perform the analysis until 3600 s. In the following GFRP thermal simulations a constant time step of 1 second is employed.

7.4.5 Modelling of the cavity geometry

The real GFRP cross section consists of a square tube with 3 mm radius round corners in the cavity. In order to simplify the geometry of the cross section, these corners were considered sharp. However, this modification of the geometry introduces four points where the radiosity field is singular. This may cause convergence problems and provide incorrect temperature fields in the vicinity of the singularity. In order to evaluate the consequences of the simplification of the cavity geometry, a mesh equivalent to mesh 2 (in terms of total number of nodes, elements and spatial distribution of the elements) was generated, but with rounded corners, mesh 2r. Figure 7.24 illustrates both meshes compared in this analysis.

The GFRP conductivity and specific heat capacity were computed using the model of Tracy (2005) and both density and emissivity were considered temperature-dependent. Figure 7.23 illustrates the temperature evolution in the thermocouples obtained with both meshes. It can be observed that only slight differences in the thermocouples positioned in the top flange are observable, which are considered acceptable (sufficiently low).

However, the consideration of the circular corners in the cavity introduces a variation in the flow of the air inside the cavity, potentiating the formation of vortex in the vicinity of

[1] Recently, Paipuri (2016) implemented the thermal FE formulation presented here in FORTRAN. The complete thermal response of the unprotected beam exposed to fire in 1-face was obtained by using the adaptive time step algorithm reported in section 5.3.3. Depending on the complexity of the calculation, at certain instants, time steps of 0.01 s or even lower were required. The results obtained can be consulted in appendix F.

the bottom face and, using a 1 second constant time step, the last time where a converged solution is computed is lower than in the mesh 2.

Considering that the objective of the numerical study is to simulate the temperature evolution in the thermocouples and that, with both meshes, the results are similar and the results of mesh 2 seem not to be affected by the singularities, mesh 2 was chosen to carry out the thermal simulations of the tubular GFRP profiles.

7.4.6 Discussion about the thermophysical properties of the GFRP

In section 7.3, three analytical models to evaluate the temperature-dependent thermal conductivity and specific heat capacity of the GFRP material were presented. In the current section, numerical simulations carried out with the different GFRP thermal properties are reported, in order to determine which model is able to simulate better the experimental results. Therefore, three nonlinear transient analyses of the tubular GFRP profiles were carried out considering the thermal conductivity and specific heat capacity computed with the models proposed by Samanta *et al.* (2004), Tracy (2005) and Bai *et al.* (2007).

The numerical simulations were performed using mesh 2. A fully implicit analysis with a time step equal to 1 second was carried out in all models.

Figure 7.14 (page 161) illustrates the numerical results obtained considering the model of Tracy (2005) and a constant emissivity. Figures 7.25 and 7.26 depict the experimental and numerical temperatures, the latter computed using the thermal properties suggested by Samanta *et al.* (2004) and Bai *et al.* (2007), respectively.

The model of Samanta *et al.* (2004) overestimates the temperatures in the bottom and top flanges, while in the web the temperatures are underestimated. Furthermore, this model only allows obtaining a converged solution until $t = 521$ s, due to the high temperature gradient in the cavity.

Both Tracy's and Bai's models provide more accurate results in the bottom flange, compared with Samanta's model. The temperatures in the web are in both cases underestimated, even if Bai's model is slightly more accurate. The numerical temperatures evolution in the top flange provided by both models are higher than the experimental ones, with Tracy's model leading to more accurate results. The last converged times were 1160 s and 1421 s for the Tracy's and Bai's models, respectively.

In the previous results the emissivity was set constant and equal to 0.7, which corresponds to the recommendation of the Eurocode 1 (1995) when the emissivity of the material is unknown. However, further simulations were carried out using Tracy's and Bai's models and considering that the emissivity is temperature-dependent (Samanta *et al.*, 2004). Figures 7.27 and 7.28 depict the temperature results obtained in the thermocouples under these assumptions.

The results obtained with constant emissivity and temperature-dependent emissivity are roughly similar. In general terms, when the emissivity is set as temperature-dependent, higher numerical temperatures are obtained in the web and top flange, while lower temperatures are obtained in the bottom flange. Regarding the last computational time for which a converged solution is attained, they were 1282 s for the Bai's model and 1058 s for the Tracy's model, both with temperature-dependent emissivity.

Based on the results reported above, it was considered that the best model to evaluate the thermal properties of the GFRP is that of Tracy with temperature-dependent emissivity. This was the model used in the thermal simulations presented in the following.

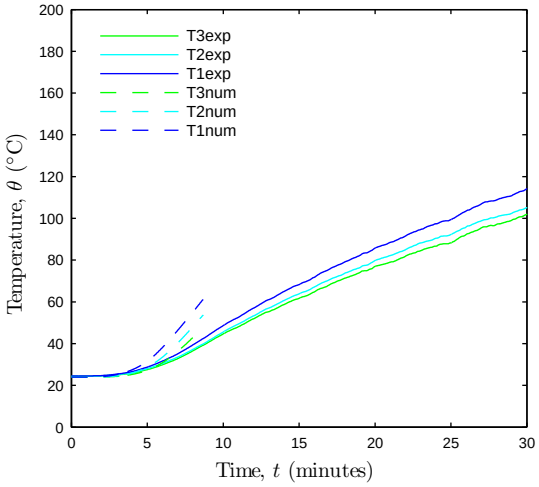

(a) Top flange.

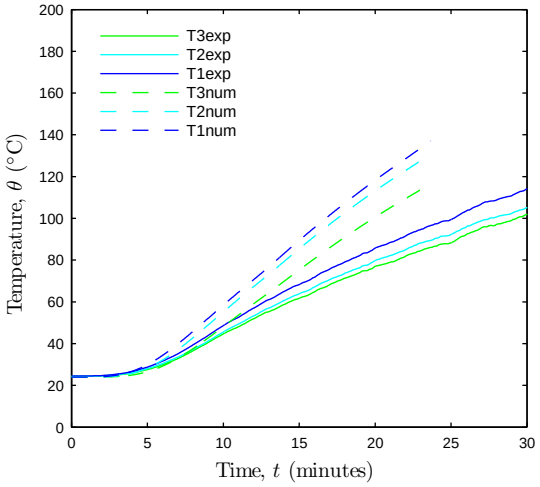

(a) Top flange.

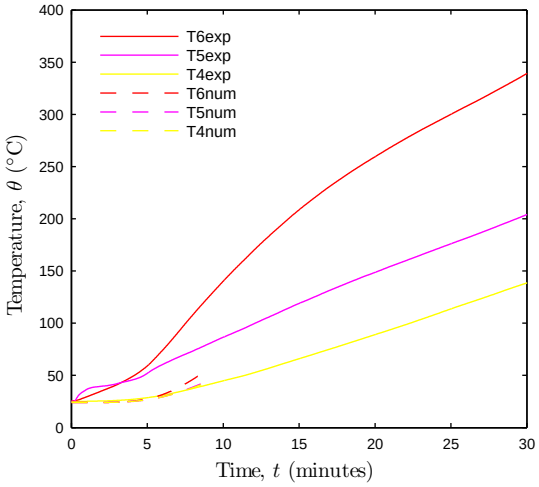

(b) Web.

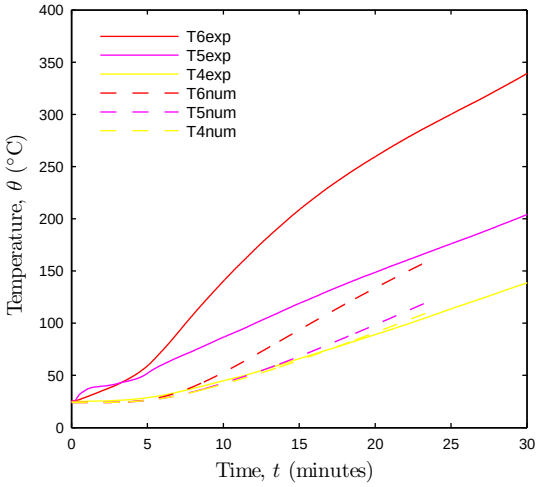

(b) Web.

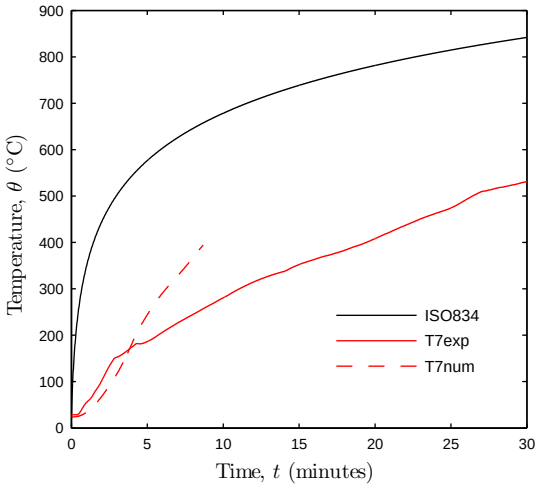

(c) Bottom flange.

Figure 7.25: Temperature profiles obtained considering the GFRP properties of Samanta *et al.* (2004).

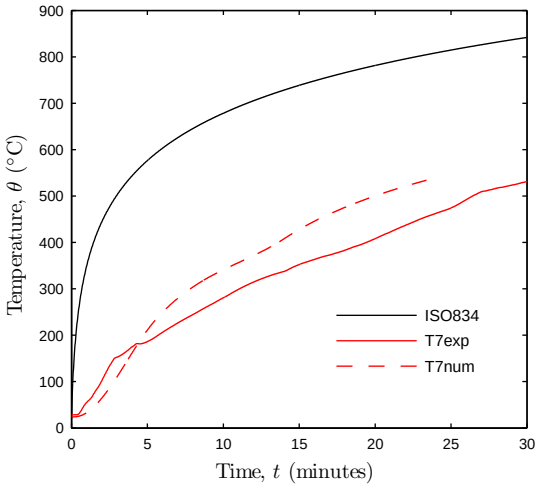

(c) Bottom flange.

Figure 7.26: Temperature profiles obtained considering the GFRP properties of Bai *et al.* (2007).

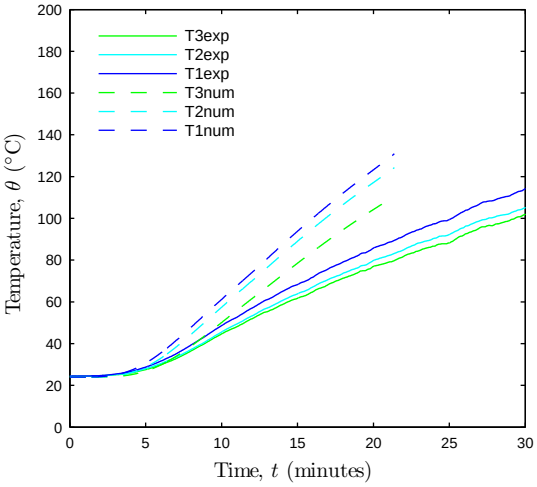

(a) Top flange.

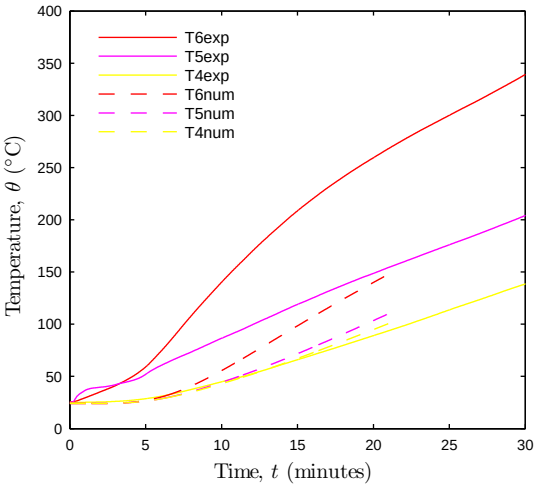

(b) Web.

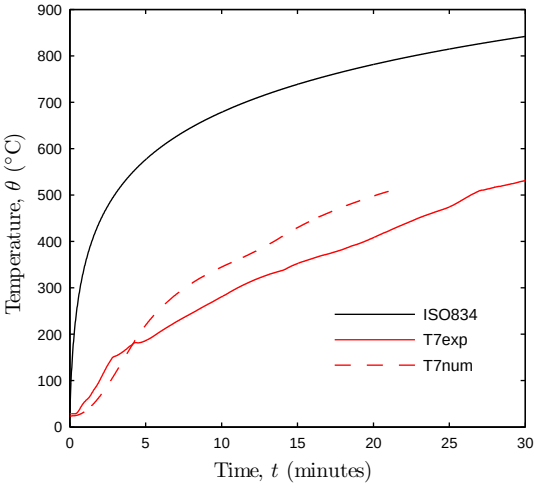

(c) Bottom flange.

Figure 7.27: Temperature profiles with Bai's model (temperature-dependent emissivity).

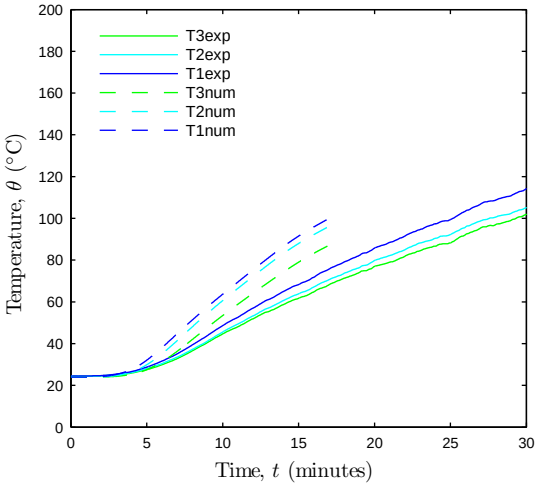

(a) Top flange.

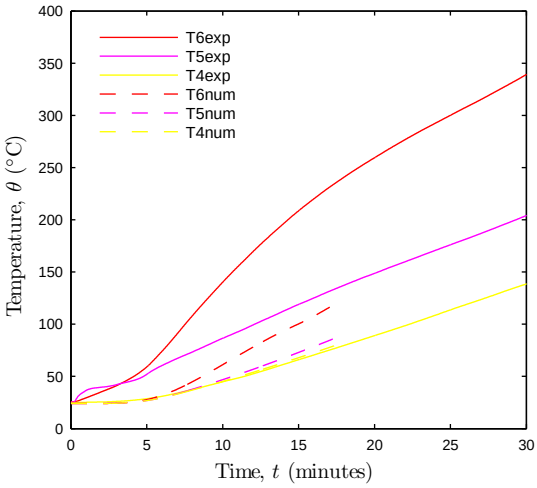

(b) Web.

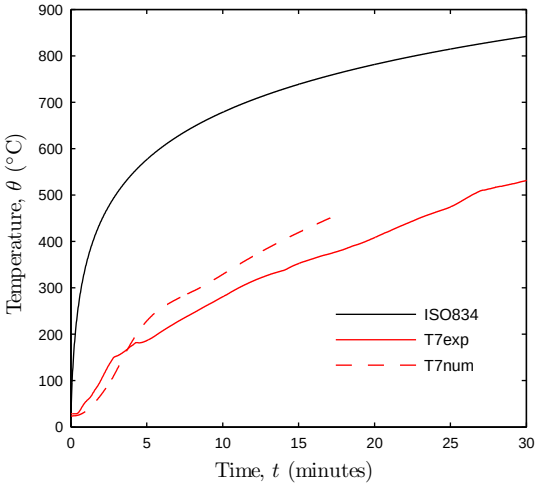

(c) Bottom flange.

Figure 7.28: Temperature profiles with Tracy's model (temperature-dependent emissivity).

7.4.7 Conclusions regarding the characteristics of the thermal simulations

The current section reports results of preliminary studies about: (i) the boundary conditions to consider in the thermal modelling of the GFRP tubular profiles, (ii) the spatial and temporal discretization, (iii) the effect of sharp corners in the cavity, and (iv) the temperature-dependent thermal conductivity, specific heat capacity and emissivity of the GFRP material.

Regarding the boundary conditions of the model, four situations were tested and the numerical results obtained were compared with the experimental data. The model that reproduced more accurately the experimental temperature distribution was the one that considers simultaneously the radiative heat exchange between the faces of the cavity and the natural convection. Both phenomena proved to be very important in order to reproduce the temperature field in the top flange. However, as the temperature gradients on the cavity walls are high, this model requires small time step sizes after the last converged time. In spite of that, this was the model chosen to compute the numerical distribution of the temperatures in the tubular and I-section GFRP profiles, as it was the one that simulated more faithfully the actual test conditions. In all models, the convective heat coefficient was modelled as linearly dependent on the temperature.

A systematic study about the spatial and temporal discretization was also carried out in order to evaluate the accuracy and robustness of the solution. In the spatial discretization study of the unprotected tubular cross section exposed to fire in 1-face, four meshes were tested. The mesh referred to as mesh 2 was chosen for the following numerical simulations. In the case of the unprotected tubular cross section exposed to fire in 3-faces, three meshes were considered. The temperature evolution in the thermocouples is similar in all meshes, being possible to conclude that the spatial discretization error can be neglected. Due to the objective of this analysis (to compare experimental and numerical results) and to the elevated computational time required to obtain the thermal response of the cross section, mesh 2 was considered more appropriate and, therefore, it was used in the final simulations presented in section 7.5.3.

In the temporal discretization study, three constant time steps were tested. All of them presented almost identical results, the only difference being the last time for which a converged solution was obtained. The convergence problems of the algorithm are associated to the time step size. When the complexity of the problem increases, small time step sizes are required to compute a converged solution. Therefore, the adaptive time step implemented should be used to obtain the complete response. This implies long CPU times and, finally, a time step of 1 second was selected to perform the thermal simulations in the tubular and I-section profiles.

Regarding the thermal properties of the GFRP, the density is considered dependent on the temperature and the values assumed were those obtained experimentally. The thermal conductivity and the specific heat capacity were computed using three analytical models (Samanta *et al.*, 2004, Tracy, 2005, Bai *et al.*, 2007) and the emissivity was considered constant and temperature-dependent (Samanta *et al.*, 2004). The analytical model that represented with more accuracy the experimental results was that with the thermal conductivity and the specific heat capacity computed with the Tracy's model and temperature-dependent emissivity for all temperatures.

7.5 Simulations of the thermal behaviour of the profiles

7.5.1 Preliminary comments

In the present section, the thermal simulations of the different profiles subjected to fire are presented. The numerical results allow evaluating the thermal response of the cross section and assessing the fluid flow in the cavities of the profiles, which depends strongly on the fire exposure. The obtained numerical results are compared with the experimental data (temperature evolution in the thermocouples obtained during the beam tests) in order to evaluate the accuracy of the model in reproducing them.

The following six numerical simulations were carried out:

1. Unprotected tubular cross section with 1-face exposed to fire (section 7.5.2).
2. Unprotected tubular cross section with 3-faces (both lateral faces and bottom face) exposed to fire (section 7.5.3).
3. CS protected tubular cross section with 1-face exposed to fire (section 7.5.4).
4. CS protected tubular cross section with 3-faces exposed to fire (section 7.5.5).
5. Unprotected I-section with 3-faces exposed to fire (section 7.5.6).
6. Protected I-section with 3-faces exposed to fire (section 7.5.7).

In all cases, transient nonlinear finite element simulations were carried out using the Euler backward scheme and considering the stabilization SUPG. The thermal properties of the GFRP and CS were considered temperature-dependent. The particularities of each analysis will be detailed in the corresponding section.

7.5.2 Unprotected tubular section with 1-face fire exposure

An unprotected tubular cross section subjected to fire exposure in the bottom face is considered (beams and columns from series S1 and S3, see tables 7.1 and 7.2). The geometry of the cross section and the position of the thermocouples are depicted in figure 7.10 and summarized in table 7.3. Regarding the installation of thermocouple T7, it was placed throughout a horizontal hole. This fact is important, as in previous tests performed on unprotected tubular sections (Correia, 2008), thermocouples were placed in the bottom flange throughout vertical holes drilled either from the top or the bottom and, in both situations, inconsistent temperatures were measured. It is possible that those temperature measurements may have been influenced by the air in the vicinity of the hole. This fact probably is also applicable to the thermocouples in the top face, which should have been placed through horizontal holes. However, in this case given the lower temperature differences between the GFRP material and the air, it is likely that this aspect was less relevant.

The numerical transient analysis was carried out with a time step size of 1 second and using the mesh referred as mesh 2 (see figure 7.24a). The boundary conditions defined are those schematically represented in figure 7.8d.

The numerical and experimental temperature evolution in the thermocouples are showed in figure 7.29.

These results are similar to those displayed in figure 7.28, except that in figure 7.29b the temperatures at thermocouples T6 and T5 are not plotted as there are concerns

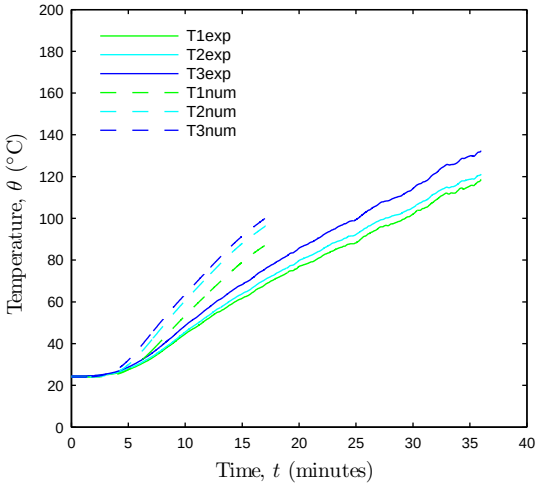

(a) Top flange.

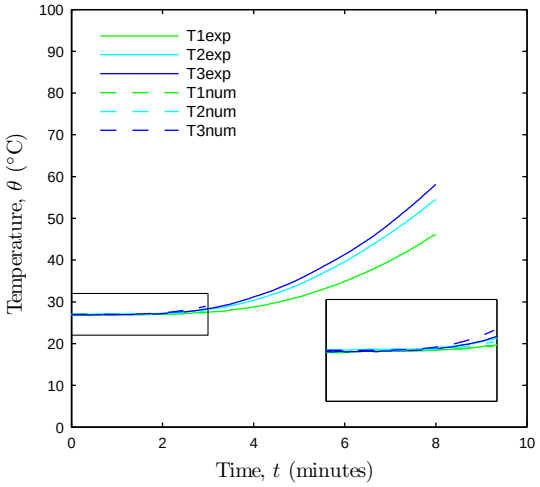

(a) Top flange.

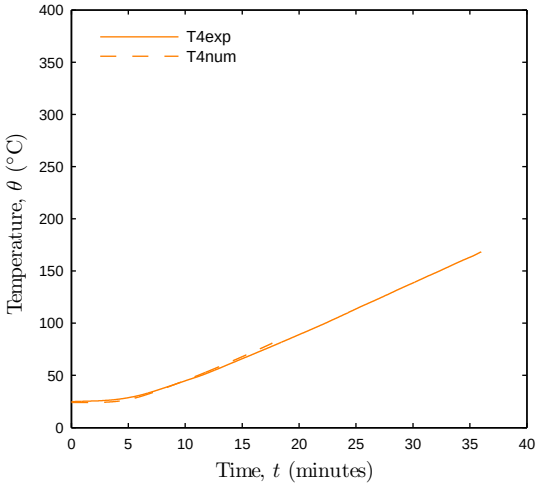

(b) Web.

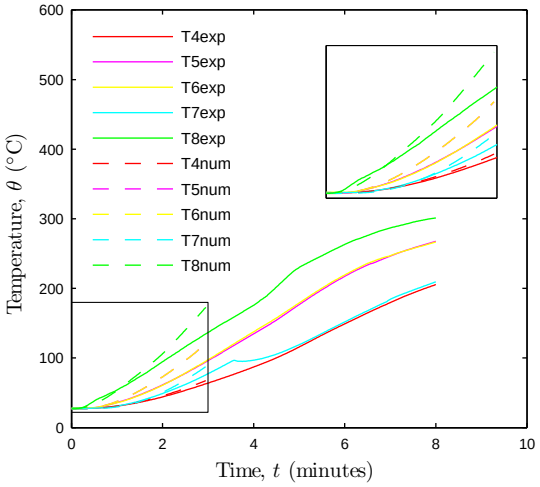

(b) Web.

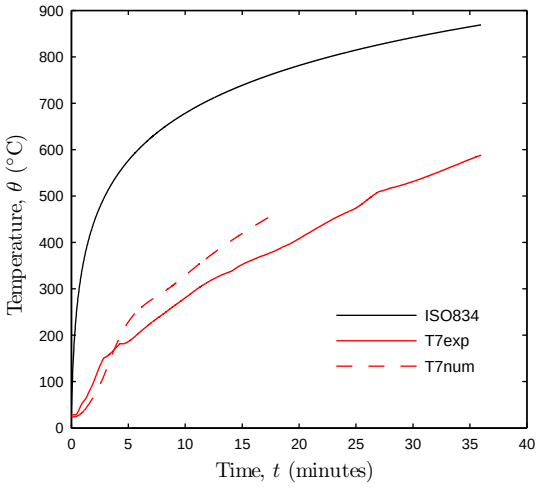

(c) Bottom flange.

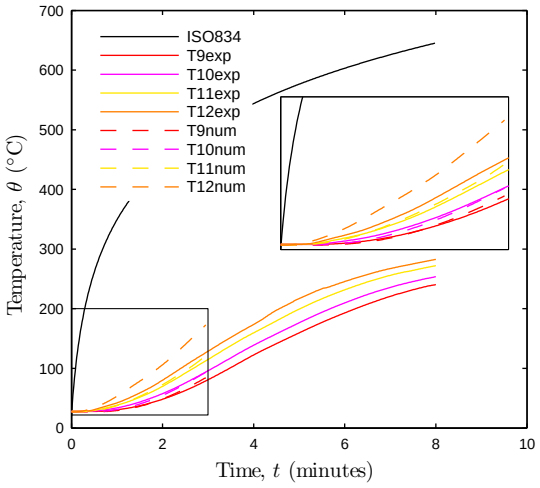

(c) Bottom flange.

Figure 7.29: Experimental and numerical temperatures in the unprotected tubular cross section with 1-face exposure.

Figure 7.30: Experimental and numerical temperatures in the unprotected tubular cross section with 3-faces exposure.

regarding the accuracy of the experimental results. In fact, the experimental temperatures in those thermocouples are much higher than those observed numerically. As mentioned, one possible reason is the inefficient lateral insulation of the profile during the test, which allowed for some heat flux on the bottom of the lateral faces (that is not quantified in the numerical simulations). Consequently, an increase of the temperatures measured in the thermocouples installed on the lateral face could be observed, especially those closer to the bottom face.

Regarding the temperatures measured in the top flange, the thermocouples were not installed laterally (as T7) and this may explain why the temperatures measured are lower than the numerical temperatures.

Recently, Paipuri (2016) computed the complete thermal response of the GFRP profile, which can be consulted in appendix F.

7.5.3 Unprotected tubular section with 3-faces partially exposed to fire

In this section, the thermal behaviour of a GFRP tubular profile with 3-faces partially subjected to fire (the bottom face and 3/4 of the lateral faces) is analysed. Figure 7.19 illustrates the geometry of the cross section and the position of the thermocouples, which is also summarized in table 7.7.

Regarding the boundary conditions, convective and radiative heat flux is prescribed in the top face, the ambient temperature being equal to 20 °C, and natural convection and radiative heat exchange is considered in the cavity. The bottom and both lateral faces are exposed to fire and, consequently, convective and radiative heat flux are prescribed; in this case, the exterior temperature varies with time according to the ISO 834 (1975) curve. The boundary conditions defined are schematically presented in figure 7.20. The numerical simulation was carried out using the mesh presented in figure 7.16d and using a time step of 1 second. Figure 7.30 depicts the numerical and experimental temperature evolution in the thermocouples until $t = 8$ min, which was the duration of the test in the beams.

The numerical temperatures are, in all thermocouples, higher than the experimental counterparts. In the bottom face, the temperature evolution of the thermocouples T9, T10 and T11 is well reproduced by the model. However, the temperature computed in thermocouple T12 is higher than the experimental one. In the web, the temperature evolution of thermocouples T4, T7 and T8 is also well represented by the model. In both numerical and experimental results, the temperatures in thermocouples T5 and T6 are similar. The temperatures evaluated in thermocouples T5, T6 and T8 are higher than the experimental ones, the maximum difference being obtained at 178 s, which is the last instant for which a converged solution was attained. In the top face, the model is able to represent the temperatures measured in the tests with reasonable accuracy. In both numerical and experimental data, the temperature in these thermocouples remain almost constant until 120 s and, after this instant, the temperatures increase. This effect is also registered numerically.

It can be observed that converged temperatures were only obtained until 178 s, and this is attributed to the time step size employed. Figure 7.31 shows that four convective cells appear due to the temperature gradient created in the lateral walls. Hence, two zones are created: a *cold* zone situated in the top of the cavity and a *warm* zone situated in the bottom. The existence of these four convective cells and the discontinuity in the boundary

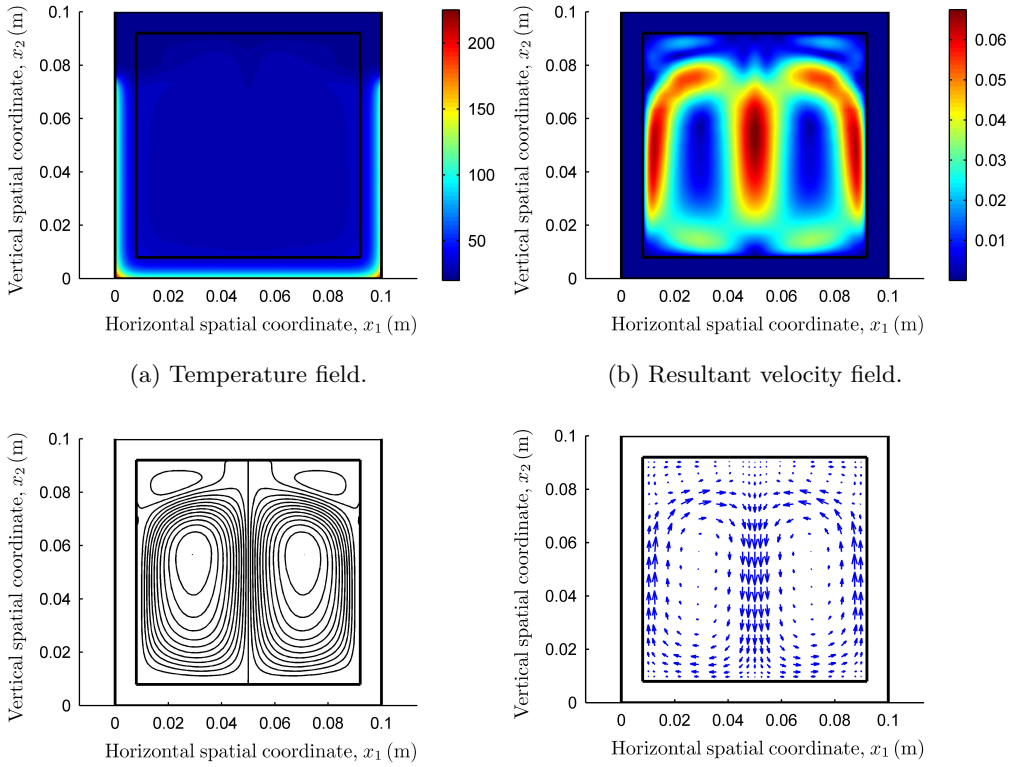

(a) Temperature field.

(b) Resultant velocity field.

(c) Streamlines.

(d) Velocity field.

Figure 7.31: Results for tubular profile exposed to fire in 3-faces (lateral faces partially exposed to fire, at $t = 100$ s).

conditions in the lateral faces hamper the convergence to the solution, which, most likely would require a very small time step size.

7.5.4 Protected tubular section with 1-face fire exposure

The thermal response of a tubular GFRP profile whose bottom face is protected with a 25 mm CS board is analysed. The geometry of the cross section and the position of the thermocouples is represented in figure 7.32. Table 7.8 summarizes the coordinates of the eleven thermocouples used in the experimental test.

The boundary conditions defined in the model are represented schematically in figure 7.33 and can be summarized as follows:

1. Top face: convective and radiative heat flux, with the ambient temperature being constant and equal to 20 °C.

2. Bottom face of the CS board: convective and radiative heat flux considering a variable ambient temperature following the ISO 834 (1975) curve.

3. Lateral faces: insulated.

4. Cavity faces: natural heat convection and radiative heat exchange.

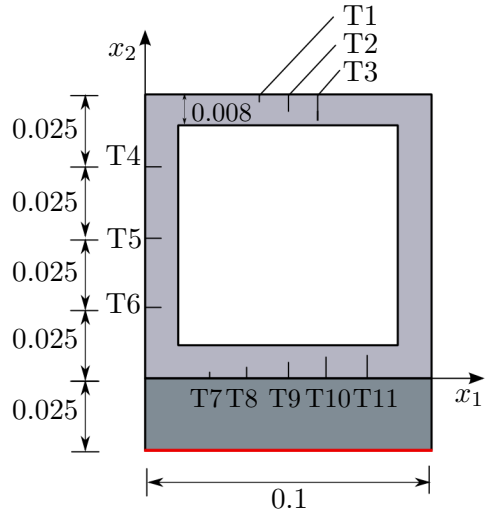

Figure 7.32: Geometry and thermocouples position of protected tubular cross section exposed to fire in 1-face (dimensions in meters).

Thermocouples	x_1 (m)	x_2 (m)
T1	0.04	0.098
T2	0.05	0.096
T3	0.06	0.094
T4	0.004	0.075
T5	0.004	0.05
T6	0.004	0.025
T7	0.03	0.0005
T8	0.04	0.002
T9	0.05	0.004
T10	0.06	0.006
T11	0.07	0.0075

Table 7.8: Coordinates of the thermocouples installed in the protected tubular GFRP cross section with 1-face exposed to fire.

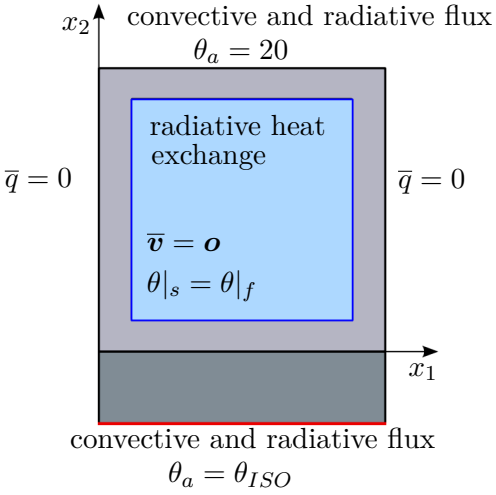

Figure 7.33: Boundary conditions in the protected tubular profile exposed to fire in the bottom face.

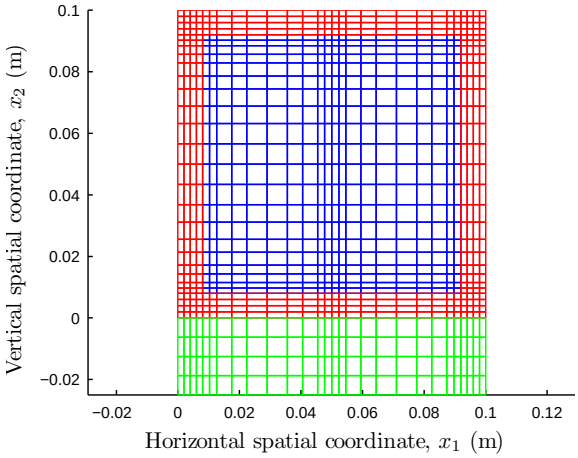

Figure 7.34: Mesh used in the modelling of the protected tubular profile exposed to fire in the bottom face.

Figure 7.34 shows the mesh used in the numerical simulation, which contains 896 quadrilateral elements (400 $Q2P1$ elements in the fluid and 496 in the solid) and 3865 nodes. In addition, the heat transfer by convection and radiation with the ambient in the bottom and top faces of the cross section were imposed along 56 sides of solid quadrilateral elements and 80 one-dimensional radiosity elements were used to account the radiative heat exchanges on the cavity walls.

A transient nonlinear simulation was carried out using a time step of 1 second until a total time of 1461 s. Figure 7.35 illustrates the numerical and experimental temperatures in the thermocouples.

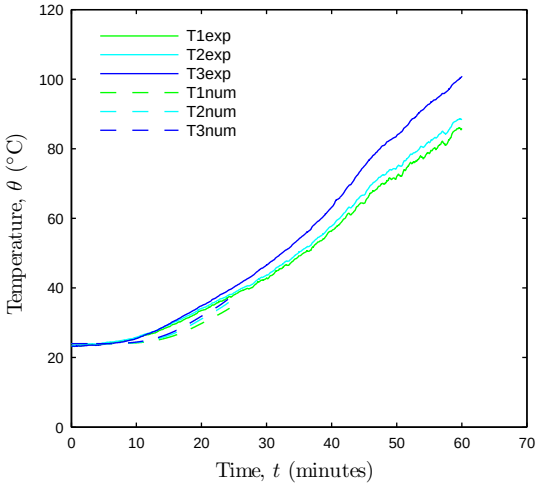

(a) Top flange.

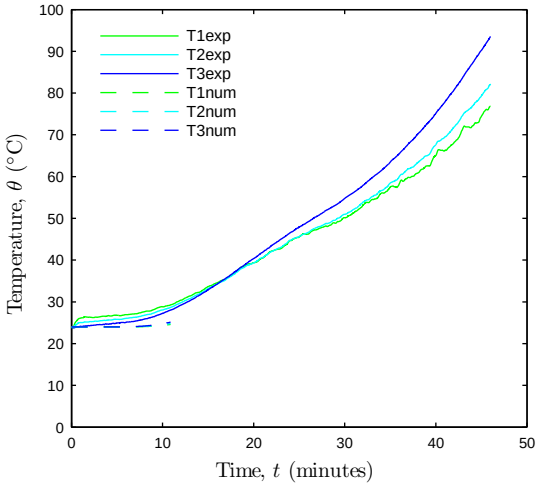

(a) Top flange.

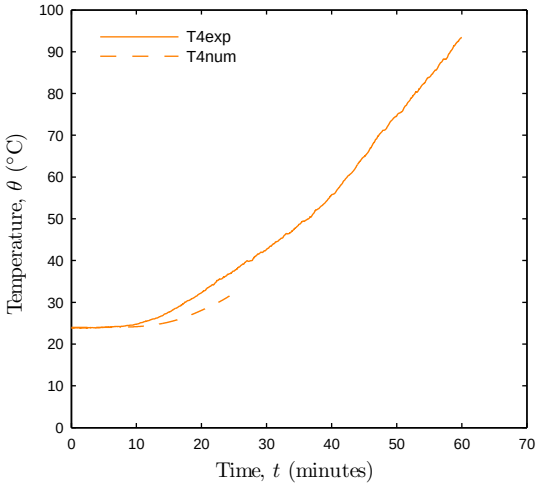

(b) Web.

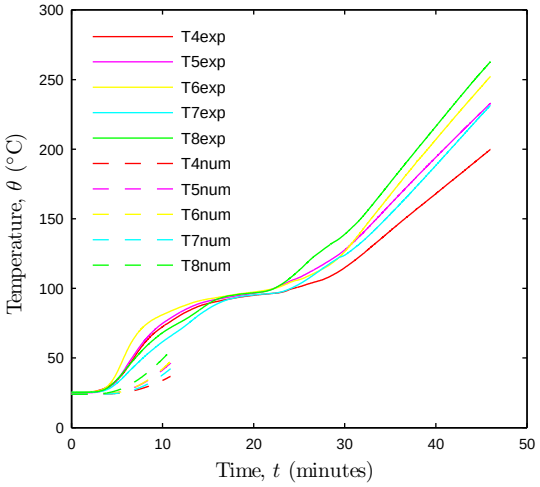

(b) Web.

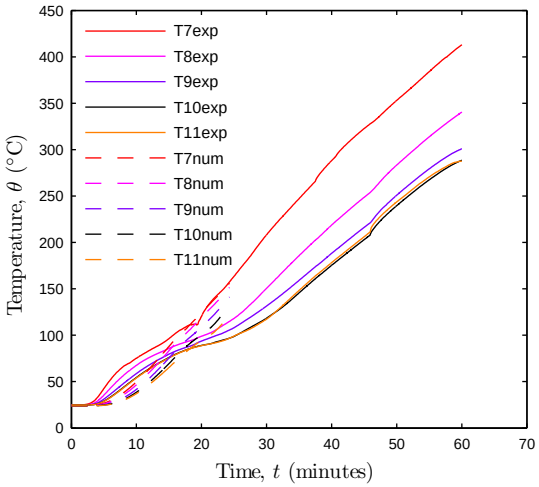

(c) Bottom flange.

Figure 7.35: Experimental and numerical temperatures in the protected tubular cross section with 1-face exposure.

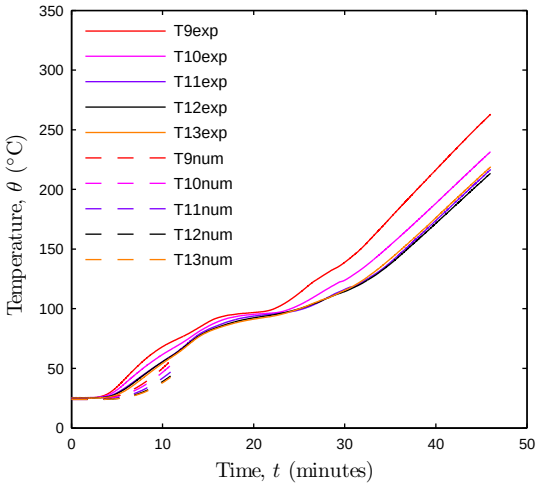

(c) Bottom flange.

Figure 7.36: Experimental and numerical temperatures in the protected tubular cross section with 3-faces exposure.

The agreement between the numerical and experimental temperatures in the thermocouples T1, T2 and T3 located in the top face is very good. In the web, three thermocouples were installed, but only the results of thermocouple T4 are presented (similarly to the unprotected profile, there were concerns regarding the efficiency of the thermal insulation of the lateral faces during the experimental test). In opposition to the thermocouples T5 and T6, the temperature evolution in T4 obtained numerically is coherent with the experimental measurements, with the differences between computed and measured temperatures being attributed to the inefficient insulation of the lateral faces, which could have also affected thermocouple T4. The temperatures at the thermocouples installed in the bottom face (*i.e.*, T7, T8, T9, T10 and T11) were well predicted by the model. The main difference between the numerical and the experimental results occurs between 10 and 20 minutes. During this period, the experimental temperatures exhibit a variation in their slope, probably due to the dehydration reaction in the CS. However, this reaction does not seem to be considered in the heat transfer capacity curved provided by the manufacturer (*cf.* figure 7.7, page 155), where a steep increase of the c_p value should occur at around 100°C (endothermic water evaporation). This is probably why the model is not able to reproduce the mentioned slope variation in the temperatures. This effect will be present in all the simulations carried out in CS protected profiles. Specific thermo-physical experiments should be performed to confirm or update the data provided by the material supplier.

A converged solution was obtained until $t = 1461$ s, this value being lower than the maximum duration of the experimental tests (almost 3600 s in both the beam and the column). A model considering only radiative heat exchange in the cavity was also developed and, in this case, it was possible to obtain a converged solution for a duration similar to that of the tests. These results complete the analysis presented in section 7.4.2, confirming the need to consider not only the radiative heat flux between the faces of the cavity, but also the natural convection of the enclosed air. The temperature evolution in the thermocouples obtained in this analysis is presented in the appendix G to keep the clarity of the text. The results presented corroborate that the model proposed is able to simulate the temperature of the GFRP tubular cross section.

7.5.5 Protected tubular section with 3-faces partially exposed to fire

A nonlinear transient simulation of the thermal behaviour of a GFRP protected tubular profile partially exposed to fire in 3-faces (the bottom face and 3/4 of the lateral faces) is presented. The cross section is protected with three CS boards, disposed as depicted in figure 7.37, which also illustrates the cross section geometry. The position of the thermocouples is detailed in table 7.9.

The boundary conditions prescribed are presented in figure 7.38 and can be defined as follows:

1. Top face: convective and radiative heat flux, with the ambient temperature being constant and equal to 20 °C.

2. Bottom face of the CS board and lateral faces of the cross section (with exception of the top 2.5 cm): convective and radiative heat flux considering that the ambient temperature follows the ISO 834 (1975) curve.

3. Top 2.5 cm of the lateral faces: insulated.

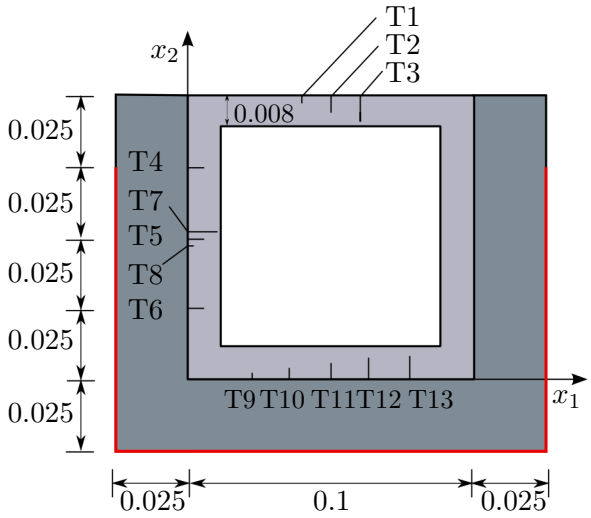

Figure 7.37: Geometry and thermocouples position of the protected tubular cross section exposed to fire partially in 3-faces (dimensions in meters).

Thermocouples	x_1 (m)	x_2 (m)
T1	0.04	0.098
T2	0.05	0.096
T3	0.06	0.094
T4	0.004	0.075
T5	0.004	0.05
T6	0.004	0.025
T7	0.007	0.05
T8	0.001	0.05
T9	0.03	0.0005
T10	0.04	0.002
T11	0.05	0.004
T12	0.06	0.006
T13	0.07	0.0075

Table 7.9: Thermocouples position in the protected GFRP tubular cross section for 3-faces partially exposed to fire.

4. Cavity faces: natural heat convection and radiative heat exchange.

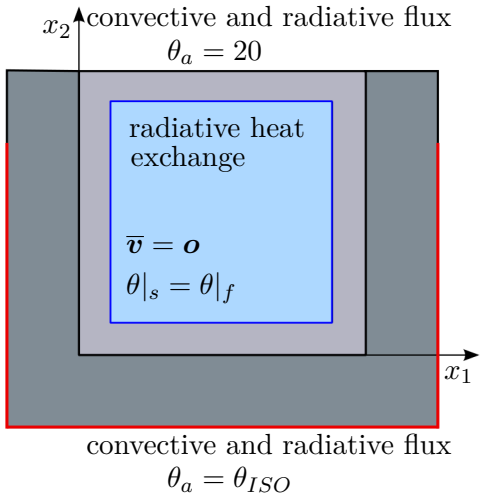

Figure 7.38: Boundary conditions in the protected tubular profile partially exposed to fire in 3-faces.

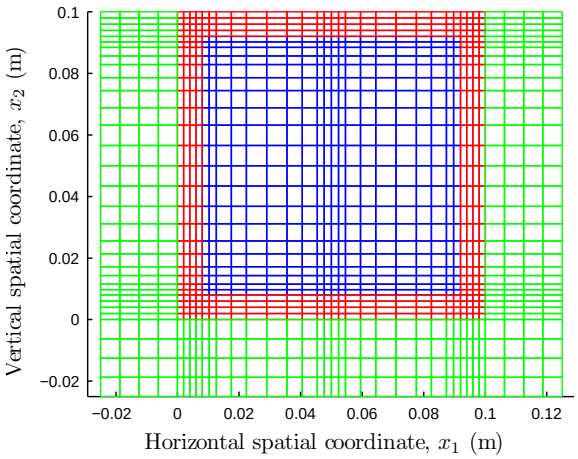

Figure 7.39: Mesh used in the modelling of the protected tubular profile partially exposed to fire in 3-faces.

The transient analysis was carried out considering the Euler backward scheme with a time step equal to 1 s. A converged solution was obtained until 654 s, while the duration of the experimental tests was around 3000 s for the beam and 2340 s for the column.

Figure 7.36 displays the temperature evolution in the thermocouples. It can be observed that, until 654 s, the agreement between the numerical and experimental temperatures is reasonable. The most relevant differences are observed in the thermocouples

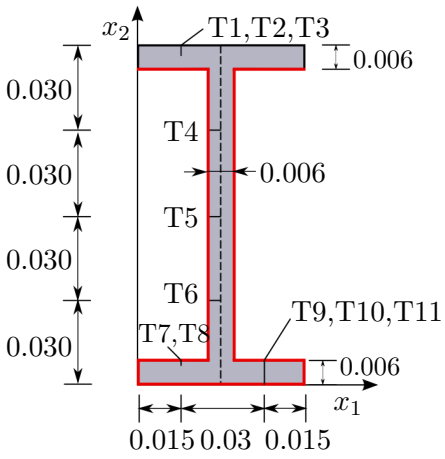

Figure 7.40: Cross section geometry and thermocouples on the GFRP I-section exposed to fire in 3-faces (dimensions in meters).

Thermocouples	x_1 (m)	x_2 (m)
T1	0.015	0.119
T2	0.015	0.117
T3	0.015	0.115
T4	0.03	0.09
T5	0.03	0.06
T6	0.03	0.03
T7	0.015	0.005
T8	0.015	0.004
T9	0.015	0.003
T10	0.015	0.002
T11	0.015	0.001

Table 7.10: Thermocouples position in the GFRP I-section with 3-faces exposed to fire.

located in the web, with the numerical temperatures being lower than the experimental ones. These differences may be due to the already mentioned possible inaccuracy in the modelling of the thermal properties of the CS (namely, the non consideration of the dehydration reactions).

7.5.6 Unprotected I-section with 3-faces fire exposure

This section presents the thermal study of the I profile subjected to fire in 3-faces. The dimensions of the profile and the position of the thermocouples are displayed in figure 7.40 and table 7.10 details the coordinates of the thermocouples.

The boundary conditions considered in the present analysis are illustrated in figure 7.41 and can be summarized as follows:

1. Top face: convective and radiative heat flux, with the ambient temperature being constant and equal to 20 °C.
2. Lateral faces of the top flange: insulated.
3. Bottom and lateral faces of the bottom flange: convective and radiative heat flux, considering an ambient temperature varying according to the ISO 834 (1975) curve.
4. Top face of the bottom flange, face of the web and bottom face of the top flange: convective and radiative heat flux, and radiative heat exchange between faces.

In order to reduce the CPU time, only half of the cross section was modelled using the mesh depicted in figure 7.42, which contains 112 9-nodes quadrilateral elements and 549 nodes. Furthermore, 65 element sides were also used to impose the convective and radiative heat exchanges with the ambient. A total of 42 radiosity elements are used to evaluate the radiative heat exchange between faces. Along the symmetry axis the normal flux value is prescribed to be equal zero.

A nonlinear transient analysis was carried out considering a time step equal to 1 second and the Euler backward scheme. The total duration of the analysis was 2.5 minutes, which

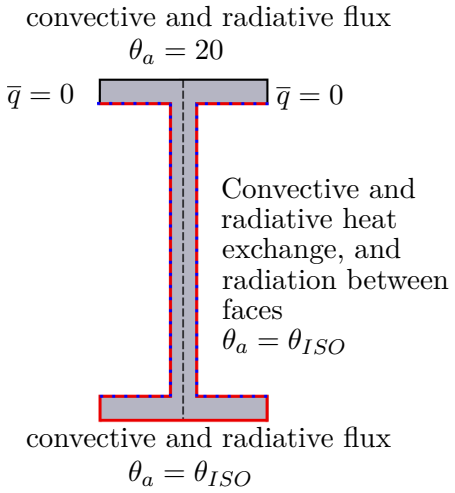

Figure 7.41: Boundary conditions in the unprotected I-profile partially exposed to fire in 3-faces.

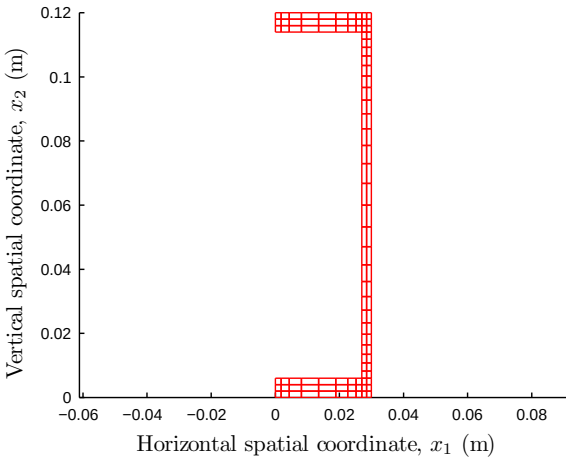

Figure 7.42: Mesh employed in the modelling of the unprotected I-section partially exposed to fire in 3-faces.

corresponds to the duration of the experimental beam test. Figure 7.43 illustrates the evolution of the numerical and experimental temperatures in the thermocouples. It can be observed that, overall, a reasonable agreement between the numerical and experimental temperatures is obtained.

Regarding the temperatures in the top flange, the model provided higher temperatures than those measured experimentally, the maximum difference occurring in thermocouples T1 and T3. To some extent, these differences can be explained by the procedure used to install the thermocouples, which could have been cooled due to the exposure to the ambient air.

In both the web and the bottom face, the numerical temperatures were lower than the experimental counterparts. This fact could be due to the very short duration of the tests (beam and column). In fact, during the first minutes of the fire resistance tests, the accurate imposition of the ISO 834 (1975) curve is generally difficult even in furnaces with gas burners such as the one used in the experiments. Particularly in these tests, it was observed that for such period the temperature in the furnace was below the nominal temperature of ISO 834 (1975), as illustrated in figure 7.45.

In the web, the numerical temperatures in thermocouples T4, T5 and T6 is almost identical. Consequently, in the numerical simulations, the temperature distribution along the vertical direction of the web is uniform. This is coherent with the temperatures observed experimentally, which are only slightly different from the numerical ones. The maximum difference between the numerical and the experimental results occurs in thermocouple T4 at approximately $t = 2$ minutes. At the end of the 2.5 minutes, the numerical results are similar to the experimental ones.

In the bottom face, the numerical results are consistent with the experimental ones. Thermocouple T7 is not presented as there were concerns regarding the validity of the temperature measured.

Figure 7.46 illustrates the temperature and the heat fluxes at each direction at the end of the test (2.5 minutes). It can be observed that the maximum heat flux occurs in the direction perpendicular to the faces exposed to fire. The flux computed in both directions

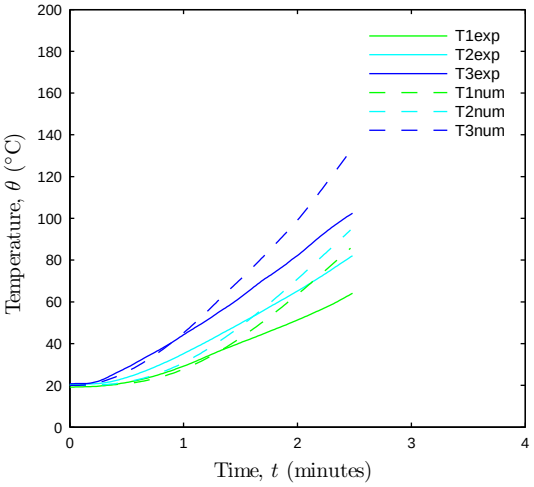

(a) Top flange.

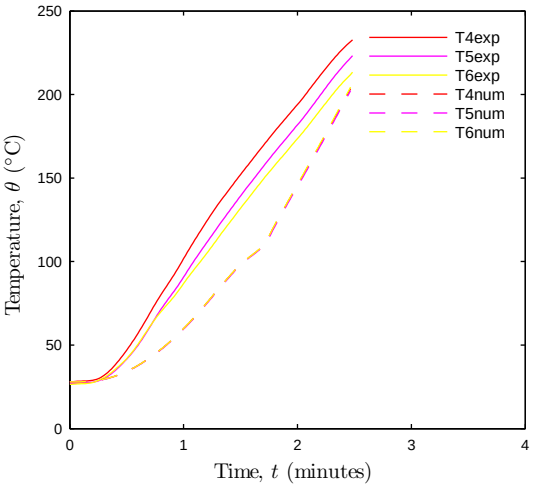

(b) Web.

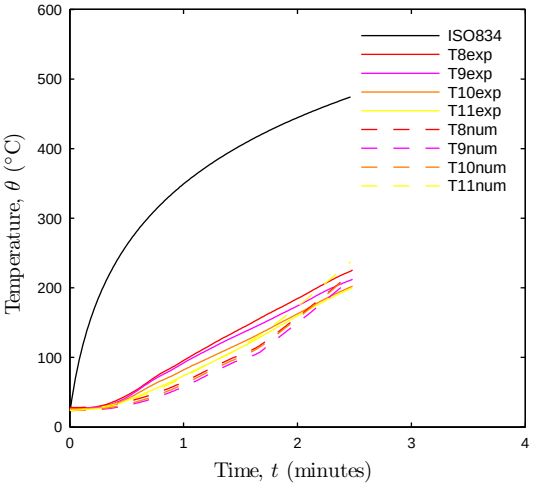

(c) Bottom flange.

Figure 7.43: Experimental and numerical temperatures in the unprotected I-section with 3-faces exposure.

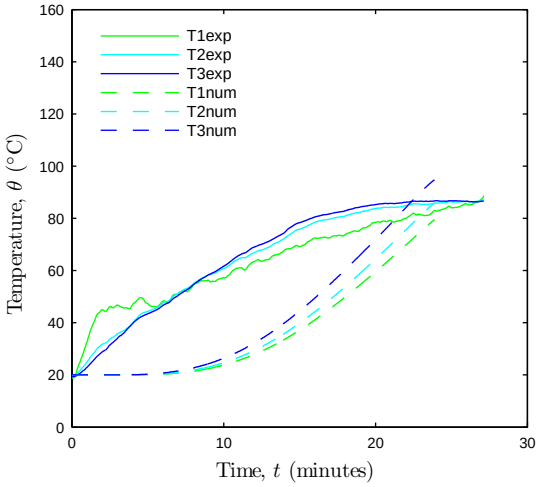

(a) Top flange.

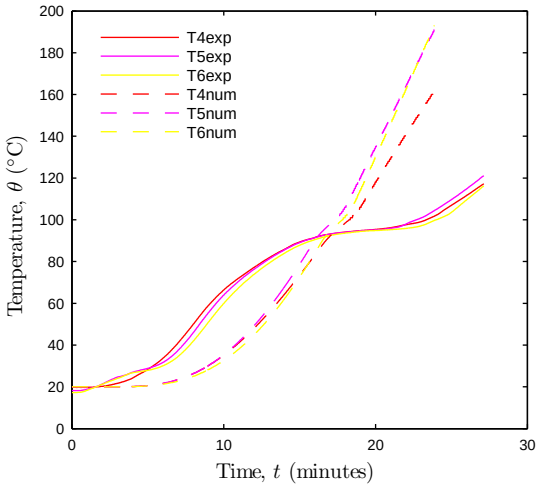

(b) Web.

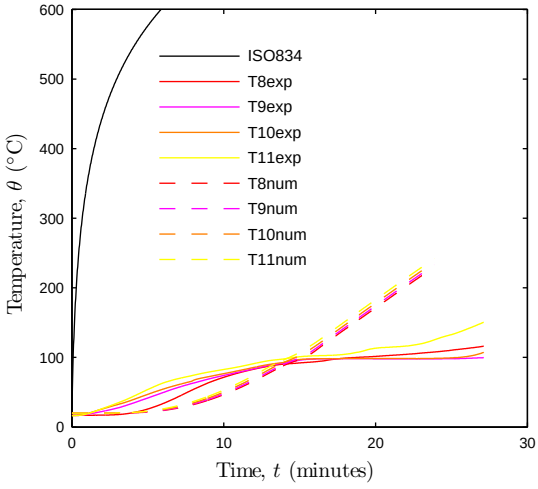

(c) Bottom flange.

Figure 7.44: Experimental and numerical temperatures in the protected I-section with 3-faces exposure.

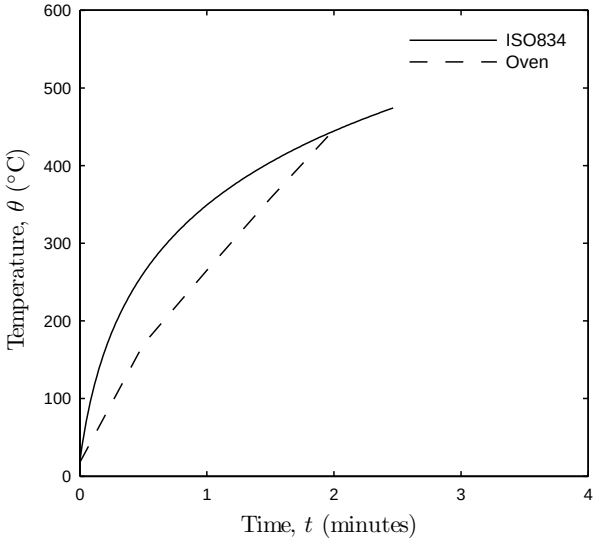

Figure 7.45: Experimental and numerical evolution of the temperature in the furnace.

is nearly continuous, confirming that the mesh used to solve the problem is adequate.

7.5.7 Protected I-section partially exposed to fire in 3-faces

The thermal response of the protected I-profile subjected to fire partially in 3-faces is reported in this section. Figure 7.47 illustrates the geometry of the cross section and the position of the thermocouples, which is also summarized in table 7.11.

A transient nonlinear analysis was carried out considering a time step of 1 second and the Euler backward scheme. The boundary conditions and the mesh are illustrated in figures 7.48 and 7.49, respectively. The mesh contains 2016 elements (832 $Q2P1$ elements in the fluid and 1184 quadrilateral elements in the solid) and a total of 8537 nodes. Furthermore, 109 element sides were employed to prescribe the radiative and convective heat fluxes and 136 one-dimensional radiosity elements to take into account the radiative heat exchanges between the cavity walls.

Figure 7.44 depicts the numerical and experimental temperature evolution in the thermocouples. Regarding the thermocouples located in the bottom face and in the web, the following comments are prompted: (i) the numerical results are lower than the experimental ones until approximately 21-23 minutes; (ii) after this instant, the numerical temperatures become higher than the measured ones; and (iii) furthermore, at approximately 100 °C, the experimental temperatures' slope is significantly reduced (the temperatures almost become constant for a certain duration), while the numerical ones continue increasing (even if in the thermocouples located in the web, a slight variation in the slope can be observed at 17 min). This relative difference was observed in all the simulations that involve CS protection and, as discussed previously, it is very likely that the model was not able to reproduce this effect due to the thermal properties of the CS material used as input (provided by the material supplier).

Regarding the temperature evolution of the thermocouples located in the top flange, the experimental results obtained in the beam test were considered inconsistent (it is very likely that the lateral insulation used in this test was not effective). Therefore, it was

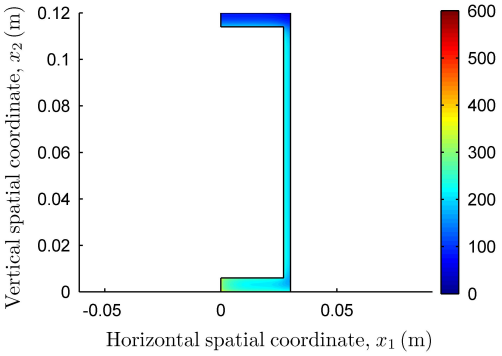

(a) Temperature field, $t = 150$ s.

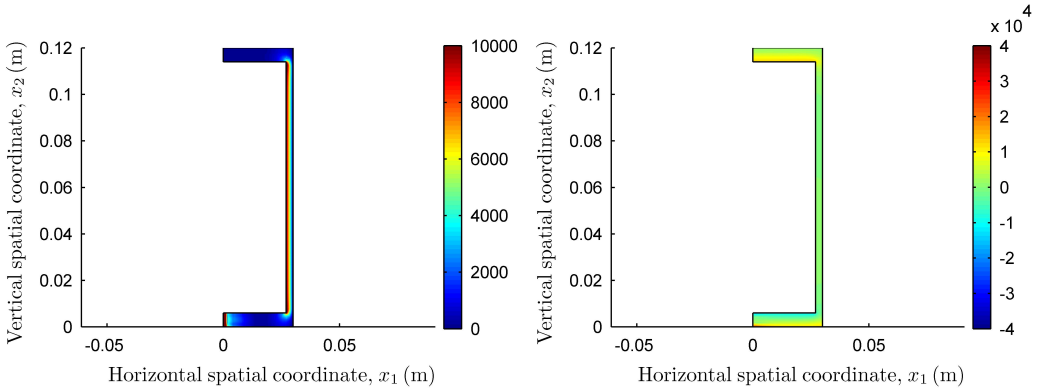

(b) Horizontal heat flux, $t = 150$ s.

(c) Vertical heat flux, $t = 150$ s.

Figure 7.46: Temperature field and heat fluxes in the unprotected I-profile subjected to fire in 3-faces.

decided to compare the numerical results with those obtained in the test of the column. Figure 7.50 illustrates such comparison. The experimental results obtained in the top flange during the column test (considered more realistic than those obtained in the beam, as they are coherent with the progression of the temperatures in the top flange and web) are in much better agreement with the results until the last solution converged.

The FE code implemented allowed obtaining a converged solution until 1737 s. Figure 7.51 displays the resultant velocity and temperature field at 200 and 1000 seconds. These images illustrate the complex development of the fluid flow, which initially presents one principal clockwise convective cell with a small convective cell in the left top corner of the cavity. At 1000 s, the small convective cell grow up displacing the principal cell and creating other convective cells in the right top corner of the cavity. Regarding the temperature field, in the mentioned instant, two areas can be clearly identified: (i) in the top of the cavity there exists cold air, while (ii) the warmer air is located in the bottom of the cavity.

7.5.8 Concluding remarks

The current section presented numerical simulations carried out in unprotected and protected GFRP tubular and I-section profiles subjected to different fire exposures.

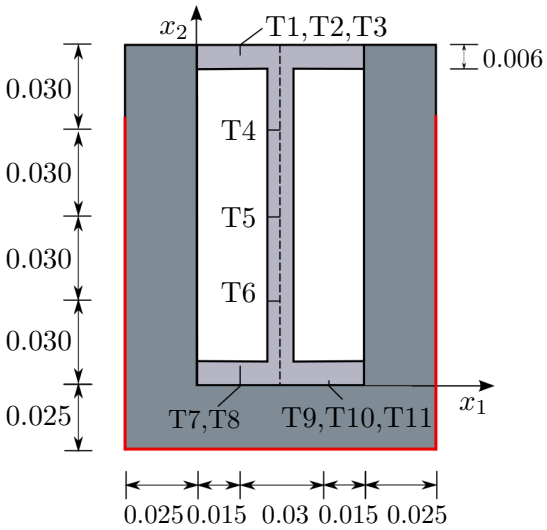

Figure 7.47: Cross section geometry and thermocouples in the protected GFRP I-profile partially exposed to fire in 3-faces (dimensions in meters).

Thermocouples	x_1 (m)	x_2 (m)
T1	0.015	0.119
T2	0.015	0.117
T3	0.015	0.115
T4	0.03	0.09
T5	0.03	0.06
T6	0.03	0.03
T7	0.015	0.005
T8	0.015	0.004
T9	0.015	0.003
T10	0.015	0.002
T11	0.015	0.001

Table 7.11: Thermocouples position in the protected GFRP I-section for 3-faces partially exposed to fire.

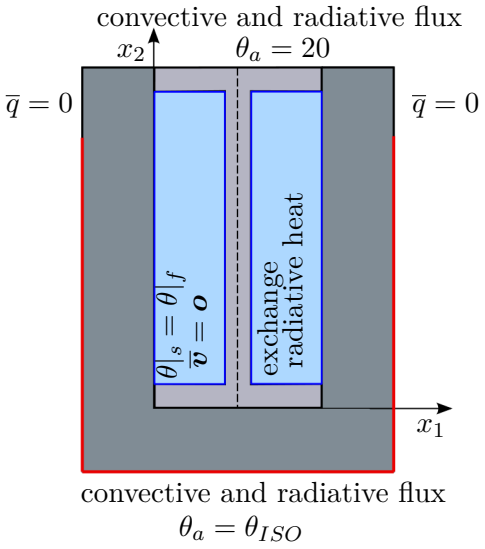

Figure 7.48: Boundary conditions in the protected I-profile partially exposed to fire in 3-faces.

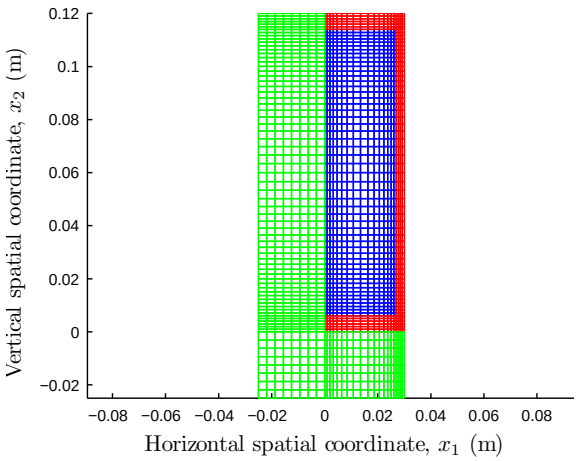

Figure 7.49: Mesh employed in the modelling of the protected I-section partially exposed to fire in 3-faces.

The studies carried out illustrate the different fluid flow patterns that are developed in the cavities of the cross sections. Hence, the code developed and the numerical simulations performed allowed understanding the physical phenomena that occur in the enclosed cavities.

In general, the numerical temperatures obtained were coherent with those measured experimentally, highlighting the necessity to consider both natural convection and radiative heat exchange in the cavities of the cross sections. The differences between the numerical and experimental results can be caused by (i) the difficulties encountered in the

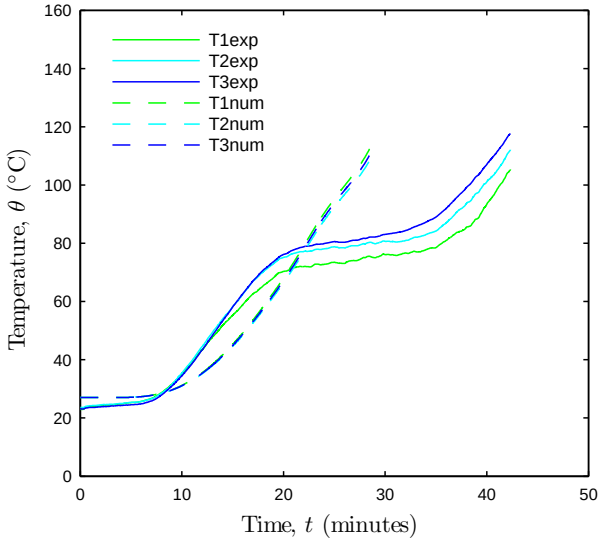

Figure 7.50: Experimental and numerical evolution of the temperature in the top flange of the protected I-profile partially exposed to fire in 3-faces (the experimental results were measured during the experimental test of the column).

experiments in accurately positioning the thermocouples and obtaining reliable measurements in some cross sections and (ii) the thermal properties assumed for the materials, which may present some differences compared to the actual properties of the materials used in the tests. This latter fact was especially relevant during the simulations of the protected profiles, where it was observed that the temperatures computed present different slopes when compared with the experimental data. In particular, it was verified that the increase of the specific heat capacity of the CS at 100 °C due to the evaporation of the water (typical in this type of fire protection materials) is not considered in the properties provided for the manufacturer.

Furthermore, the numerical results reveal convergence issues of the code, whose origin is the use of a constant time step.

Table 7.12 summarizes the last instant in which convergence was obtained in the thermal simulations and the total time required in order to reproduce completely the experiments in the beams and the columns. The percentages of the experimental results reproduced numerically are presented in parentheses. The average percentage of simulation completion among all situations tested is 62.1%. The results obtained in this study suggest that such percentage may only be increased by using the adaptive time step algorithm, that will reduce the time step size until convergence of the solution is possible. This calculations implies long computational times, which are not practically feasible using the FE code developed.

7.6 Mechanical modelling of beams and columns

7.6.1 Outline of the section

This section presents studies about the thermomechanical modelling of GFRP beams and columns. In particular, the three following aspects are addressed:

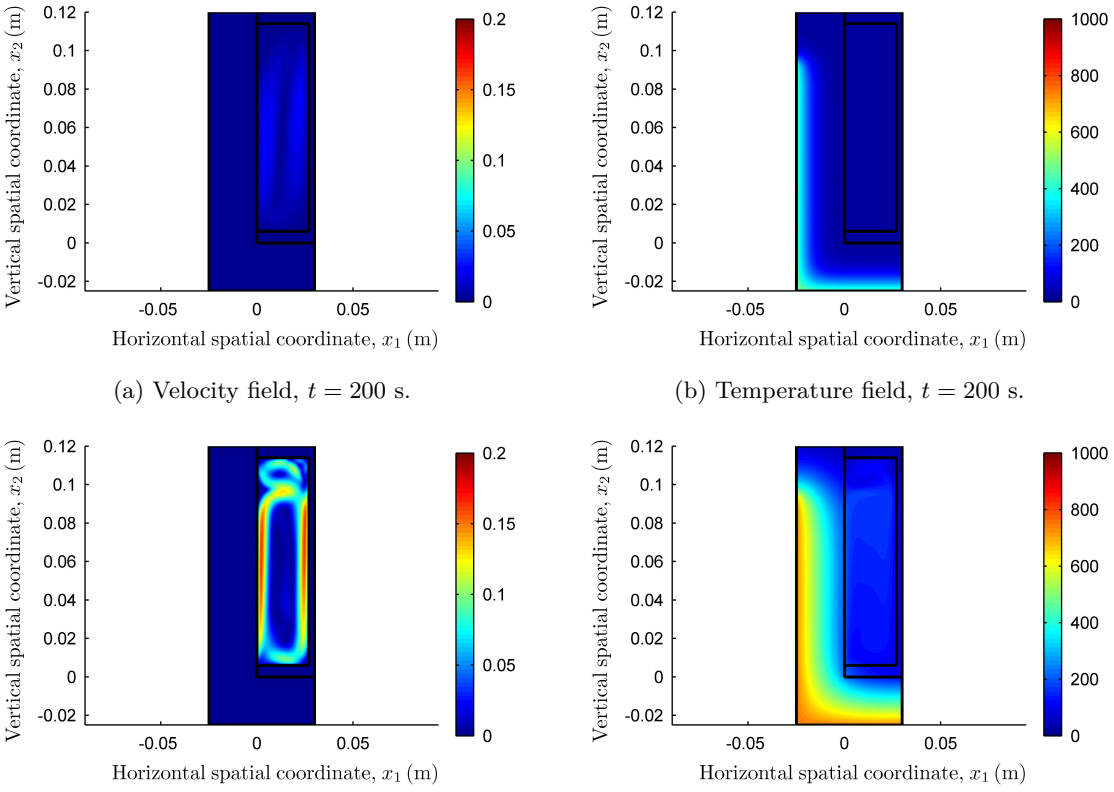

(a) Velocity field, $t = 200$ s.

(b) Temperature field, $t = 200$ s.

(c) Velocity field, $t = 1000$ s.

(d) Temperature field, $t = 1000$ s.

Figure 7.51: Resultant velocity and temperature field obtained at different computational times, when the lateral faces are partially exposed to fire (protected I-section, 3-faces exposure).

Cross section	Numerical tests	Beam (load 1)	Beam (load 2)	Column (load 1)	Column (load 2)
Unprotected tubular profile (1-face exposure)	1050	2100 (50%)	1860 (56.5%)	965 (100%)	600 (100%)
Unprotected tubular profile (3-face exposure)	178	480 (37%)	—	360 (49.4%)	—
Protected tubular profile (1-face exposure)	1461	4980 (29.3%)	3960 (36.9%)	3060 (47.7%)	2220 (65.8%)
Protected tubular profile (3-face exposure)	654	2760 (23.7%)	—	2340 (27.9%)	—
Unprotected I-profile (3-face exposure)	240	148 (100%)	—	180 (100%)	—
Protected I-profile (3-face exposure)	1737	1620 (100%)	—	2520 (68.9%)	—

Table 7.12: Experimental and numerical times computed (in seconds).

1. Evaluation of the temperature-dependent mechanical properties of the GFRP using the experimental data obtained within the Fire-FRP research project and other values reported in the literature and the description of the CS mechanical properties.
2. Study about the spatial discretization of the bars' length.
3. Influence of the unheated sections of the bars in the vertical displacement field (in the experiments, part of the bar's length was located outside the furnace and, consequently, it remained colder than the central sections).

7.6.2 Discussion about the temperature-dependent mechanical properties of the materials

GFRP material

In order to use the thermomechanical model described in chapter 6, the constitutive relations (stress-strain and shear stress-distortion curves) for the GFRP had to be defined at each temperature. The values considered are based on the experimental results obtained in the small-scale tests carried out in the scope of the Fire-FRP project and reported in Correia *et al.* (2013b).

Regarding the characterisation of the tensile behaviour of the GFRP, tests were carried out in GFRP specimens heated previously at different temperatures: 20 °C, 60 °C, 90 °C, 120 °C, 150 °C, 200 °C and 220 °C. The maximum temperature was set based on the technical difficulties (laboratory restrictions of equipment) in performing tests at higher temperatures. These difficulties included the following aspects: (i) keeping the specimens at a constant temperature; (ii) keeping the grips of the test machine sufficiently cold; and (iii) temperature limitations of the measuring equipment, including the strain gauges. The specimens used in the tests consisted of rectangular laminates obtained by sawing GFRP plates (with similar fibre architecture to that of the tubular profiles) in samples of 1800 mm length, 20 mm width and 10 mm thickness.

Regarding the compressive behaviour of the composites, tests were carried out in 50 mm long GFRP I-specimens (section similar to that used in the fire resistance tests) at 20 °C, 60 °C, 90 °C, 120 °C, 150 °C, 200 °C and 250 °C.

In both tensile and compressive tests, the instrumentation installed included: (i) strain gauges to measure the axial deformation; (ii) thermocouples to measure the temperature in the specimen; and (iii) a load cell. Furthermore, in the compressive tests, two normal temperature displacement transducers and one high-temperature displacement transducer were also used.

During the compressive tests, it was observed that the strain gauges provided unreliable results at elevated temperatures. However, the ultimate compressive strength results, being measured by the load cells were considered accurate. Consequently, given the absence of information on the literature about this property as a function of temperature, the reduction of the compressive elasticity modulus was assumed to be equal to the reduction of the ultimate compressive strength. Further experiments are needed to validate this hypothesis.

Furthermore, as in both tensile and compressive tests, a roughly linear behaviour of the composite until failure was observed, in the numerical simulations, a constant elastic modulus was adopted for each temperature.

As the temperatures reached in the tests of the beams and columns were higher than those used in the mechanical tests, the following hypotheses were considered: (i) the

Temperature (°C)	Tensile (%)	Compressive (%)	Shear (%)
20	100	100	100
60	87	68.1	100
90	86	42.5	83.1
120	83	25.1	42.8
150	82	15.3	24.2
200	83	7.8	16.9
220	74	6.76	14.7
250	71	5.2	11.3
350	61	0.1	0.1
450	52	0.1	0.1
550	40	0.1	0.1
1000	0.1	0	0.1

Table 7.13: Percentage retention of the elastic and shear moduli considered at each temperature.

compressive elastic modulus of the laminate up to 350 °C is residual and equal to 0.1% of the elastic modulus at ambient temperature, as this is the decomposition temperature of the matrix and, after this temperature, the material only contains fibres that do not develop a significant resistance to compression (if they are not surrounded by the matrix); and (ii) for the tensile behaviour, it was considered that after 350 °C the matrix of the composite is decomposed and only the glass fibres are present. Hence, based on the work of Feih *et al.* (2010), reductions of 52% and 40% of the elastic modulus (compared to ambient temperature) were assumed at 450 °C and 550 °C, respectively. At 1000 °C, a reduction to 0.1% of the ambient temperature strength was adopted, as this is the melting temperature of the glass fibres.

Regarding the shear behaviour of the composites, GFRP specimens were tested at 20 °C, 60 °C, 90 °C, 120 °C, 150 °C, 200 °C and 250 °C. The specimens consisted of GFRP rectangular laminates obtained by sawing the GFRP plates used in the tensile tests at an angle of 10° in samples of 800 mm length, 25 mm width and 10 mm thickness. In all the specimens, strain gauges were installed according to a rosette arrangement and thermocouples were used to record the temperature.

Due to the inconsistent results obtained with the strain gauges, the shear modulus at each temperature was computed considering the same reduction that was measured for the shear strength. Once more, the shear modulus at a given temperature was considered constant. As for the compressive elastic modulus, a residual value of 0.1% of the shear modulus at ambient temperature was assumed for temperatures higher than 350 °C. This hypothesis needs to be validated based one further experiments.

Table 7.13 summarizes the percentage retention of the elastic and shear moduli at each temperature, being the reference values for tensile elastic, compressive elastic and shear moduli equal to 32.93 GPa, 29.97 GPa and 3.77 GPa, respectively. Figure 7.52 illustrates the variation of the elastic and shear moduli between 20 °C and 1000 °C.

Regarding the thermal expansion coefficient of the GFRP, table 7.14 summarizes the different values reported in the literature. It can be observed that, at ambient temperature, the variability of the thermal expansion coefficient value is high, depending mainly on the composite material (volume of fibres and type of fibres and resin) and also on the geometry

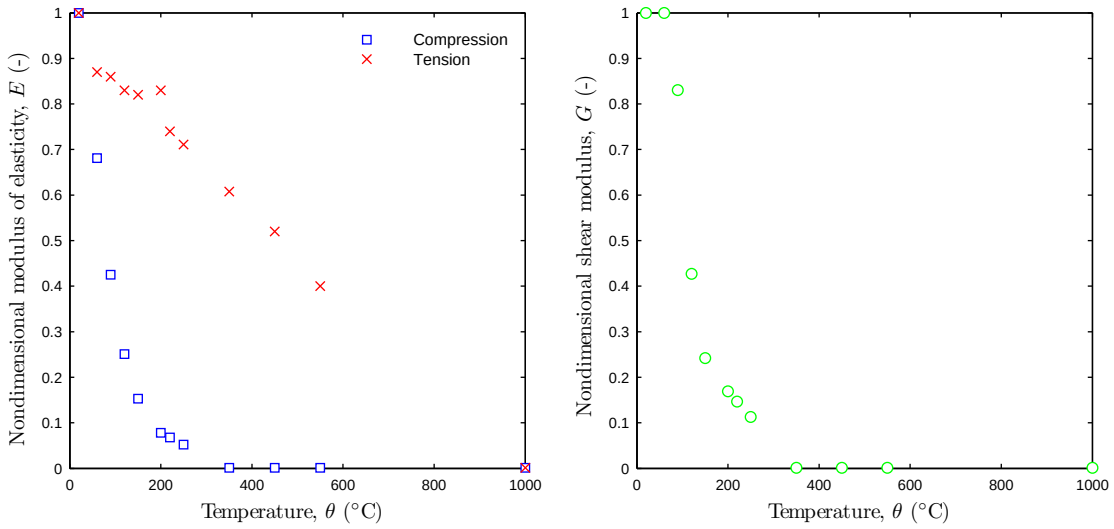

(a) Modulus of elasticity.

(b) Shear modulus.

Figure 7.52: Temperature-dependent variation of the elastic and shear moduli (divided by the respective values at a reference temperature equal to 20 °C).

of the sample tested. Furthermore, the thermal expansion coefficient is anisotropic, presenting different values in each direction (longitudinal, transverse and through-thickness). This cannot be considered in the one-dimensional thermomechanical model proposed. The experimental results presented in Tant *et al.* (1985) and Henderson *et al.* (1987) illustrate that the thermal expansion coefficient depends strongly on the temperature. However, the values reported were obtained in small samples and, consequently, the results could be affected by the scale effect. This was already discussed in section 2.3.3, where the graphical results of the mentioned references were reported.

In the present study, the thermal expansion coefficient was considered constant with the temperature, since there was no experimental data available and the values reported in the literature were not applicable to the material used in the tests. A value equal to $10^{-5}\,°C^{-1}$ was assumed. It was obtained as the average of the values reported by Tracy (2005) and the one indicated by Bank (2006) for GFRP shapes, both referring to the longitudinal direction. Both references were considered, as the corresponding materials are similar to the one used in the tests. However, the thermal expansion coefficient is dependent on the temperature and this could have an important effect, especially in the mechanical behaviour of the columns, as it will be discussed in section 7.7.3.

CS boards

In the analyses carried out, the CS elastic and shear moduli are modelled as constant and temperature-independent. The elastic modulus for tensile and compressive behaviour was set equal to 1200 MPa (value provided by the manufacturer). The shear modulus was computed considering that the material is elastic and the Poisson ratio is 0.2. Hence, a linear shear modulus of 500 MPa was obtained. The thermal coefficient expansion is equal to $-2.5 \cdot 10^{-6}\ °C^{-1}$ for temperatures between 20 and 600 °C (value provided by

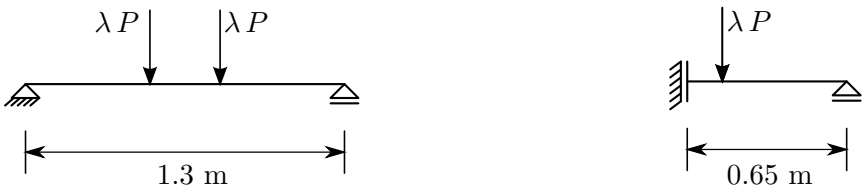

(a) Complete beam. (b) Beam simplified by symmetry.

Figure 7.53: One-dimensional mechanical model of the beam (dimensions in meters).

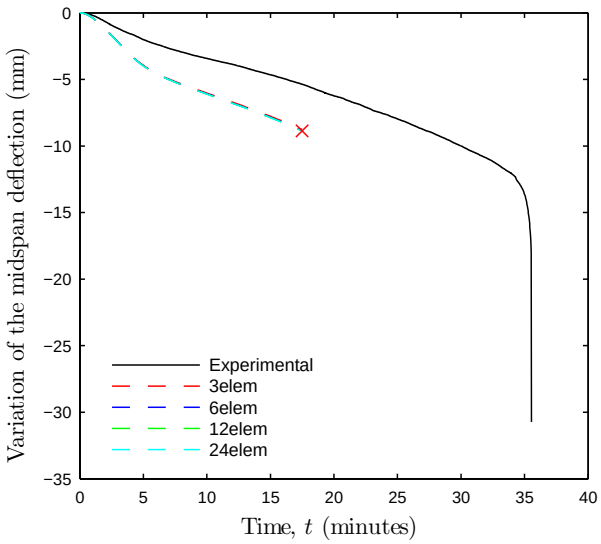

Figure 7.54: Time-deflection evolution.

the manufacturer). Since no more information was found in the literature, the mentioned value was adopted for temperatures higher than 600 °C. The contribution of the CS boards to the mechanical response of the profiles is not significant when compared with that of the GFRP profile.

7.6.3 Spatial discretization of beams

In the present section, a study about the spatial discretization along the length of the unprotected GFRP tubular beam subjected to fire in the bottom face is reported. Figure 7.53a summarizes its boundary conditions. In order to reduce the CPU time required for the simulations, the mechanical model of the beams was simplified by symmetry, hence only a half of the beam was modelled considering the boundary conditions illustrated in figure 7.53b. The load considered in the present study is equal to $P = 5.85$ kN (the one used in series S1 and S2).

Four meshes of 3, 6, 12 and 24 one-dimensional linear elements were used. Figure 7.54 depicts the experimental vertical displacement measured in the midspan of the beam and the numerical vertical displacements computed with each mesh.

It can be seen that the vertical displacement evaluated with all meshes is coincident. However, for all simulations of the thermomechanical behaviour of the GFRP profiles, the

Reference	Material	Temperature-	Value ($10^{-6}\,°C^{-1}$)	Observations
Tant *et al.* (1985) Henderson *et al.* (1987)	glass/phenolic	dependent	Graphical results (0-1600 °C)	Experimental and numerical results. Experimental thermal properties of composites.
Sullivan (1993)	glass/phenolic	independent (ambient)	$\alpha_1 = 9.0$ $\alpha_2 = 81.0$	—
Dimitrienko (1997)	epoxy composite	dependent	Not reported	The thermal expansion coefficient is computed using the results obtained for the heat deformation (graphical results between 0 and 800 °C).
Tracy (2005)	glass/polyester	independent (ambient)	$\alpha_1 = 12.6$ $\alpha_2 = 21.8$ $\alpha_3 = 37.0$	Experimental values obtained by using the rule of mixtures.
Bank (2006)	glass/vinylester	independent (ambient)	$\alpha_1 = 7.9$ $\alpha_1 = 14.4$ $\alpha_1 = 5.4$	Thin-walled shapes (wide flange 6-13 mm). Flat sheet (9-25 mm). Rods.
Liu *et al.* (2006)	glass/vinylester	independent (ambient)	$\alpha = 18.0$	—
Robert and Benmokrane (2010)	glass/vinylester	independent (ambient)	$\alpha_1 = 6.7$ $\alpha_2 = 27.2$	Experimental values obtained from bars.

Table 7.14: Thermal expansion coefficients available in the literature (1 – pultrusion direction, 2 – transverse direction and 3 – through-thickness direction).

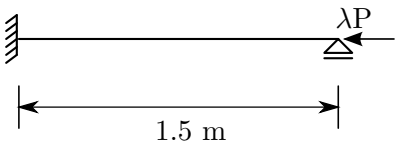

Figure 7.55: One-dimensional mechanical model of the column.

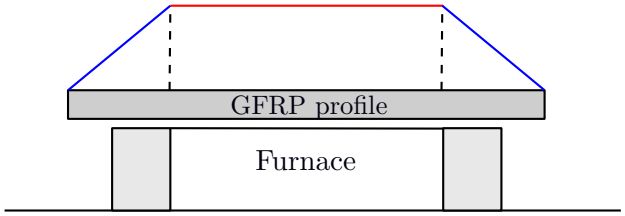

Figure 7.56: Temperature distribution assumed along the GFRP profiles length.

mesh consisting of 12 linear elements was selected because, as discussed in section 7.6.4, during the experimental tests, the extremities of the bar were colder than its central sections (as they were outside of the furnace). In order to take into account this effect and prescribe the colder temperatures at those extremity sections, a good refinement of the bar's length had to be considered.

In the simulations of the columns, a mesh of 30 linear elements was used. Figure 7.55 illustrates the one-dimensional model and the boundary conditions adopted.

7.6.4 Temperature distribution along the length bar

As mentioned, the temperature in all bar sections cannot be considered constant in the numerical simulations as, during the tests, the supports and a small length of the bars were located outside of the furnace, as illustrated in figure 7.1. Hence, the beams and columns had to be modelled considering that the central 0.95 m length of the profile was heated by the furnace (and, consequently, the temperature distribution in those cross sections was that computed in the thermal simulations), while the extremities of the bars had to be considered as being at colder temperatures. In the model, a simplifying assumption is considered that a linear reduction of the temperature takes place from the heated sections towards the supports, where the entire cross section is at ambient temperature. Figure 7.56 schematically represents the temperature distribution assumed.

In order to evaluate the effect of considering that all the cross sections are inside of the furnace and present the computed temperature distribution instead of considering that the extremities of the bars are colder, two simulations considering both cases were carried out. In these simulations, a mesh of 12 linear elements was used. The temperature distribution in the unprotected tubular profile subjected to fire in the bottom face was computed considering the model of Tracy (2005). The mechanical properties of the GFRP material are those defined in section 7.6.2.

Figure 7.57 illustrates the evolution of the vertical displacement at midspan as a function of time. The experimental curve and both numerical curves obtained considering either a constant or a variable distribution of the temperatures along the cross sections of the beam are depicted. It can be observed that the accuracy of the numerical results when

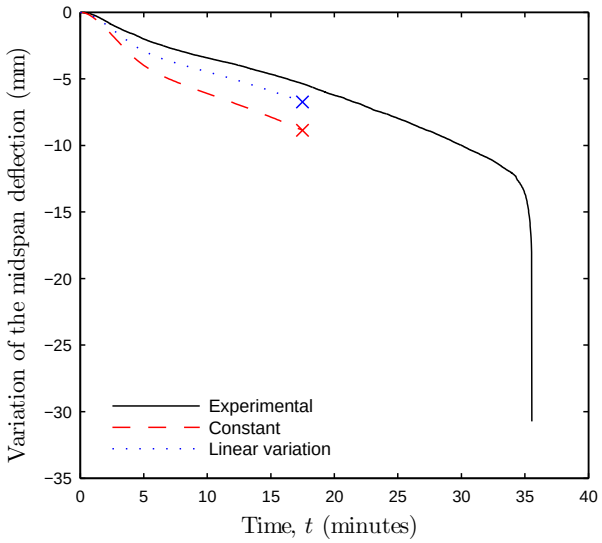

Figure 7.57: Variation of midspan deflection of unprotected tubular beam considering different temperature distributions along the length.

compared with experimental results increases when the temperatures along the length of the beam are variable.

7.6.5 Conclusions regarding the mechanical modelling and final characteristics of the mechanical simulations

The current section presented preliminary studies about the mechanical properties of the GFRP and CS materials, the spatial discretization of the bars and the effect of the temperature distribution along the bars in the vertical displacement of the beams.

Regarding the mechanical properties of the GFRP, material characterization tests obtained within the Fire-FRP project were only carried out up to a maximum temperature of 250 °C. These tests showed that the behaviour of the GFRP is almost linear until failure. For the temperatures where no experimental results were available, a linear degradation of the elastic and shear moduli was assumed.

Regarding the spatial discretization, it was demonstrated that a mesh with 3 linear elements was enough to reproduce the vertical displacement of the beams. However, in the study regarding the temperature distribution along the bar's length, this effect proved to be relevant and influenced the accuracy of the beam's midspan deflection evolution. Hence, a mesh of 12 elements was selected in order to be able to prescribe lower temperatures in the cross sections outside of the furnace. This result was applied to define the number of elements in the columns, where 30 elements were used.

7.7 Thermomechanical simulations of GFRP beams and columns

7.7.1 Introduction

The current section presents the numerical simulations of the thermomechanical behaviour of GFRP beams and columns exposed to fire.

The mechanical response is evaluated with the in-house uncoupled FE code described in chapter 6. In this model, the temperatures computed in the thermal simulations (reported in section 7.5) are used as input. The characteristics of the mechanical models are the ones described in section 7.6, namely the mechanical properties of the materials, the spatial discretization and the temperature distribution along the bars.

The cases analysed in this section are the ones summarized in tables 7.1 and 7.2 (page 150).

In the beam simulations, the numerical and experimental variation of the vertical displacement at midspan section are compared. For the column simulations, one compares the variation of the axial shortening and the variation of the vertical displacement (out of plane) at the central section. As discussed in section 7.5, for several cases, due to the time step size, it was not possible to obtain converged solutions for the entire duration of the experiments.

7.7.2 GFRP beams

The current section summarizes the numerical and experimental variation of the vertical displacement at the midspan section of the GFRP tubular and I-section profiles exposed to different fire scenarios.

Figure 7.58 depicts the variation of the vertical displacement obtained in the unprotected GFRP tubular beam subjected to fire in 1-face, for two different load levels. For both loading conditions, the FE code is able to reproduce the experimental measurements with relatively good accuracy (until the last instant for which a converged solution of the temperature field was obtained). It can be seen that for both cases, the model slightly overestimates the experimental data (20% and 10% at 1050 s when the loads applied are 11.7 kN and 18.7 kN, respectively). The results show that the relative differences in the evaluation of the temperature field throughout the cross section do not affect significantly the mechanical results. The better agreement for the mechanical response may be due to the fact that the tensile elastic modulus exhibits a progressive and very moderate reduction with temperature and, consequently, the inaccuracy in the reproduction of the temperature field does not readily propagate to the mechanical results.

The complete thermal response of the unprotected tubular cross section reported in the appendix F) was also used to evaluate the mechanical behaviour of the beam. Figure 7.59 shows the numerical and experimental variation of the vertical displacement in the unprotected GFRP tubular beam subjected to fire in 1-face. The numerical response depicted in figures 7.58 and 7.59 are coincident for the times where a converged solution was evaluated. Once more, it can be concluded that the FE code is able to reproduce the experimental results with good accuracy, specially for the second loading condition. The numerical results evidence that the model proposed is unable to represent the failure of the beam, as the material is modelled as linear (for different temperatures) and a failure criteria was not implemented.

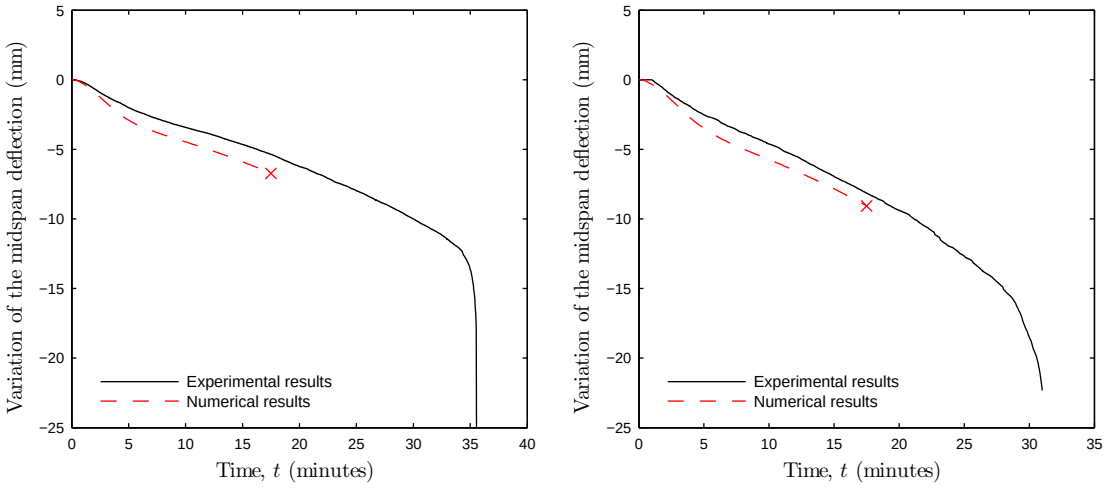

(a) Load 1 (11.7 kN). (b) Load 2 (18.7 kN).

Figure 7.58: Midspan deflection evolution in the unprotected tubular beam subjected to fire in 1-face.

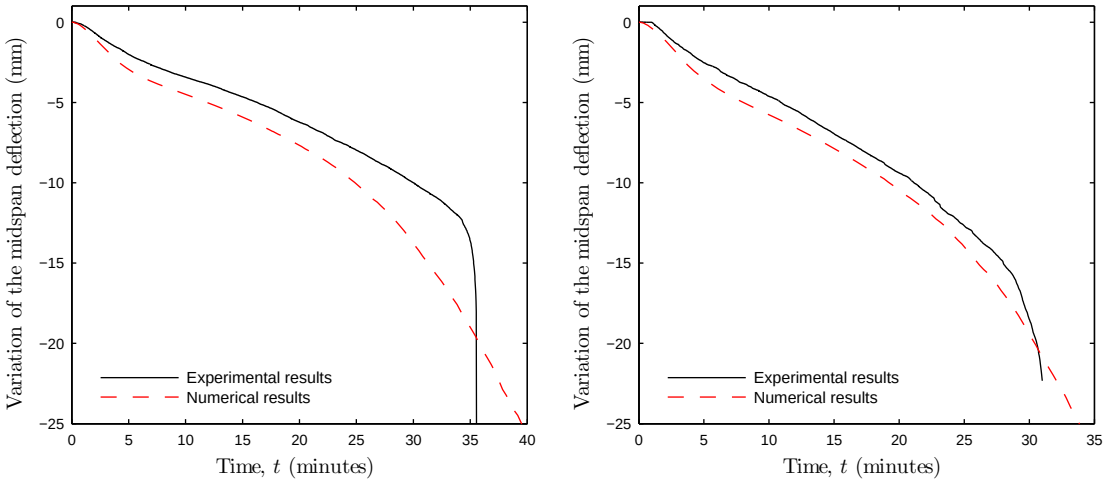

(a) Load 1 (11.7 kN). (b) Load 2 (18.7 kN).

Figure 7.59: Midspan deflection evolution in the unprotected tubular beam subjected to fire in 1-face (complete response).

Figure 7.60 displays the numerical and experimental variation of the vertical displacement in the protected GFRP tubular beam subjected to fire in 1-face. Once more, good agreement between numerical and experimental results is observed for the two load levels considered.

The variation of the vertical displacements, both computed and measured, in the unprotected and protected tubular GFRP beams exposed to fire in 3-faces is presented in figures 7.61 and 7.62, respectively. In the first case, the measured experimental variation of the vertical displacement is reproduced by the numerical solution with good accuracy. In the second case, the numerical solution indicates that the beam experiments a positive

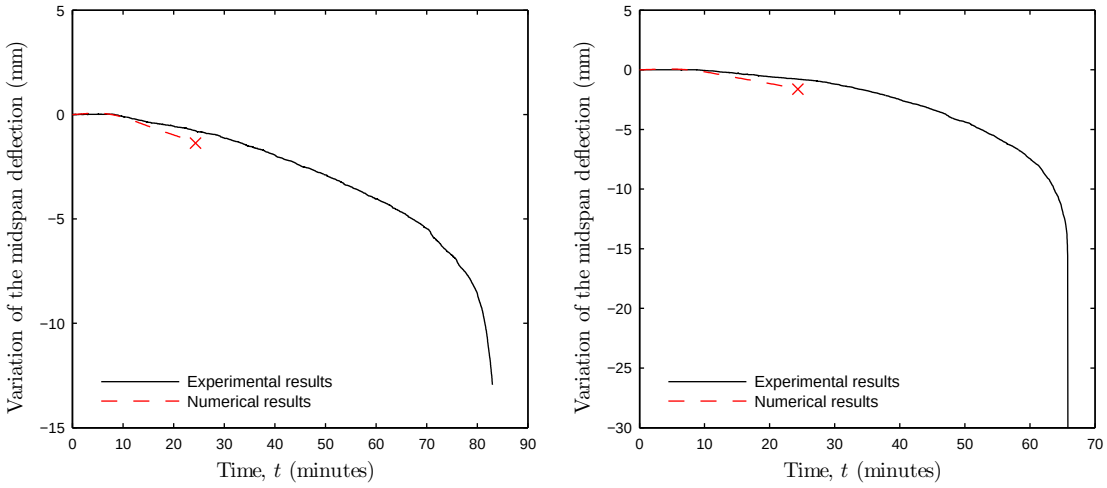

(a) Load 1 (11.7 kN). (b) Load 2 (18.7 kN).

Figure 7.60: Midspan deflection evolution in the protected tubular beam subjected to fire in 1-face.

vertical deflection variation during the first 8 minutes of exposure. However, the experimental data show that the variation of the vertical displacement oscillates from positive to negative (reduced values). After 8 minutes, the model seems to recover the experimental response of the beam. The differences encountered in this case may be due to the aforementioned possible inaccuracy in modelling the effects of thermal expansion in the GFRP material.

Finally, figures 7.63 and 7.64 display the variation of the vertical displacement in the midspan of the unprotected and protected GFRP I-section beams exposed to fire in 3-faces. The numerical results obtained in the unprotected beam are coherent with the experimental ones, even if, at the end of the simulation the numerical and the experimental values exhibit different magnitude. As discussed in section 7.5, the deviation can be due the duration of the test, which was very short and may have introduced an additional variability to the experimental results. Furthermore, the furnace temperatures during the test period were considerably lower than those defined in ISO 834 (1975).

In the case of the protected GFRP I-section beam, a positive variation of the midspan deflection is observed experimentally until 10 minutes. After this moment, the deflection variation was negative. In general terms, the variation of the vertical displacement can be considered to be well reproduced by the thermomechanical model.

7.7.3 GFRP columns

The current section presents the results obtained for the thermomechanical simulations of the GFRP tubular and I-section columns exposed to fire.

At this point, it is deemed relevant to make a remark about the experimental setup used in the fire resistance tests, namely in the tests performed on GFRP columns, and its relation with the boundary conditions defined in the thermal simulations. In section 7.4.2 a discussion about the boundary conditions needed to obtain accurate numerical results was presented. One of the conclusions was that the fluid in the cavity has to be taken into

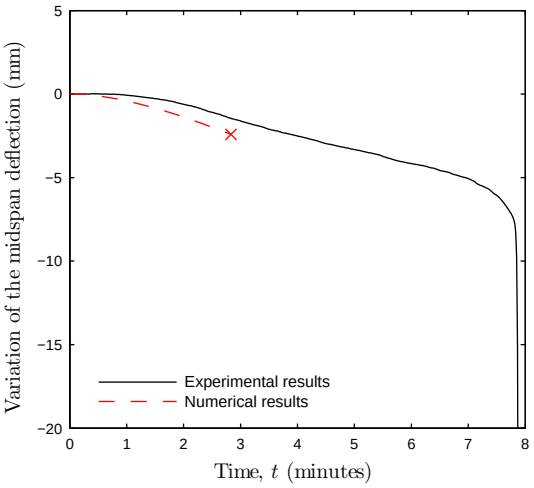

Figure 7.61: Midspan deflection evolution in the unprotected tubular beam subjected to fire in 3-faces (11.7 kN).

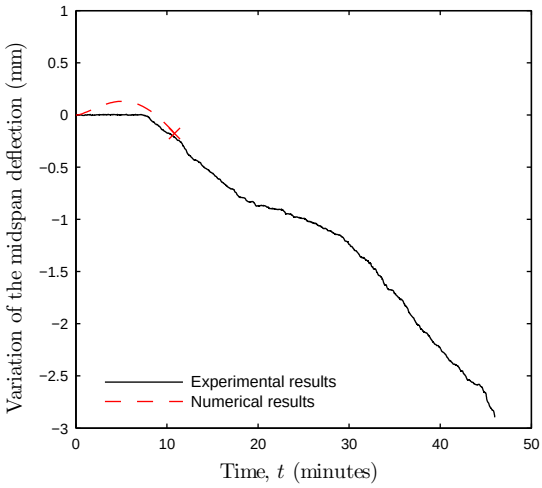

Figure 7.62: Midspan deflection evolution in the protected tubular beam subjected to fire in 3-faces (11.7 kN).

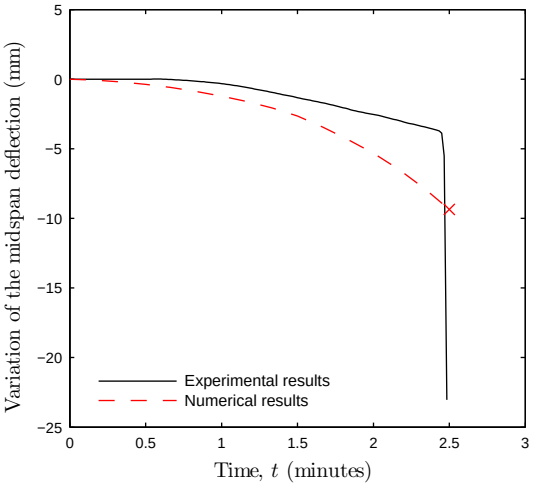

Figure 7.63: Midspan deflection evolution in the unprotected I-beam exposed to fire in 3-faces (7.4 kN).

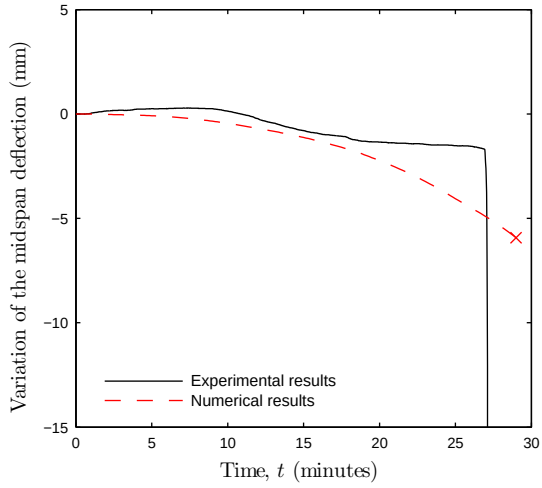

Figure 7.64: Midspan deflection evolution in the protected I-beam exposed to fire in 3-faces (7.4 kN).

account, as the natural convection in the cavity together with the radiation between the walls of the cavity, significantly influences the temperature field in the cross section. In the fire resistance tests, the columns were tested in a horizontal position, and the numerical simulations performed in this work aimed at reproducing the test conditions observed in those tests. Since natural convection is affected by gravity, it is worth pointing out that the numerical simulations performed are not valid for real columns, whose axis is along the vertical direction. In this case, in order to accurately take into account the effects of natural convection, a three-dimensional thermal model needs to be developed.

Figure 7.65 illustrates the numerical and experimental variation of the vertical displacement in the central section and the axial shortening obtained in the unprotected GFRP tubular column exposed to fire in the bottom face.

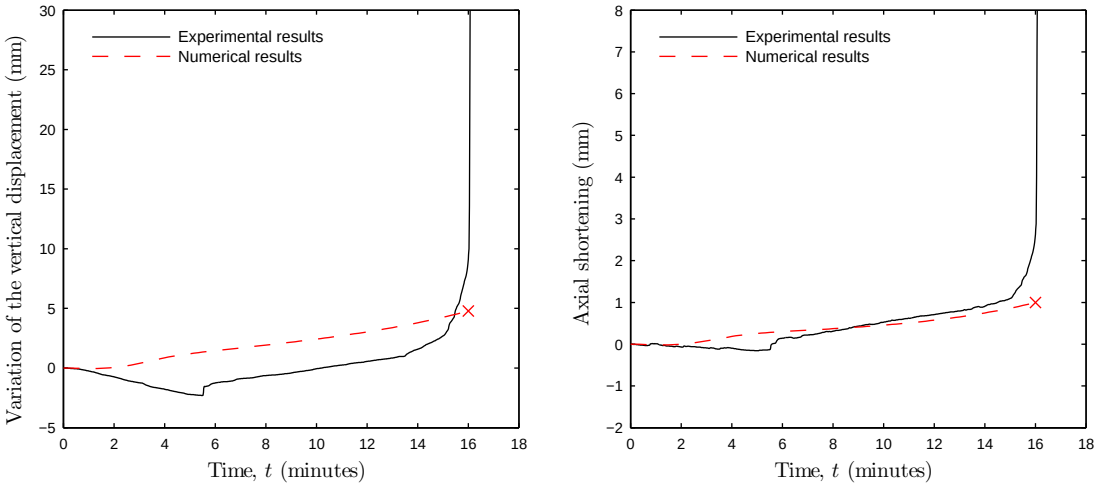

(a) Variation of the vertical displacement.

(b) Axial shortening.

Figure 7.65: Unprotected tubular column subjected to fire in 1-face (55 kN).

Analysing the experimental curves, it can be observed that, during the first 6 minutes, the rate of the variation of the vertical displacement in time of the column is negative, while the axial shortening is positive and, consequently, the column is expanding due to the temperature increase. After that instant, the sudden[2] variation of the vertical displacement is positive and the column exhibits axial shortening until failure. In the numerical results, the same effect is observed but in a different magnitude. In fact, until 2.5 minutes, the column develops a slight negative vertical displacement and axial expansion. Subsequently, the vertical displacement becomes positive and the column starts contracting. The main difference between the numerical and the experimental results occurs during the first instants, *i.e.*, during the (experimental) thermal expansion of the column. The model is not able to represent correctly this effect, probably due to the consideration of the thermal expansion coefficient as constant. Furthermore, as referred in section 7.6.2, the thermal expansion coefficient is also anisotropic and the values available in the literature — summarized in table 7.14 — point out that the thermal coefficient in the transversal and through-thickness directions can be until three times higher than in the longitudinal value. This fact cannot be considered in the one-dimensional model proposed and this may have also affected the quality of the results. Further simulations were carried out using different values of the thermal expansion coefficient — $5 \cdot 10^{-5}$ and $2 \cdot 10^{-5}$ — in order to evaluate this effect in the results. It was observed that higher values of the thermal expansion coefficient represent with more accuracy the initial behaviour of the column. The results obtained indicate that the thermal expansion coefficient strongly influences the solution and, consequently, it can be considered as a fundamental parameter for the numerical analyses of columns. Hence, deepest knowledge about its value and evolution with the temperature is required in order to reproduce correctly the mechanical response of the columns. In addition, the relative differences in the temperature field of the cross section will affect more the mechanical response of the columns than that of the beams,

[2]This sudden variation in the experimental vertical displacement is most likely due to an instantaneous rotation at the supports (associated to friction in the test setup components), which obviously can not be reproduced by the model.

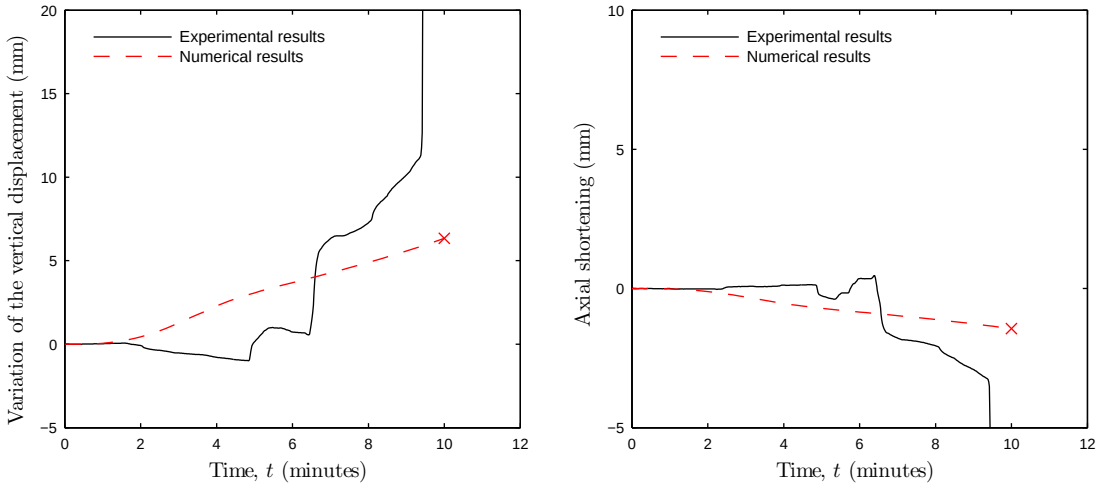

(a) Variation of the vertical displacement.

(b) Variation of the axial shortening.

Figure 7.66: Unprotected tubular column subjected to fire in 1-face (110 kN).

as the variation of the compressive elastic modulus with the temperature is more significant and steep when compared with the variation of the tensile elastic modulus. It is also very likely that the response of the columns is influenced by creep, which is also not accounted for in the model due to the lack of experimental data available. In fact, it is well known that GFRP materials present significant creep at ambient temperature, with the magnitude of such viscoelasticity increasing experimentally with temperature. This effect is expected to be much more relevant in the columns (in compression) than in the beams, where the glass fibres (that do not creep) carry the tensile stresses at the hottest part of the cross section (Dutta and Hui, 2000).

The numerical results also evidence that the model does not represent the failure of the columns, because the material was modelled as linear at each temperature and no failure criteria were defined.

In addition, the thermomechanical simulation of the unprotected tubular columns with a compressive load equal to 110 kN was also performed. Figure 7.66 depicts the numerical and experimental vertical displacement variation and axial shortening. The variation exhibited by the experimental curve is less uniform than in the previous case. This should be attributed to adjustments in the components of the test setup (due to friction between pieces, minute settlement/rotation of supports) and, to some extent, the slight changes in the applied load during the test.

Figure 7.67 displays the numerical and experimental vertical displacement variation and axial shortening obtained for the unprotected GFRP tubular column subjected to fire in 3-faces.

The experimental results illustrate that, until 1 minute of exposure, the column presents a reduced axial shortening and a positive vertical displacement. However, after this instant, the column starts to expand and the vertical displacement becomes negative until failure — when the vertical displacement suddenly changes to positive. Numerically, at the initial instants, the column presents axial expansion due to the temperature gradient and the variation of the vertical displacement is negative. After approximately 2 minutes, a modification in the slope of the curves can be observed with both variations of vertical

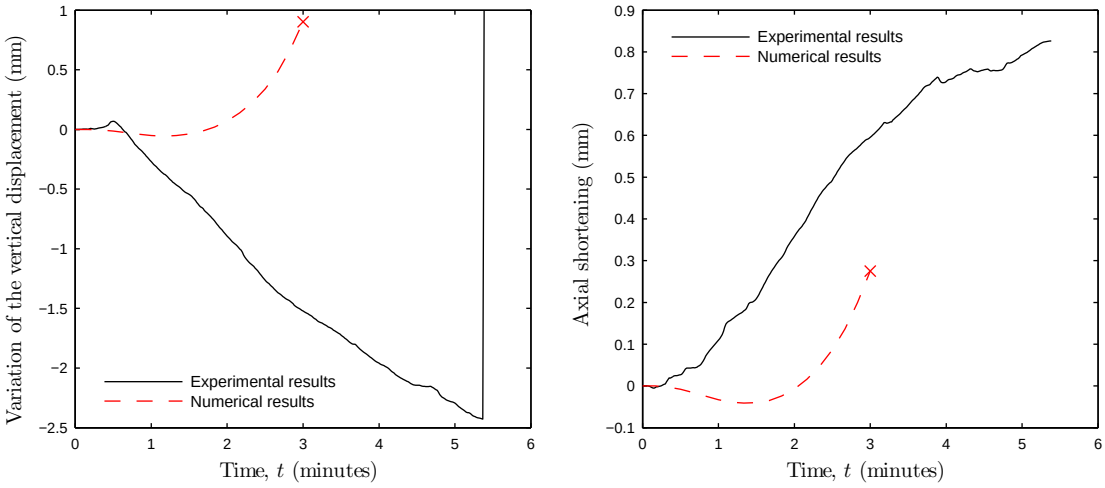

(a) Variation of the vertical displacement.

(b) Axial shortening.

Figure 7.67: Evolution of mechanical response of unprotected tubular column subjected to fire in 3-faces (55 kN).

displacement and axial shortening being positive. The causes of this disagreement between the numerical and the experimental results could be the following: (i) the adequacy of the GFRP physical-mechanical properties adopted, especially for the thermal expansion coefficient; (ii) the nonlinear elastic constitutive model employed for the material (as the stress resultants distributions in hyperstatic structures is dependent on it); (iii) the accuracy of the temperature field computed during the thermal simulations; (iv) the creep, which, as mentioned, is not considered in the simulations; and (v) the boundary conditions during the experimental test (namely, the clamped support, which may have not fully prevented the rotation at the left support).

Regarding the thermomechanical behaviour of the protected tubular columns subjected to fire in the bottom face, two simulations were carried out considering different load levels: 55 kN and 110 kN. However, as the experimental results obtained with the first load level are difficult to interpret, only the simulation of the column subjected to the second load level (110 kN) is reported and illustrated in figure 7.68.

The variation of the vertical displacement measured experimentally oscillates from positive to negative until failure, which occurs at 37 minutes with a sudden positive vertical deflection variation. During the entire duration of the test, the values of the vertical displacement were reduced (below 0.2 mm, close to the precision of the displacement transducer), while the axial shortening was positive and significant. However, in the numerical simulations, the column presents a monotonic and positive variation of the vertical displacement. Regarding the axial shortening, the numerical results indicate a continuous axial shortening of the column (as the experimental data), although the magnitude of such variation is lower than measured. The reasons mentioned before may explain these relative differences.

Additional thermomechanical simulations of GFRP tubular columns and unprotected and protected I-section columns, all exposed to fire in 3-faces, were carried out. The numerical response observed in all cases was similar: during the initial instants, the columns developed a negative variation of the vertical displacement and an expansion due to the

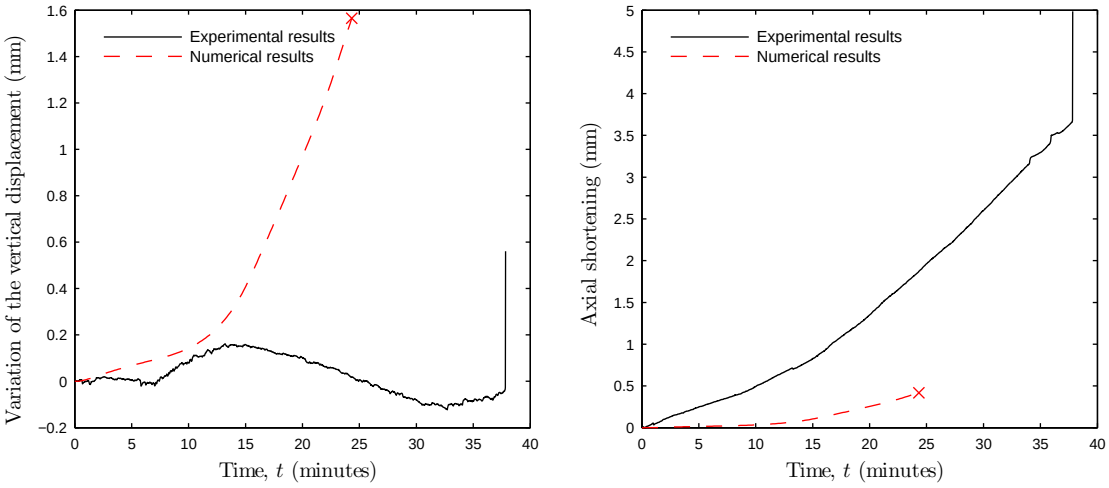

(a) Variation of the vertical displacement.

(b) Variation of the axial shortening.

Figure 7.68: Evolution of mechanical response of protected tubular column subjected to fire in 1-face (110 kN).

temperature increase. Subsequently, the variation of the vertical displacement increased progressively until attaining positive values. The same effect could be observed in the evolution of the axial shortening, with the initial expansion changing to a subsequent shortening. These results are reported and discussed in the appendix H, as they do not provide further information regarding the thermomechanical behaviour of GFRP columns.

7.7.4 Concluding remarks about the thermomechanical modelling

The current section presented the results obtained in the thermomechanical simulations of GFRP beams and columns. A brief summary of those results is presented next.

The mechanical properties of the materials involved, *i.e.*, the GFRP profiles and CS boards, were considered. For compression and shear, the moduli reduction with temperature was based on the reduction observed in the ultimate strength. The material model proposed assumed that the elastic and shear moduli at each temperature is constant. The elastic and shear moduli of the CS boards were considered constant and temperature-independent, assuming the values provided by the manufacturer.

Numerical analyses about the influence of the spatial discretization and the temperature distribution along the bars were also presented, the second study being fundamental for the thermomechanical simulation of the GFRP profiles.

In general, the thermomechanical model proposed simulated with good accuracy the variation of the midspan displacement of the beams subjected to different load levels. The differences between the numerical and experimental temperatures were not significantly propagated to the mechanical results; this was attributed to the fact that the variation of the tensile elastic modulus with temperature is slow and has relatively low magnitude. However, the model proposed was much less accurate in simulating the mechanical behaviour of the columns. One possible reason is the adequacy of the constitutive model (nonlinear elastic) employed to define the mechanical behaviour of the material. This model affects the stress resultants distributions in the columns as they are hyperstatic

structures. Contrariwise, the beams are statically determined and the reactions in the supports do not depend on it.

As pointed out along the chapter, the adequacy of the GFRP mechanical properties adopted, the accuracy of the temperature field computed, the (non) consideration of the creep effects and, finally, the boundary conditions defined in the model may explain this worse simulation accuracy.

7.8 Thermal simulation of tubular and I-profiles subjected to different fire scenarios

7.8.1 Introduction

This section presents numerical results obtained in tubular and I-sections subjected to different fire scenarios from those used in the experimental tests. The main goal is to assess the applicability of the thermal code to other possible fire scenarios during a building's service life. The following applications were tested:

- Unprotected tubular GFRP cross section completely exposed to fire in 3-faces;
- Unprotected tubular GFRP cross section exposed to fire in 4-faces;
- Protected tubular GFRP cross section exposed to fire in 4-faces;
- Protected GFRP I-section completely exposed to fire in 3-faces;
- Protected GFRP I-section exposed to fire in 4-faces.

The results presented in this section illustrates the ability of the developed code to exclusively analyse the thermal response of a given cross section exposed to a fire situation. In some cases the achieved temperatures largely exceed the temperature of decomposition of the GFRP matrix.

In all applications, convective and radiative heat flux are prescribed in the faces exposed to fire (the temperature is time dependent and follows the ISO 834 (1975) curve) and to the ambient (the ambient temperature was set equal to 20 °C). In the cavity, both the natural convection and the radiative heat exchange between faces are considered. The time step used was 1 second. The stabilization SUPG was considered in all the simulations. Further features of the numerical simulation are detailed in the corresponding subsection.

A study about the behaviour of the fluid in the cavities is carried out for all the applications, illustrating the temperature and velocity fields at different instants. Moreover, the temperature evolution in particular locations of the cross sections is also depicted.

7.8.2 Unprotected tubular GFRP cross section completely exposed to fire in 3-faces

A nonlinear transient simulation about the thermal behaviour of an unprotected tubular profile exposed to fire in 3-faces was performed using an adaptive mesh of 3409 nodes and 784 elements (see figure 7.24a). The final computational time set was 3600 seconds (1 hour).

Figure 7.69 illustrates the velocity and temperature field at different computational times. It can be observed that at the end of 1 hour the temperature of the air and of the

cross section (with exception of the top flange) is almost identical and the velocity in the fluid is almost null, indicating that the steady state is almost reached.

It can be observed that the behaviour of the fluid in the cavity when the lateral faces of the section are completely heated is contrary to the behaviour of the fluid when the cavity is heated only in the bottom face (section 7.4.3): in the present case two Bénard cells are generated in the cavity; the flow in the right cell is counter-clockwise, being clockwise in the left cell.

In order to compare these results with those reported in figure 7.31 (section 7.5.3), figure 7.70 depicts the velocity and temperature fields, the streamlines and the velocity vectors at $t = 100$ s.

These results show that small variations in the boundary conditions cause remarkable changes in the behaviour of the fluid in the cavity. This fact is important as, in future simulations, efforts will have to be carried out in order to investigate in further depth the fluid dynamics problem, as it constitutes the main handicap in the simulations of the thermal behaviour of GFRP profiles containing a cavity when using the present code.

Figure 7.71 illustrates the temperature distribution in the thermocouples, whose position is summarized in table 7.3. The temperatures in the bottom flange and in the lateral faces are almost identical in all the instants. The temperatures in the top flange are lower than the temperatures in the bottom flange and web due to the radiative and convective heat transfer between the ambient and the top flange. The results also illustrate that the temperature in the top flange is not uniform, the maximum temperature gradient being approximately equal to 300 °C at 3600 seconds (value evaluated between the thermocouples T1 and T3).

7.8.3 Unprotected tubular GFRP cross section exposed to fire in 4-faces

This example was performed using the mesh depicted in figure 7.24a. The final computational time set was 3600 seconds.

Figure 7.72 shows the velocity and temperature field at different instants. In this case, at the end of the computational time, the temperature in the fluid and in the solid can be considered identical. Regarding the velocity field, two Bénard cells are generated where the ascension of the fluid occurs in the nearest of the lateral faces. The velocity is reduced at all time steps, as well as the temperature gradient in the fluid.

Figure 7.73 depicts the velocity and temperature fields at 3600 seconds, using a different scale than that on the figures 7.72g and 7.72h . It can be observed that the velocity in the fluid is close to null and that the temperature in the cross section is almost uniform at all points, the maximum difference being 5 °C.

Finally, as in the previous section, figure 7.74 illustrates the temperature distribution in the thermocouples (table 7.3). The temperatures in the bottom face, web and thermocouple T2 are almost identical during the 3600 seconds, as these thermocouples are located at the same distance from the heated face. By analysing the temperature distribution in the top flange, it can be observed that, between 10 and 30 minutes, the temperature at each thermocouple is not coincident. The temperature decreases successively between thermocouples T1, T2 and T3. This result is coherent with the increase of the distance between the thermocouples and the top face. Figure 7.72 indicates that, between 10 and 30 minutes, the velocity of the fluid is not null and the Bénard cells are created. After

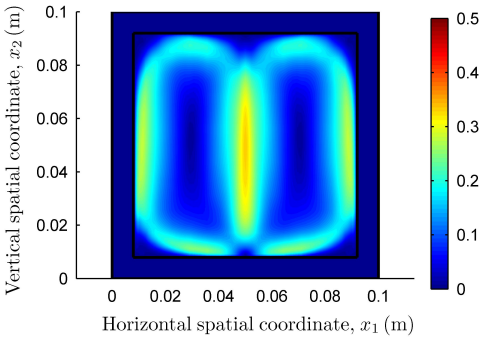

(a) Resultant velocity field, $t = 300$ s.

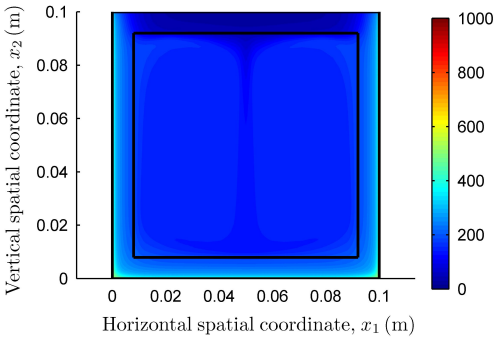

(b) Temperature field, $t = 300$ s.

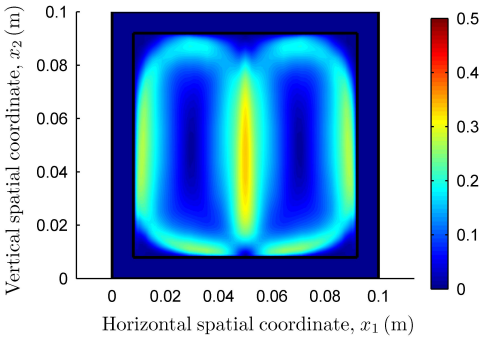

(c) Resultant velocity field, $t = 900$ s.

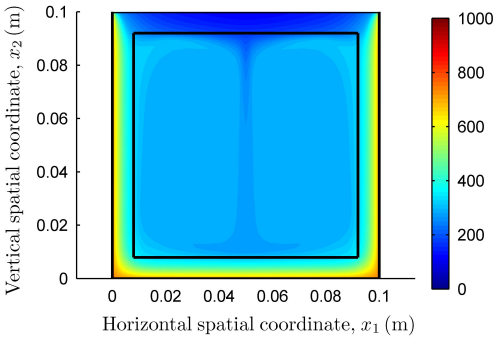

(d) Temperature field, $t = 900$ s.

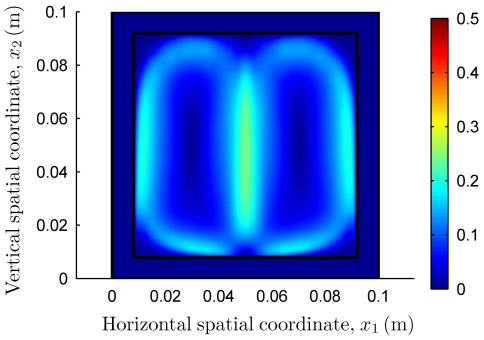

(e) Resultant velocity field, $t = 1800$ s.

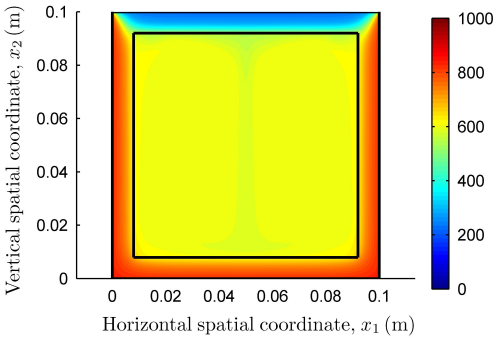

(f) Temperature field, $t = 1800$ s.

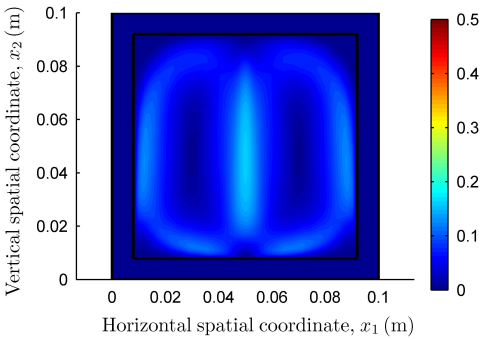

(g) Resultant velocity field, $t = 3600$ s.

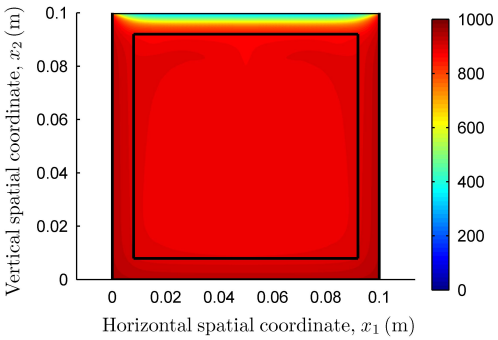

(h) Temperature field, $t = 3600$ s.

Figure 7.69: Unprotected tubular GFRP cross section with 3-faces exposed to fire.

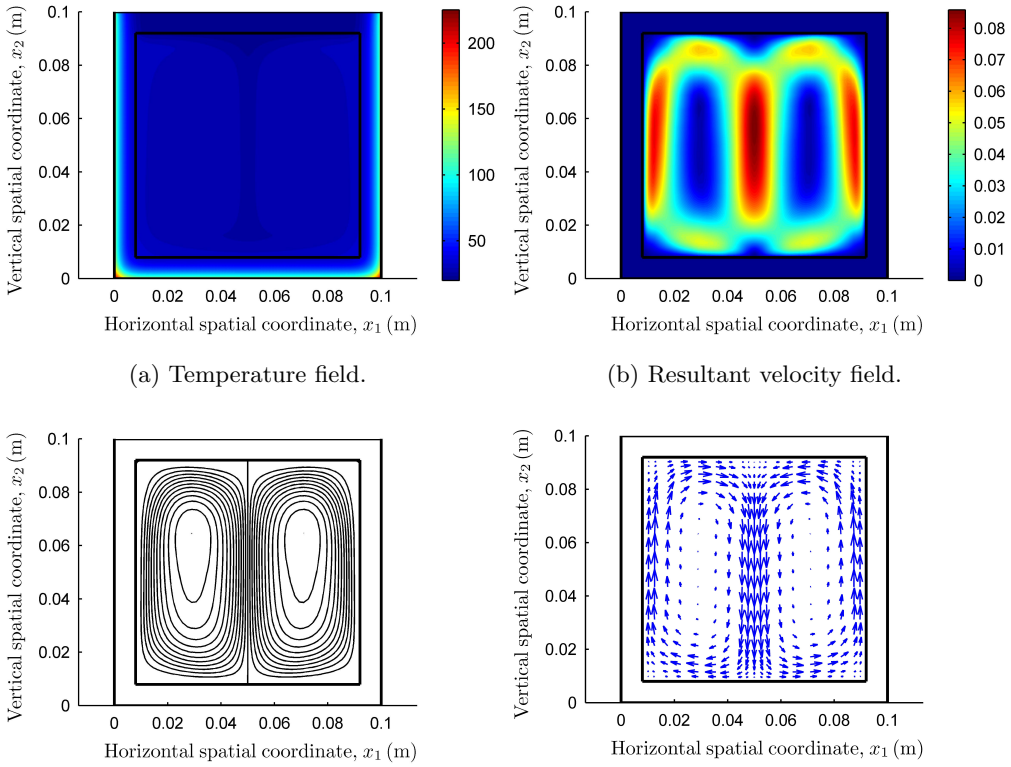

(a) Temperature field.

(b) Resultant velocity field.

(c) Streamlines.

(d) Velocity field.

Figure 7.70: Results for tubular profile exposed to fire in 3-faces (lateral faces completely exposed to fire).

30 minutes of exposure, the temperature in all the thermocouples is identical, indicating that the cross section is at uniform temperature.

7.8.4 Protected tubular GFRP cross section exposed to fire in 4-faces

A transient nonlinear analysis was performed employing a mesh of 5489 nodes and 1296 elements (896 in the solid and 400 in the cavity), the final computational time set equal to 3600 seconds. Figure 7.75 illustrates the mesh used.

Figure 7.76 depicts the temperature and velocity fields at different time steps. As in the previous case, the temperature in the cavity is uniform, as well as in the GFRP composite.

The Bénard cells are observable only at 300 seconds. At 900 seconds, the previous two vertical cells split into four cells, two reduced cells being situated in the top of the cavity. At 1800 and 2600 seconds the fluid presents a complex behaviour, where the Bénard cells break down. The behaviour of the fluid is not symmetric any more with respect to the vertical axis, even if the geometry and the boundary conditions are symmetric.

Figure 7.77 illustrates the temperature evolution in the thermocouples (whose position is detailed in table 7.3) until 1 hour, where it can be observed that the temperature in all the GFRP composite is almost uniform. However, after 30 minutes of exposure, the temperature in thermocouple T3 is higher than the temperature in the remaining thermocouples, because thermocouple T3 is closer to the heated face.

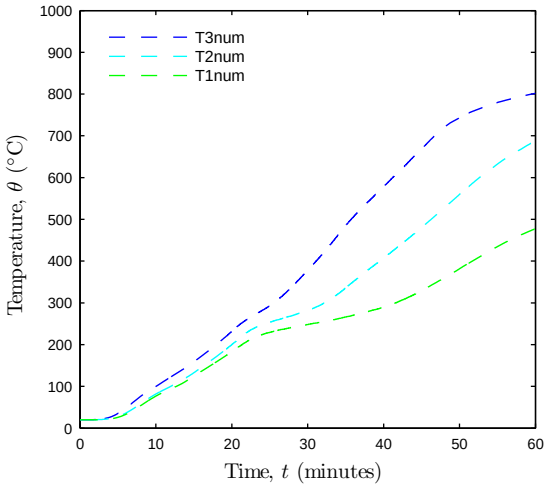

(a) Top flange.

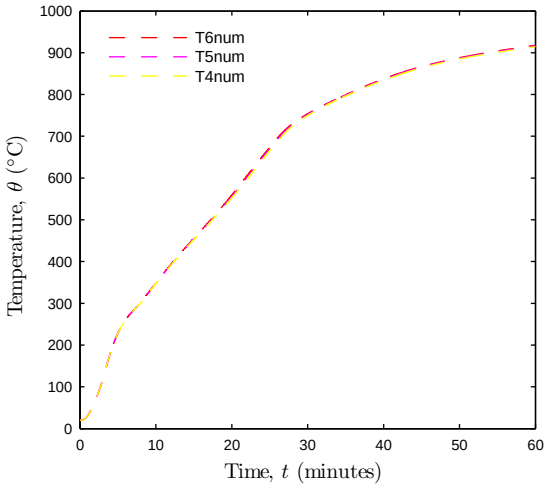

(b) Web.

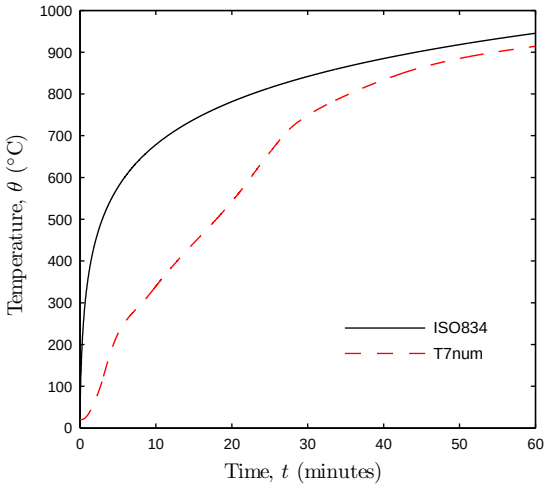

(c) Bottom flange.

Figure 7.71: Temperature evolution in the thermocouples position obtained in a tubular cross section completely exposed to fire in 3-faces.

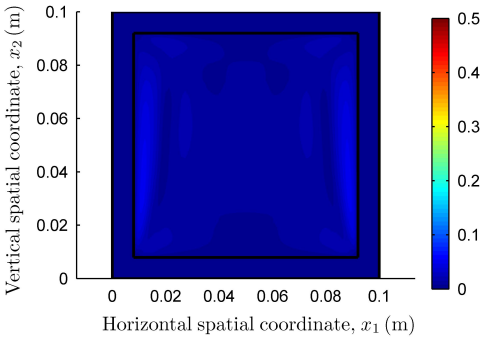

(a) Resultant velocity field, $t = 300$ s.

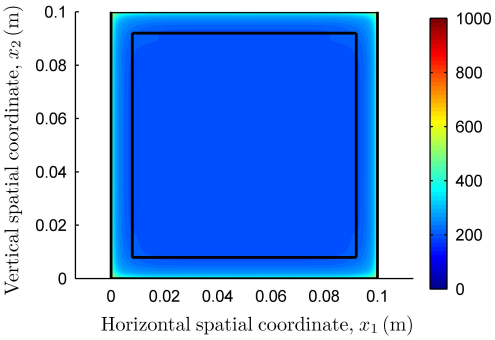

(b) Temperature field, $t = 300$ s.

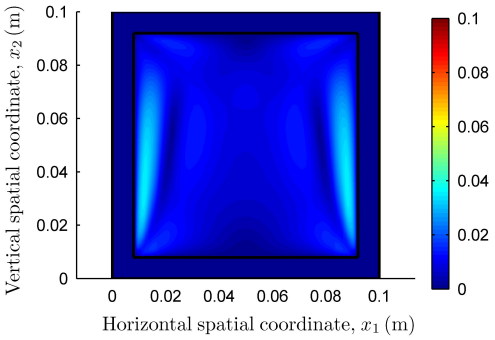

(c) Resultant velocity field, $t = 900$ s.

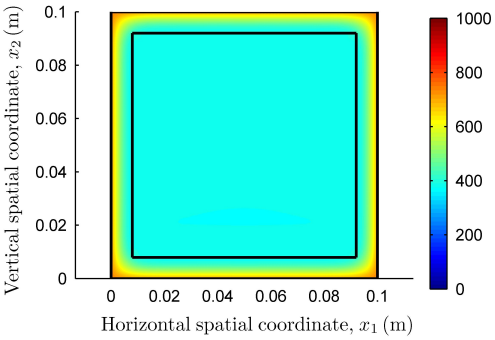

(d) Temperature field, $t = 900$ s.

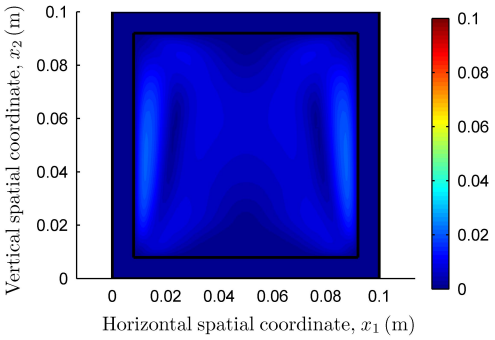

(e) Resultant velocity field, $t = 1800$ s.

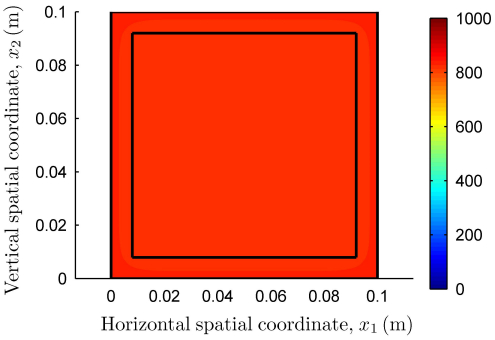

(f) Temperature field, $t = 1800$ s.

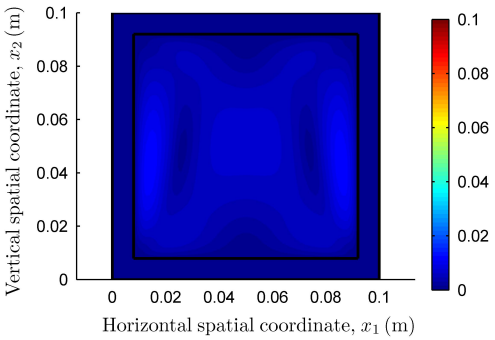

(g) Resultant velocity field, $t = 3600$ s.

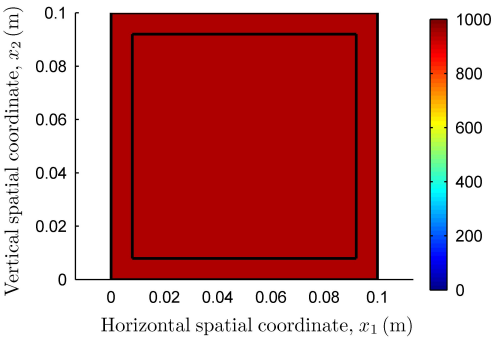

(h) Temperature field, $t = 3600$ s.

Figure 7.72: Unprotected GFRP tubular cross section with 4-faces fire exposure.

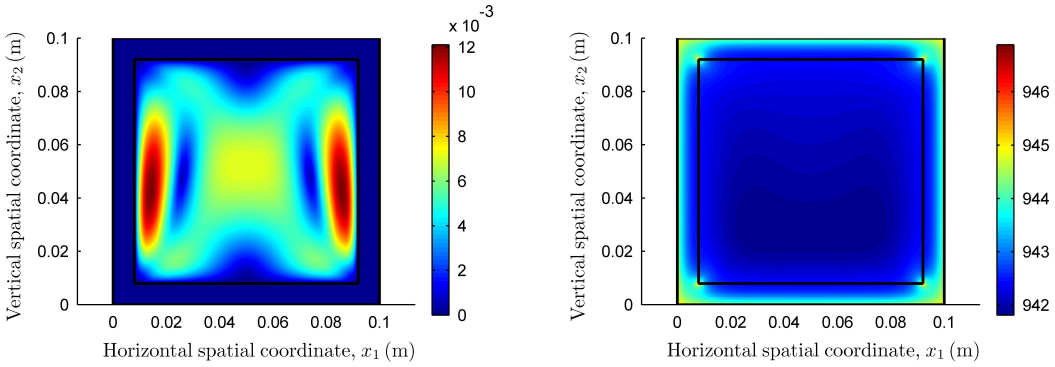

(a) Resultant velocity field, $t = 3600$ s.

(b) Temperature field, $t = 3600$ s.

Figure 7.73: Velocity and temperature field at $t = 3600$ s.

7.8.5 Protected GFRP I-section completely exposed to fire in 3-faces

A mesh of 8537 nodes and 2016 elements (*cf.* figure 7.49) is used in order to perform the transient nonlinear FE analysis. The time step was set equal to 1 second and the final computational time — where a converged solution was obtained — was 1800 seconds.

Figure 7.78 shows the temperature and velocity fields at different instants. The behaviour of the fluid is similar to that observed in the protected I-profile exposed to fire in 3-faces where the upper 2.5 cm of the lateral faces are insulated (section 7.5.7). In order to compare these results with the ones presented in section 7.5.7, the velocity and temperature fields at 1000 s are also therein depicted.

It can be observed that, in this case, only one clockwise convective cell is developed at 1000 s, contrary to the behaviour of the fluid when the lateral faces of the cavity are partially heated.

At 1800 seconds, a second convective cell is formed in the top of the cavity, this behaviour being similar to that reported in section 7.5.7.

Figure 7.79 presents the temperature evolution in the thermocouples position defined in table 7.11. It can be observed that the temperature in the thermocouples is practically uniform, this result being coherent with figure 7.78.

7.8.6 Protected GFRP I-section exposed to fire in 4-faces

In the present case, the protected I-section is exposed to fire in 4-faces. A mesh (based on the mesh employed in the previous example) of 9449 nodes and 2240 elements (1408 in the solid and 832 in the cavity) is used in order to perform the FE analysis. Figure 7.80 depicts the mesh used. The final computational set was 3600 seconds.

Figure 7.81 shows the temperature and velocity fields at different instants and figure 7.82 depicts the temperature evolution in the thermocouples position (table 7.11). In this case, the temperature in all thermocouples is identical and, consequently, the temperature in the GFRP is nearly uniform in all instants.

7.8.7 Final remarks

In the present section, further applications of the FE model were presented, in which tubular and I section profiles were subjected to fire scenarios different from those used in

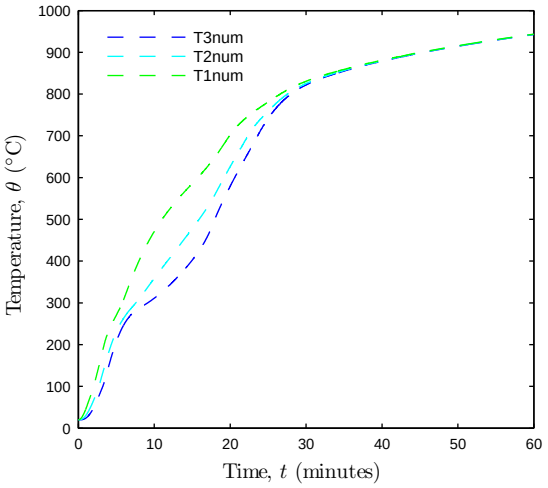

(a) Top flange.

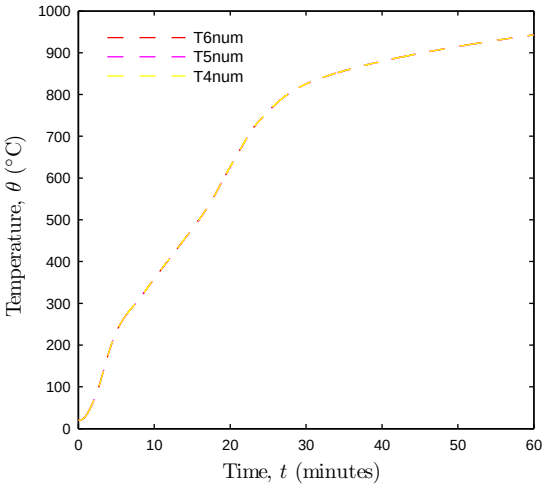

(b) Web.

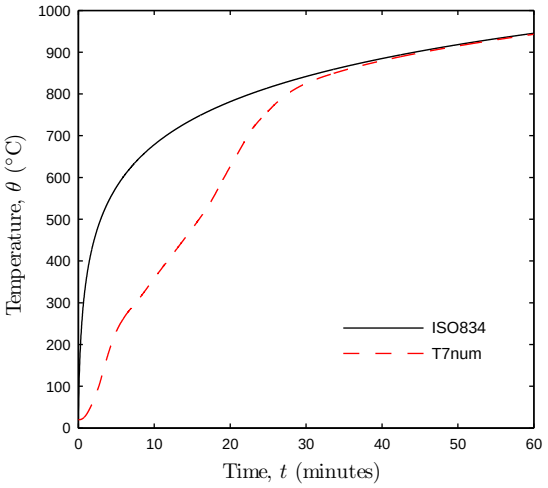

(c) Bottom flange.

Figure 7.74: Temperature evolution in the thermocouples position obtained in a tubular cross section subjected to fire completely in 4-faces.

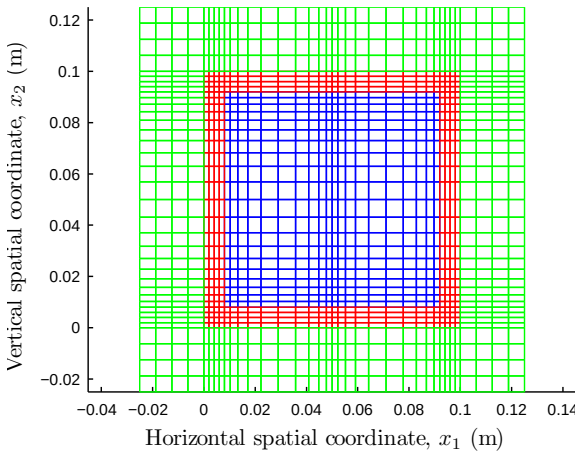

Figure 7.75: Mesh employed in the modelling of the protected tubular cross section exposed to fire in 4-faces.

the experiments. For all cases tested, relatively long computational times were obtained, always longer than 1800 seconds. In fact, with the exception of the protected I-profile completely exposed to fire in 3-faces, for all cases the final computational time was 3600 seconds.

The results presented are coherent with those reported in section 7.5, indicating, once more, the importance of investigating the fluid flow in the cavity.

7.9 Concluding remarks

The present chapter assessed the thermomechanical response of GFRP profiles (beams and columns) subjected to different fire scenarios.

The thermomechanical model presented consists of an uncoupled FE code that computes the temperature field in a generic cross section (two-dimensional FE model) and the generalized displacement field in a bar using a total Lagrangian formulation (one-dimensional FE model).

Regarding the thermal simulations of the profiles tested, the following conclusions can be drawn:

- For cross-sections containing enclosed cavities (such as tubular profiles or protected I-sections), the consideration of the radiative heat exchange between the faces of the cavity and the natural convection is essential in order to accurately simulate the temperature field.
- The consideration of the radiative heat exchange together with the natural convection considerably increases the CPU time in the simulations.
- Modelling the cavity corners as being sharp introduces singularities in the radiosity field, which affect the temperature field in their vicinity, *i.e.*, at small distances from the singularities, but not in the thermocouples position.

Different fluid flow behaviours into the cavities are observed: (i) in both protected and unprotected tubular cross sections exposed to fire in the bottom face, two convective cells

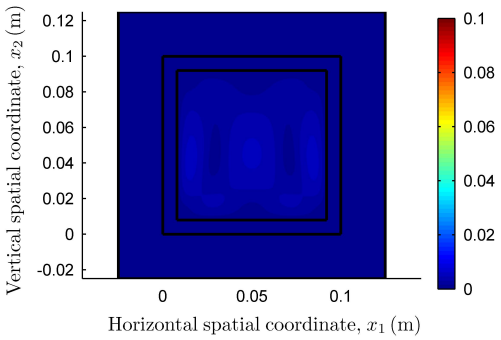

(a) Resultant velocity field, $t = 300$ s.

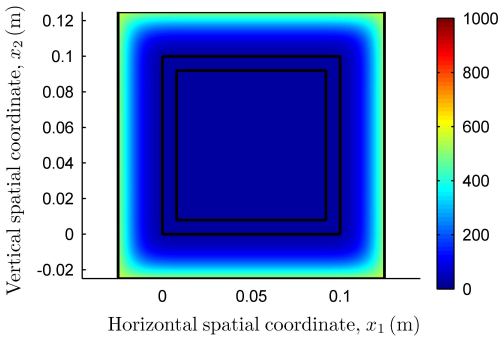

(b) Temperature field, $t = 300$ s.

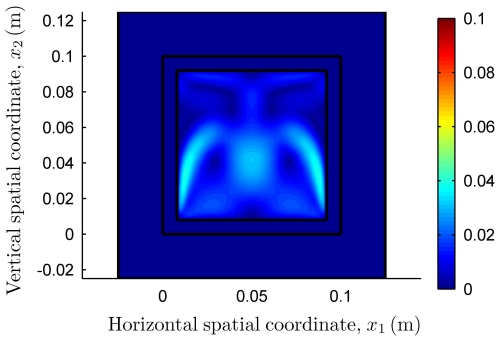

(c) Resultant velocity field, $t = 900$ s.

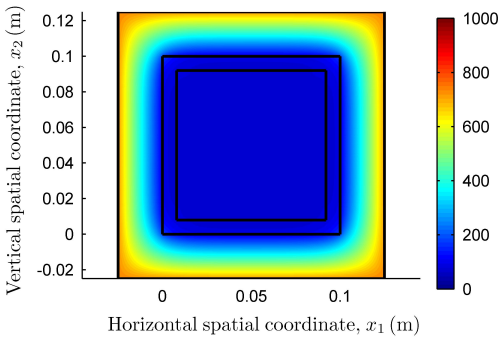

(d) Temperature field, $t = 900$ s.

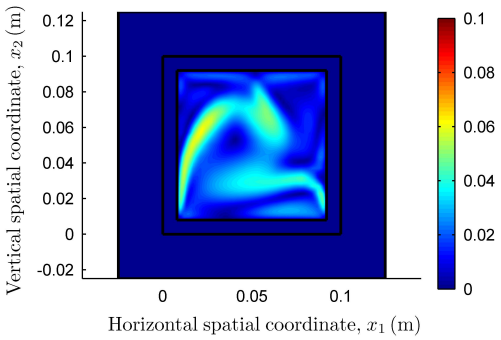

(e) Resultant velocity field, $t = 1800$ s.

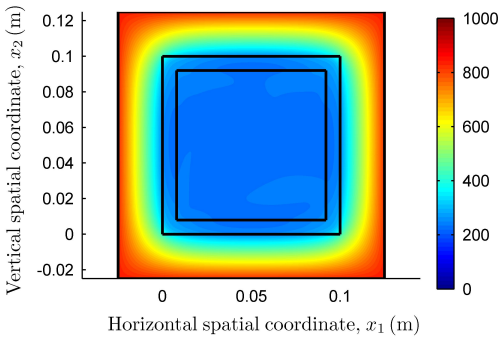

(f) Temperature field, $t = 1800$ s.

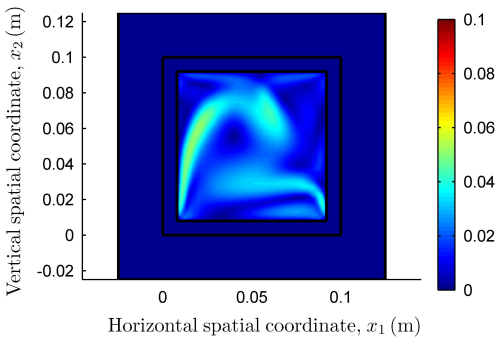

(g) Resultant velocity field, $t = 3600$ s.

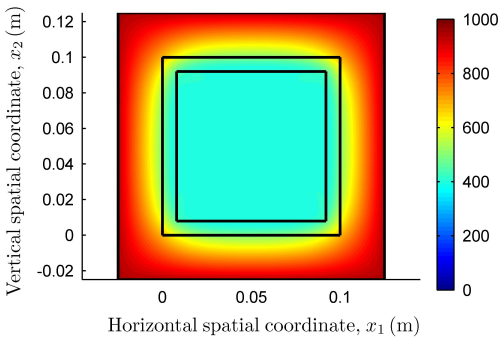

(h) Temperature field, $t = 3600$ s.

Figure 7.76: Protected tubular GFRP cross section with 4-faces exposed to fire.

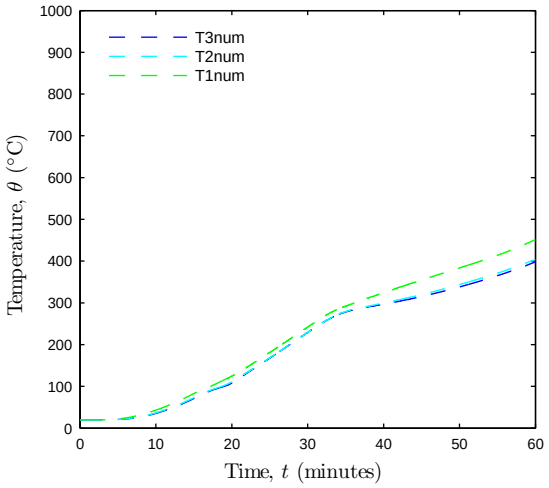

(a) Top flange.

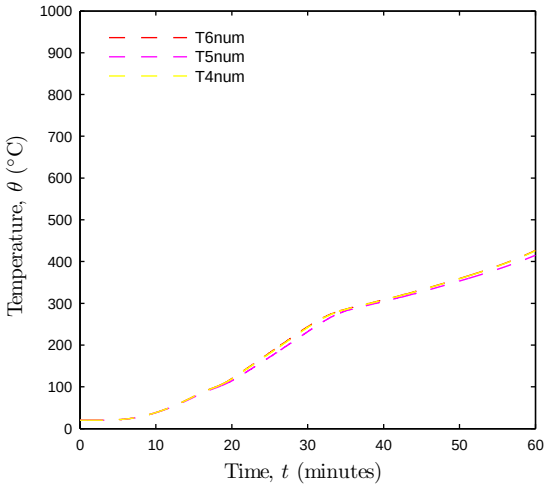

(b) Web.

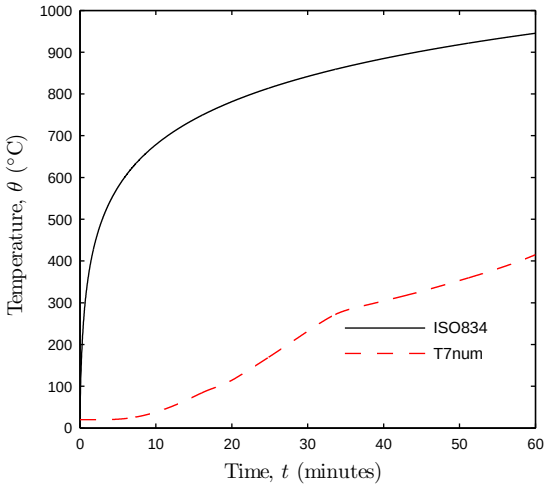

(c) Bottom flange.

Figure 7.77: Temperature evolution in the thermocouples position obtained in a protected tubular cross section subjected to fire in 4-faces.

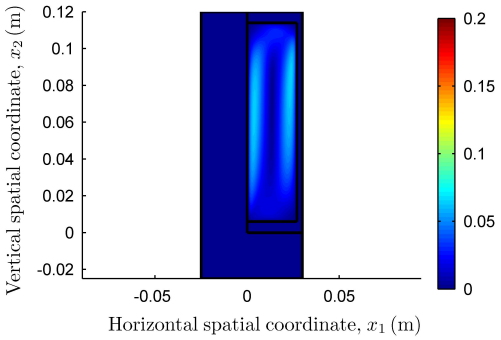

(a) Resultant velocity field, $t = 300$ s.

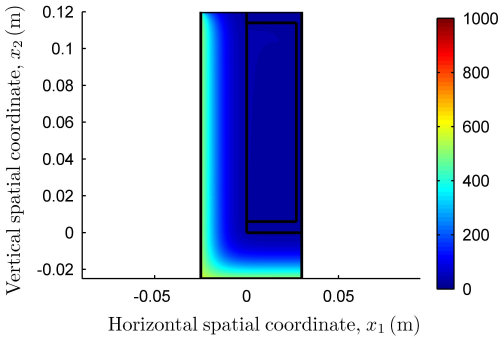

(b) Temperature field, $t = 300$ s.

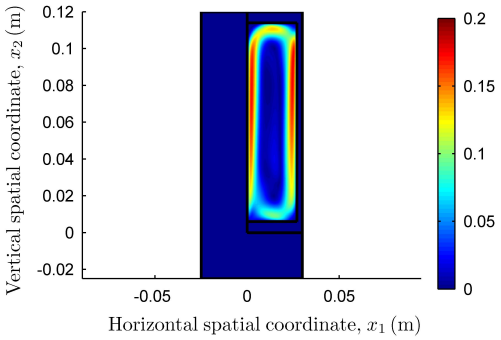

(c) Resultant velocity field, $t = 900$ s.

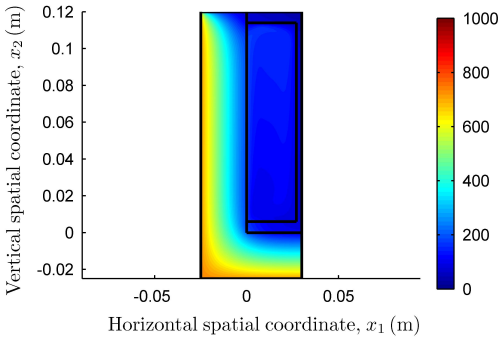

(d) Temperature field, $t = 900$ s.

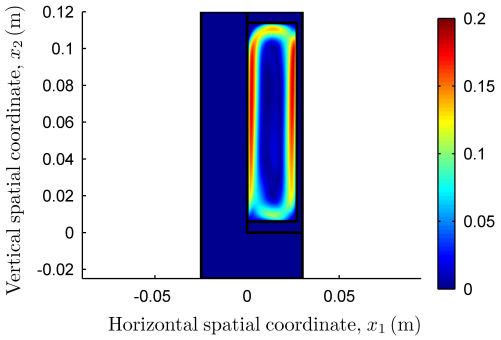

(e) Resultant velocity field, $t = 1000$ s.

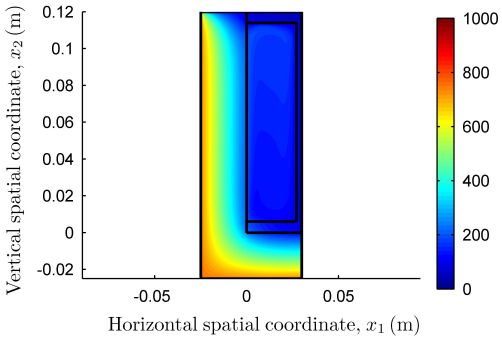

(f) Temperature field, $t = 1000$ s.

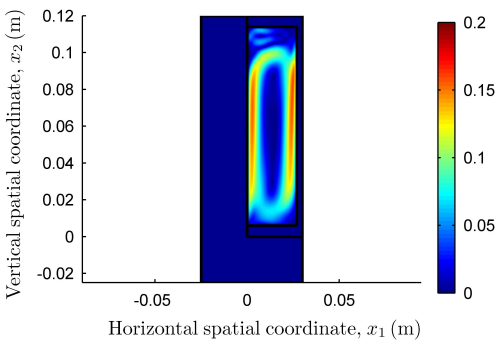

(g) Resultant velocity field, $t = 1800$ s.

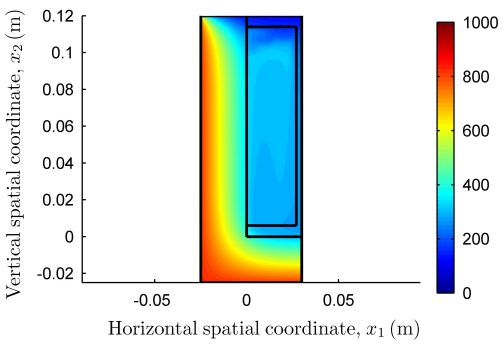

(h) Temperature field, $t = 1800$ s.

Figure 7.78: Protected GFRP I-section with 3-faces subjected to fire.

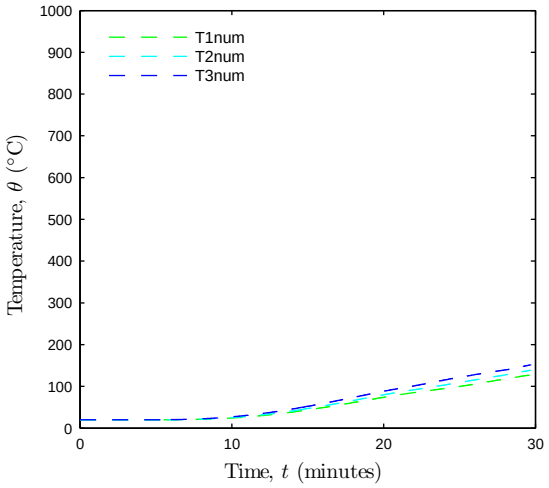

(a) Top flange.

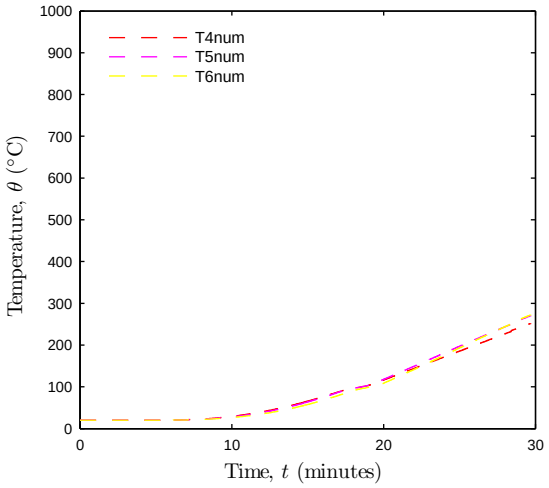

(b) Web.

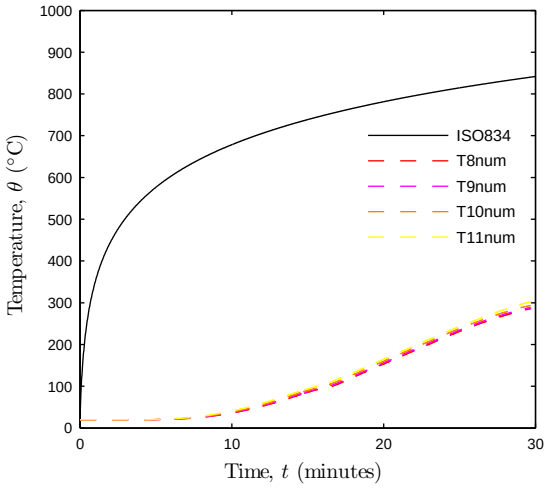

(c) Bottom flange.

Figure 7.79: Temperature evolution in the thermocouples position in a protected I-section subjected completely to fire in 3-faces.

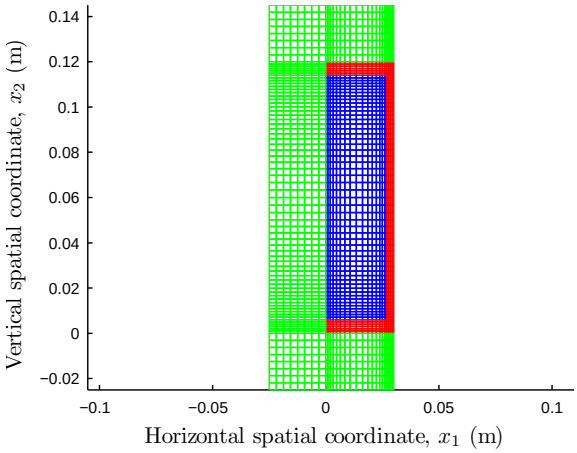

Figure 7.80: Mesh employed in the modelling of the protected I-section exposed to fire in 4-faces.

are created, with an ascending movement of the fluid in the middle of the cavity; (ii) in the cavity of the protected and unprotected tubular cross sections with 3-faces (partially) exposed to fire, four convective cells are formed. Two main parallel cells are created in the bottom of the cavity, where the ascending flow occurs in the vicinity of the lateral faces. Two secondary parallel convective cells are located in the top of the cavity, where the left and right cells present anti-clockwise and clockwise rotation, respectively and (iii) in the case of the protected I-profile, two vertical convective cells are created. The main cell is located in the bottom of the cavity and presents a clockwise movement, while a secondary anti-clockwise cell is created in the top.

In general, a good agreement between the experimental and numerical thermal responses was obtained. However, in the cases where radiative heat exchange in the cavity and natural convection are considered simultaneously, the code developed presented convergence issues. In those cases, very small time steps are required in order to obtain the complete thermal response of the profiles. This implies long CPU time when using the implemented code, being this calculation not possible.

The following reasons may explain the differences between experimental and numerical temperature results: (i) the Boussinesq assumption is inadequate when high temperature gradients are involved; (ii) the thermal and physical properties of the fluid are temperature-dependent; (iii) the thermo-physical properties of the materials (GFRP and CS) may be different from those modelled; (iv) difficulties in imposing the boundary conditions, *e.g.*, in some tests, namely those with short durations, there were significative differences between the temperature furnace and the ISO 834 (1975) curve and an efficient isolation of the lateral faces of the profile that ensures the adiabatic condition was observed; and (v) in the experiments, difficulties concerning the accurate positioning of the thermocouples and the evaluation of accurate/reliable measurements in some thermocouples (particularly for some types of fire exposure) were also reported.

Regarding de mechanical simulations, the following conclusions can be stated:

- The model proposed is able to reproduce with accuracy the variation of the vertical displacement at the midspan of the beams subjected to different fire scenarios and load levels. The consideration of the variation of the temperature along the bar's

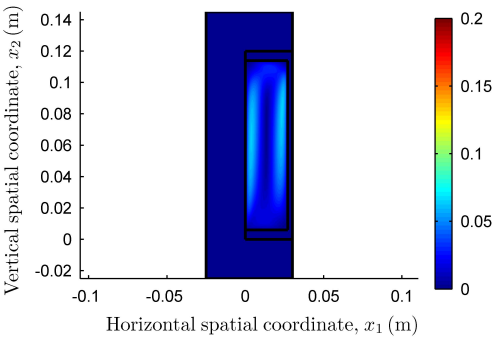

(a) Resultant velocity field, $t = 300$ s.

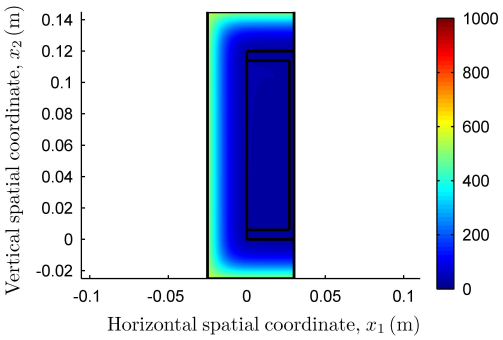

(b) Temperature field, $t = 300$ s.

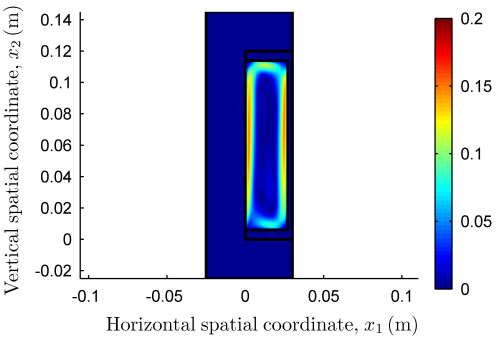

(c) Resultant velocity field, $t = 900$ s.

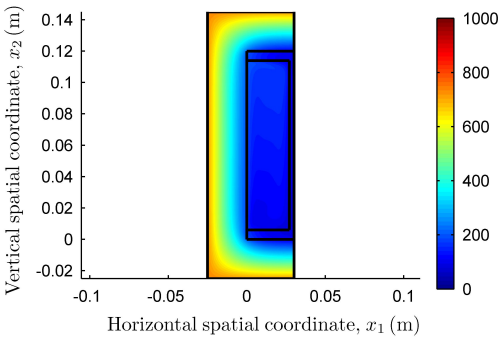

(d) Temperature field, $t = 900$ s.

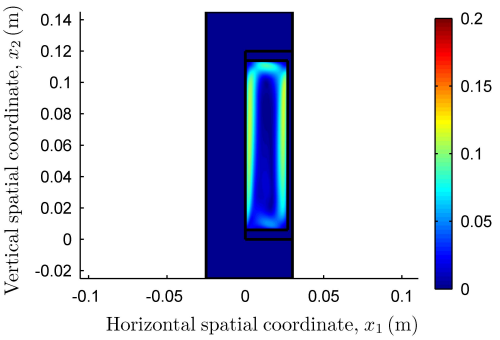

(e) Resultant velocity field, $t = 1800$ s.

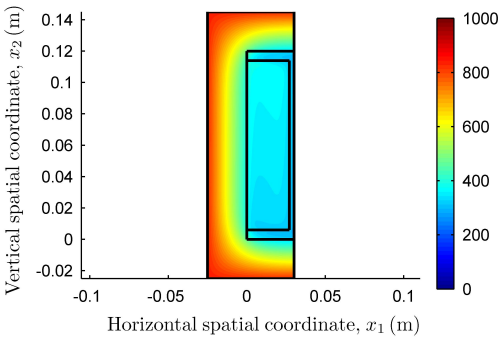

(f) Temperature field, $t = 1800$ s.

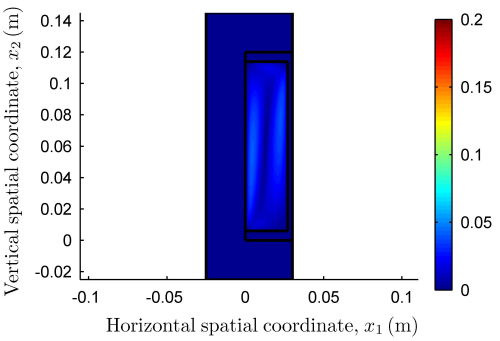

(g) Resultant velocity field, $t = 3600$ s.

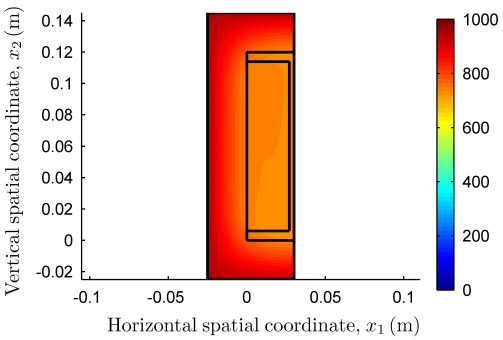

(h) Temperature field, $t = 3600$ s.

Figure 7.81: Protected GFRP I-section with 4-faces fire exposure.

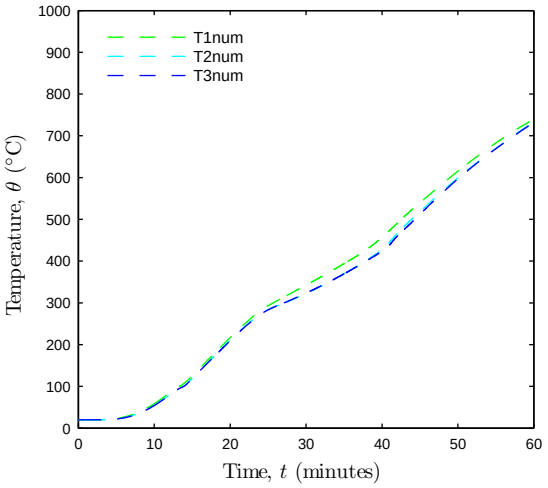

(a) Top flange.

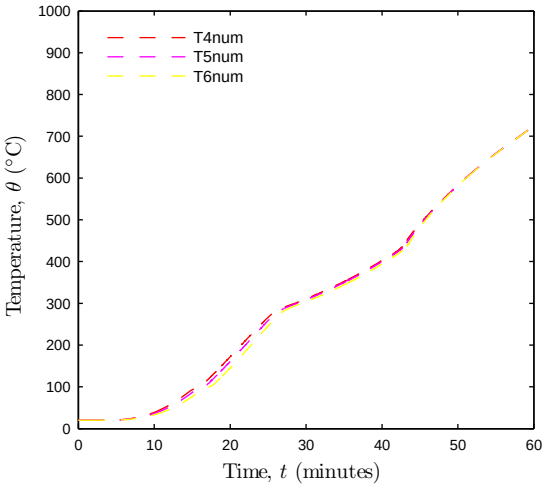

(b) Web.

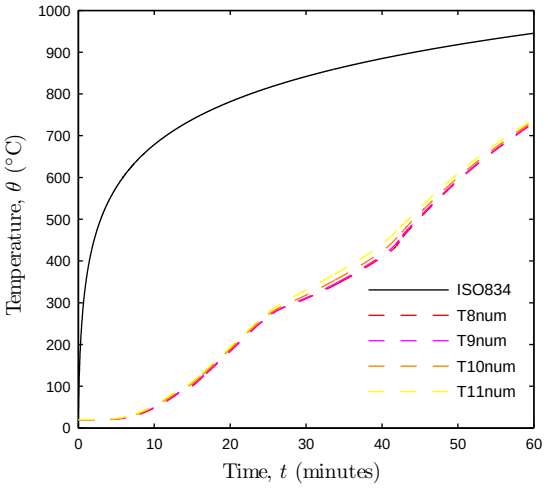

(c) Bottom flange.

Figure 7.82: Temperature evolution in the thermocouples position in a protected I-section subjected to fire in 4-faces.

length is fundamental in order to reproduce the mechanical behaviour of the beams tested.

- The mathematical model provided less accurate results regarding the mechanical response of the columns; reasonable accurate predictions were only obtained for the GFRP tubular column subjected to fire in the bottom face.
- The differences between the numerical and experimental results can be due to the adequacy of the GFRP mechanical properties adopted, the accuracy of the temperature field computed, the (non) consideration of the creep effects and the boundary conditions defined in the model.
- In order to improve the accuracy of the model to reproduce the mechanical behaviour of columns, the following modifications in the model may have to be made: consideration of the thermal expansion coefficient as temperature-dependent, implementation of a more adequate constitutive model for the GFRP, evaluation of the compressive elastic modulus reduction with temperature and consideration of creep deformations as a function of temperature.

In the final part of the chapter, additional applications of the thermal code were reported in order to assess its field of application for different fire expositions.

Chapter 8

Conclusions and future developments

8.1 Conclusions

The present thesis presented the development of a mathematical model to assess the thermomechanical behaviour of GFRP profiles subjected to fire. The FE code implemented allows computing the thermal and mechanical behaviour of GFRP profiles simultaneously subjected to elevated temperatures and mechanical loads following an uncoupled scheme.

The thermal code consists of a coupled FE formulation that allows solving fluid flow and heat transfer problems, considering the internal radiative heat exchange between the walls of a cavity. The mentioned coupled problem can be solved in both transient and steady state regime, in which the thermal properties of the material can be considered temperature-dependent, as well as the convective coefficient.

The following assumptions were considered in the fluid dynamics code: (i) the fluid is viscous and incompressible; (ii) the flow is laminar; and (iii) the density variation of the fluid due to the temperature can be evaluated by using the Boussinesq model. Furthermore, in order to improve the convergence to the solution and eliminate possible numerical oscillations, the SUPG method was implemented.

The mechanical code consists of a one-dimensional FE formulation that allows computing the generalized displacement vector at different instants by using the temperature distribution in the cross section evaluated with the thermal code. At each time step where the temperatures were obtained, a *quasi*-static analysis is performed. The algorithm implemented allows solving the geometrically exact beam theory equations, in which the Reissner–Simo kinematic assumptions were imposed. The mechanical properties of the material can be considered temperature-dependent, using the axial strain-stress and shear stress-distortion curves at each temperature.

In both FE codes, the resulting system of nonlinear equations is solved using the Newton–Raphson method.

Several benchmark problems were solved to verify the solution of the implemented algorithms, by comparing the obtained solutions with those reported in the literature or obtained through a commercial software. Analysing the benchmark problems solved, the following conclusions and comments can be stated:

- The consideration of the radiative heat exchange between faces increases significantly the CPU time due to the computation of the geometrical term in the radiosity

equation and because the radiosity matrix is full.

- The study conducted about the number of Gauss points to consider in the evaluation of the geometrical term showed that the convergence to the solution is slow and, in general, depends on the spatial discretization.
- The solution of the fluid dynamics problems depends strongly on the spatial discretization. Hence, it is important to design h-adaptive meshes considering the boundary layers location.
- The CPU time required in thermal simulations where radiative heat exchange between faces and natural convection are involved simultaneously is high. In order to reduce the CPU time, a simple adaptive time step scheme was successfully implemented.
- The mechanical code allows computing the total displacement field of a beam or column subjected to a generic temperature distribution, considering all the geometrical effects.
- Quadratic convergence of the iterative error in the asymptotic limit of the solution was observed in all the examples reported, as expected when using the Newton–Raphson method.

Regarding the thermal modelling of the GFRP profiles, the following main conclusions and remarks are drawn:

- A discussion about the adequate boundary conditions to consider in the cavity of the tubular cross section was reported. The experimental data was represented with more accuracy when using the model that simultaneously considers the radiative heat exchange between the faces of the cavity and the natural convection due to the air.
- The spatial and temporal refinement employed is sufficient to obtain a negligible numerical error in the temperatures evaluated at the thermocouples location.
- In most of the numerical simulations in which the radiative heat exchange and the natural convection are considered simultaneously, at some point the code developed presents convergence problems during the iterative solution process. To extend the duration of the numerical results, a very small time step should be employed (0.01 s or even lower). This time step is not practically feasible in the MATLAB (2012) FE code developed and a more efficient code is needed in this respect (to be developed in a different programming language).
- Regarding the influence of the geometry of the cavity in the solution, it was concluded that the consideration of sharp corners introduces singularities in the radiosity field that can interfere in the solution. It was observed that the existence of the singularities only affect the temperature field in the vicinity of the corners, while no differences were found in the thermocouples position (the control points).
- The accuracy of the model in simulating the thermal behaviour of different GFRP cross sections (in geometry) subjected to different fire exposures was carried out by comparing the numerical and experimental temperature evolutions in the thermocouples. In general, a reasonable good agreement was obtained.

- The differences between the numerical and the experimental temperatures can be due to the following reasons: (i) the actual thermal properties of the GFRP and the CS, the emissivity and the convective heat coefficient adopted were taken from the literature and, hence, may not correspond exactly to those of the experiments; (ii) the fluid is assumed incompressible and its thermal and physical properties are considered constant; however, the air is compressible and its thermal properties are temperature-dependent, which may have a non-negligible influence at high temperatures; (iii) the Boussinesq model is employed to compute the buoyancy forces developed due to the variation of the air density with the temperature, this hypothesis being valid only for reduced temperature gradients; and (iv) the fluid flow is modelled as two-dimensional, when, most probably it is 3D. Furthermore, there are also uncertainties in the experimental data reported by Morgado *et al.* (2013a,b), as for example, uncertainties regarding the real position of the thermocouples, the temperature in the furnace during the tests and inefficient insulation of the lateral faces of the profile.

In the thermomechanical simulations of unprotected and protected GFRP beams and columns subjected to different fire scenarios, due to the lack of information in the literature, it was assumed that some of the mechanical properties of the GFRP, namely, the elastic modulus in compression and the shear modulus present the same reduction with temperature as the ultimate strength. All moduli were considered constant at each temperature. Consequently, the material was modelled as linear and elastic. The CS properties were assumed to be linear and temperature independent. The model presented is not able to reproduce the failure of the beams and columns because the mechanical properties of the material were assumed constant at each temperature and a failure criterion was not implemented. The following main conclusions and remarks are drawn from the thermomechanical modelling of the GFRP beams and columns:

- In the discussion about the spatial discretization required for the bars' simulation (carried out for the unprotected tubular GFRP beam with the bottom face exposed to fire) several meshes were designed. It was concluded that no particularly refined meshes are required to reproduce with accuracy the mechanical behaviour of the beams. This conclusion was also applied in the mechanical modelling of the columns.

- In the study about the modelling of the bars' extremities (unheated during the experimental tests), it was concluded that the sections of the bars located outside the furnace have to be modelled as cold. In these tests, a linear variation of the temperature between the last section inside the furnace and the support was assumed and this led to an important improvement in the accuracy of the numerical results.

- In all the simulations of the thermomechanical behaviour of GFRP beams, the model was able to reproduce with reasonable accuracy the experimental evolution of the vertical displacement at the midspan section for different load levels.

- In the simulations of the thermomechanical behaviour of the GFRP columns less accurate results were obtained. In this case, the model was only able to reproduce with reasonable accuracy the experimental results obtained in the unprotected GFRP tubular column subjected to fire in the bottom face. In the remaining cases, the model revealed a qualitatively similar behaviour for all the columns: (i) during the first instants, a slight axial expansion of the bar due to the temperature increase

and a negative variation of the vertical displacement at the central section due to the temperature gradient are observed; and (ii) subsequently, a contraction of the column (positive axial shortening) and a positive variation of the vertical displacement was determined for the model. However, the experimental results were often different in magnitude and in sign. One reason for that could be the inadequacy of the constitutive model employed to define the mechanical behaviour of the GFRP, which influences the generalized stress field in columns.

The differences between the numerical and experimental results in the mechanical response of GFRP beams and columns can be due to the following reasons: (i) the actual mechanical properties of the GFRP material may be different from those that were assumed; (ii) the consideration of the thermal expansion coefficient of the GFRP as being constant and isotropic; this parameter was seen to have a significant influence in the columns' response; (iii) the difference encountered between the experimental and the numerical temperature fields in the cross section; the linear temperature distribution assumed along the unheated length can also be different from the actual temperature field; (iv) the non-consideration of creep effects, which are deemed to have more influence in the columns' mechanical response; and (v) the adequacy of the boundary conditions considered in the clamped support of the columns, as in the experimental tests it was not possible to entirely prevent the rotation of the cross section of the profile, thus allowing small rotations to occur.

8.2 Future developments of the research

The present thesis presented an uncoupled FE model to evaluate the thermomechanical behaviour of beams and columns subjected to elevated temperatures. The thermal model consists of a two-dimensional FE formulation that allows solving conjugate heat transfer problems following a coupled scheme. This constitutes a progress in the thermal modelling of GFRP profiles when enclosed cavities are present as, in the literature, only simple models that evaluate the temperatures in the bottom flange of the profiles are available. In fact, the present work shows the necessity of considering simultaneously the radiative heat flux between the faces of the cavity and the natural convection in order to reproduce the temperature in the cross section. However, the model developed presents a limitation: the fluid is modelled as incompressible. Consequently, the effect of the temperature gradient in the density could be miscalculated. Regarding the mechanical model, a FE code considering the geometrically exact beam theory was developed. This model allows computing the mechanical behaviour of a bar considering the geometrical and material nonlinearities, which could be significant in bars subjected to high temperatures.

For both thermal and mechanical properties of the materials involved in the simulation, especially the GFRP, there were concerns regarding the adequacy of the values assumed. Consequently, the following efforts should be developed in order to improve the quality of the input data employed in the numerical simulations:

- Validation of the temperature-dependent thermal properties of the GFRP profiles and the CS boards through experimental tests at high temperatures (if possible, up to 1000° C).

- Evaluation of the nonlinear axial stress-strain and shear stress-distortion curves of the GFRP at elevated temperatures (higher than the decomposition temperature), and for different types of loading (tension, compression and shear).
- Evaluation of the temperature-dependent thermal expansion coefficient for both GFRP and CS.

The numerical results presented in the previous chapters lead to the following steps in the future research in order to improve the thermal code:

- Elimination of the singularity in the sharp corners of the cavities, which affects the results obtained in the temperature field. One option could be to model the curved corners.
- Implementation of a thermochemical model to explicitly take into account the chemical reactions that occur during the heating process of the material, as for example, the endothermic reaction during the decomposition of the matrix.
- Consideration of the thermal properties of the fluid depending on the temperature, thus eliminating the Boussinesq approximation. The most adequate model for future developments is probably the one for low-speed compressible flows, which, as referred in Reddy and Gartling (2010), should provide the most suitable equations to simulate flows with significant variations in density and pressure and, hence, in temperature.
- Optimization of the algorithm implemented in order to allow reducing the time step to the levels required and to complete the calculations until 3600 s with an acceptable computational cost (in terms of time). This will require programming the FE code in a compiled language, as for example, FORTRAN.

Finally, the following modifications are proposed to be developed in the thermomechanical model in order to improve the results reported:

- Study about the adequate constitutive model for the GFRP, considering the creep effects, which may influence the mechanical behaviour, especially of columns (Dutta and Hui, 2000).
- Implementation of an appropriate failure criterion for composite materials at high temperatures as, for example, the Tsai-Hill criterion. This will also involve complex experimental test and numerical efforts.
- Modelling the fixed support in the columns as a pinned support with a spring. This action will allow some rotation in the support. However, this solution will introduce a new unknown parameter: the rotational stiffness of the spring, that will have to be defined based on experimental results.

Bibliography

Adams, D.F., L.A. Carlsson and R.B. Pipes (2003). *Experimental Characterization of Advanced Composite Materials*. CRC Press, third edition.

ADINA-F (2010). *Automatic Dynamic Incremental Nonlinear Analysis – Volume III: ADINA CFD & FSI Model Definition*. ADINA R & D Inc. Report ARD 10–7.

ADINA-T (2010). *Automatic Dynamic Incremental Nonlinear Analysis – Volume II: ADINA Heat Transfer Model Definition*. ADINA R & D Inc. Report ARD 10–7.

Arpaci, V.S. (1966). *Conduction Heat Transfer*. Addison-Wesley.

Babrauskas, V. and S.J. Grayson (Editors) (2006). *Heat Release in Fires*. E & FN Spon.

Bahrami, M. (2005). Radiation Heat Transfer. Undergraduate course. ECE 309 Heat Transfer & Thermodynamics (University of Waterloo). Website: http://www.mhtlab.uwaterloo.ca/courses/ece309/lectures/pdffiles/summary_ch12.pdf, visited on 31-01-2014.

Bai, Y. and T. Keller (2009). Pultruded GFRP tubes with liquid-cooling system under combined temperature and compressive loading. *Composite Structures*, *90*, 115–121.

Bai, Y., T. Keller, J.R. Correia, F.A. Branco and J.G. Ferreira (2010). Fire protection systems for building floors made of pultruded GFRP profiles. Part 2: Modeling of thermomechanical responses. *Composites Part B: Engineering*, *41*, 630–636.

Bai, Y., T. Keller and T. Vallée (2008a). Modeling of stiffness of FRP composites under elevated and high temperatures. *Composites Science and Technology*, *68*(15–16), 3099–3106.

Bai, Y., T. Keller and T. Vallée (2008b). Modeling of thermo-mechanical properties and responses for FRP composites in fire. In *Fourth International Conference on FRP Composites in Civil Engineering (CICE)*. Zurich.

Bai, Y., N.L. Post, J.J. Lesko and T. Keller (2008c). Experimental investigations on temperature-dependent thermo-physical and mechanical properties of pultruded GFRP composites. *Thermochimica Acta*, *469*(1–2), 28–35.

Bai, Y., T. Vallée and T. Keller (2007). Modelling of thermo-physical properties for FRP composites under elevated and high temperatures. *Composites Science and Technology*, *67*, 3098–3109.

Bank, L.C. (2006). *Composites for Construction: Structural Design with FRP Materials*. John Wiley & Sons, Ltd.

Basak, T., Roy S. and A.R. Balakrishnan (2006). Effects of thermal boundary conditions on natural convection flows within a square cavity. *International Journal of Heat and Mass Transfer*, *49*(23–24), 4525–4535.

Bathe, K.J. (1996). *Finite Element Procedures*. Prentice Hall.

Bathe, K.J. and M.R. Khoshgoftaar (1979). Finite element formulation and solution of nonlinear heat transfer. *Nuclear Engineering and Design*, *51*(3), 389–401.

Bausano, J.V., J.J. Lesko and S.W. Case (2006). Composite life under sustained compression and one sided simulated fire exposure: Characterization and prediction. *Composites Part A: Applied Science and Manufacturing*, *37*(7), 1092–1100.

Belazizia, A., S. Benissaad and S. Abboudi (2012). Effect of the wall conductivity on conjugate natural convection in a square enclosure with finite vertical wall thickness. *Advances in Theoretical and Applied Mechanics*, *5*(1–4), 179–190.

Bergheau, J.M. and R. Fortunier (2008). *Finite Element Simulation of Heat Transfer*. John Wiley & Sons.

Betts, P.L. and V. Haroutunian (1983). A stream function finite element solution for two-dimensional natural convection with accurate representation of Nusselt number variations near a corner. *International Journal for Numerical Methods in Fluids*, *3*(6), 605–622.

Brezzi, F. and M. Fortin (1991). *Mixed and Hybrid Finite Element Methods*. Springer Series in Computational Methematics. Springer-Verlag, New York.

Brooks, A.N. and T.J.R. Hughes (1982). Streamline upwind/Petrov-Galerkin formulations for convection dominated flows with particular emphasis on the incompressible Navier–Stokes equations. *Computer Methods in Applied Mechanics and Engineering*, *32*(1–3), 199–259.

Brown, J.R. and Z. Mathys (1997). Reinforcement and matrix effects on the combustion properties of glass reinforced polymer composites. *Composites Part A: Applied Science and Manufacturing*, *28*(7), 675–681.

Buch, J.D. (1982). Thermal expansion behavior of a thermally degrading organic matrix composite. In *Thermomechanical Behavior of High-emperature Composites*, pages 35–49. ASME, ASME publication AD-04, New York.

Buchanan, A.H. (2002). *Structural Design for Fire Safety*. John Wiley & Sons.

Burchill, P.J., Z. Mathys and C.P. Gardiner (2005). An analysis of the burning of polyester and vinylester fibre glass composites. *Fire and Materials*, *29*(4), 249–264.

Campbell, F.C. (2006). *Manufacturing Technology for Aerospace Structural Materials*. Elsevier Ltd., London, UK.

Campelo, H. (2013). *Finite element method with immersed boundaries applied to fluid dynamics and fluid-structure problems*. Ph.D. thesis, Escola Politécnica da Universidade de São Paulo, São Paulo, Brasil (in Portuguese).

Carslaw, H.S. and J.C. Jaeger (1959). *Conduction of Heat in Solids*. Oxford University Press, second edition.

Chapelle, D. and K.J. Bathe (1993). The Inf-Sup test. *Computers & Structures*, *47*(4–5), 537–545.

Chawla, K.K. (1998). *Fibrous Materials*. Cambridge University Press.

Chung, D.D.L. (2011). *Composite Materials. Science and Applications*. Springer-Verlag, London, second edition.

Codina, R. (2000). On stabilized finite element methods for linear systems of convection-diffusion-reaction equations. *Computer Methods in Applied Mechanics and Engineering*, *188*(1–3), 61–82.

Composite Construction Laboratory (2014). Website: http://cclab.epfl.ch/page-13722.html, visited on 16-01-2014.

Correia, J.R. (2008). *GFRP pultruded profiles in civil engineering: hybrid solutions, bonded connections and fire behaviour*. Ph.D. thesis, Instituto Superior Técnico, Technical University of Lisbon, Lisbon, Portugal.

Correia, J.R., Y. Bai and T. Keller (2015). A review of the fire behaviour of pultruded GFRP structural profiles for civil engineering applications. *Composite Structures*, *127*, 267–287.

Correia, J.R., F.A. Branco and J.G. Ferreira (2010a). The effect of different passive fire protection systems on the fire reaction properties of GFRP pultruded profiles for civil construction. *Composites Part A: Applied Science and Manufacturing*, *41*(3), 441–452.

Correia, J.R., F.A. Branco, J.G. Ferreira, Y. Bai and T. Keller (2010b). Fire protection systems for building floors made of pultruded GFRP profiles. Part 1: Experimental investigations. *Composites Part B: Engineering*, *41*, 617–629.

Correia, J.R., F.A. Branco and T.M. Morgado (2013a). Thermo-physical and thermomechanical experiments on GFRP and fire protection materials. Modelling of the mechanical properties of the GFRP material at elevated temperature. Report IST-2-3. Project Fire protection systems for glass fibre reinforced polymer (GFRP) pultruded profiles, PTDC/ECM/100779/2008, ICIST.

Correia, J.R., M.M. Gomes, J.M. Pires and F.A. Branco (2013b). Mechanical behaviour of pultruded glass fibre reinforced polymer composites at elevated temperature: Experiments and model assessment. *Composite Structures*, *98*, 303–313.

Cowper, G.R. (1973). Gaussian quadrature formulas for triangles. *International Journal for Numerical Methods in Engineering*, *7*(3), 405–408.

Davies, J.M. and D.W. Dewhurst (1999). The fire performance of GRE pipes in empty and dry, stagnant water filled, and flowing water filled condition. In *Second International Conference on Composites in Fire*. Newcastle Upon Tyne.

De Vahl Davis, G. (1983). Natural convection of air in a square cavity: A benchmark numerical solution. *International Journal for Numerical Methods in Fluids*, *3*(3), 249–264.

Diersch, H.J.G. (2014). *FEFLOW, Finite Element Modeling of Flow, Mass and Heat Transport in Porous and Fractured Media*. Springer-Verlag Berlin Heidelberg.

Dimitrienko, YU.I. (1995). Thermal stresses and heat-mass transfer in ablating composite materials. *International Journal of Heat and Mass Transfer*, *38*(1), 139–146.

Dimitrienko, Yu.I. (1997). Thermomechanical behaviour of composite materials and structures under high temperatures: 1. Materials. *Composites Part A: Applied Science and Manufacturing*, *28*(5), 453–461.

Dobrowolski, M. (2005). On the LBB condition in the numerical analysis of the Stokes equations. *Applied Numerical Mathematics*, *54*, 314–323.

Dodds, N., A.G. Gibson, D. Dewhurst and J.M. Davies (2000). Fire behaviour of composite laminates. *Composites Part A: Applied Science and Manufacturing*, *31*(7), 689–702.

Donea, J. and A. Huerta (2003). *Finite Element Methods for Flow Problems*. John Wiley & Sons, Ltd.

Dorfman, A. and Z. Renner (2009). Conjugate problems in convective heat transfer: Review. *Mathematical Problems in Engineering*, *2009*, 27 pages.

Drysdale, D. (Editor) (2011). *An Introduction to Fire Dynamics*. John Wiley & Sons, United Kingdom, third edition.

Du, Z.-G. and E. Bilgen (1972). Coupling of wall conduction with natural convection in a rectangular enclosure. *International Journal of Heat and Mass Transfer*, *35*(8), 1969–1975.

Dutta, P.H. and D. Hui (2000). Creep rupture of a GFRP composite at elevated temperatures. *Computers & Structures*, *76*(1–3), 153–161.

Çengel, Y. (2003). *Heat Tranfer: a Practical Approach*. McGraw-Hill, second edition.

Erturk, R., T.C. Corke and C. Gökçöl (2005). Numerical solutions of 2-D steady incompressible driven cavity flow at high Reynolds numbers. *International Journal of for Numerical Methods in Fluids*, *48*(7), 747–774.

Eurocode 1 (1995). *Basis of design and actions on structures, actions on structures exposed to fire (part 2.2)*. European Comitee for Standardization, Brussels.

Federal Aviation Administration (2014). Website: http://www.airporttech.tc.faa.gov, visited on 16-01-2014.

Feih, S., Z. Mathys, A.G. Gibson and A.P. Mouritz (2007a). Modelling the compression strength of polymer laminates in fire. *Composites Part A: Applied Science and Manufacturing*, *38*(11), 2354–2365.

Feih, S., Z. Mathys, A.G. Gibson and A.P. Mouritz (2010). Strength degradation of glass fibers at high temperatures. *Journal of Materials Science*, *44*(2), 392–400.

Feih, S., A.P. Mouritz, Z. Mathys and A.G. Gibson (2007b). Tensile strength modeling of glass fiber-polymer composites in fire. *Journal of Composite Materials*, *41*(19), 2387–2410.

Fernandes, P.R. (2009). *Simulation of the thermochemical behavior of GFRP pultruded profiles subjected to fire.* Master dissertation in Civil Engineering, Instituto Superior Técnico, Technical University of Lisbon (in Portuguese), Lisbon, Portugal.

Fernández-Carvajal, P.R.-V. (2001). *On the solution of the Navier–Stokes equations by the finite element method using a SUPG stabilization technique. Application to some wastewater treatment problems.* Ph.D. thesis, School of Civil Engineering, University of La Coruña, La Coruña, Spain.

Ferziger, J.H. and H. Perić (2000). *Computational Methods for Fluid Dynamics.* Springer-Verlag, third edition.

Fiberline Composites (2014). Website: http://www.fiberline.com, visited on 16-01-2014.

Fish, J. and T. Belytschko (2007). *A First Course in Finite Elements.* John Wiley & Sons.

Florio Jr., J., J.B. Henderson, F.L. Test and R. Hariharan (1991). A study of the effects of the assumption of local-thermal equilibrium on the overall thermally-induced response of a decomposing, glass-filled polymer composite. *International Journal of Heat and Mass Transfer*, *34*(1), 135–147.

FLUENT (2016). ANSYS FLUENT 12.0/12.1 Documentation. Website: http://www.afs.enea.it/project/neptunius/docs/fluent/html/ug/node789.htm, visited on 24-10-2016.

Franca, L.P. and S.L. Frey (1992). Stabilized finite element methods: II. The incompressible Navier-Stokes equations. *Computer Methods in Applied Mechanics and Engineering*, *99*(2–3), 209–233.

Ghia, U., K.N. Ghia and C.T. Shin (1982). High-Re solutions for incompressible flow using the Navier-Stokes equations and a multigrid method. *Journal of Computational Physics*, *48*(3), 387–411.

Gibson, A.G., P.N.H. Wright, Y.-S. Wu, A.P. Mouritz, Z. Mathys and C.P. Gardiner (2004). The integrity of polymer composites during and after fire. *Journal of Composite Materials*, *38*(15), 1283–1307.

Gibson, A.G., Y.-S. Wu, J.T. Evans and A.P. Mouritz (2006). Laminate theory analysis of composites under load in fire. *Journal of Composite Materials*, *40*(7), 639–658.

Gomes, M.M., J.R. Correia and F.A. Branco (2011). Small-scale fire resistance experiments on GFRP pultruded laminates. Small-scale tensile tests on GFRP pultruded laminates at elevated temperature – phase 1. Report IST-3-1. Project Fire protection systems for glass fibre reinforced polymer (GFRP) pultruded profiles, PTDC/ECM/100779/2008, ICIST.

Gomes, M.M., J.R. Correia, J.M. Pires and F.A. Branco (2012a). Small-scale fire resistance experiments on GFRP pultruded laminates. Small-scale compressive tests on GFRP pultruded laminates at elevated temperature. Report IST-3-4. Project Fire protection systems for glass fibre reinforced polymer (GFRP) pultruded profiles, PTDC/ECM/100779/2008, ICIST.

Gomes, M.M., J.R. Correia, J.M. Pires and F.A. Branco (2012b). Small-scale fire resistance experiments on GFRP pultruded laminates. Small-scale shear tests on GFRP pultruded laminates at elevated temperature. Report IST-3-3. Project Fire protection systems for glass fibre reinforced polymer (GFRP) pultruded profiles, PTDC/ECM/100779/2008, ICIST.

Gomes, M.M., J.R. Correia, J.M. Pires and F.A. Branco (2012c). Small-scale fire resistance experiments on GFRP pultruded laminates. Small-scale tensile tests on GFRP pultruded laminates at elevated temperature – phase 2. Report IST-3-2. Project Fire protection systems for glass fibre reinforced polymer (GFRP) pultruded profiles, PTDC/ECM/100779/2008, ICIST.

Griffis, C.A., J.A. Nemes, F.R. Stonesifer and C.I. Chang (1986). Degradation in strength of laminated composites subjected to intense heating and mechanical loading. *Journal of Composite Materials*, *20*(5), 216–235.

Hannani, S.K., M. Stanislas and P. Dupont (1995). Incompressible Navier–Stokes computations with SUPG and GLS formulations–A comparison study. *Finite Elements in Analysis and Design*, *13*(2–3), 91–104.

Hauke, G. (2008). *An Introduction to Fluid Mechanics and Transport Phenomena*. Springer.

Heinrich, J.C., P.S. Huyakorn, O.C. Zienkiewicz and A.R. Mitchell (1977). An upwind finite element scheme for two-dimensional convective transport equation. *International Journal for Numerical Methods in Engineering*, *11*(1), 131–143.

Henderson, J.B., M.R. Tant, M.P. Doherty and E.F. O'Brien (1987). Characterization of the high-temperature behaviour of a glass-filled polymer composite. *Composites*, *18*(3), 205–215.

Henderson, J.B., J.A. Wiebelt and M.R. Tant (1985). A Model for the Thermal Response of Polymer Composite Materials with Experimental Verification. *Journal of Composite Materials*, *19*, 579–595.

Hilado, J.C. (Editor) (1990). *Flammability Handbook for Plastics*. Technomic Publishing Co., Lancaster, PA, USA.

Holdeman, J.T. (2010). A Hermite finite element method for incompressible fluid flow. *International Journal for Numerical Methods in Fluids*, *64*(4), 376–408.

Holman, J.P. (1986). *Heat Transfer*. McGraw-Hill, sixth edition.

Howell, J.R. (1982). *A Catalog of Radiation Configuration Factors*. McGraw-Hill, New York, sixth edition.

Hughes, T.J.R. (2000). *The Finite Element Method: Linear Static and Dynamic Finite Element Analysis*. Dover Publications, Inc, Mineola, New York, USA.

Incropera, F.P., D.P. DeWitt, T.L. Bergman and A.S. Lavine (2006). *Fundamentals of Heat and Mass Transfer*. John Wiley & Sons, Ltd, sixth edition.

ISO 834 (1975). *Fire resistance tests. Elements of building construction.* International Standards Organization, Genève.

Jamet, P. and P.A. Raviart (1974). Numerical solution of the stationary Navier-Stokes equations by finite element methods. In R. Glowinski and J.L. Lions (Editors) *Computing Methods in Applied Sciences and Engineering Part 1*, volume 10, pages 193–223. Springer Berlin Heidelberg.

Jiang, B.-N. (1998). *The Least-Squares Finite Element Method: Theory and Applications in Computational Fluid Dynamics and Electromagnetics.* Springer-Verlag, Berlin.

Kaminski, D.A. and C. Prakash (1986). Conjugate natural convection in a square enclosure: effect of conduction in one of the vertical walls. *International Journal of Heat Mass Transfer*, *29*(12), 1979–1988.

Kanury, A.M. (1972). Thermal decomposition kinetics of wood pyrolysis. *Combustion and Flame*, *18*(1), 75–83.

Karlsson, B. and J.G. Quintiere (2000). *Enclosure Fire Dynamics.* CRC Press, Taylor & Francis, Boca Raton.

Katopodes, N.D. (1984). Fourier analysis of dissipative FEM channel flow model. *Journal of Hydraulic Engineering*, *110*(7), 927–944.

Keller, T. (2003). Use of fibre reinforced polymers in bridge construction. In *Structural Engineering Documents, 7.* IABSE-AIPC-IVBH, Zurich.

Keller, T., C. Tracy and E. Hugi (2006a). Fire endurance of loaded and liquid-cooled GFRP slabs for construction. *Composites Part A: Applied Science and Manufacturing*, *37*(7), 1055–1067.

Keller, T., C. Tracy and A. Zhou (2006b). Structural response of liquid-cooled GFRP slabs subjected to fire – Part I: Material and post-fire modeling. *Composites Part A: Applied Science and Manufacturing*, *37*(9), 1286–1295.

Keller, T., C. Tracy and A. Zhou (2006c). Structural response of liquid-cooled GFRP slabs subjected to fire – Part II: Thermo-chemical and thermo-mechanical modeling. *Composites Part A: Applied Science and Manufacturing*, *37*(9), 1296–1308.

Keller, T., A. Zhou, C. Tracy, E. Hugi and P. Schnewlin (2005). Experimental study on the concept of liquid cooling for improving fire resistance of FRP structures for construction. *Composites Part A: Applied Science and Manufacturing*, *36*(11), 1569–1580.

Kern, D.Q. (1950). *Process Heat Transfer.* McGraw-Hill Book Company, Inc., New York.

Kharbari, V.M., J.W. Chin, D. Hunston, B. Benmokrane, T. Juska, R. Morgan, J.J. Lesko, U. Sorathia and D. Reynaud (2003). Durability gap analysis for fiber-reinforced polymer composites in civil infrastructure. *Journal of Composites for Construction*, *7*(3), 238–247.

Kim, D.M. and R. Viskanta (1984). Effect of wall conduction and radiation on natural convection in a rectangular cavity. *Numerical Heat Tranfer*, *7*(4), 449–470.

Kim, J.-S., J.-C. Jeong, S.H. Cho and S.-I. Seo (2008). Fire resistance evaluation of a train carbody made of composite material by large scale tests. *Composite Structures*, *83*(3), 295–303.

Kim, S.W. (1988). A fine grid finite element computation of two-dimensional high Reynolds number flows. *Computers & Fluids*, *16*(4), 429–444.

Kodur, V.K.R. and A. Ahmed (2010). Numerical model for tracing the response of FRP-strengthened RC beams exposed to fire. *Journal of Composites for Construction*, *14*(6), 730–742.

Kondo, N. (1994). Third-order upwind finite element solutions of high Reynolds number flows. *Computer Methods in Applied Mechanics and Engineering*, *112*(1–4), 227–251.

Kung, H.-C. (1972). A mathematical model of wood pyrolysis. *Combustion and Flame*, *18*(1), 185–195.

Lattimer, B.Y., J. Ouellette and J. Trelles (2011). Thermal response of composite materials to elevated temperatures. *Fire Technology*, *47*(4), 823–850.

Layton, W. (2008). *Introduction to the Numerical Analysis of Incompressible Viscous Flows*. Society for Industrial and Applied Mathematics.

Le Quéré, P. (1991). Accurate solutions to the square thermally driven cavity at high Rayleigh number. *Computers & Fluids*, *20*(1), 29–41.

Lewis, R.W., P. Nithiarasu and K.N. Seetharamu (2004). *Fundamentals of the Finite Element Method for Heat and Fluid Flow*. John Wiley & Sons, Ltd.

Li, B.Q. (2006). *Discontinuous Finite Elements in Fluid Dynamics and Heat Transfer*. Springer-Verlag.

Lienhard IV, J.H. and J.H. Lienhard V (2011). *A Heat Transfer Textbook*. Dover Publications, fourth edition.

Liu, L., , G.A. Kardomateas, V. Birman, J.W. Holmes and G.J. Simitses (2006). Thermal buckling of a heat-exposed, axially restrained composite column. *Composites Part A: Applied Science and Manufacturing*, *37*(7), 972–980.

Looyeh, M.R.E. and P. Bettess (1998). A finite element model for the fire-performance of GRP panels including variable thermal properties. *Finite Elements in Analysis and Design*, *30*(4), 313–324.

Looyeh, M.R.E., P. Bettess and A.G. Gibson (1997). A one-dimensional finite element simulation for the fire-performance of GRP panels for offshore structures. *International Journal of Numerical Methods for Heat & Fluid Flow*, *7*(6), 609–625.

Lu, S.-Y. and I. Hamerton (2002). Recent developments in the chemistry of halogen-free flame retardant polymers. *Progress in Polymer Science*, *27*(8), 1661–1712.

Lua, J., J. O'Brien, C.T. Key, Y. Wu and B.Y. Lattimer (2006). A temperature and mass dependent thermal model for fire response prediction of marine composites. *Composites Part A: Applied Science and Manufacturing*, *37*(7), 1024–1039.

Luikov, A.V., V.A. Aleksashenko and A.A. Aleksashenko (1971). Analytical methods of solution of conjugate problems in convection heat transfer. *International Journal of Heat and Mass Transfer*, *14*, 1047–1056.

Maia, D. (2011). *Finite elements comparation on thin plate analysis*. Master dissertation in Civil Engineering, Instituto Superior Técnico, Technical University of Lisbon (in Portuguese), Lisbon, Portugal.

MATLAB (2012). *MATLAB, The Language of Technical Computing*. The MathWorks Inc. Version R2012b.

Mattiasson, K. (1981). Numerical results from large deflection beam and frame problems analysed by means of elliptic integrals. *International Journal for Numerical Methods in Engineering*, *17*(1), 145–153.

Maxwell, J.C. (1972). *Theory of Heat*. Longmans, Green, and Co., London, UK, third edition.

McManus, H.L.N. and G.S. Springer (1992a). High temperature thermomechanical behavior of carbon-phenolic and carbon-carbon composites, I. Analysis. *Journal of Composite Materials*, *26*(2), 206–229.

McManus, H.L.N. and G.S. Springer (1992b). High temperature thermomechanical behavior of carbon-phenolic and carbon-carbon composites, II. Results. *Journal of Composite Materials*, *26*(2), 230–255.

Milano, V.U. and A.G. Gibson (2009). Fire model for fibre reinforced plastic composites using apparent thermal diffusivity (ATD). *Plastics, Rubber and Composites*, *38*(2–4), 87–92.

Miller, J.R. and P.M. Weaver (2003). Temperature profiles in composite plates subject to time-dependent complex boundary conditions. *Composite Structures*, *59*(2), 267–278.

Mobedi, M. (2008). Conjugate natural convection in a square cavity with finite thickness horizontal walls. *International Communications in Heat and Mass Transfer*, *35*, 503–513.

Modest, M.F. (2003). *Radiative Heat Transfer*. Academic Press, second edition.

Morgado, T.M., J.R. Correia and F.A. Branco (2013a). Full-scale fire resistance experiments on GFRP pultruded structural elements. Fire resistance tests on GFRP pultruded columns. Report IST-5-5. Project Fire protection systems for glass fibre reinforced polymer (GFRP) pultruded profiles, PTDC/ECM/100779/2008, ICIST.

Morgado, T.M., F. Nunes, J.R. Correia and F.A. Branco (2013b). Full-scale fire resistance experiments on GFRP pultruded structural elements. Fire resistance tests on GFRP pultruded beams. Report IST-5-4. Project Fire protection systems for glass fibre reinforced polymer (GFRP) pultruded profiles, PTDC/ECM/100779/2008, ICIST.

Morgado, T.M., F. Nunes, J.R. Correia and F.A. Branco (2013c). Thermo-physical and thermomechanical experiments on GFRP and fire protection materials. Differential scanning calorimetry and thermogravimetric analyses DSC/TGA. Report IST-2-2. Project Fire protection systems for glass fibre reinforced polymer (GFRP) pultruded profiles, PTDC/ECM/100779/2008, ICIST.

Morgado, T.M., F. Nunes, J.R. Correia and F.A. Branco (2013d). Thermo-physical and thermomechanical experiments on GFRP and fire protection materials. Dynamic mechanical analyses DMA. Report IST-2-1. Project Fire protection systems for glass fibre reinforced polymer (GFRP) pultruded profiles, PTDC/ECM/100779/2008, ICIST.

Mouritz, A.P. (2002). Post-fire flexural properties of fibre-reinforced polyester, epoxy and phenolic composites. *Journal of Materials Science*, *37*(7), 1377–1386.

Mouritz, A.P. (2003). Simple models for determining the mechanical properties of burnt FRP composites. *Materials Science and Engineering: A*, *359*(1–2), 237–246.

Mouritz, A.P., S. Feih, E. Kandare, Z. Mathys, A.G. Gibson, P.E. Des Jardin, S.W. Case and B.Y. Lattimer (2009). Review of fire structural modelling of polymer composites. *Composites Part A: Applied Science and Manufacturing*, *40*, 1800–1814.

Mouritz, A.P. and A.G. Gibson (2006). *Fire Properties of Polymer Composite Materials*, volume 143. Springer-Verlag.

Mouritz, A.P. and Z. Mathys (2001). Post-fire mechanical properties of glass-reinforced polyester composites. *Composites Science and Technology*, *61*(4), 475–490.

Mouritz, A.P., Z. Mathys and A.G. Gibson (2006). Heat release of polymer composites in fire. *Composites Part A: Applied Science and Manufacturing*, *37*(7), 1040–1054.

Nicolais, L., M. Meo and E. Milella (Editors) (2011). *Composite Materials. A Vision for the Future*. Springer-Verlag, London.

Nigro, E., G. Cefarelli, A. Bilotta, G. Manfredi and E. Cosenza (2011). Fire resistance of concrete slabs reinforced with FRP bars. Part II: Experimental results and numerical simulations on the thermal field. *Composites Part B: Engineering*, *42*(6), 1751–1763–29.

Nouanegue, H.F., A. Muftuoglu and E. Bilgen (2009). Heat transfer by natural convection, conduction and radiation in an inclined square enclosure bounded with a solid wall. *International Journal of Thermal Sciences*, *48*, 871–880.

Oden, J.T. (1980). RIP-Methods for Stokesian Flows. Technical report, The Institute for Computational Engineering and Sciences, The University of Texas at Austin, Austin, Texas.

Paipuri, M. (2016). *Comparison and coupling of continuous and discontinuous Galerkin methods: application to multiphysics problems*. Ph.D. thesis (in progress), Instituto Superior Técnico, Technical University of Lisbon, Lisbon, Portugal.

Patankar, S.V. and D.B. Spalding (1972). A calculation procedure for heat, mass and momentum transfer in three-dimensional parabolic flows. *International Journal of Heat and Mass Transfer*, *15*(10), 1787–1806.

Peters, N. (2011). *Combustion Theory*. RWTH Aachen University, RWTH Aachen University.

Peyret, R. (Editor) (1996). *Handbook of Computational Fluid Mechanics*. Academic Press.

Pilato, L.A. and M.J. Michno (1994). *Advanced Composite Materials*. Springer-Verlag, second edition.

PT. Lundin Industry Invest (2014). North Sea Boats website: http://www.northseaboats.com, visited on 16-01-2014.

Quintiere, J.G. (2006). *Fundamentals of Fire Phenomena.* John Wiley & Sons, United Kingdom.

Ramaswamy, B. (1988). Finite element solution for advection and natural convection flows. *Computers & Fluids*, *16*(4), 349–388.

Reddy, J.N. (2004a). *An Introduction to Nonlinear Finite Element Analysis.* Oxford University Press.

Reddy, J.N. (2004b). *An Introduction to the Finite Element Method.* McGraw-Hill Book Company, Inc.

Reddy, J.N. (2004c). *Mechanics of Laminated Composite Plates and Shells. Theory and Analysis.* CRC Press, second edition.

Reddy, J.N. and D.K. Gartling (2010). *The Finite Element Method in Heat Transfer and Fluid Dynamics.* Taylor & Francis, third edition.

Reissner, E. (1972). On one-dimensional finite-strain beam theory: the plane problem. *Zeitschrift für Angewandte Mathematik und Physik (ZAMP)*, *23*(5), 795–804.

Reissner, E. (1981). On finite deformations of space-curved beams. *Zeitschrift für Angewandte Mathematik und Physik (ZAMP)*, *32*(6), 734–744.

Riccio, A., M. Damiano, M. Zarrelli and F. Scaramuzzino (2013). Three-dimensional modeling of composites fire behavior. *Journal of Reinforced Plastics and Composites*, *33*(7), 619–629.

Roache, P.J. (1973). Finite difference methods for the steady-state Navier-Stokes equations. In Henri Cabannes and Roger Temam (Editors) *Proceedings of the Third International Conference on Numerical Methods in Fluid Mechanics*, volume 18, pages 138–145. Springer Berlin Heidelberg.

Robert, M. and B. Benmokrane (2010). Behavior of GFRP reinforcing bars subjected to extreme temperatures. *Journal of Composites for Construction*, *14*(4), 353–360.

Samanta, A., M. Looyeh, S. Jihan and J. McConnachie (2004). *Thermo-mechanical Assessment of Polymer Composites Subjected to Fire.* Engineering and Physical Science Research Council & The Robert Gordon University, Aberdeen, UK.

Schlichting, H. (1960). *Boundary Layer Theory.* McGraw-Hill.

Scudamore, M.J. (1994). Fire performance studies on glass-reinforced plastic laminates. *Fire and Materials*, *18*(5), 313–325.

Shakib, F., T.J.R. Hughes and Z. Johan (1991). A new finite element formulation for computational fluid dynamics: X. The compressible Euler and Navier-Stokes equations. *Computer Methods in Applied Mechanics and Engineering*, *89*(1–3), 141–219.

Shen, S.F. and W. Habashi (1976). Local linearization of the finite element method and its applications to compressible flows. *International Journal for Numerical Methods in Engineering*, *10*(3), 565–577.

Simo, J.C. (1985). A finite strain beam formulation. The three-dimensional dynamic problem. Part I. *Computer Methods in Applied Mechanics and Engineering*, *49*(1), 55–70.

Simo, J.C. and L. Vu-Quoc (1986). A three-dimensional finite strain rod model. Part II: Computational aspects. *Computer Methods in Applied Mechanics and Engineering*, *58*(1), 79–116.

Smith, G.D. (1985). *Numerical Solution of Partial Differential Equations: Finite Difference Methods.* Oxford University Press, third edition.

Solomon, T.H. and J.P. Gollub (1990). Thermal boundary layers and heat flux in turbulent convection: the role of recirculating flows. *Physical Review A*, *43*(12), 6683–6693.

Sorathia, U., C. Beck and T. Dapp (1993). Residual strength of composites during and after fire exposure. *Journal of Fire Sciences*, *11*(3), 255–270.

Sparrow, E.M. (1962). Heat radiation between simply-arranged surfaces having different temperatures and emissivities. *American Institute of Chemical Engineers (A.I.Ch.E. Journal)*, *8*(1), 12–18.

Sparrow, E.M., R.B. Husar and R.J. Goldstein (1970). Observations and other characteristics of thermals. *Journal of Fluid Mechanics*, *41*(4), 793–800.

Springer, G.S. (1984). Model for predicting the mechanical properties of composites at elevated temperatures. *Journal of Reinforced Plastics and Composites*, *3*(1), 85–95.

Sullivan, R.M. (1993). A coupled solution method for predicting the thermostructural response of decomposing, expanding polymeric composites. *Journal of Composite Materials*, *27*(4), 408–434.

Sullivan, R.M. and N.J. Salamon (1992a). A finite element method for the thermochemical decomposition of polymeric materials – I. Theory. *Journal of Composite Materials*, *30*(4), 431–441.

Sullivan, R.M. and N.J. Salamon (1992b). A finite element method for the thermochemical decomposition of polymeric materials – II. Carbon phenolic composites. *International Journal of Engineering Science*, *30*(7), 939–951.

Suzuki (2014). Website: http://www.suzuki-cup.at, visited on 16-01-2014.

Swiss Society of Engineers and Architects (1997). *The fire protection in construction.* SN 520—183. Swiss Association for Standardization (in French), Zurich.

Tant, M.R., J.B. Henderson and C.T. Boyer (1985). Measurement and modelling of the thermochemical expansion of polymer composites. *Composites*, *16*(2), 121–126.

Taylor, C. and P. Hood (1973). A numerical solution of the Navier-Stokes equations using the finite element technique. *Computers & Fluids*, *1*(1), 73–100.

Team One Composites (2014). Website: http://www.indiamart.com, visited on 16-01-2014.

Tezduyar, T.E., S. Mittal, S.E. Ray and R. Shih (1992). Incompressible flow computations with stabilized bilinear and linear equal-order-interpolation velocity-pressure elements. *Computer Methods in Applied Mechanics and Engineering*, *95*(2), 221–242.

Tezduyar, T.E. and Y. Osawa (2000). Finite element stabilization parameters computed from element matrices and vectors. *Computer Methods in Applied Mechanics and Engineering*, *190*(3–4), 411–430.

Thatcher, R.W. (1990). Locally mass-conserving Taylor-Hood elements for two- and three-dimensional flow. *International Journal for Numerical Methods in Fluids*, *11*(3), 341–353.

Tiago, C. (2007). *Meshless methods: Extending the linear formulation and its generalization to geometrically exact structural analysis*. Ph.D. thesis, Instituto Superior Técnico, Technical University of Lisbon, Lisbon, Portugal.

Timoshenko, S.P. (1953). *History of Strength of Materials*. McGraw-Hill Book Company, Inc., New York.

Tracy, C. (2005). *Fire endurance of multicellular panels in an FRP building system*. Ph.D. thesis, École Polytechnique Fédérale de Lausanne, Lausanne, Switzerland.

Troitzsch, J.H. (1983). Methods for the fire protection of plastics and coatings by flame retardant and intumescent systems. *Progress in Organic Coatings*, *11*(1), 41–69.

Turek, S. (1998). *Efficient Solvers for Incompressible Flow Problems: An Algorithmic Approach*. Springer, Berlin.

Versteeg, H.K. and W. Malalasekera (1995). *An Introduction to Computational Fluid Dynamics. The Finite Volume Method*. Longman Scientific & Technical, England.

Wolfram Research, Inc. (2010). *Mathematica Edition: Version 8.0*. Wolfram Research, Inc., Champaign, Illinois.

Wriggers, P. (2008). *Nonlinear Finite Element Methods*. Springer-Verlag Berlin Heidelberg.

Yücel, A., S. Acharya and M.L. Williams (1989). Natural convection and radiation in a square enclosure. *Numerical Heat Tranfer*, *15*, 261–278.

Zienkiewicz, O.C. and R.L. Taylor (2005). *Finite Element Method for Solid and Structural Mechanics*, volume 2. Elsevier Butterworth-Heinemann, sixth edition.

Zienkiewicz, O.C., R.L. Taylor and P. Nithiarasu (2005a). *Finite Element Method for Fluid Dynamics*, volume 3. Elsevier Butterworth-Heinemann, sixth edition.

Zienkiewicz, O.C., R.L. Taylor and J.Z. Zhu (2005b). *Finite Element Method: Its Basis and Fundamentals*, volume 1. Elsevier Butterworth-Heinemann, sixth edition.

Zoghi, M. (Editor) (2014). *The International Handbook of FRP Composites in Civil Engineering*. CRC Press, Taylor & Francis.

Zudin, Y.B. (2011). *Theory of Periodic Conjugate Heat Transfer*. Mathematical Engineering. Springer-Verlag, United Kingdom, second edition.

Appendix A

Heat transfer problem

A.1 Weak form of the heat transfer equation

The weak form of the transient heat transfer equation is given by equation (3.24). Integrating by parts the first term of the first member, one obtains,

$$-\int_{\Omega} \delta\theta \,\mathrm{div}\,\boldsymbol{q}\,\mathrm{d}\Omega = -\int_{\Omega} \boldsymbol{\nabla}\cdot(\delta\theta\,\boldsymbol{q})\,\mathrm{d}\Omega + \int_{\Omega} \boldsymbol{\nabla}\delta\theta\cdot\boldsymbol{q}\,\mathrm{d}\Omega \tag{A.1}$$

and applying the divergence theorem[1] in the first term of the second member:

$$\int_{\Omega} \delta\theta \,\mathrm{div}\,\boldsymbol{q}\,\mathrm{d}\Omega = -\int_{\Gamma} \delta\theta\, q_i\, n_i\,\mathrm{d}\Gamma + \int_{\Omega} \boldsymbol{\nabla}\delta\theta\cdot\boldsymbol{q}\,\mathrm{d}\Omega = \\ = -\int_{\Gamma} \delta\theta\, q_n\,\mathrm{d}\Gamma + \int_{\Omega} \boldsymbol{\nabla}\delta\theta\cdot\boldsymbol{q}\,\mathrm{d}\Omega \tag{A.3}$$

Since $\Gamma = \Gamma_\theta \cup \Gamma_{q_n}$ and $\Gamma_{q_n} = \Gamma_{\overline{q}} \cup \Gamma_h \cup \Gamma_r \cup \Gamma_R$, it is possible to write,

$$\int_{\Gamma} \delta\theta\, q_n\,\mathrm{d}\Gamma = \int_{\Gamma_\theta} \delta\theta\, q_n\,\mathrm{d}\Gamma_\theta + \int_{\Gamma_q} \delta\theta\, q_n\,\mathrm{d}\Gamma_q + \int_{\Gamma_h} \delta\theta\, q_n\,\mathrm{d}\Gamma_h + \int_{\Gamma_r} \delta\theta\, q_n\,\mathrm{d}\Gamma_r + \int_{\Gamma_R} \delta\theta\, q_n\,\mathrm{d}\Gamma_R \tag{A.4}$$

where $\int_{\Gamma_\theta} \delta\theta\, q_n\,\mathrm{d}\Gamma_\theta = 0$ as $\delta\theta = 0$ on Γ_θ.

Replacing the expressions (A.3) and (A.4) into the weak form (3.24), renders,

$$-\int_{\Gamma} \delta\theta\, q_n\,\mathrm{d}\Gamma + \int_{\Omega} \boldsymbol{\nabla}\delta\theta\cdot\boldsymbol{q}\,\mathrm{d}\Omega + \int_{\Omega} \delta\theta\, G\,\mathrm{d}\Omega - \int_{\Omega} \delta\theta\,\rho\, c_p\,\frac{\partial\theta}{\partial t}\,\mathrm{d}\Omega + \int_{\Gamma_{\overline{q}}} \delta\theta\,\left(q_n + \overline{q}\right)\,\mathrm{d}\Gamma_{\overline{q}} + \\ + \int_{\Gamma_h} \delta\theta\,\left(q_n + h\,\left(\theta_a - \theta\right)\right)\,\mathrm{d}\Gamma_h + \int_{\Gamma_r} \delta\theta\,\left(q_n + \epsilon\,\sigma\,\left(\theta_a^4 - \theta^4\right)\right)\,\mathrm{d}\Gamma_r + \\ + \int_{\Gamma_R} \delta\theta\,\left(q_n - \frac{\epsilon}{1-\epsilon}\,\left(\sigma\,\theta^4 - R\right)\right)\,\mathrm{d}\Gamma_R = 0 \tag{A.5}$$

where the terms regarding Γ_{q_n} cancel and the final form of the weak equation, (3.25), is obtained.

[1] The divergence theorem can be stated as follows:

$$\int_{\Omega} \mathrm{div}\,\boldsymbol{f}\,\mathrm{d}\Omega = \int_{\Gamma} \boldsymbol{f}\cdot\boldsymbol{n}\,\mathrm{d}\Gamma \Leftrightarrow \int_{\Omega} \frac{\partial f_i}{\partial x_i}\,\mathrm{d}\Omega = \int_{\Gamma} f_i n_i\,\mathrm{d}\Gamma \tag{A.2}$$

where $\boldsymbol{f}$ is a vector function and $\boldsymbol{n}$ is the unit normal vector.

A.2 Particularization of the weak form of the radiosity equation to the 2D space

The equation that expresses the radiosities in a three-dimensional space is presented in several publications, *e.g.*, Bathe (1996), Bergheau and Fortunier (2008) or Reddy and Gartling (2010), and it can be written as:

$$R^e = \sigma\,\epsilon^e\,(\theta^e)^4 + (1-\epsilon^e)\sum_{\substack{k=1\\k\neq e}}^{n}\int_{S_R^k} R_k\,\frac{\cos\alpha^e\cos\alpha^k}{\pi\,d^2}\,\mathrm{d}S_R^k \tag{3.7}$$

The weak form of the previous equation is:

$$\begin{aligned}\int_{S_R^e}\delta R^e\frac{R^e}{(1-\epsilon^e)}\,\mathrm{d}S_R^e = \int_{S_R^e}\delta R^e\,\sigma\,\frac{\epsilon^e}{(1-\epsilon^e)}\,(\theta^e)^4\,\mathrm{d}S_R^e + \\ +\sum_{\substack{k=1\\k\neq e}}^{n}\int_{S_R^e}\int_{S_R^k}\delta R^e\,R^k\,\frac{\cos\alpha^e\cos\alpha^k}{\pi\,d^2}\,\mathrm{d}S_R^k\,\mathrm{d}S_R^e\end{aligned} \tag{3.26}$$

For the particular case of the 2D space, the differential surfaces may be evaluated through:

$$\mathrm{d}S_R^e = \mathrm{d}\Gamma_R^e\,\mathrm{d}x_3 \tag{A.6a}$$

$$\mathrm{d}S_R^k = \mathrm{d}\Gamma_R^k\,\mathrm{d}x_3 \tag{A.6b}$$

Hence, replacing the previous result into equation (3.26), one obtains:

$$\begin{aligned}\int_{\Gamma_R^e}\int_{-h/2}^{h/2}\delta R^e\frac{R^e}{(1-\epsilon^e)}\,\mathrm{d}x_3\,\mathrm{d}\Gamma_R^e = \int_{\Gamma_R^e}\int_{-h/2}^{h/2}\delta R^e\,\sigma\,\frac{\epsilon^e}{(1-\epsilon^e)}\,(\theta^e)^4\,\mathrm{d}x_3\,\mathrm{d}\Gamma_R^e + \\ +\sum_{\substack{k=1\\k\neq e}}^{n}\int_{\Gamma_R^e}\int_{\Gamma_R^k}\int_{-h/2}^{h/2}\int_{-h/2}^{h/2}\delta R^e\,R^k\,\frac{\cos\alpha^e\cos\alpha^k}{\pi\,d^2}\,\mathrm{d}x_3\,\mathrm{d}x_3\,\mathrm{d}\Gamma_R^k\,\mathrm{d}\Gamma_R^e\end{aligned} \tag{A.7}$$

From figure 3.1, $\cos\alpha^e$ and $\cos\alpha^k$ are given by:

$$\cos\alpha^e = \boldsymbol{n}^e\cdot\frac{\boldsymbol{d}}{d} \tag{A.8a}$$

$$\cos\alpha^k = \boldsymbol{n}^k\cdot\frac{-\boldsymbol{d}}{d} \tag{A.8b}$$

where the vector $\boldsymbol{d}$ joins a point of the surface S_{R^e} to a point of the surface S_{R^k}. Therefore, if $\boldsymbol{x}^e$ is a point in S_{R^e} and $\boldsymbol{x}^k$ is a point in S_{R^k}, their difference vector is $\boldsymbol{d} = \boldsymbol{x}^k - \boldsymbol{x}^e$ and, the distance, d, between two points can be expressed as:

$$d^2 = \underbrace{\left(x_1^k - x_1^e\right)^2 + \left(x_2^k - x_2^e\right)^2}_{c^2} + \left(x_3^k - x_3^e\right)^2 \tag{A.9}$$

Replacing equation (A.8) into (A.7), it is obtained:

$$\begin{aligned}\int_{\Gamma_R^e}\delta R^e\frac{R^e}{(1-\epsilon^e)}\,\mathrm{d}\Gamma_R^e = \int_{\Gamma_R^e}\delta R^e\,\sigma\,\frac{\epsilon^e}{(1-\epsilon^e)}\,(\theta^e)^4\,\mathrm{d}\Gamma_R^e + \\ +\sum_{\substack{k=1\\k\neq e}}^{n}\int_{\Gamma_R^e}\int_{\Gamma_R^k}\delta R^e\,R^k\,(\boldsymbol{n}^e\cdot\boldsymbol{d})\left(-\boldsymbol{n}^k\cdot\boldsymbol{d}\right)\int_{-h/2}^{h/2}\int_{-h/2}^{h/2}\frac{1}{\pi\,h\,d^4}\,\mathrm{d}x_3\,\mathrm{d}x_3\,\mathrm{d}\Gamma_R^k\,\mathrm{d}\Gamma_R^e\end{aligned} \tag{A.10}$$

The weak form of the radiosity equation in the two-dimensional space can be obtained determining the limit of the expression (A.10) when $h \to \infty$. This calculus was carried out using Mathematica (Wolfram Research, 2010), rendering the following intermediate results:

$$\int_{-h/2}^{h/2}\int_{-h/2}^{h/2} \frac{1}{\pi\, h\, d^4}\, \mathrm{d}x_3\, \mathrm{d}x_3\, \mathrm{d}\Gamma_R^k\, \mathrm{d}\Gamma_R^e = \frac{-2\tan^{-1}\left(\frac{c}{h}\right) + 2\tan^{-1}\left(\frac{h}{c}\right) + \pi}{4\pi c^3} \tag{A.11a}$$

$$\lim_{h\to\infty} \frac{-2\tan^{-1}\left(\frac{c}{h}\right) + 2\tan^{-1}\left(\frac{h}{c}\right) + \pi}{4\pi c^3} = \frac{1}{2\, r^3} \tag{A.11b}$$

Hence, the weak form of the radiosity equation in a 2D space is,

$$\begin{aligned}\int_{\Gamma_R^e} \delta R^e \frac{R^e}{(1-\epsilon^e)}\, \mathrm{d}\Gamma_R^e = \int_{\Gamma_R^e} \delta R^e\, \sigma\, \frac{\epsilon^e}{(1-\epsilon^e)}\, (\theta^e)^4\, \mathrm{d}\Gamma_R^e + \\ + \sum_{\substack{k=1\\k\neq e}}^{n} \int_{\Gamma_R^e}\int_{\Gamma_R^k} \delta R^e\, R^k\, (\boldsymbol{n}^e\cdot\boldsymbol{c})\left(-\boldsymbol{n}^k\cdot\boldsymbol{c}\right) \frac{1}{2\, r^3}\, \mathrm{d}\Gamma_R^k\, \mathrm{d}\Gamma_R^e\end{aligned} \tag{A.12}$$

where:

$$\boldsymbol{c} = \left(x_1^k - x_1^e\right)\boldsymbol{e}_1 + \left(x_2^k - x_2^e\right)\boldsymbol{e}_2 \tag{A.13}$$

Considering that,

$$\boldsymbol{n}^e\cdot\boldsymbol{c} = c\,\cos\alpha^e \tag{A.14a}$$

$$\boldsymbol{n}^k\cdot\boldsymbol{c} = c\,\cos\alpha^k \tag{A.14b}$$

the previous expression (A.12) leads to (3.27), written in section 3.5.

Appendix B

Finite element method

B.1 Introduction to the finite element formulation

The finite element method involves the discretization of the domain and the governing equations. In this process, a relation between the differential equations and the elements is established by dividing the domain into a number of regions — *finite elements* — and approximating the solution over these by suitable approximation functions — *shape functions*. These functions are used to approximate the value field variables within an element by interpolating the nodal values.

The strong form of the problem consists of the governing equations and the boundary conditions for the physical problem. The weak form is an integral form of the strong form and it is convenient to formulate the finite element method (FEM).

Generally, the FEM can be subdivided in the following six steps (adapted from Fish and Belytschko, 2007):

1. Formulation of the strong form (governing equations and boundary conditions);
2. Calculation of the weak form;
3. Determination of the elemental equations (usually, this step requires the development of the partial differential equations for the problem and its weak form, obtained by replacing the approximation of the elemental unknowns on the elemental domain using the *shape functions*);
4. Obtaining the global system of equations to solve by assembling the elemental ones;
5. Solving the equations;
6. Postprocessing the results to determine the quantities of interest, as for example, heat flux in heat transfer problems.

In the case of transient problems, a two-stage procedure is usually employed: (i) a finite element space discretization to transform the differential equations in a set of ordinary differential equations in time, and (ii) a time discretization (commonly using the finite difference method) to obtain the algebraic equations to solve.

Based on Reddy (2004a), three sources of error in a finite element solution are possible:

- the approximation of the domain, *i.e.*, the spatial approximation,

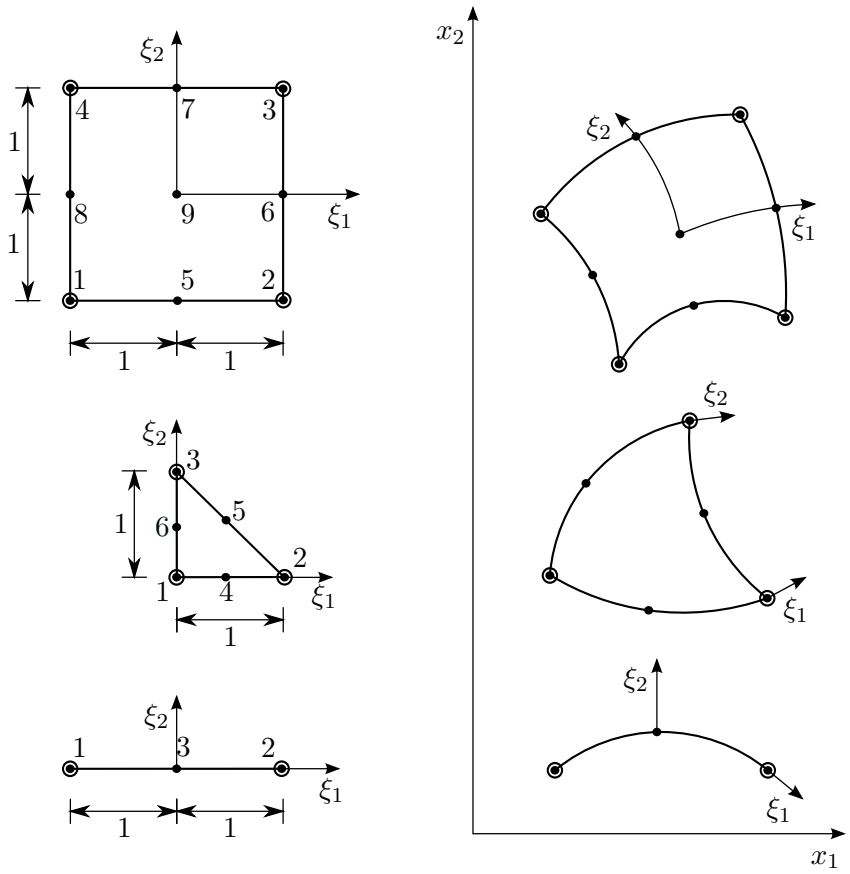

Figure B.1: Mapping of the Taylor-Hood elements and one-dimensional quadratic element (adapted from Zienkiewicz *et al.*, 2005b).

- the time discretization and,
- numerical computation, *e.g.* numerical integration.

B.2 Isoparametric elements and shape functions

In the present thesis, an isoparametric formulation is used to compute the shape functions of the elements. One characteristic of these elements is that they are not restricted to have straight sides and evenly spaced nodes. Hence, it is possible to solve practical problems which have curved boundaries using a reduced number of elements with a consequent reduction in the total number of variables in the system. The method used to create the curved elements is mapping from isoparametric elements (natural coordinates, ξ_1 and ξ_2) to regular elements (global coordinates, x_1 and x_2). Figure B.1 illustrates the mapping of the Taylor–Hood elements and the 3-nodes one-dimensional element. Several specific literature about this topic is available, as for example, the works of Bathe (1996), Hughes (2000) or Zienkiewicz *et al.* (2005b).

In the present section the computation of the first and second order derivatives of the shape functions with respect to the global coordinates is presented.

Assuming that the shape functions are given by,

$$\boldsymbol{\psi}^{(e)} = \begin{Bmatrix} \psi_1 & \psi_2 & ... & \psi_n \end{Bmatrix} \tag{B.1}$$

where each component ψ_i is function of (ξ_1, ξ_2).

The first derivatives of a generic component of the shape function vector with respect to the global coordinates are:

$$\begin{Bmatrix} \frac{\partial \psi_i}{\partial x_1} \\ \frac{\partial \psi_i}{\partial x_2} \end{Bmatrix} = \begin{bmatrix} \frac{\partial \xi_1}{\partial x_1} & \frac{\partial \xi_2}{\partial x_1} \\ \frac{\partial \xi_1}{\partial x_2} & \frac{\partial \xi_2}{\partial x_2} \end{bmatrix} \begin{Bmatrix} \frac{\partial \psi_i}{\partial \xi_1} \\ \frac{\partial \psi_i}{\partial \xi_2} \end{Bmatrix} \tag{B.2}$$

The matrix presented in expression (B.2) can be computed as the inverse of the Jacobian matrix, which is given by:

$$\boldsymbol{J} = \begin{bmatrix} \frac{\partial x_1}{\partial \xi_1} & \frac{\partial x_1}{\partial \xi_2} \\ \frac{\partial x_2}{\partial \xi_1} & \frac{\partial x_2}{\partial \xi_2} \end{bmatrix} \tag{B.3}$$

The components of the Jacobian matrix can be obtained explicitly in terms of natural coordinates by deriving the parametric equations representing the elements geometry,

$$x_1 = \boldsymbol{\psi}^{(e)}\, \mathbf{x}_1^{(e)} \tag{B.4a}$$

$$x_2 = \boldsymbol{\psi}^{(e)}\, \mathbf{x}_2^{(e)} \tag{B.4b}$$

where $\mathbf{x}_1^{(e)}$ and $\mathbf{x}_2^{(e)}$ are respectively vectors that contain the horizontal and vertical coordinates of the element nodes.

Consequently, the inverse of the Jacobian matrix is,

$$\begin{bmatrix} \frac{\partial \xi_1}{\partial x_1} & \frac{\partial \xi_1}{\partial x_2} \\ \frac{\partial \xi_2}{\partial x_1} & \frac{\partial \xi_2}{\partial x_2} \end{bmatrix} = \boldsymbol{J}^{-1} \Leftrightarrow \boldsymbol{J}^{-1} = \frac{1}{J} \begin{bmatrix} \frac{\partial x_2}{\partial \xi_2} & -\frac{\partial x_1}{\partial \xi_2} \\ -\frac{\partial x_2}{\partial \xi_1} & \frac{\partial x_1}{\partial \xi_1} \end{bmatrix} \tag{B.5a}$$

$$J = \det(\boldsymbol{J}) = \frac{\partial x_1}{\partial \xi_1}\frac{\partial x_2}{\partial \xi_2} - \frac{\partial x_1}{\partial \xi_2}\frac{\partial x_2}{\partial \xi_1} \tag{B.5b}$$

where J is the determinant of the Jacobian matrix.

Hence, the first derivatives of the shape function vector with respect to the natural coordinate are required to compute the Jacobian matrix and, in the next sections, they are given for each element, in the following form:

$$\mathbf{B}^{(e)} = \begin{bmatrix} \psi_{1,1} & \psi_{2,1} & ... & \psi_{n,1} \\ \psi_{1,2} & \psi_{2,2} & ... & \psi_{n,2} \end{bmatrix} \tag{B.6}$$

In order to compute the matrices $\mathbf{C}_{SUPG}^{(e)t+\Delta t}$ and $\mathbf{F}_{SUPG}^{(e)t+\Delta t}$ defined in equations (4.61), the second derivatives of the shape function vector with respect to the global coordinates have to be evaluated.

Similarly to (B.2), the second derivatives of each component of the shape function vector can be computed as (Maia, 2011):

$$\begin{Bmatrix} \frac{\partial^2 \psi_i}{\partial {x_1}^2} \\ \frac{\partial^2 \psi_i}{\partial x_1 \partial x_2} \\ \frac{\partial^2 \psi_i}{\partial {x_2}^2} \end{Bmatrix} = \begin{bmatrix} \frac{\partial^2 \xi_1}{\partial {x_1}^2} & \frac{\partial^2 \xi_2}{\partial {x_1}^2} & \left(\frac{\partial \xi_1}{\partial x_1}\right)^2 & 2\,\frac{\partial \xi_1}{\partial x_1}\frac{\partial \xi_2}{\partial x_1} & \left(\frac{\partial \xi_2}{\partial x_1}\right)^2 \\ \frac{\partial^2 \xi_1}{\partial x_1 \partial x_2} & \frac{\partial^2 \xi_2}{\partial x_1 \partial x_2} & \frac{\partial \xi_1}{\partial x_1}\frac{\partial \xi_1}{\partial x_2} & \frac{\partial \xi_1}{\partial x_1}\frac{\partial \xi_2}{\partial x_2} + \frac{\partial \xi_1}{\partial x_2}\frac{\partial \xi_2}{\partial x_1} & \frac{\partial \xi_2}{\partial x_1}\frac{\partial \xi_2}{\partial x_2} \\ \frac{\partial^2 \xi_1}{\partial {x_2}^2} & \frac{\partial^2 \xi_2}{\partial {x_2}^2} & \left(\frac{\partial \xi_1}{\partial x_2}\right)^2 & 2\,\frac{\partial \xi_1}{\partial x_2}\frac{\partial \xi_2}{\partial x_2} & \left(\frac{\partial \xi_2}{\partial x_2}\right)^2 \end{bmatrix} \begin{Bmatrix} \frac{\partial \psi_i}{\partial \xi_1} \\ \frac{\partial \psi_i}{\partial \xi_2} \\ \frac{\partial^2 \psi_i}{\partial {\xi_1}^2} \\ \frac{\partial^2 \psi_i}{\partial \xi_1 \partial \xi_2} \\ \frac{\partial^2 \psi_i}{\partial {\xi_2}^2} \end{Bmatrix} \tag{B.7}$$

To evaluate the expression (B.7), the second derivatives of the natural coordinates with respect to the global ones have to be obtained. As it was done with the first order derivatives, the second derivatives can be computed using the definition of the Jacobian matrix and are given by (Maia, 2011):

$$\begin{Bmatrix} \frac{\partial^2 \xi_1}{\partial {x_1}^2} \\ \frac{\partial^2 \xi_2}{\partial {x_1}^2} \end{Bmatrix} = \frac{1}{J^3} \begin{bmatrix} \frac{\partial x_2}{\partial \xi_2} & -\frac{\partial x_1}{\partial \xi_2} \\ -\frac{\partial x_2}{\partial \xi_1} & \frac{\partial x_1}{\partial \xi_1} \end{bmatrix} \begin{Bmatrix} -\frac{\partial^2 x_1}{\partial {\xi_1}^2}\left(\frac{\partial x_2}{\partial \xi_2}\right)^2 + 2\,\frac{\partial^2 x_1}{\partial \xi_1 \partial \xi_2}\frac{\partial x_2}{\partial \xi_1}\frac{\partial x_2}{\partial \xi_2} - \frac{\partial^2 x_1}{\partial {\xi_2}^2}\left(\frac{\partial x_2}{\partial \xi_1}\right)^2 \\ -\frac{\partial^2 x_2}{\partial {\xi_1}^2}\left(\frac{\partial x_2}{\partial \xi_2}\right)^2 + 2\,\frac{\partial^2 x_2}{\partial \xi_1 \partial \xi_2}\frac{\partial x_2}{\partial \xi_1}\frac{\partial x_2}{\partial \xi_2} - \frac{\partial^2 x_2}{\partial {\xi_2}^2}\left(\frac{\partial x_2}{\partial \xi_1}\right)^2 \end{Bmatrix} \tag{B.8a}$$

$$\begin{Bmatrix} \frac{\partial^2 \xi_1}{\partial x_1 \partial x_2} \\ \frac{\partial^2 \xi_2}{\partial x_1 \partial x_2} \end{Bmatrix} = \frac{1}{J^3} \begin{bmatrix} \frac{\partial x_2}{\partial \xi_2} & -\frac{\partial x_1}{\partial \xi_2} \\ -\frac{\partial x_2}{\partial \xi_1} & \frac{\partial x_1}{\partial \xi_1} \end{bmatrix} \begin{Bmatrix} \frac{\partial^2 x_1}{\partial {\xi_1}^2}\frac{\partial x_2}{\partial \xi_2}\frac{\partial x_1}{\partial \xi_2} - \frac{\partial^2 x_1}{\partial \xi_1 \partial \xi_2}\left(\frac{\partial x_2}{\partial \xi_1}\frac{\partial x_1}{\partial \xi_2} + \frac{\partial x_2}{\partial \xi_2}\frac{\partial x_1}{\partial \xi_1}\right) + \frac{\partial^2 x_1}{\partial {\xi_2}^2}\frac{\partial x_2}{\partial \xi_1}\frac{\partial x_1}{\partial \xi_1} \\ \frac{\partial^2 x_2}{\partial {\xi_1}^2}\frac{\partial x_2}{\partial \xi_2}\frac{\partial x_1}{\partial \xi_2} - \frac{\partial^2 x_2}{\partial \xi_1 \partial \xi_2}\left(\frac{\partial x_2}{\partial \xi_1}\frac{\partial x_1}{\partial \xi_2} + \frac{\partial x_2}{\partial \xi_2}\frac{\partial x_1}{\partial \xi_1}\right) + \frac{\partial^2 x_2}{\partial {\xi_2}^2}\frac{\partial x_2}{\partial \xi_1}\frac{\partial x_1}{\partial \xi_1} \end{Bmatrix} \tag{B.8b}$$

$$\begin{Bmatrix} \frac{\partial^2 \xi_1}{\partial {x_2}^2} \\ \frac{\partial^2 \xi_2}{\partial {x_2}^2} \end{Bmatrix} = \frac{1}{J^3} \begin{bmatrix} \frac{\partial x_2}{\partial \xi_2} & -\frac{\partial x_1}{\partial \xi_2} \\ -\frac{\partial x_2}{\partial \xi_1} & \frac{\partial x_1}{\partial \xi_1} \end{bmatrix} \begin{Bmatrix} -\frac{\partial^2 x_1}{\partial {\xi_1}^2}\left(\frac{\partial x_1}{\partial \xi_2}\right)^2 + 2\,\frac{\partial^2 x_1}{\partial \xi_1 \partial \xi_2}\frac{\partial x_1}{\partial \xi_1}\frac{\partial x_1}{\partial \xi_2} - \frac{\partial^2 x_1}{\partial {\xi_2}^2}\left(\frac{\partial x_1}{\partial \xi_1}\right)^2 \\ -\frac{\partial^2 x_2}{\partial {\xi_1}^2}\left(\frac{\partial x_1}{\partial \xi_2}\right)^2 + 2\,\frac{\partial^2 x_2}{\partial \xi_1 \partial \xi_2}\frac{\partial x_1}{\partial \xi_1}\frac{\partial x_1}{\partial \xi_2} - \frac{\partial^2 x_2}{\partial {\xi_2}^2}\left(\frac{\partial x_1}{\partial \xi_1}\right)^2 \end{Bmatrix} \tag{B.8c}$$

The second derivatives of the shape function vector with respect to the natural coordinates are also required. Hence, in the next sections they are presented, for each element, in the following form:

$$\mathbf{C}^{(e)} = \begin{bmatrix} \psi_{1,11} & \psi_{2,11} & \dots & \psi_{n,11} \\ \psi_{1,12} & \psi_{2,12} & \dots & \psi_{n,12} \\ \psi_{1,22} & \psi_{2,22} & \dots & \psi_{n,22} \end{bmatrix} \tag{B.9}$$

B.2.1 Two-dimensional 3-nodes element

$$\boldsymbol{\psi}^{(e)} = \begin{Bmatrix} -\xi_1 - \xi_2 + 1 \\ \xi_1 \\ \xi_2 \end{Bmatrix}^T$$

$$\mathbf{B}^{(e)} = \begin{bmatrix} -1 & 1 & 0 \\ -1 & 0 & 1 \end{bmatrix} \quad ; \quad \mathbf{C}^{(e)} = \begin{bmatrix} 0 & 0 & 0 \\ 0 & 0 & 0 \\ 0 & 0 & 0 \end{bmatrix}$$

B.2.2 Two-dimensional 6-nodes element

$$\boldsymbol{\psi}^{(e)} = \begin{Bmatrix} (-1+\xi_2+\xi_1)\ (-1+2\,\xi_2+2\,\xi_1) \\ \xi_1\ (-1+2\,\xi_1) \\ \xi_2\ (-1+2\,\xi_2) \\ -4\,\xi_1\ (-1+\xi_2+\xi_1) \\ 4\,\xi_2\,\xi_1 \\ -4\,\xi_2\ (-1+\xi_2+\xi_1) \end{Bmatrix}^T$$

$$\mathbf{B}^{(e)} = \begin{bmatrix} -3+4\,\xi_2+4\,\xi_1 & -3+4\,\xi_2+4\,\xi_1 \\ -1+4\,\xi_1 & 0 \\ 0 & -1+4\,\xi_2 \\ -4\ (-1+\xi_2+2\,\xi_1) & -4\,\xi_1 \\ 4\,\xi_2 & 4\,\xi_1 \\ -4\,\xi_2 & -4\ (-1+2\,\xi_2+\xi_1) \end{bmatrix}^T \ ; \ \mathbf{C}^{(e)} = \begin{bmatrix} 4 & 4 & 4 \\ 4 & 0 & 0 \\ 0 & 0 & 4 \\ -8 & -4 & 0 \\ 0 & 4 & 0 \\ 0 & -4 & -8 \end{bmatrix}^T$$

B.2.3 Two-dimensional 4-nodes element

$$\boldsymbol{\psi}^{(e)} = \begin{Bmatrix} 1/4\ (1-\xi_1)\ (1-\xi_2) \\ 1/4\ (1+\xi_1)\ (1-\xi_2) \\ 1/4\ (1+\xi_1)\ (1+\xi_2) \\ 1/4\ (1-\xi_1)\ (1+\xi_2) \end{Bmatrix}^T$$

$$\mathbf{B}^{(e)} = \begin{bmatrix} 1/4\ (-1)\ (1-\xi_2) & 1/4\ (1-\xi_1)\ (-1) \\ 1/4\ (1)\ (1-\xi_2) & 1/4\ (1+\xi_1)\ (-1) \\ 1/4\ (1)\ (1+\xi_2) & 1/4\ (1+\xi_1)\ (1) \\ 1/4\ (-1)\ (1+\xi_2) & 1/4\ (1-\xi_1)\ (1) \end{bmatrix}^T \ ;\ \mathbf{C}^{(e)} = \begin{bmatrix} 0 & 1/4 & 0 \\ 0 & -1/4 & 0 \\ 0 & 1/4 & 0 \\ 0 & -1/4 & 0 \end{bmatrix}^T$$

B.2.4 Two-dimensional 9-nodes element

$$\boldsymbol{\psi}^{(e)} = \begin{Bmatrix} ((-1+\xi_2)\ \xi_2\ (-1+\xi_1)\ \xi_1)/4 \\ ((-1+\xi_2)\ \xi_2\,\xi_1\ (1+\xi_1))/4 \\ (\xi_2\ (1+\xi_2)\ \xi_1\ (1+\xi_1))/4 \\ (\xi_2\ (1+\xi_2)\ (-1+\xi_1)\ \xi_1)/4 \\ -\left((-1+\xi_2)\ \xi_2\ (-1+\xi_1^2)\right)/2 \\ -\left((-1+\xi_2^2)\ \xi_1\ (1+\xi_1)\right)/2 \\ -\left(\xi_2\ (1+\xi_2)\ (-1+\xi_1^2)\right)/2 \\ -\left((-1+\xi_2^2)\ (-1+\xi_1)\ \xi_1\right)/2 \\ (-1+\xi_2^2)\ (-1+\xi_1^2) \end{Bmatrix}^T$$

B.3 Temporal discretization

The elemental transient residual vector involves a differential operator in time. There are several time approximation schemes to discretize it, and some of them can be consulted in the works of Reddy and Gartling (2010), Donea and Huerta (2003) and Lewis *et al.* (2004). In this section, a particular application of the finite difference method (FDM) is presented: the generalized trapezoidal family of methods.

A linear interpolation of the unknown vector, $\mathbf{u}^{t+\Delta t}$, can be done as a function of the parameter γ:

$$\mathbf{u}^{t+\gamma\,\Delta t} = \gamma\,\mathbf{u}^{t+\Delta t} + (1-\gamma)\ \mathbf{u}^t \tag{B.10}$$

The equation (B.10) can be differentiated in order to t to obtain:

$$\frac{\partial \mathbf{u}^{t+\gamma\,\Delta t}}{\partial t} = \gamma\,\frac{\partial \mathbf{u}^{t+\Delta t}}{\partial t} + (1-\gamma)\ \frac{\partial \mathbf{u}^t}{\partial t} \tag{B.11}$$

The time derivative at the instant $t+\gamma\,\Delta t$ may be approximated by:

$$\frac{\partial \mathbf{u}^{t+\gamma\,\Delta t}}{\partial t} \simeq \frac{\mathbf{u}^{t+\Delta t} - \mathbf{u}^t}{\Delta t} \tag{B.12}$$

Replacing equation (B.12) into (B.11), one obtains,

$$\dot{\mathbf{u}}^{t+\Delta t} = \frac{1}{\gamma\,\Delta t}\left(\mathbf{u}^{t+\Delta t} - \mathbf{u}^t - (1-\gamma)\ \Delta t\,\dot{\mathbf{u}}^t\right) \tag{B.13}$$

$$
\mathbf{B}^{(e)} = \begin{bmatrix}
((-1+\xi_2)\,\xi_2\,(-1+\xi_1))/4 + ((-1+\xi_2)\,\xi_2\,\xi_1)/4 & ((-1+\xi_2)\,(-1+\xi_1)\,\xi_1)/4 + (\xi_2\,(-1+\xi_1)\,\xi_1)/4 \\
((-1+\xi_2)\,\xi_2\,\xi_1)/4 + ((-1+\xi_2)\,\xi_2\,(1+\xi_1))/4 & ((-1+\xi_2)\,\xi_1\,(1+\xi_1))/4 + (\xi_2\,\xi_1\,(1+\xi_1))/4 \\
(\xi_2\,(1+\xi_2)\,\xi_1)/4 + (\xi_2\,(1+\xi_2)\,(1+\xi_1))/4 & (\xi_2\,\xi_1\,(1+\xi_1))/4 + ((1+\xi_2)\,\xi_1\,(1+\xi_1))/4 \\
(\xi_2\,(1+\xi_2)\,(-1+\xi_1))/4 + (\xi_2\,(1+\xi_2)\,\xi_1)/4 & (\xi_2\,(-1+\xi_1)\,\xi_1)/4 + ((1+\xi_2)\,(-1+\xi_1)\,\xi_1)/4 \\
-((-1+\xi_2)\,\xi_2\,\xi_1) & -((-1+\xi_2)\,(-1+\xi_1^2))/2 - (\xi_2\,(-1+\xi_1^2))/2 \\
-((-1+\xi_2^2)\,\xi_1)/2 - ((-1+\xi_2^2)\,(1+\xi_1))/2 & -(\xi_2\,\xi_1\,(1+\xi_1)) \\
-(\xi_2\,(1+\xi_2)\,\xi_1) & -(\xi_2\,(-1+\xi_1^2))/2 - ((1+\xi_2)\,(-1+\xi_1^2))/2 \\
-((-1+\xi_2^2)\,(-1+\xi_1))/2 - ((-1+\xi_2^2)\,\xi_1)/2 & -(\xi_2\,(-1+\xi_1)\,\xi_1) \\
2\,(-1+\xi_2^2)\,\xi_1 & 2\xi_2\,(-1+\xi_1^2)
\end{bmatrix}^T
$$

$$
\mathbf{C}^{(e)} = \begin{bmatrix}
((-1+\xi_2)\,\xi_2)/2 & ((-1+2\,\xi_2)\,(-1+2\,\xi_1))/4 & ((-1+\xi_1)\,\xi_1)/2 \\
((-1+\xi_2)\,\xi_2)/2 & ((-1+2\,\xi_2)\,(1+2\,\xi_1))/4 & (\xi_1\,(1+\xi_1))/2 \\
(\xi_2\,(1+\xi_2))/2 & ((1+2\,\xi_2)\,(1+2\,\xi_1))/4 & (\xi_1\,(1+\xi_1))/2 \\
-((-1+\xi_2)\,\xi_2) & \xi_1 - 2\,\xi_2\,\xi_1 & 1-\xi_1^2 \\
1-\xi_2^2 & -(\xi_2\,(1+2\,\xi_1)) & -(\xi_1\,(1+\xi_1)) \\
-(\xi_2\,(1+\xi_2)) & -((1+2\,\xi_2)\,\xi_1) & 1-\xi_1^2 \\
1-\xi_2^2 & \xi_2 - 2\,\xi_2\,\xi_1 & -((-1+\xi_1)\,\xi_1) \\
2\,(-1+\xi_2^2) & 4\,\xi_2\,\xi_1 & 2\,(-1+\xi_1^2)
\end{bmatrix}^T
$$

γ	Type of the scheme	Name of the scheme
0.0	Fully explicit	Euler Forward difference method
0.5	Semi implicit	Crank–Nicolson method
1.0	Fully implicit	Euler Backward difference method

Table B.1: Time-stepping schemes (adapted from Lewis *et al.*, 2004).

where:

$$\dot{\mathbf{u}}^t = \frac{\partial \mathbf{u}^t}{\partial t} \qquad \text{and} \qquad \dot{\mathbf{u}}^{t+\Delta t} = \frac{\partial \mathbf{u}^{t+\Delta t}}{\partial t}$$

By varying the parameter γ, different transient schemes can be constructed, *e.g.*, taking $\gamma = 0$, $\gamma = 0.5$ and $\gamma = 1$, the fully explicit, semi-implicit and fully implicit schemes are obtained, respectively (see table B.1).

It may be noticed that equation (B.13) cannot be directly used when $\gamma = 0$. In that case, the aforementioned equation should be rewritten as:

$$\gamma\, \Delta t\, \dot{\mathbf{u}}^{t+\Delta t} = \mathbf{u}^{t+\Delta t} - \mathbf{u}^t - (1-\gamma)\ \Delta t\, \dot{\mathbf{u}}^t \tag{B.14}$$

The terms in the residual vector and tangent matrix where time derivatives occur should be multiplied by $\gamma\, \Delta t$ and approximated by expression (B.14).

The order of convergence of the presented scheme is linear for all the values of γ, except for $\gamma = 0.5$, for which the convergence is quadratic.

The term $\dot{\mathbf{u}}^0$ has to be evaluated from the assembled discrete system of equations at the initial time, as indicated in Hughes (2000). Notice that the term $\mathbf{u}^0$ is known.

B.4 Gauss integration

In general, the integrals involved in the weak form of a problem cannot be solved in closed form due to the complexity of the integrands. The finite element formulation approximates the weak form in each element by using the shape functions, which in the present thesis are polynomials. Over each element, the weak form is evaluated numerically using the Gauss quadrature, which is valid in the parent domain. Hence, schematically, the numerical integration process can be summarized as follows:

1. Definition of the integral in the elemental domain or boundary (Ω and Γ),
2. transformation of coordinates to evaluate the integral in the parent domain or boundary,
3. application of the Gauss quadrature.

In the case of one-dimensional and quadrilateral elements, the Gauss–Legendre quadrature was implemented. This method is based on the idea that, in a one dimensional-space, given an appropriate finite number of points, n_G, with coordinates $(\xi_1)_i$ and its corresponding weight factors, w_i, the Gauss-Legendre quadrature allows to evaluate exactly polynomials of degree equal or minor than $(2\, n_G + 1)$. The Gauss–Legendre formula for a one-dimensional generic function $f(x_1)$ is given by,

$$\int_\Gamma f\,(x_1)\ \mathrm{d}\Gamma = \int_{-1}^{1} \hat{f}\,(\xi_1)\ \ \mathrm{d}\xi_1 \approx \sum_{i=1}^{nG} \hat{f}\,((\xi_1)_i)\ w_i \tag{B.15}$$

n_G	p	ξ_1	w
1	1	0.0	2.0
2	3	$\pm 1/\sqrt{3}$	1.0
3	5	$\pm\sqrt{3}/\sqrt{5}$	5/9
		0.0	8/9
4	7	± 0.8611363116	0.3478548451
		± 0.3399810436	0.6521451549

Table B.2: Position of Gauss points and corresponding weights for the integration of one-dimensional or quadrilateral regions (adapted from Fish and Belytschko, 2007).

where $(\xi_1)_i$ are the based points and $\hat{f}$ is the transformed integrand,

$$\hat{f}\left(\xi_1\right) = f\left(x_1\left(\xi_1\right)\right)\, J\left(\xi_1\right) \tag{B.16}$$

and J is the Jacobian of the transformation.

The Gauss–Legendre is one of the most efficient techniques to integrate polynomial functions as it requires fewer based points than other techniques. Table B.2 summarizes the position of the Gauss points and their corresponding weights for the first four rules, being n_G the number of Gauss points, p the maximum polynomial degree which can be exactly integrated, ξ_1 the coordinate of the Gauss point and w the corresponding weight factor.

Considering the evaluation of the integral of a generic two-dimensional function, $f(x_1, x_2)$, one has,

$$\int_\Omega f(x_1, x_2)\, \mathrm{d}\Omega = \int_{-1}^{1}\int_{-1}^{1} \hat{f}\left(\xi_1, \xi_2\right)\, \mathrm{d}\xi_1\, \mathrm{d}\xi_2 \approx \sum_{i=1}^{nG}\sum_{j=1}^{nG} \hat{f}\left(\left(\xi_1\right)_i, \left(\xi_2\right)_j\right)\, w_i\, w_j \tag{B.17}$$

where $\hat{f}$ is the transformed integrand expressed by:

$$\hat{f}\left(\xi_1, \xi_2\right) = f\left(x_1\left(\xi_1, \xi_2\right), x_2\left(\xi_1, \xi_2\right)\right)\, J\left(\xi_1, \xi_2\right) \tag{B.18}$$

In the case of triangular elements, the Gauss quadrature formula employed is,

$$\int_\Omega f(x_1, x_2)\, \mathrm{d}\Omega = \int_0^1 \int_0^{1-\xi_1} \hat{f}\left(\xi_1, \xi_2\right)\, \mathrm{d}\xi_1\, \mathrm{d}\xi_2 \approx \sum_{i=1}^{nG} \hat{f}\left(\left(\xi_1\right)_i, \left(\xi_2\right)_i\right)\, w_i \tag{B.19}$$

where $\hat{f}$ is the transformed integrand expressed by (B.18). As an example, table B.3 summarizes sampling points and weights required for integrating exactly polynomials of 1, 2 and 3 degree.

B.5 Global system of equations and global tangent matrix

The global system of equations to be solved is obtained by *assembling* the elemental ones. It is a process where the elemental matrices and vectors are added in the appropriate locations of the global matrices and vectors. The assembly of elements, in a general case,

n_G	p	ξ_1	ξ_2	w
1	1	1/3	1/3	1/2
3	2	1/2	0.0	1/6
		1/2	1/2	1/6
		0.0	1/2	1/6
4	3	1/3	1/3	−27/96
		1/5	1/5	25/96
		3/5	1/5	25/96
		1/5	3/5	25/96

Table B.3: Position of Gauss points and corresponding weights for the integration in triangular regions.

is based on the idea that the solution is continuous at the interelement boundaries and it is subjected to boundary and/or initial conditions.

Following the notation of Hughes (2000), the assembly operation of the residual and tangent matrix at $(t + \Delta t)$ can be expressed respectively by,

$$\mathbf{r}^{t+\Delta t} = \mathop{\mathbf{A}}_{e=1}^{m} \mathbf{r}^{(e)t+\Delta t} \qquad \text{and} \qquad \overline{\mathbf{K}}^{t+\Delta t} = \mathop{\mathbf{A}}_{e=1}^{m} \overline{\mathbf{K}}^{(e)t+\Delta t} \tag{B.20}$$

where $\mathbf{A}$ is the finite element assembly operator and m is the total number of elements.

B.6 Newton–Raphson method

The Newton–Raphson method is an incremental/iterative numerical method to solve nonlinear systems of equations. The problem consists of finding the unknowns at each time step, $\mathbf{u}^{t+\Delta t}$, such that:

$$\mathbf{r}\left(\mathbf{u}^{t+\Delta t}\right) = \mathbf{0} \tag{B.21}$$

The iterative process is carried out until the convergence of the solution — which is evaluated through the convergence test — is attained. In the developed code, one indicator of the convergence was considered: the dimensionless residual norm, computed as the quotient between the norm of the residual vector and the norm of the initial residual vector. The Euclidean norm was programmed. The convergence to the solution will be attained when the indicator is equal or lower than a threshold value, ε_{TOL}, defined by the user. In the present thesis, this value is set as 10^{-8}.

In this method, the unknown vector correction is calculated from a first order Taylor expansion series of the residual in the vicinity of the solution,

$$\mathbf{r}\left(\mathbf{u}^{t+\Delta t}\right) \cong \mathbf{r}\left(\mathbf{u}^{t+\Delta t}\right)_i + \left.\frac{\partial \mathbf{r}\left(\mathbf{u}^{t+\Delta t}\right)}{\partial \mathbf{u}^T}\right|_i \left(\mathbf{u}^{t+\Delta t} - \left(\mathbf{u}^{t+\Delta t}\right)_i\right) \tag{B.22}$$

where i refers to the iteration number. A linear approximation of the residual vector in the vicinity of the solution is obtained and, in order to cancel it, equation (B.21) will be considered. Hence, the iterative incremental nodal solution vector, $\delta\mathbf{u}^{t+\Delta t}$, can be computed from,

$$\mathbf{r}\left(\mathbf{u}^{t+\Delta t}\right)_i = -\left(\mathbf{A}^{t+\Delta t}\right)_i \delta\mathbf{u}^{t+\Delta t} \tag{B.23}$$

where $\left(\mathbf{A}^{t+\Delta t}\right)_i$ is the tangent matrix at $(t+\Delta t)$, given by,

$$\left(\mathbf{A}^{t+\Delta t}\right)_i = \left.\frac{\partial \mathbf{r}\left(\mathbf{u}^{t+\Delta t}\right)}{\partial \mathbf{u}^T}\right|_i \tag{B.24}$$

and:

$$\delta \mathbf{u}^{t+\Delta t} = \mathbf{u}^{t+\Delta t} - \left(\mathbf{u}^{t+\Delta t}\right)_i \tag{B.25}$$

The update of the iterative solution vector is expressed by:

$$\left(\mathbf{u}^{t+\Delta t}\right)_{i+1} = \left(\mathbf{u}^{t+\Delta t}\right)_i + \delta \mathbf{u}^{t+\Delta t} \tag{B.26}$$

The Newton–Raphson method presents quadratic convergence of the iterative error in the asymptotic limit of the solution.

Appendix C

Navier–Stokes problem

C.1 Navier–Stokes equations and weak form

The Navier–Stokes equations are a set of equations (momentum and mass-conservation equations) that govern the time-dependent laminar flow of viscous, incompressible and Newtonian fluids. The strong form of the problem is given by:

$$\operatorname{div} \boldsymbol{v} = 0 \qquad \text{in} \quad \Omega \tag{C.1a}$$

$$\dot{\boldsymbol{v}} + (\boldsymbol{\nabla v})\,\boldsymbol{v} - \nu\,\boldsymbol{\nabla}^2\boldsymbol{v} + \boldsymbol{\nabla} p = \boldsymbol{b} \qquad \text{in} \quad \Omega \tag{C.1b}$$

$$\boldsymbol{v} = \overline{\boldsymbol{v}} \qquad \text{on} \quad \Gamma_v \tag{C.1c}$$

$$\boldsymbol{t} = \bar{\boldsymbol{t}} \qquad \text{on} \quad \Gamma_t \tag{C.1d}$$

$$\boldsymbol{v}_0 = \overline{\boldsymbol{v}}_0 \qquad \text{at} \quad t = t_0 \text{ in } \overline{\Omega} \tag{C.1e}$$

The weak form of the Navier–Stokes equation is:

$$-\int_\Omega \delta p \operatorname{div} \boldsymbol{v}\, \mathrm{d}\Omega = 0 \tag{4.29b}$$

$$\int_\Omega \delta \boldsymbol{v} \cdot \left(\dot{\boldsymbol{v}} + (\boldsymbol{\nabla v})\,\boldsymbol{v} - \nu\,\boldsymbol{\nabla}^2\boldsymbol{v} + \boldsymbol{\nabla} p - \boldsymbol{b}\right) \mathrm{d}\Omega + \\ + \int_{\Gamma_t} \delta \boldsymbol{v} \cdot \left((\nu\,\boldsymbol{\nabla v} - p\,\boldsymbol{I})\,\boldsymbol{n} - \bar{\boldsymbol{t}}\right) \mathrm{d}\Gamma_t = 0 \tag{C.2a}$$

Integrating by parts and applying the divergence theorem to the forth and fifth terms of the left part in expression (C.2a), it is obtained:

$$\int_\Omega \delta \boldsymbol{v} \cdot \boldsymbol{\nabla}^2 \boldsymbol{v}\, \mathrm{d}\Omega = \int_\Gamma \delta \boldsymbol{v} \cdot (\boldsymbol{\nabla v})\,\boldsymbol{n}\, \mathrm{d}\Gamma - \int_\Omega \boldsymbol{\nabla}\delta \boldsymbol{v} : \boldsymbol{\nabla v}\, \mathrm{d}\Omega \tag{C.3a}$$

$$\int_\Omega \delta \boldsymbol{v} \cdot \boldsymbol{\nabla} p\, \mathrm{d}\Omega = \int_\Gamma \delta \boldsymbol{v} \cdot p\,\boldsymbol{n}\, \mathrm{d}\Gamma - \int_\Omega \operatorname{div} \delta \boldsymbol{v}\, p\, \mathrm{d}\Omega \tag{C.3b}$$

Replacing (C.3) into (C.2a) and taking into account that $\Gamma = \Gamma_v \cup \Gamma_t$ and $\delta \boldsymbol{v} = \boldsymbol{o}$ on Γ_v, the final weak form of the problem is,

$$\int_\Omega \delta \boldsymbol{v} \cdot \dot{\boldsymbol{v}}\, \mathrm{d}\Omega + \int_\Omega \delta \boldsymbol{v} \cdot (\boldsymbol{\nabla v})\,\boldsymbol{v}\, \mathrm{d}\Omega + \int_\Omega \boldsymbol{\nabla}\delta \boldsymbol{v} : \nu \boldsymbol{\nabla v}\, \mathrm{d}\Omega - \\ - \int_\Omega \operatorname{div} \delta \boldsymbol{v}\, p\, \mathrm{d}\Omega - \int_{\Gamma_t} \delta \boldsymbol{v} \cdot \bar{\boldsymbol{t}}\, \mathrm{d}\Gamma_t - \int_\Omega \delta \boldsymbol{v} \cdot \boldsymbol{b}\, \mathrm{d}\Omega = 0 \tag{C.4}$$

which corresponds to the equation (4.29a), when the fluid is considered iso-thermal.

C.2 Ladyzhenskaya-Babŭska-Brezzi condition

Including the spatial discretization of the variables into the weak form, operating similarly to section 4.6 and assembling the elemental matrices and vectors, the global matrix system which governs the discrete Stokes problem assumes the form,

$$\begin{bmatrix} \mathbf{M}_v & \mathbf{O} \\ \mathbf{O} & \mathbf{O} \end{bmatrix} \begin{Bmatrix} \dot{\mathbf{v}} \\ \dot{\mathbf{p}} \end{Bmatrix} + \begin{bmatrix} \mathbf{K}_v & \mathbf{G} \\ \mathbf{G}^T & \mathbf{O} \end{bmatrix} \begin{Bmatrix} \mathbf{v} \\ \mathbf{p} \end{Bmatrix} = \begin{Bmatrix} \mathbf{f}_v \\ \mathbf{0} \end{Bmatrix} \tag{C.5}$$

which, in the steady state regime, is expressed as:

$$\begin{bmatrix} \mathbf{K}_v & \mathbf{G} \\ \mathbf{G}^T & \mathbf{O} \end{bmatrix} \begin{Bmatrix} \mathbf{v} \\ \mathbf{p} \end{Bmatrix} = \begin{Bmatrix} \mathbf{f}_v \\ \mathbf{0} \end{Bmatrix} \tag{C.6}$$

Equation (C.6) presents an algebraic system of equations that contains a null submatrix in the diagonal. From the first equation, one obtains,

$$\mathbf{K}_v\,\mathbf{v} + \mathbf{G}\,\mathbf{p} = \mathbf{f}_v \tag{C.7}$$

and replacing it into the second equation, the pressure can be computed using the so called Schur complement matrix:

$$\left(\mathbf{G}^T\,\mathbf{K}_v^{-1}\,\mathbf{G}\right)\,\mathbf{p} = \mathbf{G}^T\,\mathbf{K}_v^{-1}\,\mathbf{f}_v \tag{C.8}$$

It can be demonstrated that, provided $\mathbf{G}$ such that its kernel[1] is null, the pressure matrix $\left(\mathbf{G}^T\,\mathbf{K}_v^{-1}\,\mathbf{G}\right)$ is positive definite (besides symmetric and full) and the global matrix of system (C.6) is non-singular. Under these conditions, the existence and uniqueness of the solution is guaranteed.

The Ladyzhenskaya-Babŭska-Brezzi (*LBB*) condition states that velocity and pressure spaces cannot be chosen arbitrarily. The LBB condition, thus, is a sufficient compatibility condition that continuous and discrete spaces of approximation of velocity and pressure must satisfy to guarantee the stability of the solution (avoiding numerical oscillations in the pressure field). Hence, the velocity-pressure pairs that satisfy the LBB condition, allow obtaining a discrete gradient operator such that $\ker \mathbf{G} = \mathbf{0}$.

Following Donea and Huerta (2003), the LBB condition states that:

> *The existence of a stable finite element approximate solution* ($\boldsymbol{v}$, p) *to the steady Stokes problem depends on choosing a pair of spaces* $\boldsymbol{\mathcal{V}}$ *and* $\mathcal{Q}$*, such that the following* inf-sup condition *holds,*
>
> $$\inf_{\delta p \in \mathcal{Q}} \sup_{\delta \boldsymbol{v} \in \boldsymbol{\mathcal{V}}} \frac{\int_\Omega \delta p\ (\operatorname{div} \delta \boldsymbol{v})\ \mathrm{d}\Omega}{\|\delta p\|\ \|\delta \boldsymbol{v}\|} \geq \alpha > 0 \tag{C.9}$$
>
> *where* $\boldsymbol{\mathcal{V}}$ *and* $\mathcal{Q}$ *are the finite-dimensional spaces of functions for velocity and pressure, respectively, and* α *is a constant independent of the mesh size.*

An extensive discussion of the LBB condition is beyond the scope of this thesis. Further information and details about the theory of mixed methods and LBB condition can be consulted in Oden (1980), Brezzi and Fortin (1991), Chapelle and Bathe (1993), Peyret (1996), Jiang (1998), Donea and Huerta (2003), Dobrowolski (2005) and Layton (2008).

[1] The kernel of a generic matrix, $\mathbf{G}$, is the set of vectors, $\mathbf{q}$, such that $\mathbf{G}\,\mathbf{q} = \mathbf{0}$.

Appendix D

Numerical results of the lid-driven problem

In this appendix the numerical results obtained for the lid-driven cavity for $Re = 100$, $Re = 1000$ and $Re = 5000$ are presented. Nonlinear transient analyses were carried out until the steady state solution of the problem was reached. Due to the increasing complexity of the problems performed for higher Reynolds number, different adaptive meshes had to be generated. $P2P1$ elements were employed in all the analyses.

Tables D.1 and D.2 report the velocities obtained with the in-house code using non-uniform meshes of 40×40 and 16×16 $P2P1$ elements, respectively. Table D.3 summarizes the results presented in Ghia *et al.* (1982) and table D.4 lists those reported in Erturk *et al.* (2005). Figure D.1 graphically represents the numerical results obtained with the implemented code and the numerical solution of the referenced papers. It can be observed that the solution of the problem when $Re = 5000$ and meshes of 16×16 $P2P1$ elements are used is not represented as convergence was not attained.

Vertical velocity along $x_1 = 0.5$ m			Horizontal velocity along $x_2 = 0.5$ m		
x_2 (m)	Re		x_1 (m)	Re	
	1000	5000		1000	5000
0	0	0	0	0	0
0.003429	0.024285	0.054178	0.003429	0.024285	0.054178
0.006859	0.047328	0.103913	0.006859	0.047328	0.103913
0.010288	0.069131	0.148388	0.010288	0.069131	0.148388
0.013717	0.089715	0.187491	0.013717	0.089715	0.187491
0.017147	0.109076	0.220639	0.017147	0.109076	0.220639
0.020576	0.127250	0.248759	0.020576	0.127250	0.248759
0.024005	0.144241	0.272025	0.024005	0.144241	0.272025
0.027435	0.160105	0.291752	0.027435	0.160105	0.291752
0.033981	0.187288	0.322245	0.033981	0.187288	0.322245
0.040527	0.210867	0.347017	0.040527	0.210867	0.347017
0.047073	0.231150	0.368163	0.047073	0.231150	0.368163

(Continued on next page)

Table D.1: Numerical results of the velocity computed using a 40×40 nonuniform mesh of $P2P1$ elements.

Vertical velocity along $x_1 = 0.5$ m			Horizontal velocity along $x_2 = 0.5$ m		
x_2 (m)	Re		x_1 (m)	Re	
	1000	5000		1000	5000
0.053619	0.248712	0.386042	0.053619	0.248712	0.386042
0.060165	0.263965	0.400153	0.060165	0.263965	0.400153
0.066711	0.277376	0.410734	0.066711	0.277376	0.410734
0.073257	0.289325	0.417074	0.073257	0.289325	0.417074
0.079803	0.300095	0.420354	0.079803	0.300095	0.420354
0.091386	0.316788	0.417480	0.091386	0.316788	0.417480
0.102968	0.330960	0.408425	0.102968	0.330960	0.408425
0.114550	0.342877	0.394980	0.114550	0.342877	0.394980
0.126133	0.352341	0.380797	0.126133	0.352341	0.380797
0.137715	0.359180	0.366568	0.137715	0.359180	0.366568
0.149298	0.363264	0.353338	0.149298	0.363264	0.353338
0.160880	0.364514	0.340225	0.160880	0.364514	0.340225
0.172462	0.363059	0.328404	0.172462	0.363059	0.328404
0.190448	0.355552	0.310104	0.190448	0.355552	0.310104
0.208433	0.342814	0.292484	0.208433	0.342814	0.292484
0.226419	0.326032	0.273891	0.226419	0.326032	0.273891
0.244404	0.306591	0.256261	0.244404	0.306591	0.256261
0.262389	0.285709	0.238482	0.262389	0.285709	0.238482
0.280375	0.264249	0.220894	0.280375	0.264249	0.220894
0.298360	0.242876	0.202769	0.298360	0.242876	0.202769
0.316346	0.221993	0.185481	0.316346	0.221993	0.185481
0.339303	0.196114	0.163863	0.339303	0.196114	0.163863
0.362259	0.170990	0.142046	0.362259	0.170990	0.142046
0.385216	0.146400	0.120143	0.385216	0.146400	0.120143
0.408173	0.122158	0.098617	0.408173	0.122158	0.098617
0.431130	0.098090	0.076714	0.431130	0.098090	0.076714
0.454086	0.074087	0.055121	0.454086	0.074087	0.055121
0.477043	0.050088	0.033482	0.477043	0.050088	0.033482
0.522957	0.001924	−0.009925	0.522957	0.001924	−0.009925
0.545914	−0.022294	−0.031569	0.545914	−0.022294	−0.031569
0.568870	−0.046639	−0.053227	0.568870	−0.046639	−0.053227
0.591827	−0.071203	−0.075143	0.591827	−0.071203	−0.075143
0.614784	−0.096030	−0.097573	0.614784	−0.096030	−0.097573
0.637741	−0.121099	−0.119970	0.637741	−0.121099	−0.119970
0.660697	−0.146354	−0.142131	0.660697	−0.146354	−0.142131
0.683654	−0.171924	−0.164694	0.683654	−0.171924	−0.164694
0.701640	−0.191969	−0.183381	0.701640	−0.191969	−0.183381
0.719625	−0.212069	−0.201982	0.719625	−0.212069	−0.201982
0.737611	−0.232033	−0.220340	0.737611	−0.232033	−0.220340
0.755596	−0.252096	−0.239142	0.755596	−0.252096	−0.239142
0.773581	−0.272572	−0.258654	0.773581	−0.272572	−0.258654
0.791567	−0.294049	−0.278191	0.791567	−0.294049	−0.278191

(Continued on next page)

Table D.1: Numerical results of the velocity computed using a 40×40 nonuniform mesh of $P2P1$ elements.

Vertical velocity along $x_1 = 0.5$ m			Horizontal velocity along $x_2 = 0.5$ m		
x_2 (m)	Re		x_1 (m)	Re	
	1000	5000		1000	5000
0.809552	−0.318459	−0.297594	0.809552	−0.318459	−0.297594
0.827538	−0.347386	−0.317651	0.827538	−0.347386	−0.317651
0.839120	−0.369911	−0.330579	0.839120	−0.369911	−0.330579
0.850702	−0.395684	−0.344029	0.850702	−0.395684	−0.344029
0.862285	−0.424669	−0.357814	0.862285	−0.424669	−0.357814
0.873867	−0.455072	−0.371130	0.873867	−0.455072	−0.371130
0.885450	−0.483116	−0.384403	0.885450	−0.483116	−0.384403
0.897032	−0.505235	−0.396254	0.897032	−0.505235	−0.396254
0.908614	−0.512758	−0.409051	0.908614	−0.512758	−0.409051
0.920197	−0.502425	−0.426443	0.920197	−0.502425	−0.426443
0.926743	−0.485583	−0.443280	0.926743	−0.485583	−0.443280
0.933289	−0.461017	−0.464745	0.933289	−0.461017	−0.464745
0.939835	−0.428570	−0.492372	0.939835	−0.428570	−0.492372
0.946381	−0.389056	−0.521114	0.946381	−0.389056	−0.521114
0.952927	−0.343720	−0.540425	0.952927	−0.343720	−0.540425
0.959473	−0.293893	−0.543292	0.959473	−0.293893	−0.543292
0.966019	−0.241785	−0.509051	0.966019	−0.241785	−0.509051
0.972565	−0.188882	−0.440838	0.972565	−0.188882	−0.440838
0.975995	−0.161765	−0.389823	0.975995	−0.161765	−0.389823
0.979424	−0.135213	−0.331291	0.979424	−0.135213	−0.331291
0.982853	−0.109534	−0.268542	0.982853	−0.109534	−0.268542
0.986283	−0.084875	−0.204138	0.986283	−0.084875	−0.204138
0.989712	−0.061486	−0.142702	0.989712	−0.061486	−0.142702
0.993141	−0.039456	−0.086233	0.993141	−0.039456	−0.086233
0.996571	−0.018948	−0.038469	0.996571	−0.018948	−0.038469
1	0	0	1	0	0

(End of table)

Table D.1: Numerical results of the velocity computed using a 40×40 nonuniform mesh of $P2P1$ elements.

x_2 (m)	Re	
	100	1000
0	0	0
0.005836	−0.004281	−0.018717
0.011673	−0.008455	−0.036683
0.021020	−0.014935	−0.063999
0.030366	−0.021180	−0.089732
0.045058	−0.030575	−0.126982
0.059750	−0.039527	−0.161807
0.082180	−0.052494	−0.211957
0.104610	−0.064820	−0.260346
0.137372	−0.082057	−0.322359
0.170135	−0.098772	−0.363139
0.215025	−0.121320	−0.359456
0.259914	−0.143563	−0.306063
0.316319	−0.170061	−0.247807
0.372723	−0.192769	−0.182685
0.436362	−0.206931	−0.124876
0.500000	−0.204657	−0.066996
0.563638	−0.178786	−0.002982
0.627277	−0.129285	0.061310
0.683681	−0.067523	0.127795
0.740086	0.009078	0.192123
0.784975	0.082845	0.251191
0.829865	0.176039	0.304342
0.862628	0.266026	0.339342
0.895390	0.385003	0.366685
0.917820	0.488076	0.381041
0.940250	0.609835	0.414455
0.954942	0.699303	0.468589
0.969634	0.794520	0.579686
0.978980	0.857347	0.687173
0.988327	0.920824	0.819573
0.994164	0.960563	0.909776
1	1	1

(a) Vertical velocity along $x_1 = 0.5$ m.

x_1 (m)	Re	
	100	1000
0	0	0
0.005836	0.010460	0.037761
0.011673	0.020520	0.072438
0.021020	0.035807	0.121037
0.030366	0.050094	0.162252
0.045058	0.070588	0.210993
0.059750	0.088773	0.247140
0.082180	0.112385	0.284977
0.104610	0.131372	0.312492
0.137372	0.151954	0.340975
0.170135	0.165198	0.352167
0.215025	0.174042	0.329952
0.259914	0.173897	0.291705
0.316319	0.163518	0.226042
0.372723	0.142348	0.160967
0.436362	0.105468	0.092977
0.500000	0.053804	0.028701
0.563638	−0.011126	−0.037232
0.627277	−0.087577	−0.104262
0.683681	−0.154871	−0.170049
0.740086	−0.214297	−0.233179
0.784975	−0.240583	−0.280917
0.829865	−0.242943	−0.349012
0.862628	−0.224480	−0.422804
0.895390	−0.187979	−0.506854
0.917820	−0.155229	−0.495017
0.940250	−0.116092	−0.415867
0.954942	−0.088660	−0.315706
0.969634	−0.059953	−0.197075
0.978980	−0.041494	−0.129158
0.988327	−0.022964	−0.065500
0.994164	−0.011446	−0.030911
1	0	0

(b) Horizontal velocity along $x_2 = 0.5$ m.

Table D.2: Numerical results of the velocity computed using a 16×16 nonuniform mesh of $P2P1$ elements.

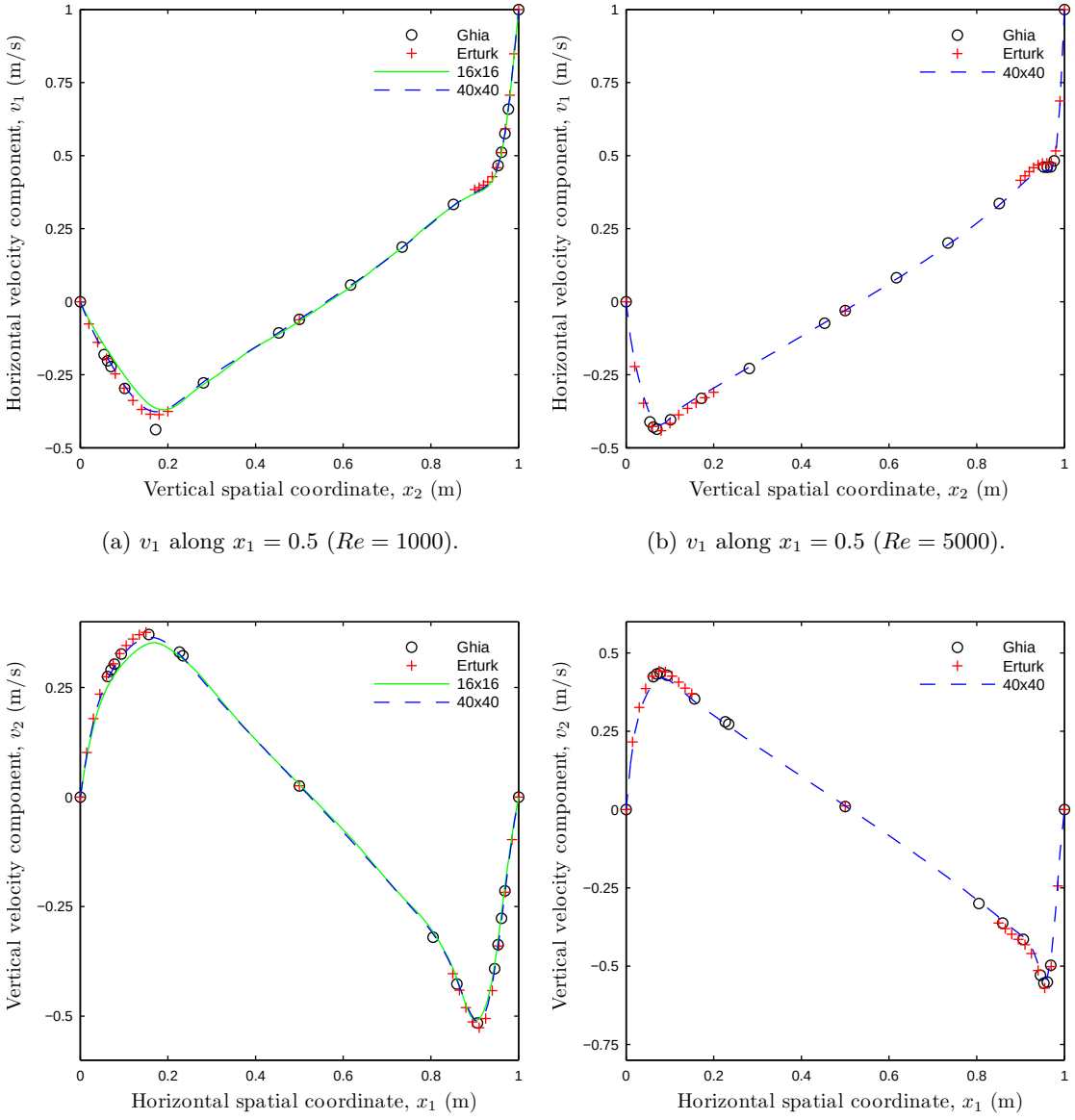

(a) v_1 along $x_1 = 0.5$ ($Re = 1000$).

(b) v_1 along $x_1 = 0.5$ ($Re = 5000$).

(c) v_2 along $x_2 = 0.5$ ($Re = 1000$).

(d) v_2 along $x_2 = 0.5$ ($Re = 5000$).

Figure D.1: Vertical and horizontal velocity distributions in the lid-driven problem.

x_2 (m)	Re		
	100	1000	5000
1	1	1	1
0.9766	0.84123	0.65928	0.48223
0.9688	0.78871	0.57492	0.4612
0.9609	0.73722	0.51117	0.45992
0.9531	0.68717	0.46604	0.46036
0.8516	0.23151	0.33304	0.33556
0.7344	0.00332	0.18719	0.20087
0.6172	−0.13641	0.05702	0.08183
0.5	−0.205810	−0.0608	−0.03039
0.4531	−0.2109	−0.10648	−0.07404
0.2813	−0.15662	−0.27805	−0.22855
0.1719	−0.1015	−0.438289	−0.3305
0.1016	−0.06434	−0.2973	−0.40435
0.0703	−0.04775	−0.2222	−0.43643
0.0625	−0.04192	−0.20196	−0.42901
0.0547	−0.03717	−0.18109	−0.41165
0	0	0	0

(a) Vertical velocity along $x_1 = 0.5$ m.

x_1 (m)	Re		
	100	1000	5000
1	0	0	0
0.9688	−0.05906	−0.21388	−0.49774
0.9609	−0.07391	−0.27669	−0.55069
0.9531	−0.08864	−0.33714	−0.55408
0.9453	−0.10313	−0.39188	−0.52876
0.9063	−0.16914	−0.5155	−0.41442
0.8594	−0.22445	−0.42665	−0.36214
0.8047	−0.24533	−0.31966	−0.30018
0.5	0.05454	0.02526	0.00945
0.2344	0.17527	0.32235	0.2728
0.2266	0.17507	0.33075	0.28066
0.1563	0.16077	0.37095	0.35368
0.0938	0.12317	0.32627	0.4291
0.0781	0.1089	0.30353	0.43648
0.0703	0.10091	0.29012	0.43329
0.0625	0.09233	0.27485	0.42447
0	0	0	0

(b) Horizontal velocity along $x_2 = 0.5$ m.

Table D.3: Numerical results of the velocity obtained by Ghia *et al.* (1982).

x_2 (m)	Re	
	1000	5000
1	1	1
0.99	0.8486	0.6866
0.98	0.7065	0.5159
0.97	0.5917	0.4749
0.96	0.5102	0.4739
0.95	0.4582	0.4738
0.94	0.4276	0.4683
0.93	0.4101	0.4582
0.92	0.3993	0.4452
0.91	0.3913	0.4307
0.9	0.3838	0.4155
0.5	−0.062	−0.0319
0.2	−0.3756	−0.31
0.18	−0.3869	−0.3285
0.16	−0.3854	−0.3467
0.14	−0.369	−0.3652
0.12	−0.3381	−0.3876
0.1	−0.296	−0.4168
0.08	−0.2472	−0.4419
0.06	−0.1951	−0.4272
0.04	−0.1392	−0.348
0.02	−0.0757	−0.2223
0	0	0

(a) Vertical velocity along $x_1 = 0.5$ m.

x_1 (m)	Re	
	1000	5000
1	0	0
0.985	−0.0973	−0.2441
0.97	−0.2173	−0.5019
0.955	−0.34	−0.57
0.94	−0.4417	−0.5139
0.925	−0.5052	−0.4595
0.91	−0.5263	−0.4318
0.895	−0.5132	−0.4147
0.88	−0.4803	−0.3982
0.865	−0.4407	−0.3806
0.85	−0.4028	−0.3624
0.5	0.0258	0.0117
0.15	0.3756	0.3699
0.135	0.3705	0.3878
0.12	0.3605	0.407
0.105	0.346	0.426
0.09	0.3273	0.4403
0.075	0.3041	0.4426
0.06	0.2746	0.4258
0.045	0.2349	0.3868
0.03	0.1792	0.3263
0.015	0.1019	0.216
0	0	0

(b) Horizontal velocity along $x_2 = 0.5$ m.

Table D.4: Numerical results of the velocity reported in Erturk *et al.* (2005).

Appendix E

Differentially heated square cavity

In this appendix the numerical values of velocity and temperature of the differentially heated square cavity problem are presented, considering different Rayleigh numbers (10^3, 10^4 and 10^5). Due to the complexity of the problems, two regular meshes with $Q2Q1$ elements are used: (i) 8×8 and (ii) 32×32 elements.

The geometry and the boundary conditions of the problem are illustrated in figure E.1. The value of the constants considered is reported in table E.1[1].

The reference results are reported in Betts and Haroutunian (1983) and summarized in table E.2. Table E.3 provides the numerical results obtained with a mesh of 8×8 elements. The numerical results obtained with the 32×32 mesh are only presented in graphical mode, as they are too extensive. Figures E.2, E.3 and E.4 compare the numerical results computed with both meshes *versus* the reference values. The mesh with 32×32 elements presents good agreement with the reference results. However, the representation of the solution provided by the 8×8 elements mesh clearly deteriorates for increasing Ra number. At first, these limitations are only perceptible in the velocity fields, but they are gradually extended to the temperature field as well.

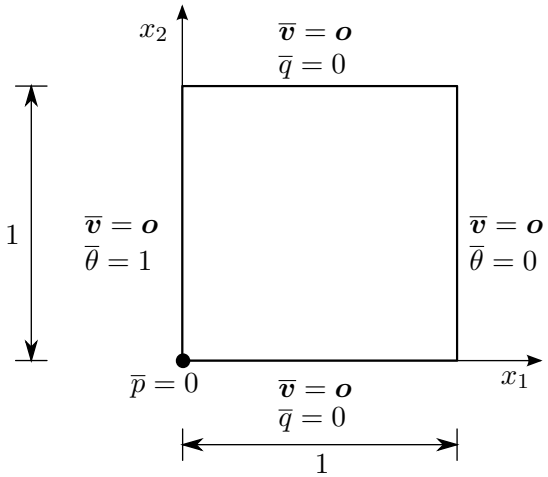

Figure E.1: Geometry and boundary conditions.

Ra	ν	β
10^3	0.71	71
10^4	0.71	710
10^5	0.71	7100

Table E.1: Constants values for the different analyses carried out.

[1]The reader should notice that the data used in this appendix is different than the one employed in section 4.11.6, even if the problem is the same.

x_2 (m)	$Ra = 10^3$			$Ra = 10^4$			$Ra = 10^5$		
	v_1	v_2	θ	v_1	v_2	θ	v_1	v_2	θ
0.00	0	0	1	0	0	1	0	0	1
0.05	0.030	2.001	0.943	0.400	14.100	0.880	0.675	65.910	0.772
0.10	0.094	3.139	0.887	1.054	19.290	0.766	0.525	59.060	0.594
0.15	0.149	3.633	0.832	1.215	18.890	0.667	−2.735	33.430	0.500
0.20	0.182	3.666	0.778	0.912	15.840	0.592	−5.256	13.790	0.471
0.25	0.189	3.375	0.726	0.409	12.050	0.541	−6.133	3.644	0.473
0.30	0.173	2.874	0.677	−0.051	8.605	0.512	−5.735	−0.332	0.481
0.35	0.141	2.240	0.630	−0.334	5.771	0.498	−4.677	−1.355	0.489
0.40	0.098	1.527	0.585	−0.380	3.514	0.494	−3.256	−1.224	0.495
0.45	0.050	0.773	0.542	−0.240	1.659	0.496	−1.664	−0.655	0.498
0.50	0	0	0.5	0	0	0.5	0	0	0.5

(a) Results along the line $x_1 = 0.5$ m.

x_1 (m)	$Ra = 10^3$			$Ra = 10^4$			$Ra = 10^5$		
	v_1	v_2	θ	v_1	v_2	θ	v_1	v_2	θ
1.00	0	0	0.634	0	0	0.784	0	0	0.812
0.95	1.901	0.012	0.635	8.599	−0.146	0.783	19.830	−1.386	0.810
0.90	3.021	0.040	0.635	13.670	−0.441	0.777	31.460	−4.380	0.801
0.85	3.549	0.074	0.632	15.910	−0.681	0.762	34.670	−7.207	0.782
0.80	3.639	0.105	0.624	16.010	−0.809	0.737	31.280	−8.642	0.756
0.75	3.409	0.127	0.612	14.630	−0.839	0.704	24.600	−8.614	0.725
0.70	2.951	0.132	0.596	12.340	−0.786	0.666	17.410	−7.378	0.689
0.65	2.334	0.120	0.575	9.507	−0.663	0.625	11.210	−5.519	0.649
0.60	1.610	0.091	0.552	6.420	−0.483	0.584	6.507	−3.553	0.603
0.55	0.821	0.049	0.526	3.225	−0.255	0.542	2.955	−1.718	0.553
0.50	0	0	0.5	0	0	0.5	0	0	0.5

(b) Results along the line $x_2 = 0.5$ m.

Table E.2: Numerical results of the velocity and temperature reported in Betts and Haroutunian (1983).

x_2 (m)	$Ra = 10^3$			$Ra = 10^4$			$Ra = 10^5$		
	v_1	v_2	θ	v_1	v_2	θ	v_1	v_2	θ
0	0	0	1	0	0	1	0	0	1
0.0625	0.047	2.174	0.929	0.682	14.463	0.851	1.968	58.351	0.729
0.1250	0.124	3.478	0.859	1.117	20.167	0.714	−1.734	55.146	0.528
0.1875	0.182	3.725	0.791	1.271	17.305	0.607	−3.193	22.005	0.456
0.2500	0.187	3.408	0.726	0.527	12.480	0.538	−4.936	5.774	0.450
0.3125	0.171	2.757	0.665	−0.101	8.112	0.503	−6.700	−0.090	0.461
0.3750	0.119	1.917	0.607	−0.351	4.757	0.490	−5.115	−1.309	0.472
0.4375	0.063	0.986	0.553	−0.344	2.189	0.489	−2.830	−0.976	0.478
0.5000	0.000	0.018	0.500	−0.059	0.037	0.495	−0.565	−0.222	0.482
0.5625	−0.064	−0.950	0.447	0.237	−2.097	0.500	1.716	0.572	0.486
0.6250	−0.118	−1.879	0.392	0.284	−4.607	0.500	4.061	1.027	0.492
0.6875	−0.169	−2.717	0.335	0.094	−7.858	0.488	5.788	0.131	0.501
0.7500	−0.185	−3.367	0.274	−0.454	−12.072	0.454	5.030	−4.627	0.511
0.8125	−0.180	−3.686	0.209	−1.140	−16.730	0.387	3.931	−17.979	0.507
0.8750	−0.122	−3.448	0.141	−1.011	−19.558	0.284	2.432	−45.427	0.445
0.9375	−0.046	−2.352	0.071	−0.631	−15.991	0.148	−1.190	−67.250	0.264
1	0	0	0	0	0	0	0	0	0

(a) Results along the line $x_1 = 0.5$ m.

x_1 (m)	$Ra = 10^3$			$Ra = 10^4$			$Ra = 10^5$		
	v_1	v_2	θ	v_1	v_2	θ	v_1	v_2	θ
0	0	0	0.366	0	0	0.215	0	0	0.191
0.0625	−2.239	−0.016	0.365	−10.165	0.231	0.217	−23.010	2.148	0.194
0.1250	−3.337	−0.052	0.366	−15.097	0.512	0.228	−33.832	4.604	0.210
0.1875	−3.638	−0.090	0.374	−16.123	0.829	0.255	−32.655	8.243	0.238
0.2500	−3.395	−0.123	0.388	−14.608	0.754	0.294	−24.715	8.573	0.275
0.3125	−2.798	−0.116	0.409	−11.682	0.797	0.341	−15.713	7.000	0.317
0.3750	−1.974	−0.096	0.436	−8.012	0.574	0.392	−8.587	4.265	0.366
0.4375	−1.018	−0.043	0.467	−4.082	0.349	0.443	−3.848	2.234	0.422
0.5000	0.000	0.018	0.500	−0.059	0.037	0.495	−0.565	−0.222	0.482
0.5625	1.017	0.077	0.532	3.974	−0.273	0.546	2.649	−2.831	0.542
0.6250	1.973	0.128	0.563	7.932	−0.505	0.598	7.355	−5.055	0.596
0.6875	2.798	0.143	0.590	11.645	−0.735	0.648	14.736	−8.089	0.642
0.7500	3.395	0.144	0.611	14.621	−0.709	0.696	24.396	−10.135	0.682
0.8125	3.639	0.103	0.626	16.186	−0.814	0.736	33.138	−9.731	0.718
0.8750	3.337	0.059	0.633	15.196	−0.511	0.763	34.835	−5.500	0.748
0.9375	2.240	0.018	0.634	10.255	−0.236	0.775	23.716	−2.517	0.765
1	0	0	0.633	0	0	0.776	0	0	0.769

(b) Results along the line $x_2 = 0.5$ m.

Table E.3: Numerical results of the velocity and temperature obtained using a 8×8 mesh of $Q2Q1$ elements.

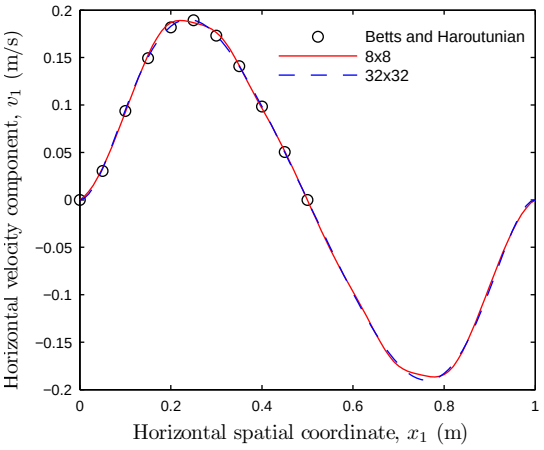

(a) Horizontal velocity along $x_1 = 0.5$.

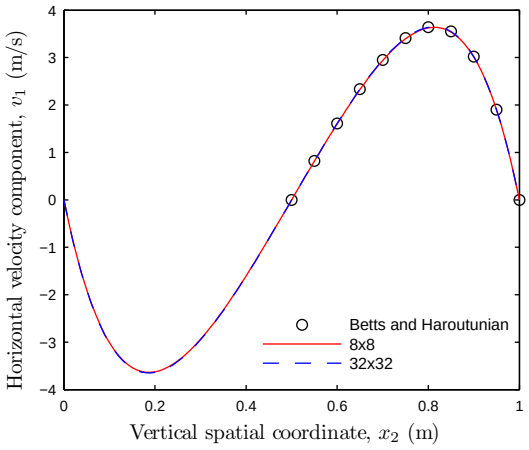

(b) Horizontal velocity along $x_2 = 0.5$.

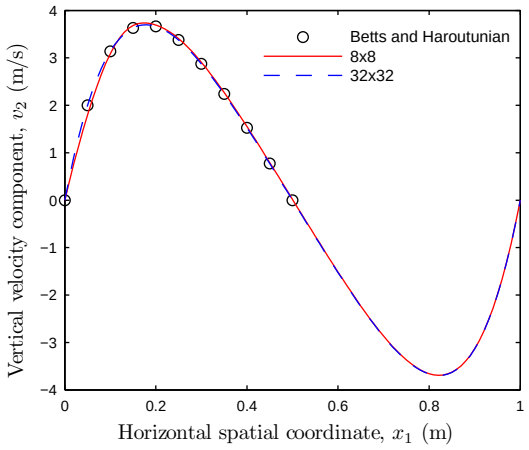

(c) Vertical velocity along $x_1 = 0.5$.

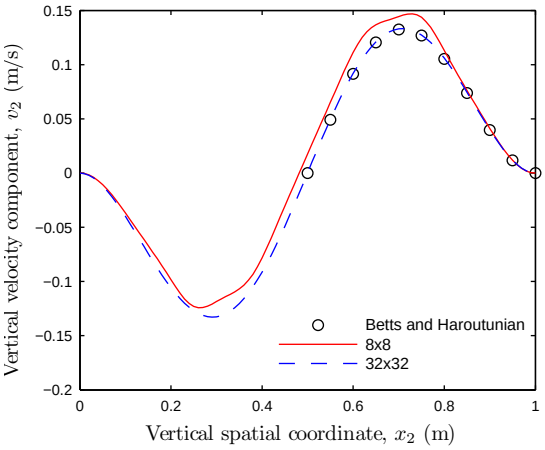

(d) Vertical velocity along $x_2 = 0.5$.

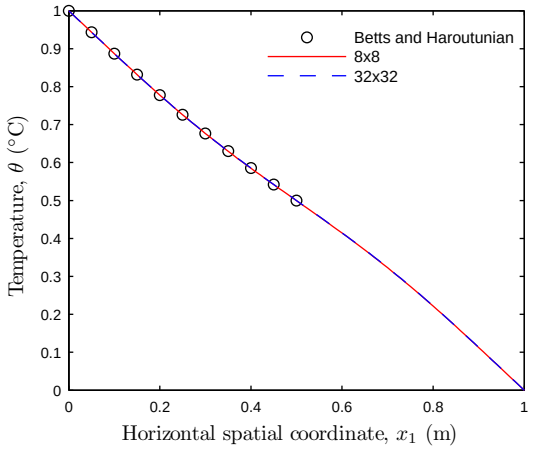

(e) Temperature along $x_1 = 0.5$.

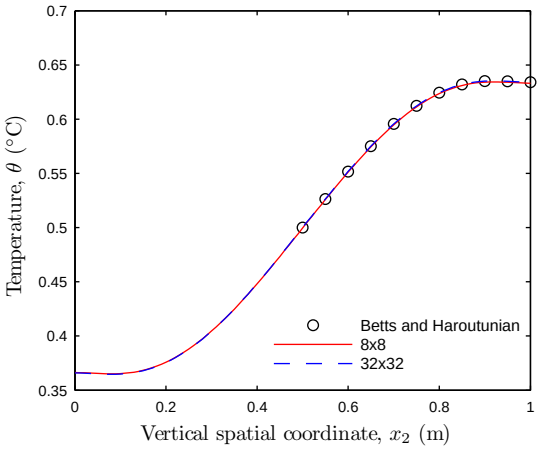

(f) Temperature along $x_2 = 0.5$.

Figure E.2: Numerical results of vertical and horizontal velocities and temperature along the lines $x_1 = 0.5$ and $x_2 = 0.5$ when $Ra = 10^3$.

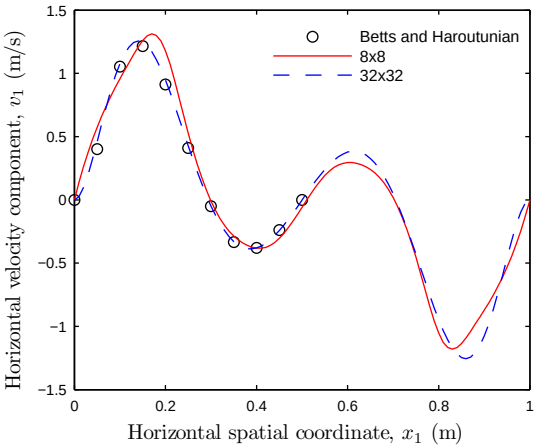

(a) Horizontal velocity along $x_1 = 0.5$.

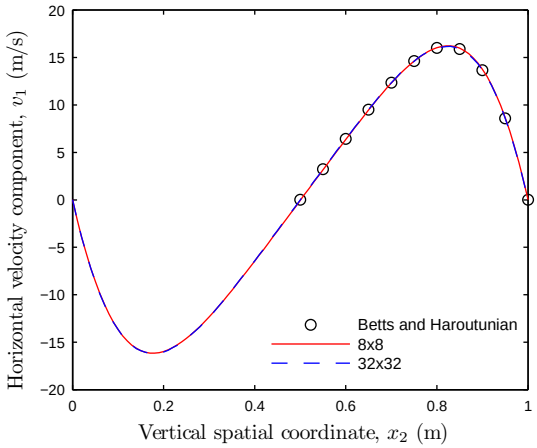

(b) Horizontal velocity along $x_2 = 0.5$.

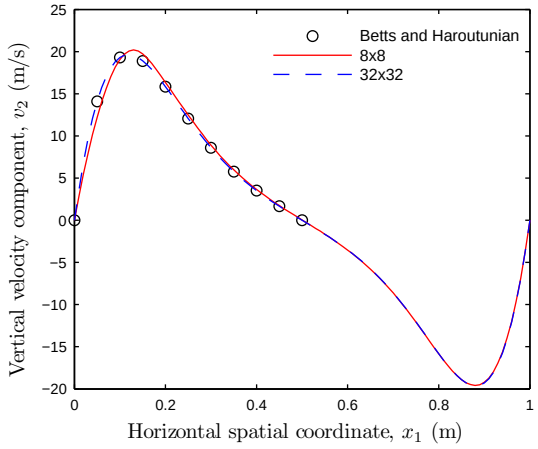

(c) Vertical velocity along $x_1 = 0.5$.

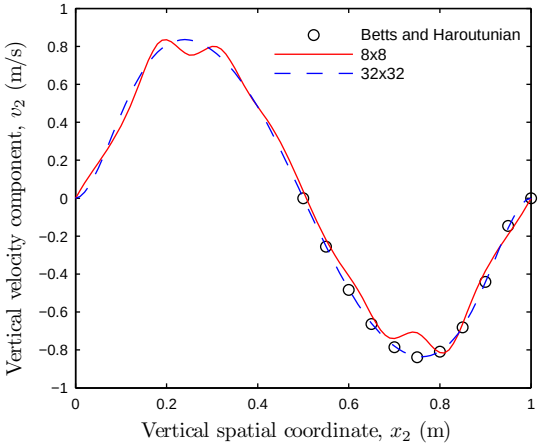

(d) Vertical velocity along $x_2 = 0.5$.

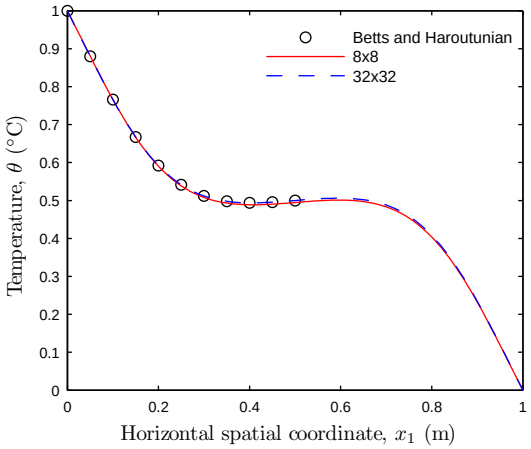

(e) Temperature along $x_1 = 0.5$.

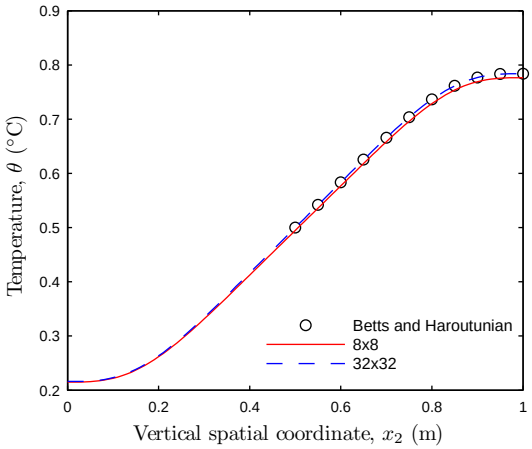

(f) Temperature along $x_2 = 0.5$.

Figure E.3: Numerical results of vertical and horizontal velocities and temperature along the lines $x_1 = 0.5$ and $x_2 = 0.5$ when $Ra = 10^4$.

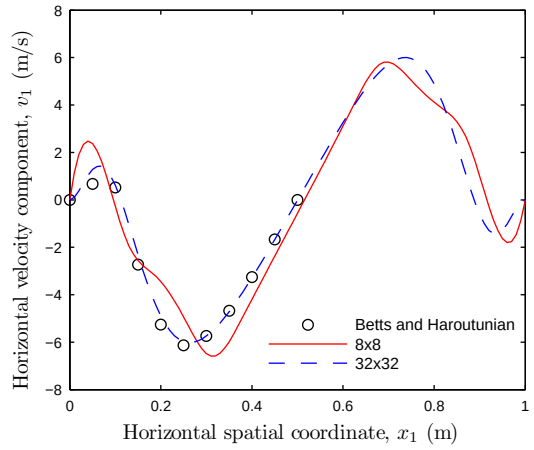

(a) Horizontal velocity along $x_1 = 0.5$.

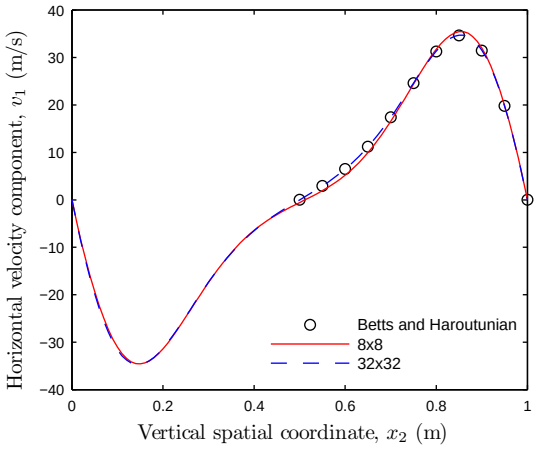

(b) Horizontal velocity along $x_2 = 0.5$.

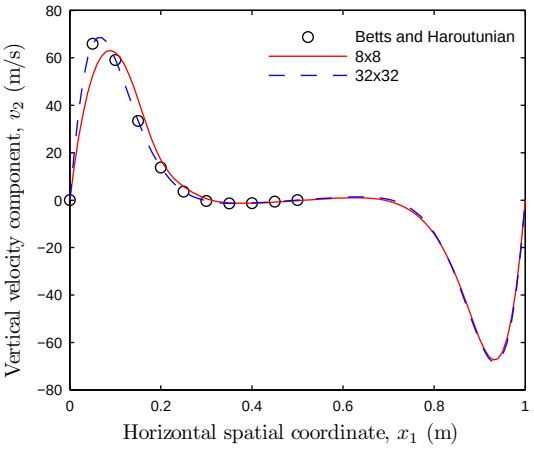

(c) Vertical velocity along $x_1 = 0.5$.

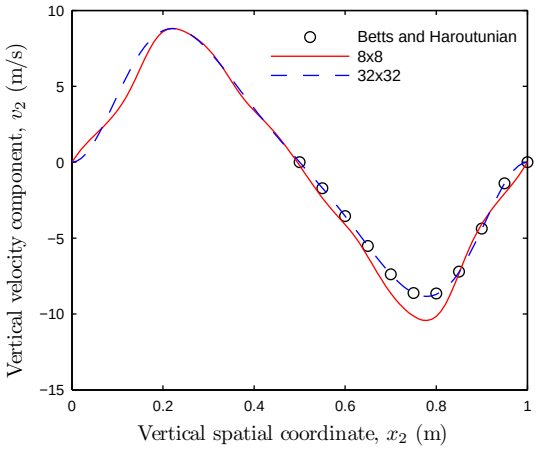

(d) Vertical velocity along $x_2 = 0.5$.

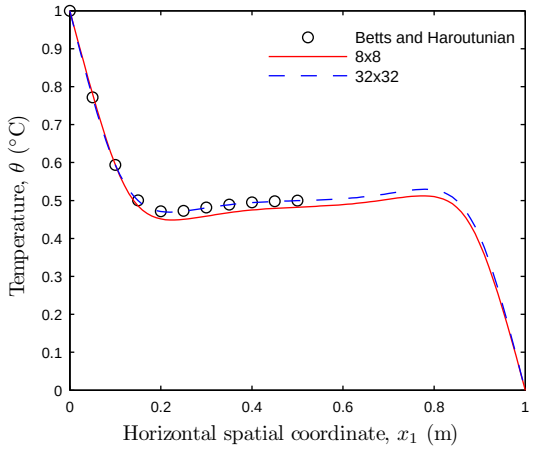

(e) Temperature along $x_1 = 0.5$.

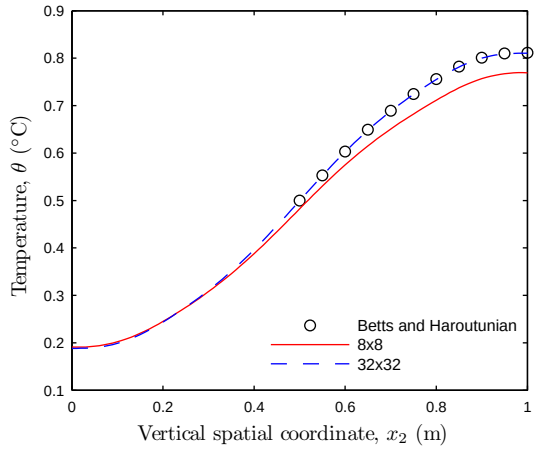

(f) Temperature along $x_2 = 0.5$.

Figure E.4: Numerical results of vertical and horizontal velocities and temperature along the lines $x_1 = 0.5$ and $x_2 = 0.5$ when $Ra = 10^5$.

Appendix F

Complete thermal response of the unprotected tubular profile with the bottom face subjected to fire

This appendix reports the complete thermal response of the unprotected tubular profile subjected to fire in the bottom face. These results were obtained by Paipuri (2016), who implemented the equations reported in the present thesis in FORTRAN, in order to reduce the CPU time required for the calculations. The adaptive time step scheme described in section 5.3.3 was also implemented.

The results were obtained using the boundary conditions reported in section 7.4.2, model (iv) and using the thermo-physical properties of the GFRP evaluated by Tracy (2005).

Figure F.1 depicts the evolution of the time step size as a function of time. The maximum and minimum time step sizes are 66.60486 s and 0.00122 s, respectively.

Figure F.2 illustrates the evolution of the maximum elemental Courant number along the computational time. Two peak values can be identified: (i) at 624.58 s and (ii) at 1005.5 s. Both the peak values are associated to the formation of vortices in the lower corners of the cavity: at 624.58 s the vortices appear and at 1005.5 s the vortices develop

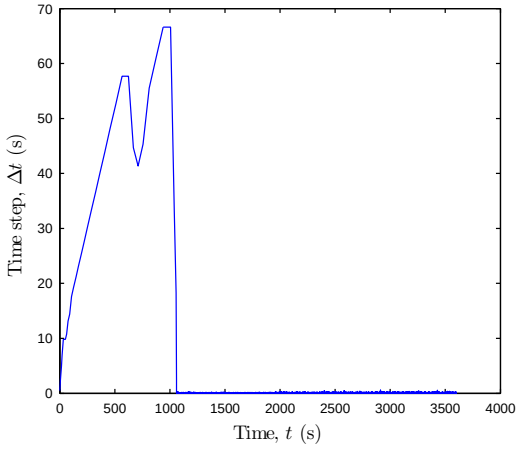

Figure F.1: Variable time step size along time (data from Paipuri, 2016).

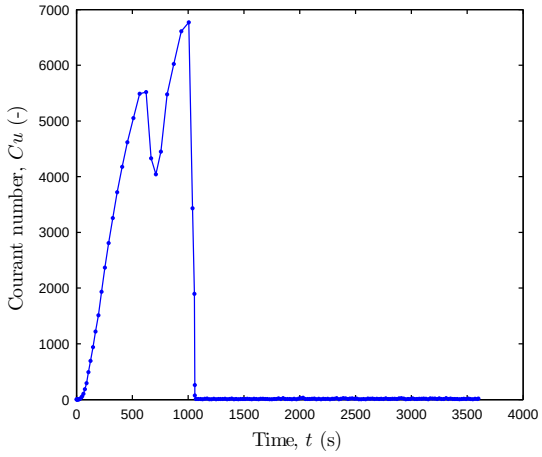

Figure F.2: Courant number evolution along time (data from Paipuri, 2016).

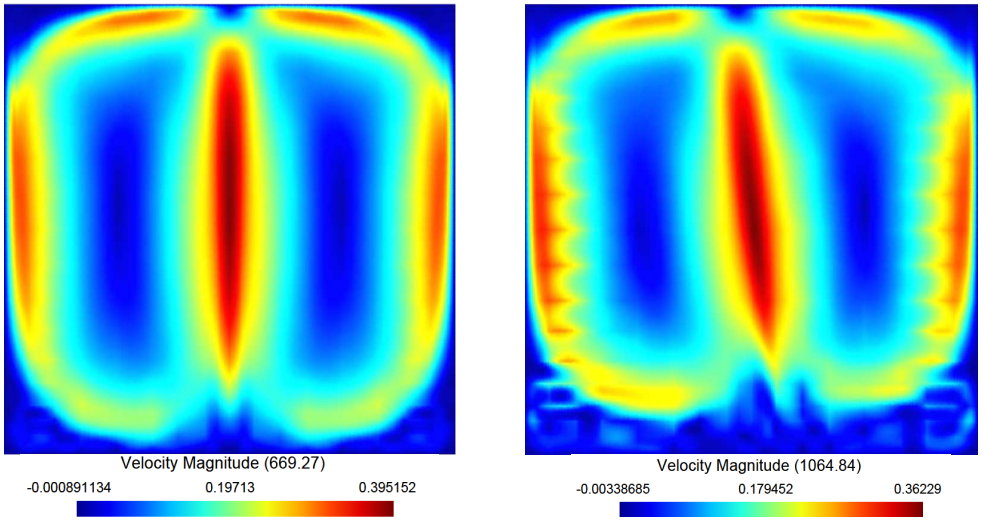

(a) Velocity field at $t = 669$ s.

(b) Velocity field at $t = 1064$ s.

Figure F.3: Velocity field in the cavity (data from Paipuri, 2016).

and the Bénard cells separate from the bottom of the cavity, and the fluid flow loses its symmetry. Figure F.3 depicts the velocity magnitude in the cavity at 669 s and 1064 s, where both phenomena previously stated can be recognized.

After 1005.5 s (the Cu number is 6770.5, this value being the maximum), a sudden reduction of the Cu numbers is observed. This is attributed to the complexity (and high nonlinearity) of the flux in the cavity, which starts being asymmetric. The minimum Cu number calculated after this time is approximately 4.739. Figure F.4 shows the velocity field at 3600 s.

The results depicted in figures F.6b and F.4 indicate that the mesh employed is too coarse to represent accurately (and continuously) the velocity magnitude, the mesh being visible in the results. This is relevant in the vicinities of the walls of the cavity, where elevated velocity gradients are expected.

By comparing figure F.1 and figure F.2, the influence of the time step size in the Cu

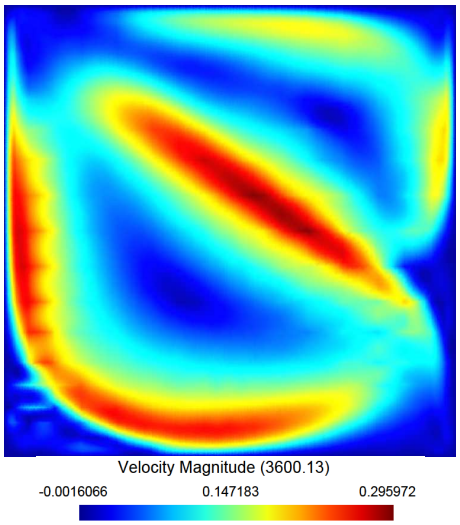

Figure F.4: Velocity field at $t = 3600$ s (data from Paipuri, 2016).

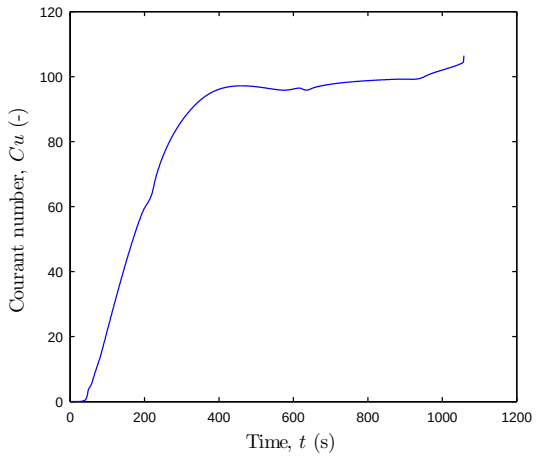

Figure F.5: Courant number evolution along time.

number can be clearly observed, as both the graphics present almost the same shape.

Figure F.5 depicts the evolution of the maximum elemental Courant number along the time, when a constant time step equal to 1 s is considered (the description of the analysis can be consulted in section 7.5.2). Between 0 and 400 s, the Cu number increases from 0 to 100. For these initial computational times, higher time step sizes could be employed, as the Cu number remains relatively low. After 400 s and until 1000 s, the Cu number is approximately equal to 100 for all the time steps. This Cu number is high, but the algorithm implemented is still able to evaluate a converged solution. After 1000 s, the Cu number continues increasing, attaining a value of 106 at the last time step computed. After this instant, the algorithm implemented requires a smaller time step size in order to compute a converged solution.

The Courant numbers obtained when using a constant time step and a variable time step are significantly different, as the Cu numbers obtained with the time step variable are the maximum Cu numbers that can be used to obtain a converged solution.

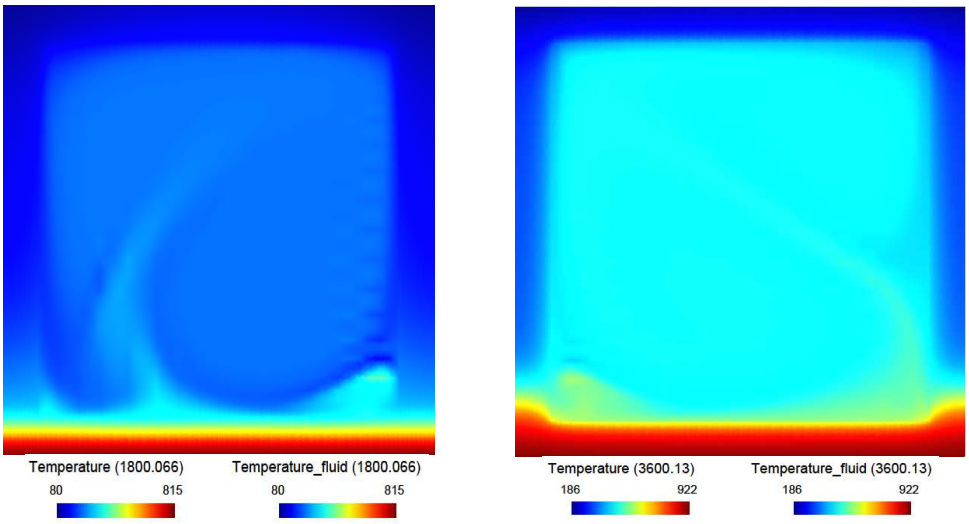

(a) Temperature field at $t = 1800$ s. (b) temperature field at $t = 3600$ s.

Figure F.6: Temperature field in the squared tubular cross section (data from Paipuri, 2016).

The complete thermal response was also obtained by Paipuri (2016). Figure F.7 shows the temperature field in the solid and fluid domain at 1800 s and 3600 s. Figure F.7 depicts the numerical and experimental temperatures obtained along the time in the seven thermocouples installed in the cross section.

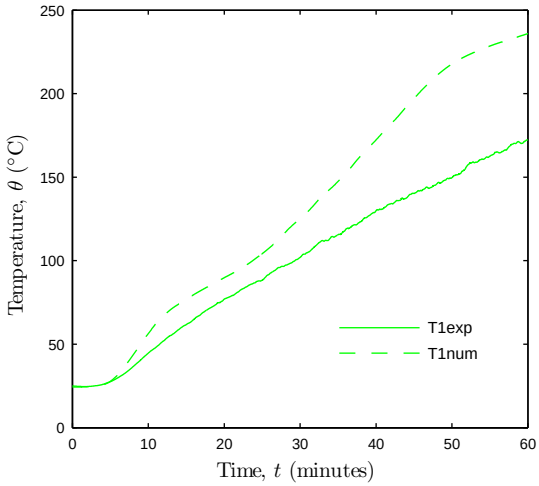

(a) Thermocouple T1.

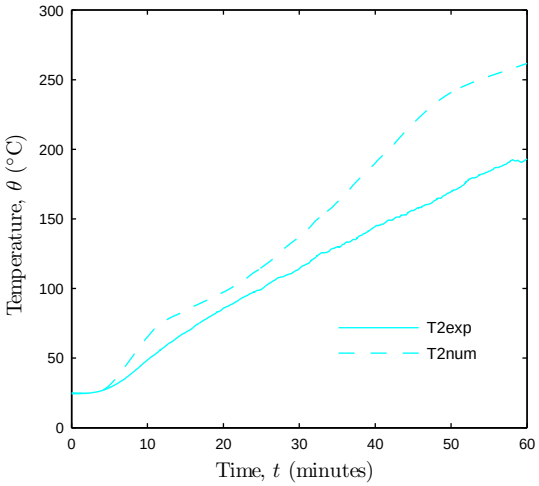

(b) Thermocouple T2.

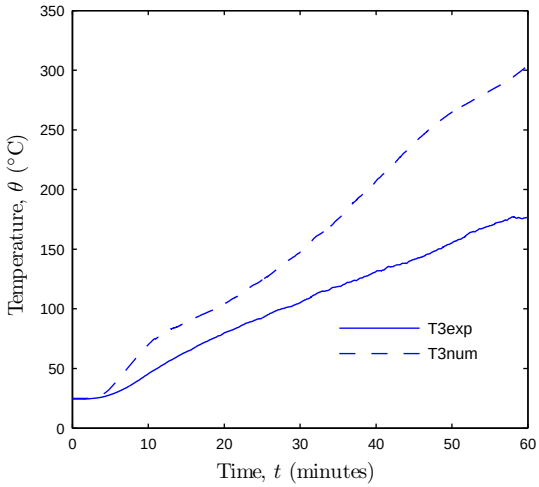

(c) Thermocouple T3.

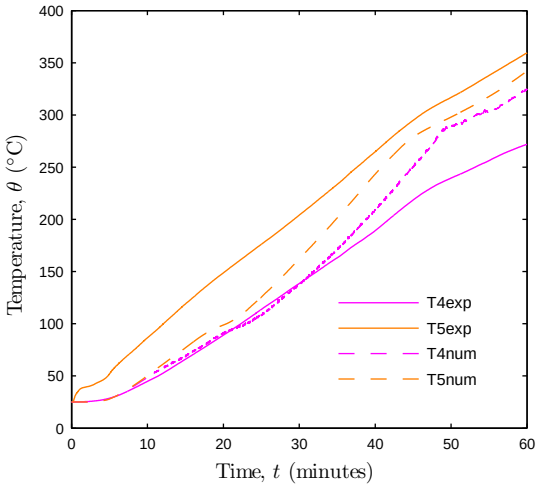

(d) Thermocouples T4 and T5.

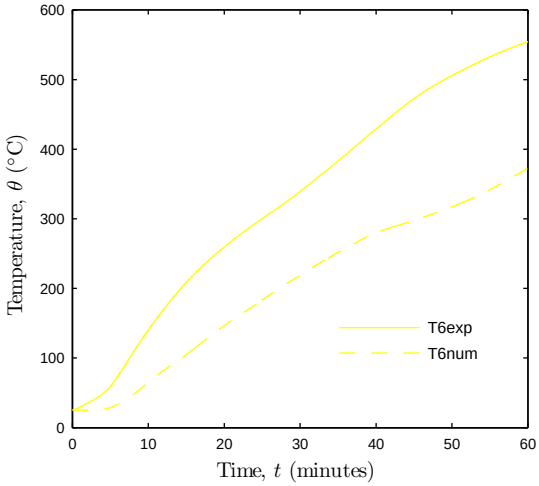

(e) Thermocouple T6.

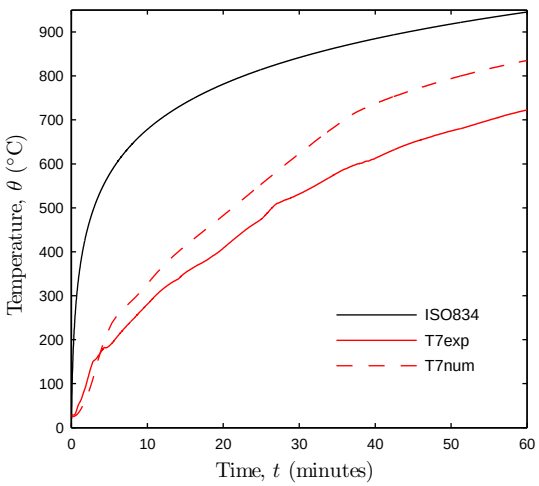

(f) Thermocouple T7.

Figure F.7: Experimental and numerical temperatures in the unprotected tubular cross section with 1-face exposure (data from Paipuri, 2016).

Appendix G

Modelling of the tubular protected profile with the bottom face subjected to fire

In the present appendix, the numerical results obtained in the simulation of the thermal behaviour of a protected tubular GFRP profile subjected to fire in the bottom face is presented. In the simulation, the bottom and top faces are modelled as being subjected to a radiative and convective heat transfer with the ambient, the lateral faces are modelled as insulated and, in the cavity, only radiative exchange between the faces is considered. The boundary conditions defined are schematized in figure G.1. The mesh used is that presented in 7.34 in section 7.5.4.

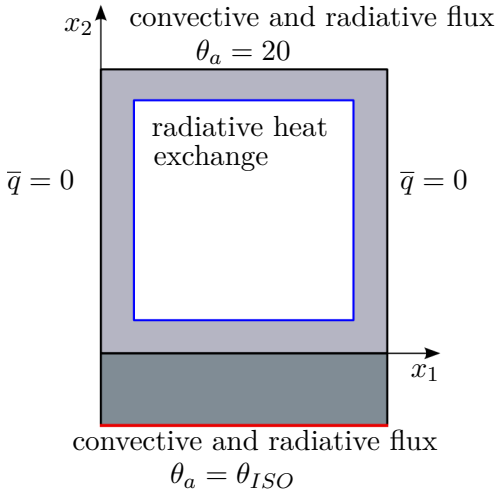

Figure G.1: Thermal boundary conditions prescribed in the protected GFRP cross section, with the bottom face subjected to fire.

A nonlinear transient analysis was carried out with a time step of 10 s. The results obtained are depicted in figure G.2. It can be observed that the numerical results are lower than the experimental ones in all the thermocouples, the relative difference between them being very high. Consequently, the model presented does not reproduce correctly the thermal behaviour of the protected tubular profile subjected to fire in the bottom

face. This conclusion points out the necessity of considering simultaneously the radiative exchange and the natural convection in the cavity.

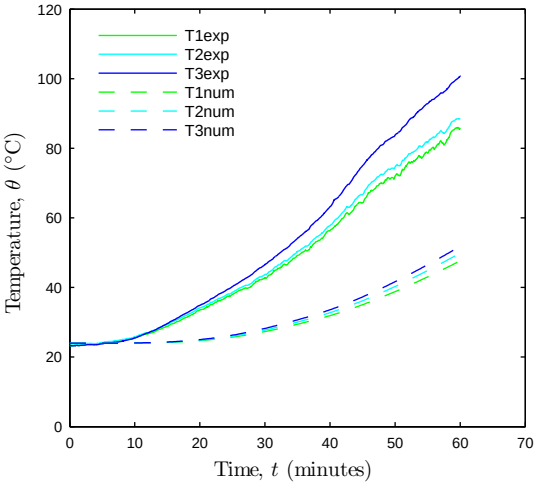

(a) Top flange.

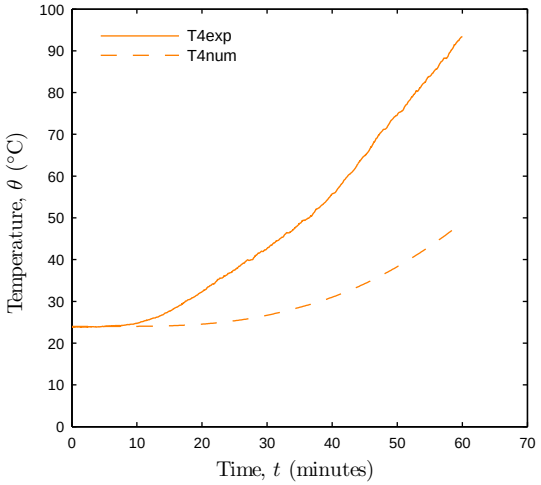

(b) Web.

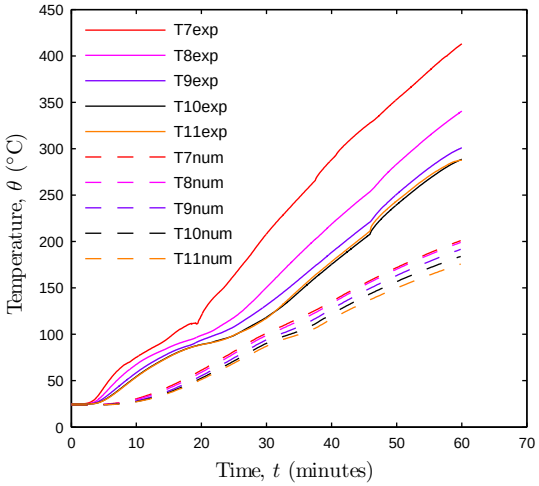

(c) Bottom flange.

Figure G.2: Tubular protected cross section with 1-face exposure when only radiative heat transfer in the cavity is considered.

Appendix H

Numerical results of the thermomechanical simulation of columns

The mechanical performance of the protected tubular and unprotected/protected I-section columns, all exposed to fire in 3-faces, are displayed in figures H.1, H.2 and H.3, respectively.

The experimental results presented in figure H.1 indicate that the column presents a positive variation of the vertical deflection at midspan and axial shortening during all the test.

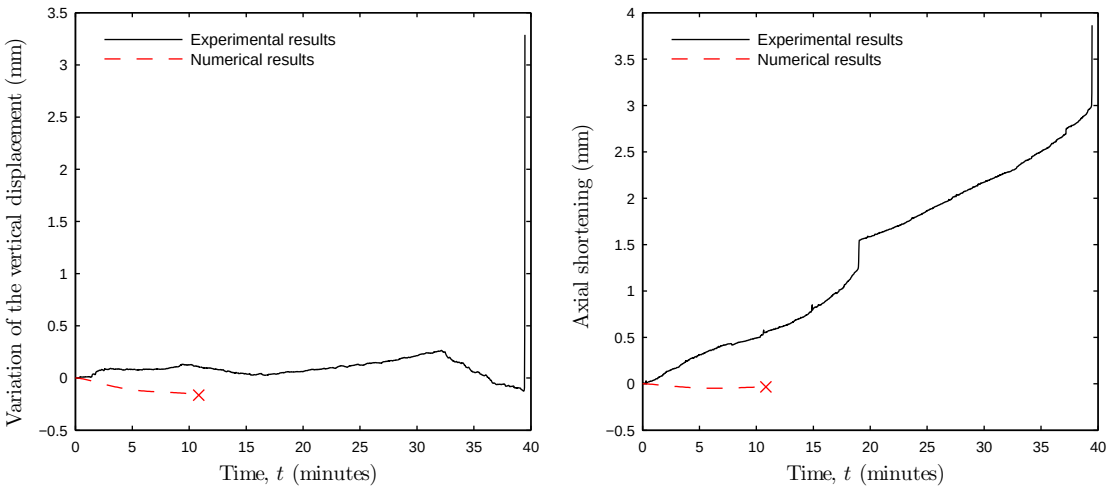

(a) Variation of the vertical displacement.

(b) Variation of the axial shortening.

Figure H.1: Protected tubular column subjected to fire in 3-faces (55 kN).

The variation of the central section vertical deflection observed in the test has very low magnitude and presents a non-monotonic trend. The numerical results obtained were only able to simulate the mechanical behaviour of the column during the first 10 minutes. During this period, the variation of the vertical deflection at the central section is negative and the axial shortening is positive, but both are lower than the results measured

experimentally, particularly the axial shortening.

The structural response of the GFRP I-section column subjected to fire in 3-faces is illustrated in figure H.2. The experimental results indicate that the column suffers a negative variation of the vertical displacement in the central section and a minor axial shortening (the maximum value measured was −0.5 mm). These results are difficult to interpret as the duration of the test was very short. Numerically, the column develops a negative variation of the vertical displacement and a slight expansion due to the temperature increase (negative shortening), during the initial instants. Subsequently, the variation of the vertical displacement augments progressively until attaining positive values. For the axial shortening, the same effect can be observed, with the initial expansion changing to contraction.

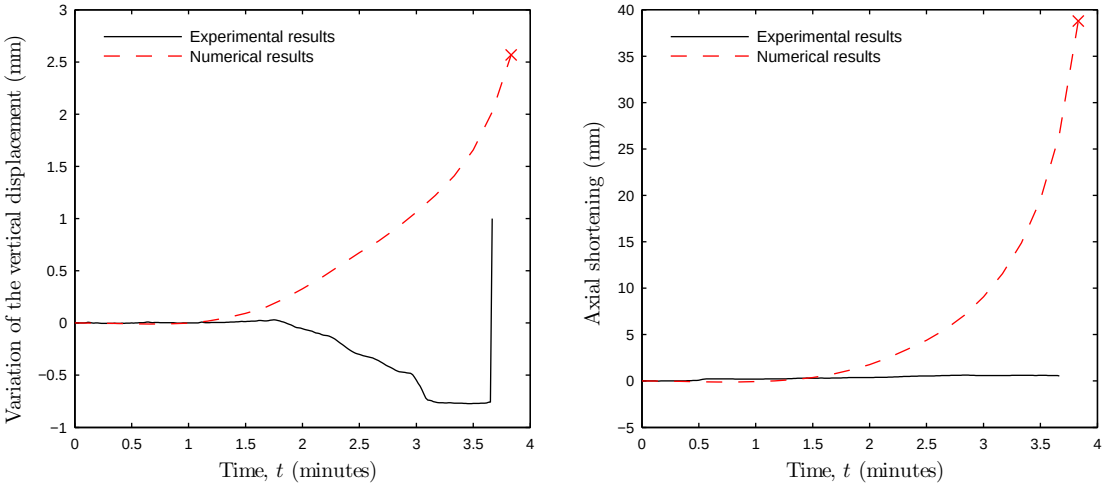

(a) Variation of the vertical displacement. (b) Variation of the axial shortening.

Figure H.2: Unprotected I column subjected to fire in 3-faces (25 kN).

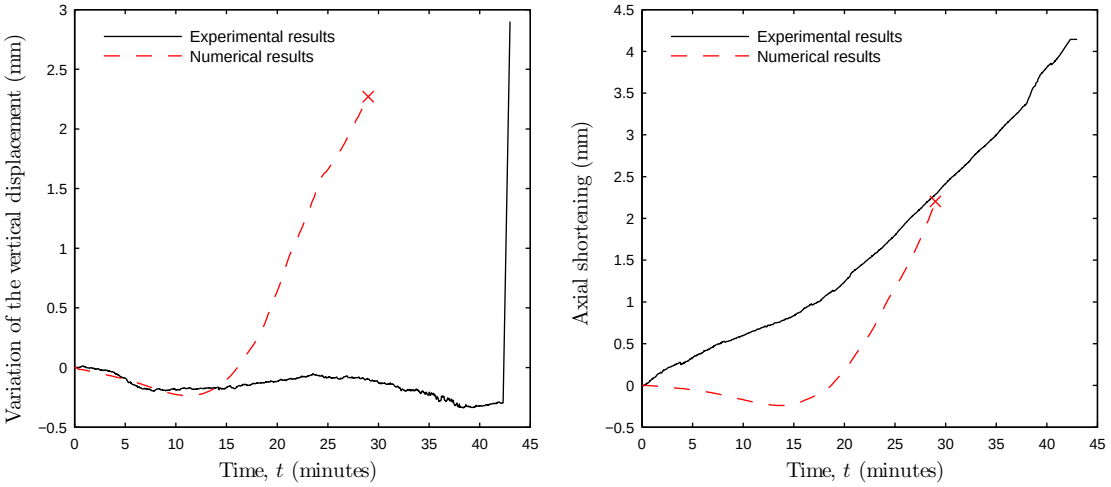

(a) Variation of the vertical displacement. (b) Variation of the axial shortening.

Figure H.3: Protected I column subjected to fire in 3-faces (25 kN).

Figure H.3 displays the numerical and experimental results obtained for the protected GFRP I-column exposed to fire in 3-faces. The experimental data reflect an axial shortening of the column (almost linear up to failure) with little variation of the vertical displacement. The numerical simulation shows a different behaviour of the column, with the variation of the vertical displacement being negative until approximately 13 minutes and positive afterwards.